SCUOLA NORMALE SUPERIORE

PHD THESIS

Development of computational methods for the simulation of vibrational and electronic spectra of medium-to-large sized molecular systems

Author:
Alberto BAIARDI

Supervisor:
Vincenzo BARONE
Julien BLOINO

A thesis submitted in fulfillment of the requirements for the degree of Doctor of Philosophy

in

Methods and models for molecular sciences

SCUOLA NORMALE SUPERIORE

Abstract

Classe di Scienze

Doctor of Philosophy

Development of computational methods for the simulation of vibrational and electronic spectra of medium-to-large sized molecular systems

by Alberto BAIARDI

Computational spectroscopy has become in the recent years an essential tool for the interpretation of experimental spectra. Thanks to the development of electronic structure methods of increasing accuracy and more efficient algorithms coupled with even more powerful hardware, energies and properties of ground and excited electronic states can be computed accurately also for medium- and large-size systems. In most cases, data arising from purely electronic structure calculations are not sufficient and the inclusion of nuclear effects is crucial to be comparable to experimental data. Hence, in order to achieve the accuracy needed to support laboratory results, theoretical models for the description of nuclear effects need to be developed. The main goal of this research project has been the development of efficient algorithms for the inclusion of those effects on vibrational and vibro-electronic (vibronic) processes for medium-sized systems, which may exhibit some flexibility, targeting molecules of several dozens of atoms. The first part of this thesis focuses on the development of theoretical models for the inclusion of anharmonic effects in spectroscopies involving a single electronic state (i.e. vibrational spectroscopies). The main feature of this framework is the use of curvilinear internal coordinates for the description of molecular vibrations. In fact, an accurate choice of the internal coordinates set allows a significant reduction of the couplings between different modes, enabling the development of multi-scale schemes, where different modes are treated at different levels of accuracy. Based on this idea, an hybrid variational-harmonic scheme has been proposed, where anharmonic effects are included for a single degree of freedom, whereas the other modes are treated as harmonic. The model extends the Reaction Path Hamiltonian (RPH) theory to the use of a general set of curvilinear coordinates, and is effective for systems displaying some limited flexibility, where most of the anharmonicity is concentrated on a single degree of freedom. However, for more complex systems, the definition of a single coordinate to treat as anharmonic is not possible, and variational approaches including multiple degrees of freedom are necessary.

However, the computational cost associated to standard variational methods grows exponentially with the size of the system, thus algorithms for solving efficiently the vibrational Schrödinger equation need to be devised. In the present thesis, the first formulation of the Density Matrix Renormalization Group (DMRG), a theory normally applied to electronic structure problems, for vibrational structure problems is presented. Particular care has been paid during its development to support advanced diagonalization schemes to target directly excited states, using stochastic algorithms to characterize the resulting vibrational wavefunctions. The second part of this thesis is a generalization of the internal coordinates-based framework presented in the previous section to electronic transitions. Unlike vibrational spectroscopy, the difference between Cartesian and internal coordinates appears already at the harmonic level in vibronic spectroscopy and not at the anharmonic level, since multiple electronic states are treated simultaneously with the same coordinates system. The main advantage of using internal coordinates is a strong reduction of mode couplings, leading to much more accurate results for flexible systems, undergoing significant structural changes upon electronic excitation. Within this framework, based on internal coordinates, general time-independent (TI) and time-dependent (TD) approaches are presented and applied to the actual calculation of vibronic spectra. As a first step, the TD approach is applied to the calculation of spectra and rates related to radiative processes, both for absorption and emission. Then, the formalism is generalized to the calculation of rates of different non-radiative processes, such as inter-system crossing (ISC) internal conversion (IC) and electronic energy transfer (EET). For each case, the impact of the choice of the coordinates on the results is discussed and illustrated. Finally, the TD framework is extended to the calculation of resonance Raman (RR) and resonance Raman optical activity (RROA) spectra, where the intensity of these vibrational spectroscopies depends directly on vibronic effects. The internal coordinates-based harmonic framework is not sufficient to treat cases where large-amplitude modes (LAMs) have a strong impact on the experimental observable, due to their strong anharmonicity, and an higher level of theory is required to get exploitable results. To increase the reliability of such simulations also in those cases, the hybrid anharmonic-harmonic scheme validated for vibrational spectroscopies has been generalized to vibronic transition energies and properties. This has been done by keeping the framework as general as possible, therefore supporting all vibronic models already available for the harmonic case. The last part of this thesis focuses on the application of the theoretical models introduced in the preceding sections to core-spectroscopies, namely near-edge X-ray absorption spectroscopy (NEXAFS) and X-ray photoelectron spectroscopies (XPS). Even if the resolution of NEXAFS and XPS spectra is usually lower than their valence counterpart. The accuracy of experimental spectra has been quickly increasing, thanks to the increasing power of synchrotron light sources, and the inclusion of vibronic

effects has become crucial to match those advances. For NEXAFS, the different vibronic models have been applied to the simulation of the spectra of different pyridine derivatives, employing electronic structure calculations carried out at the transition state density functional theory (TS-DFT) level. For XPS, Green Function-based (GF) techniques are employed to compute ionization energies. However, for core ionization, high-order GF approaches are needed to obtain reliable results, and their computational cost makes them not affordable for large-size systems. To increase the efficiency of the simulation, a new GF-based approach is presented, which is based on the use of the orbitals arising from a grand-canonical calculation to compute the one-particle Green function. As is proven with several test cases, the use of those orbitals leads to accurate results already with a second-order approximation of the GF, therefore with a limited computational cost.

Acknowledgements

First of all, I would like to thank my PhD thesis advisor, Prof. Vincenzo Barone, who guided me in the world of scientific research with constant enthusiasm. From when I was an undergraduate, he has always be ready and willing to support my work and to share his wealth of knowledge and experience. I am also deeply in debt with Dr. Julien Bloino. His door office was always open whenever I was in trouble or had a question about my research project. Without their constant support from the beginning of my work to the writing of the thesis, this PhD project would not have been possible.
The members of my group have contributed to my personal and professional development. They have been a source of friendships as well as good advice and collaboration. First of all I would like to acknowledge the other people of my research group who were involved in the development of some of the research reported in the thesis. Hence, my thanks go to Franco, Marco F. and Marco M., Shiladitya and Lorenzo. Last but not least, I really want to thank Goska, or better Prof. Malgorzata Biczysko at the University of Shanghai.
I would like to acknowledge also Prof. Mauro Stener, Prof. Giovanna Fronzoni and Gustavo Adolfo Cardenas Jimenez from the University of Trieste, Prof. Ugo Cosentino, Dr. Claudio Greco and Damiano Gerosa from the University of Milano Bicocca for the fruitful collaborations that has enabled me to apply the models I have developed throughout this thesis to "real life" chemical systems.
An important part of my work is the output of fruitful periods I have spent abroad in collaborations with foreign universities. In this respect, I am grateful to Prof. Vincent Ortiz and Dr. Viatcheslav V. Zakjevskii for the kindness with which they received in their group at the University of Auburn, and for letting me live my first "true" american experience.
Lastly, it is a pleasure to acknowledge Prof. Dr. Markus Reiher for offering me the opportunity to work in his group, and to Christopher Stein, for his constant support during my stay in Zürich.

Contents

List of Figures

List of Tables

List of publications

- M.H. Palmer, M. Coreno, M. de Simone, S.V. Hoffmann, N.C. Jones, C. Grazioli, K.A. Peterson, A. Baiardi, T. Zhang, M. Biczysko, *A combined theoretical and experimental study of the ionic states of iodopentafluorobenzene*, J. Chem. Phys., **2017**, *146*, 084302

- A. Baiardi, C.J. Stein, V. Barone, M. Reiher, *Vibrational Density Matrix Renormalization Group*, J. Chem. Theo. Comput., **2017**, *13*, 3764

- M.H. Palmer, S.V. Hoffmann, N.C. Jones, M. Coreno, M. de Simone, C. Grazioli, K.A. Peterson, A. Baiardi, T. Zhang, M. Biczysko, *A combined theoretical and experimental study of the valence and Rydberg states of iodopentafluorobenzene*, J. Chem. Phys., **2017**, *146*, 174301

- A. Baiardi, L. Paoloni, V. Barone, V.G. Zakrzewski, J.V. Ortiz, *Assessment of electron propagator methods for the simulation of vibrationally-resolved valence and core photoionization spectra*, J. Chem. Theo. Comput., **2017**, *13*, 3120

- F. Egidi, D.B. Williams-Young, A. Baiardi, J. Bloino, G. Scalmani, M.J. Frisch, X. Li, V. Barone, *Effective Inclusion of Mechanical and Electrical Anharmonicity in Excited Electronic States: VPT2-TDDFT Route*, J. Chem. Theo. Comput., **2017**, *13*, 2789

- A. Baiardi, J. Bloino, V. Barone, *Simulation of vibronic spectra of flexible systems: hybrid DVR-harmonic approaches*, J. Chem. Theo. Comput., **2017**, *13*, 2804

- C. Puzzarini, A. Baiardi, J. Bloino, V. Barone, T.E. Murphy, H.D. Drew, A. Ali, *Spectroscopic Characterization of Key Aromatic and Heterocyclic Molecules: A Route toward the Origin of Life*, The Astronomical Journal, **2017**, *154*, 82

- M.H. Palmer, M. Biczysko, A. Baiardi, M. Coreno, M. De Simone, C. Grazioli, S.V. Hoffmann, N.C. Jones, K.A. Peterson, *The ionic states of difluoromethane: A reappraisal of the low energy photoelectron spectrum including ab initio configuration interaction computations*, J. Chem. Phys., **2017**, *147*, 074305

- U. Cosentino, C. Greco, D. Pitea, S. Binetti, A. Le Donne, G. Moro, A. Baiardi *Theoretical and experimental investigation of UV–Vis absorption spectrum in a Eu(3+) based complex for luminescent downshifting applications*, Theo. Chem. Acc., **2017**, *136*, 117

- J. Bloino, A. Baiardi, M. Biczysko, *Aiming at an accurate prediction of vibrational and electronic spectra for medium-to-large molecules: An overview*, Int. J. Quantum. Chem., **2016**, *116*, 1543

- S. Banerjee, A. Baiardi, J. Bloino, V. Barone, *Vibronic effects on rates of excitation energy transfer and their temperature dependence*, J. Chem. Theo. Comput., **2016**, *12*, 2357

- M.H. Palmer, T. Ridley, S.V. Hoffmann, N.C. Jones, M. Coreno, M. de Simone, C. Grazioli, T. Zhang, M.Biczysko, A. Baiardi, K.A. Peterson, *Combined theoretical and experimental study of the valence, Rydberg and ionic states of chlorobenzene*, J. Chem. Phys., **2016**, *144*, 124302

- A. Baiardi, J. Bloino, V. Barone, *General formulation of vibronic spectroscopy in internal coordinates*, J. Chem. Phys., **2016**, *144*, 084114

- S. Banerjee, A. Baiardi, J. Bloino, V. Barone, *Temperature dependence of radiative and non-radiative rates from time-dependent correlation function methods*, J. Chem. Theo. Comput., **2016**, *12*, 774

- M.H. Palmer, T. Ridley, S.V. Hoffmann, N.C. Jones, M. Coreno, M. de Simone, C. Grazioli, T. Zhang, M. Biczysko, A. Baiardi, K.A. Peterson, *Combined theoretical and experimental study of the valence, Rydberg and ionic states of fluorobenzene*, J. Chem. Phys., **2016**, *144*, 204305

- D. Licari, A. Baiardi, M. Biczysko, F. Egidi, C. Latouche, V. Barone, *Implementation of a graphical user interface for the multifrequency virtual spectrometer: the VMS-draw tool*, J. Comput. Chem., **2015**, *36*, 321

- C. Latouche, A. Baiardi, V. Barone, *Virtual Eyes Designed for Quantitative Spectroscopy of Inorganic Complexes: Vibronic Signatures in the Phosphorescence Spectra of Terpyridine Derivatives*, J. Phys. Chem. B, **2015**, *119*, 7235

- M.H. Palmer, T. Ridley, S.V. Hoffmann, N.C. Jones, M. Coreno, M. de Simone, C. Grazioli, M. Biczysko, A. Baiardi, *Interpretation of the vacuum ultaviolet photoabsorption spectrum of iodobenzene by ab initio computations*, J. Chem. Phys., **2015**, *142*, 134302

- M.H. Palmer, T. Ridley, S.V. Hoffmann, N.C. Jones, M. Coreno, M. de Simone, C. Grazioli, M. Biczysko, A. Baiardi, *The ionic states of iodobenzene studied by photoionization and ab initio configuration interaction and DFT computations*, J. Chem. Phys., **2015**, *142*, 134301

- A. Baiardi, J. Bloino, V. Barone, *Accurate simulation of Resonance Raman spectra of flexible molecules: an internal coordinates approach*, J. Chem. Theo. Comput., **2015**, *11*, 3267

- A. Baiardi, M. Mendolicchio, V. Barone, G. Fronzoni, G.A. Cardenas Jimenez, M. Stener, C. Grazioli, M. de Simone, M. Coreno *Vibrationally resolved NEXAFS at C and N K-edges of pyridine, 2-fluoropyridine and 2,6-difluoropyridine: A combined experimental and theoretical assessment*, J. Chem. Phys., **2015**, *103*, 204102

- M.H. Palmer, T. Ridley, S.V. Hoffmann, N.C. Jones, M. Coreno, M. de Simone, C. Grazioli, T. Zhang, M. Biczysko, A. Baiardi, *Interpretation of*

the photoelectron, ultraviolet and vacuum ultraviolet photoabsorption spectra of bromobenzene by ab initio configuration interaction and DFT computations, J. Chem. Phys., **2015**, *143*, 164303

- A. Baiardi, J. Bloino, V. Barone, *A general time-dependent route to Resonance-Raman spectroscopy including Franck-Condon, Herzberg-Teller and Duschinsky effects*, J. Chem. Phys., **2014**, *141*, 114108

Chapter 1

Introduction

Molecular spectroscopy is nowadays routinely used for the characterization of molecular systems, and is currently an active field of research in chemistry, both from a theoretical and an experimental point of view.[1,2,3] In all spectroscopic techniques, the molecular system under investigation is exposed to an electromagnetic radiation and, from the response of the molecule to the interaction with the light, information on the molecular system are derived. In the last decades, a wide range of spectroscopic techniques have been developed, whose systematic classification is far from being straightforward. The most natural classification is based on the energy of the radiation, which determines the class of molecular transitions which are excited.
The spectroscopic techniques using the lowest-energy radiation are nuclear magnetic resonance (NMR) and electronic paramagnetic resonance (EPR), in which radiowaves (with a frequency of the order of magnitude of approximately 1 MHz) are employed.[4,5,6,7] In both cases, transitions between different spin states are studied, associated to nuclei for NMR and to electrons for EPR. Transition energies between different spin states of a given nucleus are strongly influenced by the other nuclei surrounding it, thus NMR is widely used as a tool for the structural characterization of molecular systems. Similarly, transition energies between different spin states of an electron are determined by its electronic environment, so EPR is used as a probe of the electronic density. The main limitations of these techniques is that, at least under standard conditions, spin states are often degenerate, and high-intensity magnetic fields must be employed to induce measurable splittings between them.
Another class of techniques, which is widely employed as a tool for the structural characterization of molecular systems, is rotational spectroscopy,[8,9] employing radiations in the microwave (MW) region (with frequencies of the order of magnitude of $\approx$ 1GHz, thus about 10^3 times higher than for NMR and EPR), which excite transitions between different levels associated to the overall rotation of the molecule. Thanks to its high-resolution, rotational spectroscopy is the election tool for the characterization of molecular systems in the gas phase. In recent years, this technique has been widely applied in the field of astrochemistry:[10,11,12] several hundreds of inorganic and organic compounds were identified from the analysis of the MW region of the radiation arising from the interstellar medium (ISM). From a computational point of view, to match the high-accuracy of rotational spectra, parallel highly-accurate quantum mechanical (QM) simulations are needed.[13,14]

In this connection, semi-experimental (SE) approaches, where experimental data obtained from MW spectroscopy are combined with QM calculations are receiving growing attention in recent years due to their effectiveness in determining highly-accurate molecular structures.[15,16]
The present thesis focuses on the development of theoretical models for the simulation of vibrational effects on molecular spectra. The average energy of a vibrational state lies in the infrared (IR) region (*i.e.* with an energy approximately between 10^2 and 10^4 cm^{-1}), thus above the energies involved in the techniques outlined above, which were outside the research activity presented in the following. Spectroscopic techniques based on transitions between vibrational states are referred to, in broad terms, as vibrational spectroscopies,[17,18,19] the most standard one being IR absorption. Vibrational spectroscopies are the methods of choice for the study of dynamical aspects, since they directly probe the motion of the nuclei. For example, specific functional groups display characteristic absorption patterns in an IR spectrum, strongly localized in a narrow specific energy range, which depends on the functional group and is only weakly tuned by its chemical environment. The position of these bands is often used to follow the nuclear dynamics of a molecular system. This is the case for instance of the CO stretching mode, whose absorption band lies between 1400 and 1700 cm^{-1} and is widely used to track conformational changes both in inorganic and organic compounds.[20,21] From a computational point of view, the simulation of IR spectra poses several challenges. The nuclear motion is determined by the potential energy generated by the electrons, better known as potential energy surface (PES), which can be obtained from electronic structure calculations (ESCs).[22,23,24] If molecular vibrations are simulated using simplified models, the output of ESCs are sufficient to simulate vibrational spectra. For example, it is well-known that the simulation of a vibrational spectrum at the harmonic level is possible directly from the harmonic frequencies of the electronic state of interest, together with the derivatives of the dipole moment. However, harmonic models cannot be used to simulate accurate IR spectra. In fact, a "true" one-dimensional PES is never equivalent to a parabola, as assumed in the harmonic approximation. This is displayed in Fig. 1.1 for the stretching mode of a diatomic molecule. The parabolic expansion of the PES leads to a divergence of the electronic energy in the limit of infinite interatomic distance. However, the same asymptotic limit of the "true" PES is finite and corresponds to the dissociation energy. This simple example shows that corrections to the harmonic model, usually referred to as anharmonic contributions, must be included to get a reliable reproduction of experimental spectra.[25,26] Differently from the harmonic case, the inclusion of anharmonic effects cannot be done directly from the outputs of ESCs, and requires the explicit solution of the vibrational Schrödinger equation, and this usually leads to an increase in the computational cost of the simulation. In fact, anharmonic calculations often require the calculation of high-order derivatives of potential energy and property surfaces, which leads to a steep raise in the overall computational cost. This cost can be further increased depending on the method chosen to solve the vibrational Schrödinger equation itself, in some cases this latter step being

even more expensive than the underlying ESCs themselves. This is the case, for example, for variational approaches,[27,28] whose high computational costs limits their application to small-size molecules.

The highest-energy transitions of a molecule are the ones involving excitations of the electrons, and can be investigated by further increasing the energy of the probe electromagnetic field, above the IR region. The energetic range spanned by electronic excitations is much higher than for other spectroscopic techniques, going from the visible region, at about 400-800 nm, corresponding to the average excitation energies of valence electrons of chromophores, to the X-ray region, between 100 and 400 eV, which produces excitations of core electrons. The simulation of electronic spectra is more challenging than that of IR for several reasons. First of all, the calculation of properties is intrinsically more complex for electronic excited states. Even if significant work has been done in recent years to produce reliable and black-box approaches for the calculation of electronic excited states,[29,30] especially in connection with the time-dependent extension of density functional theory (TD-DFT),[31,32,33] they are still far from being comparable to their counterparts for ground states. Another difficulty arises from the fact that the number of phenomena occurring after an electronic excitation is much larger than for other spectroscopies. Furthermore, also spectroscopic techniques, based on emission processes subsequent to an electronic excitation, such as fluorescence,[34] have also been devised. Of course, electronic states are characterized also by their spin and, especially for metal complexes, transitions between states of different spins are possible. A proper reproduction of those phenomena, which are at the basis, for example, of phosphorescence spectroscopy,[35] requires, from a theoretical point of view, the inclusion of relativistic effects in the simulation,[36] therefore increasing the complexity of ESCs. All those effects need to be included in the simulation, in order to get results directly comparable to experimental data, and this increases significantly the complexity of modeling electronic spectroscopies.

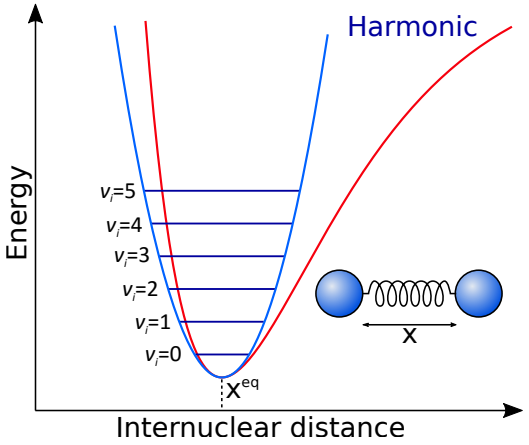

FIGURE 1.1: Schematic representation of the harmonic and anharmonic potential energy surfaces of a biatomic molecule.

The spectroscopic techniques mentioned above (*i.e.* NMR, EPR, MW spectroscopy, IR and electronic absorption) have been known for several decades, and have been constantly improved in terms of reliability and accuracy. As a consequence, for a given spectroscopic technique, the fine-structure of experimental spectra is determined by lower-energy transitions. For example, in high-resolution electronic spectra, transitions between vibrational levels

of different electronic states can be singled out. In a similar way, the broadening of high-resolution IR spectra is modulated by rotational transitions. For the most accurate electronic spectra, usually recorded for very small-molecules, both rotational and vibrational transitions between levels of different electronic states can be detected.[37,38] The simulation of such high-resolution spectra requires very refined models, supporting combined excitations involving different types of molecular levels. For example, the reproduction of vibrational signatures in electronic spectra requires the calculation of potential energy surfaces of excited states, which means in practice getting the energy gradients and Hessians from the corresponding methods.[39,40,41] For this reason, simulations of vibronic spectra carried out at the harmonic level are already challenging for medium-sized molecules, and the further inclusion of anharmonic effects is possible only for the smallest systems.[42,43,44] The energy of the light is not the only possible criterion to classify different spectroscopic techniques. Another possible categorization is based on the modulation of the electromagnetic wave used in the experiment. In fact, even if for the spectroscopic techniques outlined above, standard, unpolarized light is in most cases employed, a proper control of the polarization allows to extract additional information on a molecular system. For example, it is known that chiral molecules interact differently with left- and right-handed circularly polarized light. This effect, known as circular dichroism (CD), is at the basis of all chiroptical measurement instruments,[45] which are the primary tools for the assignment of absolute configurations of chiral systems. The CD counterparts of most of the spectroscopies outlined above have been developed, the most known ones being vibrational circular dichroism (VCD),[46] the chiral version of IR absorption, and electronic circular dichroism (ECD), the chiral counterpart of electronic absorption spectroscopy.[47] More recently, also the chiral parallel of fluorescence and phosophorescence, known as circularly polarized luminescence (CPL)[48] and phosphorescence (CPP)[49] have been developed, which are particularly appealing for studying transition metal complexes. The simulation of chiroptical spectroscopies involves additional challenges with respect to their standard counterparts, since band intensities are, in most cases, given by mixed electric-magnetic transition properties, such as the magnetic transition dipole moment, and the calculation of those properties is less straightforward than for pure electronic properties.[50,51] Furthermore, chiroptical spectra are recorded as differences between the spectra obtained with left- and right-handed circularly polarized light. For this reason, an experimental spectrum can display both positive and negative bands and, in most cases, has a weaker intensity. This makes the simulation of chiroptical spectra even more sensitive to the quality of the underlying quantum mechanical model. In fact, different contributions to the overall bandshape, such as the harmonic and anharmonic parts for a VCD spectrum, might have different signs and thus they do not necessarily add up, and can even cancel each other. For this reason, a small change in the individual terms can lead to strong variations in the overall spectrum.[52] This is the case also for ECD, where the theoretical spectrum can change sign depending on the vibronic model.[53,54]

A common feature of all the techniques outlined up to this point is that they are related to linear-optical effects. However, by increasing the intensity of the laser, non-linear optical effects become relevant, and are the basis of more advanced spectroscopic techniques, such as the ones based on multiphoton absorption processes, like two-photon absorption (TPA).[56,57] The simulation of this class of spectroscopies requires the calculation of high-order response properties, which increases the complexity of the simulations. Furthermore, the inclusion of several electronic states is often mandatory, with an increase in the computational cost of the ESCs. A second class of spectroscopic techniques based on non-linear optical effects is related to scattering, such as Raman[58,59,60] and resonance Raman (RR).[61,62] In particular, RR is challenging from a computational point of view, since it combines vibrational and electronic processes. Indeed, the initial and final levels of a RR transition are vibrational levels of the same electronic state, thus from this point of view RR can be considered a vibrational spectroscopy. However, RR experiment are carried out with a laser, whose energy matches an electronic transition (the corresponding electronic state is usually referred to as the intermediate state), and the intensity of the RR spectrum is determined by this intermediate state. In this respect, RR is an electronic spectroscopy, which makes its simulation more difficult than for standard vibrational spectra. Once again, chiral versions of those spectroscopies have been recently developed.[63]

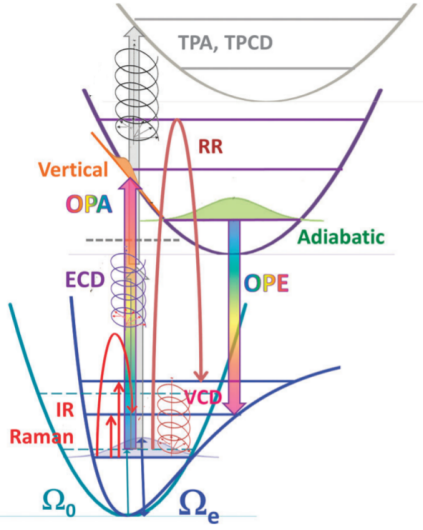

FIGURE 1.2: General theoretical framework for different kind of vibrational and vibronic (one and two photon) transitions (Figure taken from Ref. 55).

The previous discussion showed that, by varying the frequency and the nature (*i.e.* its polarization and intensity) of the light source of a spectroscopic experiment, a wide range of spectroscopic techniques are obtained. A graphical representation of some of the processes at the basis of the vibrational and electronic spectroscopies mentioned up to now is reported in Fig. 1.2. In most cases, different techniques give access to a complementary set of information about the molecular system under study. For this reason, a full characterization is often reached through a multifrequency approach, combining multiple experimental techniques. In order to reliably support the interpretation of data arising from different techniques, theoretical frameworks covering the highest number of spectroscopies possible with a nearly constant accuracy over the whole energy range need to be devised. This requires, in practice, the development of a general and modular theoretical framework.

With the aim of building such a computational tool, one of the major research

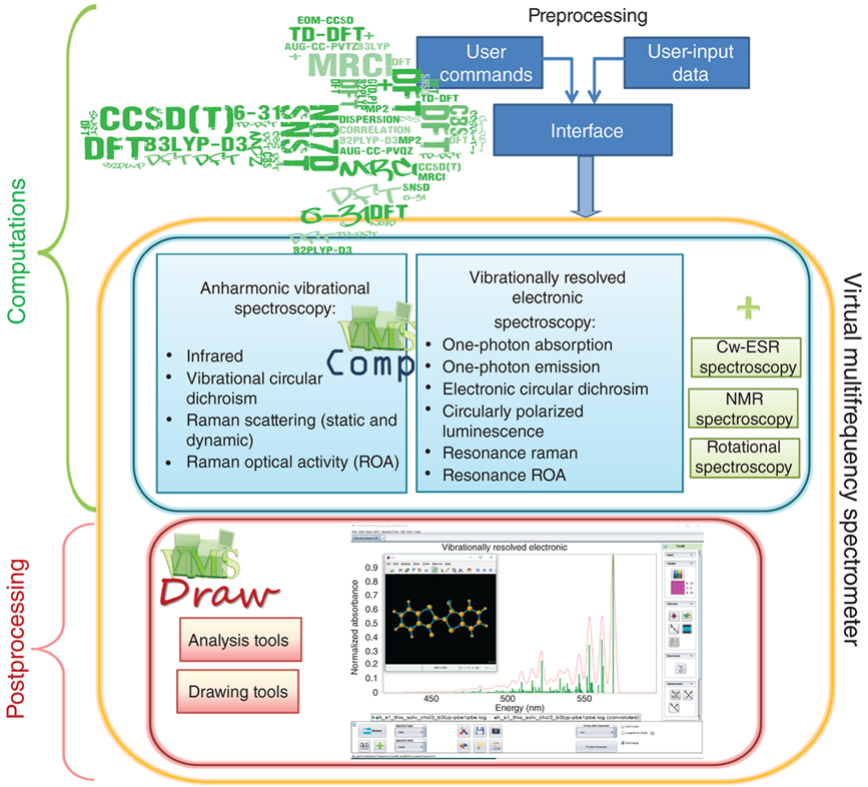

FIGURE 1.3: Structure of the Multifrequency Virtual Spectrometer (VMS) (Figure taken from Ref. 64).

lines of the group where I have been working has been focused on the development of the so-called multifrequency virtual spectrometer (VMS),[55,64,65] which is a computational parallel of an experimental multifrequency instrument. As shown in the graphical representation of VMS given in Fig. 1.3, this tool is composed of two modules. The first one is in charge of the spectral simulation, and takes data from electronic structure calculations. The second module is dedicated to the visualization of the results in a natural and user-friendly way. The main objective ot this thesis is to extend the range of applicability of VMS, and more precisely its first module, to large-sized, possibly flexible systems, by focusing on vibrational and for vibronic spectroscopies. The first part of the thesis will focus on the development of new, efficient methods for the simulation of vibrational spectra at the anharmonic level. The anharmonic models developed over the last decades can be broadly divided in two classes, variational[27,28,66] and perturbative.[67,68,69] The former methods are based on the explicit solution of the vibrational Schrödinger equation in a given basis set and, even if they provide results of systematically increasing quality, their high computational cost, which formally scales exponentially with the size of the systems, makes their application to large-sized systems difficult. As a side note, it should be mentioned that the quality of the variational correction is entirely dependent on the quality of the description of the PES. We note that, in recent years, several ways to reduce the computational cost of variational calculations, such as basis-pruning algorithms[70,71] or local modes-based approaches[72,73,74] extended significantly

the range of applicability of variational approaches, but systems with more than 20 atoms is still however challenging. On the other hand, perturbative approaches are particularly appealing due to their relatively low computational cost, but their reliability strongly depends on the partition of the Hamiltonian in a reference and a perturbation part. For example, second-order perturbation theory (VPT2),[67,75] where the harmonic Hamiltonian is taken as a reference, is effective for semi-rigid systems, but its accuracy decreases for low-frequency, highly-anharmonic large-amplitude modes. With the aim of increasing the range of applicability of variational approaches, two different algorithms have been devised in this thesis, each one tailored for a specific class of problems. The first approach is based on an hybrid scheme, where a single degree of freedom is treated variationally, while the harmonic approximation is used for the remaining degrees of freedom. In more detail, the method generalizes the internal coordinates path Hamiltonian (ICPH)[76] and the reaction path Hamiltonian (RPH)[66,77,78,79] models to curvilinear internal coordinates, and has been developed to support the largest number possible of large-amplitude modes, including torsions, inversion and stretching coordinates. Such an approach is effective for systems, where anharmonic effects are mostly concentrated in a single degree of freedom. For more complex systems, with multiple, strongly coupled anharmonic degrees of freedom, multidimensional anharmonic approaches are required. To target those systems, the density matrix renormalization group (DMRG),[80,81,82] which is commonly applied in electronic structure calculations for the solution of large variational problems, has been extended to vibrational structure calculations. This extension requires two steps. First, electrons obey the Fermi-Dirac statistics, whereas nuclei obey the Bose-Einstein one, and thus the DMRG algorithm must be generalized to support bosons. Furthermore, in electronic structure calculations, the ground state is much more important than for vibrational structure calculations, where highly-excited states need to be in most cases computed. For this reason, an energy-specific version of DMRG, which allows a direct targeting of excited states, has been devised following ideas already used for the electronic structure case.[83,84,85]
The second part of this thesis focuses on the development of theoretical models for the simulation of vibrational signatures in electronic spectra. In order to target large-size, potentially flexible systems, harmonic vibronic models in Cartesian coordinates have been generalized to support curvilinear, internal coordinates. Such an extension is scarcely discussed in the literature[86,87,88] and improves significantly the reliability of vibronic models when targeting large-sized system, since it allows to strongly reduce mode-couplings. This results, in practice, in much more accurate band-shapes already at the harmonic level for systems characterized by highly-anharmonic large-amplitude deformations. Furthermore, a general time-dependent (TD)[89,90,91] algorithm for the calculation of the bandshape has been developed. Unlike the parallel time-independent (TI) approach, where the vibronic bandshape is obtained as the sum of all the contributions from each vibronic transition, within TD approaches rely on the Fourier transform of transition dipole moments autocorrelation function. The time-evolution of the autocorrelation function can

be, in principle, obtained from quantum dynamics calculations.[92,93] However, in the present thesis, where the harmonic approximation is employed, it will be computed analytically based on the Feynmann path-integral theory. The resulting TD approach is particularly appealing for the study of large-size systems, since it does not require the evaluation of any infinite summation, even when temperature effects are included, and its computational costs scales favorably with the size of the system.
As discussed above, a wide range of phenomena can occur following an electronic excitation, including both radiative and non-radiative decays. In particular, emission spectroscopies, such as fluorescence and phosphorescence, are strongly influenced by competitive, non-radiative decay processes. In order to build a complete framework, where all those phenomena are properly taken into accounts, the TD framework has been extended to the calculation of rates of several non-radiative processes, including intersystem-crossing (ISC) and internal conversion (IC).[94,95,96]
As already remarked above, a computational tool covering the largest number possible of spectroscopies requires also the support of non-linear optical effects must be included. In this thesis, we will focus on two non-linear spectroscopies, resonance Raman and its chiral counterpart, resonance Raman (RR) optical activity (RROA).[58] The experimental process at the basis of RR involves an electronic transition to an excited, intermediate state, so vibronic models, and in particular the TD algorithm, can be extended to RR and RROA spectroscopies.[61,97,98] Following the lines sketched above, the derivation has been kept as general as possible, thus without introducing any additional approximation compared to the one already made for the linear spectroscopy case. In particular, the TD theory of RR and RROA spectroscopies has been formulated in a general set of curvilinear, internal coordinates, thus providing reliable results also for flexible systems.
All the vibronic models described in the second part of this thesis rely on the harmonic approximation of the PES involved in the transition. In the last part of the thesis, this limitation will be lifted, and two different models for the inclusion of anharmonic effects on electronic excited states will be described. Even if the use of internal coordinates reduces mode-couplings, flexible systems usually display low-frequency, large-amplitude modes (LAMs), whose correct treatment requires the inclusion of anharmonic effects. With the aim of targeting systems with a limited flexibility, the RPH-based anharmonic approach introduced in the first part of the thesis has been extended to vibronic spectroscopy.[99] Not only does this method allow to compute anharmonic frequencies of excited states along a LAM, but also provides transition properties between vibrational levels of different electronic states. This paves the way toward the simulation of anharmonic vibronic spectra. Clearly, as mentioned above, such a method has the same limitations as already mentioned in the context of vibrational spectroscopy, so it is effective only for systems, where a single coordinate, for which anharmonic effects are relevant, can be identified. To target also more complex systems, VPT2 has been coupled with the recent development of analytic second derivatives of

time-dependent DFT (TD-DFT) energies,[100,101] to compute anharmonic vibrational spectra of electronic excited states. Unlike the RPH-based model, VPT2 provides a more balanced representation of anharmonic effects, since all degrees of freedom are treated at the same footing. However, the theory can be used to compute frequencies and transition properties between vibrational levels of the same electronic states, thus cannot be extended to the calculation of band intensities in vibronic spectra.
As a conclusion, the algorithms developed throughout the thesis have been applied to the simulation of vibrationally-resolved near edge X-ray absorption fine structure (NEXAFS) and X-ray photoelectron (XPS) spectroscopies. In particular, for XPS, a new electronic structure method, based on Green function (GF) techniques, has been developed.[102,103] This method, referred to as transition-operator second-order electron-propagator (TOEP2),[104,105] generalizes the standard, second-order electron propagator (EP2) approach to grand-canonical HF orbitals. In fact, with a careful choice of these orbitals, results of the same quality, or even more accurate, than high-order GF methods, can be obtained at the low, second-order perturbation level.
To conclude, the thesis is organized as follows:

- in Chapter 2, the general theory used for the modeling of molecular vibrations both for vibrational and vibronic spectroscopy will be presented, with particular attention to the framework employed to build non-redundant internal coordinates.

- Chapter 3 focuses on the theoretical model for the simulation of anharmonic vibrational spectra. In the first part of the chapter, the hybrid anharmonic-harmonic approach based on the RPH-model and a general set of internal coordinates will be introduced. In the second part, the extension of DMRG to vibrational problems (referred to as vibrational DMRG, VDMRG) will be presented, with particular emphasis on the difference with the formulation of DMRG for electronic structure problems. Both algorithms will be tested on some organic molecules to show their strengths and weaknesses.

- in Chapter 4, the harmonic models for vibronic spectroscopy will be presented. First, the definition of all the quantities arising from ESCs and needed to define the reference vibronic model will be presented, together with their extension to internal coordinates. Then, the general TD framework as applied to one-photon spectroscopies is discussed. Finally, the TD framework is extended to support the calculation of non-radiative decay rates. The reliability of the TD approach is checked against molecular systems, with particular care on the impact of the choice of the coordinates system on the final computed spectrum.

- in Chapter 5, the TD extension of the TD framework to RR and RROA spectroscopies is presented, highlighting the additional challenges that are present with respect to the TD formulation for one-photon spectroscopies. The TD theory is then applied to the simulation of the RR and RROA spectra of several organic systems.

- in Chapter 6 the extension of the RPH-based model to excited states is presented. In particular, the approximation needed to extend it to the calculation of transition properties of vibronic transitions are presented. Moreover, several ways of including the effects associated to the vibrational degrees of freedom different from the LAM at the harmonic level are described. Finally, the extension of VPT2 to electronic excited states, is discussed along with its application to correct band positions in vibronic spectra.

- in Chapter 7, the application of the previous vibronic models to the calculation of vibrationally-resolved NEXAFS an XPS spectra is presented. In both cases, it is shown that, for spectra recorded at high-resolution using synchrotron light sources, even if single vibronic bands cannot be singled out, the inclusion of vibronic effects is critical to get a correct reproduction of the relative intensity of the bands. For XPS, the main features of GF-based approaches are highlighted, and the theoretical formulation and implementation of the new, TOEP2 approach is described.

- finally, Chapter 8 summarizes the results obtained in this thesis, and sketches possible future developments.

Chapter 2

General theory of computational spectroscopy

2.1 The main challenge: calculation of transition properties

All spectroscopic techniques rely on one or more transitions between molecular states, either spontaneous or stimulated by an external perturbation. This perturbation is, in most cases, caused by the electromagnetic radiation, and depending on its frequency (*i.e.* on the energy), different processes occur. From the nature of the transitions induced by the radiation (such as their rate or intensity), the character of the molecular states can be investigated, thus providing information on a chemical compound.
In order to simulate *ab-initio* molecular spectra, two steps are required: the first one is the determination of the molecular states involved for a given system of interest, whereas the second one focuses on the description of transitions between these states induced by the electromagnetic radiation. The first step is the same for all spectroscopic techniques, whereas the second one depends on the spectroscopy of interest. The first part of this chapter will focus on the approximations employed in this thesis to describe molecular levels. Then, the Fermi Golden Rule (FGR), which is the basis for the representation of a wide range of spectroscopic processes, will be introduced. Since, as already mentioned in the introduction, this thesis will focus on both vibrational and electronic spectroscopies, the framework will be kept as general as possible, introducing only a minimum number of approximations.

2.1.1 The molecular Hamiltonian

In the non-relativistic limit, the vibrational Hamiltonian for a molecule of N_{at} atoms and N_{ele} electrons is defined as,

$$\begin{aligned}\mathcal{H}_{\text{mol}} =& -\frac{1}{2}\sum_{a=1}^{N_{\text{at}}}\sum_{\tau=x,y,z}\frac{1}{M_a}\frac{\partial^2}{\partial R_{a\tau}^2} - \frac{1}{2}\sum_{i=1}^{N_{\text{ele}}}\frac{\partial^2}{\partial r_i^2} + \sum_{i\neq j}^{N_{\text{ele}}}\frac{1}{|\boldsymbol{r}_i - \boldsymbol{r}_j|^2} \\ &+ \sum_{a\neq b}^{N_{\text{at}}}\frac{Z_a\, Z_b}{|\boldsymbol{R}_a - \boldsymbol{R}_b|^2} - \sum_{i=1}^{N_{\text{ele}}}\sum_{a=1}^{N_{\text{at}}}\frac{Z_a}{|\boldsymbol{R}_a - \boldsymbol{r}_i|^2} \\ =& \mathcal{T}_{\text{nuc}}(\boldsymbol{R}) + \mathcal{T}_{\text{ele}}(\boldsymbol{r}) + \mathcal{V}_{ee}(\boldsymbol{r}) + \mathcal{V}_{NN}(\boldsymbol{R}) + \mathcal{V}_{Ne}(\boldsymbol{r},\boldsymbol{R})\end{aligned} \tag{2.1}$$

where $\boldsymbol{R}_a$ is the vector of the Cartesian coordinates of the a-th nucleus, with charge Z_a and mass M_a, and $\boldsymbol{r}_i$ its counterpart for the i-th electron. The fourth term of Eq. 2.1, that couples nuclear and electronic coordinates, makes the molecular Hamiltonian not separable in a purely electronic and nuclear parts. As a consequence, the molecular wavefunction $\Psi_m(\boldsymbol{r},\boldsymbol{R})$, computed as an eigenfunction of $\mathcal{H}_{\text{mol}}$, cannot be factorized. However, it is well-known that, due to the difference in their masses, the nuclei are moving much more slowly than the electrons. For this reason, an adiabatic separation, usually known as the Born-Oppenheimer (BO) approximation,[106] is employed to simplify the solution of the Schrödinger equation associated with $\mathcal{H}_{\text{mol}}$. Within the BO approximation, a fixed-nuclei equation, where the kinetic energy of the nuclei is neglected, is solved:

$$\left[\mathcal{T}_{\text{ele}} + \mathcal{V}_{ee}(\boldsymbol{r}) + \mathcal{V}_{Ne}(\boldsymbol{r},\boldsymbol{R}) + \mathcal{V}_{NN}(\boldsymbol{R})\right]\phi_{\underline{m}}(\boldsymbol{r},\boldsymbol{R}) = E_{\underline{m}}^{\text{ele}}(\boldsymbol{R})\,\phi_{\underline{m}}(\boldsymbol{r},\boldsymbol{R}) \tag{2.2}$$

We note that no differential operator involving the nuclear coordinates are present in Eq. 2.2, thus the equation depends only parametrically on $\boldsymbol{R}$. This means that the nuclear coordinates $\boldsymbol{R}$ determine the potential to be used in the solution of the Schrödinger equation, which involves only the electronic degrees of freedom. As the potential energy, the eigenvalue $E_{\underline{m}}^{\text{ele}}$ of Eq. 2.2 depends on the nuclear coordinates, and determines the electronic potential energy in which the nuclei move. Starting from the fixed-nuclei equation, it is natural now to factorize the molecular wavefunction in two contributions, as follows:

$$\Psi_m(\boldsymbol{r},\boldsymbol{R}) = \phi_{\underline{m}}(\boldsymbol{r},\boldsymbol{R}) \times \psi_{r(\underline{m})}(\boldsymbol{R}) \tag{2.3}$$

where $\underline{m}$ labels the index of the electronic state and r the nuclear one related to molecular state m. The nuclear wavefunction depend also on $\underline{m}$ since the potential in which the nuclei move changes with the electronic state. Using this factorization to solve Eq. 2.1, the following equation is obtained:

$$\left[\mathcal{T}_{\text{nuc}} + E_{\underline{m}}^{\text{ele}} + \sum_{\underline{n}\neq\underline{m}}\Delta\mathcal{T}_{\underline{n},\underline{m}}\right]\phi_{\underline{m}}(\boldsymbol{r},\boldsymbol{R})\,\psi_{r(\underline{m})}(\boldsymbol{R}) = E_{\text{mol}}\,\phi_{\underline{m}}(\boldsymbol{r},\boldsymbol{R})\,\psi_{r(\underline{m})}(\boldsymbol{R}) \tag{2.4}$$

with,[106]

$$\Delta\mathcal{T}_{\underline{n},\underline{m}} = \langle\, \phi_{\underline{n}} \mid \mathcal{T}_{\text{nuc}} \mid \phi_{\underline{m}} \,\rangle - \sum_{a=1}^{N_{\text{at}}} \sum_{\tau=x,y,z} \langle\, \phi_{\underline{n}} \mid \frac{\partial}{\partial R_{a\tau}} \mid \phi_{\underline{m}} \,\rangle \frac{\partial}{\partial R_{a\tau}} \tag{2.5}$$

The coupling operators $\Delta\mathcal{T}_{\underline{n},\underline{m}}$, known as non-adiabatic couplings, are expressed as sum of two terms. The first one is the cross matrix element of the nuclear kinetic energy operator between the two electronic wavefunctions, and is non-null since both $|\, \phi_{\underline{m}} \,\rangle$ and $|\, \phi_{\underline{n}} \,\rangle$ depend on the nuclear coordinates $\boldsymbol{R}$. As a constant energy shift has no effects in the relative energies of the vibrational states, this first term can be neglected. This is not the case for the second term, which is proportional to the momentum associated to the a-th nuclear coordinate, and couples different electronic states. If non-adiabatic couplings are included in the Hamiltonian, it is not possible to solve a vibrational Schrödinger equation for each electronic state separately. Within the BO approximation, those terms are neglected, and Eq. 2.4 becomes, in this case,

$$\left[\mathcal{T}_{\text{nuc}} + \mathcal{V}_{\underline{m}}\left(\boldsymbol{R}\right)\right] \psi_{r(\underline{m})}\left(\boldsymbol{R}\right) = E_{\text{mol}}\, \psi_{r(\underline{m})}\left(\boldsymbol{R}\right) \tag{2.6}$$

where the potential operator $\mathcal{V}_{\underline{m}}\left(\boldsymbol{R}\right)$ corresponds to the eigenvalue $E^{\text{ele}}_{\underline{m}}$ of the electronic Hamiltonian, usually referred to as potential energy surface (PES). The previous equation does not involve couplings between different electronic states, thus can be separately solved for each PES.

2.1.2 Calculation of transition rates

The previous section introduced the general framework, based on the Born-Oppenheimer approximation, which will allow us to separate the molecular wavefunction in an electronic and in a nuclear parts. In the present section, we will discuss how external, time-dependent perturbations can induce transitions between molecular states. Here, we will consider a specific case, where the external perturbation is represented by the electromagnetic radiation. In the next chapters, other perturbations, such as the spin-orbit coupling or non-adiabatic effects, will be considered.
The theoretical framework introduced here relies on a semi-classical model, in which the light is treated in a classical way, while the molecule is treated at the quantum level. Interacting with the light introduces a time-dependent perturbation $\Delta\mathcal{H}\left(t\right)$ to the molecular Hamiltonian $\mathcal{H}_{\text{mol}}$ such that,

$$\mathcal{H}\left(t\right) = \mathcal{H}_{\text{mol}} + \Delta\mathcal{H}\left(t\right) \tag{2.7}$$

Treating the light as classical allows to express the light-matter interaction Hamiltonian $\Delta\mathcal{H}\left(t\right)$ as a classical multipolar expansion. By including only the two leading terms of this expansion, corresponding to the electric and magnetic dipole terms, $\Delta\mathcal{H}\left(t\right)$ can be expressed as,

$$\Delta\mathcal{H} = -\boldsymbol{\mu} \cdot \boldsymbol{E}\left(t\right) - \boldsymbol{m} \cdot \boldsymbol{B}\left(t\right) \tag{2.8}$$

where $\boldsymbol{E}(t)$ and $\boldsymbol{B}(t)$ are the time-dependent electric and magnetic fields associated to the incident radiation. Additional terms could be included in the expansion given in Eq. 2.8, such as the interaction induced by the electric quadrupole moment, but those terms will not be considered for the moment, and their effect will be discussed later, when dealing with non-linear spectroscopies.
If the eigenfunctions Ψ_i of the molecular Hamiltonian $\mathcal{H}_{\text{mol}}$ and the corresponding eigenvalues E_i^{mol} are known, the effect of the interaction term $\Delta\mathcal{H}(t)$ can be included *a posteriori* by first-order time-dependent perturbation theory. Because of the presence of this perturbation, the molecular levels Ψ_i are not anymore stationary, and transitions between them are possible. The probability $p_{if}(t)$ that a transition happens between two states Ψ_i and Ψ_f at time t (where $t = 0$ corresponds to the moment in which the perturbations starts) is given by the well-known Fermi golden rule;[106]

$$p_{if}(t) = \frac{1}{\hbar^2}\left|\int_0^t \mathrm{d}t \,\langle\, \Psi_f \mid \Delta\mathcal{H} \mid \Psi_i \,\rangle\right|^2 \tag{2.9}$$

In the following, we will assume that the incident light is a monochromatic electromagnetic wave with frequency equal to ω, so that the electric field can be written as $\mathbf{E} = \mathbf{E}_0\, e^{i\omega t}$. Furthermore, the magnetic term will be neglected for the moment. By using the explicit expression for the electric field, it is possible to carry out the integral given in Eq. 2.9 to express the probability as,

$$p_{if}(t) = \frac{4\pi}{3\hbar^2 c} I(\omega)\left|\langle\, \Psi_f \mid \boldsymbol{\mu} \mid \Psi_i \,\rangle\right|^2 t\, \delta\left(\omega_{if} - \omega\right) \tag{2.10}$$

where $I(\omega)$ is the intensity of the incident radiation and $\omega_{if} = \left(E_f - E_i\right)/\hbar$. The previous equation shows that the transition probability is mainly determined by two quantities, the resonance frequency ω_{if} and the transition dipole moment $\langle\, \Psi_f \mid \boldsymbol{\mu} \mid \Psi_i \,\rangle$. The presence of the Dirac delta function in Eq. 2.10 shows that transitions can occur only when the frequency of the incident light matches ω_{if}. If this condition is met, the rate is proportional to the modulus of the transition dipole moment. We note that the previous formulation can be easily generalized to support also the inclusion of the magnetic dipole moment (see Eq. 2.8), and the transition probability would be, in this case, proportional to the transition magnetic dipole moment $\left|\langle\, \Psi_f \mid \boldsymbol{m} \mid \Psi_i \,\rangle\right|^2$. The constant factor would be the same as for the electric dipole moment, scaled by the fine-structure constant. Because of the presence of this term, the magnetic term is usually much smaller than the electric one, and is neglected in most cases. The successive correction is related to the quadrupole moment, and its contribution would be in this case proportional to the transition quadrupole moment $|\langle\, \Psi_m \mid \boldsymbol{\Theta} \mid \Psi_n \,\rangle|^2$.
In order to keep the derivation as general as possible, let us consider an arbitrary operator $\mathcal{O}$ and its integral between two molecular states, $|\, \Psi_m \,\rangle$ and $|\, \Psi_n \,\rangle$,

$$\langle \mathcal{O} \rangle_{mn} = \frac{\langle \Psi_m \mid \mathcal{O} \mid \Psi_n \rangle}{\sqrt{\langle \Psi_m \mid \Psi_m \rangle \langle \Psi_n \mid \Psi_n \rangle}} \tag{2.11}$$

where the normalization factor has been included to support also the case of non-orthogonal wavefunctions. The Born-Oppenheimer (BO) approximation can be used to simplify the previous equation. In fact, using the factorization given in Eq. 2.3, the previous integral can be rewritten as follows:

$$\langle \mathcal{O} \rangle_{mn} \approx \frac{\langle \psi_{r(\underline{m})} \mid \langle \phi_m \mid \mathcal{O} \mid \phi_n \rangle \mid \psi_{s(\underline{n})} \rangle}{\sqrt{\langle \psi_{r(\underline{m})} \mid \psi_{r(\underline{m})} \rangle \langle \psi_{s(\underline{n})} \mid \psi_{s(\underline{n})} \rangle}} \tag{2.12}$$

where the orthonormality of the electronic wavefunctions has been used to simplify the denominator. The nuclear contribution of Eq. 2.12 can be further simplified. First of all, even if the number of the nuclear coordinates $\boldsymbol{R}$ is equal to $3N_{\text{at}}$, in absence of external perturbation the Hamiltonian is invariant by an overall translation of the molecule. In other words, the nuclear coordinates $\boldsymbol{R}$ can be separated in the 3 coordinates of the center of mass (CM) ($\boldsymbol{R}_{\text{CM}}$) and $3N_{\text{at}} - 3$ coordinates relative to the center of mass. Since $\mathcal{H}_{\text{mol}}$ does not depend on $\boldsymbol{R}_{\text{CM}}$, only contributions associated to the remaining coordinates can be considered.
A further simplification is obtained by considering that the potential is also invariant from rotations of the whole molecule. This condition is not trivially satisfied in all coordinate systems, at variance with the translational motion, but a particular set of reference axis has to be chosen. For a given molecular arrangement, this frame is the so-called Eckart frame (f_x, f_y, f_z),[107,108] whose definition is presented, for example, in Ref. 109. By expressing the equilibrium geometry of the molecule within this frame ($\boldsymbol{R}^{\text{eq}}_{\text{Eck}}$), and by defining as $\boldsymbol{d}$ the displacements from this equilibrium position, it is possible to show that the following equality holds:

$$\begin{aligned} \sum_{a=1}^{N_{\text{at}}} M_i \boldsymbol{d}_a &= 0 \\ \sum_{a=1}^{N_{\text{at}}} M_i \boldsymbol{R}^{\text{eq}}_{\text{Eck},a} \times \boldsymbol{d}_a &= 0 \end{aligned} \tag{2.13}$$

that are usually referred to as Eckart conditions. From the previous equation, it can be proven that the displacement vector $\boldsymbol{d}$ has no components along the overall rotation of the molecule. This means, in practice, that rotational effects are included in the definition of the Eckart frame, and displacements within this frame include only pure vibrational motions. By adopting this frame, translational and rotational components of the nuclear wavefunction can be factored out, so that only pure vibrational part is kept, which will be at the center of our discussion in the present thesis.
Within this framework, Eq. 2.11 becomes,

$$\langle \mathcal{O} \rangle_{mn} \approx \frac{\langle \psi^v_{r(\underline{m})} | \langle \phi_m \mid \mathcal{O} \mid \phi_n \rangle | \psi^v_{s(\underline{n})} \rangle}{\sqrt{\langle \psi^v_{r(\underline{m})} \mid \psi^v_{r(\underline{m})} \rangle \langle \psi^v_{s(\underline{n})} \mid \psi^v_{s(\underline{n})} \rangle}} \tag{2.14}$$

where the same notation has been used for vibrational and nuclear states. Even if not explicitly indicated in the previous equation, the property $\hat{\mathcal{O}}$ depends both on the nuclear and on the electronic coordinate, thus the expectation value given in the previous equation cannot be, in general, simplified. While such a calculation becomes straightforward for vibrational spectroscopies, where only one electronic state is involved ($| \phi_f \rangle = | \phi_i \rangle$), this is not the case for electronic spectroscopies since the initial and final vibrational states are generally expressed with different coordinate sets.
In the following, except if stated otherwise, we will assume that the property or quantity of interest and the associated electronic transition dipole moment ($\langle \phi_m \mid \hat{\mathcal{O}} \mid \phi_n \rangle$) are known, and will be noted $\mathcal{O}^e$.

2.2 PES and PS representation

2.2.1 Harmonic models

The BO approximation introduced in the previous section allows the decoupling of the electronic component of the molecular wavefunction from the nuclear one. Here, we will focus on the solution of the vibrational part of the Schrödinger equation,

$$[\mathcal{T}_{\text{nuc}} + \mathcal{V}_{\underline{m}}(\boldsymbol{x})] \psi_{r(\underline{m})} = E_{r(\underline{m})} \psi_{n(\underline{m})} \tag{2.15}$$

where $\mathcal{V}_{\underline{m}}(\boldsymbol{x})$ is the PES of the m-th electronic state, obtained from the solution of Eq. 2.2. Unlike Eq. 2.6, where a general coordinate system $\boldsymbol{R}$ is used for the nuclear motion, in Eq. 2.15 $\boldsymbol{x}$ label the Cartesian coordinates of the nuclei. The main issue associated to the solution of Eq. 2.15 is that no analytical formulas for $\mathcal{V}_{\underline{m}}(\boldsymbol{x})$ are known. For this reason, the potential energy surface (PES) is usually approximated as a Taylor expansion,

$$\begin{aligned} \mathcal{V}_{\underline{m}}(\boldsymbol{x}) = \mathcal{V}_{\underline{m}}(\boldsymbol{x}^{\text{eq}}) &+ \sum_{a=1}^{N_{\text{at}}} \sum_{\tau=x,y,z} \left(\frac{\partial \mathcal{V}_{\underline{m}}}{\partial x_{a\tau}} \right)_{eq} \left(x_{a\tau} - x^{\text{eq}}_{a\tau} \right) \\ &+ \frac{1}{2} \sum_{a,b=1}^{N_{\text{at}}} \sum_{\tau,\rho=x,y,z} \left(\frac{\partial^2 \mathcal{V}_{\underline{m}}}{\partial x_{a\tau} \partial x_{b\rho}} \right)_{\text{eq}} \left(x_{a\tau} - x^{\text{eq}}_{a\tau} \right) \left(x_{b\rho} - x^{\text{eq}}_{b\rho} \right) \end{aligned} \tag{2.16}$$

The constant term $\mathcal{V}_{\underline{m}}(\boldsymbol{x}^{\text{eq}})$ can be set to zero by taking the energy of the equilibrium geometry as a reference. At a minimum of the PES, the gradient is null, so also the second term is null. Thus, the first non-null term in the previous expansion is the second-order one. Eq. 2.16 can be used to rewrite the vibrational Schrödinger equation as,

$$\left(-\sum_{a=1}^{N_{\text{at}}} \sum_{\tau=x,y,z} \frac{1}{2M_a} \frac{\partial^2}{\partial x_{a\tau}^2} + \sum_{a,b=1}^{N_{\text{at}}} \sum_{\tau,\rho=x,y,z} \frac{1}{2} H^{\underline{m},eq}_{\boldsymbol{x},a\tau b\rho} x_{a\tau} x_{b\rho} \right) \psi_{r(\underline{m})} = E_{r(\underline{m})} \psi_{r(\underline{m})} \tag{2.17}$$

where $\boldsymbol{H}^{\underline{m},eq}_{\boldsymbol{x}}$ is the Hessian matrix of the PES of the $\underline{m}$-th electronic state calculated at the equilibrium position $\boldsymbol{x}^{\text{eq}}$ expressed with respect to the Cartesian coordinates. For the sake of compactness, the superscript indicating the electronic state m will be dropped out in the following. The form of the kinetic energy operator is simplified by introducing the mass-weighted Cartesian coordinates, defined as $X_{a\tau} = \sqrt{M_a}\left(x_{a\tau} - x^{\text{eq}}_{a\tau}\right)$ or, in matrix notation, as $\boldsymbol{X} = \boldsymbol{M}^{1/2}\left(\boldsymbol{x} - \boldsymbol{x}^{\text{eq}}\right)$. Eq. 2.17 can be rewritten in terms of the $\boldsymbol{X}$ as,

$$\left(-\frac{1}{2} \sum_{a=1}^{N_{\text{at}}} \sum_{\tau=x,y,z} \frac{\partial^2}{\partial X_{a\tau}^2} + \frac{1}{2} \sum_{a,b=1}^{N_{\text{at}}} \sum_{\tau,\rho=x,y,z} H^{eq}_{\boldsymbol{X},a\tau b\rho} X_{a\tau} X_{b\rho} \right) \psi_{r(\underline{m})} = E_{r(\underline{m})} \psi_{r(\underline{m})} \tag{2.18}$$

where $\mathbf{H}^{eq}_{\boldsymbol{X}} = \boldsymbol{M}^{1/2} \boldsymbol{H}^{eq}_{\boldsymbol{x},ij} \boldsymbol{M}^{1/2}$ is the Hessian matrix calculated with respect to the mass-weighted Cartesian. The Hessian of a function calculated in a minimum point is positive definite, and thus can be diagonalized by unitary transformation $\boldsymbol{L}$. The $\boldsymbol{L}$ matrix is defined such that $\boldsymbol{L}^T\boldsymbol{L} = \boldsymbol{I}$ and $\boldsymbol{L}^T \boldsymbol{H}^{eq}_{\boldsymbol{X}} \boldsymbol{L} = \boldsymbol{\Omega}^2$, where $\boldsymbol{\Omega}$ is the diagonal matrix of the eigenvalues. $\boldsymbol{L}$ defines a new set of coordinates, referred to as mass-weighted normal coordinates, in which the Hessian matrix is diagonal through the following relation:

$$\boldsymbol{Q} = \boldsymbol{L}^T \left(\boldsymbol{X} - \boldsymbol{X}^{eq} \right) \tag{2.19}$$

The vibrational Hamiltonian given in Eq. 2.18 can be now rewritten in terms of the coordinates $\boldsymbol{Q}$. The kinetic energy operator is invariant under unitary transformation, and therefore does not change. The potential energy term becomes diagonal, as expressed in the following,

$$\sum_{i=1}^{N_{\text{vib}}} \left(-\frac{1}{2} \frac{\partial^2}{\partial Q_i^2} + \frac{1}{2} \omega_i^2 Q_i^2 \right) \psi_{r(\underline{m})} = E_{r(\underline{m})} \psi_{r(\underline{m})} \tag{2.20}$$

where ω_i^2 are the diagonal elements of the eigenvalue matrix $\boldsymbol{\Omega}$. Let us recall that the eigenvalues of a positively definite matrix are positive, and thus the elements ω_i are all real. Eq. 2.20 shows that the vibrational Hamiltonian expressed in terms of the normal coordinates can be written as sum of N_{vib} monodimensional operators $\mathcal{H}_i\left(Q_i\right)$ corresponding harmonic oscillators,

$$\mathcal{H}_{\text{vib}} = \sum_{i=1}^{N_{\text{vib}}} \left(-\frac{1}{2} \frac{\partial^2}{\partial Q_i^2} + \frac{1}{2} \omega_i^2 Q_i^2 \right) \tag{2.21}$$

The methods for computing eigenvalues and eigenfunctions of the Hamiltonian give in Eq. 2.21 are well known.[18] The eigenfunctions associated to the i-th mode, $\psi^{(i),n}_{r(\underline{m})}$, can be written as,[106]

$$\psi_{r(\underline{m})}^{(i),n} = \left(\frac{\sqrt{\omega_i/\hbar}}{2^n n!\sqrt{\pi}}\right)^{1/2} H_n\left(\omega_i/\hbar\right) \exp\left(-\frac{1}{2}\frac{\omega_i}{\hbar}Q_i^2\right) \tag{2.22}$$

where n is the vibrational quantum number of the state $\psi_{r(\underline{m})}^{(i),n}$, and H_n is the n-th order Hermite polynomial. Furthermore, the eigenvalues can be expressed as,

$$E_{r(\underline{m})}^{(i),n_i} = \hbar\omega_i\left(n_i + \frac{1}{2}\right) \tag{2.23}$$

The eigenvalues of Eq. 2.21 are the product of the eigenfunction of each monodimensional Hamiltonan, thus,

$$\psi_{r(\underline{m})} = \prod_{i=1}^{N_{\text{vib}}} \psi_{r(\underline{m})}^{(i),n_i} \tag{2.24}$$

Furthermore, the total vibrational energy E_{vib} is the sum of the energies of the single modes,

$$E_{vib} = \sum_{i=1}^{3N_{\text{at}}} E_{r(\underline{m})}^{(i),n_i} = \sum_{i=1}^{3N_{\text{at}}} \hbar\omega_i\left(n_i + \frac{1}{2}\right) \tag{2.25}$$

The previous equations can be easily derived within the bosonic second-quantization (SQ) algebra.[110,111] For each mode, a couple of creation and annihilation operators is defined as follows:

$$\begin{aligned} \hat{b}_i &= \sqrt{\frac{\omega_i}{2}}Q_i + \frac{i}{\sqrt{2\omega_i}}P_i \\ \hat{b}_i^\dagger &= \sqrt{\frac{\omega_i}{2}}Q_i - \frac{i}{\sqrt{2\omega_i}}P_i \end{aligned} \tag{2.26}$$

where $\boldsymbol{P}_i$ is the conjugate momentum operator of $\boldsymbol{Q}_i$. The SQ operators obey the following rules:

$$\begin{aligned} \hat{b}_i^\dagger|\, n_1, ..., n_i, ..., n_L \,\rangle &= \sqrt{n_i+1}|\, n_1, ..., n_i+1, ..., n_L \,\rangle \\ \hat{b}_i|\, n_1, ..., n_i, ..., n_L \,\rangle &= \sqrt{n_i}|\, n_1, ..., n_i-1, ..., n_L \,\rangle \end{aligned} \tag{2.27}$$

where $|\, n_1, ...n_i, ..., n_L \,\rangle$ is the occupation number vector (ONV) associated to the state where the quantum number of the i-th mode is n_i. Thus, in practice, operator $\hat{b}_i^\dagger$ increases by one the quantum number of the i-th mode, whereas $\hat{b}_i$ decreases it by one. In the following, a product of SQ operators will be referred to as "string". The second-quantized form of the Hamiltonian given in Eq. 2.21 can be readily obtained by replacing the position and the momentum operators by their SQ counterparts, and the final results is the following:

$$\mathcal{H}_{\text{vib}} = \sum_{i=1}^{N_{\text{vib}}} \omega_i\left(\hat{b}_i^\dagger\hat{b}_i + \frac{1}{2}\right) \tag{2.28}$$

Using the properties of the SQ creation/annihilation operators, it is easy to show that the eigenvalues of the vibrational Hamiltonian given in Eq. 2.28 are the ones of Eq. 2.25

2.2.2 Internal coordinates framework

The theory presented in the previous section holds for Cartesian coordinates. However, it is well-know, already from chemical intuition, that molecular vibrations are more accurately described in terms of internal coordinates. For example, molecular structures are expressed in terms of the so-called primitive internal coordinates (PICs), that are listed in the following:

- the bond lengths r_{ab} bewteen atoms a and b
- the valence angles α_{abc} between the bonds a-b and b-c
- the dihedral angles γ_{abcd} between the planes defined by a-b-c and b-c-d

In order to extend the harmonic framework developed in the previous section to such set of coordinates, the force field in Cartesian coordinates must be converted to this new set. The first step needed to perform this transformation is the definition of a relation between the Cartesian coordinates $\boldsymbol{x}$ and the internal ones, referred to in the following as $\boldsymbol{s}$. From pure geometrical considerations, it is easy to see that, for PICs, these relations are the following:

$$\begin{aligned} r_{ab} &= \sqrt{(x_b - x_a)^2 + (y_b - y_a)^2 + (z_b - z_a)^2} \\ \cos(\alpha_{abc}) &= \hat{\boldsymbol{r}}_{ab} \cdot \hat{\boldsymbol{r}}_{bc} \\ \cos(\gamma_{ijkl}) &= \frac{(\hat{\boldsymbol{r}}_{ab} \times \hat{\boldsymbol{r}}_{bc}) \cdot (\hat{\boldsymbol{r}}_{bc} \times \hat{\boldsymbol{r}}_{cd})}{\sin(\alpha_{abc}) \sin(\alpha_{bcd})} \end{aligned} \tag{2.29}$$

where $\hat{\boldsymbol{r}}_{ab} = (\boldsymbol{r}_a - \boldsymbol{r}_b) / |\boldsymbol{r}_a - \boldsymbol{r}_b|$ is the unit vector joining atom a to atom b. It is clear that the transformations given in Eq. 2.29 are non-linear functions of $\boldsymbol{r}_{ab}$, which in turns is also a non-linear function of the Cartesian coordinates of atoms a and b. Instead of using directly Eq. 2.29, it is useful to approximate the relations given in Eq. 2.29 as a Taylor series,

$$\begin{aligned} s_i = &\sum_{a=1}^{N_{\text{at}}} \sum_{\tau=x,y,z} \left(\frac{\partial s_i}{\partial x_{a\tau}} \right)_{\text{eq}} \left(x_j - x_j^{\text{eq}} \right) \\ &+ \sum_{a,b=1}^{N_{\text{at}}} \sum_{\tau,\rho=x,y,z} \left(\frac{\partial^2 s_i}{\partial x_{a\tau} \partial x_{b\rho}} \right)_{\text{eq}} \left(x_{a\tau} - x_{a\tau}^{\text{eq}} \right) \left(x_{b\rho} - x_{b\rho}^{\text{eq}} \right) + \mathcal{O}\left(|\boldsymbol{x}|^2 \right) \end{aligned} \tag{2.30}$$

where the value of the internal coordinates at the equilibrium position is assumed to be equal to zero. The expansion given in Eq. 2.30 has been truncated to the second order, since, as will be discussed in the following, only first- and second-order terms are needed for the harmonic frequencies. The

matrix containing the first order derivatives $(\partial s_i/\partial x_{a\tau})_{\text{eq}}$ (i.e. the Jacobian of the transformation between the two sets of coordinates) is usually referred to as the Wilson $\boldsymbol{B}$ matrix, and the tensor with the second derivatives as Wilson $\boldsymbol{B}$ matrix derivatives, $\boldsymbol{B}'$,

$$B_{ia} = \left(\frac{\partial s_i}{\partial x_a}\right)_{\text{eq}} \qquad B'_{iab} = \left(\frac{\partial s_i}{\partial x_k \partial x_k}\right)_{\text{eq}} \tag{2.31}$$

We note that the $\boldsymbol{B}'$ tensor is symmetric under permutation of the two lower indexes (a and b in Eq. 2.31), whereas $\boldsymbol{B}$ is not symmetric. In general, the Wilson $\boldsymbol{B}$ matrix is not even square, since the number of internal coordinates $N_{\boldsymbol{s}}$ can be different from $3N_{\text{at}}$. If $N_{\boldsymbol{s}} = N_{\text{vib}}$ and all the internal coordinates are linearly independent, the set is defined non-redundant, otherwise redundant. For example, in a planar, tricoordinated center, if two out of three valence angles are known, the third one is defined univocally. Thus, if all the three valence angles are included in the internal coordinate set, the resulting set will be redundant. This is a peculiarity of internal coordinates, whose definition, unlike the one of Cartesian coordinates, is not unique for a given molecular topology. The problem of building a non-redundant set of internal coordinates will be discussed in more detail in the next section. Here, we will assume that a non-redundant set of internal coordinates is available.
For a non-redundant set of internal coordinates, $\boldsymbol{B}$ is a $N_{\boldsymbol{s}} \times 3N_{\text{at}}$ rectangular matrix. Thus, the transformation between the $\boldsymbol{x}$ and $\boldsymbol{s}$ sets of coordinates not invertible, making the conversion of the force-field not trivial. To obtain a square $\boldsymbol{B}$ matrix, it is necessary to include the coordinates describing the overall rotations and translations. Following the procedure proposed by Page and co-workers,[78] the three coordinates are obtained from the expression of an infinitesimal displacement of the center of mass of the molecule:

$$dx_{\text{CM}} = \sum_{a=1}^{N_{\text{at}}} M_a dx_a \qquad dy_{\text{CM}} = \sum_{a=1}^{N_{\text{at}}} M_a dy_a \qquad dz_{\text{CM}} = \sum_{a=1}^{N_{\text{at}}} M_a dz_a \tag{2.32}$$

Analogously, infinitesimal overall rotation of the molecule can be expressed as,

$$\begin{aligned} ds^x_{\text{rot}} &= \sum_{a=1}^{N_{\text{at}}} \left(\sqrt{M_a} y_a dz_a - z_a dy_a\right) \\ ds^y_{\text{rot}} &= \sum_{a=1}^{N_{\text{at}}} \left(\sqrt{M_a} z_a dx_a - x_a dz_a\right) \\ ds^z_{\text{rot}} &= \sum_{a=1}^{N_{\text{at}}} \left(\sqrt{M_a} x_a dy_a - y_a dx_a\right) \end{aligned} \tag{2.33}$$

The coordinates given in Eqs. 2.32 and 2.33 are expressed as infinitesimal, and thus the calculation of the derivatives with respect to the Cartesian coordinates (i.e. of the elements of $\boldsymbol{B}$) is trivial. The transformation between the

force constants in Cartesian and internal coordinates is obtained by substituting in the Taylor expansion given in Eq. 2.16 the expression given in Eq. 2.30. The relation between the gradient vector and the Hessian matrix in the two representations is the following,[112,113]

$$\begin{aligned} \boldsymbol{g_x} &= \boldsymbol{B_F}^T \boldsymbol{g_s} \\ \boldsymbol{H_x} &= \boldsymbol{B_F}^T \boldsymbol{H_s} \boldsymbol{B_F} + \boldsymbol{B'_F}^T \boldsymbol{g_s} \end{aligned} \tag{2.34}$$

where the multiplication between the $\boldsymbol{B'}$ tensor and the gradient in internal coordinates $\boldsymbol{g_s}$ is performed by contracting the index associated to the internal coordinate set (i in Eq. 2.31). Furthermore, the F subscript indicates that the $\boldsymbol{B}$ matrix is computed from the full, $3N_{\text{at}}$-dimensional set of coordinates, thus including rotational and translational coordinates. We note that no truncation of the Taylor expansion given in Eq. 2.30 is assumed in the derivation of Eq. 2.34. The conversion of the gradient is equivalent to keeping only the first-order term in Eq. 2.30, thus neglecting the non-linearity in the transformation between the two sets of coordinates. This is however not the case for the Hessian matrix, since, by keeping only first order terms, only the first term of Eq. 2.34 would be obtained. The second term, which arises from the non-linearity of the coordinates system, is null only at stationary points of the PES, where $\boldsymbol{g_s} = \boldsymbol{0}$. In Ref. 113 it has been noted that this additional, gradient term makes the derivatives, as computed with Eq. 2.34, non-covariant. However, it has been shown[112,114,115] that the inclusion of this second term improves the description of the PES, and thus Eq. 2.34 will be employed in the present work.
It is worth noting that, in electronic structure calculations, the gradient and the Hessian are, in most cases, computed in Cartesian coordinates, and then converted to the internal representation. Thus, the inverse of Eq. 2.34 is used in practice:

$$\begin{aligned} \boldsymbol{g_s} &= \{\boldsymbol{B_F}^T\}^{-1} \boldsymbol{g_s} \\ \boldsymbol{H_s} &= \{\boldsymbol{B_F}^T\}^{-1} \left[\boldsymbol{H_x} - \boldsymbol{B'_F}^T \{\boldsymbol{B_F}^T\}^{-1} \boldsymbol{g_x} \right] \boldsymbol{B_F}^{-1} \end{aligned} \tag{2.35}$$

As stated above, in the present thesis we will focus mainly on molecular vibrations, thus neglecting any effect associated to the overall translations and rotations of the molecule. For this reason, it is more suitable to express Eq. 2.34 using the non-redundant $\boldsymbol{B}$ matrix, with dimensions $N_{\boldsymbol{s}} \times 3N_{\text{at}}$, referred in the following as $\boldsymbol{B}_{\text{NR}}$:

$$\begin{aligned} \boldsymbol{g}_{\boldsymbol{x}}^{\text{NR}} &= \boldsymbol{B}_{\text{NR}}{}^T \boldsymbol{g_s} \\ \boldsymbol{H}_{\boldsymbol{x}}^{\text{NR}} &= \boldsymbol{B}_{\text{NR}}{}^T \boldsymbol{H_s} \boldsymbol{B}_{\text{NR}} + \boldsymbol{B'}_{\text{NR}}{}^T \boldsymbol{g_s} \end{aligned} \tag{2.36}$$

where non-redundant quantities are labeled with a NR superscript. As noted in Ref. 113, the Cartesian Hessian matrices obtained from Eqs. 2.34 and 2.36 differ when evaluated in a non-stationary point. Indeed, at non-stationary points, the Hessian matrix given in Eq. 2.34 has only 3 null eigenvalues, meaning that its rank is $3N_{\text{at}} - 3$, since overall rotations couple with the vibrational motion, and thus have non-null harmonic frequency. However,

since both $\boldsymbol{B}_{\mathrm{NR}}$ and $\boldsymbol{H}_{\boldsymbol{s}}$ have rank $3N_{\mathrm{at}} - 6$, the Hessian matrix in Cartesian coordinates computed with Eq. 2.36 will have rank $3N_{\mathrm{at}} - 6$ too, thus differing from the one in Eq. 2.34. The reason of this difference is that, in practice, in Eq. 2.36 rotations and translations are implicitly removed by projection. The relations given in Eq. 2.36 can be inverted using the Moore-Penrose pseudoinverse of $\{\boldsymbol{B}_{\mathrm{NR}}{}^{T}\}^{+}$ of $\boldsymbol{B}_{\mathrm{NR}}^{T}$, defined as:[113,116]

$$\{\boldsymbol{B}_{\mathrm{NR}}{}^{T}\}^{+} = \left(\boldsymbol{B}_{\mathrm{NR}}\boldsymbol{U}\boldsymbol{B}_{\mathrm{NR}}{}^{T}\right)^{-1}\boldsymbol{B}_{\mathrm{NR}}\boldsymbol{U} \tag{2.37}$$

where $\boldsymbol{U}$ is an arbitrary, $3N_{\mathrm{at}} \times 3N_{\mathrm{at}}$ diagonal matrix and $\{\boldsymbol{B}_{\mathrm{NR}}{}^{T}\}^{+}\boldsymbol{B}_{\mathrm{NR}}^{T} = \boldsymbol{I}$. The inverse of Eq. 2.36 reads,

$$\begin{aligned}\boldsymbol{g}_{\boldsymbol{s}} &= \{\boldsymbol{B}_{\mathrm{NR}}{}^{T}\}^{+}\boldsymbol{g}_{\boldsymbol{x}}{}^{\mathrm{NR}} \\ \boldsymbol{H}_{\boldsymbol{s}} &= \{\boldsymbol{B}_{\mathrm{NR}}{}^{T}\}^{+}\left(\boldsymbol{H}_{\boldsymbol{x}}{}^{\mathrm{NR}} - \boldsymbol{B}'_{\mathrm{NR}}{}^{T}\{\boldsymbol{B}_{\mathrm{NR}}{}^{T}\}^{+}\boldsymbol{g}_{\boldsymbol{x}}^{\mathrm{NR}}\right)\boldsymbol{B}_{\mathrm{NR}}{}^{+}\end{aligned} \tag{2.38}$$

Again, the gradient and Hessian computed from Eq. 2.35 are different from the ones given in Eq. 2.38, since all the quantities are $N_{\boldsymbol{s}}$-dimensional. However, the latter formulation is better suited for the study of vibrational problems, since provides an Hessian with the correct rank (N_{vib}) even for non-stationary points. On the contrary, Eq. 2.35 defines an Hessian, where residual vibro-rotational couplings are present. However, to compute $\boldsymbol{g}_{\boldsymbol{s}}$ and $\boldsymbol{H}_{\boldsymbol{s}}$ from Eq. 2.38, the projected quantities $\bar{\boldsymbol{g}}_{\boldsymbol{x}}$ and $\bar{\boldsymbol{H}}_{\boldsymbol{x}}$ must be obtained from their non-projected counterpart, $\boldsymbol{g}_{\boldsymbol{x}}$ and $\boldsymbol{H}_{\boldsymbol{x}}$. This step can be done by noting that the former matrices contain the pure vibrational contributions of the latter. Using the theory of the Moore-Penrose pseudoinverse,[116] it is possible to prove that the projector onto the rank of $\boldsymbol{B}_{\mathrm{NR}}$ can be expressed as,

$$\boldsymbol{P}_{\mathrm{NR}} = \boldsymbol{B}_{\mathrm{NR}}{}^{+}\boldsymbol{B}_{\mathrm{NR}} \tag{2.39}$$

Using the definition given in the previous equation, the following relations are obtained:[113,117]

$$\begin{aligned}\boldsymbol{g}_{\boldsymbol{x}}{}^{\mathrm{NR}} &= \boldsymbol{P}_{\mathrm{NR}}{}^{T}\boldsymbol{g}_{\boldsymbol{x}} \\ \boldsymbol{H}_{\boldsymbol{x}}{}^{\mathrm{NR}} &= \boldsymbol{P}_{\mathrm{NR}}{}^{T}\boldsymbol{H}_{\boldsymbol{x}}\boldsymbol{P}_{\mathrm{NR}}\end{aligned} \tag{2.40}$$

Thus, the gradient and the Hessian in internal coordinates are obtained by combining Eqs. 2.38 and 2.40. To conclude, we note that several approaches for computing the force constants by using directly redundant internal coordinates (such as PICs), have been proposed.[115,118,119] The main advantage of those approaches is that the extraction of a non-redundant subset of internal coordinates is avoided, therefore making the simulations on systems characterized by a complex topology simpler. However, a major drawback is that a force field in redundant internal coordinates contains more parameter than the one in Cartesian coordinates. Thus, the transformation of the force-field from the latter to the former representation is not unique, and prone to arbitrariness. Again, this issue is usually solved by employing the Moore-Penrose pseudoinverse of the redundant $\boldsymbol{B}$ matrix ($\boldsymbol{B}_{\mathrm{R}}$) to perform the transformation given in Eq. 2.38. However, the relations reported in Eq. 2.38 are

exact, for full-rank matrices (i.e. the rows are linearly independent) as $\boldsymbol{B}_{\mathrm{NR}}$, thus ${\boldsymbol{B}_{\mathrm{NR}}}^{+}\boldsymbol{B}_{\mathrm{NR}} = \boldsymbol{I}$. On the contrary, $\boldsymbol{B}_{\mathrm{R}}$ is not full-rank if calculated for a redundant set of coordinates, since linear dependences are present amongst its rows by definition, and in those cases ${\boldsymbol{B}_{\mathrm{NR}}}^{+}\boldsymbol{B}_{\mathrm{NR}} \neq \boldsymbol{I}$. However, the Moore-Penrose pseudoinverse provides the best approximation for the inverse matrix, in a least-squares sense. As has been discussed in detail in Ref. 120, a direct use of redundant coordinates is equivalent to extracting the non-redundant set of coordinates by Singular Value Decomposition (SVD) of $\boldsymbol{B}_{\mathrm{R}}$. For geometry optimizations, where the non-redundant set of coordinates is computed at each step, there is a computational advantage in the use of redundant set of coordinates.[112,115] However, for spectroscopy, where a single geometry is relevant, there is no advantage in using directly redundant internal coordinates. For this reason, in the following, all the theoretical derivations will hold for a non-redundant set of internal coordinates.
The theory developed up to this point supports also the definition of harmonic PESs in internal coordinates. However, the use of curvilinear coordinates modifies the definition for the kinetic energy operator $\mathcal{T}$. The correct expression has been widely discussed in the literature,[121,122] with its most common form being,

$$\mathcal{T} = -\frac{\hbar^2}{2}\sum_{i,j=1}^{N_{\boldsymbol{s}}} g^{1/4}\frac{\partial}{\partial s_i}g^{-1/2}G_{ij}\frac{\partial}{\partial s_j}g^{1/4} \tag{2.41}$$

where Wilson $\boldsymbol{G}$ matrix is defined as follows,

$$G_{ij} = \sum_{a=1}^{N_{\mathrm{at}}}\sum_{\tau=x,y,z}\frac{1}{M_a}\left(\frac{\partial s_i}{\partial x_{a\tau}}\right)_{eq}\left(\frac{\partial s_j}{\partial x_{a\tau}}\right)_{eq} = \sum_{a=1}^{N_{\mathrm{at}}}\sum_{\tau=x,y,z}\frac{B_{ia\tau}B_{ja\tau}}{M_a} \tag{2.42}$$

and $g = \det(\boldsymbol{G})$. The Wilson $\boldsymbol{G}$ matrix is a function of $\boldsymbol{s}$, and thus the expansion of the derivatives in Eq. 2.41 would lead to terms involving the first and second derivatives of $\boldsymbol{G}$. However, as a first approximation, the dependence of $\boldsymbol{G}$ on $\boldsymbol{s}$ can be neglected. Under this approximation, g is constant and $\mathbf{G}$ can be approximated with its value at the reference geometry (usually the equilibrium one). In this case, Eq. 2.41 becomes,

$$\mathcal{T} = -\frac{\hbar^2}{2}\sum_{i,j=1}^{N} G_{ij}\frac{\partial^2}{\partial s_i \partial s_j} \tag{2.43}$$

$\boldsymbol{G}$ and $\boldsymbol{H_s}$, also known as as Wilson $\boldsymbol{F}$ matrix, are the two quantities needed to obtain harmonic frequencies and normal modes in terms of curvilinear coordinates through the so-called Wilson GF method.[18] As shown by Wilson,[18] the normal modes in internal coordinates are the eigenvectors of the $\boldsymbol{GH_s}$ matrix:

$$\boldsymbol{GH_sL_s} = \boldsymbol{L_s\Lambda} \tag{2.44}$$

At variance with the Cartesian coordinate case, the normal modes obtained from internal coordinates are eigenvectors of a non-symmetric matrix, and

therefore are not orthogonal. However, as proven by Miyazawa[123], it is possible to recast Eq. 2.44 in a symmetric form as,

$$\begin{aligned} \boldsymbol{G}^{1/2}\boldsymbol{G}^{1/2}\boldsymbol{H}_{\boldsymbol{s}}\boldsymbol{G}^{1/2}\boldsymbol{G}^{-1/2}\boldsymbol{L}_{\boldsymbol{s}} &= \boldsymbol{L}_{\boldsymbol{s}}\boldsymbol{\Lambda} \\ \left(\boldsymbol{G}^{1/2}\boldsymbol{H}_{\boldsymbol{s}}\boldsymbol{G}^{1/2}\right)\boldsymbol{G}^{-1/2}\boldsymbol{L}_{\boldsymbol{s}} &= \boldsymbol{G}^{-1/2}\boldsymbol{L}_{\boldsymbol{s}}\boldsymbol{\Lambda} \end{aligned} \tag{2.45}$$

Here, the columns of $\boldsymbol{G}^{-1/2}\boldsymbol{L}_{\boldsymbol{s}}$ are the eigenvectors of a symmetric matrix, namely $\boldsymbol{G}^{1/2}\boldsymbol{H}_{\boldsymbol{s}}\boldsymbol{G}^{1/2}$, and therefore are orthogonal. Thus, the orthogonality constraint for the $\boldsymbol{L}_{\boldsymbol{s}}$ reads,

$$\boldsymbol{L}_{\boldsymbol{s}}^{T}\boldsymbol{G}^{-1}\boldsymbol{L}_{\boldsymbol{s}} = \boldsymbol{I} \tag{2.46}$$

2.2.3 Selection of the non-redundant internal coordinates

The theoretical framework presented in the previous paragraph holds for a non-redundant set of internal coordinates. However, for a given molecule and molecular topology, the definition of such set is neither univocal nor straightforward. In this section, several algorithms for the definition of a non-redundant set of coordinates, already employed for geometry optimization schemes,[24] will be presented and compared.
All the algorithms that will be presented builds the non-redundant set of coordinates as linear combinations of primitive internal coordinates (PICs). In order to define unambiguously PICs, a threshold δ_{ij} must be set and two atoms i and j are connected if and only if $\left|r_i - r_j\right| \leq \delta_{ij}$. The bond connectivity defines unambiguously both valence and dihedral angles. The non-redundant set of coordinates, referred to as $\boldsymbol{s}$, can thus be expressed in terms of the PICs $\boldsymbol{s}_{\mathrm{PIC}}$ as follows:

$$s_i = \sum_{j=1}^{N_{\mathrm{PIC}}} A_{ij}\, s_{\mathrm{PIC},j} \tag{2.47}$$

The definition of matrix $\boldsymbol{A}$ changes with the algorithm used to define the non-redundant coordinates. The first method is based on the so-called delocalized internal coordinates (DICs), which are becoming the most used coordinates in geometry optimizations.[115,120] The algorithm used to generate the DICs is based on the singular value decomposition (SVD) to determine the range and the null space of $\boldsymbol{B}_{\mathrm{R}}$. The SVD of $\boldsymbol{B}_{\mathrm{R}}$ is obtained as,

$$\boldsymbol{B}_R = \boldsymbol{U}\boldsymbol{\Lambda}\boldsymbol{V}^{\dagger} \tag{2.48}$$

where $\mathbf{U}$ and $\mathbf{V}$ are $N_{\mathrm{PIC}} \times N_{\mathrm{PIC}}$ and $3N_{\mathrm{at}} \times 3N_{\mathrm{at}}$ square matrices, respectively, whereas $\boldsymbol{\Lambda}$ is a rectangular diagonal matrix (only the elements Λ_{ii} of $\boldsymbol{\Lambda}$ are different from zero). The number of non-null elements of $\boldsymbol{\Lambda}$ is equal to the rank of $\mathbf{B}$, which is, in turn, equal to the number of vibrational degrees of freedom of the molecule for a complete set of internal coordinates. From the definition of SVD[124] it follows that the columns of $\mathbf{U}$ corresponding to non-zero diagonal elements of $\boldsymbol{\Lambda}$ span the rank of $\mathbf{B}$. Thus, DICs are defined as,

$$s_{\mathrm{DIC},i} = \sum_{j=1}^{N_{\mathrm{PIC}}} U'_{ij} s_{\mathrm{PIC},j} \tag{2.49}$$

where $\mathbf{U}'$ is a $N_{\mathrm{vib}} \times N_{\mathrm{PIC}}$ matrix containing only the columns of $\mathbf{U}$ corresponding to non-null singular values. This set of internal coordinates has been introduced by Baker and co-workers[120] and is usually referred to as delocalized, since it includes linear combinations of internal coordinates of different types localized on different portions of the molecule. When applied to geometry optimization algorithms, DICs are nearly equivalent to redundant internal coordinates. In fact, when geometry optimizations are performed using redundant internal coordinates, the pseudo-inverse of the redundant Wilson matrix $\mathbf{B}$ is calculated by means of SVD for each step of the optimization procedure, and this is equivalent to the calculation of DICs at every step. Conversely, for spectroscopy, DICs are calculated only once, taking a single geometry (usually the equilibrium structure of an electronic state) as a reference.

A major limitation of DICs is that every coordinate is treated on the same footing as the others. For this reason, different types of coordinates will be combined in the linear combination defining the non-redundant set (see Eq. 2.47). Different methods have been proposed to avoid the mixing of coordinates of different types. Amongst them, let us recall the so-called weighted internal coordinates (WICs), introduced by Lindh[125], where the redundant Wilson matrix $\boldsymbol{B}_{\mathrm{R}}$ is scaled by a square, $N_{\mathrm{PIC}} \times N_{\mathrm{PIC}}$ weight matrix $\boldsymbol{W}$ before identifying the redundancies. Thus, the non-redundant set of coordinates is obtained from the SVD of $\boldsymbol{W}\boldsymbol{B}_{\mathrm{R}}$. The final set of non-redundant internal coordinates changes with $\boldsymbol{W}$ since PICs associated to elements of $\boldsymbol{W}$ of significantly different orders of magnitude are not mixed. Even if in the original formulation of Lindh, $\boldsymbol{W}$ is an approximation of the exact energy Hessian of the molecule,[126] a simpler but still effective procedure has been proposed more recently by Swart,[127] where $\boldsymbol{W}$ is a diagonal matrix whose elements are expressed in terms of the bond order ρ_{ab} of the atoms involved in the internal coordinate,

$$\rho_{ab} = e^{-[(r_{ab}/C_{ab})-1]} \tag{2.50}$$

where r_{ab} is the distance between the a-th and the b-th atom and C_{ab} is the sum of their covalent radii. Then, the diagonal elements of $\boldsymbol{W}$ are calculated using the following relations,

$$\begin{aligned} W_{\mathrm{bond}} &= \rho_{ab} \\ W_{\mathrm{angle}} &= (\rho_{ab}\rho_{bc})^{1/2} \left[f + (1-f)\sin\theta_{abc}\right] \\ W_{\mathrm{dihed}} &= (\rho_{ab}\rho_{bc}\rho_{cd})^{1/2} \left[f + (1-f)\sin\theta_{abc}\right] \left[f + (1-f)\sin\theta_{bcd}\right] \end{aligned} \tag{2.51}$$

where the first expression given in Eq. 2.51 is used for each bond between atoms a and b, the second one is used for each angle between atoms a, b and

c, where b is the central atom, and the third equation is used for each dihedral angle between atoms a, b, c, d, where the bond between atoms b and c is the central bond. f is a fixed parameter, set to 0.12 in the original work of Swart.[127] For the sake of completeness, let us recall that using WICs, a smooth delocalization of the internal coordinates is obtained. The mixing between coordinates of different types cannot be minimized by calculating the SVD of $\boldsymbol{B}_{\mathrm{R}}$ separately for different types of coordinates, since this procedure may produce an incorrect number of non redundant internal coordinates.[128] This happens, for example, if the redundancies couple different types of PICs, such as for molecules containing cyclic structures.
Both DICs and WICs give the correct number of non-redundant internal coordinates, except when separate, non-bonded fragments are present in the system under investigation. However, in this case, for each pair of fragments a bond between the two nearest atoms can be added to overcome this problem.
Even if the use of WICs limits the mixing of PICs of different types, the non-redundant internal coordinates may be still delocalized on different portions of the molecule. This drawback may be overcome by employing the so-called Natural Internal Coordinates (NICs), introduced by Pulay.[129,130] NICs are built as linear combinations of PICs localized on the same atom, built based on the local molecular symmetry. Even if NICs minimize the couplings between different coordinates both at the harmonic and at the anharmonic level, they are ill-suited for a general implementation since they are not defined for every atom type and for each molecular topology. In the following, a generalized procedure to build Natural Internal Coordinates will be presented, based on the procedure recently proposed by Arnim and coworkers[131] and supporting any molecular topology. We will refer to this set of coordinates as generalized natural internal coordinates (GNICs). Unlike the original formulation of Arnim,[131] here the PICs are divided in the following subsets:

1. all bond lengths are included in the same set
2. for each non-terminal atom, a separate set is built, including all the valence angles (and possibly out-of-planes) centered on this atom
3. for each bond between non-terminal atoms, a separate set is built including all the dihedral angles centered around this bond

We will refer to the $\boldsymbol{B}$ matrix of the i-th set of PICs as $\boldsymbol{B}^{(i)}$, and to its SVD as $\boldsymbol{U}^{(i)}\boldsymbol{\Lambda}^{(i)}\boldsymbol{V}^{(i),\dagger}$. In the previous expression, $\boldsymbol{B}^{(i)}$ is $N^{(i)} \times 3N_{\mathrm{at}}$ matrix, $N^{(i)}$ is the number of primitive internal coordinates of the i-th group, while $\boldsymbol{U}^{(i)}$ and $\boldsymbol{V}^{(i)}$ are $N^{(i)} \times N^{(i)}$ and $3N_{\mathrm{at}} \times 3N_{\mathrm{at}}$ orthogonal matrices, respectively. The complete procedure to generate GNICs is given below:

- the first set of internal coordinates, including all bond lengths, is built, and the SVD of the corresponding Wilson matrix $\mathbf{B}^{(1)}$ is computed. If this set of coordinates is non-redundant (every singular value is non-null) the PICs of the first group $\boldsymbol{s}^{(1)}$ are included in the GNICs set. On

the other hand, if some of the singular values are null, a non-redundant subset $\boldsymbol{s}^{(1)'}$ can be defined as follows:

$$\boldsymbol{s}^{(1)'} = \boldsymbol{U}^{(1)'}\boldsymbol{s}^{(1)} \tag{2.52}$$

where $\boldsymbol{U}^{(1)'}$ is built from $\boldsymbol{U}^{(1)}$ by neglecting the rows corresponding to non-zero singular values.

- the coordinates of the second set $\boldsymbol{s}^{(2)}$ must be orthogonalized to $\mathbf{s}^{(1)'}$ before identifying the redundancies, otherwise the final number of non-redundant coordinates will be incorrect. As in the original formulation of Arnim,[131] a Gram-Schmidt procedure is employed here to perform this projection step. Democratic orthogonalization schemes, like the one derived from the SVD, are not appealing in this context, since they might mix coordinates of $\boldsymbol{s}^{(1)'}$ and $\boldsymbol{s}^{(2)}$, whereas the use of sequential algorithms, like the Gram-Schmidt procedure, avoids this problem. The Wilson $\boldsymbol{B}$ matrix for the coordinates of the second set, after the orthogonalization, (referred to as $\boldsymbol{B}^{(2)}_{\text{ort}}$), can be expressed as follows:

$$\boldsymbol{B}^{(2)}_{\text{ort},i} = \boldsymbol{B}^{(2)}_{i} - \sum_{j=1}^{N^{(1)}} \frac{\{\boldsymbol{B}^{(2)}_{i}\}^{T}\boldsymbol{B}^{(1)}_{\text{ort},j}}{\{\boldsymbol{B}^{(1)}_{\text{ort},j}\}^{T}\boldsymbol{B}^{(1)}_{\text{ort},j}}\,\boldsymbol{B}^{(1)}_{\text{ort},j} \tag{2.53}$$

where $\boldsymbol{B}^{(1)}_{\text{ort},j}$ is the j-th row of $\boldsymbol{B}^{(1)}_{\text{ort}}$ and $\boldsymbol{B}^{(2)}_{i}$ is the i-th row of $\boldsymbol{B}^{(2)}$. Even if Eq. 2.53 holds only for the linearized approximation of the internal coordinates, it can be used to define the orthogonalized coordinates of the second set $\boldsymbol{s}^{(2)}_{\text{ort}}$:

$$s^{(2)}_{\text{ort},i} = s^{(2)}_{i} - \sum_{j=1}^{N^{(1)}} \frac{\{\boldsymbol{B}^{(2)}_{i}\}^{T}\boldsymbol{B}^{(1)}_{\text{ort},j}}{\{\boldsymbol{B}^{(1)}_{\text{ort},j}\}^{T}\boldsymbol{B}^{(1)}_{\text{ort},j}}\,s^{(1)}_{j} \tag{2.54}$$

Finally, the SVD of $\boldsymbol{B}^{(2)}_{\text{ort}}$ is used to define the non-redundant subset of coordinates $s^{(2)'}$ as,

$$\begin{aligned} s^{(2)'}_{j} &= \sum_{i=1}^{N^{(2)}} U^{(2)'}_{ij}\, s^{(2)}_{i,\text{ort}} \\ &= \sum_{i=1}^{N^{(2)}} U^{(2)'}_{ij} \left(s^{(2)}_{i} - \sum_{k=1}^{N^{(1)}} U_{ij} \frac{\{\boldsymbol{B}^{(2)}_{i}\}^{T}\boldsymbol{B}^{(1)}_{\text{ort},k}}{\{\boldsymbol{B}^{(1)}_{\text{ort},k}\}^{T}\boldsymbol{B}^{(1)}_{\text{ort},k}}\, s^{(1)}_{k} \right) \end{aligned} \tag{2.55}$$

This equation shows that the $\boldsymbol{s}^{(2)'}$ coordinates are linear combinations of $\boldsymbol{s}^{(2)}$ and $\boldsymbol{s}^{(1)'}$. Since the $\boldsymbol{s}^{(1)'}$ coordinates are already included in the definition of the non-redundant coordinates, their contribution can be

safely neglected and the following definition of $\boldsymbol{s}^{(2)'}$ can be used:

$$s_j^{(2)'} = \sum_{i=1}^{N^{(2)}} U_{ij}^{(2)'} s_i^{(2)} \tag{2.56}$$

- the procedure outlined above can be used to identify the redundancies in all subsequent sets of coordinates. Each set of coordinates $\boldsymbol{s}^{(m)}$ is orthogonalized with respect to the previous ones ($\boldsymbol{s}_{\text{ort}}^{(k)}$, with $k < m$) and then the SVD is performed. At the end, the components of $\boldsymbol{s}_{\text{ort}}^{(k)}$ are neglected in the definition of $\mathbf{s}^{(m)}$, in order to enforce the localization of the coordinates.

The main features of the procedure outlined above can be summarized in the following way. First of all, the algorithm will give the correct number of internal coordinates for every molecular topology, thanks to the orthogonalization step, except for molecules containing non-bonded fragments. Similarly to DICs and WICs, additional coordinates can be added *a-posteriori* to describe the relative motion of fragments. Anyway, in most cases, increasing the threshold used to select the bonded pairs of atoms is sufficient to avoid the presence of non-bonded fragments, and the procedure described above can be safely used. One of the main advantage of GNICs over the other sets of non-redundant internal coordinates is their flexibility. In fact, the procedure presented above can be easily modified to include special internal coordinates, that are known to describe efficiently a particular vibration, and thus should be included in the non-redundant set of coordinates. For example, ring puckering coordinates, which are linear combinations of dihedral and valence angles inside a ring structure, θ_k and γ_k respectively, and are known to provide an accurate description of ring deformations. The definition of those coordinates, $s_{\theta,m}$ and $s_{\gamma,m}$, is given below[129,130]

$$\begin{aligned} s_{\theta,m} &= \sum_{k=1}^{n} \cos\left(\frac{2\pi(k-1)m}{n}\right) \theta_k \\ s_{\gamma,m} &= \sum_{k=1}^{n} \cos\left(\frac{2\pi(k-1)m}{n}\right) \gamma_k \end{aligned} \tag{2.57}$$

where n is the number of atoms of the ring and m runs from 2 to $n/2$ (the integer part of $n/2$ if n is even). Even if more complex definitions of ring-puckering coordinates have been proposed,[132] they will not be used in the following since the associated Wilson matrix $\boldsymbol{B}_{\text{R}}$ diverges for planar cyclic structures.[133,134] In order to include the coordinates defined in Eq. 2.57 in the GNICs set, introducing an additional set of internal coordinates containing them suffices. The procedure outlined above can be applied, starting from this set, and then by performing the Gram-Schmidt orthogonalization for every other set of coordinates, including in this case also the bond lengths.
Let us finally recall that the so-called Z-matrix coordinates (ZICs) are still also widely used, since this set is non-redundant by definition. However, as already pointed out for geometry optimizations,[135] ZICs are ill-suited for

a general and robust implementation. In fact, in the presence of complex molecular topologies, like fused rings of bicyclic structures, it is not straightforward to define a non-redundant Z-matrix with the correct number of parameters. Even worse, if standard Z-matrices are used, unreliable results are obtained. As a consequence, ZICs will not be considered in the following.

2.2.4 Special cases: out-of-plane and linear angles

The procedure outlined above to build PICs must be modified in presence of particular molecular arrangements in order to reliably build any kind of non-redundant set of coordinates (DICs, WICs and GNICs). For example, for planar tricoordinated centers, *ad-hoc* out-of-plane coordinates can be profitably added to describe deformations from the planar geometry better. This coordinate is defined, as the angle between one of the bonds, and the plane defined by the other two bonds[18,26] The number of out-of-plane coordinates to add, as well as the bond used to define them, changes with the number of terminal atoms bonded to the tri-coordinated center based on the following rules:

1. in presence of one terminal atom, a single out-of-plane coordinate is added, defined from the bond involving the terminal atom. When two terminal atoms are present, the out-of-plane coordinate defined by the bond involving the third, non-terminal atom, is added.

2. if no terminal atoms are present, a symmetric, linear combination of the three out-of-plane coordinates is included.

3. if the tricoordinated center is part of a ring, the out-of-plane coordinates defined by the bond, which is not part of the ring, is added. The same procedure is adopted when three terminal centers are present (as, for example, in ammonia)

Let us recall that usually, even if the out-of-plane coordinates are not added, the algorithm used to generate DICs and WICs will produce the correct number of non-redundant coordinates. However, the vibrations involving out-of-plane motions would be described in terms of linear combinations of valence and dihedral angles, increasing the magnitude of the coupling between different internal coordinates.
The procedure outlined above to build a non-redundant set of internal coordinates can be further generalized in order to support also linear chains. Let us consider, for example, a generic situation sketched in the left panel of Fig. 2.1, where the collinear atoms are identified as A, B and D. Using the procedure outlined above, the angle $\widehat{\mathrm{ABD}}$, as well as all dihedral angles R_i–A–B–D and A–B–D–L_i (where i is an integer number ≤ 3) are included in the definition of the PICs. However, as already pointed out,[136] the values of $\boldsymbol{B}$ and $\boldsymbol{B}'$ for linear angles diverge, and therefore the numerical stability of the overall procedure is poor. To overcome this limitation, the A–B–D angle is substituted by two appropriate linear bending coordinates, whose definition can be found, for example, in refs.[18,26] Furthermore, the dihedral angles

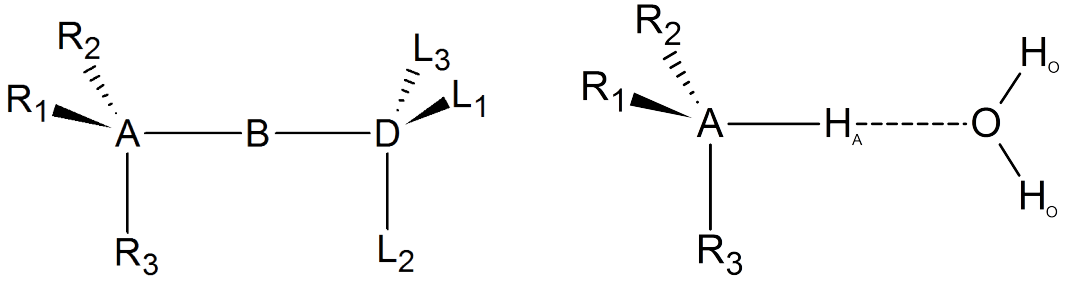

FIGURE 2.1: Upper panel: graphical representation of linear structures within a molecule. The three collinear atoms are labeled as A, B and D, and the atoms bonded to A and D are indicated as L_i and R_i, respectively, where i is an integer number. Lower panel: graphical representation of an hydrogen bond between the hydrogen atom bonded to the generic atom A and a water molecule. For the sake of clarity, the hydrogen bonded to A has been labeled as H_A, while the hydrogen atoms of the water as H_O.

involving the A–B–D chain are removed, and all dihedrals R_i–A–C–L_j are added.

By using this protocol, the Wilson $\boldsymbol{B}$ matrix and its derivatives can be safely computed, and the final number of non-redundant internal coordinates is correct. The computational protocol can be further modified to improve the description of linear angles, where the central atom (B in the left panel of Fig. 2.1) is a light atom, as occurs, for instance, in hydrogen bonds. In fact, as will be discussed in the following sections, for those systems, an incorrect definition of the internal coordinates involving the linear chain may lead to a large coupling between internal coordinates. For the sake of simplicity, let us consider the situation reported in the right panel of Fig. 2.1, where the linear chain involves an hydrogen bond with a water molecule. Despite the specificity of the case, the discussion can be easily extended to other hydrogen-bond patterns, or even other light atoms. The main limitation of the definition of PICs outlined above for linear chains lies in the two linear bending coordinates. In fact, the definition of the Wilson $\boldsymbol{G}$ matrix, which is central to the calculation of the normal modes in internal coordinates, changes significantly even for small displacements from the linear arrangement, and this introduces the unwanted couplings. In order to overcome this problem, the molecular topology can be modified by substituting the hydrogen bond with the A-O bond. Then, PICs are built following the strategy outlined above, without including the H_A–A–O angle, as well as the two H_O–O–A–H_A dihedral angles. This procedure can be used also when the linear angle does not correspond to an hydrogen bond. For example, if a valence angle is linear at the equilibrium geometry of only one electronic state, the linear bending coordinates should not be used, since they are ill-suited for the description of the electronic state, where the linear configuration is not present. On the other hand, by using the second procedure, only standard valence coordinates are introduced.

2.3 The diabatic representation

For most of the applications presented in this thesis, the BO approximation will be assumed to stand, and thus Eq. 2.6 will be employed. Only in Chapter 4, the impact of non-adiabatic couplings on the rate of vibronic effects will be analyzed. Without going into details, which will be addressed in the next chapters, it is sufficient noting here that, for most applications, the BO Hamiltonian is taken as a reference, and non-adiabatic effects are included using perturbative approaches. While this approach has proven to be reliable when the separation between the PESs is large compared to the vibrational energies, perturbation theory can become ill-suited as the PESs become closer in energies.

An alternative approach for the description of the electronic states is the so-called diabatic representation. The diabatic electronic states $\phi_{\underline{m}}^{\text{dia}}$ are obtained by applying a linear transformation of the adiabatic ones (indicated in the following as $\phi_{\underline{m}}^{\text{adia}}$). This transformation is chosen to minimize the non-adiabatic couplings $\Delta\mathcal{T}_{\underline{n},\underline{m}}$ coupling term of Eq. 2.5. As a consequence, this transformation introduces couplings between different electronic states in the potential operator, which however varies more smoothly with the nuclear geometry, even for electronic states that are close in energy. For two electronic states, the transformation from the adiabatic to the diabatic representation can be expressed as a rotation by an angle θ, as follows:

$$\begin{pmatrix} \phi_{\underline{m}}^{\text{dia}} \\ \phi_{\underline{n}}^{\text{dia}} \end{pmatrix} = \begin{pmatrix} \cos\theta & \sin\theta \\ -\sin\theta & \cos\theta \end{pmatrix} \begin{pmatrix} \phi_{\underline{m}}^{\text{adia}} \\ \phi_{\underline{n}}^{\text{adia}} \end{pmatrix} \tag{2.58}$$

As a consequence of this rotation of the electronic states, the adiabatic potential energy surfaces $E_{\underline{m}}^{\text{ele}}$ and $E_{\underline{n}}^{\text{ele}}$, as well as the non-adiabatic couplings change. The diabatic representation is defined as the rotation that makes the non-adiabatic couplings null, meaning that,

$$\langle\, \phi_{\underline{m}}^{\text{dia}} \mid \frac{\partial}{\partial R_a} \mid \phi_{\underline{n}}^{\text{dia}} \,\rangle = 0 \tag{2.59}$$

The representation in which the previous relation is satisfied exactly is usually referred to as the exact diabatic representation. However, as proven by Truhlar,[137] such representation does not exist, except for very simple cases, such as for electronic states of diatomic molecules of different symmetry. Thus, an approximate diabatic representation is usually employed, where the couplings in Eq. 2.59 are not null, but only minimized.

Several algorithms have been proposed in the literature for building approximate diabatic states. In the most direct approaches, the matrix with the couplings $\mathcal{T}_{\underline{m},\underline{n}}$ is computed in the basis of the adiabatic states, and the rotation matrix is determined by explicitly minimizing those couplings. A strong limitation of such approaches[138,139] is the necessity of computing non-adiabatic couplings, which is far from being straightforward for most electronic structure approaches.[101,140]

Most diabatization schemes developed over the last years avoid the calculation of the matrix elements of the non-adiabatic coupling operator, and build

the diabatic basis on other quantities, such as configuration interaction (CI) coefficients or molecular properties, and the diabatic character of the basis is then verified only *a-posteriori*. For example, diabatization schemes based on the configurational uniformity[141,142,143] use the CI expansion coefficients to build the diabatic transformation. In fact, it is known that the shape of diabatic state varies smoothly by changing the nuclear coordinates. This means, in practice, that, if the diabatic states are expressed in the CI basis, the expansion coefficients are expected to vary smoothly along with the nuclear displacements. As discussed, for example, in Ref.[141], this property can be expressed in a more rigorous way by defining the diabatic transformation as the one which diagonalizes the overlap matrix $\boldsymbol{S}$ in the CI basis.
More recently, another class of approaches has been introduced, where diabatic states are determined based on molecular properties, such as the electric dipole moment. Those methods include the Werner-Meyer[144] and the generalized Mulliken-Hush (GMH)[145] schemes, that have been recently generalized to multiple electronic states with the Boys[146,147,148] localization algorithm. In the Boys algorithm, the diabatic states are determined by maximizing the following functional:

$$f_{\text{Boys}} = \sum_{\underline{m},\underline{n}=1}^{M} |\langle \phi_{\underline{m}} \mid \boldsymbol{\mu} \mid \phi_{\underline{m}} \rangle - \langle \phi_{\underline{n}} \mid \boldsymbol{\mu} \mid \phi_{\underline{n}} \rangle|^2 \tag{2.60}$$

where the sum over M includes all the states to be diabatized. It is clear that the maximization of the functional given in Eq. 2.60 leads to states, with centers of charge well separated. Thus, as has been already noticed, the previous scheme is efficient in describing electronic excitation transfer (EET) processes, where excited states are well localized on different portions of the molecule. However, even if the Boys diabatization scheme has been applied also to the modeling of phenomena other than EET,[147] it has been shown to fail for states characterized by a weak charge separation. In those cases, an additional re-diagonalization step is required to obtain quasi-diabatic states.[146] For this reason, the Boys localization scheme has been recently extended by Truhlar and co-workers to the dipole-quadrupole (DQ)[149] and dipole-quadrupole-potential (DQΦ) approaches. In DQ and DQΦ, both electric dipole and electric quadrupole moments, together with the electrostatic potential for the latter, are used to build the diabatic states. In this way, even states characterized by weak charge separation can be efficiently diabatized. In the DQΦ approach, the following functional is maximized:

$$\begin{aligned} f_{\text{DQ}\Phi} = \sum_{\underline{m}=1}^{M} \Big[&|\langle \phi_{\underline{m}} \mid \boldsymbol{\mu} \mid \phi_{\underline{m}} \rangle|^2 + \alpha \, |\text{Tr}\left(\langle \phi_{\underline{m}} \mid \boldsymbol{\Theta} \mid \phi_{\underline{m}} \rangle\right)|^2 \\ &+ \beta \, |\langle \phi_{\underline{m}} \mid \Phi\left(\boldsymbol{r}_k\right) \mid \phi_{\underline{m}} \rangle|^2 \Big] \end{aligned} \tag{2.61}$$

where $\boldsymbol{\mu}$ is the dipole moment operator, $\boldsymbol{\Theta}$ its quadrupole moment and $\Phi\left(\boldsymbol{r}_k\right)$ its electrostatic potential computed at a certain point $\boldsymbol{r}_k$ of the space. α and β are real constants that parametrize the model. The DQ model is obtained

when $\beta = 0$, and by further putting α=0 the original Boys algorithm is recovered. For two electronic states, labeled as $\underline{m}$ and $\underline{n}$, $f_{\mathrm{DQ\Phi}}$ can be rewritten as,[149]

$$\begin{aligned} f_{\mathrm{DQ\Phi}} = |\boldsymbol{\mu}_{\underline{m}\,\underline{m}}|^2 + |\boldsymbol{\mu}_{\underline{n}\,\underline{n}}|^2 + \alpha \left(\mathrm{Tr}\left(\boldsymbol{Q}_{\underline{m}\,\underline{m}}\right) + \mathrm{Tr}\left(\boldsymbol{\Theta}_{\underline{n}\,\underline{n}}\right)^2\right)^2 \\ + \beta \left(\Phi_{\underline{m}\,\underline{m}}\left(\boldsymbol{r}_k\right)^2 + \Phi_{\underline{n}\,\underline{n}}\left(\boldsymbol{r}_k\right)^2\right) \\ + A + \sqrt{\left(A^2 + B^2\right)} \cos\left(4(\theta - \gamma)\right) \end{aligned} \tag{2.62}$$

where A and B are computed from each state's dipole and quadrupole moments, as well as the associated transition moments,

$$\begin{aligned} B = & \boldsymbol{\mu}_{\underline{m}\,\underline{m}} \cdot \boldsymbol{\mu}_{\underline{m}\,\underline{n}} - \boldsymbol{\mu}_{\underline{m}\,\underline{n}} \cdot \boldsymbol{\mu}_{\underline{n}\,\underline{n}} \\ & + \beta \left(\Phi_{\underline{m}\,\underline{m}}\left(\boldsymbol{r}_k\right) \Phi_{\underline{m}\,\underline{n}}\left(\boldsymbol{r}_k\right) - \Phi_{\underline{n}\,\underline{n}}\left(\boldsymbol{r}_k\right) \Phi_{\underline{m}\,\underline{n}}\left(\boldsymbol{r}_k\right)\right) \\ & + \alpha \left[\mathrm{Tr}\left(\boldsymbol{\Theta}_{\underline{m}\,\underline{m}}\right) \mathrm{Tr}\left(\boldsymbol{\Theta}_{\underline{m}\,\underline{n}}\right) - \mathrm{Tr}\left(\boldsymbol{\Theta}_{\underline{m}\,\underline{n}}\right) \mathrm{Tr}\left(\boldsymbol{\Theta}_{\underline{n}\,\underline{n}}\right)\right] \end{aligned} \tag{2.63}$$

and,

$$\begin{aligned} A = & - \frac{|\boldsymbol{\mu}_{\underline{m}\,\underline{m}}|^2 + |\boldsymbol{\mu}_{\underline{n}\,\underline{n}}|^2}{4} + |\boldsymbol{\mu}_{\underline{m}\,\underline{n}}|^2 + \frac{\boldsymbol{\mu}_{\underline{m}\,\underline{m}} \cdot \boldsymbol{\mu}_{\underline{n}\,\underline{n}}}{2} \\ & - \beta \left[\frac{\Phi_{\underline{m}\,\underline{m}}\left(\boldsymbol{r}_k\right)^2 + \Phi_{\underline{n}\,\underline{n}}\left(\boldsymbol{r}_k\right)^2}{4} + \Phi_{\underline{m}\,\underline{n}}\left(\boldsymbol{r}_k\right)^2 + \frac{\Phi_{\underline{m}\,\underline{m}}\left(\boldsymbol{r}_k\right) \Phi_{\underline{n}\,\underline{n}}\left(\boldsymbol{r}_k\right)}{2}\right] \\ & - \alpha \left[\frac{\mathrm{Tr}\left(\boldsymbol{\Theta}_{\underline{m}\,\underline{m}}\right)^2 + \mathrm{Tr}\left(\boldsymbol{\Theta}_{\underline{n}\,\underline{n}}\right)^2}{4} - \mathrm{Tr}\left(\boldsymbol{\Theta}_{\underline{m}\,\underline{n}}\right)^2 - \frac{\mathrm{Tr}\left(\boldsymbol{\Theta}_{\underline{m}\,\underline{m}}\right) \mathrm{Tr}\left(\boldsymbol{\Theta}_{\underline{n}\,\underline{n}}\right)}{2}\right] \end{aligned} \tag{2.64}$$

with,

$$\gamma = \arctan(-B/A) \tag{2.65}$$

In Eqs. 2.63 and 2.64, the dipole moment of the electronic states $\underline{m}$ and $\underline{n}$ has been labeled as $\boldsymbol{\mu}_{\underline{m}\,\underline{m}}$ and $\boldsymbol{\mu}_{\underline{n}\,\underline{n}}$, respectively, and the transition dipole moment between them as $\boldsymbol{\mu}_{\underline{m}\,\underline{n}}$. The same notation has been used for the quadrupole moment and for the electrostatic potential.
By direct minimization of Eq. 2.62, the values of θ for which $f_{DQ\Phi}$ is maximized are,

$$\theta = \gamma, \gamma + \pi/2, \ldots \tag{2.66}$$

In this thesis, diabatic states will be build from both the DQ and DQΦ algorithms.

Chapter 3

Effective models for anharmonic vibrational spectroscopy

Due to the availability of analytical second derivatives of the electronic energy with respect to the nuclear coordinates for a wide range of electronic structure methods, the harmonic models introduced in Chapter 2 are nowadays commonly used to simulate vibrational spectra. However, these models are in most cases not reliable enough for an accurate simulation of vibrational spectra. For example, they systematically overestimate transitions frequencies, which are intrinsically anharmonic, and their reliability worsens for highly anharmonic effects. Furthermore, some phenomena, such as non-null intensity for overtones and combination bands, are not predicted at the harmonic level. Scaling schemes, in which the harmonic transition frequencies are multiplied by a scaling factor α to obtain the anharmonic frequency, have been proposed to cope with this shortcomings. Several variants of those approaches have been proposed, where either the frequencies[150] or the force constants (possibly in internal coordinates)[151] are scaled. However, scaling factors are in most cases obtained by firring fitting the scaled anharmonic frequencies to highly accurate theoretical or experimental data,[152] often intended to correct the X–H stretching region, which can lead to an overcorrection of frequencies in the mid-IR region. Furthermore, scaling factors are in most cases fitted to fundamentals transition frequencies, and thus they can hardly be extended to overtones or combination bands, as well as to the calculation of transition properties. Finally, scaled force-fields are strongly dependent on the level of calculation which is employed, and thus different sets of scaling factors have to be developed for different electronic structure methods.[153,154]

A proper inclusion of anharmonic effects is thus mandatory for overcoming those limitations, but this leads to a steep increase in the computational cost of both the preliminary electronic structure calculations to generate the necessary data, and in the vibrational part itself. For this reason, efficiency becomes critical in anharmonic calculations. Among all the algorithms that have been developed in the last decades, second-order vibrational perturbation theory (VPT2) has proven to be the best compromise between computational cost and accuracy for treating semi-rigid systems. However, VPT2 suffers from severe limitations when dealing with flexible systems, displaying highly anharmonic, large-amplitude modes, such as torsions or umbrella inversion vibrations. In those cases, variational approaches are usually needed

to get reliable results, where the vibrational Schrödinger equation is solved by expanding the wavefunctions in a certain basis, with the coefficients determined by direct minimization of the energy functional. Even if variational approaches are particularly appealing, since they allow to obtain converged results by systematically increasing the basis set, their computational cost is very high, making them applicable only to small-size systems, up to 10-20 atoms, depending on the model.
With the aim of developing anharmonic models for larger systems characterized by some degree of flexibility, two anharmonic algorithms have been developed. The first one is based on an hybrid scheme, where a single degree of freedom is treated variationally, using a full numerical treatment based on the discrete variable representation (DVR), while the other degrees of freedom are treated as harmonic. The theory generalizes the Reaction Path Hamiltonian (RPH) model to curvilinear coordinates, and is well suited for systems characterized by a single, well-defined large-amplitude degree of freedom. The second approach is based on a full-dimensional anharmonic treatment, and uses the Density Matrix Renormalization Group (DMRG) algorithm for the parametrization of the vibrational wavefunction. Unlike RPH-based approaches, this method is well suited for studying systems, with multiple, strongly coupled and highly anharmonic modes.
This chapter is organized as follows: the first section presents briefly the state-of-the-art approaches for computing vibrational spectra at the anharmonic level. Then, the theoretical formulation of the hybrid variational-harmonic approach will be presented, together with some representative applications to show its reliability. Then, the vibrational formulation of DMRG, referred to as VDMRG, will be introduced, with particular emphasis on its specificity with respect to its electronic-structure counterpart. Furthermore, an energy-specific formulation of VDMRG, developed to target directly vibrational excited states, will be described. Finally, the reliability of VDMRG will be shown using several, medium-sized organic systems as test-cases.

3.1 Standard anharmonic approaches

In order to develop robust anharmonic approaches, not replying on any empirical factors, a reference Hamiltonian, including anharmonic effects, has to be chosen, and this choice is not unique. This is a major difference between electronic and vibrational structure calculations, since in the former case an exact (in the non-relativistic limit) form for the Hamiltonian is available (Eq. 2.1), whereas in the latter case approximations have to be introduced. If the harmonic oscillator is taken as a reference choice, it is natural to choose the Cartesian normal coordinates $\boldsymbol{Q}$ as a reference set for the Hamiltonian $\mathcal{H}_{\text{vib}}$,

$$\mathcal{H}_{\text{vib}} = \mathcal{T}\left(q_1, ..., q_{N_{\text{vib}}}\right) + \mathcal{V}\left(q_1, ..., q_{N_{\text{vib}}}\right) \tag{3.1}$$

where $\mathcal{T}\left(q_1,...,q_{N_{\text{vib}}}\right)$ and $\mathcal{V}\left(q_1,...,q_{N_{\text{vib}}}\right)$ are the kinetic and potential energy operators, respectively, and $\boldsymbol{q}$ are the dimensionless normal coordinates, defined in terms of the mass-weighted ones ($\boldsymbol{Q}$) as,

$$q_i = \sqrt{\frac{\hbar}{\omega_i}} Q_i \tag{3.2}$$

where ω_i is the harmonic frequency of the i-th mode. At the anharmonic level, vibro-rotational couplings become relevant, thus vibrational and rotational degrees of freedom cannot be fully decoupled. As proved by Watson,[155] the full kinetic energy operator in Cartesian normal modes, with the proper account of vibro-rotational couplings, can be written as follows:

$$\mathcal{T}_{\text{Watson}} = -\frac{\omega_i}{2}\sum_{i=1}^{N_{\text{vib}}}\frac{\partial^2}{\partial q_i^2} + \frac{1}{2}\sum_{\tau<\rho}^{x,y,z}\frac{1}{I_{\tau\rho}}\left(\mathcal{J}_\tau - \mathcal{P}_\rho\right)\left(\mathcal{J}_\tau - \mathcal{P}_\rho\right) - \frac{1}{8}\sum_{\tau}^{x,y,z}\frac{1}{I_{\tau\tau}^{\text{eq}}}, \tag{3.3}$$

where $I_{\tau\rho}$ is the inertia tensor, and $I_{\tau\tau}^{\text{eq}}$ is its equilibrium value. Furthermore, $\mathcal{P}_\tau$ and $\mathcal{J}_\tau$ are the τ component of vibrational and rotational angular momenta, respectively. The first term is the same as in the harmonic case, whereas the second one accounts for the vibro-rotational couplings. The third term is a constant shift of the potential, and will be neglected in the following. The rotational angular momentum can be expressed as,

$$\mathcal{P}_\tau = \sum_{ij=1}^{N_{\text{vib}}}\zeta_{ij}^{\tau}\sqrt{\frac{\omega_i}{\omega_j}}q_i p_j \tag{3.4}$$

By considering only rotational ground states, for which $\mathcal{J} = 0$, and approximating the inertia tensor with its equilibrium value, the following relation is obtained,

$$\mathcal{T}_{\text{Watson}} = -\frac{\omega_i}{2}\sum_{i=1}^{N_{\text{vib}}}\frac{\partial^2}{\partial q_i^2} + \sum_{\tau=x,y,z}B_\tau^{\text{eq}}\sum_{i\neq j}\sum_{k\neq l}\zeta_{ij}^{\tau}\zeta_{kl}^{\tau}q_i p_j q_k p_l\sqrt{\frac{\omega_j\omega_l}{\omega_i\omega_k}} - \frac{1}{8}\sum_{\tau=x,y,z}\frac{1}{I_{\tau\tau}^{\text{eq}}}, \tag{3.5}$$

where $\boldsymbol{\zeta}$ is the matrix of the Coriolis coupling constants, which is defined in terms of the geometrical parameters of the molecule[156] and $\boldsymbol{B}^{\text{eq}}$ are the equilibrium rotational constants. The vibrational Hamiltonian obtained combining Eqs. 3.5 and 3.1 is usually referred to as Watson Hamiltonian.
The form of the kinetic energy operator given in Eq. 3.5 holds only if Cartesian normal modes are employed. If internal coordinates are used, a new definition has to be used, due to the non-linearity of the relation between Cartesian and internal coordinates. We recall here its definition in terms of the $\boldsymbol{G}$ matrix given in Eq. 2.41,[122]

$$\mathcal{T} = -\frac{1}{2}\sum_{i,j=1}^{N_{\text{vib}}}G_{ij}\frac{\partial^2}{\partial Q_i\partial Q_j} - \frac{1}{2}\sum_{i=1}^{N_{\text{vib}}}\left(G_{ij}\ln g + \frac{\partial G_{ij}}{\partial Q_j}\right)\frac{\partial}{\partial Q_i} \tag{3.6}$$

The second term of the previous equation is usually small, and so neglected in most applications. In harmonic models, the first term is further approximated by neglecting the variation of $\boldsymbol{G}$ with the nuclear coordinates. At the anharmonic level, a Taylor expansion is usually employed to approximate the dependence of G_{ij} on $\boldsymbol{Q}$, by keeping terms up to the second order,

$$G_{ij}\left(\boldsymbol{Q}\right) = G_{ij}\left(\boldsymbol{Q}^{\mathrm{eq}}\right) + \sum_{k=1}^{N_{\mathrm{vib}}} \left(\frac{\partial G_{ij}}{\partial Q_k}\right)_{\mathrm{eq}} Q_k + \frac{1}{2}\sum_{kl=1}^{N_{\mathrm{vib}}} \left(\frac{\partial^2 G_{ij}}{\partial Q_k \partial Q_l}\right)_{\mathrm{eq}} Q_k Q_l \tag{3.7}$$

By substituting G_{ij} in Eq. 3.6 with this new definition, contributions formally equivalent to Coriolis couplings are obtained. If internal coordinates-based normal modes are used in the simulation, the equilibrium value of G_{ij} is the identity matrix, since the normal modes $\boldsymbol{L_s}$ diagonalize the Wilson $\boldsymbol{G}$ matrix.[157,158] However, if internal coordinates are used directly in the simulation without performing the GF analysis, $\boldsymbol{G}$ is in general different from the identity matrix, and off-diagonal terms appear in Eq. 3.6.
Once a closed-form expression of the kinetic energy operator is obtained, the potential energy operator needs to be determined. Taking the harmonic oscillator model as a reference, the most natural choice is to include higher-order terms in the Taylor expansion of the potential in terms of the Cartesian-based normal coordinates. For example, by including terms up to the fourth-order, the potential $\mathcal{V}$ reads,

$$\mathcal{V}\left(\boldsymbol{q}\right) = \frac{1}{2}\sum_{i=1}^{N_{\mathrm{vib}}} \omega_i q_i^2 + \frac{1}{6}\sum_{ijk=1}^{N_{\mathrm{vib}}} k_{ijk} q_i q_j q_k + \frac{1}{24}\sum_{ijkl=1}^{N_{\mathrm{vib}}} k_{ijkl} q_i q_j q_k q_l \tag{3.8}$$

where the reduced force constants are defined as,

$$\begin{aligned} k_{ijk} &= \left(\frac{\partial^3 \mathcal{V}}{\partial q_i \partial q_j \partial q_k}\right) = \frac{1}{\sqrt{\omega_i \omega_j \omega_k}}\left(\frac{\partial^3 \mathcal{V}}{\partial Q_i \partial Q_j \partial Q_k}\right) = \frac{K_{ijk}}{\sqrt{\omega_i \omega_j \omega_k}} \\ k_{ijkl} &= \left(\frac{\partial^4 \mathcal{V}}{\partial q_i \partial q_j \partial q_k \partial q_l}\right) = \frac{1}{\sqrt{\omega_i \omega_j \omega_k \omega_l}}\left(\frac{\partial^4 \mathcal{V}}{\partial Q_i \partial Q_j \partial Q_k \partial Q_l}\right) = \frac{K_{ijkl}}{\sqrt{\omega_i \omega_j \omega_k \omega_l}} \end{aligned} \tag{3.9}$$

where K_{ijk} and K_{ijkl} are commonly referred to as third- and fourth-order force constants, respectively, which can be obtained, for example, by finite differentiation of the harmonic force constants. A major advantage of the expansion given in Eq. 3.8 is that a compact second quantization form can be readily obtained using the bosonic SQ operators of the harmonic oscillator model introduced in the previous section (see Eq. 2.26). However, the potential given in Eq. 3.8 has not the correct asymptotic behavior, since it diverges (either positively or negatively depending on the sign of the anharmonic force constants), whereas the "true" potential should reach a constant, finite limiting value. Furthermore, for low frequencies modes, the anharmonic correction is usually of the same order of magnitude, or even higher,

than the harmonic part, and thus additional terms (fifth and sixth-order) are needed for a correct representation of the potential.[159,160]
A more flexible expression for the potential expansion is given by the following expansion, usually referred to as the n-mode representation,[161]

$$\mathcal{V}\left(q_1,\ldots,q_{N_{\text{vib}}}\right) = \sum_{i=1}^{N_{\text{vib}}} \mathcal{V}_i^{[1]} + \sum_{i<j}^{N_{\text{vib}}} \mathcal{V}_{ij}^{[2]} + \sum_{i<j<k}^{N_{\text{vib}}} \mathcal{V}_{ijk}^{[3]} \tag{3.10}$$

where $\mathcal{V}_i^{[1]}$ collects all the terms depending only on the i-th mode, $\mathcal{V}_{ij}^{[2]}$ the terms depending on the i-th and j-th mode and so on (note that the $\mathcal{V}_i^{(1)}$ term must be subtracted from $\mathcal{V}_{ij}^{[2]}$ in order to avoid double counting, as suggested in Ref. 161). The main advantage of the n-mode representation over the Taylor expansion given in Eq. 3.8 is that it holds for general basis sets and general functional form of the potential. For this reason, e Eq. 3.10 can support also non-linear function of the normal modes, such as the Morse potential, with correct asymptotic behaviors. We note that SQ algebra of the creation and annihilation operators of the harmonic oscillator cannot be used to express Eq. 3.10 in second quantization. However, a more general SQ formalism has been recently proposed,[110,162] supporting a general-order n-mode representation. The main difference with the harmonic oscillator-based SQ algebra is that a pair of creation and annihilation operators has to be defined for each mode as before, but for each basis set. For this reason, the number of SQ operators grows quickly.
Turning back to the vibrational Schrödinger equation, the reference Hamiltonian in constructed from the kinetic term given in Eq. 3.5 and the potential expansion in Eq. 3.8. The algorithms used to solve in practice this equation and to compute vibrational wavefunctions and energies, can be divided in two main classes, perturbative and variational. In the former approaches, a reference Hamiltonian is taken, for which eigenvalues and eigenfunctions are known, and corrections are added through perturbation theory. A natural choice for this reference Hamiltonian is the harmonic one, whose eigenvalues and eigenfunctions are known. For example, in VPT2, the harmonic model is used as a reference, and cubic terms are treated as a first-order perturbation, while the quartic ones are treated as a second-order perturbation.[75]. At the VPT2 level, the vibrational energies can be computed as a quadratic function of the quantum numbers,[1]

$$\varepsilon_m^v = \varepsilon_0^v + \sum_{i=1}^{N} v_i^m \omega_i + \sum_{i,j=1}^{N} \chi_{ij}\left[v_i^m v_j^m + \frac{1}{2}\left(v_i^m + v_j^m\right)\right], \tag{3.11}$$

where m labels the vibrational state where the quantum number of the i-th mode is v_i. χ_{ij} are the elements of the anharmonic $\boldsymbol{\chi}$ matrix, which represents the anharmonic correction to transition energies (a full definition of $\boldsymbol{\chi}$ in terms of the anharmonic force constants can be found, for example, in

[1] for systems with degenerate modes, additional terms functions of the angular vibrational number are present (see Ref. 163)

Ref.[67,75]). A major advantage of VPT2 is the limited computational cost of the electronic-structure calculations needed to generate the PES, since only a semi-diagonal quartic force field is needed. Furthermore, its reliability is high for semi-rigid systems, not characterized by strongly anharmonic large-amplitude modes, for which the harmonic oscillator is a good reference model. However, a significant drawback of VPT2 is the problem of resonances, i.e. the potential presence of divergent terms in the expression for the χ matrix. The most critical situation comes from the so-called Fermi resonances (FR), thus when a fundamental harmonic state is close to an overtone of another mode (type 1, $\omega_i \approx 2\omega_j$), or to a combination of two other modes (type 2, $\omega_i \approx \omega_j + \omega_k$). In those cases, some denominators in the expression for χ become almost negligible, leading to divergences in the anharmonic correction.

In order to overcome this limitation of VPT2, several strategies have been adopted.[67,68,164,165] In the so-called deperturbed VPT2 (DVPT2), a two-step procedure is used for the identification and the subsequent removal of resonant terms. The states close in energy are first identified (low frequency difference) and then the resonance magnitude is estimated from the deviation of the VPT2 term from a model variational treatment. The latter step is commonly known as Martin's test.[164] Once identified as resonant, these terms are removed from the anharmonic treatment. A major drawback of DVPT2 is the need to set thresholds to identify the resonant terms, which may cause side effects in the overall results when applied over a broad range of systems or computational setups. An alternative strategy is to replace all potentially resonant terms with non-resonant equivalents. Such an approach was for instance proposed by Kuhler, Truhlar and Isaacson as the degeneracy-corrected PT2 (DCPT2)[166]. One important drawback of this approach is its inaccuracy with respect to the original VPT2 formulation, especially far from resonance, but this can be significantly reduced by introducing an *ad hoc* transition function to recover the VPT2 term in this case (the hybrid approach is referred to as hybrid DCPT2-VPT2, HDCPT2)[68].

Going back to the DVPT2 model, an important shortcoming of the removal of resonances is that the anharmonic treatment becomes truncated. A solution to this problem is to reintroduce those terms through a successive variational step, where the variational matrix is built by placing the DVPT2 energies ($\varepsilon_m^{\mathrm{DVPT2}}$) on the diagonal and the variational terms corresponding to the resonances as off-diagonal elements. The final vibrational energies are obtained after diagonalization of the full variational matrix, and the overall procedure (DVPT2 + variational correction) will be called generalized VPT2 (GVPT2). GVPT2 is the most complete model, since the resonant terms, that are removed from the perturbative treatment, are included *a-posteriori* variationally. However, due to this second variational treatment, the simple form given in Eq. 3.11 does not hold anymore, and the vibrational wavefunctions change with respect to the harmonic ones.[68] To conclude this part, it is noteworthy that the problem of a successive variational treatment is not present for DCPT2/HDCPT2 since it is done automatically as the replacement of the potentially resonant form.

Even if the previous formulations of VPT2 theory allow recovering the inaccuracy of VPT2 in case of resonances, perturbation theory is intrinsically ill-suited to account for strong anharmonic effects, since in this case they cannot be considered perturbations to the harmonic Hamiltonian. In those cases, variational approaches are more appropriate. The general principle is that a basis function is chosen for each degree of freedom, and the vibrational wavefunction $|\,\psi_i\,\rangle$ is expanded as a linear combination of Hartree product of those basis functions. For example, if the harmonic oscillator eigenfunctions are employed as a reference basis set, the expansion can be written in terms of ONVs as follows:

$$|\,\psi_i\,\rangle = \sum_{n_1,\ldots,n_L} \boldsymbol{C}_{n_1,\ldots,n_\mathrm{L}} |\,n_1,\ldots,n_\mathrm{L}\,\rangle\,, \tag{3.12}$$

where $\boldsymbol{C}_{n_1,\ldots,n_\mathrm{L}}$ is a tensor collecting the parameters to be optimized variationally, and $|\,n_1,\ldots,n_\mathrm{L}\,\rangle$ are basis functions expressed as ONVs. A variational minimization of the energy starting from the linear expansion given in Eq. 3.12 leads to the secular equation $\boldsymbol{HC} = E\boldsymbol{C}$, where $\boldsymbol{C}$ is a vector obtained from $\boldsymbol{C}_{n_1,\ldots,n_\mathrm{L}}$ by collecting all the indexes in a single dimension. However, the main limitation of such an approach is that the dimension of the variational matrix grows exponentially with the size of the system, and thus calculations are feasible only for small-size systems, even when subspace iteration techniques (such as the Davidson or the Jacobi-Davidson algorithms[167,168]) are employed.[159,160] For this reason, several strategies have been derived to reduce the computational cost of the simulation. For example, it is known that the harmonic oscillator wavefunction is not the optimal choice for the basis set to use in the variational expansion. Conversely, functions (usually referred to as modals) obtained from vibrational self consistent field (VSCF)[161] are known to be better suited for variational calculation, since they provide a faster convergence of the expansion given in Eq. 3.12 with respect to the number of basis functions. However, a reference state needs to be set for VSCF calculations, and thus the basis set is optimized for a specific vibrational level. As a result, to compute the energies of multiple states, either the same basis is used each time, even if not properly optimized for each level, or a different basis is chosen each time. Finally, VSCF modals arising from calculations performed on different vibrational levels are, in general, not orthogonal, and this leads to an increase of the computational effort.
An alternative approach proposed to reduce the computational cost of simulations is to change the coordinate systems used to express the vibrational Hamiltonian to reduce off-diagonal mode-couplings. As already mentioned above, the use of curvilinear internal coordinates usually allows to reduce the coupling between modes,[169,170] but this requires the inclusion of terms depending on $\boldsymbol{G}$ and its derivatives (see Eq. 3.6), which is not straightforward, especially for large-size systems. Alternatively, as shown by Reiher and coworkers,[72] also Cartesian-based normal modes can be localized too, using the same algorithms as in electronic structure calculations. Those localized modes have been recently applied by several groups[73,74,171,172] to perform anharmonic calculations on large, biologically-relevant molecules.

However, even if this approach is very efficient for strongly localized vibrations (such as stretching modes), it fails for intrinsically delocalized modes, such as overall rotations or ring deformations.

3.2 Monodimensional anharmonic treatment: a DVR-based approach

As discussed in the previous section, variational approaches are the most used methods for studying highly anharmonic, flexible systems. However, their high computational costs makes those approaches applicable to systems up to 10-20 atoms in the best case. A full variational treatment is however not necessary in most cases, since there are usually only a few highly anharmonic modes. For the simplest deformations, such as torsions, ring deformations or umbrella inversions, the LAM can be associated to a single coordinate. This section will present a theoretical framework designed to tackle this class of systems. The theory is based on an hybrid scheme, where a full variational treatment is employed for the calculation of the vibrational levels of the LAM, whereas the harmonic approximation is used for the other modes.

3.2.1 Selection of the coordinates describing large-amplitude motions

The main assumption of the hybrid variational-harmonic approach presented in this section is that the molecular motion can be described in terms of two different kinds of coordinates:

1. the LAM coordinate (z), along which the molecule is not forced to do small displacements. The PES along this coordinates is not approximated with a Taylor expansion, but is computed explicitly through a scan calculation. Vibrational levels are then computed using a variational approach.

2. N_{vib}-1 harmonic coordinates ($\boldsymbol{Q}_{\text{ortho}}$), along which, at each value of the LAM, the molecule undergoes small-amplitude deformations, which can evolve along the LAM.

This means in practice that each Cartesian coordinate $\boldsymbol{x}$ can be expressed as,

$$\boldsymbol{x} = \boldsymbol{a}_{\text{LAM}}(z) + \boldsymbol{Q}_{\text{ortho}}(z) \tag{3.13}$$

where the LAM is represented by a curve $\boldsymbol{a}_{\text{LAM}}(z)$ in the coordinates space, which is a function of a general parameter z. The first step is to define $\boldsymbol{a}_{\text{LAM}}(z)$, which will depend on the LAM. The latter is defined univocally only at the reference geometry (usually, the equilibrium geometry, at which vibrational calculations are done), where it coincides with one of the harmonic modes, labeled in the following as Q_1. However, the LAM curve must

be defined also for finite displacements from the equilibrium position to obtain the curve and, for the hybrid scheme to be effective, the curve should be defined to minimize the couplings between the LAM and the coordinates $\boldsymbol{Q}_{\text{ortho}}$.
The most natural choice is to use the same coordinates (thus, mode Q_1) also for finite displacements from the equilibrium position. This means, in practice, that the curve $\boldsymbol{a}_{\text{LAM}}(z)$, and the corresponding PES, is computed through a non-relaxed scan along Q_1. This model will be referred to in the following as the non-relaxed internal coordinates path Hamiltonian (NR-ICPH). Even if it is particularly appealing for studying large systems, since no geometry optimization is needed along the scan, NR-ICPH provides a poor description of the PES for large-displacements from the equilibrium position in most cases. In fact, even if Q_1 is decoupled from the other modes at the reference geometry, this is not true in general for large displacements from the equilibrium position, where significant couplings can appear. In those cases, a more accurate definition of the LAM, taking into account geometry relaxation effects, is needed.
A more refined model is obtained by adopting the so-called internal coordinates path Hamiltonian (ICPH) model, introduced by Handy and co-workers to describe tunneling processes in malonaldehyde,[76] and more recently applied to vibronic spectroscopies.[173] In the ICPH model, the curve $\boldsymbol{a}_{\text{LAM}}(z)$ is obtained by fixing Q_1 at different values along the path and optimizing, at each step, all other degrees of freedom. Unlike its non-relaxed version, the ICPH model includes geometry relaxation effects, since the N_{vib}-1 harmonic coordinates are optimized at each step of the scan. For this reason, in ICPH, the LAM does not coincide anymore with Q_1, but its expression in terms of the internal coordinates will change with the z parameter. This means also that the N_{vib}-1 $\boldsymbol{Q}_{\text{ortho}}$ coordinates can change along the LAM.
A third approach is obtained by describing the LAM using the intrinsic reaction coordinate (IRC)[174,175,176] combined to the reaction path Hamiltonian (RPH).[77,177] Within this model, the LAM is defined as the minimum energy path (MEP) connecting a transition state to a minimum. Starting from the geometry $\boldsymbol{x}_{\text{TS}}$ (or $\boldsymbol{s}_{\text{TS}}$, if internal coordinates are used) corresponding to the transition state, the IRC is defined as the curve where the displacement along each Cartesian coordinates is directly proportional to the PES gradient. Thus, the infinitesimal displacements along the IRC are defined as:[178]

$$\frac{M_1 dx_1}{g_{x,1}} = \frac{M_1 dy_1}{g_{y,1}} = \ldots = \frac{M_{N_{\text{at}}} dz_{N_{\text{at}}}}{g_{z,N_{\text{at}}}} = dl \tag{3.14}$$

Eq. 3.14 diverges when the gradient is null, thus at stationary points, where however the IRC corresponds to one of the normal modes (i.e. the imaginary frequency mode at the transition state) and thus Eq. 3.14 is not needed. Eq. 3.14 defines the IRC through the following differential equation:[176,179]

$$\frac{\mathrm{d}\boldsymbol{x}_{\text{IRC}}(l)}{\mathrm{d}l} = -C\boldsymbol{g} \tag{3.15}$$

where C is a constant proportionality constant. If $C = |\boldsymbol{g}|^{-1}$, parameter l

corresponds to the length of the curve defined by the IRC in the coordinate space (also known as the IRC parameter). As has been discussed by Fukui,[180] the IRC is the trajectory that the molecule would follow starting from the transition state with an infinitesimal, positive kinetic energy in the direction of the mode Q_1. From a practical point of view, the IRC is computed using numerical algorithms, where Eq. 3.15 is integrated numerically.[78,181,182,183] Without going into the details, here we note only that all these algorithms are based on a two-step procedure: first of all, a new coordinate lying on the IRC curve is estimated from the gradient computed at the previous point (prediction step), then the geometry is corrected if components orthogonal to the IRC are present (correction step). Unlike ICPH, RPH can be used only for PESs with a transition state, such as double-well potentials. On the other hand, it is more general, since it does not require to perform the constrained optimization.

Once the algorithm required to compute the curve $\boldsymbol{a}_{\mathrm{LAM}}(z)$ has been defined, this curve needs to be parametrized, i.e. an algorithm to compute z must be developed. This task is particularly important since, depending on the choice of z, a different form for the kinetic energy operator will be obtained. For the simplest, NR-ICPH, the LAM can be expressed as,

$$\boldsymbol{a}_{\mathrm{LAM}}(z) = \boldsymbol{x}^{\mathrm{eq}} + z \cdot Q_1 \tag{3.16}$$

where $\boldsymbol{x}^{\mathrm{eq}}$ are the Cartesian coordinates of the nuclei at the equilibrium geometry and Q_1 is the normal mode associated to the LAM, expressed as a linear combination of Cartesian coordinates. Even if this parametrization has been widely used in the literature,[88,184,185,186] it cannot be applied to the ICPH or RPH models, since the expression of the LAM in terms of normal modes changes along the scan due to structural relaxation. A more general parametrization is obtained by defining the length (l) of the curve $\boldsymbol{a}_{\mathrm{LAM}}$,[187]

$$l(z) = \int_0^z \mathrm{d}z' \left| \boldsymbol{\nabla} \boldsymbol{a}_{\mathrm{LAM}}(z') \right|^2 \tag{3.17}$$

$l(z)$ can be used to parametrize the LAM as $\boldsymbol{a}_{\mathrm{LAM}}(l)$, and this choice brings several advantages. First, the definition of l holds for any kind of deformation, and therefore supports both ICPH and RPH. Next, the expression of the kinetic energy operator can be simplified. Next, the expression of the kinetic energy operator, given in Eq. 2.41 for a general, curvilinear set of coordinates, can be simplified to,

$$\mathcal{T} = -\frac{\hbar^2}{2} g^{1/4} \frac{\mathrm{d}}{\mathrm{d}l} g^{1/2} \frac{\mathrm{d}}{\mathrm{d}l} g^{1/4} \tag{3.18}$$

where,

$$g = \sum_{a=1}^{3N_{\mathrm{at}}} \left| \frac{\mathrm{d}x_a}{\mathrm{d}l} \right|^2 = \left| \frac{\mathrm{d}\boldsymbol{x}}{\mathrm{d}l} \right|^2 \tag{3.19}$$

In theory, g is a function of l, and so Eq. 3.18 can be rewritten as a sum of terms containing the first and second derivatives of g with respect to l (see

Eq. 3.6). Since they are usually small, these terms are usually neglected so that Eq. 3.18 can be simplified as,[179]

$$\mathcal{T}(l) = -\frac{\hbar^2}{2}\frac{\mathrm{d}}{\mathrm{d}l}g\frac{\mathrm{d}}{\mathrm{d}l} \tag{3.20}$$

From the definition of l in equation 3.17, $g = 1$, and therefore the kinetic energy is proportional to the second derivative operator, the same as for mass-weighted Cartesian coordinates. This simplification holds only for monodimensional large-amplitude modes, whereas for multidimensional systems, the Wilson **G** matrix must be known explicitly to calculate the kinetic energy operator.[188,189,190]

3.2.2 The discrete variable representation

The previous section presented several algorithms for computing the geometries along the LAM and the corresponding PES $\mathcal{V}_{\mathrm{LAM}}(l)$. Furthermore, the parametrization of the LAM curve along as a function of Cartesian coordinates determines the kinetic energy operator $\mathcal{T}(l)$. With those two quantities, the monodimensional vibrational Hamiltonian specific to the LAM can be expressed in terms of l as follows:

$$\mathcal{H}_{\mathrm{LAM}}(l) = \mathcal{T}(l) + \mathcal{V}(l) = -\frac{\hbar^2}{2}\frac{\mathrm{d}^2}{\mathrm{d}l^2} + \mathcal{V}(l) \tag{3.21}$$

where, for the moment, the effects of the $N_{\mathrm{vib}} - 1$ small-amplitude coordinates (SAMs) have been neglected. To get a correct account of the anharmonicity of the LAM, the eigenvalues and eigenfunctions of $\mathcal{H}_{\mathrm{LAM}}(l)$ will be computed with a variational approach. Here, the Discrete Variable Representation (DVR) method will be employed. The DVR approach has been introduced by Light and co-workers,[191] and later re-derived by Colbert and Miller[192] as a numerical method to solve the Schrödinger equation. The DVR theory is strictly related to the variational basis representation (VBR). In VBR, the monodimensional Schrödinger equation is solved by expanding the eigenfunctions as linear combinations of a basis set $\boldsymbol{\chi}_{\mathrm{VBR}}(l)$. The matrix representation of $\mathcal{H}_{\mathrm{LAM}}$ in the VBR basis is obtained as follows:

$$H_{\mathrm{LAM},ij} = -\frac{1}{2}\langle\, \chi_i^{\mathrm{VBR}} \mid \frac{d^2}{dl^2} \mid \chi_j^{\mathrm{VBR}} \,\rangle + \langle\, \chi_i^{\mathrm{VBR}} \mid \mathcal{V}_{\mathrm{LAM}}(l) \mid \chi_j^{\mathrm{VBR}} \,\rangle \tag{3.22}$$

Even if, for a wide range of basis sets, the matrix element of the second derivative (i.e. the first term of Eq. 3.22) can be computed analytically, this is usually not true for the potential. In fact, in our approach the potential operator is computed through a scan, and thus an analytical representation of $\mathcal{V}_{\mathrm{LAM}}$ is not available, which makes the analytical calculation of the matrix elements $\langle\, \chi_i^{\mathrm{VBR}} \mid \mathcal{V}_{\mathrm{LAM}} \mid \chi_j^{\mathrm{VBR}} \,\rangle$ not practical. A possible solution is to approximate the integrals using Gaussian quadratures,

$$\langle \chi_i^{\mathrm{VBR}} \mid \mathcal{V}^{\mathrm{LAM}} \mid \chi_j^{\mathrm{VBR}} \rangle \approx \sum_{k=1}^{2n} m_k \, \chi_i^{\mathrm{VBR}}(l_k) \, \mathcal{V}^{\mathrm{LAM}}(l_k) \, \chi_j^{\mathrm{VBR}}(l_k) \, , \tag{3.23}$$

where the weight m_k and the grid points $l(z_k)$ (written l_k for simplicity) depend on the quadrature algorithm. From an algorithmic perspective, the grid points are the zeros of a set of $2n$ polynomials $\varphi_k(l)$, each one of degree k, which are orthogonal with respect to a weight function $m(l)$ in the interval $[a, b]$ where the Hamiltonian $\mathcal{H}_{\mathrm{LAM}}$ is defined,

$$\int_a^b \mathrm{d}l \, m(l) \, \varphi_i(l)^\dagger \, \varphi_j(l) = \delta_{ij} \tag{3.24}$$

If the matrix representation of $\mathcal{H}(l)$ in the VBR is obtained by computing the integrals involving the kinetic energy operator exactly and the potential operator using Eq. 3.23, the so-called finite basis representation (FBR) is obtained. In VBR calculations, the only source of error is the truncation of the basis expansion, whereas in FBR another source of inaccuracy is the approximation in the calculation of the matrix elements. As noticed in early theoretical works,[191] methods relying on the FBR, unlike those based on VBR, are not variational.

The DVR can be easily introduced starting from the VBR approach presented above. Let us consider a matrix $\boldsymbol{Y}$ giving the change of basis from the VBR to the position representation:[191]

$$Y_{i\alpha} = \langle \chi_i^{\mathrm{VBR}} \mid l_\alpha \rangle = \chi_i^{\mathrm{VBR}}(l_\alpha) \tag{3.25}$$

where i is the index of a basis function and α a continuous index labeling all the values taken by the position coordinate. If the coordinate representation is obtained only on a grid of n values $(l_1, \ldots, l_n)$, where n is the number of basis functions, then $\boldsymbol{Y}$ becomes square and its entries are obtained from the value of the basis functions in the grid points. $\boldsymbol{Y}$ can be used to define the DVR basis set from the VBR one as,

$$\boldsymbol{\chi}^{\mathrm{DVR}} = \boldsymbol{Y}^\dagger \boldsymbol{\chi}^{\mathrm{VBR}} \tag{3.26}$$

If the representation of an operator is known in the VBR, its DVR counterpart can be obtained by simply applying the $\boldsymbol{Y}$ transformation matrix. This is however not particularly useful, since, as already remarked above, the main problem is that, for the potential operator, the VBR representation is not available. An interesting feature of the DVR basis set is however its localization property. In fact, it can be easily shown that,

$$\begin{aligned} \chi_i^{\mathrm{DVR}}(l_j) &= \sum_{k=1}^{n} Y_{ik} \chi_k^{\mathrm{VBR}}(l_j) = \sum_{k=1}^{n} Y_{ik} Y_{jk} \\ &= \left(\boldsymbol{Y} \boldsymbol{Y}^\dagger \right)_{ij} \end{aligned} \tag{3.27}$$

Thus, $\chi_i^{\mathrm{DVR}}(l_j) = \delta_{ij}$ provided that $\boldsymbol{Y}$ is orthogonal. This can be ensured

with the proper transformation,[191] for example through Löwdin orthogonalization. The localization property can be used to approximate operators depending on the position (such as the potential $\mathcal{V}^{\mathrm{LAM}}$) as being diagonal,

$$\left(\boldsymbol{V}^{\mathrm{LAM}}\right)_{ij}^{\mathrm{DVR}} \approx V\left(l_i\right)\delta_{ij} \tag{3.28}$$

The matrix elements of the kinetic energy operator $\mathcal{T}(l)$ are usually known analytically in the VBR, and thus its representation in the DVR can be obtained by applying the $\boldsymbol{Y}$ transformation matrix. Up to now the Gaussian quadrature has not been invoked, and the derivation holds for a general grid point. However, depending on the grid, the reliability of the diagonal approximation (Eq. 3.28) varies. Let us now select a quadrature algorithm, and choose the quadrature grid to be the DVR grid. By defining the elements of $\boldsymbol{Y}$ as,

$$Y_{ij} = \sqrt{\frac{m_i}{m\left(l_i\right)}}\chi_j^{\mathrm{DVR}}\left(l_i\right) \tag{3.29}$$

the diagonal approximation given in Eq. 3.28 reads,

$$\left(\boldsymbol{V}_{\mathrm{LAM}}\right)_{ij}^{\mathrm{DVR}} = \sum_{k=1}^{n}\frac{m_k}{m\left(l_l\right)}\chi_i^{\mathrm{DVR}}\left(l_k\right)V\left(l_k\right)\chi_i^{\mathrm{DVR}}\left(l_k\right) \tag{3.30}$$

The previous equation shows that the DVR basis combined with the diagonal approximation leads to the FBR, where the matrix elements of the potential are computed using the Gaussian quadrature. However, the DVR theory presented above is not limited to grids connected to Gaussian quadratures, but holds for any grid points. For the study of chemical processes, the more general formulation is usually needed. In fact, the DVR grid points correspond in practice to the point where the potential is computed. In most the applications, those points are not know *a priori*, and thus they does not coincide with the grid arising from a quadrature. Furthermore, for multidimensional problems, the definition of a quadrature grid is less straightforward than for the monodimensional case, and in this situation, a general grid is preferred. In the present thesis, three DVR basis sets, which have been proposed in the literature,[193,194,195] will be used. Each one corresponds to three different choice of the interval $[a, b]$ and of the boundary conditions where to solve the vibrational Schrödinger equation,

1. the $[0, 2\pi]$ interval with periodic boundary conditions. This setup can be adapted to any periodic potentials as, for example, rotations along dihedral angles.[192,196,197] In this case, a consistent choice for the VBR is the trigonometric basis,

$$\chi_n^{\mathrm{DVR}}\left(l\right) = \frac{e^{inl}}{2\pi} \tag{3.31}$$

with the grid points defined as $l_n = i\frac{2\pi}{2N+1}$. The matrix element of the kinetic energy operator in this basis are given by:

$$\langle \chi_i^{\mathrm{DVR}} \mid \frac{d^2}{dl^2} \mid \chi_j^{\mathrm{DVR}} \rangle = \begin{cases} (-1)^{i-j} \times \frac{N(N+1)}{3} & i \neq j \\ \frac{(-1)^{i-j}}{2} \times \frac{\cos\left(\frac{\pi(i-j)}{2N+1}\right)}{2\sin^2\left(\frac{\pi(i-j)}{2N+1}\right)} & i = j \end{cases} \tag{3.32}$$

2. a bounded interval $[a, b]$, with the boundary conditions that the wavefunction must be null at the two extremal point. In this case, a proper choice of the orthogonal polynomials is the Fourier basis, given in the following:

$$\chi_n^{\mathrm{DVR}}(l) = \sqrt{\frac{2}{b-a}} \sin\left(\frac{n\pi(l-a)}{b-a}\right) \tag{3.33}$$

where the grid is given by $l_i = a + i(b-a)/n$, where n is the total number of DVR basis functions. In this case, the matrix element of the second derivative operator is given by the following expression:

$$\langle \chi_i^{\mathrm{DVR}} \mid \frac{\mathrm{d}^2}{\mathrm{d}s^2} \mid \chi_j^{\mathrm{DVR}} \rangle = \begin{cases} \frac{(-1)^{i-j}\pi}{2(b-a)^2} \times \left[\frac{1}{\sin^2\left(\frac{\pi(i-j)}{2n}\right)} - \frac{1}{\sin^2\left(\frac{\pi(i+j)}{2n}\right)}\right] & i \neq j \\ \frac{\pi}{2(b-a)^2} \times \left[\frac{3}{2n^2+1} - \frac{1}{\sin^2\left(\frac{i\pi}{n}\right)}\right] & i = j \end{cases} \tag{3.34}$$

3. the third case corresponds to an unbound interval $(-\infty, +\infty)$, with the boundary condition that the wavefunction vanishes for $l \to \pm\infty$. This corresponds, for example, to inversion modes in a molecular system. As discussed in Ref.[192], the matrix elements of the DVR basis set can be derived in this case from the previous case, and is the following:

$$\langle \chi_i^{\mathrm{DVR}} \mid \frac{\mathrm{d}^2}{\mathrm{d}s^2} \mid \chi_j^{\mathrm{DVR}} \rangle = \begin{cases} \frac{(-1)^{i-j}\pi}{2} \times \frac{\pi^2}{3} & i \neq j \\ \frac{(-1)^{i-j}\pi}{2} \times \frac{2}{(i-j)^2} & i = j \end{cases} \tag{3.35}$$

For a DVR based on a set of orthogonal polynomials, the DVR grid $(l_1, ..., l_n)$ used to compute numerically the Hamiltonian matrix $\boldsymbol{H}_{\mathrm{vib}}$ is defined *a priori*, independently of the molecular system under analysis. However, in practice, the grid of l-points in which the energy is computed during a scan calculation (the corresponding points will be noted with a tilde) is known only when the NR-ICPH model is employed. For the other two models of interest here, namely ICPH and RPH, the geometry is optimized during the scan, and for this reason the differences between the values of l corresponding to two consecutive point of the scan vary. As a consequence, the value of the PES is not known in the points of the DVR grid. To overcome this problem, a two-steps procedure is adopted. An analytical representation of the PES ($\mathcal{V}^{\mathrm{fit}}(l)$) is obtained by fitting the $\tilde{n}$ energies computed at $(\tilde{l}_1, ..., \tilde{l}_{\tilde{n}})$ using a cubic B-spline.[124,198] We note that, in the literature, other functional

forms for the fitting have been employed, such as the Fourier basis[184,199,200] or Morse-like potentials.[201,202] However, these representations are specific to particular types of potentials (such as periodic ones for the former and inversion potential for the latter) and lack of generality. On the contrary, the B-spline representation, which is obtained by approximating the curve as a cubic function of l by imposing continuity of the first and second derivative at each grid point, can be used for any kind of potential. The Hamiltonian matrix to be diagonalized in the DVR calculation is built using $\mathcal{V}^{\text{fit}}(l)$ instead of the exact potential. Since $\mathcal{V}^{\text{fit}}(l)$ is known analytically thanks to the B-spline representation, its value at the grid points $(l_1, ..., l_n)$ can be obtained for a negligible computational cost.
We note that this double-step approach reduces significantly the computational cost. In fact, the number of points needed to obtain a converged representation of the PES from B-splines is usually far lower than the number of grid points needed to reach convergence in the DVR expansion, meaning that, in most cases, $\tilde{n} \ll n$. Thus, electronic structure calculations, which are the bottleneck of the simulation, are performed over a smaller number of points than the ones employed for the DVR basis.

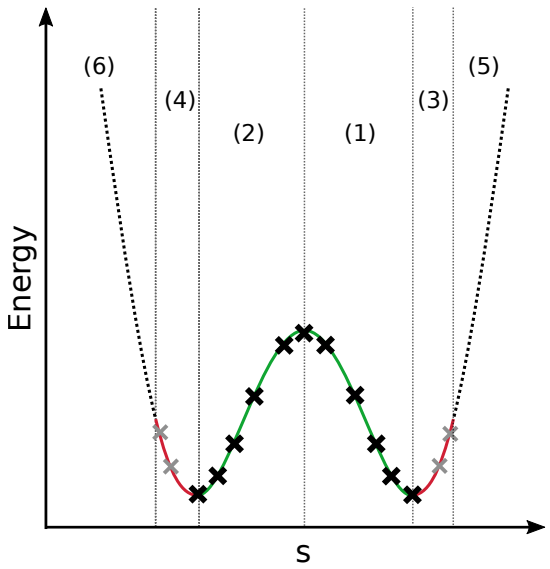

FIGURE 3.1: Graphical representation of the extrapolation procedure used for RPH. In the first two steps (labeled as 1 and 2) IRC calculations are used to compute PES between the saddle point and each of the two minima (black crosses) of the double well, which is then fitted using a B-spline representation (solid, green line). Then (steps 3 and 4) the PES beyond the stationary points (solid, red line) is obtained through a relaxed scan along the mode associated to the LAM (gray crosses). To limit the number of points of the scan calculation (steps 5 and 6), the PES can be extrapolated by fitting it to a double Morse potential (dashed, black line). Note that, for symmetric double-well potentials, steps 2, 4 and 6 are equivalent to 1, 3 and 5, and therefore can be avoided. (Source: Ref. 203)

This fitting procedure can be easily coupled to the ICPH model, but the integration into the RPH model is less straightforward. Indeed, as shown in Fig. 3.1 and mentioned in the previous section, the IRC is defined only between a minimum and the transition state (green line in Fig. 3.1) obtained by following the normal mode Q_1. However, the curve $\boldsymbol{a}_{\mathrm{LAM}}(l)$ needs to be known also beyond this path. Nevertheless, it can be shown that,[77,179] for infinitesimal displacements from the equilibrium position, the IRC is equivalent to the normal coordinate associated to the LAM and therefore the ICPH model can be used to complement RPH, providing data on $\boldsymbol{a}_{\mathrm{LAM}}(l)$ beyond the minima (solid, red line in Fig. 3.1). For double-well potentials, it is possible to reduce the number of grid points for the ICPH step, by extrapolating the PES using the a double Morse potential, with a functional form,[201,202]

$$\mathcal{V}_{\mathrm{Morse}}(l) = A_1\left[1 - e^{-b_1(l-l_1)}\right] + A_2\left[1 - e^{-b_2(l-l_2)}\right] \tag{3.36}$$

where A_1, b_1, l_1, A_2, b_2 and l_2 are parameters determined through least-squares fitting. The B-spline fitting preliminary to the DVR calculation of the PES along the LAM is then fitted from two components, the analytical expression $V_{\mathrm{Morse}}(l)$ beyond the two end points of the ICPH calculations (dashed, black line in Fig. 3.1) and the set of points obtained from quantum chemical computations built from RPH+ICPH calculations (black and grey crosses in Fig. 3.1).

3.2.3 Hybrid DVR-harmonic models

The previous section described a theoretical framework for building the vibrational Hamiltonian $\mathcal{H}_{\mathrm{LAM}}(l)$ describing the motion along a LAM, and a variational approach for computing its eigenpairs. As already mentioned at the beginning of the previous section, up to this point, the couplings with the other modes have been neglected. In order to analyze the impact of those couplings, the l coordinate must be complemented by a set of $N'_{\mathrm{vib}} = N_{\mathrm{vib}} - 1$ coordinates $\tilde{\mathbf{Q}}(l) = (\tilde{Q}_1(l), ..., \tilde{Q}_{N'_{\mathrm{vib}}}(l))$ describing the remaining degrees of freedom which are, in the most general case, function of l themselves.
For a single electronic state, the RPH model provides a consistent definition of $\tilde{\mathbf{Q}}(l)$.[77,204] Within this framework, the l coordinate is complemented by the N'_{vib} normal modes orthogonal to $\boldsymbol{a}_{\mathrm{LAM}}(l)$ (referred to as $\boldsymbol{Q}^p$ in the following). For practical purposes, it is useful to introduce a vector $\mathbf{n}$ tangent to $\boldsymbol{a}_{\mathrm{LAM}}(l)$ as,[187]

$$\boldsymbol{n}(l) = \frac{1}{\left\| \frac{\mathrm{d}\boldsymbol{a}_{\mathrm{LAM}}(l)}{\mathrm{d}l} \right\|} \frac{\mathrm{d}\boldsymbol{a}_{\mathrm{LAM}}(l)}{\mathrm{d}l} \tag{3.37}$$

which can be used to compute the projector operator in Cartesian coordinates on the space parallel to the curve $\boldsymbol{a}_{\mathrm{LAM}}(l)$ as $\mathbf{P}_{\boldsymbol{x}} = \boldsymbol{n}\boldsymbol{n}^T$. Within the RPH model, $\boldsymbol{P}_{\boldsymbol{x}}$ can be rewritten as,

$$\mathbf{P}_{\boldsymbol{x}}(l) = \frac{\boldsymbol{g}_{\boldsymbol{x}}(l)\,\boldsymbol{g}_{\boldsymbol{x}}(l)^T}{\|\boldsymbol{g}_{\boldsymbol{x}}(l)\|^2} \tag{3.38}$$

where $\boldsymbol{g_x}$ is the energy gradient in Cartesian coordinates. Then, $\boldsymbol{Q}^p$ are defined as the eigenvalues of the mass-weighted projected Hessian matrix,

$$\mathbf{P}_{\boldsymbol{x}} \left(\boldsymbol{M}^{1/2} \boldsymbol{H}_{\mathbf{x}} \boldsymbol{M}^{1/2} \right) \mathbf{P}_{\boldsymbol{x}} \boldsymbol{L}_{\boldsymbol{x}}^{p} = \left(\boldsymbol{\Omega}^{p} \left(l \right) \right)^2 \boldsymbol{L}_{\boldsymbol{x}}^{p} \tag{3.39}$$

where $\boldsymbol{\Omega}^p$ is the $N'_{\text{vib}} \times N'_{\text{vib}}$ diagonal matrix of the projected harmonic frequencies, and $\boldsymbol{L}_{\mathbf{x}}^{p}$ is the $N'_{\text{vib}} \times N_{\text{vib}}$ transformation matrix from Cartesian coordinates to the projected normal modes $\boldsymbol{Q}^p$. For a fixed value of the LAM coordinate l_{ref}, any geometry $\boldsymbol{x}_{\text{ref}}$ can be expressed as,

$$\boldsymbol{x}_{\text{ref}} = \boldsymbol{a}_{\text{LAM}} \left(l_{\text{ref}} \right) + \{ \boldsymbol{L}_{\mathbf{x}}^{p} \}^T \boldsymbol{Q}^p \tag{3.40}$$

This relation can be used to build the expression of the full-dimensional vibrational Hamiltonian in the $(l, \boldsymbol{Q}^p)$ representation as,[77]

$$\begin{aligned} \mathcal{H}_{\text{vib}} =& \mathcal{T}_{\text{LAM}}(l) + \mathcal{V}_{\text{LAM}}(l) + \mathcal{T}_{N'_{\text{vib}}}(\boldsymbol{Q}^p) + \sum_{i=1}^{N'_{\text{vib}}} \frac{1}{2} \{ \omega_i^p \}^2 (l) Q_i^p (l)^2 \\ &+ \frac{1}{2} \frac{\left(p\left(l\right) - \boldsymbol{P}\left(\boldsymbol{Q}^p\right)^T \boldsymbol{\Gamma} \boldsymbol{Q}^p \right)^2}{\left(1 + \boldsymbol{\zeta}^T \boldsymbol{Q}^p\right)^2} \end{aligned} \tag{3.41}$$

where $p\left(l\right)$ is the momentum operator for the LAM coordinate, whereas $\boldsymbol{P}\left(\boldsymbol{Q}^p\right)$ is its counterpart for the orthogonal modes. The $\boldsymbol{\Gamma}$ matrix introduces a coupling between the orthogonal modes, and can be expressed as:

$$\boldsymbol{\Gamma} = \{ \boldsymbol{L}_{\boldsymbol{x}}^{p} \}^T \frac{d \boldsymbol{L}_{\boldsymbol{x}}^{p}}{\mathrm{d}l} \tag{3.42}$$

and a similar expression can be written for the $\boldsymbol{\zeta}$ vector, which couples the modes with the overall rotation of the molecule. We note that the magnitude of the couplings grows with the derivative of the mode with respect to l. Thus, if the projected modes are constant along the LAM, no couplings are present, and the Hamiltonian given in Eq. 3.41 can be expressed as a sum of a term depending only on l ($\mathcal{H}_{\text{LAM}}$), and another term, corresponding to the harmonic oscillator Hamiltonian for the N'_{vib} orthogonal modes, where the harmonic frequency depends parametrically on the LAM coordinate. The model in which those couplings are neglected is usually referred to as the adiabatic approximation. As mentioned above, the accuracy of the adiabatic approximation can be checked by monitoring the variation of the orthogonal modes with the LAM coordinate.

Before commenting on the calculation of the eigenfunctions of the Hamiltonian given in Eq. 3.41 can be computed, let us generalize this Hamiltonian to internal coordinates. As discussed by Natanson and co-workers[79,114,179] when a non-orthogonal set of coordinates is employed, equation 3.38 does not hold anymore. The expression for the projector $\mathbf{P}_{\boldsymbol{s}}$ in internal coordinates is the following:

$$\mathbf{P}_{\boldsymbol{s}} = \frac{\boldsymbol{n_s} \boldsymbol{n_s}^T}{\boldsymbol{n_s}^T \boldsymbol{G} \boldsymbol{n_s}} \tag{3.43}$$

where, similarly to the Cartesian case, $\boldsymbol{n_s}$ is a vector tangent to the curve $\boldsymbol{a}_{\mathrm{LAM}}(l)$ expressed in internal coordinates. The main difference between Eqs. 3.38 and 3.43 is the presence of a normalization factor in the latter case ($\boldsymbol{n_s}^T \boldsymbol{G} \boldsymbol{n_s}$) which is equal to 1 in the Cartesian case. For RPH, Eq. 3.43 can be expressed as,

$$\mathbf{P}_{\boldsymbol{s}}(l) = \frac{\boldsymbol{g_s}(l) \boldsymbol{g_s}(l)^T}{\boldsymbol{g_s}^T(l) \boldsymbol{G}(l) \boldsymbol{g_s}(l)} \tag{3.44}$$

where the gradient in internal coordinates ($\boldsymbol{g_s}$) is obtained from its Cartesian counterpart $\boldsymbol{g_x}$ from the same relation already used for the full-dimensional case in Eq. 2.38,

$$\boldsymbol{g_s}(l) = \{\boldsymbol{B}^T\}^+(l) \boldsymbol{g_x}(l) \tag{3.45}$$

In Ref.[79], an alternative equation, where the pseudo-inverse is built from the matrix of the atomic masses $\boldsymbol{M}$ has been proposed. However, as already remarked in the previous section, the definition of the pseudoinverse matrix is not unique, and for this reason the two formulations are equivalent.
As for the full-dimensional case, the orthogonal modes $\boldsymbol{Q}^p$ are computed with the GF method introduced in the previous chapter. In a similar way to Cartesian coordinates, the projected modes are here the eigenvectors of $\boldsymbol{G}\boldsymbol{H}_{\boldsymbol{s}}^p$, with the projected Hessian matrix $\boldsymbol{H}_{\boldsymbol{s}}^p$ defined as,

$$\boldsymbol{H}_{\boldsymbol{s}}^p(l) = [\mathbf{1} - \mathbf{P}_{\boldsymbol{s}}(l) \boldsymbol{G}(l)] \boldsymbol{H_s}(l) [\mathbf{1} - \boldsymbol{G}(l) \mathbf{P}_{\boldsymbol{s}}(l)] \tag{3.46}$$

where $\boldsymbol{H_s}$ is the full-dimensional Hessian in internal coordinates. Those quantities change along the curve $\boldsymbol{a}_{\mathrm{LAM}}(l)$ and therefore are functions of l. As mentioned in the previous chapter, the calculation of the full-dimensional Hessian $\boldsymbol{H_s}$ from its cartesian counterpart $\boldsymbol{H_x}$ requires both the Wilson $\boldsymbol{B}$ matrix and its first derivative $\boldsymbol{B}'$,[113,205]

$$\boldsymbol{H_s}(l) = \{\boldsymbol{B}(l)^T\}^+ \left[\boldsymbol{H_x}(l) - \boldsymbol{g_s}(l)^T \boldsymbol{B}'(l)\right] \boldsymbol{B}(l)^+ \tag{3.47}$$

where $\boldsymbol{B}^+$ is the pseudo-inverse of $\boldsymbol{B}$. It is worth noting that the equivalence between harmonic models in Cartesian and internal coordinates is lost when working with projected modes, for two reasons:

- the projector operator is different in the two representations.
- the gradient is, in general, non-null along the LAM, thus the second term of the conversion of the Hessian given Eq. 2.36 is not null as well.

As already done for the Cartesian case, the internal coordinates-based eigenvectors associated to non-null eigenvalues can be collected as columns of a matrix $\boldsymbol{L}^p(l)$, defining the projected normal modes $\boldsymbol{Q}^p$ in terms of the internal coordinates as,

$$\boldsymbol{L}^{p}\left(l\right)\boldsymbol{Q}^{p}=\boldsymbol{s}-\boldsymbol{s}^{\mathrm{eq}}\left(l\right) \tag{3.48}$$

where $\boldsymbol{s}^{\mathrm{eq}}\left(l\right)$ are the internal coordinates of the geometry corresponding to the IRC parameter l. The full vibrational Hamiltonian can be built as for the Cartesian case, but the final result is different from the one given in Eq. 3.41 since, for example, vibro-rotational couplings are null in internal coordinates, since their contribution are projected out from the transformation given in Eq. 3.46, while they are non-null in Cartesian coordinates. However, in the adiabatic approximation, where all couplings are neglected, the same Hamiltonian is obtained,

$$\mathcal{H}_{\mathrm{vib}}^{\mathrm{ad}}=\mathcal{T}_{\mathrm{LAM}}(l)+\mathcal{V}_{\mathrm{LAM}}(l)+\mathcal{T}_{N'_{\mathrm{vib}}}(\boldsymbol{Q}^{p})+\sum_{i=1}^{N'_{\mathrm{vib}}}\frac{1}{2}\{\omega_{i}^{p}\}^{2}(l)Q_{i}^{p}(l)^{2} \tag{3.49}$$

Even if the expression of $\mathcal{H}_{\mathrm{vib}}$ obtained using equation 3.49 does not contain any direct coupling between the LAM and the orthogonal normal modes, an indirect coupling is present due to the parametric dependence of ω_{i}^{p} and $\boldsymbol{Q}^{p}$ on l. This parametric dependence is analogous to the separation of slow and fast motion in the Born-Oppenheimer approximation, where the electronic Schrödinger equation is solved for a fixed value of the nuclear coordinate. In this case, the "slow" coordinate is the LAM, and the Schrödinger equation for the "fast" coordinates, i.e. the projected modes.
The vibrational wavefunctions $\chi(l,\boldsymbol{Q}^{p})$ of the adiabatic Hamiltonian given in Eq. 3.49 can be then computed following the same strategy employed as for the Born-Oppenheimer separation.[106] $\chi(l,\boldsymbol{Q}^{p})$ is factorized as the product of a LAM wavefunction, $\chi_{\mathrm{LAM},i(k)}\left(l\right)$, and the one of the harmonic modes, $\chi_{N'_{\mathrm{vib}},k}\left(l,\boldsymbol{Q}^{p}\right)$, depending on the IRC parameter, where k labels the wavefunction for the harmonic modes, and i the one of the LAM. By inserting,

$$\chi(l,\boldsymbol{Q}^{p})=\chi_{\mathrm{LAM},i(k)}\left(l\right)\times\chi_{N'_{\mathrm{vib}},k}\left(l,\boldsymbol{Q}^{p}\right) \tag{3.50}$$

in the eigenvalue equation for $\mathcal{H}_{\mathrm{vib}}^{\mathrm{ad}}$, two coupled Schrödinger equations are obtained, one for each component of the overall wavefunction:

$$\begin{aligned}\mathcal{H}_{N'_{\mathrm{vib}}}\chi_{N'_{\mathrm{vib}},k}\left(l,\boldsymbol{Q}^{p}\right)&=\left[\mathcal{T}_{N'_{\mathrm{vib}}}(\boldsymbol{Q}^{p})+\mathcal{V}_{N'_{\mathrm{vib}}}(\boldsymbol{Q}^{p};l)\right]\chi_{N'_{\mathrm{vib}},k}\left(l,\boldsymbol{Q}^{p}\right)\\&=E_{N'_{\mathrm{vib}},k}(l)\,\chi_{N'_{\mathrm{vib}},k}\left(l,\boldsymbol{Q}^{p}\right)\end{aligned} \tag{3.51}$$

$$\left[\mathcal{T}_{\mathrm{LAM}}(l)+\mathcal{V}_{\mathrm{LAM}}(l)+E_{N'_{\mathrm{vib}},k}(l)\right]\chi_{\mathrm{LAM},i(k)}\left(l\right)=E_{\mathrm{tot},i(k)}\,\chi_{\mathrm{LAM},i(k)}\left(l\right) \tag{3.52}$$

where $\mathcal{H}_{\mathrm{LAM}}$ is defined in Eq. 3.21, $\mathcal{H}_{N'_{\mathrm{vib}}}$ is the sum of N'_{vib} harmonic oscillator Hamiltonians, $E_{\mathrm{tot},i(k)}^{\mathrm{tot}}$ is the total vibrational energy and,

$$E_{N'_{\text{vib}},k}(l) = \sum_{i=1}^{N'_{\text{vib}}} \omega_i^p(l) \left(n_i + \frac{1}{2}\right) \tag{3.53}$$

Eqs. 3.51 and 3.52 highlight the indirect coupling between $\boldsymbol{Q}^p$ and l. In fact, the potential used to compute the LAM wavefunctions ($\chi_{\text{LAM},i(k)}(l)$) contains, besides the pure electronic contribution $\mathcal{V}^{\text{LAM}}(l)$, the energy of the wavefunction for the "N'_{vib}" harmonic modes ($E_{N'_{\text{vib}},k}(l)$). Analogously, the Schrödinger equation for the harmonic modes change along the LAM, since the Hessian matrix, as well as the projection operator, are functions of l. As a consequence, a different set of nuclear wavefunctions for the LAM is obtained for each level of the "N'_{vib}" harmonic modes. In practice, the calculation of the vibrational levels requires the following computational protocol:

1. calculation of the electronic energy along the PES through a scan calculation (non-relaxed, relaxed, IRC).

2. at each step of the scan, calculation of the Hessian and determination of the projected modes using Eq. 3.46 (for NR-ICPH) or Eq. 3.40 (for RPH).

3. fitting of the PES with a cubic spline to obtain a semi-analytical representation, to be used in the subsequent variational calculation.

4. fitting of the projected harmonic frequencies $\omega_i^p(l)$ through a B-spline fitting. This step is necessary to add the contribution from the N'_{vib} harmonic modes (third term in Eq. 3.52) to the PES obtained from electronic structure calculations. The fitting can be done only if each projected normal mode can be tracked and consistently labeled along the scan, and thus if $\boldsymbol{Q}^p$ does not change quickly along the IRC. This assumption has to be met since, otherwise, large elements in $\boldsymbol{\Gamma}$ are present and the adiabatic approximation is not accurate.

5. a vibrational level k of the N'_{vib} orthogonal modes is selected, its energy along the LAM is computed ($E_{N'_{\text{vib}},k}(l)$) and added to the PES obtained from the electronic structure calculation.

6. the vibrational levels of the LAM associated to the k-th state of the N'_{vib} orthogonal modes are computed with the DVR-based method outlined above.

To conclude this section, a significant simplification can be obtained by neglecting the dependence of the harmonic frequencies and normal modes on l since, in this case, the potential $\mathcal{V}_{N'_{\text{vib}}}$ and the vibrational energies $E_{N'_{\text{vib}},k}$ do not depend on l. As a consequence, this last term is a constant and the LAM wavefunctions are the same for each vibrational level of the N'_{vib} harmonic coordinates. Under those approximations, no couplings, neither parametric nor direct, are present between the LAM and the other modes, and it is sufficient to solve the vibrational Schrödinger equation for the LAM only once.

3.3 Selected applications

The reliability of the hybrid harmonic-variational framework introduced in the previous section will be now tested using two molecules as test-cases. The first one is a small-size system, ammonia (NH_3), which will be used to check the reliability of the code. A more complex system, bithiophene, will be used to highlight the difference between the various formulations of the hybrid DVR-harmonic schemes, with particular care on the impact of the choice of the coordinates system on the simulated spectrum.

3.3.1 Ammonia: benchmark of the model.

The first test-case is ammonia, which is, as it is well known, pyramidal in the equilibrium geometry of its neutral ground state. The lowest frequency vibrational mode is a LAM corresponding to the umbrella inversion coordinate. The PES of the ground state along this LAM has a symmetric double-well shape, where the two minima correspond to two, equivalent pyramidal geometries, and the transition state corresponds to the planar configuration. As already mentioned above, double-well potentials are the classical cases that are poorly described in terms of harmonic models, since several geometries, that could be used as a reference for the harmonic expansion, are present.
As a first step, ammonia has been used to check the numerical stability of the DVR-based approach with respect to the density of the two grids used in the scan and in the variational calculation. As a reminder, the first grid is employed for the QM calculations, and is used to fit the PES with the cubic spline representation. The second grid is used in the DVR-based variational calculation on the fitted PES. In Tab. 3.1, the energies of the five lowest vibrational levels of the inversion mode of ammonia, computed with different grids, are reported. The PES along the umbrella mode has been computed from a non-relaxed scan along the inversion mode from 50° to 130° (therefore using the NR-ICPH model). The results reported in Tab. 3.1 show that, for a given step-size and a given number of points of the non-relaxed scan (which gives a unique representation of the PES in terms of B-splines), 150 DVR basis functions (corresponding to a grid spacing of 0.53°) are sufficient to reach a convergence of the energy levels within 1 cm^{-1}. On the other hand, a significantly larger step-size, of 4°, can be safely used in the first scan, where discrete geometries are taken at regular intervals along the large-amplitude coordinate, to reach convergence in the B-spline fitting. Those findings are in line with the discussions in the previous section, and confirm that a fitting step preceding the DVR calculation significantly reduces the number of QM calculations needed with respect to a direct approach, where QM calculations are performed directly on the DVR grid.
The last column of Tab. 3.1 contains the energies of the 5 lowest vibrational states for the ground, neutral electronic state of ammonia computed after a relaxed scan of the PES along the inversion coordinates, therefore using the ICPH model. The difference between the frequencies computed within the

Scan step-size		Number of DVR basis functions			
		100	150	200	150(rel)
		519.69	521.58	521.79	504.32
		520.67	522.56	522.77	505.72
	2°	1451.14	1453.05	1453.27	1392.42
		1496.07	1497.99	1498.21	1449.91
		2106.84	2108.78	2109.02	2021.75
		519.75	521.65	521.86	504.36
		520.74	522.63	522.84	505.77
	4°	1451.28	1453.19	1453.41	1392.50
		1496.28	1498.20	1498.42	1450.05
		2107.04	2108.98	2109.22	2021.88
		520.25	522.18	522.40	505.61
		521.25	523.17	523.39	507.03
	8°	1451.76	1453.70	1453.93	1393.91
		1497.16	1499.10	1499.34	1451.95
		2107.44	2109.41	2109.67	2023.04
		521.48	521.49	522.14	499.87
		522.54	522.55	523.21	501.34
	16°	1443.77	1443.79	1444.46	1369.87
		1495.29	1495.32	1495.99	1433.99
		2071.20	2071.26	2071.94	1970.31

TABLE 3.1: Vibrational energies (in cm^{-1}) of the 5 lowest-energy vibrational states of ammonia computed using the DVR-based approach with different step sizes in the PES scan calculation (expressed in degrees) and with a different number of basis functions. The energies are reported in wavenumbers. All electronic structure calculations were performed at the B3LYP/SNSD level. In all cases, non-relaxed scans have been performed, except for the last column, where the results issuing from a relaxed scan are reported. (Source Ref. 203)

ICPH and NR-ICPH is, in all cases, above 15 cm^{-1}, with a maximum reached for the highest-frequency modes, where it is above 100 cm^{-1}. This discrepancy can be understood from the PES that are obtained with the two models, which are plotted in Fig. 3.2. As expected, the energy barrier between the minimum and the transition state is higher in the NR-ICPH framework than in the ICPH one, with a difference of about 1.68 kJ/mol. In fact, for ICPH, the geometry is optimized at each step of the scan, leading to a lower energy. The height of the barrier (of about 1760 cm^{-1}) is higher than the vibrational frequency of the inversion mode, and for this reason, the two lowest-energy states are nearly degenerate (as can be seen from tab. 3.1), corresponding to the symmetric and antisymmetric combinations of wavefunctions localized in the two minima. Since the coupling between the two localized states decreases as the barrier gets higher, the energy difference between those wavefunctions, also known as tunneling splitting Δ, becomes smaller. This can be seen also by combining the tunneling splitting of NH_3 computed at the NR-ICPH ($\Delta_{\text{NR-ICPH}}$) and ICPH (Δ_{ICPH}) level. In fact, $\Delta_{\text{ICPH}} < \Delta_{\text{NR-ICPH}}$, in agreement with the relative value of the energy barrier. The difference between NR-ICPH and ICPH is even more evident for higher-energy states, that are not localized in the two energy minima, but are delocalized over all the range of the IRC parameter. In fact, the NR-ICPH and ICPH models coincide only at the two equilibrium positions, and the deviation between them increases with the displacement from those nuclear configurations.

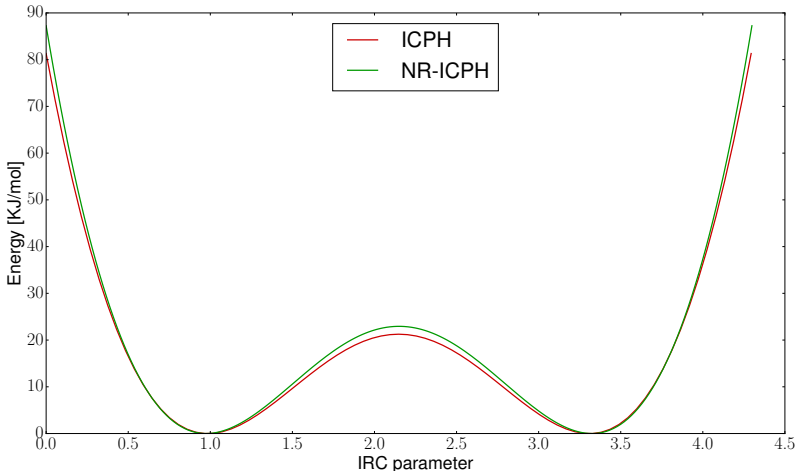

FIGURE 3.2: Plot of the PES of the neutral, ground state of NH_3 computed within the NR-ICPH (solid, green line) and ICPH (solid, red line) models. Electronic structure calculations were performed at the B3LYP/SNSD level.

Since the PES along the inversion coordinate of NH_3 is a double-well, the RPH framework can be employed to study the LAM too. Ammonia is also an ideal case to test the extrapolation procedure coupled to RPH since, due to the symmetry of the system, only one degree of freedom (the N–H distance) needs to be optimized along the scan, and therefore RPH should be equivalent to ICPH. The vibrational energies computed using ICPH and RPH with

different extrapolation schemes are reported in Tab. 3.2. Based on the previous results, 150 DVR basis functions have been used for each simulation and, for ICPH, a step-size of 4° has been employed. The results show that, if the extrapolation is performed including only the points obtained from an IRC calculation (second column of Tab. 3.2), large deviations, above 60 cm^{-1} in all cases, from the frequencies computed at the ICPH level are observed. The quality of the results can be significantly improved by computing the electronic energies for geometries beyond the minima, following the normal mode correlating with the IRC coordinate (which is in this case the umbrella-inversion mode). The discrepancy with the ICPH results decreases, and is approximately 10 cm^{-1} if 8 points (4 for each side of the IRC) are added. From those results, it is clear that the extrapolation is mandatory to minimize the error for a given number of scan points.

	LAM model	ICPH	RPH	RPH	RPH	RPH	RPH	RPH (no extr.)
	Added points		0	2	4	6	8	8
Vib. level	n=0	504.36	573.57	551.37	527.66	508.67	496.74	697.33
	n=1	505.77	575.61	553.22	529.27	510.14	498.10	734.43
	n=2	1392.50	1509.51	1478.74	1446.97	1419.36	1399.21	1687.33
	n=3	1450.05	1605.41	1564.33	1521.50	1486.44	1460.06	1904.33
	n=4	2021.88	2188.32	2145.46	2105.10	2070.83	2045.91	2558.45

TABLE 3.2: Vibrational energies of the 5 lowest-energy vibrational states of ammonia computed within the ICPH (column 1) and RPH frameworks (column 2-7). For RPH calculations, calculations have been performed adding scan points beyond the minima (the number of the additional point is reported in the "Added points" row). All electronic structure calculations have been performed at the B3LYP/SNSD level.

Up to this point, the vibrational energies along the LAM have been computed using $\mathcal{H}_{\mathrm{LAM}}$, therefore neglecting the energy arising from the other harmonic modes. However, this contribution is negligible only if the harmonic modes do not change along the LAM. With the aim of checking the reliability of this approximation, the projected frequencies $\omega_i^p(l)$ are plotted in Figs. 3.3 and 3.4. For the two degenerate bending modes (Fig. 3.3), a variation of up to 100 cm^{-1} occurs along the scan, with a maximum value obtained close to the two minima, and the minimum corresponding to the planar configuration. The degeneracy of the modes is preserved along the scan, since the minimal point group of the molecule is C_{3v} along all the scan.
For the N–H stretching modes (reported in Fig. 3.4), the variation of the harmonic wavenumber is even more pronounced, and has a maximum of more than 500 cm^{-1}. It is worth noticing that two crossing points between the three curves, associated to the three N–H stretching modes, are detected. In correspondence of those two points, the energetic order of the two, degenerate, antisymmetric and symmetric N–H modes changes. Those crossings are the vibrational analogues of conical intersections for electronic structure calculations.

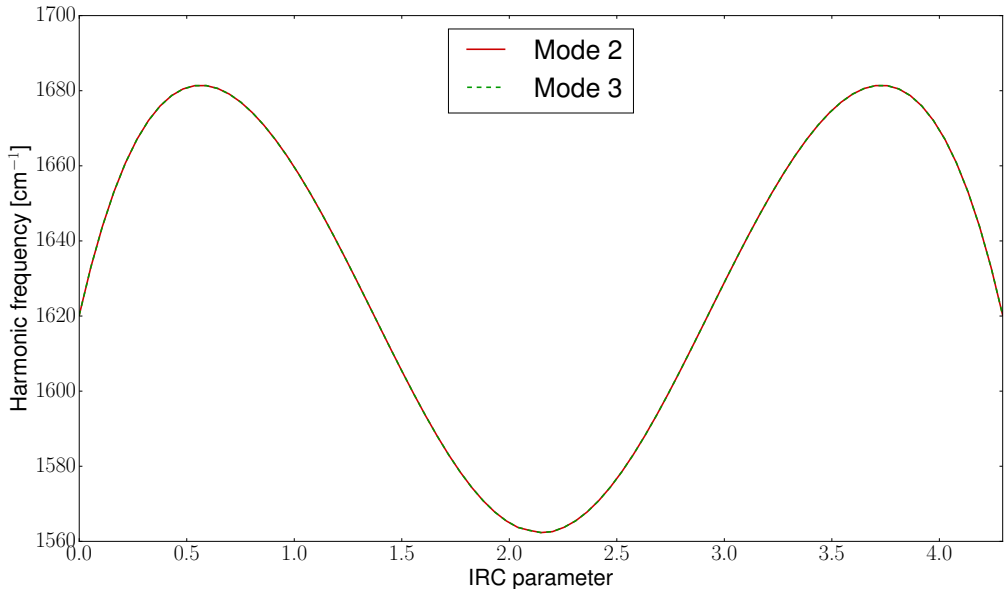

FIGURE 3.3: Graphical representation of the variation of the wavenumber of the bending modes along the LAM.

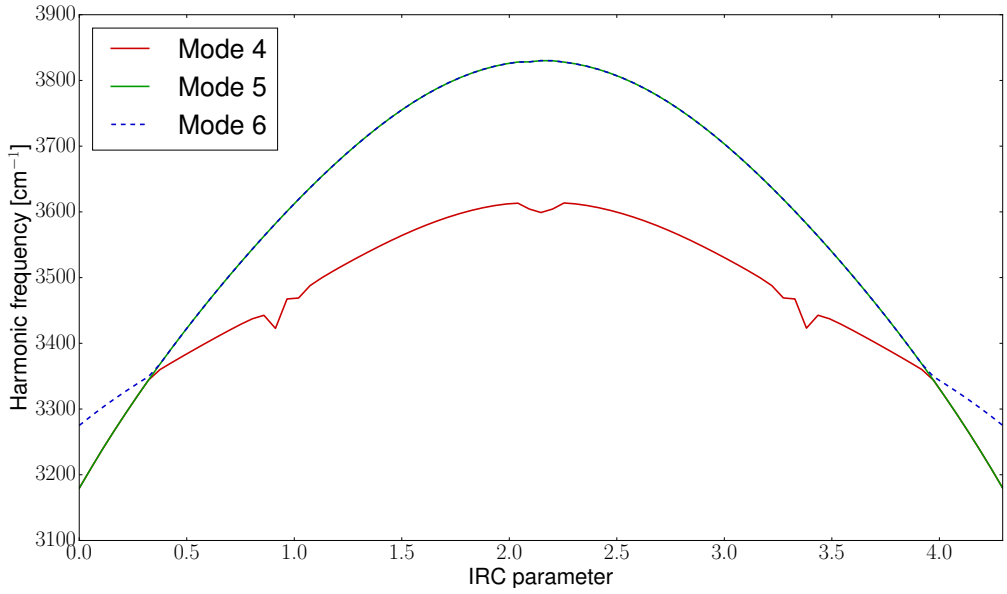

FIGURE 3.4: Graphical representation of the variation of the frequency of the N−H stretching modes along the LAM.

Up to now, all calculations have been performed in Cartesian coordinates. However, as already mentioned above, the projected harmonic frequencies, unlike the full-dimensional ones, change with the coordinate system. To highlight this effect, the wavenumber of mode 2, corresponding to one of the two H−N−H bending modes, is plotted as a function of the IRC coordinates in Fig. 3.5.

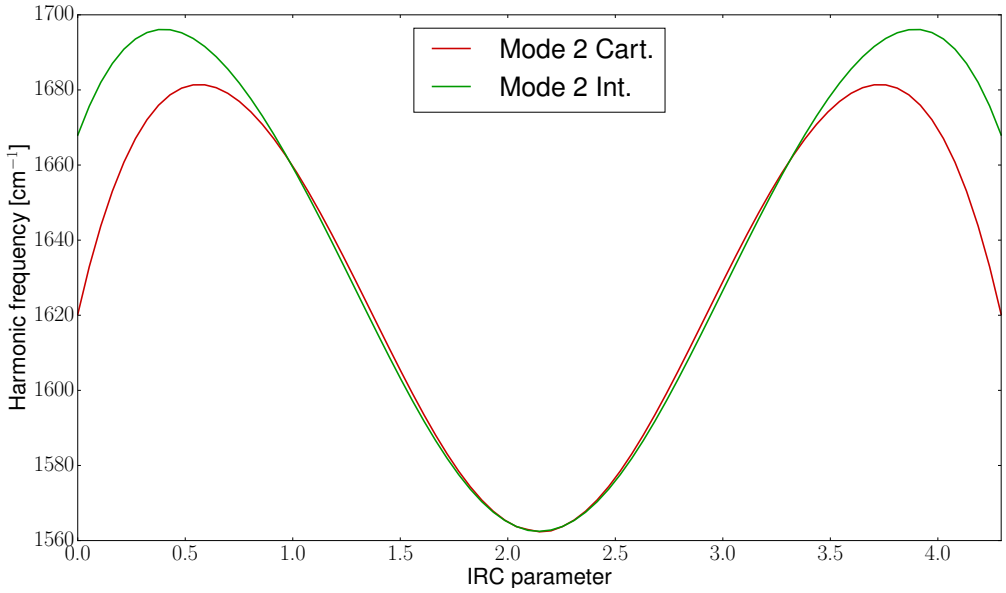

FIGURE 3.5: Plot of the projected wavenumber of the H−N−H modes of ammonia along the IRC coordinate corresponding to the bending mode.

It is noteworthy that the two representations are equivalent for three values of the IRC parameter, namely at the center, corresponding to the planar configuration (associated to the saddle point of the PES) and at the two minima (at about 1 and 3.5 $\sqrt{\text{amu}} \times$ Bohr). In fact, those three points are stationary points of the PES, meaning that $\boldsymbol{g} = \mathbf{0}$, and thus the projector is null and the second term of Eq. 3.47 is null. As already mentioned in the previous chapter, in those cases Cartesian and internal coordinates provide equivalent results. The deviation between the two representations increases with the distance from the stationary points, and is maximal in the two boundary regions. In fact, those regions correspond to a steep increase in the potential, and thus the difference between the representations is expected to increase as well.
The orthogonal harmonic frequencies influence the calculation of the vibrational energies through the $E_{N'_{\text{vib}},k}(l)$ term in Eq. 3.49 If the variation of the frequencies along the LAM is small, this term is just a constant shift of the Hamiltonian. However, the frequency changes non-negligible, this term will change with l. As a consequence, the shape of the PES will change as well, and this will have a significant impact on the vibrational levels and wavefunctions. The $E_{N'_{\text{vib}},k}(l)$ term depends on k, thus on the vibrational level for the N'_{vib} modes for which the LAM level is computed. For the sake of simplicity, only the ground state of the N'_{vib} modes will be considered, and thus:

$$E_{N'_{\text{vib}},0}(l) = \frac{1}{2}\sum_{i=1}^{N'_{\text{vib}}} \omega^p(l) \tag{3.54}$$

The comparison of the PESs obtained from the scan calculation, where the contribution of the orthogonal modes has not been included, with the adiabatic one, where this term is taken into account, is reported in Fig. 3.6.

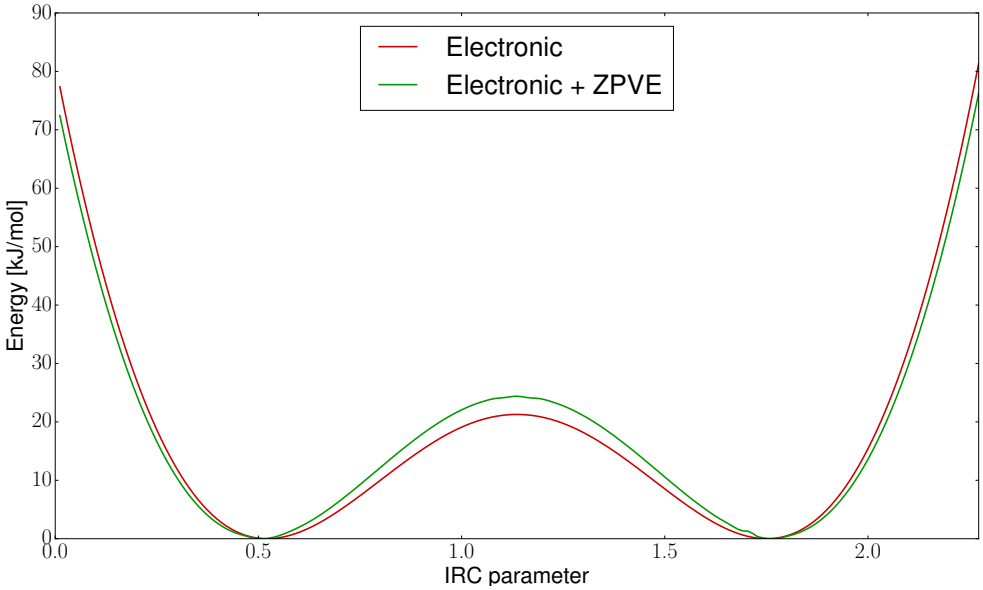

FIGURE 3.6: Graphical representation of the PES along the inversion coordinates of ammonia obtained from an IRC calculation by including only the pure electronic contribution (solid, red line) or by adding the ZPVE of the N'_{vib} orthogonal mode (solid, green line).

The main difference between the two PESs is observed at the the saddle point, where the height of the barrier increases by adding the contribution of the zero-point vibrational energy (ZPVE). This is in line with the plot reported in Fig. 3.4, where the maximum of the N−H stretching frequencies is reached at the saddle point. We note that, however, the value of the H−N−H bending is minimum at the saddle point. However, the variation of this frequency is smaller than the one of the NH stretching, and thus the latter contribution is dominant. The vibrational energies for the two PESs with the DVR variational approach described in the previous section are reported in Tab. 3.3 As expected, the tunneling splitting is lower for the PES obtained including the ZPVE, since the barrier is higher. It is worth noting that the deviation between the vibrational energies decreases for the higher-energy vibrational states. In fact, the energy of those states is much higher than the barrier, and thus those states are less sensitive to its height and more to the shape of the PES in the boundary regions. In those regions the deviation between the two PESs is smaller, and thus the deviation between the vibrational energies decreases as well.

Vib. Level	No ZPVE	With ZPVE
ZPVE	863.86	922.25
1	94.74	69.48
2	1313.05	1379.14
3	2087.38	2081.56
4	3268.01	3243.75
5	4604.04	4567.03

TABLE 3.3: Energy (in cm^{-1}) of the five lowest-energy vibrational levels for the inversion mode of ammonia computed with the DVR variational approach from the PES obtained from QM calculations (No ZPVE) and including the $E_k^{N'_{vib}}(l)$ term (With ZPVE)

3.4 Vibrational Density Matrix Renormalization Group (VDMRG)

The hybrid variational-harmonic scheme used up to now can be efficiently employed for a specific category of flexible systems, where a single coordinate can be found to describe the motion, for which the anharmonic effects are more pronounced. For most cases, however, such a convenient representation is not possible and a multidimensional, variational treatment is required. As already mentioned in Section 3.1, the main limitation of variational approaches such as VCI, is the exponential growth of their computational cost with the size of the problem. Several strategies for reducing the cost of variational approaches have been explored. For example, with an accurate choice of the coordinates (such as curvilinear internal coordinates[69,158,206] or localized modes[72,171,172]), it is possible to partition the vibrational Hamiltonian into non-interacting blocks of coordinates, and thus block-diagonalization schemes can be employed to efficiently compute vibrational energies. Alternatively, basis-pruning algorithms[70,71] have been developed, to identify *a priori* the basis functions with the largest CI coefficients, and to include only them in the variational treatment. From a purely algorithmic point of view, the computational cost of the diagonalization of the vibrational Hamiltonian matrix can be strongly reduced by using iterative subspace expansion algorithms (such as Davidson[167] and Jacobi-Davidson[168,207]), which are commonly used in electronic structure calculations.[85,208]

In this section, an alternative approach based on the density matrix renormalization group (DMRG) algorithm will be presented, with the aim of carrying out variational calculations on large-sized systems with a limited computational effort. In DMRG, the wavefunction is expressed as a matrix product state (MPS), providing a parametrization, which is much more compact than the standard VCI one (see Eq. 3.12). The resulting theory will be defined vibrational DMRG (VDMRG). As will be discussed more in detail in the following, VDMRG can be seen as a refined pruning algorithm, where the basis

function are chosen to obtain, in a least-squares sense, the best approximation of the "true" wavefunction. Furthermore, even if in the following VDMRG will be formulated only for the Watson Hamiltonian in Cartesian-based normal modes, the theory is general enough to support any kind of Hamiltonian and basis function, provided that the SQ expression for the Hamiltonian is known.

3.4.1 Basic theory of DMRG

Before describing VDMRG, it is useful to introduce the theory of DMRG for general Hamiltonians, not necessarily describing molecular vibrations. DMRG was introduced several decades ago[80,209] as a method for the calculation of the ground state of large, strongly correlated systems, and was initially mainly applied to the calculation of the ground state of spin chains. For this reason, here the main features of the DMRG theory will be presented for spin chains Hamiltonians. Its extension to more general problems will be discussed only later.

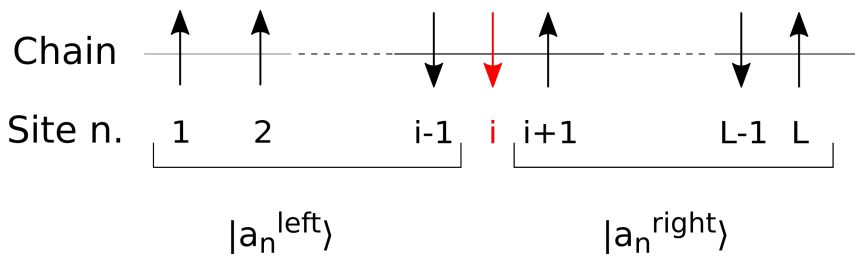

FIGURE 3.7: Graphical representation of the sweep-based optimization of a spin chain with L sites, where the optimization is performed for the i-th site.

Let us suppose to study a chain of L spin (referred to as sites in the following), where the state of each site is described with a vector space (referred to as local basis) of N_{basis} functions. The j-th function of the local basis of the i-th site will be referred to as $|\,\psi^{\text{loc}}_{j,i}\,\rangle$. The size of the local basis is, in general, different for each site, but here, for the sake of simplicity, we will assume that N_{basis} is the same for all the sites. Starting from the $|\,\psi^{\text{loc}}_{i}\,\rangle$ sets, it is possible to build a basis for the full system of L spins as direct product of all the local basis functions. The overall dimension of the resulting basis grows with the N_{basis}-th power of the chain size L, and this exponential increase of the size, also known as curse of dimensionality, makes variational approaches feasible only for small-size systems. DMRG offers a way to avoid the curse of dimensionality, based on two ideas:

1. the variational parameters are not optimized together, to avoid the solution of a full-dimensional secular equation, that would require the diagonalization of a N^{L}_{basis}-dimensional matrix. Instead, the variational parameter of each site are optimized one after the other, starting from the first site (see Fig. 3.7 for a graphical representation of the chain)

and going back and forth along the chain. This algorithm is known as sweep-based optimization.[82]

2. after the optimization of the variational parameters for a given site, only m basis functions are kept in the variational space, in order to avoid the curse of dimensionality. This algorithm is usually known as decimation, and we will refer to m as the number of renormalized block states.

The efficiency of DMRG is obtained through the combination of the sweep-based optimization and the decimation step. Let us now analyze more in detail these two algorithms. As already mentioned above, in DMRG each site is optimized separately from the others. Let us denote the site, on which the optimization is performed, as i (see Fig. 3.7). The other sites are divided in two groups, the left and right blocks, where the former includes sites 1-$i-1$, while the latter the $i+1$-L ones. Let us suppose to know a basis set $|\, a_n^{\text{left}} \,\rangle$ with n_l elements describing the states of the left block, and another set $|\, a_n^{\text{right}} \,\rangle$ with size n_r describing the right block. The ground state wavefunction $|\, \Psi_{\text{GS}} \,\rangle$ can thus be expressed as,

$$|\, \Psi_{\text{GS}} \,\rangle = \sum_{l=1}^{n_l} \sum_{r=1}^{n_r} \sum_{j=1}^{N_{\text{basis}}} C_{lr}^{k} |\, a_l^{\text{left}} \psi_{j,i}^{\text{loc}} a_r^{\text{right}} \,\rangle \tag{3.55}$$

where the C_{lr}^{k} tensor is optimized variationally by solving the secular equation in the $|\, a_l^{\text{left}} \psi_{j,i}^{\text{loc}} a_r^{\text{right}} \,\rangle$ basis. The optimization is then shifted to the following, i+1-th site (forward sweep). The sweep-based optimization alone does not bring any computational advantage since, if a complete set is used as a basis for the two blocks, the dimension of the C_{lr}^{k} tensor still grows exponentially with the chain size. However, in DMRG, after each optimization, only the m eigenvalues giving the largest contribution to the one-body density matrix are kept and included in the left boundary. It is thus evident that m, also known as "number of renormalized states", As can be noticed from the previous discussion, the m parameter controls the accuracy of DMRG simulations. By systematically increasing m, the full-CI representation is recovered, but the advantages of DMRG are lost. However, it has been shown that, for Hamiltonians not involving long-ranged interactions, converged energy are obtained with low values of m. For example, for the electronic structure case, converged electronic energies can be obtained with $m \approx$100-1000,[210,211,212] allowing a significant reduction of the computational cost with respect to standard CI approaches.
The previous formulation of is known as first-generation DMRG,[82] and corresponds to the first theoretical formulations. The main drawback of this formulation is that the wavefunction is not computed explicitly, which makes the calculation of properties different from the energies cumbersome. This issue has been solved by Östlund and Rommer,[213] who proved that the DMRG algorithm is equivalent to a standard variational calculation, where however the ground state wavefunction $|\, \Phi_{\text{GS}} \,\rangle$ is parametrized as follows,

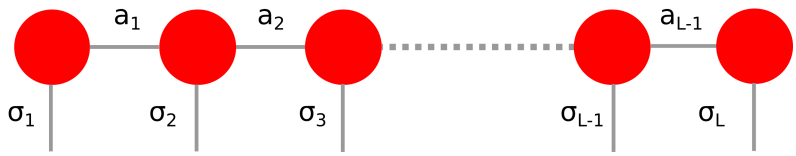

FIGURE 3.8: Graphical representation of a matrix product state. The $\boldsymbol{M}$ tensors are represented by red circles. Horizontal, gray bars represent the a_i indexes, whereas the σ_i ones are represented with vertical, gray bars.

$$
\begin{aligned}
|\,\Phi_{\mathrm{GS}}\,\rangle &= \sum_{\sigma_1=1}^{N_{\max}} \cdots \sum_{\sigma_L=1}^{N_{\max}} \sum_{a_1=1}^{m} \cdots \sum_{a_{L-1}=1}^{m} M^{\sigma_1}_{1,a_1} M^{\sigma_2}_{a_1,a_2} \ldots M^{\sigma_{L-1}}_{a_{L-1},1} |\,\sigma_1,\ldots,\sigma_L\,\rangle \\
&= \sum_{\sigma_1=1}^{N_{\max}} \cdots \sum_{\sigma_L=1}^{N_{\max}} \boldsymbol{M}^{\sigma_1}\boldsymbol{M}^{\sigma_2}\ldots\boldsymbol{M}^{\sigma_L} |\,\sigma_1,\ldots,\sigma_L\,\rangle
\end{aligned}
\tag{3.56}
$$

The parametrization given in the previous equation is usually referred to as matrix product state (MPS). Furthermore, $|\,\sigma_1,\ldots,\sigma_L\,\rangle$ is a SQ occupation number vectors obtained from the direct product of the local basis of the single sites, each one of dimension $N_{\max}$. Furthermore, for a given value of σ_i, $\boldsymbol{M}^{\sigma_i}$ is a $m \times m$ matrix, where m corresponds to the number of renormalized block states of first-generation DMRG. By comparing Eq. 3.56 to a standard CI expansion, we note that, in an MPS, the CI matrix $\boldsymbol{C}_{\sigma_1,\ldots,\sigma_L}$ is expressed as,

$$
\boldsymbol{C}_{\sigma_1,\ldots,\sigma_L} = \sum_{a_1=1}^{m} \cdots \sum_{a_{L-1}=1}^{m} M^{\sigma_1}_{1,a_1} M^{\sigma_2}_{a_1,a_2} \ldots M^{\sigma_{L-1}}_{a_{L-1},1} \tag{3.57}
$$

The previous equation shows that the number of parameters needed to define an MPS scales as $m^2 \times N_{max} \times L$, and this allow to avoid the curse of dimensionality. We note that the previous parametrization is general, and not necessarily limited for spin-chains Hamiltonians. For example, in electronic structure calculation, the parametrization given in Eq. 3.56 can be used if the number of sites L corresponds to the number of orbitals of the molecule. Similarly, for vibrational structure calculation, the number of sites corresponds to the number of modes of the molecule. To facilitate the following discussion, a graphical representation of the tensor defined in Eq. 3.57 is given in Fig. 3.8, where the DMRG tensors $\boldsymbol{M}^{\sigma_i}$ are represented by red circles. The index σ_i of each tensor is represented by a vertical bar, whereas the index associated to the renormalized block states a_i is represented by horizontal, gray lines. Indexes over which a contraction is performed, such as the a_i ones, correspond to lines in which both ends are connected to MPS tensors, while lines associated to non contracted indexes, such as the σ_i ones, have a free extreme. The main advantage of the MPS-based formulation of DMRG over the first-generation one is that a precise form for the wavefunction is given, and this

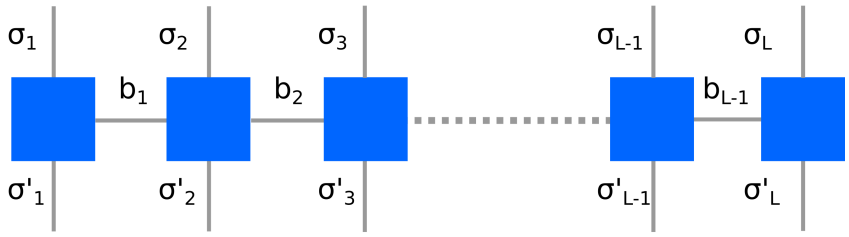

FIGURE 3.9: Graphical representation of a matrix product operator. The $\boldsymbol{W}$ tensors are represented by blue squares. The representation of the indexes as gray bars is obtained as in Fig. 3.8.

allows to manipulate the MPS, for example computing the action of an operator on it. An efficient calculation of the action of an operator $\mathcal{W}$ on an MPS requires to express $\mathcal{W}$ as a matrix product operator (MPO) as,

$$\begin{aligned}\mathcal{W} &= \sum_{\sigma_1,\ldots,\sigma_L}^{N_{\max}} \sum_{\sigma'_1,\ldots,\sigma'_L}^{N_{\max}} \boldsymbol{W}^{\sigma_1,\sigma'_1} \ldots \boldsymbol{W}^{\sigma_L,\sigma'_L} |\, \sigma_1,\ldots,\sigma_L \,\rangle\langle\, \sigma'_1,\ldots,\sigma'_L \,| \\ &= \sum_{\sigma_1,\ldots,\sigma_L}^{N_{\max}} \sum_{\sigma'_1,\ldots,\sigma'_L}^{N_{\max}} \sum_{b_1=1}^{b_{1,\max}} \cdots \sum_{b_{L-1}=1}^{b_{L-1,\max}} W_{1,b_1}^{\sigma_1,\sigma'_1} \ldots W_{b_{L-1},1}^{\sigma_{L-1},\sigma'_{L-1}} |\, \sigma_1,\ldots,\sigma_L \,\rangle\langle\, \sigma'_1,\ldots,\sigma'_L \,|\end{aligned} \tag{3.58}$$

Despite the similarity between Eqs. 3.56 and 3.58, two major differences are present; first of all, the tensors $\boldsymbol{W}$ have two upper indexes (σ and σ') corresponding to the local basis, since the operator is expressed in terms of a bra and a ket, instead of only a ket as for a wavefunction. Furthermore, the dimension of the $\boldsymbol{W}^{\sigma_i,\sigma'_i}$ tensors $b_{i,\max}$ is not a parameter that is changed to tune the accuracy of an MPS, but a constant value that depends on the form of the Hamiltonian. To highlight the difference between MPOs and MPSs, a graphical representation of an MPO is given in Fig. 3.9, where the $\boldsymbol{W}^{\sigma_i,\sigma'_i}$ are represented as blue squares. A direct comparison of Figs. 3.8 and 3.9 show that in MPS only a single set of vertical lines is present whereas, for the MPO, two vertical lines are present for each tensor. This is a direct consequence of the fact that $\boldsymbol{M}^{\sigma_i}$ has a single upper index, whereas $\boldsymbol{W}^{\sigma_i,\sigma'_i}$ has two upper indexes. Different algorithms have been proposed for encoding a general Hamiltonian in an MPO format.[214,215,216,217] Without going into the details, in the present work the algorithm proposed by Reiher and co-workers[216] will be employed. Here it is sufficient to recall that, for the quantum chemical electronic Hamiltonian, within this efficient construction the dimension of the $\boldsymbol{W}$ tensors scales as L^4.

Also in the second-generation formulation of DMRG, the variational parameters are optimized for each site one at the time. In fact, for an MPS, the energy functional is an highly non-linear function of the $\boldsymbol{M}^{\sigma_i}$ tensors. For this reason, a direct optimization of the MPS is not practical. However, the structure of an MPO given in Eq. 3.58 can be exploited to express the expectation value as:[216]

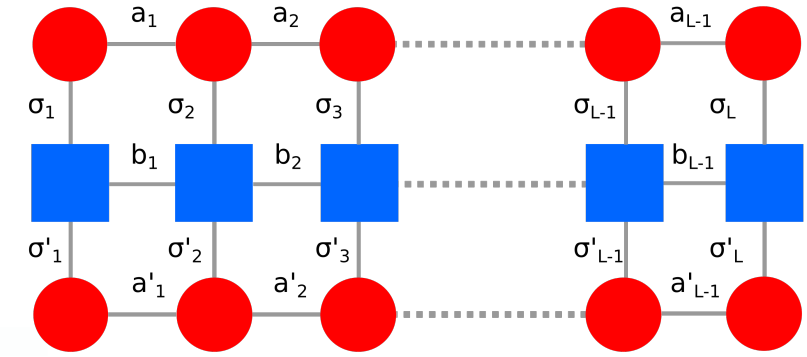

FIGURE 3.10: Graphical representation of the evaluation of the average of an operator $\mathcal{W}$, expressed as MPO over a matrix product state, obtained combining the representations given in Figs. 3.8 and 3.9.

$$\begin{aligned}\langle \Phi \mid \mathcal{W} \mid \Phi \rangle = & \sum_{\sigma_L,\sigma'_L=1}^{N_{\max}} \sum_{a_{L-1},a'_{L-1}=1}^{m} \sum_{b_l=1}^{b_{l,\max}} N^{\sigma_L,\dagger}_{1,a_{L-1}} W^{\sigma_L,\sigma'_L}_{b_{L-1},1} \\ & \times \left(\dots \sum_{\sigma_1,\sigma'_1=1}^{N_{\max}} M^{\sigma_1,\dagger}_{a_1,1} W^{\sigma_1,\sigma'_1}_{1,b_1} M^{\sigma'_1}_{1,a'_1} \dots \right) M^{\sigma'_L}_{a'_{L-1},1}\end{aligned} \tag{3.59}$$

where the $\boldsymbol{M}$ and $\boldsymbol{W}$ matrices are defined in Eqs. 3.58 and 3.56. Combining the graphical representations of a MPS and a MPO, given in Figs. 3.8 and 3.9, the evaluation of the average of $\mathcal{W}$ can be represented as in Fig. 3.10. It is worth noting that, in the latter figure, all the gray lines have both extreme connected to a tensor. In fact, all the indexes are contracted in Eq. 3.59. Based on Eq. 3.59, the expectation value can be evaluated by contracting the $\boldsymbol{M}$ tensors with the $\boldsymbol{W}$ ones one site after the others. In Eq. 3.59, the contractions are performed starting from the first site, but a similar expression can be obtained, for example, starting from the last, L-th site. If the contractions are started from site i, the following relation is obtained:

$$\langle \Phi \mid \mathcal{W} \mid \Phi \rangle = \sum_{a_i,a'_i=1}^{m} \sum_{b_i=1}^{b_{i,\max}} L^{b_i}_{a_i,a'_i} R^{b_i}_{a'_i,a_i} \tag{3.60}$$

where the boundaries matrices $\boldsymbol{L}$ and $\boldsymbol{R}$ are built from the following recursive relations:

$$\begin{aligned} L^{b_i}_{a_i,a'_i} &= \sum_{\sigma_i,\sigma'_i=1}^{N_{\max}} \sum_{a_{i-1},a'_{i-1}=1}^{m} \sum_{b_{i-1}=1}^{b_{i-1,\max}} L^{b_{i-1}}_{a_{i-1},a'_{i-1}} M^{\sigma_i,\dagger}_{a_{i-1},a_i} M^{\sigma'_i}_{a'_{i-1},a'_i} W^{\sigma_i,\sigma'_i}_{b_{i-1},b_i} \\ R^{b_{i-1}}_{a_{i-1},a'_{i-1}} &= \sum_{\sigma_i,\sigma'_i=1}^{N_{\max}} \sum_{a_i,a'_i=1}^{m} \sum_{b_i=1}^{b_{i,\max}} R^{b_i}_{a_i,a'_i} M^{\sigma_i}_{a_{i-1},a_i} M^{\sigma'_i,\dagger}_{a'_{i-1},a'_i} W^{\sigma_i,\sigma'_i}_{b_{i-1},b_i} \ , \end{aligned} \tag{3.61}$$

Eq. 3.60 is particularly useful in connection with the sweep-based optimization introduced above. In fact, if the energy is minimized with respect to the i-th set of matrices $\boldsymbol{M}^{\sigma_i}$ by keeping all the other tensors constants, the following eigenvalue equation is obtained.

$$\sum_{a'_{i-1},a'_i=1}^{m} \sum_{b_{i-1}=1}^{b_{i-1,\max}} \sum_{b_i=1}^{b_{i,\max}} \sum_{\sigma'_i=1}^{N_{\max}} W^{\sigma_i,\sigma'_i}_{b_{i-1},b_i} M^{\sigma'_i}_{a'_{i-1},a'_i} L^{b_{i-1}}_{a_{i-1},a'_{i-1}} R^{b_i}_{a'_i,a_i} = \mathrm{E}\, M^{\sigma_i}_{a_{i-1},a_i}\,, \tag{3.62}$$

which is formally equivalent to a standard eigenvalue problem. However, we note that, unlike the secular equation, which is obtained in CI problems, here the representation of the operator is not simply given by a matrix, but is the combination of several contractions with the MPO and with the boundaries. As already discussed above, in a sweep-base optimization, once Eq. 3.62 has been solved for the i-th site, the next, "i+1"-th site is optimized. To do so, the left (for forward sweep) and right (for backward sweeps) boundaries have to be updated at each iteration. A naive update of the boundary would lead to an exponential increase of their dimensions. However, if the update is performed through a Singular Value Decomposition (SVD), by keeping only the singular vectors corresponding to the largest singular values, the dimension of the boundaries can be controlled, and an increase of m is avoided.
The previous optimization scheme, where one site is optimized at each step, which is usually referred to as single-size optimization, can lead to convergence to local minima, as shown, for example, in Ref. 218. A possible solution is to introduce an *ad-hoc* noise term, built from perturbation theory.[218] An alternative solution is offered by the so-called two-sites optimization algorithm, where the matrices of two, adjacent sites are optimized simultaneously at each iteration. In this case, a two site tensor $\boldsymbol{T}$, defined as,

$$T^{\sigma_l,\sigma_{l+1}}_{a_{l-1},a_{l+1}} = \sum_{a_l=1}^{m} M^{\sigma_l}_{a_{l-1},a_l} M^{\sigma_{l+1}}_{a_l,a_{l+1}}\,, \tag{3.63}$$

is optimized at each iteration. As discussed in Ref. 216, an eigenvalue equation equivalent to Eq. 3.62 can be built for $\boldsymbol{T}$, by adapting the definition of the MPO. However, we note that the dimension of $\boldsymbol{T}$ is $N^2_{\max} \times m^4$, whereas for $\boldsymbol{M}$ it is $N_{\max} \times m^2$, thus the computational cost of a two-site optimization, in particular the diagonalization step, is higher than for single-site optimizations.

3.4.2 Theoretical formulation of VDMRG

The theoretical framework presented in the previous chapter holds for a general quantum system. The only quantity needed to perform the calculation is the Hamiltonian of the system, expressed in a SQ form. In the present section, VDMRG will be introduced, where the general DMRG theory is used for computing vibrational energies and wavefunctions.

In the following, the Watson Hamiltonian in Cartesian-based normal coordinates will be applied for the calculation of vibrational energies. By combining the potential expression given in Eq. 3.8 with the kinetic energy operator given in Eq. 3.5, the following definition is obtained:

$$\begin{aligned}\mathcal{H}_{\text{vib}} =& \frac{1}{2}\sum_{i=1}^{N_{\text{vib}}}\omega_i\left(p_i^2+q_i^2\right)\\ &+\frac{1}{6}\sum_{ijk=1}^{N_{\text{vib}}}k_{ijk}q_iq_jq_k+\frac{1}{24}\sum_{ijkl=1}^{N_{\text{vib}}}k_{ijkl}q_iq_jq_kq_l\\ &+\frac{1}{24}\sum_{\tau=x,y,z}B_\tau^{\text{eq}}\sum_{ijkl=1}^{N_{\text{vib}}}\zeta_{ij}^\tau\zeta_{kl}^\tau\left(\frac{\omega_j\omega_l}{\omega_i\omega_k}\right)^{1/2}q_ip_jq_kp_l\end{aligned} \tag{3.64}$$

where p_i is the conjugate momentum of the i-th dimensionless normal coordinate $\hat{q}_i$, defined in Eq. 3.2. Furthermore, the harmonic frequencies ω_i, the force constants k_{ijk} and k_{ijkl} are the third- and fourth-order reduced force constants, which can be defined in terms of the third- and fourth-order derivatives (k_{ijk} and k_{ijkl}), the equilibrium rotational constants B_τ^{eq} and the Coriolis couplings ζ_{ij}^τ are defined in the previous section. For the sake of simplicity, only terms up to fourth-order have been included in Eq. 3.64, but the generalization to higher-order terms is straightforward.
By replacing the reduced coordinates and momenta by the bosonic creation and annihilation operators $\hat{b}_i^+$ and $\hat{b}_i$, from their definition given in Eq. 2.26, we obtain the second-quantized form of the vibrational Hamiltonian,

$$\begin{aligned}\mathcal{H}_{\text{vib}} =& \sum_{i=1}^{N_{\text{vib}}}\omega_i\left(\hat{b}_i^+\hat{b}_i+\frac{1}{2}\right)\\ &+\frac{1}{12\sqrt{2}}\sum_{ijk=1}^{N_{\text{vib}}}k_{ijk}\left(\hat{b}_i^++\hat{b}_i\right)\left(\hat{b}_j^++\hat{b}_j\right)\left(\hat{b}_k^++\hat{b}_k\right)\\ &+\frac{1}{96}\sum_{ijkl=1}^{N_{\text{vib}}}k_{ijkl}\left(\hat{b}_i^++\hat{b}_i\right)\left(\hat{b}_j^++\hat{b}_j\right)\left(\hat{b}_k^++\hat{b}_k\right)\left(\hat{b}_l^++\hat{b}_l\right)\\ &-\frac{1}{96}\sum_{\tau=x,y,z}B_\tau^{\text{eq}}\sum_{ijkl=1}^{N_{\text{vib}}}\zeta_{ij}^\tau\zeta_{kl}^\tau\left(\frac{\omega_j\omega_l}{\omega_i\omega_k}\right)^{1/2}\left(\hat{b}_i^++\hat{b}_i\right)\left(\hat{b}_j^+-\hat{b}_j\right)\\ &\qquad\times\left(\hat{b}_k^++\hat{b}_k\right)\left(\hat{b}_l^+-\hat{b}_l\right)\end{aligned} \tag{3.65}$$

Eq. 3.65 shows that, for example, the third-order potential term can be written as a sum of all possible products of creation or annihilation operators localized on sites i, j, k (such as, for example $\hat{b}_i\hat{b}_j^+\hat{b}_k$). A similar result is obtained for the fourth-order potential term, but in this case 24 terms are present. More attention must be paid to the evaluation of the sign associated to a Coriolis term due to the presence of the momentum operator. The length

of the strings of SQ operators present in the Hamiltonian has a critical impact on the efficiency of DMRG, since longer strings require a larger bond dimension of the MPO, therefore resulting in an increase of the computational cost to obtain expectation values of the Hamiltonian. In electronic structure calculations, strings with up to four SQ operators are present, whereas in vibrational structure theory longer strings also exists. For example, it is well-known that sixth-order terms are often necessary in variational calculations to obtain accurate results.[159,160,219] To support those cases as well, the procedure reported in Ref. 216 to build MPOs has been generalized to support strings with 5 and 6 SQ operators as well. Another major difference between electronic and vibrational structure Hamiltonians is that the SQ form of the vibrational Hamiltonian given in Eq. 3.65 contains strings of SQ operators with a different number of creation and annihilation operators. As a consequence, the number of particles is not conserved for each individual mode or, in more theoretical terms, the Hamiltonian does not belong to the $U(1)$ symmetry group.
We note that, in Refs. 110 and 162, a different second-quantized form of the vibrational Hamiltonian has been proposed, based on the n-mode representation of the potential energy, where a general, one-dimensional basis set is used for each mode instead of the eigenfunctions of the harmonic oscillator Hamiltonian (i.e. the Hermite polynomials). Within this framework, a couple of creation and annihilation operators needs to be introduced for each basis function of each mode, and the SQ form of a vibrational wavefunction is obtained as follows:

$$| \Psi \rangle = | \{n_1^1, \ldots, n_{N_{\max}^1}^1\}, \ldots, \{n_1^L, \ldots, n_{N_{\max}^L}^L\} \rangle \tag{3.66}$$

where n_j^h is the occupation number of the j-th basis set of the h-th mode. Unlike the previous formulation, in this case the occupation number of each basis function cannot exceed 1, as in the electronic structure case. However, an additional constraint is present, since only one basis function per mode can have occupation number equal to 1 and the occupation numbers for the other basis has to be null. Even if symmetry constraints can be included in the MPO-MPS formulation of DMRG, as already discussed in Refs. 216,220,221 an implementation of VDMRG based on this formulation would be more difficult than the one based on the harmonic oscillator basis set. For this reason, the SQ form of the vibrational Hamiltonian given in Eq. 3.65 has been used. We note however that two major differences would be present between the two formulations of VDMRG. In the harmonic oscillator-based one, the size of the DMRG chain is equal to the number of modes, whereas in the other one, it is equal to the number of overall basis functions. Thus, in the second case, the size of the chain is much larger. However, in the n-mode representation, the number of SQ operators associated to each term of the Hamiltonian depends on the number of couplings present in the term, and not on the order of the Taylor expansion as in Eq. 3.65. Thus, for example, diagonal quartic (q_i^4) and sextic (q_i^6) terms would correspond to the same number of SQ operators in the n-mode representation. As a consequence, it

is still not clear which representation would be more efficient for VDMRG.
As already remarked above, the vibrational wave function of a molecule with L degrees of freedom can be expressed in a CI expansion as in Eq. 3.12. Within VDMRG, the L-dimensional tensor $\boldsymbol{C}_{n_1,\ldots,n_\mathrm{L}}$ is parametrized as,

$$\boldsymbol{C}_{n_1,\ldots,n_\mathrm{L}} = \sum_{a_1,\ldots,a_{L-1}}^{m} \boldsymbol{N}^{n_1}_{1,a_1} \boldsymbol{N}^{n_2}_{a_1,a_2} \ldots \boldsymbol{N}^{n_L}_{a_{L-1},1} \tag{3.67}$$

where the DMRG matrices are labeled as $\boldsymbol{N}$ to avoid confusion with the electronic case. For electronic wavefunctions, the Fermi-Dirac statistic prevents the occupation number of each orbital to exceed 1, whereas in the vibrational wave function it is unbounded. To limit, in practice, the size of the basis set appearing in Eq. 3.12, an upper bound ($N^\mathrm{i}_\mathrm{max}$) for the occupation number of each mode has to be defined. This means that the convergence of a VDMRG calculation has to be checked with respect to both the $N^\mathrm{i}_\mathrm{max}$ parameter and the bond dimension m.

3.4.3 Excited-state targeting in VDMRG

The standard formulation of VDMRG gives the ground-state energy. In practice, iterative eigensolvers, such as the Davidson[167] or Jacobi-Davidson[168] algorithms, are employed to compute the lowest energy state. However, for vibrational structure calculations, the most important quantities are vibrational frequencies, corresponding to transition energies to excited states. For this reason, a generalization of the previous theory to excited states needs to be formulated.
In standard variational calculations, excited states are in most cases computed by optimizing the wavefunction in the space orthogonal to the lower-energy states. The extension of this class of approaches to first-generation DMRG algorithms is not possible. In fact, the left- and right-boundary states are built from the density matrix of the ground state, and for this reason the same density cannot be used to compute also excited states. To overcome this issue, it has been proposed to build the boundary states with a state-average reduced density matrix, obtained by averaging all the states of interest.[222,223] While this provides a balanced representation of every state, the boundaries are not optimized for any specific level, and thus an higher value of m is usually needed to reach convergence.
In the MPO-MPS formulation of DMRG, the calculation of excited states is easier since an explicit form for the wavefunction is available. Let us consider the case where the first excited state $|\,\psi_1\,\rangle$ needs to be optimized after the optimization of the ground state $|\,\psi_0\,\rangle$. To perform a constrained optimization in the space orthogonal to $|\,\psi_0\,\rangle$, the scalar product between the ground and the first excited states needs to be computed. The overlap between two MPSs can be efficiently computed as:

$$\langle\,\psi_0\,|\,\psi_1\,\rangle = \sum_{\sigma_L}^{N_\mathrm{max}} \boldsymbol{M}^{\sigma_L\dagger} \ldots \left(\sum_{\sigma_1}^{N_\mathrm{max}} \boldsymbol{M}^{\sigma_1\dagger} \boldsymbol{N}^{\sigma_1} \right) \ldots \boldsymbol{N}^{\sigma_L} \tag{3.68}$$

where $\boldsymbol{M}$ are the tensors expressing the ground state as MPS, and $\boldsymbol{N}$ those, not optimized, associated to the first excited state. By computing the contractions one site at a time, it is easy to prove that the computational cost associated to the evaluation of Eq. 3.68 is $\mathcal{O}\left(m^3 \times N_{\max} \times L\right)$, thus the exponential increase of the cost is avoided in this case too. However, in the sweep-based method, the tensors are optimized sequentially, and thus the scaling can be further reduced by a factor equal to L, since only one tensors is modified at each step. Following the derivation described in refs.[216,224], it is useful to introduce the partial overlap matrices $\boldsymbol{C}$ and $\boldsymbol{D}$, defined as follows:

$$\begin{aligned} \boldsymbol{C}^l &= \sum_{\sigma_l=1}^{N_{\max}} \{\boldsymbol{M}^{\sigma_l}\}^\dagger \dots \left(\sum_{\sigma_1=1}^{N_{\max}} \{\boldsymbol{M}^{\sigma_1}\}^\dagger \boldsymbol{N}^{\sigma_1} \right) \dots \boldsymbol{N}^{\sigma_l} \\ \boldsymbol{D}^l &= \sum_{\sigma_{l+1}=1}^{N_{\max}} \boldsymbol{N}^{\sigma_{l+1}} \dots \left(\sum_{\sigma_L}^{N_{\max}} \boldsymbol{N}^{\sigma_L} \{\boldsymbol{M}^{\sigma_L}\}^\dagger \right) \dots \{\boldsymbol{M}^{\sigma_{l+1}}\}^\dagger \end{aligned} \tag{3.69}$$

It is easy to show that $\langle\, \Phi_0 \mid \Phi_1 \,\rangle = \mathrm{Tr}\left(\boldsymbol{C}^l \boldsymbol{D}^l\right)$. The main advantage associated with the introduction of the partial overlaps is that, at each sweep, only one element of the partial overlap vectors must be updated, therefore reducing the computational cost of the overlap computation by a factor of L. Let us consider the case where the i-th site is optimized in a single-site optimization (the extension to the two-site case is trivial). The overlap can be expressed as,[216]

$$\langle\, \psi_0 \mid \psi_1 \,\rangle = \mathrm{Tr}\left(\{\boldsymbol{M}^{\sigma_i}\}^\dagger \boldsymbol{V} \right) \tag{3.70}$$

where,

$$\boldsymbol{V} = \sum_{\sigma_i=1}^{N_{\max}} \boldsymbol{C}^{i-1} \boldsymbol{N}^{\sigma_i} \boldsymbol{D}^i \tag{3.71}$$

Thus, the overlap between the two MPSs can be computed as the scalar product between the DMRG tensors $\{\boldsymbol{M}^{\sigma_i}\}^\dagger$ and $\boldsymbol{V}$, where the tensors are seen as vectors, by grouping all the dimensions in a single index. This means, in practice, that components parallel to $\mid \Phi_0 \,\rangle$ can be projected out simply by applying the standard projection operator $\boldsymbol{I} - \boldsymbol{V}\boldsymbol{V}^T$. It is important noting that the overlap is not given simply by the scalar product between $\boldsymbol{M}^{\sigma_i}$ and $\boldsymbol{N}^{\sigma_i}$ since the other DMRG tensors, and thus the boundaries, are in general different. This approach, usually referred to as state-specific DMRG, can be easily generalized to the calculation of several eigenpairs, by applying successive projections with respect to the lower-energy states. The main limitation of this approach is that, in order to optimize an excited state, all the lower-energy states need to be optimized. Thus, for large-size systems, with several low-energy vibrations, a huge number of states needs to be optimized before reaching, for example, the fingerprint region. To make VDMRG applicable to large-size systems, algorithms to target directly excited states need to be developed.

In the present thesis, we employ the shift-and-invert (S&I) algorithms to

overcome the limitations described above. Before describing in details the S&I algorithm, we recall the main feature of subspace iterative diagonalization schemes. Within those schemes, the target eigenvector $|\,\boldsymbol{\nu}\,\rangle$ is expanded as a linear combination of a subspace $|\,\boldsymbol{\eta}\,\rangle = (|\,\boldsymbol{\eta}_1\,\rangle, \ldots, |\,\boldsymbol{\eta}_n\,\rangle)$ (we refer to this space as the search space) of the full vector space,

$$|\,\boldsymbol{\nu}^n\,\rangle = \sum_{i=1}^{n} c_{ni} |\,\boldsymbol{\eta}_i\,\rangle\,, \tag{3.72}$$

where n is the dimension of the subspace, which is updated at each iteration of the algorithm, and $|\,\boldsymbol{\nu}^n\,\rangle$ is the n-th approximation of the eigenvector. In the first iteration, the search space includes only one basis function, corresponding to the guess of the algorithm, and one function is added per iteration. Thus, the dimension n corresponds to the number of iteration. At each iteration, the coefficients are determined variationally, by solving the following secular equation:

$$\boldsymbol{H}^n_{\text{vib}} \boldsymbol{c}_n = E_{1,n} \boldsymbol{c}_n \tag{3.73}$$

where $\boldsymbol{H}^n_{\text{vib}}$ is the representation of the vibrational Hamiltonian $\mathcal{H}_{\text{vib}}$ in the $|\,\boldsymbol{\eta}\,\rangle$ basis and $E_{1,n}$ is the n-th approximation of the lowest eigenvalue. After solving Eq. 3.73 (diagonalization step), a new vector must be added to the subspace (expansion step). Here, two different algorithms will be presented, the Davidson[167] and the Jacobi-Davidson[168], that differ in the second step. In the Davidson algorithm, the new subspace vector is obtained from:

$$|\,\boldsymbol{\eta}_{n+1}\,\rangle = \frac{1}{\text{diag}\,(\mathcal{H}_{\text{vib}}) - E_{1,n}} |\,\boldsymbol{r}^n\,\rangle \tag{3.74}$$

where $|\,\boldsymbol{r}^n\,\rangle$ is the error vector, computed as,

$$|\,\boldsymbol{r}^n\,\rangle = \mathcal{H}_{\text{vib}} |\,\boldsymbol{\nu}^n\,\rangle - E_{1,n} |\,\boldsymbol{\nu}^n\,\rangle \tag{3.75}$$

We note that, even though the diagonalization step is performed within the subspace, the error is computed exactly from the full operator $\mathcal{H}_{\text{vib}}$. While being widely applied in quantum chemistry,[225,226,227] the Davidson algorithm is the most efficient for nearly-diagonal matrices, its efficiency being low for sparse ones. In the Jacobi-Davidson algorithm, which is more robust than the Davidson one, the new vector is obtained from the following correction equation:

$$\mathcal{H}_{\text{vib}} \left(|\,\boldsymbol{\nu}^n\,\rangle + |\,\boldsymbol{\eta}_{n+1}\,\rangle\right) = E_{1,n} \left(|\,\boldsymbol{\nu}^n\,\rangle + |\,\boldsymbol{\eta}_{n+1}\,\rangle\right) \tag{3.76}$$

with the constraint that $\langle\,\boldsymbol{\eta}_{n+1}\,|\,\boldsymbol{\nu}^n\,\rangle = 0$. If $E_1^{(n)}$ was equal to the "exact" eigenvalue, $|\,\boldsymbol{\eta}_{n+1}\,\rangle$ would correspond to the component of the exact eigenvector in the space orthogonal to the subspace, and only a single iteration of Eq. 3.76 would be needed to reach convergence. However, $E_{1,n}$ is an approximation of the exact ground-state energy, thus the Jacobi-Davidson algorithm takes more than a single step. Eq. 3.76 can be expressed in an alternative form as,

$$(\mathcal{I} - |\,\boldsymbol{\nu}^n\,\rangle\langle\,\boldsymbol{\nu}^n\,|)\,(\mathcal{H}_{\text{vib}} - E_{1,n})\,(\mathcal{I} - |\,\boldsymbol{\nu}^n\,\rangle\langle\,\boldsymbol{\nu}^n\,|)\,|\,\boldsymbol{\eta}_{n+1}\,\rangle = -|\,\boldsymbol{r}^n\,\rangle \tag{3.77}$$

where the orthogonality constraint is expressed through explicit projection operators. We note that, unlike the secular equation, Eq. 3.77 does not necessarily have to be solved exactly, since the solution is only used to add a vector to the subspace.
Both Davidson and Jacobi-Davidson algorithms allow one to compute the lowest-energy eigenpair of the Hamiltonian. As already mentioned above, the S&I form of those algorithms will be used in the following to target directly excited states. In S&I algorithms, the auxiliary operator Ω_ω (also known as S&I operator) is defined in terms of the vibrational Hamiltonian $\mathcal{H}_{\text{vib}}$ as,

$$\Omega_\omega = \frac{1}{\omega\mathcal{I} - \mathcal{H}_{\text{vib}}} = \frac{1}{\mathcal{H}_\omega} \tag{3.78}$$

where ω is an energy shift parameter. The eigenfunction of Ω_ω corresponding to the smallest eigenvalue is also the eigenfunction of $\mathcal{H}_{\text{vib}}$ corresponding to the first eigenvalue larger than ω. Hence, this interior eigenvalue of $\mathcal{H}_{\text{vib}}$ can be obtained, in principle, with standard iterative eigensolvers by working with Ω_ω instead of with $\mathcal{H}_{\text{vib}}$. The lowest energy eigenvalue of Ω_ω is estimated by minimizing the functional $1/E_{\omega,n}$ defined as,

$$\frac{1}{E_{\omega,n}} = \frac{\langle\,\boldsymbol{\nu}^n\,|\,\Omega_\omega\,|\,\boldsymbol{\nu}^n\,\rangle}{\langle\,\boldsymbol{\nu}^n\,|\,\boldsymbol{\nu}^n\,\rangle} \tag{3.79}$$

with respect to the c_{in} coefficients. The minimization leads to a standard eigenvalue problem:

$$\boldsymbol{\Omega}_\omega \mathbf{c}^{(n)} = \left(\mathbf{E}_\omega^{(n)}\right)^{-1} \mathbf{c}^{(n)} \tag{3.80}$$

where $\boldsymbol{\Omega}_\omega$ is the matrix representation of Ω_ω in the $|\,\boldsymbol{\eta}\,\rangle$ basis, $\mathbf{c}^{(n)}$ is the matrix containing the eigenvectors and $\mathbf{E}_\omega^{(n)}$ is the diagonal matrix of the eigenvalues of $\mathcal{H}_\omega$ both computed at the n-th iteration (also known as harmonic Ritz values of $\mathcal{H}_{\text{vib}}$). The n-th approximation of the targeted interior eigenvalue $\mathrm{E}_{\text{vib},t}^{(n)}$ of the original, non-inverted operator $\mathcal{H}_{\text{vib}}$ is then obtained as $\left(\omega - \mathrm{E}_{\omega,1}^{(n)}\right)$. In this setup, the form of the Davidson correction would be,

$$|\,\boldsymbol{\eta}_{n+1}\,\rangle = \frac{\left(\Omega_\omega - \mathcal{I}\,/\mathrm{E}_{\omega,1}^{(n)}\right)}{\text{diag}(\Omega_\omega) - \mathcal{I}/\mathrm{E}_{\omega,1}^{(n)}} |\,\boldsymbol{\nu}^n\,\rangle \tag{3.81}$$

The major drawback of this approach with respect to the standard Davidson procedure is the need to calculate the inverse of the operator $\mathcal{H}_\omega$. As pointed out in Ref. 228, no efficient algorithm to directly invert MPOs are currently available in the literature. Thus, an alternative formulation of the S&I algorithm, where the inversion of the MPO is avoided, must be derived.

For all subspace iterative diagonalization schemes described up to this point, the subspace $|\,\boldsymbol{\eta}\,\rangle$ represents both the test space, used for the wavefunction expansion, and the search space, against which the eigenvalue equation is projected to build Eq. 3.62. The inversion of the operator $\mathcal{H}_\omega$ can be avoided if the search space and the test space are different vector spaces. Keeping $|\,\boldsymbol{\eta}\,\rangle$ as the search space, we define the test space $|\,\tilde{\boldsymbol{\eta}}\,\rangle$ as,

$$|\,\tilde{\boldsymbol{\eta}}\,\rangle = \mathcal{H}_\omega |\,\boldsymbol{\eta}\,\rangle\,. \tag{3.82}$$

As discussed in Refs. 229 and 168, this procedure, also known as oblique projection, leads to the following generalized eigenvalue problem;

$$\langle\,\tilde{\boldsymbol{\eta}}\mid\mathcal{H}_\omega\mid\boldsymbol{\eta}\,\rangle\,\mathbf{c}_1^{(n)} = \mathrm{E}_{\omega,1}^{(n)}\langle\,\tilde{\boldsymbol{\eta}}\mid\boldsymbol{\eta}\,\rangle\,\mathbf{c}_1^{(n)}\,, \tag{3.83}$$

where $\mathbf{c}_1^{(n)}$ is the vector of the coefficients of the lowest-energy eigenfunction expressed in the $|\,\boldsymbol{\eta}\,\rangle$ basis set (vector space) at the n-th iteration of the diagonalization. Eq. 3.83 can now be rearranged as follows:

$$\langle\,\boldsymbol{\eta}\mid\mathcal{H}_\omega\mid\boldsymbol{\eta}\,\rangle\,\mathbf{c}_1^{(n)} = \frac{1}{\mathrm{E}_{\omega,1}^{(n)}}\langle\,\tilde{\boldsymbol{\eta}}\mid\tilde{\boldsymbol{\eta}}\,\rangle\,\mathbf{c}_1^{(n)} \tag{3.84}$$

In this way, the lowest eigenvalue $\mathrm{E}_{\omega,1}^{(n)}$ of Ω_ω is calculated without explicitly inverting the operator. However, the overlap matrix of the auxiliary basis $\langle\,\tilde{\boldsymbol{\eta}}\mid\tilde{\boldsymbol{\eta}}\,\rangle$ is, in general, different from the identity matrix, since the $\tilde{\boldsymbol{\eta}}$ basis set is not necessarily orthogonal. For this reason, Eq. 3.84 is a generalized eigenvalue problem. Following an approach already introduced for first-generation DMRG,[222] an orthogonal basis set $|\,\tilde{\boldsymbol{\eta}}'\,\rangle$ for the search space $|\,\tilde{\boldsymbol{\eta}}\,\rangle$ can be built through a Gram-Schmidt algorithm,

$$|\,\tilde{\eta}_i'\,\rangle = |\,\mathcal{H}_\omega\eta_i'\,\rangle = |\,\tilde{\eta}_i\,\rangle - \sum_{j<i}\frac{\langle\,\tilde{\eta}_i\mid\tilde{\eta}_j'\,\rangle}{\langle\,\tilde{\eta}_j'\mid\tilde{\eta}_j'\,\rangle}|\,\tilde{\eta}_j'\,\rangle\,. \tag{3.85}$$

This simplifies the eigenvalue problem given in Eq. 3.84, since the overlap matrix is equal to the identity matrix in the $|\,\tilde{\boldsymbol{\eta}}'\,\rangle$ basis set, thus Eq. 3.84 becomes a standard eigenvalue problem. However, even the vector space $|\,\boldsymbol{\eta}\,\rangle$ needs to be updated consequently to the transformation given in Eq. 3.85. It is easy to see that the required transformation from the old vector space $|\,\boldsymbol{\eta}\,\rangle$ to the new one $|\,\boldsymbol{\eta}'\,\rangle$,

$$|\,\eta_i'\,\rangle = |\,\eta_i\,\rangle - \sum_{j<i}\frac{\langle\,\tilde{\eta}_i\mid\tilde{\eta}_j'\,\rangle}{\langle\,\tilde{\eta}_j'\mid\tilde{\eta}_j'\,\rangle}|\,\eta_j'\,\rangle\,. \tag{3.86}$$

The generalized eigenvalue equation given in Eq. 3.83 can be expressed as a standard eigenvalue problem in the now orthogonal basis $|\,\tilde{\boldsymbol{\eta}}'\,\rangle$ as,

$$\frac{1}{\mathrm{E}_{\omega,1}^{(n)}}\mathbf{c}_1^{(n)} = \langle\,\boldsymbol{\eta}'\mid\mathcal{H}_\omega\mid\boldsymbol{\eta}'\,\rangle\,\mathbf{c}_1^{(n)}\,, \tag{3.87}$$

With this procedure, the diagonalization step of the Davidson algorithm to the S&I operator can be generalized. The diagonalization must now be complemented by the expansion step. As suggested in Ref. 222, the search space can be expanded with the relation,

$$| \boldsymbol{\eta}_{\mathrm{n+1}} \rangle = \frac{1}{\mathrm{diag}(\mathcal{H}_\omega) - \mathcal{I}\,\tilde{\mathrm{E}}^{(n)}_{\omega,1}} \left(\mathcal{H}_\omega - \mathcal{I}\tilde{\mathrm{E}}^{(n)}_{\omega,1} \right) | \boldsymbol{\nu}^n \rangle \tag{3.88}$$

where $\tilde{\mathrm{E}}^{(n)}_{\omega,1}$ is the Rayleigh quotient obtained from the n-th approximation of the eigenvalue,

$$\tilde{\mathrm{E}}^{(\mathrm{n})}_{\omega,1} = \frac{\langle\, \nu_n \mid \mathcal{H}_\omega \mid \nu_n \,\rangle}{\langle\, \nu_n \mid \nu_n \,\rangle} \tag{3.89}$$

We note that the Rayleigh quotient is equal to $\mathrm{E}^{(n)}_{\omega,1}$ only for fully-converged eigenfunctions, since otherwise,

$$\mathrm{E}^{(n)}_{\omega,1} = \frac{1}{\langle\, \eta_n \mid \mathcal{H}_\omega \mid \eta_n \,\rangle} \neq \tilde{\mathrm{E}}^{(\mathrm{n})}_{\omega,1} \tag{3.90}$$

As already mentioned above, the efficiency of the Davidson algorithm is maximal for nearly-diagonal matrices, but it decreases as the sparsity of the target matrix increases. In those cases, the Jacobi-Davidson (JD) algorithm is more efficient. Thus, in order to build a robust and general implementation, the latter is preferred and needs to be adapted to S&I algorithms. The diagonalization step, with the inclusion of the orthogonalization of the $| \tilde{\boldsymbol{\eta}} \rangle$ basis set, introduced for the S&I Davidson algorithm, can be used also for the Jacobi-Davidson one. The generalization of the correction equation is however less straightforward. In fact, even if the extension of the JD method to the calculation of harmonic Ritz values is known in the literature,[168] its application in quantum chemistry is scarce, especially in the context of DMRG, where mostly harmonic Davidson methods are used.[222]
Following the same approach as for the Davidson algorithm, we rewrite the correction equation (Eq. 3.76) for the shifted inverse of $\mathcal{H}_{\mathrm{vib}}$ as;

$$(\mathcal{I} - | \tilde{\boldsymbol{\nu}}^n \rangle\langle \tilde{\boldsymbol{\nu}}^n |) \left(\Omega_\omega - \frac{\mathcal{I}}{\mathrm{E}^{(n)}_{\omega,1}} \right) (\mathcal{I} - | \tilde{\boldsymbol{\nu}}^n \rangle\langle \tilde{\boldsymbol{\nu}}^n |)\, | \tilde{\boldsymbol{\eta}}_{n+1} \rangle = -| \tilde{\boldsymbol{r}}_{\mathrm{n}} \rangle \tag{3.91}$$

and, as before, Eq. 3.91 would require the explicit calculation of ${\mathcal{H}_\omega}^{-1}$, which is not trivial, especially for operators expressed in a MPO format. Again, this can be circumvented with $| \tilde{\boldsymbol{\eta}} \rangle$ (defined in Eq. 3.82) as the test space. Expressing Eq. 3.91 in this basis, we obtain the following result;[168,230]

$$(\mathcal{I} - | \tilde{\boldsymbol{\nu}}^n \rangle\langle \tilde{\boldsymbol{\nu}}^n |) \left({\mathcal{H}_\omega}^{-1} - \frac{\mathcal{I}}{\mathrm{E}^{(n)}_{\omega,1}} \right) (\mathcal{I} - | \tilde{\boldsymbol{\nu}}^n \rangle\langle \tilde{\boldsymbol{\nu}}^n |)\, \mathcal{H}_\omega | \boldsymbol{\eta}_{\mathrm{n+1}} \rangle = -| \tilde{\boldsymbol{r}}^n \rangle \tag{3.92}$$

which is equivalent to,

$$(\mathcal{I} - |\,\tilde{v}_n\,\rangle\langle\,\tilde{v}_n\,|)\left(\mathcal{H}_\omega - \mathrm{E}^{(n)}_{\omega,1}\mathcal{I}\right)(\mathcal{I} - |\,\nu_n\,\rangle\langle\,\nu_n\,|\mathcal{H}_\omega)\,|\,\eta_{n+1}\,\rangle = |\,\tilde{\boldsymbol{r}}^n\,\rangle\mathrm{E}^{(n)}_{\omega,1}\,, \tag{3.93}$$

an equation not involving the inverse of $\mathcal{H}_\omega$. It is important stressing out that the error $|\,\tilde{\boldsymbol{r}}^n\,\rangle$ is computed from the inverse operator as,

$$\begin{aligned} |\,\tilde{\boldsymbol{r}}_n\,\rangle &= \mathcal{H}_\omega^{-1}|\,\mathcal{H}_\omega\boldsymbol{\nu}_n\,\rangle - \frac{1}{\mathrm{E}^{(n)}_{\omega,1}}|\,\mathcal{H}_\omega\boldsymbol{\nu}_n\,\rangle \\ &= |\,\boldsymbol{\nu}_n\,\rangle - \frac{1}{\mathrm{E}^{(n)}_{\omega,1}}|\,\mathcal{H}_\omega\boldsymbol{\nu}_n\,\rangle = -\frac{1}{\mathrm{E}^{(n)}_{\omega,1}}|\,\boldsymbol{r}_n\,\rangle \end{aligned} \tag{3.94}$$

Thus, even the calculation of the error does not require the explicit inversion of the Hamiltonian operator. As in the standard JD algorithm, Eq. 3.93 does not need to be solved exactly, but can be solved approximately with a least-squares solver such as the generalized minimal residue method (GMRES) algorithm. The only additional step with respect to the standard Jacobi-Davidson algorithm is the Gram-Schmidt orthogonalization of the search vector space (see Eq. 3.85 and 3.86).
As suggested in Ref. 168, an alternative form of the correction equation is,

$$\left(\mathcal{I} - \frac{|\,\boldsymbol{\nu}^n\,\rangle\langle\,\tilde{\boldsymbol{\nu}}^n\,|}{\langle\,\tilde{\boldsymbol{\nu}}^n\,|\,\boldsymbol{\nu}^n\,\rangle}\right)\left(\mathcal{H}_\omega - \mathrm{E}^{(n)}_{\omega,1}\mathcal{I}\right)\left(\mathcal{I} - \frac{|\,\boldsymbol{\nu}^n\,\rangle\langle\,\tilde{\boldsymbol{\nu}}^n\,|}{\langle\,\tilde{\boldsymbol{\nu}}^n\,|\,\boldsymbol{\nu}^n\,\rangle}\right)|\,\boldsymbol{\eta}^{n+1}\,\rangle = -|\,\tilde{\boldsymbol{r}}^n\,\rangle\,. \tag{3.95}$$

In our implementation, this second form will be used, since, as will be discussed in the following, it can be more easily coupled with a deflation process (i.e. orthogonalization with respect to converged root). We note that a third correction equation has been proposed in Ref. 230, where skew projection are not present. However, this third formulation does not lead to any computational advantage, and has not been considered in the following.

3.4.4 MO-VDRMG

Even if the S&I algorithm introduced in the previous section significantly increases the range of applicability of VDMRG, it has still some significant drawbacks. First, the root toward which the algorithm will converge strongly depends strongly on the value of ω. Clearly, ω should be as close as possible to, and lower than, the target eigenvalue. However, this eigenvalue is not known before the calculation, and thus needs to be estimated in some way. In VDMRG, ω can be set based on the harmonic energy of the states, by scaling the value by a factor < 1 to ensure that ω is lower than the anharmonic frequency. However, in regions with a high density of states, such

as the C−H stretching region of a medium-sized molecule, a lot of closely-lying states are present, and in this case a small change in ω can lead to convergence to the wrong root. This effect has already been noticed for electronic structure calculations in Ref.[222], and is expected to be an even more severe problem in VDMRG, where more closely lying excited states are usually targeted. With the aim of solving these issues, two modifications of S&I VDMRG are presented here. The first one, which is based on root-homing diagonalization algorithms,[231] is that the root to be followed in the iterative subspace expansion must be chosen based on a maximum-overlap (MO) criterion.[232] This allows to ensure that the correct root is followed consistently during the optimization, avoiding root-flipping effects. The second approach is a generalization of the state-specific formulation of DMRG introduced in the previous section where, however, several roots are optimized together, and not sequentially, as in standard state-specific DMRG. In this section, we will describe the first approach, while the second one will be discussed in the next section.

The first approach, based on the MO method, is similar to the DMRG-X algorithm proposed recently in the literature,[233,234] where the localization in the DMRG lattice of the eigenstates is used to improve the convergence of DMRG. This is interesting for vibrational states, since even states close in energy will generally involve different modes, which means, in the DMRG formalism, that they will be localized on different sites of the lattice. Thus, if an estimate of the MPS is known *a priori*, it is possible to use the eigenvector with the maximum overlap onto this estimate during the subspace iteration algorithm to build the error vector $|\, \boldsymbol{r}^n \,\rangle$ to use in the correction equation (Eq. 3.74 and 3.77). This procedure is different from the one used in standard Davidson and Jacobi-Davidson diagonalization schemes, where the error vector obtained from the lowest-energy eigenfunction is employed at each iteration. Thus, the choice of the eigenfunction to be used in the correction equation, usually referred to as *root-homing*,[231] is based on the locality of the wavefunction, instead of on purely energetic criteria. Root-homing algorithms have already been used in vibrational structure calculations, in the context of mode-tracking algorithms[84,235] where harmonic normal modes are built iteratively, without diagonalizing the full Hamiltonian matrix. More recently, the same theory has been extended to the solution of Casida's equations in time-dependent density functional theory (TD-DFT)[85,208] for large-size systems. Root-homing approaches are equivalent to the maximum-overlap methods (MOM) that are commonly applied for electronic structure problems,[104,232,236] when SCF problems with fractional occupation numbers are solved. In those cases, the root homing is used to consistently follow the orbitals during the SCF cycles.

As already discussed in Refs. 84 and 208, root-homing algorithms can be divided in two main classes, depending on the vector used for the calculation of the overlap (referred to in the following as "test vector"):

1. the initial guess of the diagonalization is used as test vector, and is kept constant during the optimization. This approach is well-suited if the initial guess is a good approximation of the final wavefunction, but

might result in slow convergence (or even fail) for inaccurate guesses. This is the case, for example, if two states close in energy, have both a large component along the test vector. In those cases, the subspace diagonalization algorithm most likely will oscillate between the two roots, without reaching convergence. The application of this scheme to VDMRG will be referred in the following as constant maximum-overlap VDMRG (cMO-VDMRG).

2. alternatively, the test vector can be updated at each cycle of the iterative diagonalization, with the approximation of the eigenfunction obtained at the previous iteration used as test vector. The combination of this scheme with VDMRG will be referred in the following as updated maxium-overlap VDMRG (uMO-VDMRG).

3. in DMRG, where the matrices of each site are optimized sequentially, a third root-homing approach is possible, where the guess vector is updated in the same way as in uMO-VDMRG, but at the end of each sweep, and not at the end of each microiteration within a sweep. We define this third approach as sweep-based maximum-overlap VDMRG (sMO-VDMRG)

The main advantage of MO-DMRG over the state-average algorithms outlined above is that only a single MPS is optimized, therefore avoiding the problem of using the same effective basis (i.e. the same boundaries) for several eigenstates. The price to pay is the calculation of the overlaps at each iteration.
Each root-homing algorithm requires the calculation of overlaps between vibrational MPSs, which can be done using the theory introduced above. We note however that, in cMO-VDMRG, the guess of the optimization is in most cases built as a fixed linear combination of ONVs;

$$| \Phi_{\text{track}} \rangle = \sum_{i=1}^{N_{\text{bases}}} C_i | \sigma_1^{(i)}, ..., \sigma_L^{(i)} \rangle , \tag{3.96}$$

where the previous expansion is usually limited to only one or a few terms. In those cases, instead of converting Eq. 3.96 to MPS and using Eq. 3.68, it is convenient to compute the overlap with the single basis vectors $| \sigma_1^{(i)}, ..., \sigma_L^{(i)} \rangle$ included in the expansion given in Eq. 3.96. In fact, the $\boldsymbol{N}^{\sigma_j,(i)}$ tensors for an ONV are simply given by,

$$\boldsymbol{N}^{\sigma_j,(i)} = \boldsymbol{I}\delta_{\sigma_j,\sigma_j^{(i)}} \tag{3.97}$$

and thus the contraction over the σ index in Eq. 3.68 is trivial. Furthermore, as already remarked in the previous section, the partial overlap objects defined in Eq. 3.69 can be stored to reduce the computational effort associated to the calculation of the overlaps by a factor of L.
Calculation of the overlap in uMO-VDMRG and sMO-VDMRG is even easier, since the test MPS differs from the targeted one only by the DMRG tensor

$\boldsymbol{M}^{\sigma_l}$ of the site which is optimized, whereas all the other tensors are the same. For this reason, the two MPSs share the same boundary, and the overlap can be simply computed as,

$$\langle \Psi \mid \Phi_{\text{track}} \rangle = \sum_{\sigma_l=1}^{\boldsymbol{N}_{\max}} \boldsymbol{M}^{\sigma_l \dagger} \boldsymbol{N}^{\sigma_l} \tag{3.98}$$

where $\mid \Psi \rangle$ is the MPS that is currently being optimized. For all the formulations of MO-VDMRG, an additional parameter has to be introduced. Indeed, in standard Davidson and Jacobi-Davidson algorithms, only the lowest eigenvalue of the matrix giving the representation of the operator in the subspace basis is computed, together with the corresponding eigenvalue. In MO-VDMRG, multiple eigenpairs have to be computed, and among them the root to be followed is chosen with the root-homing procedure. Hence, the additional parameter to be set is the number of roots $N_{\text{states}}^{\text{MO}}$ to compute at each microiteration (i.e. at each step of the iterative optimization of the DMRG tensors of the i-th site).
MO-VDMRG is even more effective if combined with the S&I algorithms introduced above. In principle, root-homing should obviate the need for the S&I operator Ω_ω to target an eigenpair other than the lowest-energy one, since the MO scheme allows following the correct state during the optimization. However, in practice, for high-energy states, a large value of $N_{\text{states}}^{\text{MO}}$ would need to be chosen, in order to ensure that the targeted eigenpair is always present in the working set at each microiteration, so this would reduce significantly the computational efficiency of MO-VDMRG. However, if MO-VDMRG is combined with S&I algorithms, the targeted eigenpair can be one of the lowest-energy ones, and a relatively small value for $N_{\text{states}}^{\text{MO}}$ can be safely employed every time. We note also that the combination of S&I with MO approaches makes the limitation of the former less stringent. Indeed, the MO criterion avoids the root-flipping effects that characterize standard, S&I approaches in regions with an high-density of states. For this reason, the choice of ω becomes less important since, even if several eigenpairs are present in the energy range between ω and the target eigenvalue, $N_{\text{states}}^{\text{MO}}$ eigenpairs are computed at each iteration, thus this parameter can be tuned to include the target state.
To conclude, we note that the previous models can be modified to improve their efficiency further. In the previous derivation of S&I algorithms, it has been assumed that ω is constant during the sweep-based optimization algorithm. This assumption is mandatory for standard diagonalization schemes, where the full variational matrix has to be diagonalized once. However, in VDMRG, the full diagonalization is replaced by repeated, smaller eigenvalue problems, solved sequentially. For this reason, the shift parameter ω can be updated after each microiteration using the approximation of the energy obtained at the previous iteration. We will refer to this approach as adaptive MO-VDMRG (aMO-VDMRG). However, since the energy is expected to decrease during the sweep-based optimization, ω will be in most cases (but not

necessarily) higher than the target energy. To ensure that the target eigenvector is included in the set, in which the root-homing is performed, the MO algorithm is modified, and both the $N^{\mathrm{MO}}_{\mathrm{states}}$ higher and $N^{\mathrm{MO}}_{\mathrm{states}}$ lowest eigenpairs of the matrix are computed at each microiteration.

3.4.5 Multistate VDMRG

An alternative algorithm for targeting excited states is the state-average extension of DMRG (referred to in the following as SA-DMRG). In SA algorithms based on first-generation DMRG,[222,223] the environment states are obtained by diagonalizing the reduced density matrix averaged over the first N_{exc} excited states, as:

$$\hat{\rho}_{\mathrm{SA}} = \sum_{i=1}^{N_{\mathrm{SA}}} \alpha_i | \Phi_i \rangle \langle \Phi_i | \tag{3.99}$$

where, in standard SA-DMRG, α_i is equal to $\frac{1}{N_{\mathrm{exc}}}$ for each state. The first N_{exc} eigenpairs of the local Hamiltonian are computed, and then contracted with the respective boundaries to obtain the environment states for the following iteration. SA-DMRG has two main disadvantages: first of all, it is limited to low-lying excited states, that can be reached with a relatively small value of N_{SA}. Furthermore, the convergence of the energies with respect to the number of renormalized block states m is usually slower than for standard DMRG, since the boundaries are not optimized for any of the states of interest.
The second-generation formulation of SA-DMRG is obtained by optimizing the following functional in place of the ground state energy:

$$\mathrm{E}_{\mathrm{SA}} = \sum_{i=1}^{N_{\mathrm{exc}}} \alpha_i \langle \Phi_i \mid \mathcal{H} \mid \Phi_i \rangle \tag{3.100}$$

By expressing the states $| \Phi_i \rangle$ as MPSs and by minimizing the functional E_{SA} with respect to the i-th DMRG tensor, the following eigenvalue equation is obtained:

$$\sum_{k=1}^{N_{\mathrm{exc}}} \sum_{\sigma_i'} \alpha_i \left(\sum_{a'_{i-1} a'_i} \sum_{b_{i-1}, b_i} W^{\sigma_i, \sigma_i'}_{b_{i-1}, b_i} M^{\sigma_i'}_{a'_{i-1}, a'_i} L^{b_{i-1}}_{a_{i-1}, a'_{i-1}} R^{b_i}_{a'_i, a_i} \right) = \mathrm{E}\, M^{\sigma_i}_{a_{i-1}, a_i}\,, \tag{3.101}$$

which is equivalent to the eigenvalue equation given in Eq. 3.62, with the difference that the boundaries are averaged-out over the target states. Recently, it has been proposed[237] to select one of the N_{exc} states to build the boundaries, and to use those boundaries also for the calculation of the energy of the other states. This corresponds, in the previous equations, to setting $\alpha_i = 1$ for one state and 0 for all the others. However, this approach introduces a bias toward one of the states, which is described better than the others, and will not be analyzed in the following.

The necessity of building a common boundary for all the states is mandatory for first-generation DMRG algorithms, where an explicit expression for the wavefunction is not available. In second-generation algorithms, however, this is not necessary since a state-specific formulation of DMRG is possible, for which excited states are obtained by optimizing the MPS in the space orthogonal to all lower-energy states. As already discussed above, the projector onto this space can be built from the partial overlap tensors, through the $\boldsymbol{V}$ tensor defined in Eq. 3.71. In practice, the optimization is carried out with the following, deflated operator instead of the standard one:

$$\left(\boldsymbol{I} - \boldsymbol{V}\boldsymbol{V}^T\right)\left(\mathcal{H}_{\text{vib}} - E\boldsymbol{I}\right)\left(\boldsymbol{I} - \boldsymbol{V}\boldsymbol{V}^T\right) \tag{3.102}$$

In most state-specific formulations of DMRG,[216] the ground state is optimized, and only when the ground state is converged can the optimization of the first excited state be done, using the deflated operator given in Eq. 3.102 with $\boldsymbol{V}$ obtained from the $\boldsymbol{N}$ tensors of the optimized wavefunction. For VDMRG, we will use a modified version of the previous algorithm for the computation of excited states. In the original formulation, it is necessary to fully optimize all lower $n-1$ states to optimize the n-th excited state and this task can be challenging in regions with high density of states, where root-flipping effects are common. To avoid those issues, the first n eigenfunctions can be computed at each microiteration (i.e. during the optimization of each site), by calculating the $\boldsymbol{V}^l$ vectors *on-the-fly*. Even if this approach is similar to SA-DMRG, it does not require a common basis for the environment states of all the targeted states. The price to be paid is the need to update the partial overlaps at each microiteration, since they are build from non-converged wavefunctions.

3.4.6 Stochastic sampling of the determinant space

A drawback of VDMRG with respect to standard variational approaches is that the vibrational wavefunction is expressed as MPSs, and thus the CI coefficients are not known. Consequently, it is not possible to determine easily the basis functions with the largest coefficients in the CI expansion, and so, for example, to characterize the MPS in terms of fundamentals, overtones or combination bands. In principle, the CI coefficients can be determined by computing the overlap of the converged MPS with all the possible basis functions, using Eqs. 3.68 and 3.69 to efficiently evaluate the contractions. A similar approach has already been used in Ref. 238 for electronic structure calculations, but is limited to very small systems, due to the exponential increase of the CI space with the number of DMRG sites (i.e. the number of modes N_{vib} for VDMRG).
To target also larger size systems, a more efficient way to sample the variational space is needed. Here, the sampling reconstruction complete active space (SR-CAS) algorithm, developed for electronic structure problems in Ref. 239 and based on the stochastic algorithms proposed in Refs. 240 and

241 to optimize tree tensor network states (TTNS), is used to efficiently determine the ONVs with the largest coefficients in the CI expansion. In SR-CAS, the variational space is sampled through a Metropolis-Hastings Markov chain, where the probability density $\rho_{i_1,\dots,i_L}$ is given by the squared value of the CI coefficient $C_{i_1,\dots,i_L}$,[242]

$$\rho_{i_1,\dots,i_L} = \left|C_{i_1,\dots,i_L}\right|^2 \tag{3.103}$$

We note that $\rho_{i_1,\dots,i_L}$ can be interpreted as a probability distribution function since $\sum_{i_1} \dots \sum_{i_L} \rho_{i_1,\dots,i_L} = 1$. The Metroplis-Hastings algorithm is designed to sample more often region of the CI space with higher probability density, therefore avoiding the calculation of nearly-negligible overlaps. The workflow of the algorithm can be described in the following steps;

1. set a starting ONV, known to have a large CI coefficient, as reference ONV. Computes its CI coefficient C_{old}. For MO-VDMRG algorithms, the test MPS can be used as a first guess.

2. generate randomly an integer $N_{\text{exc}} < L \times N_{\text{max}}$, representing the overall number of simultaneously excited modes.

3. generate randomly N_{exc} integer numbers

$$\left(n^{(1)}_{\text{modes}}, \dots, n^{(i)}_{\text{modes}}, \dots, n^{(N_{\text{exc}})}_{\text{modes}}\right) , \tag{3.104}$$

   representing the indexes of the modes to be excited.

4. generate a new ONV, obtained from the one of the previous cycle, by exciting the reference ONV by the number of occurrences of its index in the $n^{(i)}_{\text{modes}}$ list. If the occupation number exceeds N_{max}, it is replaced by its modulo with respect to N_{max}, since the occupation numbers cannot exceed N_{max}.

5. compute the overlap between the optimized MPS and the new ONV, to obtain the CI coefficient C_{new}. Store the determinant if the overlap is greater than η_{store}, which is a parameter of the algorithm. η_{store} is used to store only relevant determinants, avoiding this way an exponential increase of the database of the stored determinants.

6. replace the reference ONV with the newly generated one with a probability P_{t} given by,

$$P_{\text{t}} = \min\left[1, \frac{C_{\text{new}}}{C_{\text{old}}}\right] \tag{3.105}$$

   This is done, in practice, by generating a random, positive number < 1 and replacing the old determinant with the new one if the number is $> P_{\text{t}}$.

7. iterate points 2-6 until convergence.

The convergence of the algorithm can be assessed through the completeness measure COM, defined as,

$$\xi_{\mathrm{COM}} = 1 - \sum_i |C_i|^2 , \tag{3.106}$$

where the sum over i includes only the stored determinants. Convergence is reached when $\xi_{\mathrm{COM}} < \eta_{\mathrm{COM}}$, given as input of the algorithm. We note that the main difference between the present algorithm and the original SR-CAS, formulated for electronic structure problems lies in the generation of the determinants. For the electrons, the occupation number of each orbital is either 0 or 1 due to the Fermi-Dirac statistic, whereas for molecular vibrations the occupation number is bounded by the N_{max} parameter.
To conclude, we note that other algorithms to reconstruct the CI expansion have been recently proposed[243] where quantum entanglement measures are used to enhance the efficiency of the stochastic sampling. The quantum entanglement could be in principle determined also for molecular vibrations, following the same strategy already employed for electronic structure calculations[244,245] and employing vibrational density matrices,[246] but a similar analysis goes beyond the scope of this thesis. The SR-CAS algorithm can be used also to compute vibrational averages of generic operators, as well as their transition counterpart. In fact, in most cases, the matrix representation properties in the CI basis is readily available, such as when they are expanded as a Taylor series in terms of Cartesian-based normal modes. Thus, the SR-CAS algorithm can be employed to extract the determinant giving the largest CI coefficients, and then to use the expansion in terms of CI basis to compute matrix elements of properties. A possible drawback of such an approach would be that the CI configuration with the largest coefficients are not necessarily the ones with the largest contribution to properties. Thus, the convergence of the SR-CAS would be probabily slower for properties than for energies. In any case, the evaluation of the same quantities by using directly vibrational wavefunctions encoded as MPSs is more difficult than by using the SR-CAS algorithm, and would require to express also the property surface as MPO.

3.5 Selected applications of VDMRG

The VDMRG theory is now applied to the calculation of vibrational properties of three molecular systems. The first one is a three-atom molecule (ClO_2), which will be used as a test case to check the reliability of the implementation. Indeed, thanks to its small size, full variational results, which will serve as our reference, are available in the literature. The second test-case is ethylene (C_2H_4), which already represents a challenge for standard variational calculations, and for which the reliability of VDMRG in reproducing experimental data will be checked. Finally, a large-size systems, the

sarcosyn-glycine dipeptide ($SarGly^+$), which is not treatable with most standard, variational algorithms, will be studied, with the aim of checking the scalability of VDMRG for large-sized systems.

3.5.1 Benchmark: vibrational levels of ClO_2

As a first step, VDMRG is validated for the triatomic molecule ClO_2 in its electronic ground state, of X^2B_1 symmetry. The PES obtained from multi-reference configuration interaction (MRCI) calculations, which is available in the literature,[159,247] will be employed. Fully converged vibrational energies up to 3300 cm^{-1} were calculated from this PES with variational approaches,[159,247] thus those energies can be used as reference to check the VDMRG results. The high accuracy of these calculated wavenumbers was demonstrated by comparison to high-resolution experimental data, so no further comparison with the experimental data will be needed.[248,249,250]
Before discussing the results of our calculations, it is useful to compare the VDMRG approach with the variational approaches of the reference papers. In the study by Peterson,[247] the PES is expressed as a 4th-order Taylor expansion in terms of the internal coordinates (the two bond lengths and the valence angle) of the molecule. The variational calculations of the vibrational problem are then carried out directly in these coordinates, with Morse oscillator eigenfunctions as a basis set for the two stretching coordinates and a DVR for the bond angle.[251] In a more recent work,[159] this quartic force field in internal coordinates is first transformed to a sixth-order force field in Cartesian-based normal coordinates, by a direct tensor transformation,[26,159] and the variational calculation is then carried out using the harmonic-oscillator wavefunctions as the basis set. In this work, we employ the latter representation of the PES, since the second-quantized expression of the vibrational Hamiltonian given in Eq. 3.65 holds for a basis of harmonic-oscillator wave functions. This representations is, in principle, different from the internal coordinates' one since the latter are non-linear functions of the Cartesian normal modes. However, the two approaches result in equivalent computed fundamental anharmonic frequencies,[160,247] and this seems to suggest that a sextic force-field in terms of Cartesian-based normal modes provides a sufficiently reliable reproduction of the PES. Although more recent results are reported in Ref. 160, the data reported in Ref. 247 include also the theoretical energies for overtones and combination bands, so they will serve as our reference.
As already pointed out before, two parameters control the convergence of VDMRG vibrational wave function and energy. The first, N_{max}, corresponds to the number of basis functions that describe each mode and its value must match the anharmonicity of each mode. The second parameter, the number of renormalized block states m, controls the degree of dimension reduction of the final MPS wavefunction and has to be increased with increasing anharmonic mode coupling. These two parmeters are, in general, independent and the convergence with respect to both has to be analyzed.
VDMRG vibrational energies up to 3000 cm^{-1} calculated with different values for N_{max} and m are reported in Table 3.4, together with the harmonic

TABLE 3.4: VDMRG zero-point energy and energies of the 17 lowest vibrational transitions from the ground state (in cm^{-1}) for ClO_2. Each state was calculated with different values for the parameters N_{max} and m.

Mode	Ref.	$N_{max} = 10$			$N_{max} = 12$		Harm.
		$m = 2$	$m = 5$	$m = 10$	$m = 5$	$m = 10$	
ZPE		1264.5	1264.5	1264.5	1264.5	1264.5	
ν_2	449.9	449.5	449.5	449.5	449.5	449.5	455.62
$2\nu_2$	898.7	898.0	898.1	898.1	898.0	898.2	911.24
ν_1	940.7	940.7	940.7	940.7	940.7	940.5	960.15
ν_3	1105.5	1105.2	1105.2	1105.2	1105.2	1105.2	1127.82
$3\nu_2$	1346.5	1345.6	1345.5	1345.5	1345.5	1345.8	1366.86
$\nu_1 + \nu_2$	1386.5	1386.2	1386.2	1386.3	1386.1	1385.8	1415.77
$\nu_2 + \nu_3$	1549.9	1548.7	1548.7	1548.7	1548.6	1548.6	1573.44
$\nu_1 + 2\nu_2$	1831.2	1830.7	1830.6	1830.6	1830.6	1828.8	1871.39
$2\nu_1$	1872.1	1872.4	1872.3	1872.3	1872.3	1872.2	1920.30
$2\nu_2 + \nu_3$	1993.2	1991.2	1991.2	1992.8	1991.1	1991.1	2039.06
$\nu_1 + \nu_3$	2029.3	2029.3	2028.9	2029.1	2029.2	2029.2	2087.97
$2\nu_3$	2200.1	2201.0	2199.5	2199.5	2199.5	2199.6	2255.64
$2\nu_1 + \nu_2$	2313.8	2318.4	2313.5	2313.6	2313.6	2313.7	2375.92
$\nu_1 + \nu_2 + \nu_3$	2469.8	2468.3	2468.5	2468.5	2468.1	2468.4	2543.59
$3\nu_1$	2794.0	2797.5	2794.6	2794.6	2794.7	2794.7	2880.45
$2\nu_1 + \nu_3$	2943.2	2947.9	2943.8	2943.2	2943.5	2943.7	3048.12

results and theoretical reference data taken from Ref. 247. The number of VDMRG sweeps was set to 40 for all states, to ensure convergence with respect to the number of sweeps. With ten basis functions per mode ($N_{max} = 10$), converged results are obtained for energies up to 2000 cm^{-1} with as little as two renormalized states, and variations below 0.1 cm^{-1} are obtained by increasing m to 5 and 10. By further increasing the dimension of the local basis to 12, no further variations occur and the energies can therefore be considered converged with respect to the basis set size. The VDMRG results are in good agreement with the reference values and confirm that a sixth-order Taylor expansion in Cartesian-based normal modes is sufficient to obtain accurate anharmonic frequencies. However, for some of the higher-energy transitions, two renormalized states are not sufficient to reach convergence, with variations above 1 cm^{-1}. This is particularly evident for the transitions from the ground state to $2\nu_1 + \nu_2$, $3\nu_1$ and $2\nu_1 + \nu_3$, where results obtained with $m = 2$ and $m = 10$ deviate by more than 2 cm^{-1}. It should be noted that these vibrations are 3-quanta overtones and combination bands, and thus are localized in regions of the PES far from the equilibrium position. Thus, for those states, the expansion of the PES as a 6th-order Taylor expansion is expected to be less

accurate.

3.5.2 Comparison with accurate experimental data: C_2H_4

The second example with which we demonstrate the reliability of the VDMRG ansatz is ethylene (C_2H_4). Here, we adapt a highly accurate *ab initio* PES from the literature[252] and compare the results with previous calculations and experimental data.[253]

The force-field of C_2H_4 has been widely studied over the years, using different electronic structure approaches. Several years ago, an accurate PES of ethylene was constructed from CCSD(T) calculations by Martin and coworkers.[164] This PES was then used to determine vibrational energies and spectra with different variational approaches, such as basis-pruning algorithms[71] and VCI calculations based on VSCF modals.[254] Recently, a new PES was constructed from CCSD(T) calculations with a larger, quadruple-ζ orbital basis, from which more accurate vibrational energies could be calculated, again using basis-pruning algorithm.[252] Here, we will apply the latter PES in our VDMRG calculations. We note however, as for ClO_2, that the analytical expression of the PES computed in Ref. 252 is given in terms of non-linear functions of the valence, internal coordinates (5 bond lengths, 4 valence angles, 2 dihedrals and an out-of-plane coordinate). As already done for ClO_2, this PES must converted to a Taylor series in cartesian normal modes. This has been done following the procedure discussed in Refs. 159 and 160 using the `PyPES` package. As already remarked above, an infinite-order expansion in Cartesian-based normal modes is required to match a quartic force-field in internal coordinates. Here, fourth- and sixth-order Taylor series expansion of the potential, with and without the inclusion of Coriolis effects, were used in the VDMRG calculations. The order of the Taylor expansion was chosen based on the variational results reported in Ref. 160, where it was shown that a sixth-order expansion is sufficient to reach convergence within 1 cm^{-1}. If not otherwise specified, vibro-rotational Coriolis couplings were neglected.

First, the standard formulation of VDMRG has been used to compute the ZPVE of C_2H_4 by varying the bond dimension n, for a given order of the Taylor expansion of the potential (a fixed Hamiltonian) and for a given value of N_{max} (a fixed local basis set), with the results shown in Fig. 3.11. With five renormalized states, inaccurate results, with deviations larger than 10 cm^{-1} with respect to the converged values, are obtained. Convergence (with deviations below 1 cm^{-1}) is reached with ten renormalized block states for all Hamiltonians (both quartic and sextic force fields). Thus, the inclusion of higher-order terms in the potential does not affect significantly the structure of the Hamiltonian, i.e. it does not introduce further long-range correlations, which would require a larger number of renormalized block states and DMRG sweeps to converge the MPS.

Regarding the convergence of the ZPVE with respect to the maximum quantum of excitation N_{max} for each site (i.e. the size of the local basis), the results stabilize for $N_{max} = 6$, and with $N_{max} = 8$, the change in the ZPVE becomes negligible (below 0.01 cm^{-1}). For C_2H_4, the lowest-energy mode has a wavenumber of approximately 850 cm^{-1}, thus low-energy frequencies

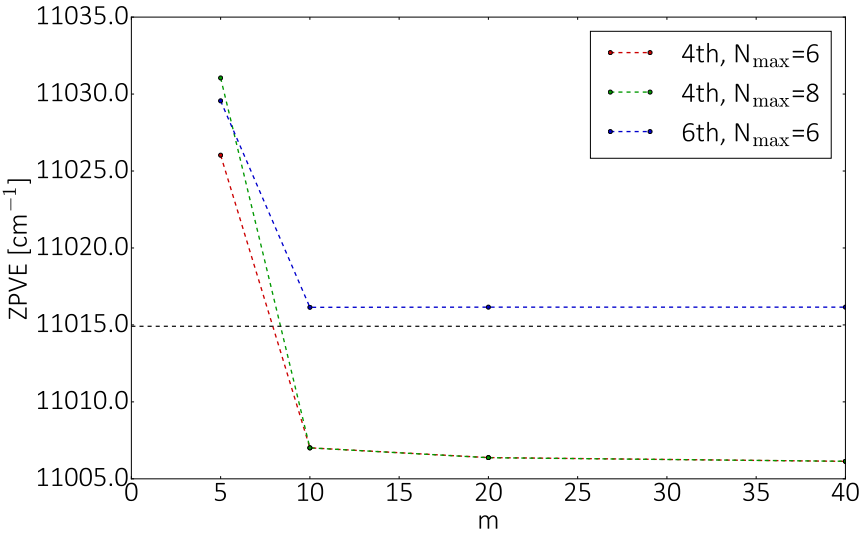

FIGURE 3.11: Plot of the VDMRG ZPVE of C_2H_4 as a function of the number of renormalized states m. Calculations were performed with a quartic force field and setting $N_{max} = 6$ (dashed, red line) and $N_{max} = 8$ (dashed, green line) and with a sextic force-field and with $N_{max} = 6$ (dashed, blue line). The reference theoretical ZPVE, taken from Ref. 252, is represented as a black dotted line.

characterized by strong anharmonic effects are not present. For this reason, a reliable representation of the vibrational wave function can be obtained from a relatively small number of Hermite polynomials (6 in this case) as local basis functions. This is particularly true for the ZPVE, since the ground state is localized about the equilibrium geometry, where the representation of the PES as Taylor series in terms of Cartesian coordinates is accurate. For systems with an higher anharmonicity, an higher value for N_{max} would be needed.
Regarding the convergence of the ZPVE with respect to the order of the Taylor series expansion, we note that, with a fourth-order PES, the ZPVE is underestimated by approximately 7 cm^{-1}. The further inclusion of fifth- and sixth-order terms reduces the error to less than 1 cm^{-1}, therefore providing satisfactory convergence, in agreement with the results obtained for ClO_2. This result is in line also with the analysis reported in Refs. 159 and 160, where results converged within 1 cm^{-1} were obtained from a full sextic potential and including Coriolis couplings in the kinetic energy operator. To conclude, the VDMRG ZPVE obtained with the sextic potential and with $N_{max} = 6$ and $m = 20$ is 11016.15, and agrees well with the reference theoretical value of 11014.91 cm^{-1},[252] computed without the inclusion of Coriolis couplings.
Due to the relatively small size of C_2H_4, transition frequencies lying in the fingerprint region (800-2000 cm^{-1}) can be computed with SS-VDMRG, without using the S&I algorithm. A complete list of the 15 lowest vibrational wavenumbers (including both overtones and combination bands) of C_2H_4

TABLE 3.5: Comparison of the wavenumber of the 20 lowest states of C_2H_4 (in cm^{-1})computed with VDMRG applying a fourth- (labeled as 4th) and a sixth-order (labeled as 6th) Taylor expansion of the PES with reference theoretical data from Ref. 252, and experimental data from Ref. 253. VDMRG calculations were performed with different values for the parameters N_{max} and m.

Mode	Assign.	Quartic		Sextic		Sextic + C	Ref.[252]	Exp.[253]
		N_{max}=6 m=10	N_{max}=6 m=20	N_{max}=6 m=10	N_{max}=6 m=20	N_{max}=6 m=10		
ZPVE		11007.01	11006.19	11016.14	11016.15	11021.39	11014.91	
1	ν_{10}	810.27	809.03	831.13	831.17	834.64	822.42	825.92
2	ν_8	916.61	915.29	933.48	933.47	942.26	934.29	939.86
3	ν_7	929.76	928.31	948.26	948.26	957.15	949.51	948.77
4	ν_4	1008.46	1007.13	1018.26	1018.26	1026.64	1024.94	1025.58
5	ν_6	1217.88	1217.17	1227.08	1227.05	1229.68	1224.96	1225.41
6	ν_3	1339.55	1338.87	1343.46	1343.46	1344.25	1342.96	1343.31
7	ν_{12}	1431.74	1430.47	1441.50	1441.52	1444.94	1441.11	1442.44
8	ν_2	1619.69	1622.11	1628.26	1629.04	1628.41	1624.43	1626.17
9	$2\nu_{10}$	1626.57	1625.56	1682.30	1682.18	1685.54	1658.39	1664.16
10	$\nu_8 + \nu_{10}$	1723.42	1722.77	1769.89	1770.02	1764.78	1757.70	1765.78
11	$\nu_7 + \nu_{10}$	1739.03	1729.53	1787.02	1786.99	1781.17	1778.34	1781.01
12	$\nu_4 + \nu_{10}$	1814.03	1810.47	1840.52	1852.60	1865.89	1848.61	1851.51
13	$2\nu_8$	1830.01	1825.99	1878.67	1878.42	1890.40	1873.73	1879.72
14	$\nu_7 + \nu_8$	1830.71	1856.77	1886.15	1886.16	1897.34	1885.12	1888.63
15	$2\nu_7$	1855.82	1870.92	1905.44	1906.02	1901.04	1901.61	1899.74

computed at the VDMRG level is reported in Tab. 3.5. Based on the results obtained for the ZPVE, all calculations were carried out with $N_{max} = 6$, with quartic and sextic potential and 10 or 20 renormalized states. First of all, these results show that 10 renormalized states are sufficient to get an accuracy within 1 cm^{-1} for the lowest energy states, up to 1500 cm^{-1}. The difference between the results obtained with $m = 10$ and $m = 20$ increases for higher excited states, but still remains below 10 cm^{-1} even for states up to 1800 cm^{-1}. These observations hold whatever the expansion of the potential chosen, therefore suggesting once again that the introduction of fifth- and sixth-order terms improves the agreement with the experimental results without modifying the overall structure of the vibrational Hamiltonian.
The VDMRG results obtained with $N_{max} = 6$ and $m = 20$ are in good agreement with experimental data, taken from Ref. 253, and, as for ClO_2, the inclusion of sixth-order terms is crucial for accuracy, especially for higher-energy levels. To further assess the reliability of our simulations, vibrational wavefunctions and energies were computed by including Coriolis couplings, using the sixth-order Taylor expansion for the potential. Rotational effects were included in the reference theoretical work[252] for two, high-energy fundamental transitions (ν_{11} and ν_9, with harmonic wavenumbers of 3140.91 and 3248.71, respectively), but were neglected for all other transitions. For the ν_{11} and ν_9 bands, however, the rotational correction amounted to approximately 3 cm^{-1}, and is therefore on the same order of magnitude as the discrepancy between VDMRG and experimental data. For this reason, the inclusion of rotational effects might further improve the quality of VDMRG results. The results obtained with the inclusion of Coriolis terms (reported in Tab. 3.5 as "Sextic + C") confirm that vibro-rotational corrections are relevant for several bands (e.g. ν_7 and ν_8), for which this effect amounts to up to 9 cm^{-1}. In general, the inclusion of vibro-rotational corrections improves the agreement between VDMRG and experimental data.

3.5.3 Toward large-size systems: the sarcosyn-glycine dipeptide

The last example studied here is the protonated sarcosine-glycine dipeptide (referred to as $SarGly^+$ in the following, the molecular structure is reported in figure 3.12). Computational studies of the anharmonic vibrational properties of medium-size biomolecules have been limited mostly to VSCF[255,256] and VPT2[257,258] approaches, and only recently VCI studies were published mainly based on local-mode approaches to reduce the computational cost of variational simulations.[72,73,74] Here, $SarGly^+$ will be used as an example of a large-size system not treatable with standard variational approaches, in order to check if converged results can be obtained with VDMRG, using a small value for m. It is important to note that the use of local-modes changes the expression for the vibrational Hamiltonian, but does not affects the algorithm used for its diagonalization. Thus, local-modes approaches can be coupled with VDMRG as well. This combination would probably make VDMRG even more efficient, since long-range interactions would be reduced, and this

would reduce the value of m needed to reach convergence for VDMRG. First, the effect of the number of renormalized block states m on the vibrational energies is assessed. If the value of m required to reach convergence turns out to be small and largely independent of the system size, VDMRG would be a valuable alternative to local mode approaches for large systems.
Due to the size of SarGly$^+$, theoretical results with fully-converged VCI calculations are not available. However, a theoretical study of the vibrational properties of SarGly$^+$ was performed recently with VSCF and a local mode ansatz employing a B3LYP/6-311+G(d,p) quartic force-field.[171] For consistency, the same electronic structure method is used here to compute the semi-quartic force field, where the quartic force constants k_{ijkl} with four different indexes are neglected, together with those smaller than 1 cm^{-1}. Based on the results of the previous sections, $N_{\max}$ is set to 6 and values of m range from 5 to 20 in the calculations. To limit the computational cost, the reduced-dimensionality (RD) scheme presented in Refs. 259 and 260 is employed so that all the modes below 900 cm^{-1} are considered as harmonic, therefore neglecting all couplings between those modes and the other ones (i.e. setting all the anharmonic force-constants where at least an index corresponds to a mode below 500 cm^{-1} to 0). Such a selection of the modes might seem, in general, crude and prone to arbitrariness, and for larger systems a more accurate definition of the reduced-dimensionality model is certainly required. However, the aim is to demonstrate the efficiency of the VDMRG method for large systems, without an exact reproduction of experimental results that will in general also be limited by the electronic structure approach. Therefore, a RD potential, consisting of 35 modes (corresponding to 35 DMRG sites), represents a viable setup for VDMRG, because VCI calculations on systems of this size are unfeasible for standard variational approaches.
The VDMRG fundamental wavenumbers of SarGly$^+$ in the fingerprint region are reported in Table 3.6. For comparison, results from localized VSCF (l-VSCF) taken from Ref. 171 are reported as well, together with the GVPT2[68] results obtained with the same RD potential as for VDMRG. GVPT2 calculations were performed using the standard parameters as implemented in the last release of GAUSSIAN.[262] Experimental values from Ref. 261 are included where available. The convergence of the energies with respect to the number of renormalized block states m is similar to that observed for smaller systems as analyzed in the previous sections. Almost fully converged results are obtained already with $m = 10$ and corrections below 2 cm^{-1} are observed upon increasing m to 20. This confirms that VDMRG can be used also for large-size systems, with a limited number of renormalized states.
In Figure 3.12, the spectrum obtained with VDMRG anharmonic transition energies of SarGly$^+$ with $N_{\max} = 6$ and $m = 20$ and harmonic dipole strengths is compared to the experimental spectrum.[261] As expected, the inclusion of anharmonic effects leads to an overall shift of the frequencies toward lower energies, providing a considerably better agreement with the experimental data. This is pronounced for the band at 1147 cm^{-1} (C–O–H bending), whose energy is overestimated by approximately 50 cm^{-1} with harmonic calculations, whereas it is correctly reproduced by VDMRG. Similarly, the

TABLE 3.6: VDMRG vibrational energies for $SarGly^+$ with $N_{max} = 6$ and varying number of renormalized states m. Reference theoretical data (from Ref. 171) and experimental data (from Ref. 261) are also reported.

	Harm	m=5	m=10	m=20	GVPT2	l-VSCF	Exp.
ZPVE	39054.82	38601.40	38590.02	38572.25	38611.75		
1	987.26	962.90	960.60	958.01	973.56		
2	1011.54	988.72	986.85	986.53	992.70		
3	1038.64	1028.06	1027.18	1028.65	1038.57		
4	1100.19	1073.27	1073.33	1074.75	1084.04	1110	1088
5	1148.05	1123.05	1113.58	1112.64	1131.87	1169	1147
6	1187.57	1141.80	1139.91	1138.55	1162.39		
7	1190.81	1147.04	1141.08	1140.44	1174.23		
8	1242.55	1214.50	1210.85	1209.25	1216.47		
9	1257.74	1217.62	1211.53	1214.81	1232.04		
10	1287.33	1229.23	1242.64	1243.30	1263.71		
11	1317.02	1277.39	1279.26	1279.27	1287.62		
12	1337.91	1290.34	1299.94	1291.30	1309.18		
13	1405.94	1344.23	1347.04	1350.35	1369.52		
14	1432.43	1358.03	1361.04	1376.33	1389.17	1394	1384
15	1435.01	1407.78	1404.80	1407.65	1418.96		
16	1464.25	1426.97	1413.36	1416.71	1432.58		
17	1484.39	1436.63	1431.33	1437.38	1445.66		
18	1491.29	1443.39	1443.08	1443.91	1453.07		
19	1500.94	1457.25	1459.48	1448.32	1458.22		
20	1505.58	1474.20	1467.00	1455.07	1466.01		
21	1565.36	1566.85	1566.85	1566.06	1538.98		

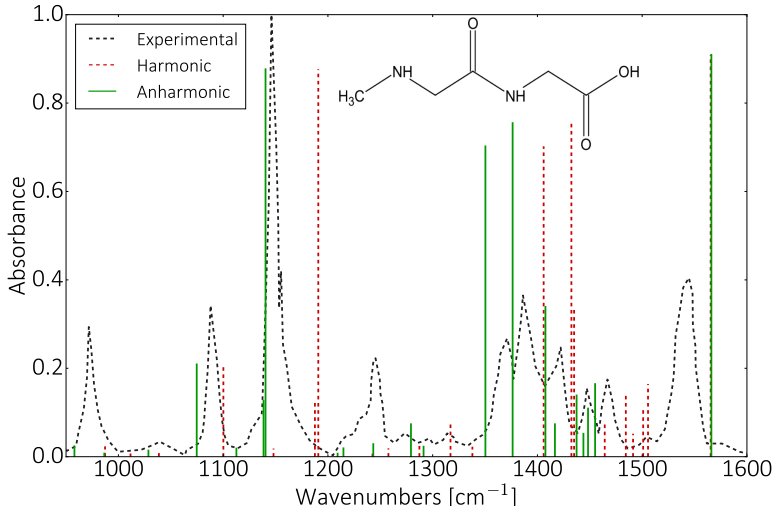

FIGURE 3.12: Experimental[261] and theoretical infrared spectrum of SarGly$^+$ computed from harmonic (red lines) and anharmonic VDMRG wavenumbers (green lines). The parameters of the VDMRG calculations are $N_{\max} = 6$ and $m = 20$. In all cases, harmonic dipole strengths were employed.

pattern recorded between 1350 and 1450 cm^{-1}, that is composed of three, nearly equidistant bands with the same intensity, is reproduced more accurately by VDMRG, whereas two of the three bands have nearly the same energy in a harmonic approximation. Therefore, although a higher-order potential is usually required to obtain reliable variational energies, anharmonic variational calculations from a quartic potential considerably improve the description of this system.

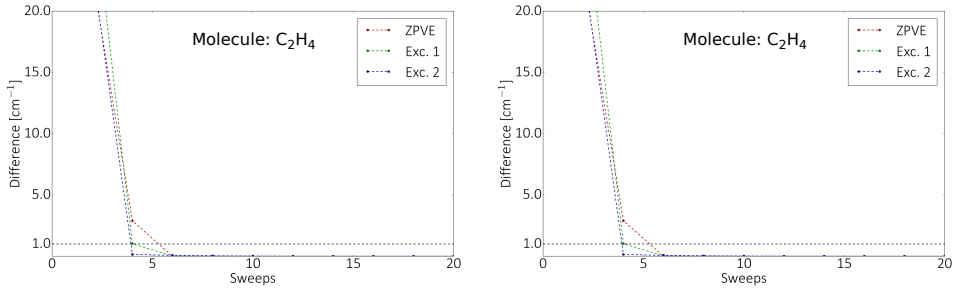

FIGURE 3.13: Energy of the ground and first two excited states of C_2H_4 (left panel) and SarGly$^+$ (right panel) as a function of the number of sweeps. In all cases, VDMRG calculations were performed with $N_{\max} = 6$ and $m = 10$. For C_2H_4, the full quartic potential from Ref. 159 was used. For SarGly$^+$, the semi-diagonal quartic force-field computed at the B3LYP/6-311+G(d,p) level was employed.

As already noted above, an additional factor determining the efficiency of the calculation is the iterative, sweep-based optimization algorithm used to minimize the DMRG energy. In fact, the number of renormalized block states

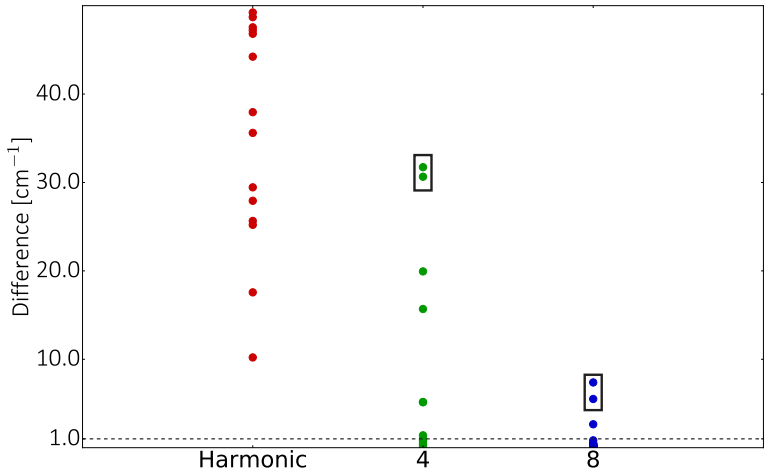

FIGURE 3.14: Difference between vibrational energies of SarGly$^+$, computed with different number of sweeps in the optimization procedure, and converged energies (obtained with 10 sweeps). VDMRG calculations were performed with a semi-diagonal quartic potential computed with B3LYP/6-311+G(d,p). Data corresponding to modes 36 and 37 are highlighted with a black box.

m and the dimension of the local basis $N_{\max}$ determine the computational cost of a single sweep but, in order to make VDMRG applicable to large molecules, the number of sweeps required to reach convergence should be largely independent of the system size, and kept as low as possible.
In Figure 3.13, the energies of the first three vibrational states of SarGly$^+$ (right panel) and C_2H_4 (left panel) are reported as a function of the number of sweeps. In all cases, the harmonic vibrational wave function served as the initial guess for the MPS. The VDMRG calculations were performed with quartic force-fields (semi-diagonal for SarGly$^+$) with $N_{\max} = 6$ and $m = 10$. For ethylene, the convergence of the optimization algorithm is fast, with deviations below 1 cm^{-1} from the fully converged value (obtained with 10 sweeps) already within three sweeps for both the ground and the excited states. The efficiency of the procedure is only slightly lower for SarGly$^+$, even if to obtain a ground-state energy with an accuracy within 1 cm^{-1}, at least four sweeps are required (eight for the fist excited state).
A graphical representation of the difference with respect to fully converged results as a function of the number of sweeps is reported in Fig. 3.14. With only 4 sweeps, most of the vibrational frequencies are converged within 1 cm^{-1}, with the exception of only five frequencies. With 8 sweeps, only three frequencies are not converged which demonstrates the efficiency of the optimization procedure also for highly-excited states. It is interesting to note that the frequencies that convergence slowest, ν_{36} and ν_{37}, are involved in a Darling-Dennison 1-1 resonance (as can be checked performing the test described, for example, in Ref. 52) and, as remarked above, anharmonic corrections are usually relevant for resonant states. This indicates once more

that the number of sweeps required to reach convergence increases with the magnitude of anharmonic corrections.

Chapter 4

Vibronic models tailored for larger-size systems

This section will present the generalization of transition moments and energies to transitions between vibrational levels belonging to different electronic states (referred in the following as vibronic transitions). Vibronic transitions involve electronic excited states, and the computational cost of electronic structure calculations on excited states is, in most cases, much more expensive than the one for ground states. This issue is even more critical for computational spectroscopy, where excitation energies computed at a given geometry (typically, the equilibrium structure of the initial state) are in most cases not sufficient, and the gradient and Hessian of the PES(s) are required. This high computational cost limits further the applicability of anharmonic models for spectroscopies involving multiple electronic states, and both perturbative[42,43] and variational[44,263] approaches are only feasible for to very small systems, totaling less than 10 atoms. Since the main objective of this thesis is to support rather larger systems, possibly with dozens of atoms, all the models presented in this section will be based on the harmonic approximation. This choice is motivated also by the fact that the number of vibronic models based on the harmonic approximation is significantly larger than for vibrational spectroscopy, since multiple excited states are treated simultaneously. For example, a reference geometry for the harmonic expansion has to be chosen for each state, which is not necessarily the same for all the states. Another issue, which is not present in the pure vibrational case, is that molecular vibrations are inherently described with a different set of coordinates for each electronic state. All those points make harmonic vibronic models less straightforward than their vibrational counterpart.
An additional challenge associated to the modeling of vibronic effects is related to the nature of molecular transitions. For vibrational spectroscopies, only radiative transitions induced by the absorption of IR radiation are usually of interest. However, the lifetime of electronic excited states is usually much longer than the one of vibrational levels. For this reason, emission processes, happening after an electronic excitation, can also be recorded in experiments. Those transitions are usually determined by the interplay of radiative and non-radiative processes, and a theoretical model accounting for both phenomena needs to be developed in order to reproduce reliably experimental data.

Based on those observations, a theoretical framework for the simulation of vibronic effects at the harmonic level will be presented in this section. This framework has been designed to target systems of several dozens of atoms, displaying some degree of flexibility, while keeping it as general as possible, to support a wide range of effects and computational protocols. The first goal has been accomplished by developing a framework supporting a general set of curvilinear coordinates. As already mentioned before and as will be commented in details within this chapter, differences between Cartesian and internal coordinates are already visible at the harmonic level in vibronic spectroscopy. As a result, using the latter clearly improves the description of systems characterized by some flexible degrees of freedom. The extension to internal coordinates puts also the basis for hybrid anharmonic treatments, that will be presented in the next chapters. The second goal has been reached by developing a generalized framework, based on the time-dependent (TD) Feynmann path integral theory, supporting different kinds of radiative and non-radiative phenomena.
The present chapter is organized as follows: the first section will focus on the definition of an harmonic vibronic model in Cartesian-based normal coordinates, that will be extended to a general set of curvilinear, internal coordinates in the second section. Based on this theoretical framework, an efficient algorithm, based on the TD theory, for the simulation of different kinds of vibronic processes is presented in the third section. In the last part of the chapter, the extension of this framework to support the calculation of rates of non-radiative processes, including internal conversion (IC) and intersystem crossing (ISC), is presented.

4.1 General framework of vibronic spectroscopy

The starting point for the definition of the vibronic models is Eq. 2.11, where the matrix element of a general operator $\mathcal{O}$ between two molecular wavefunctions Ψ_m and Ψ_n was expressed as,

$$\mathcal{O}_{mn} = \frac{\langle \psi^v_{r(\underline{m})} | \langle \phi_m \mid \mathcal{O}(\boldsymbol{R}, \boldsymbol{r}) \mid \phi_n \rangle | \psi^v_{s(\underline{n})} \rangle}{\sqrt{\langle \psi^v_{r(\underline{m})} \mid \psi^v_{r(\underline{m})} \rangle \langle \psi^v_{s(\underline{n})} \mid \psi^v_{s(\underline{n})} \rangle}} \tag{4.1}$$

Under the harmonic approximation, the nuclear wavefunctions of each electronic state are orthonormal, and thus the denominator of Eq. 4.1 is equal to 1. Unlike vibrational spectroscopy, where the previous equation was simplified by assuming that $\phi_m = \phi_n$, in vibronic spectroscopy ϕ_m and ϕ_n are different. It is useful to introduce a short notation to represent the transition moment of $\mathcal{O}$ between the two electronic states ϕ_m and ϕ_n as,

$$\mathcal{O}^e_{\underline{m}\,\underline{n}}(\boldsymbol{R}) = \langle \phi_{\underline{m}} \mid \mathcal{O} \mid \phi_{\underline{n}} \rangle \tag{4.2}$$

Combining Eqs. 4.1 and 4.2, the final result is,

$$\mathcal{O}_{mn} = \langle \psi^v_{r(\underline{m})}(\boldsymbol{R}) \mid \mathcal{O}^e_{\underline{m}\,\underline{n}}(\boldsymbol{R}) \mid \psi^v_{s(\underline{n})}(\boldsymbol{R}) \rangle \tag{4.3}$$

where the dependence of all the quantities on the nuclear coordinates has been explicitly stated. The calculation of transition properties from Eq. 4.3 requires the definition of the vibrational wavefunctions $\psi^v_{r(\underline{m})}$ and $\psi^v_{s(\underline{n})}$ and of a relation giving the variation of the transition property $\mathcal{O}^e_{\underline{m}\,\underline{n}}$ with the molecular geometry. Both these issues will be addressed in the following. Within this chapter, only transitions between 2 electronic states will be considered, so a slight change of notation will be introduced for the sake of readability. The explicit reference to the electronic state to which the vibrational state belongs will be dropped out, as well as the "v" superscript, so a more compact notation can be used, $\psi^v_{r(\underline{m})} \rightarrow \psi_r$. Moreover, the underscore will be dropped out for the electronic state.

4.1.1 The vibronic Hamiltonian

To calculate vibrational wavefunctions, a reference Hamiltonian describing both electronic and nuclear degrees of freedom must be developed. For two electronic states (the extension to more electronic states is trivial), the reference Hamiltonian $\mathcal{H}_{\text{ve}}$ (referred in the following as vibronic Hamiltonian) can be expressed in the basis of the Born-Oppenheimer electronic wavefunctions as,

$$\mathcal{H}_{\text{ve}} = \begin{pmatrix} \mathcal{T}_m & \mathcal{T}_{mn} \\ \mathcal{T}_{mn} & \mathcal{T}_n \end{pmatrix} + \begin{pmatrix} \mathcal{V}_m & \mathcal{V}_{mn} \\ \mathcal{V}_{mn} & \mathcal{V}_n \end{pmatrix} \tag{4.4}$$

where $\mathcal{T}_m$ and $\mathcal{T}_n$ are the nuclear kinetic energy operators for the first and second electronic state, respectively and $\mathcal{V}_m$ and $\mathcal{V}_n$ are their potential energy operators. In the most general formulation, couplings between the two states appear both in the potential ($\mathcal{V}_{mn}$) and in the kinetic energy energy operator ($\mathcal{T}_{mn}$). As discussed in Chapter 2, in the adiabatic representation, $\mathcal{V}_{mn} = \mathcal{V}_{nm} = 0$, but a non-null kinetic energy coupling is present. Conversely, in the diabatic representation, the kinetic energy coupling is neglected, but a non-null off-diagonal term in the potential energy operator is present. For both representations, we will take as reference the diagonal part in Eq. 4.4, and treat the off-diagonal contributions by perturbation theory. The zeroth-order Hamiltonian can thus be expressed as follows,

$$\mathcal{H}^{(0)}_{\text{ve}} = \begin{pmatrix} \mathcal{T}_m & 0 \\ 0 & \mathcal{T}_n \end{pmatrix} + \begin{pmatrix} \mathcal{V}_m & 0 \\ 0 & \mathcal{V}_n \end{pmatrix} \tag{4.5}$$

The main advantage of the Hamiltonian given in Eq. 4.5 is that each electronic state can be treated independently, since the off-diagonal terms have been neglected. To further simplify the notation, in the following, instead of the m and n subscripts, the electronic states will be labeled with overbars, using a single one for the initial state and a double overbar for the final state. We note that, for absorption spectroscopies, the initial state coincides with the lower (typically the ground) electronic level, and the final state to an higher, excited

electronic level. For emission spectroscopies, the opposite equivalence holds. The harmonic approximation of both $\overline{\mathcal{V}}$ and $\overline{\overline{\mathcal{V}}}$ leads to,

$$\begin{aligned}\overline{\mathcal{V}}\left(\overline{\boldsymbol{Q}}\right) &= \overline{\mathcal{V}}\left(\overline{\boldsymbol{Q}}^{\text{ref}}\right) + \sum_{i=1}^{N_{\text{vib}}}\left(\frac{\partial\overline{\mathcal{V}}}{\partial\overline{Q}_i}\right)_{\text{ref}}\overline{Q}_i + \frac{1}{2}\sum_{i=1}^{N_{\text{vib}}}\left(\frac{\partial^2\overline{\mathcal{V}}}{\partial\overline{Q}_i^2}\right)_{\text{ref}}\overline{Q}_i^2 \\ &= \overline{E}_0 + \overline{\boldsymbol{g}}^T\overline{\boldsymbol{Q}} + \frac{1}{2}\overline{\boldsymbol{Q}}^T\overline{\boldsymbol{\Omega}}^2\overline{\boldsymbol{Q}}\end{aligned} \tag{4.6}$$

$$\begin{aligned}\overline{\overline{\mathcal{V}}}\left(\overline{\overline{\boldsymbol{Q}}}\right) &= \overline{\overline{\mathcal{V}}}\left(\overline{\overline{\boldsymbol{Q}}}\right)^{\text{ref}} + \sum_{i=1}^{N_{\text{vib}}}\left(\frac{\partial\overline{\overline{\mathcal{V}}}}{\partial\overline{\overline{Q}}_i}\right)_{\text{ref}}\overline{\overline{Q}}_i + \frac{1}{2}\sum_{i=1}^{N_{\text{vib}}}\left(\frac{\partial^2\overline{\overline{\mathcal{V}}}}{\partial\overline{\overline{Q}}_i^2}\right)_{\text{ref}}\overline{\overline{Q}}_i^2 \\ &= \overline{\overline{E}}_0 + \overline{\overline{\boldsymbol{g}}}^T\overline{\overline{\boldsymbol{Q}}} + \frac{1}{2}\overline{\overline{\boldsymbol{Q}}}^T\overline{\overline{\boldsymbol{\Omega}}}^2\overline{\overline{\boldsymbol{Q}}}\end{aligned} \tag{4.7}$$

In vibrational spectroscopy, the harmonic expansion is usually performed at stationary points, thus the gradient contribution is null. This is not always the case in vibronic spectroscopy, depending on the mode, thus the more general expansion given in Eqs. 4.6 and 4.7 needs to be used. In any case, the normal modes for the two states ($\overline{\boldsymbol{Q}}$ and $\overline{\overline{\boldsymbol{Q}}}$) are defined as the eigenvectors of the force-constant matrices ($\overline{\boldsymbol{L}}_{\boldsymbol{x}}$ and $\overline{\overline{\boldsymbol{L}}}_{\boldsymbol{x}}$), where the $\boldsymbol{x}$ subscript has been added to highlight that all the quantities have been computed in Cartesian coordinates) as,

$$\begin{aligned}\overline{\boldsymbol{Q}} &= \overline{\boldsymbol{L}}_{\boldsymbol{x}}{}^T\boldsymbol{M}^{1/2}\left(\boldsymbol{x} - \overline{\boldsymbol{x}}^{\text{eq}}\right) \\ \overline{\overline{\boldsymbol{Q}}} &= \overline{\overline{\boldsymbol{L}}}_{\boldsymbol{x}}{}^T\boldsymbol{M}^{1/2}\left(\boldsymbol{x} - \overline{\overline{\boldsymbol{x}}}^{\text{eq}}\right)\end{aligned} \tag{4.8}$$

where $\overline{\boldsymbol{x}}_{\text{eq}}$ and $\overline{\overline{\boldsymbol{x}}}_{\text{eq}}$ are the Cartesian geometries of the equilibrium structures of the initial and final states, respectively. The vibrational eigenfunctions obtained from the Hamiltonian operators given in Eqs. 4.6 and 4.7 are expressed in terms of two different set of coordinates ($\overline{\boldsymbol{Q}}$ and $\overline{\overline{\boldsymbol{Q}}}$), and thus, in order to carry out the integral given in Eq. 4.3, a relation between the two sets of normal coordinates needs to be derived. Here, the affine transformation proposed by Duschinsky is employed;[264]

$$\overline{\boldsymbol{Q}} = \boldsymbol{J}\overline{\overline{\boldsymbol{Q}}} + \boldsymbol{K} \tag{4.9}$$

where $\boldsymbol{J}$ is a $N_{\text{vib}} \times N_{\text{vib}}$ matrix, called the Duschinsky matrix, while $\boldsymbol{K}$ is a N_{vib}-dimensional vector, the shift vector. In practice, $\boldsymbol{K}$ expresses the shift between the equilibrium geometries of the two electronic states involved in the transition, while $\boldsymbol{J}$ expresses the modes of the initial electronic state as linear combinations of the ones of the final electronic state. For semi-rigid systems, where electronic excitations are accompanied by limited structural rearrangement, the normal modes of the two states are similar, so $\boldsymbol{J}$ is nearly diagonal. Off-diagonal terms increase when strong structural changes happens upon the transition.

The normal modes are linear combinations of the Cartesian coordinates, and this might suggest that the relation given in Eq. 4.9 is formally exact. However, this is not true, as already noticed in Ref. 265. Indeed, the number

of normal modes is smaller than the Cartesian coordinates, since the space spanned by the normal modes is a subspace of the $3N_{at}$-dimensional Cartesian space, corresponding to pure vibrational motions. As already discussed above, this vibrational subspace depends on the reference geometry. Since the equilibrium geometry of the two electronic states are, in general, different, the subspaces spanned by $\overline{\boldsymbol{Q}}$ and $\overline{\overline{\boldsymbol{Q}}}$ are different as well, and thus Eq. 4.9 is a good approximation only in the limit of semi-rigid systems, for which the difference between the two equilibrium geometries is small. For more flexible systems, higher-order terms (such as quadratic) need to be added in Eq. 4.9. To conclude this discussion, we recall the definition of the normal modes changes with the reference coordinate system used in the simulation. Thus, also the Duschinsky transformation given in Eq. 4.9 will change depending on the coordinate system used to compute $\overline{\boldsymbol{L}}_{\boldsymbol{x}}$ and $\overline{\overline{\boldsymbol{L}}}_{\boldsymbol{x}}$. As mentioned in the previous chapter, for a single electronic state, normal modes are usually compute within the Eckart frame, to minimize vibro-rotational effects. However, in vibronic spectroscopy two reference geometries are usually present, corresponding to the equilibrium structures of the initial and final electronic states, each one associated to a different Eckart frame. In the present work, calculations are performed within the Eckart frame obtained for the equilibrium geometry of the initial state. The final state geometry is then oriented in order to maximize the overlap with the initial state one. In this way, vibro-rotational couplings can be minimized.[266]

The definition of $\boldsymbol{J}$ and $\boldsymbol{K}$ changes with the reference geometry employed for the expansions given in Eqs. 4.6 and 4.7. A first choice is to expand each PES about its own minimum (see left panel of Fig. 4.1). Vibronic models based on this approximation are usually referred to as adiabatic, and their main advantage is that the harmonic expansion is performed about a stationary point for each state. However, when strong structural changes occur upon electronic excitation, the equilibrium geometries of the two PESs become significantly shifted. For this reason, even if an accurate description of the PES of the final state about its equilibrium position is obtained, an inaccurate representation in the so-called Franck-Condon region, that is to say about the equilibrium geometry of the initial state, where the most intense transitions are localized, is obtained.

A more accurate reproduction of the PES in this region is possible within the so-called vertical models, where both the PESs are expanded about the equilibrium geometry of the initial state (see right panel of Fig. 4.1). The main limitation of vertical models is that the harmonic expansion is performed about a non-stationary point, which is often significantly different from the minimum, thus the frequencies, and so the position of the bands, are less accurate.

The definition of the Duschinsky transformation is different in adiabatic and vertical models. In the first case, the normal modes of the two states are obtained from Eq. 4.8. By combining the two definitions given in Eq. 4.8, the following relation is straightforwardly obtained,

$$\overline{\boldsymbol{Q}} = \overline{\boldsymbol{L}}_{\boldsymbol{x}}{}^{T}\overline{\overline{\boldsymbol{L}}}_{\boldsymbol{x}}\overline{\overline{\boldsymbol{Q}}} + \overline{\boldsymbol{L}}_{\boldsymbol{x}}{}^{T}\left(\overline{\overline{\boldsymbol{x}}}^{\mathrm{eq}} - \overline{\boldsymbol{x}}^{\mathrm{eq}}\right) , \tag{4.10}$$

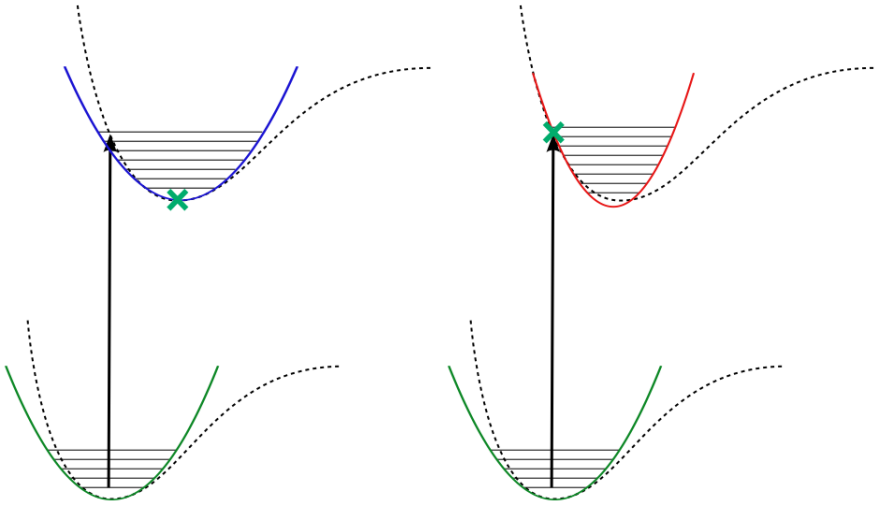

FIGURE 4.1: Graphical representation of the different expansion of the final state PES for the adiabatic (on the left) and vertical (on the right) models. For the sake of simplicity, only the case of absorption spectroscopy is reported, so the final state is the one higher in energy.

and thus,

$$\begin{aligned} \boldsymbol{J}_{\boldsymbol{x}} &= \overline{\boldsymbol{L}}_{\boldsymbol{x}}{}^{T}\overline{\overline{\boldsymbol{L}}}_{\boldsymbol{x}} \\ \boldsymbol{K}_{\boldsymbol{x}} &= \overline{\boldsymbol{L}}_{\boldsymbol{x}}{}^{T}\left(\overline{\overline{\boldsymbol{x}}}^{\mathrm{eq}} - \overline{\boldsymbol{x}}^{\mathrm{eq}}\right) \end{aligned} \tag{4.11}$$

Regarding vertical models, we will describe present here only the most important steps in the definition of the Duschinsky transformation,[267] since this derivation will be discussed more in detail in the next section for internal coordinates. As already mentioned above, in vertical models the expansion of the final state PES is performed at the equilibrium geometry of the initial state, where both the gradient $\overline{\overline{\boldsymbol{g}}}_{\boldsymbol{x}}$ and the Hessian $\overline{\overline{\boldsymbol{H}}}_{\boldsymbol{x}}$ are computed. Even if the harmonic expansion is performed at a non-stationary point of the final-state PES, the normal modes $\overline{\overline{\boldsymbol{L}}}_{\boldsymbol{x}}$ are still defined as the eigenvectors of the force-constant matrix $\overline{\overline{\boldsymbol{H}}}_{\boldsymbol{x}}$ is still used,

$$\overline{\overline{\boldsymbol{L}}}^{T}\overline{\overline{\boldsymbol{H}}}_{\boldsymbol{x}}\overline{\overline{\boldsymbol{L}}} = \overline{\overline{\boldsymbol{\Omega}}}^{2} \tag{4.12}$$

$\overline{\overline{\boldsymbol{H}}}_{\boldsymbol{x}}$ is not evaluated at a stationary point, thus the elements of $\boldsymbol{\Omega}^2$ are not necessarily all positive. Anyway, the definition of the Duschinsky matrix given in Eq. 4.10 still holds, and can be used to express Eq. 4.12 as,

$$\boldsymbol{J}^{T}\overline{\boldsymbol{L}}^{T}\overline{\overline{\boldsymbol{H}}}_{\boldsymbol{x}}\overline{\boldsymbol{L}}\boldsymbol{J} = \boldsymbol{\Omega}^{2} \tag{4.13}$$

which means that $\boldsymbol{J}$ can also be obtained by diagonalizing the Hessian matrix $\overline{\overline{\boldsymbol{H}}}_{\boldsymbol{x}}$ expressed in the basis of the normal modes of the initial state ($\overline{\boldsymbol{L}}$). The calculation of the shift vector $\boldsymbol{K}$ is less trivial than for adiabatic models, since the equilibrium position of the final state is not explicitly computed.

However, it can be extrapolated as the minimum of the parabolic expansion given in Eq. 4.7. The gradient of $\overline{\overline{\mathcal{V}}}(\boldsymbol{x})$ reads,

$$\nabla_{\boldsymbol{x}}\overline{\overline{\mathcal{V}}}(\boldsymbol{x}) = \overline{\overline{\boldsymbol{g}}}_{\boldsymbol{x}} + \overline{\overline{\boldsymbol{H}}}_{\boldsymbol{x}}\left(\boldsymbol{x} - \overline{\overline{\boldsymbol{x}}}^{\mathrm{eq}}\right) \tag{4.14}$$

By setting $\nabla_{\boldsymbol{x}}\overline{\overline{\mathcal{V}}}(\boldsymbol{x}) = 0$ and using the definition of $\boldsymbol{J}$ given in Eq. 4.13, the following definition is obtained:

$$\boldsymbol{K} = -\boldsymbol{J}\overline{\overline{\boldsymbol{\Omega}}}^{-2}\boldsymbol{J}^{T}\overline{\overline{\boldsymbol{g}}}_{\boldsymbol{x}} \tag{4.15}$$

The adiabatic model where the definition of $\boldsymbol{J}$ and $\boldsymbol{K}$ given in Eq. 4.11 are employed is referred to as Adiabatic Hessian (AH), whereas the vertical one based on the definitions given in Eqs. 4.13 and 4.15 is known as Vertical Hessian (VH).[268] Both models require the calculation of harmonic frequencies of electronic excited states, which is not trivial for large-sized systems, and is the most expensive step of the overall simulation. Simplified models, where the harmonic frequencies of the final state are not required, are obtained by assuming that the PES are equal, with a first consequence that $\boldsymbol{J} = \boldsymbol{I}$. The resulting adiabatic model is known as Adiabatic Shift (AS), and its vertical counterpart is known as Vertical Gradient (VG).
To conclude, it is noteworthy that vertical and adiabatic models are equivalent only for exactly harmonic PESs or if the minima are superimposed to each other. Otherwise, they diverge from one another as the shift between the PESs increase the magnitude of the differences growing faster with the anharmonicity of the PES. As will be discussed in the next section, this problem can be limited also by using internal coordinates to describe molecular vibrations.

4.1.2 Expansion of the transition property

The definition of the vibronic Hamiltonian $\mathcal{H}_{\mathrm{ve}}$ presented in the previous section allows to compute the vibrational wavefunctions of each electronic state and transition properties. Those quantities can be used to express Eq. 4.3 as,

$$\langle \mathcal{O} \rangle_{if} = \langle\, \overline{\psi} \mid \mathcal{O}^{e}_{if} \mid \overline{\psi}\, \rangle \tag{4.16}$$

where the electronic states involved in the transition (if) are not explicitly indicated anymore. As already noted above, $\mathcal{O}^{e}_{if}$ depends parametrically on the nuclear coordinates, and thus on the normal modes $\boldsymbol{Q}$. However, with the exception of the simplest models, analytical expressions for $\mathcal{O}^{e}_{if}(\boldsymbol{Q})$ are not available. Since electronic excitations are usually much faster than the average timescales of nuclear motions, the electronic transition moment $\mathcal{O}^{e}_{if}$ can be approximated in practice by its value at the equilibrium geometry of the initial electronic state. This approximation is usually known as Franck-Condon (FC) approximation,[269,270] and corresponds to a zeroth-order Taylor expansion of $\mathcal{O}^{e}_{if}$ in terms $\boldsymbol{Q}$. If also higher-order terms are included, we obtain the following expression,

$$\mathcal{O}^e_{if}\left(\boldsymbol{Q}\right) = \mathcal{O}^e_{if}\left(\boldsymbol{Q}_{\text{eq}}\right) + \sum_{k=1}^{N_{\text{vib}}} \left(\frac{\partial \mathcal{O}^e_{if}}{\partial Q_k}\right)_{\text{eq}} Q_k + \frac{1}{2}\sum_{k,l=1}^{N_{\text{vib}}} \left(\frac{\partial^2 \mathcal{O}^e_{if}}{\partial Q_k \partial Q_l}\right)_{\text{eq}} Q_k Q_l \quad (4.17)$$

where the sum of the first-order contributions is known as Herzberg-Teller (HT) term.[271] For a wide range of applications, such as when studying fully-allowed electronic transitions, reliable results are generally obtained already at FC level. However, the HT term become relevant for specific systems and spectroscopies. This is the case, for example, of weakly-allowed transitions, where the equilibrium value of the transition dipole moment is smaller than or of the same order of magnitude of the first-order terms. Another case in which the FC approximation is insufficient are chiroptical spectroscopies, where, as will be discussed more in detail in the following, the FC term is given by the scalar product of the electronic component of the electric and magnetic dipole moments, that are in several cases nearly orthogonal. The second-order term in Eq. 4.17 is only rarely relevant, except for highly symmetric systems, and will be included only in the last part of this chapter, when diabatic models are discussed. Eq. 4.17 was expressed in terms of a general set of normal modes $\boldsymbol{Q}$, without specifying the electronic state of reference. Following the original formulation introduced by Herzberg and Teller,[271] the expansion is usually performed with respect to the normal modes of the initial electronic state ($\overline{\boldsymbol{Q}}$). However, in electronic structure calculations, the derivatives of the transition properties are computed, in practice, with respect to the excited states, corresponding to the final only one for absorption spectroscopy. For emission spectroscopies, the output of electronic structure calculations are the derivatives with respect to $\overline{\overline{\boldsymbol{Q}}}$. Depending on the preferred state of reference, data from electronic structure calculations may need to be converted. This can be done by assuming that Eq. 4.17, with the inclusion of FC and HT terms, is exact, and equating the two expansions:

$$\mathcal{O}^e_{if}\left(\overline{\boldsymbol{Q}}^{\text{eq}}\right) + \sum_{k=1}^{N_{\text{vib}}} \left(\frac{\partial \mathcal{O}^e_{if}}{\partial \overline{Q}_k}\right)_{\text{eq}} \overline{Q}_k = \mathcal{O}^e_{if}\left(\overline{\overline{\boldsymbol{Q}}}_{\text{eq}}\right) + \sum_{k=1}^{N_{\text{vib}}} \left(\frac{\partial \mathcal{O}^e_{if}}{\partial \overline{\overline{Q}}_k}\right)_{\text{eq}} \overline{\overline{Q}}_k \quad (4.18)$$

Following Herberg and Teller's formalism and assuming the case of an absorption spectrum, then the conversion of the transition moment with respect to $\overline{\overline{\boldsymbol{Q}}}$ to a Taylor expansion about $\overline{\boldsymbol{Q}}^{\text{eq}}$ can be done using the Duschinsky transformation given in Eq. 4.9,

$$\begin{aligned} \mathcal{O}^e_{if}\left(\overline{\boldsymbol{Q}}^{\text{eq}}\right) &= \mathcal{O}^e\left(\overline{\overline{\boldsymbol{Q}}}^{\text{eq}}\right) - \sum_{k=1}^{N_{\text{vib}}} \left(\frac{\partial \mathcal{O}^e_{if}}{\partial \overline{\overline{Q}}_k}\right)_{\text{eq}} \left(\boldsymbol{J}^T \boldsymbol{K}\right)_k \\ \left(\frac{\partial \mathcal{O}^e}{\partial \overline{\overline{Q}}_p}\right)_{\text{eq}} &= \sum_{k=1}^{N_{\text{vib}}} \left(\boldsymbol{J}^{-1}\right)_{pk} \left(\frac{\partial \mathcal{O}^e_{if}}{\partial \overline{\overline{Q}}_k}\right)_{\text{eq}} \end{aligned} \quad (4.19)$$

4.2 Extension to internal coordinates

The framework outlined in the previous section can be used to compute different kinds of vibronic spectra using harmonic models in Cartesian-based normal coordinates. The two main limitations of the framework are the harmonic approximation, and the underlying description of molecular vibrations in terms of Cartesian coordinates, which limits reliability outside semi-rigid systems. In order to extend its range of applicability of the model also to more flexible systems, one of the two limitations just described must be overcome. Here, we will present the extension of the Cartesian-based harmonic models mentioned above to a general set of curvilinear, internal coordinates. As will discussed in the next section, this generalization allows to significantly improve the reliability of the simulations for flexible systems in a cost-effective way.

4.2.1 Adiabatic and vertical models in internal coordinates

As will be clearer in the following, the quantities needed to compute a vibronic spectrum within the harmonic approximation are the harmonic frequencies of at least one electronic state, $\boldsymbol{J}$, $\boldsymbol{K}$ and the transition dipole moment (together with its derivative, for HT simulations). The harmonic frequencies do not depend on the reference coordinates system, and the same holds for the equilibrium value of the transition dipole moment. Thus, at the FC level, generalizing the Duschinsky transformation to internal coordinates is sufficient to develop harmonic vibronic models in internal coordinates. Before going into the details of the theory, let us discuss briefly the difference between internal coordinates-based frameworks for vibrational and vibronic spectroscopy. As already noted above,[18,128] in vibrational spectroscopy the difference between the two representations appears only at the anharmonic level, provided that calculations are computed at a stationary point. In fact, for infinitesimal displacements from the equilibrium position, the first non-null term arising from the non-linearity of the transformation between Cartesian and internal coordinates appears for cubic force-constants. This is not true in vibronic spectroscopy, where two geometries (i.e. the reference geometries of the two electronic states) have to be described with the same coordinates system. Since the difference between those two geometries is, in general, not infinitesimal, a change is detected already at the harmonic level. Following the same strategy used for Cartesian coordinates, the Duschinky transformation can be derived from the expression for the gradient and the Hessian in internal coordinates, which is given in the following,

$$\begin{aligned} \boldsymbol{g_s} &= \{\boldsymbol{B}^T\}^+ \boldsymbol{P}^T \boldsymbol{g_x} \\ \boldsymbol{H_s} &= \{\boldsymbol{B}^T\}^+ \boldsymbol{P}^T \left(\boldsymbol{H_x} - \boldsymbol{g_s}^T \boldsymbol{B'} \right) \boldsymbol{P} \boldsymbol{B}^+ \end{aligned} \tag{4.20}$$

where, as discussed in Chapter 2, $\boldsymbol{P} = \boldsymbol{B}^+ \boldsymbol{B}$ is a projection operator that removes the translational and rotational contributions from the Cartesian force

constants. In internal coordinates, normal modes $\boldsymbol{L_s}$ are the eigenvectors of $\boldsymbol{GH_s}$, and satisfy the following generalized orthogonality relation;

$$\boldsymbol{L_s}^T \boldsymbol{G}^{-1} \boldsymbol{L_s} = \boldsymbol{I} \tag{4.21}$$

As a consequence, $\boldsymbol{L_s}$ is not orthogonal, since $\boldsymbol{G}$ is not diagonal. Anyway, the definition of the Duschinsky matrix and shift vector in internal coordinates can be derived following the same strategy as for the Cartesian case by using the pseudo-inverse of $\boldsymbol{L}$ instead of its transpose. Let us start from the definition of the curvilinear normal modes $\overline{\boldsymbol{Q}}_{\boldsymbol{s}}$ and $\overline{\overline{\boldsymbol{Q}}}_{\boldsymbol{s}}$, reported below:

$$\begin{aligned} \overline{\boldsymbol{L}}_{\boldsymbol{s}} \overline{\boldsymbol{Q}}_{\boldsymbol{s}} &= \boldsymbol{s} - \overline{\boldsymbol{s}}^{\mathrm{eq}} \\ \overline{\overline{\boldsymbol{L}}}_{\boldsymbol{s}} \overline{\overline{\boldsymbol{Q}}}_{\boldsymbol{s}} &= \boldsymbol{s} - \overline{\overline{\boldsymbol{s}}}^{\mathrm{eq}} \end{aligned} \tag{4.22}$$

In a way similar to what was done for Eq. 4.10, the second relation of Eq. 4.22 is used to express $\boldsymbol{s}$ in terms of $\overline{\overline{\boldsymbol{Q}}}_{\boldsymbol{s}}$, which is then inserted in the first equation, leading to the following expressions for $\boldsymbol{J_s}$ and $\boldsymbol{K_s}$,[86,88]

$$\begin{aligned} \boldsymbol{J_s} &= \overline{\boldsymbol{L}}_{\boldsymbol{s}}^{\,T} \overline{\overline{\boldsymbol{L}}}_{\boldsymbol{s}} \\ \boldsymbol{K_s} &= \overline{\boldsymbol{L}}_{\boldsymbol{s}}^{\,T} \left(\overline{\overline{\boldsymbol{s}}}^{\mathrm{eq}} - \overline{\boldsymbol{s}}^{\mathrm{eq}} \right) \end{aligned} \tag{4.23}$$

where $\overline{\boldsymbol{L}}_{\boldsymbol{s}}$ and $\overline{\overline{\boldsymbol{L}}}_{\boldsymbol{s}}$ are the transformation matrices from internal coordinates to curvilinear normal modes for the initial and final states, respectively. The previous equation is a starting point ot highlight the origin of the differences between $\boldsymbol{J_s}$ and $\boldsymbol{J_x}$. Since our derivation holds for adiabatic models, $\boldsymbol{g_x}$ vanishes for both electronic states. Therefore, using Eq. 4.20, $\boldsymbol{J_s}$ can be expressed as follows:

$$\boldsymbol{J_s} = \overline{\boldsymbol{L}}_{\boldsymbol{x}}^{\,T} \boldsymbol{M}^{1/2} \overline{\boldsymbol{B}}^{-1} \overline{\overline{\boldsymbol{B}}} \boldsymbol{M}^{-1/2} \overline{\overline{\boldsymbol{L}}}_{\boldsymbol{x}} \tag{4.24}$$

From the previous equation, it is clear that $\boldsymbol{J_x} = \boldsymbol{J_s}$ only if $\overline{\boldsymbol{B}}^{-1} \overline{\overline{\boldsymbol{B}}} = \boldsymbol{I}$, otherwise the two matrices differ. Since the reference geometry used to compute the first-order derivatives needed to build $\boldsymbol{B}$ is different for the two electronic states, $\overline{\boldsymbol{B}}^{-1} \overline{\overline{\boldsymbol{B}}} \neq \boldsymbol{I}$, and the deviation of the product from the identity matrix increases with the extent of the geometry change. For this reason, for systems undergoing large-amplitude deformations, $\boldsymbol{J_x}$ and $\boldsymbol{J_s}$ may be significantly different.
A similar analysis can be done for the shift vector $\boldsymbol{K}$. Following the same strategy as above, it is easy to show that,

$$\boldsymbol{K_s} = \overline{\boldsymbol{L}}_{\boldsymbol{x}}^{\,T} \boldsymbol{M}^{1/2} \overline{\boldsymbol{B}}^{-1} \left(\overline{\overline{\boldsymbol{s}}}^{\mathrm{eq}} - \overline{\boldsymbol{s}}^{\mathrm{eq}} \right) \tag{4.25}$$

In this case, the identity $\boldsymbol{K_x} = \boldsymbol{K_s}$ holds when $\overline{\overline{\boldsymbol{s}}}^{\mathrm{eq}} - \overline{\boldsymbol{s}}^{\mathrm{eq}} = \overline{\boldsymbol{B}} \left(\overline{\overline{\boldsymbol{x}}}^{\mathrm{eq}} - \overline{\boldsymbol{x}}^{\mathrm{eq}} \right)$, thus if only the first-order term in Eq. 2.30 is kept in the Taylor expansion of the internal coordinates in terms of the Cartesian ones. This approximation is valid when the geometrical rearrangement (i.e. the difference "$\Delta \boldsymbol{x} = \overline{\overline{\boldsymbol{x}}}_{\mathrm{eq}} - \overline{\boldsymbol{x}}_{\mathrm{eq}}$") is small, but this is not the case for flexible systems, where the deformation can be significant.

In order to derive the Duschinsky transformation for vertical models in internal coordinates, a different procedure must be followed.[267] In this case, the difference between Cartesian and internal coordinates is not caused by the presence of two different equilibrium structures, since the reference geometry is the same for both PESs. However, the PES of the final state is expanded about a non-stationary point, and therefore the Wilson $\boldsymbol{B}$ matrix and its derivative $\boldsymbol{B}'$ are needed to calculate the Hessian in internal coordinates $\boldsymbol{H_s}$. The presence of $\boldsymbol{B}'$ generates the difference between Cartesian and internal coordinates, for the same reason as for the RPH model in internal coordinates.
As a first step, let us express the final-state potential energy $\overline{\overline{\mathcal{V}}}$ as a Taylor expansion in terms of the curvilinear normal coordinates $\overline{\boldsymbol{Q}}_{\boldsymbol{s}}$ of the initial state,

$$\begin{aligned}\overline{\overline{\mathcal{V}}}\left(\overline{\boldsymbol{Q}}_{\boldsymbol{s}}\right) =& \overline{\overline{\mathcal{V}}}\left(\overline{\boldsymbol{Q}}_{\boldsymbol{s}}^{\mathrm{eq}}\right) + \left(\frac{\partial\overline{\overline{\mathcal{V}}}}{\partial\overline{\boldsymbol{Q}}_{\boldsymbol{s}}}\right)_{\mathrm{eq}}\overline{\boldsymbol{Q}}_{\boldsymbol{s}} + \frac{1}{2}\overline{\boldsymbol{Q}}_{\boldsymbol{s}}^{T}\left(\frac{\partial^2\overline{\overline{\mathcal{V}}}}{\partial\overline{\boldsymbol{Q}}_{\boldsymbol{s}}^2}\right)_{\mathrm{eq}}\overline{\boldsymbol{Q}}_{\boldsymbol{s}} \\ =& \overline{\overline{\mathcal{V}}}\left(\overline{\boldsymbol{Q}}_{\boldsymbol{s}}^{\mathrm{eq}}\right) + \overline{\overline{\boldsymbol{g}}}\left(\overline{\boldsymbol{Q}}_{\boldsymbol{s}}^{\mathrm{eq}}\right)^{T}\overline{\boldsymbol{Q}}_{\boldsymbol{s}} + \frac{1}{2}\overline{\boldsymbol{Q}}_{\boldsymbol{s}}^{T}\overline{\overline{\boldsymbol{H}}}\left(\overline{\boldsymbol{Q}}_{\boldsymbol{s}}^{\mathrm{eq}}\right)\overline{\boldsymbol{Q}}_{\boldsymbol{s}}\end{aligned} \tag{4.26}$$

where $\overline{\overline{\boldsymbol{g}}}\left(\overline{\boldsymbol{Q}}_{\boldsymbol{s}}^{\mathrm{eq}}\right)$ and $\overline{\overline{\boldsymbol{H}}}\left(\overline{\boldsymbol{Q}}_{\vec{s}}^{\mathrm{eq}}\right)$ are the gradient and Hessian of the final state PES calculated at the equilibrium geometry of the initial state and expressed in terms of the normal modes of the initial state. Since the curvilinear coordinates $\boldsymbol{Q_s}$ are related to the internal ones $\mathbf{s}$ through a linear transformation, the derivatives with respect to the former can be straightforwardly rewritten as,

$$\begin{aligned}\overline{\overline{\boldsymbol{g}}}\left(\overline{\boldsymbol{Q}}_{\boldsymbol{s}}^{\mathrm{eq}}\right) &= \overline{\boldsymbol{L}}_{\boldsymbol{s}}^{\ T}\overline{\overline{\boldsymbol{g}}}_{\boldsymbol{s}} \\ \overline{\overline{\boldsymbol{H}}}\left(\overline{\boldsymbol{Q}}_{\boldsymbol{s}}^{\mathrm{eq}}\right) &= \overline{\boldsymbol{L}}_{\boldsymbol{s}}^{\ T}\overline{\overline{\boldsymbol{H}}}_{\boldsymbol{s}}\overline{\boldsymbol{L}}_{\boldsymbol{s}}\end{aligned} \tag{4.27}$$

Alternatively, the final-state potential energy can be expressed also as a Taylor series in terms of the final-state normal coordinates $\overline{\overline{\boldsymbol{Q}}}_{\boldsymbol{s}}$ about their equilibrium position $\overline{\overline{\boldsymbol{Q}}}_{\boldsymbol{s}}^{\mathrm{eq}}$ as,

$$\overline{\overline{\mathcal{V}}}\left(\overline{\overline{\boldsymbol{Q}}}_{\boldsymbol{s}}\right) = \mathrm{E_{ad}} + \frac{1}{2}\overline{\overline{\boldsymbol{Q}}}_{\boldsymbol{s}}^{\ T}\overline{\overline{\boldsymbol{\Omega}}}^2\overline{\overline{\boldsymbol{Q}}}_{\boldsymbol{s}} \tag{4.28}$$

where the definition of the matrix containing the harmonic frequencies $\overline{\overline{\boldsymbol{\Omega}}}^2$ is the same, as for Cartesian coordinates. Furthermore, E_{ad} is the energetic separation between the minima of the two PESs. In order to express both Taylor expansions in terms of the same coordinate system, the Duschinsky transformation reported in Eq. 4.9 can be inverted to express $\overline{\overline{\boldsymbol{Q}}}_{s}$ in terms of $\overline{\boldsymbol{Q}}_{\boldsymbol{s}}$ as,

$$\overline{\overline{\boldsymbol{Q}}}_{\boldsymbol{s}} = \boldsymbol{J_s}^{-1}\overline{\boldsymbol{Q}}_{\boldsymbol{s}} - \boldsymbol{J_s}^{-1}\boldsymbol{K_s} \tag{4.29}$$

Thanks to the previous relation, Eq. 4.28 can be written as,

$$\begin{aligned}\overline{\overline{\mathcal{V}}}\left(\overline{\boldsymbol{Q}}_s\right) =& \frac{1}{2}\overline{\boldsymbol{Q}}_s{}^T\{\boldsymbol{J}_s{}^{-1}\}^T\overline{\overline{\boldsymbol{\Omega}}}^2\boldsymbol{J}_s{}^{-1}\overline{\boldsymbol{Q}}_s - \mathbf{K}_s{}^T\{\boldsymbol{J}_s{}^{-1}\}^T\overline{\overline{\boldsymbol{\Omega}}}^2\boldsymbol{J}_s{}^{-1}\overline{\boldsymbol{Q}}_s \\ &+ \frac{1}{2}\boldsymbol{K}_s{}^T\{\boldsymbol{J}_s{}^{-1}\}^T\overline{\overline{\boldsymbol{\Omega}}}^2\boldsymbol{J}_s{}^{-1}\boldsymbol{K}_s + \mathrm{E}_{\mathrm{ad}}\end{aligned} \tag{4.30}$$

Under the harmonic approximation, Eqs. 4.26 and 4.30 must be equivalent for each value of $\overline{\boldsymbol{Q}}_s$. As a consequence, the coefficients of the zeroth-, first- and second-order terms in $\overline{\boldsymbol{Q}}_s$ must be equal. The equivalence between the second-order terms can be used to derive the following expression for the Duschinsky matrix $\boldsymbol{J}_s$:

$$\overline{\overline{\boldsymbol{H}}}\left(\overline{\boldsymbol{Q}}_s^{\mathrm{eq}}\right) = \{\boldsymbol{J}_s{}^{-1}\}^T\overline{\overline{\boldsymbol{\Omega}}}^2\boldsymbol{J}_s{}^{-1} \tag{4.31}$$

Thus, $\boldsymbol{J}_s$ can be obtained by diagonalizing the Hessian matrix in internal coordinates $\overline{\overline{\boldsymbol{H}}}\left(\overline{\boldsymbol{Q}}_s\right)$. On the other hand, the equivalence of the first-order terms of Eqs. 4.26 and 4.30 can be used to derive the following expression for the shift vector $\mathbf{K}_s$;

$$\begin{aligned}\boldsymbol{K}_s =& -\overline{\overline{\boldsymbol{H}}}\left(\overline{\boldsymbol{Q}}_s^{\mathrm{eq}}\right)^{-1}\overline{\overline{\boldsymbol{g}}}\left(\overline{\boldsymbol{Q}}_s^{\mathrm{eq}}\right) = -\overline{\overline{\boldsymbol{H}}}\left(\overline{\boldsymbol{Q}}_s^{\mathrm{eq}}\right)^{-1}\overline{\boldsymbol{L}}_s{}^T\overline{\overline{\boldsymbol{g}}}_s \\ =& -\boldsymbol{J}_s\overline{\overline{\boldsymbol{\Omega}}}^{-2}\boldsymbol{J}_s^T\overline{\boldsymbol{L}}_s{}^T\overline{\overline{\boldsymbol{g}}}_s\end{aligned} \tag{4.32}$$

The previous expressions can be simplified within the VG model, where the Duschinsky matrix $\boldsymbol{J}$ is assumed to be equal to identity $\boldsymbol{I}$. In this case, Eq. 4.32 can be recast as,

$$\boldsymbol{K}_s = -\overline{\overline{\boldsymbol{\Omega}}}^{-2}\overline{\boldsymbol{L}}_s{}^T\overline{\overline{\boldsymbol{g}}}_s \tag{4.33}$$

The normal modes in internal coordinates ($\boldsymbol{L}_s$) can be expressed in terms of the ones in Cartesian coordinates ($\boldsymbol{L}_x$) as,

$$\boldsymbol{L}_s = \boldsymbol{B}\boldsymbol{M}^{-1/2}\boldsymbol{L}_x \tag{4.34}$$

Using the relation between the gradient in internal and Cartesian coordinates given in Eq. 2.34, it can be proven that, at the VG level, $\boldsymbol{K}_x = \boldsymbol{K}_s$. This strict equivalence does not hold for the VH model due to the presence of the term $\boldsymbol{B}'\boldsymbol{g}_s$ in the definition of $\boldsymbol{H}_s$ (see Eq. 2.34). Thus, VG is the only vibronic model, among the ones employed here, for which Cartesian and internal coordinates provide the same results. This equivalence has been overlooked in previous studies[88,186,272,273] and explains the claimed accuracy of the VG implementation based on Cartesian coordinates.

4.2.2 Reduced-dimensionality schemes

The theoretical framework introduced in the previous section can be coupled to reduced-dimensionality (RD) schemes, to reach even larger systems. The main idea behind RD schemes is to perform the vibronic calculations only on a fraction of the normal modes, neglecting the contributions arising from the other vibrations. RD schemes are particularly appealing when the final state PES, in vertical models, displays an imaginary frequency (i.e. when the

harmonic force constants matrix has a negative eigenvalue). Such frequency, at the harmonic level, would describe an unbounded motion, thus leading to unphysical results. In those cases, the adoption of RD schemes allows the removal of contributions from this mode. Similarly, those schemes can be used to neglect contributions from low-frequency, highly-anharmonic modes which are described inaccurately at the harmonic level, leading to an inaccurate definition of the Duschinsky transformation. For this reason, in most cases more accurate results are obtained by neglecting their contribution, since they usually give rise to a large number of closely-spaced transitions, whose overall effect is to broaden the main vibronic transitions. Their contribution can be recovered *a posteriori* using symmetric distribution functions for each vibronic peak. Finally, a primary reason to using the RD schemes is to reduce the overall computational cost when dealing with large systems. Often, only a part of the system is actively contributing to photochemical properties, while the rest has a minor role. By selecting the modes, which will have a predominant role in the final band-shape, the computational cost to generate the frequencies can potentially be strongly reduced.
In practice, when RD models are built, a subset of n_{RD} normal modes of one of the states is selected, referred to in the following as active modes, and calculations are performed only on those modes. However, in order to build a consistent RD model, the same number n_{RD} of active modes in the other electronic state must be chosen. Since the modes of the first state are, in the most general case, coupled with all the other modes of the second electronic state, the selection of the active set of modes for this second state is not trivial. To illustrate the algorithm used here to construct this active ensemble, let us consider as a starting point a subset $\overline{\mathrm{S}}$ of $\overline{n}_{\mathrm{RD}}$ normal modes chosen from the initial state. The extent of coupling tolerated in the construction of the active block is defined through a positive parameter η, whose value should not exceed 1. A high value for η ensures that this coupling will be very small. For each mode in $\overline{\mathrm{S}}$, its projection onto the basis set of the final state $\overline{\overline{Q}}$ is given by ${J_{ij}}^2$. The list of the N_{vib} ${J_{ij}}^2$ values are sorted by decreasing order and the first $\overline{\overline{\mathrm{n}}}_{\mathrm{RD}}$ element are chosen so that:

$$\sum_{j=1}^{\overline{\overline{\mathrm{n}}}_{\mathrm{RD}}-1} {J_{ij}}^2 < \eta \qquad \text{and} \qquad \sum_{j=1}^{\overline{\overline{\mathrm{n}}}_{\mathrm{RD}}} {J_{ij}}^2 \geq \eta \tag{4.35}$$

All selected modes are then added to $\overline{\overline{\mathrm{S}}}$ and the selection proceeds until all elements of $\overline{\mathrm{S}}$ have been treated. The same is done after this with the modes of $\overline{\overline{\mathrm{S}}}$, inverting the states in the procedure described above. Succinctly, the conditions for the construction of the blocks can be summarized as,

$$\sum_{i\in\overline{\mathrm{S}}} {J_{ij}}^2 \geq \eta \qquad\qquad \sum_{j\in\overline{\overline{\mathrm{S}}}} {J_{ij}}^2 \geq \eta \tag{4.36}$$

The construction of $\overline{\mathrm{S}}$ and $\overline{\overline{\mathrm{S}}}$ is done iteratively, until their content has been stabilized ($\overline{\mathrm{n}} = \overline{\overline{\mathrm{n}}}$). The number of modes included in $\overline{\overline{\mathrm{S}}}$ changes with η. If

the mode-mixing is negligible for the modes in $\overline{\mathrm{S}}$, the elements of $\overline{\overline{\mathrm{S}}}$ are n_{RD} even for values of η close to 1, otherwise smaller values of η can be used. In this case, a potentially significant portion of $\boldsymbol{J}$ may be neglected, lowering the reliability of the reduced-dimensionality approximation.[274,275]
Some care must be paid when this framework is generalized to internal coordinates. Indeed, the relation given in Eq. 4.36 assumes that $\boldsymbol{J}$ is orthogonal. Since, in this case the sums of the squared elements of a row or a column of $\boldsymbol{J}$ are equal to 1, and therefore η needs not exceed 1. In order to extend this definition to support curvilinear internal coordinates as well, Eq. 4.36 must be modified as follows:

$$\frac{\sum_{i\in\overline{S}} {J_{ij}}^2}{\sum_{i=1}^{N_{\mathrm{vib}}} {J_{ij}}^2} > \eta \qquad\qquad \frac{\sum_{j\in\overline{\overline{S}}} {J_{ij}}^2}{\sum_{j=1}^{N_{\mathrm{vib}}} {J_{ij}}^2} > \eta \tag{4.37}$$

The normalization factor of Eq. 4.37 sets the upper limit of the sums to 1, and therefore the same definition of η as in the Cartesian case can be used.
Once the active normal modes have been selected, the Duschinsky transformation for the reduced-dimensionality scheme must be defined. For curvilinear sets of coordinates, this definition is not as straightforward as in the Cartesian case. Let us start from the definition of the curvilinear normal modes given in Eq. 4.22 where, for reduced-dimensionality schemes, $\overline{\boldsymbol{L}}_{\boldsymbol{s}}$ and $\overline{\overline{\boldsymbol{L}}}_{\boldsymbol{s}}$ are $n_{\mathrm{RD}} \times 3N_{\mathrm{at}}$ rectangular matrices. The counterpart of Eq. 4.22 for the RD case is the following;

$$\overline{\boldsymbol{L}}_{\boldsymbol{s}}\overline{\boldsymbol{Q}}_{\boldsymbol{s}} = \overline{\overline{\boldsymbol{L}}}_{\boldsymbol{s}}\overline{\overline{\boldsymbol{Q}}}_{\boldsymbol{s}} + \overline{\overline{\boldsymbol{s}}}^{\mathrm{eq}} - \overline{\boldsymbol{s}}^{\mathrm{eq}} \tag{4.38}$$

Particular care must be taken when Eq. 4.38 is inverted, since $\overline{\boldsymbol{L}}_{\boldsymbol{s}}$ is rectangular. However, Eq. 4.21 still holds also for $\overline{\boldsymbol{L}}_{\boldsymbol{s}}$ and $\overline{\overline{\boldsymbol{L}}}_{\boldsymbol{s}}$, and therefore Eq. 4.38 can be inverted by multiplying both lhs and rhs by ${\overline{\boldsymbol{L}}_{\boldsymbol{s}}}^T\overline{\boldsymbol{G}}^{-1}$. The resulting definition of $\boldsymbol{J}_{\boldsymbol{s}}$ and $\boldsymbol{K}_{\boldsymbol{s}}$ is,

$$\begin{aligned} \boldsymbol{J}_{\boldsymbol{s}} &= {\overline{\boldsymbol{L}}_{\boldsymbol{s}}}^T\overline{\boldsymbol{G}}^{-1}\overline{\overline{\boldsymbol{L}}}_{\boldsymbol{s}} \\ \boldsymbol{K}_{\boldsymbol{s}} &= {\overline{\boldsymbol{L}}_{\boldsymbol{s}}}^T\overline{\boldsymbol{G}}^{-1}\left(\overline{\overline{\boldsymbol{s}}}^{\mathrm{eq}} - \boldsymbol{s}^{\mathrm{eq}}\right) \end{aligned} \tag{4.39}$$

Let us remark that the relations given in Eq. 4.39 are equivalent to those derived in Ref. 86 and used more recently by Santoro and coworkers in Ref. 88. For full-dimensional systems, Eqs. 4.23 and 4.39 are equivalent, so the latter is more appealing for implementations since more general.

4.2.3 Inclusion of Herzberg-Teller effects

In order to build an internal coordinates-based framework as general as the Cartesian one, it is necessary to support HT terms in internal coordinates as well. As highlighted before, inclusion of HT effects is mandatory for some cases, such as for weakly-allowed transitions, so the framework cannot be limited to the FC leve as often done in the literature before.[88,273,276]

As a first step, the derivatives of the transition dipole moment must be converted from the Cartesian representation to the internal one. This step can be done following the same strategy as for the energy gradient. The final transformation is given in the following:

$$\frac{\partial \mathcal{O}^e_{if}}{\partial \boldsymbol{x}} = \boldsymbol{B}^T \frac{\partial \mathcal{O}^e_{if}}{\partial \boldsymbol{s}} \tag{4.40}$$

However, $\boldsymbol{B}$ must be inverted to use Eq.4.40 in order to express $(\partial \mathcal{O}^e_{if}/\partial \boldsymbol{s})$ in terms of $(\partial \mathcal{O}^e_{if}/\partial \boldsymbol{x})$. Following the procedure used in the previous section, this transformation can be safely performed by using the projector operator $\boldsymbol{P} = \boldsymbol{B}^+\boldsymbol{B}$ to remove translational and vibrational contributions from the gradient in Cartesian coordinates, and then applying the pseudo-inverse $\{\boldsymbol{B}^T\}^+$ to get the derivatives with respect to the internal coordinates,

$$\frac{\partial \mathcal{O}^e_{if}}{\partial \boldsymbol{s}} = \{\boldsymbol{B}^T\}^+ \boldsymbol{P}^T \frac{\partial \mathcal{O}^e_{if}}{\partial \boldsymbol{x}} \tag{4.41}$$

The derivatives of the transition dipole moment with respect to the internal coordinates $\boldsymbol{s}$ must then be expressed in terms of curvilinear normal-modes. Since the transformation between $\boldsymbol{s}$ and $\boldsymbol{Q_s}$ is linear, $\boldsymbol{L_s}$ is sufficient to perform this second conversion,

$$\frac{\partial \mathcal{O}^e_{if}}{\partial \boldsymbol{Q_s}} = \boldsymbol{L_s}^T \frac{\partial \mathcal{O}^e_{if}}{\partial \boldsymbol{s'}} = \boldsymbol{L_s}^T \{\boldsymbol{B}^T\}^+ \boldsymbol{P}^T \frac{\partial \mathcal{O}^e_{if}}{\partial \boldsymbol{x}} \tag{4.42}$$

Let us remark that, even if no overbars are specified in Eq. 4.42, both $\boldsymbol{B}$ and $\boldsymbol{L_s}$ must be calculated with respect to the same reference geometry, which can be either the initial- or the final-state equilibrium geometries, depending on the vibronic model which is used. Even if, for adiabatic models, the previous relation can be further simplified using the same strategy as for Eq. 4.24, Eq. 4.42 will be preferred in order to make the theoretical derivation as general as possible.

As discussed for the Cartesian case, for emission spectroscopies, the derivatives of the transition dipole moment must be converted from $\overline{\boldsymbol{Q}}_{\boldsymbol{s}}$ to $\overline{\overline{\boldsymbol{Q}}}_{\boldsymbol{s}}$. This step requires the generalization of the procedure presented for the Cartesian case to internal coordinates.

To do so, we will derive both the general transformation of the transition dipole moment derivatives from $\overline{\boldsymbol{Q}}_{\boldsymbol{s}}$ to $\overline{\overline{\boldsymbol{Q}}}_{\boldsymbol{s}}$ and the inverse transformation, from $\overline{\overline{\boldsymbol{Q}}}_{\boldsymbol{s}}$ to $\overline{\boldsymbol{Q}}_{\boldsymbol{s}}$. By assuming that the HT approximation is exact, the following relation holds:

$$\mathcal{O}^e_{if}\left(\overline{\boldsymbol{Q}}^{\mathrm{eq}}_{\boldsymbol{s}}\right) + \sum_{k=1}^{N_{\mathrm{vib}}} \left(\frac{\partial \mathcal{O}^e_{if}}{\partial \overline{Q}_{\boldsymbol{s},k}}\right)_{\mathrm{eq}} \overline{Q}_{\boldsymbol{s},k} = \mathcal{O}^e_{if}\left(\overline{\overline{\boldsymbol{Q}}}^{\mathrm{eq}}_{\boldsymbol{s}}\right) + \sum_{k=1}^{N_{\mathrm{vib}}} \left(\frac{\partial \mathcal{O}^e_{if}}{\partial \overline{\overline{Q}}_{\boldsymbol{s},k}}\right) \overline{\overline{Q}}_{\boldsymbol{s},k} \tag{4.43}$$

Using the Duschinsky transformation in Eq. 4.9 and the definitions in Eq. 4.23, $\overline{\overline{\boldsymbol{Q}}}_{\boldsymbol{s}}$ can be directly expressed in terms of $\overline{\boldsymbol{Q}}_{\boldsymbol{s}}$ and so the transition moments

in the state of choice, here the final state. Then, by equivalence of the zeroth- and first-order terms of the expansions in the lhs and rhs of Eq. 4.43, the following relations can be derived;

$$\begin{aligned} \mathcal{O}^e_{if}\left(\overline{\overline{\boldsymbol{Q}}}^{\mathrm{eq}}_{\boldsymbol{s}}\right) &= \mathcal{O}^e_{if}\left(\overline{\boldsymbol{Q}}^{\mathrm{eq}}_{\boldsymbol{s}}\right) + \sum_{k=1}^{N_{\mathrm{vib}}} \left(\frac{\partial \mathcal{O}^e_{if}}{\partial \overline{\overline{Q}}_{\boldsymbol{s},j}}\right)_{\mathrm{eq}} K_k \\ \left(\frac{\partial \mathcal{O}^e_{if}}{\partial \overline{\overline{Q}}_{\boldsymbol{s},k}}\right) &= \sum_{l=1}^{N_{\mathrm{vib}}} \left(\boldsymbol{J}_{\boldsymbol{s}}\right)_{kl} \left(\frac{\partial \mathcal{O}^e_{if}}{\partial \overline{Q}_{\boldsymbol{s},l}}\right) \end{aligned} \tag{4.44}$$

On the other hand, if the derivatives expressed in terms of the coordinates $\overline{\overline{\mathbf{Q}}}_{\boldsymbol{s}}$ must be expressed in terms of the normal coordinates of the initial state, Eq. 4.29 must be used instead,

$$\begin{aligned} \mathcal{O}^e_{if}\left(\overline{\boldsymbol{Q}}^{\mathrm{eq}}_{\boldsymbol{s}}\right) &= \mathcal{O}^e_{if}\left(\overline{\overline{\boldsymbol{Q}}}^{\mathrm{eq}}_{\boldsymbol{s}}\right) - \sum_{k=1}^{N_{\mathrm{vib}}} \left(\frac{\partial \mathcal{O}^e_{if}}{\partial \overline{\overline{Q}}_{\boldsymbol{s},k}}\right)_{\mathrm{eq}} \left(\boldsymbol{J}_{\boldsymbol{s}}{}^{-1}\, \boldsymbol{K}_{\boldsymbol{s}}\right)_k \\ \left(\frac{\partial \mathcal{O}^e_{if}}{\partial \overline{Q}_{\boldsymbol{s},k}}\right) &= \sum_{l=1}^{N_{\mathrm{vib}}} \left(\boldsymbol{J}_{\boldsymbol{s}}^{-1}\right)_{kl} \left(\frac{\partial \mathcal{O}^e_{if}}{\partial \overline{\overline{Q}}_{\boldsymbol{s},l}}\right)_{\mathrm{eq}} \end{aligned} \tag{4.45}$$

4.3 Sum-over-states formulation

The theoretical framework introduced in the previous section allows to compute the transition probability between vibrational levels through Eq. 2.10. If the expansion of $\mathcal{O}^e_{if}$ given in Eq. 4.17 is employed, Eq. 4.3 can be rewritten as,

$$\begin{aligned} \langle\, \overline{\psi} \mid \mathcal{O}^e_{if} \mid \overline{\overline{\psi}}\, \rangle &= \mathcal{O}^e\left(\boldsymbol{Q}^{\mathrm{eq}}\right) \langle\, \overline{\overline{\psi}} \mid \overline{\psi}\, \rangle \\ &+ \sum_{k=1}^{N_{\mathrm{vib}}} \left(\frac{\partial \mathcal{O}^e_{if}}{\partial Q_k}\right)_{\mathrm{eq}} \langle\, \overline{\overline{\psi}} \mid \mathcal{Q}_i \mid \overline{\psi}\, \rangle \\ &+ \frac{1}{2} \sum_{k,l=1}^{N_{\mathrm{vib}}} \left(\frac{\partial^2 \mathcal{O}^e_{if}}{\partial Q_k \partial Q_l}\right)_{\mathrm{eq}} \langle\, \overline{\overline{\psi}} \mid \mathcal{Q}_i \mathcal{Q}_j \mid \overline{\psi}\, \rangle \end{aligned} \tag{4.46}$$

Thus, within the FC approximation, the calculation of transition properties requires the calculation of overlap integrals between vibrational wavefunctions $\langle\, \overline{\overline{\psi}} \mid \overline{\psi}\, \rangle$, also known as FC integrals. As a matter of fact, the expectation values of the product of position operators $\mathcal{Q}_k$ can be recast in terms of FC integrals, using the SQ expression for $\mathcal{Q}_k$ given in Eq. 2.26. For example, the first-order term can be expressed as follows:

$$\langle\, \overline{\overline{\psi}} \mid \mathcal{Q}_i \mid \overline{\psi}\, \rangle = \sqrt{\frac{\hbar}{2\omega_k}} \left[\langle\, \overline{\overline{\psi}} \mid \hat{b}^+_k \mid \overline{\psi}\, \rangle + \langle\, \overline{\overline{\psi}} \mid \hat{b}_k \mid \overline{\psi}\, \rangle \right] \tag{4.47}$$

where the quantities appearing in the rhs of the previous equation are FC integrals, where the occupation numbers of the k-th mode of one vibrational

wavefunction are increased (for the first term) and decreased (for the second term) by 1. At the harmonic level, analytical expressions for the FC integrals can be derived, by employing the properties of the Hermite polynomials.[277,278] Such approaches, where the FC integrals are computed directly from those expressions are referred to as analytical approaches. The main disadvantage of those methods is that their use is not practical for a general implementation, since a different expression need to be implemented for each class of integrals. This issue can be overcome by using recursion formulas instead. In practice, only the FC integral involving the vibrational ground states ($\langle \overline{\overline{\mathbf{0}}} \mid \overline{\mathbf{0}} \rangle$) is computed explicitly, and all the other integrals are derived from this one. In the most general case, only 2 formulas are needed for this task, depending if the recursion relation must be adapted with respect to the initial or final states. If temperature effects are ignored, then only the latter is relevant,[266,267,279]

$$\begin{aligned}\langle \overline{\mathbf{0}} \mid \overline{\overline{\boldsymbol{v}}} \rangle = &\frac{1}{\sqrt{2\overline{\overline{v}}_i}} \Big[D_i \langle \overline{\mathbf{0}} \mid \overline{\overline{\boldsymbol{v}}} - \overline{\overline{\mathbf{1}}}_i \rangle + 2\sqrt{\overline{\overline{v}}_i - 1} C_{ii} \langle \overline{\mathbf{0}} \mid \overline{\overline{\boldsymbol{v}}} - \overline{\overline{\mathbf{2}}}_i \rangle \\ &+ \sum_{j \neq i}^{N_{\text{vib}}} \sqrt{2\overline{\overline{v}}_j}\, C_{ij} \langle \overline{\mathbf{0}} \mid \overline{\overline{\boldsymbol{v}}} - \overline{\overline{\mathbf{1}}}_i - \overline{\overline{\mathbf{1}}}_j \rangle \Big]\end{aligned} \tag{4.48}$$

where the vibrational levels, previously indicated as $\overline{\psi}$ and $\overline{\overline{\psi}}$, have been represented here as ONVs $\overline{\boldsymbol{v}}$ and $\overline{\overline{\boldsymbol{v}}}$. The Sharp and Rosenstock matrices $\boldsymbol{C}$ and $\boldsymbol{D}$ are defined as,[277]

$$\begin{aligned}\boldsymbol{C} &= 2\overline{\overline{\boldsymbol{\Gamma}}}^{1/2} \left(\boldsymbol{J}^T \overline{\boldsymbol{\Gamma}} \boldsymbol{J} + \overline{\overline{\boldsymbol{\Gamma}}} \right)^{-1} \overline{\overline{\boldsymbol{\Gamma}}}^{1/2} - \boldsymbol{I} \\ \boldsymbol{D} &= \overline{\overline{\boldsymbol{\Gamma}}}^{1/2} \left(\boldsymbol{J}^T \overline{\boldsymbol{\Gamma}} \boldsymbol{J} + \overline{\overline{\boldsymbol{\Gamma}}} \right)^{-1} \boldsymbol{J}^T \overline{\boldsymbol{\Gamma}} \boldsymbol{K}\end{aligned} \tag{4.49}$$

where $\overline{\boldsymbol{\Gamma}}$ and $\overline{\overline{\boldsymbol{\Gamma}}}$ are diagonal matrices containing the reduced frequencies of the initial and the final state, respectively. By applying recursively Eq. 4.48, it is straightforward to show that only the overlap integral between the vibrational ground states $\langle \overline{\mathbf{0}} \mid \overline{\overline{\mathbf{0}}} \rangle$ needs to be known analytically. From there, and considering only the FC case for the sake of simplicity, one can see that vibrational progressions (overtones) will be determined from D_i and the diagonal elements of $\boldsymbol{C}$, while the intensity of combination bands will depend on the off-diagonal elements C_{ij}. Thus, for combination bands to give a significant contribution to the band-shape, the elements C_{ij} must have significant magnitude. For this reason, in the following, the $\boldsymbol{C}$ matrix will also be used to visualize the impact of the mixing on transition intensities, how this impact the band-shape and the difference a change of coordinate systems can bring to this mixing. The $\boldsymbol{C}$ matrix is better suited than $\boldsymbol{J}$ as analysis tool for two reasons. Indeed, in absence of mode-mixing effects, $\boldsymbol{J}$ is equal to $\boldsymbol{I}$, whereas $\boldsymbol{C}$ is null (as can be easily seen from Eq. 4.49 by setting $\boldsymbol{J} = \boldsymbol{I}$). Second, unlike $\boldsymbol{J}$, the elements of $\boldsymbol{C}$ directly give access to the strength of the coupling.
Similarly, $\boldsymbol{D}$ also gives a better idea about the impact of the shift on the vibrational progression, that is to say the relative intensity of the fundamental

and overtones with respect to the number of quanta. This can be easily seen in the special case where the PESs are equal (thus in the AS and VG models). Within those models, the recursion formulas given in Eq 4.48 can be simplified as follows,

$$\begin{aligned} \langle \overline{\mathbf{0}} \mid \overline{\overline{v}} \rangle &= \frac{1}{\sqrt{2\overline{\overline{v}}_i}} D_i \langle \overline{\mathbf{0}} \mid \overline{\overline{v}} - 1_i \rangle \\ &= \frac{1}{\sqrt{\overline{\overline{v}}_i!}} \left(\frac{D_i}{\sqrt{2}} \right)^n \langle \overline{\mathbf{0}} \mid \overline{\overline{\mathbf{0}}} \rangle \end{aligned} \tag{4.50}$$

with $\boldsymbol{D} = -\overline{\boldsymbol{\Gamma}}^{1/2}\boldsymbol{K}/2$ and n the overall number of quanta of the i-th mode in the $|\,\overline{\overline{v}}\,\rangle$ state. Eq. 4.50, shows that the intensity of the vibrational progression involving the i-th mode, in the limit of large quantum number $\overline{\overline{v}}_i$ decays with the exponential of the i-th element of the $\boldsymbol{D}$ vector. Thus, large-components of $\boldsymbol{D}$ are associated to modes giving a large contribution to the overall spectrum.

Starting from the FGR with the definition of the transition moment of the properties introduced above, it is possible to compute the transition probability p_{if}, which is a microscopic molecular property. To compare theoretical results to their experimental data, p_{if} must be related to a macroscopic quantities. For OPA spectroscopy the quantity usually measured is the molar absorption coefficient $\epsilon(\omega)$, which is proportional to the absorption cross section $\sigma(\omega)$. The latter quantity is obtained summing the cross section σ_{if} of each possible transition. In presence of temperature effects, each initial state i must be weighted by its Boltzmann population. σ_{if} is in turn proportional to the probability of transition p_{if}, and therefore the final relation is given by,

$$\epsilon(\omega) = \frac{4\pi^2 \omega N_a}{3 \times 10^3 \ln(10)\, \hbar c Z} \sum_{i,f} e^{-\beta E_i} \left| \langle\, \overline{\overline{\psi}}_f \mid \boldsymbol{\mu}^e_{if} \mid \overline{\psi}_i \,\rangle \right|^2 \delta\left(\left|\omega_{if}\right| - \omega \right) \tag{4.51}$$

where N_a is the Avogadro number and Z is the canonical partition function. E_i is the vibrational energy of the initial state i, $\omega_{if} = \omega_f - \omega_i$ and $\beta = 1/k_{\mathrm{B}}T$, where k_{B} is the Boltzmann constant. Eq. 4.51, usually referred to as sum-over-states (SOS) expression, can be combined with the recursive or analytical methods described above to compute the FC integrals to obtain the overall vibronic spectrum once the property has been expanded to the desired order. Approaches based on those schemes are usually referred to as time-independent (TI) approaches. Their main problem is that Eq. 4.51 involves infinite summations, that must be truncated in some way. In order to make TI approaches feasible in practice, they must be coupled with some prescreening schemes, to select *a priori* the most relevant vibronic transitions. In this thesis, we use a *class*-based prescreening scheme, in which the transitions are divided in so-called *classes*, depending on the number of simultaneously excited modes in the final state.[266,280] So, *class* 1 (C_1) corresponds to fundamentals and overtones, C_2 to 2-modes combinations and so on. Within the

prescreening system, the FC overlaps belonging to classes C_1 and C_2 are computed up to a set maximum number of quanta (C_1^{max} and C_2^{max}, respectively) using the analytical or recursive formulas already introduced above. Data related to the probability and intensity of each transition are stored to build an internal database, which is used to estimate the probability of transitions to states belonging to the other, higher classes. Such an approach is very efficient for semi-rigid systems, characterized by a limited flexibility. However, it loses it efficiency for flexible systems, when mode-mixing effects are strong. Moreover, it is often less reliable when the transition probability and intensity are not directly related, such as for chiroptical spectroscopies.
The SOS expression given in Eq. 4.51 holds for one-photon absorption spectroscopy. However, it can be easily generalized to other kinds of spectroscopy and processes. For example, let us consider the case of emission spectroscopy. When a molecular system is excited by an electromagnetic wave, two different emission processes can occur, i.e. spontaneous and stimulated emission. In the UV region, stimulated emission processes are negligible with respect to spontaneous ones, and thus can be safely neglected. Following the Einstein model of light absorption, the rate of spontaneous emission, (A_{if}) can be expressed in terms of the rate of stimulated emission (B_{if}), through the following equations,

$$A_{mn} = \frac{2\hbar\omega^3}{\pi c^3} B_{mn} \tag{4.52}$$

This link between absorption and emission rates can be used to derive the following sum-over-states formula of the intensity of the emitted light I_{em} starting from the expression given in Eq. 4.51

$$I_{\text{em}}(\omega) = \frac{8\pi\omega^4}{3c^3 Z} \sum_{i,f} e^{-\beta E_i} \left| \langle\, \overline{\overline{\psi}}_f \mid \boldsymbol{\mu}^e_{if} \mid \overline{\psi}_i \,\rangle \right|^2 \delta\left(|\omega_{nm}| - \omega\right) \tag{4.53}$$

The previous framework can support chiroptical spectroscopies as well. In ECD spectroscopy, the experimentally recorded quantity is the difference of the molar extinction coefficient obtained with left-circularly and right-circularly polarized lights $\Delta\epsilon = \epsilon_l - \epsilon_r$. This quantity is proportional to the rotatory strength of the transitions, defined as the scalar product between the electric and magnetic transition dipole moments $\Im\left(\boldsymbol{\mu}_{if} \cdot \boldsymbol{m}_{fi}\right)$.[281] Starting from this relation and using the same strategy employed for OPA, it is possible to derive the following sum-over-states formula,

$$\begin{aligned} \Delta\epsilon(\omega) = \frac{16 N_a \pi^2 \omega}{3 \cdot 10^3 \ln(10)\hbar c} \sum_{i,f} & e^{-\beta E_i} \delta\left(|\omega_{nm}| - \omega\right) \\ & \times \Im\left(\langle\, \overline{\psi}_i \mid \boldsymbol{\mu}^e \mid \overline{\overline{\psi}}_f \,\rangle \cdot \langle\, \overline{\overline{\psi}}_f \mid \boldsymbol{m}^e \mid \overline{\psi}_i \,\rangle \right) \end{aligned} \tag{4.54}$$

where $\boldsymbol{m}^e_{if}$ is the electric component of the electronic transition magnetic dipole moment. Let us remark that Eq. 4.54 has the same form as equation 4.51, but the rotatory strength must be used in place of the dipole strength.

An additional type of spectroscopy that can be supported within the previous framework, is circularly polarized luminescence (CPL). In CPL spectroscopy, the sample is irradiated with a non-polarized light and the difference between the number of emitted photon with left-handed and right-handed polarization is measured. The extension of the SOS formula for ECD, given in Eq. 4.54 to its emission counterpart is not as straightforward as for the OPA case, since the Einstein model holds only for the absorption case. However, as proved by Emeis and co-workers proved in Refs. 282,283, and later confirmed by Riehl and Richardson in Refs. 48,284, ECD and CPL cross sections are both proportional to the rotatory strength, similarly to OPA and OPE spectroscopies. The difference between the intensities of emitted light ΔI_{em} can be related to the rotatory strength through the following equation,

$$\Delta I_{\text{em}} = \frac{8\pi\omega^4}{3\epsilon_0 c^4} \Im\left(\boldsymbol{\mu}_{if} \cdot \mathbf{m}_{if}\right) \tag{4.55}$$

At first glance, the support of those spectroscopy seems to require the implementation of 4 different equations. However, it is possible to gather them in a unique framework by adopting a general sum-over-state formula[268,285]:

$$I = \alpha\omega^{\beta} \sum_i \sum_f \rho_i \boldsymbol{P}_{if}^{\text{A},e} \boldsymbol{P}_{if}^{\text{B},e*} \delta\left(\frac{\left|\overline{\overline{E}}_f - \overline{E}_i\right|}{\hbar} - \omega\right) \tag{4.56}$$

where ω is the frequency of the incident (OPA, ECD) or emitted (OPE,CPL) photon, ρ is the Boltzmann population. The parameters I, α, β, $\boldsymbol{P}_{if}^{\text{A},e}$ and $\boldsymbol{P}_{if}^{\text{B},e}$ depend on the kind of spectroscopy, following the equivalency given in Table 4.1.

	OPA	OPE	ECD	CPL
I	$\epsilon(\omega)$	I_{em}	$\Delta\epsilon(\omega)$	ΔI_{em}
α	$\frac{10\pi N_a}{3\epsilon_0 \ln(10)\hbar c}$	$\frac{2}{3\epsilon_0 c^3}$	$\frac{40\pi N_a}{3\epsilon_0 \ln(10)\hbar c^2}$	$\frac{8N_a}{3\epsilon_0 c^4}$
β	1	4	1	4
$\boldsymbol{P}_{if}^{\text{A},e}$	$\boldsymbol{\mu}_{if}$	$\boldsymbol{\mu}_{if}$	$\boldsymbol{\mu}_{if}$	$\boldsymbol{\mu}_{if}$
$\boldsymbol{P}_{if}^{\text{A},e}$	$\boldsymbol{\mu}_{if}$	$\boldsymbol{\mu}_{if}$	$\Im\left(\mathbf{m}_{if}\right)$	$\Im\left(\mathbf{m}_{if}\right)$

TABLE 4.1: Equivalence table defining the parameters appearing in Eq. 4.56 for each kind of spectroscopy.

4.4 General time-dependent framework

The time-dependent (TD) approach of molecular spectroscopy has been introduced in the pioneering works of Heller and co-workers[89] as a way to compute spectra without explicitly computing the eigenstates of the molecular Hamiltonian. This is done, in practice, by expressing the spectra in the

time domain instead of the frequency domain as for the SOS formulation. In TD approaches, the spectra are obtained as Fourier transforms of appropriate autocorrelation or cross-correlation functions. The calculation of those functions requires the simulation of the time-evolution of the molecular wavefunction. The TD models which have been proposed in the literature can be classified based on the way in which this time-evolution is simulated.
One way of simulating the time-evolution of the vibrational wavefunction is are so-called semiclassical methods. Within this class of approaches, the vibrational wavefunction is approximated as a multidimensional Gaussian function, whose center and width evolve under classical laws of motion. The advantage of using a Gaussian function to represent the molecular wavefunction is that it is exact in the limit of low temperatures and its evolution is analytic for harmonic potentials. Thanks to this property, analytical formulae for the transition dipole moment autocorrelation function can be derived by assuming that only the short-time evolution contributes to the overall spectrum (within the so-called short-time propagation methods).[286,287]
The limitations of semiclassical models can be overcome with the Green function formalism, which allows to derive an analytic expression for the dipole moment autocorrelation function for the time evolution of the ground-state wavefunction of an harmonic oscillator over an harmonic PES.[90,288] The flexibility of this formalism allows an easy inclusion of temperature effects, without any additional computational cost.[91,289] The same framework can be easily extended also to the computation of rates of non-radiative decay processes,[87,290] as well as to the simulation of vibronic phosphorescence spectra.[291,292] However, all those approaches are limited to the FC approximation, and the extension to HT terms has been discussed only over the last years.[293]

4.4.1 Franck-Condon formulation

Let us begin with the description of the TD formalism applied to one-photon spectroscopies. For the sake of simplicity, we will restrict our analysis to absorption spectroscopy. The subscript indicating the electronic states involved in the transition will be dropped from the symbol of the transition dipole moment, so only the superscript e will remain.
The mathematical property which allows to switch from the sum-over-states problem to a time-dependent picture is the following definition of the Dirac distribution function,

$$\delta(\omega) = \frac{1}{2\pi} \int_{-\infty}^{+\infty} e^{i\omega t}\, dt \tag{4.57}$$

By replacing the Dirac delta function in Eq. 4.56 with the previous expression we obtain:

$$I = \frac{\alpha\omega^{\beta}}{Z}\sum_{i,f} e^{-\beta\overline{E}_i}\langle\,\overline{\psi}_i \mid \boldsymbol{P}^{\mathrm{A},e} \mid \overline{\overline{\psi}}_f\,\rangle\langle\,\overline{\overline{\psi}}_f \mid \{\boldsymbol{P}^{\mathrm{B},e}\}^{*} \mid \overline{\psi}_i\,\rangle \int_{-\infty}^{+\infty} e^{i\left[\frac{\left|\breve{\overline{E}}_f-\breve{E}_i\right|+E_{\mathrm{ad}}}{\hbar}-\omega\right]t} dt \tag{4.58}$$

where $\breve{E}_i$ and $\breve{\overline{E}}_f$ are the energies of the initial and the final vibrational states, respectively. The canonical vibrational partition function Z can be expressed, at the harmonic level, as,

$$Z = \prod_{i=1}^{N_{\mathrm{vib}}}\sum_{n_i=1}^{+\infty} e^{-\hbar\beta\overline{\omega}_i\left(v_i+\frac{1}{2}\right)} = \prod_{i=1}^{N_{\mathrm{vib}}}\left[2\sinh\left(\frac{\hbar\overline{\omega}_i}{2k_BT}\right)\right]^{-1} \tag{4.59}$$

Since Z is a constant, we can integrate it in α and will use from now on the constant factor $\alpha' = \alpha/Z$. Let us define the vibrational Hamiltonian of the ground and excited state as $\overline{\mathcal{H}}$ and $\overline{\overline{\mathcal{H}}}$, and their respective time-evolution operators $e^{-i\overline{\mathcal{H}}t/\hbar}$ and $e^{-i\overline{\overline{\mathcal{H}}}t/\hbar}$. From the definition of $\overline{E}_m$ and $\overline{\overline{E}}_n$ as eigenvalues of $\overline{\mathcal{H}}$ and $\overline{\overline{\mathcal{H}}}$ respectively, Eq. 4.58 can be rewritten as,

$$I = \alpha'\omega^{\beta}\int_{-\infty}^{+\infty} dt \sum_{i,f}\langle\,\overline{\psi}_i \mid \boldsymbol{P}^{\mathrm{A},e}e^{-\overline{\tau}\,\overline{\overline{\mathcal{H}}}} \mid \overline{\overline{\psi}}_f\,\rangle\langle\,\overline{\overline{\psi}}_f \mid \{\boldsymbol{P}^{\mathrm{B},e}\}^{*}e^{-\overline{\tau}\,\overline{\mathcal{H}}} \mid \overline{\psi}_i\,\rangle e^{i(E_{\mathrm{ad}}-\omega)t} \tag{4.60}$$

where $\overline{\tau}$ and $\overline{\overline{\tau}}$ are defined as,

$$\overline{\tau} = \frac{1}{k_BT} - \frac{it}{\hbar} \quad ; \quad \overline{\overline{\tau}} = \frac{it}{\hbar} \tag{4.61}$$

We note that $\overline{\overline{\tau}}$ is proportional to time t and is purely imaginary, whereas $\overline{\tau}$ has a also a real component, which allows to include temperature effects in the time-evolution operator. By using the closure relation for the $\mid\overline{\overline{\psi}}_f\,\rangle$ basis set,

$$\sum_{f=1}^{+\infty} \mid\overline{\overline{\psi}}_f\,\rangle\langle\,\overline{\overline{\psi}}_f \mid = \boldsymbol{I}$$

Eq. 4.60 becomes,

$$\begin{aligned} I &= \alpha'\omega^{\beta}\int_{-\infty}^{+\infty} dt \sum_{i=1}^{+\infty}\langle\,\overline{\psi}_i \mid \boldsymbol{P}^{\mathrm{A},e}e^{-\overline{\tau}\,\overline{\overline{\mathcal{H}}}}\{\boldsymbol{P}^{\mathrm{B},e}\}^{*}e^{-\overline{\tau}\,\overline{\mathcal{H}}} \mid \overline{\psi}_i\,\rangle e^{i(\omega_{\mathrm{ad}}-\omega)t} \\ &= \alpha'\omega^{\beta}\int_{-\infty}^{+\infty} dt\ \mathrm{Tr}\left(\boldsymbol{P}^{\mathrm{A},e}e^{-\overline{\tau}\,\overline{\overline{\mathcal{H}}}}\{\boldsymbol{P}^{\mathrm{B},e}\}^{*}e^{-\overline{\tau}\,\overline{\mathcal{H}}}\right)e^{i(\omega_{\mathrm{ad}}-\omega)t} \\ &= \alpha'\omega^{\beta}\int_{-\infty}^{+\infty} dt\,\chi_{\mathrm{full}}(t)\,e^{i(\omega_{\mathrm{ad}}-\omega)t} \end{aligned} \tag{4.62}$$

where, in going from the first to the second equality in the previous equation, the completeness of the basis $|\,\overline{\psi}_i\,\rangle$ has been employed to write the sum of a trace. The second equality introduces the definition of the transition dipole moment autocorrelation function $\chi_{\text{full}}(t)$.
The trace of an operator is the same irrespective of the basis set chosen, and therefore the autocorrelation function $\chi(t)$ can be expressed in terms of the continuous basis set formed by the normal coordinates of the initial state $\overline{\boldsymbol{Q}}$;

$$\chi_{\text{full}}(t) = \int_{-\infty}^{+\infty} d\overline{\boldsymbol{Q}} \langle\, \overline{\boldsymbol{Q}} \,|\, \boldsymbol{P}^{\text{A},e} e^{-\overline{\overline{\tau}}\,\overline{\overline{\mathcal{H}}}} \{\boldsymbol{P}^{\text{B},e}\}^{+} e^{-\overline{\tau}\,\overline{\mathcal{H}}} \,|\, \overline{\boldsymbol{Q}} \,\rangle \tag{4.63}$$

The main advantage of Eq. 4.63 over the previous formulation is that the definition of the vibrational Hamiltonian in the position operator given in Eq. 2.21, makes easier the derivation of a closed form for the autocorrelation function. In order to derive an analytical expression for $\chi_{\text{full}}(t)$, it is however necessary to express also the transition properties as a function of the normal modes. By using the expansion given in Eq. 4.17 and keeping, for the sake of simplicity, terms up to the first-order, the following relation is obtained:

$$\begin{aligned}
\chi_{\text{full}}(t) =& \boldsymbol{P}^{\text{A},e}\left(\overline{\overline{\boldsymbol{Q}}}_{eq}\right) \{\boldsymbol{P}^{\text{B},e}\}^{\star}\left(\overline{\overline{\boldsymbol{Q}}}_{eq}\right) \int_{-\infty}^{+\infty} d\overline{\boldsymbol{Q}} \langle\, \overline{\boldsymbol{Q}} \,|\, e^{-\overline{\overline{\tau}}\,\overline{\overline{\mathcal{H}}}} e^{-\overline{\tau}\,\overline{\mathcal{H}}} \,|\, \overline{\boldsymbol{Q}} \,\rangle \\
&+ \sum_{k=1}^{N_{\text{vib}}} \left(\frac{\partial \boldsymbol{P}^{\text{A},e}}{\partial \overline{\overline{Q}}_k}\right)_{\text{eq}} \{\boldsymbol{P}^{\text{B},e}\}^{\star}\left(\overline{\overline{\boldsymbol{Q}}}_{eq}\right) \int_{-\infty}^{+\infty} d\overline{\boldsymbol{Q}} \langle\, \overline{\boldsymbol{Q}} \,|\, \overline{\overline{Q}}_k e^{-\overline{\overline{\tau}}\,\overline{\overline{\mathcal{H}}}} e^{-\overline{\tau}\,\overline{\mathcal{H}}} \,|\, \overline{\boldsymbol{Q}} \,\rangle \\
&+ \sum_{k=1}^{N_{\text{vib}}} \left(\frac{\partial \{\boldsymbol{P}^{\text{B},e}\}^{\star}}{\partial \overline{\overline{Q}}_k}\right)_{\text{eq}} \boldsymbol{P}^{\text{A},e}\left(\overline{\overline{\boldsymbol{Q}}}_{eq}\right) \int_{-\infty}^{+\infty} d\overline{\boldsymbol{Q}} \langle\, \overline{\boldsymbol{Q}} \,|\, e^{-\overline{\overline{\tau}}\,\overline{\overline{\mathcal{H}}}} \overline{\overline{Q}}_k e^{-\overline{\tau}\,\overline{\mathcal{H}}} \,|\, \overline{\boldsymbol{Q}} \,\rangle \\
&+ \sum_{k,l=1}^{N_{\text{vib}}} \left(\frac{\partial \boldsymbol{P}^{\text{A},e}}{\partial \overline{\overline{Q}}_k}\right)_{\text{eq}} \left(\frac{\partial \{\boldsymbol{P}^{\text{B},e}\}^{\star}}{\partial \overline{\overline{Q}}_l}\right)_{\text{eq}} \int_{-\infty}^{+\infty} d\overline{\boldsymbol{Q}} \langle\, \overline{\boldsymbol{Q}} \,|\, \overline{\overline{Q}}_k e^{-\overline{\overline{\tau}}\,\overline{\overline{\mathcal{H}}}} \overline{\overline{Q}}_l e^{-\overline{\tau}\,\overline{\mathcal{H}}} \,|\, \overline{\boldsymbol{Q}} \,\rangle
\end{aligned} \tag{4.64}$$

where $\overline{\overline{Q}}_k$ is the operator associated to the k-th final-state normal coordinate, with eigenvalue $\overline{\overline{Q}}_k$. From Eq. 4.64, it is clear that the evaluation of the transition dipole moment autocorrelation function will follow the calculation of one or more correlation functions, which may contain position operators. To make thediscussion more clear, we collect those quantities as elements of a matrix as,

$$\begin{aligned}
\chi(t) &= \int_{-\infty}^{+\infty} d\overline{\boldsymbol{Q}} \langle\, \overline{\boldsymbol{Q}} \,|\, e^{-i\overline{\overline{\mathcal{H}}}\overline{\overline{\tau}}} e^{-i\overline{\mathcal{H}}\overline{\tau}} \,|\, \overline{\boldsymbol{Q}} \,\rangle \\
\chi^{l}(t) &= \int_{-\infty}^{+\infty} d\overline{\boldsymbol{Q}} \langle\, \overline{\boldsymbol{Q}} \,|\, e^{-i\overline{\overline{\mathcal{H}}}\overline{\overline{\tau}}} \overline{\overline{Q}}_l e^{-i\overline{\mathcal{H}}\overline{\tau}} \,|\, \overline{\boldsymbol{Q}} \,\rangle \\
\chi_{l}(t) &= \int_{-\infty}^{+\infty} d\overline{\boldsymbol{Q}} \langle\, \overline{\boldsymbol{Q}} \,|\, \overline{\overline{Q}}_l e^{-i\overline{\overline{\mathcal{H}}}\overline{\overline{\tau}}} e^{-i\overline{\mathcal{H}}\overline{\tau}} \,|\, \overline{\boldsymbol{Q}} \,\rangle \\
\chi_{l}^{j}(t) &= \int_{-\infty}^{+\infty} d\overline{\boldsymbol{Q}} \langle\, \overline{\boldsymbol{Q}} \,|\, e^{-i\overline{\overline{\mathcal{H}}}\overline{\overline{\tau}}} \overline{\overline{Q}}_l e^{-i\overline{\mathcal{H}}\overline{\tau}} \overline{\overline{Q}}_j \,|\, \overline{\boldsymbol{Q}} \,\rangle
\end{aligned} \tag{4.65}$$

and, more in general,

$$\chi_{ijk\ldots}^{lmn\ldots}(t) = \int_{-\infty}^{+\infty} d\overline{\boldsymbol{Q}} \langle\, \overline{\boldsymbol{Q}} \mid \overline{\overline{\mathcal{Q}}}_i \overline{\overline{\mathcal{Q}}}_j \overline{\overline{\mathcal{Q}}}_k \ldots e^{-i\overline{\overline{\mathcal{H}}}\overline{\tau}} \overline{\overline{\mathcal{Q}}}_l \overline{\overline{\mathcal{Q}}}_m \overline{\overline{\mathcal{Q}}}_n \ldots e^{-i\overline{\mathcal{H}}\overline{\tau}} \mid \overline{\boldsymbol{Q}} \,\rangle \quad (4.66)$$

Thus, the general cross-correlation function $\chi_{ijk\ldots}^{lmn\ldots}(t)$ is defined by two sets of indexes, the lower one $(ijk\ldots)$, corresponding to position operators multiplying the time-evolution operator on the left, and the upper one $(lmn\ldots)$, corresponding to position operators multiplying it from right. Under the Franck-Condon approximation, only one term, $\chi(t)$, needs to be computed. However, when HT and higher-order terms are included in the sum, other tensors $\chi_{ijk\ldots}^{lmn\ldots}(t)$ appear.

The FC autocorrelation function $\chi(t)$ can be calculated by following the derivation presented by Pollack and co-workers.[91] Starting from Eq. 4.64, we introduce an additional set of orthonormal coordinates for the initial state $\overline{\boldsymbol{Q}}'$ and two for the final state $\overline{\overline{\boldsymbol{Q}}}$ and $\overline{\overline{\boldsymbol{Q}}}'$. All those sets correspond to complete base, thus satisfy the closure relation,

$$\int_{-\infty}^{+\infty} d\overline{\boldsymbol{Q}}' |\, \overline{\boldsymbol{Q}}' \,\rangle\langle\, \overline{\boldsymbol{Q}}' \,| = \int_{-\infty}^{+\infty} d\overline{\overline{\boldsymbol{Q}}} |\, \overline{\overline{\boldsymbol{Q}}} \,\rangle\langle\, \overline{\overline{\boldsymbol{Q}}} \,| = \int_{-\infty}^{+\infty} d\overline{\overline{\boldsymbol{Q}}}' |\, \overline{\overline{\boldsymbol{Q}}}' \,\rangle\langle\, \overline{\overline{\boldsymbol{Q}}}' \,| = \boldsymbol{I} \quad (4.67)$$

By using the closure relation given above, Eq. 4.63 can be rewritten as,

$$\begin{aligned} \chi(t) = \int_{-\infty}^{+\infty} d\overline{\boldsymbol{Q}} \int_{-\infty}^{+\infty} d\overline{\overline{\boldsymbol{Q}}} \int_{-\infty}^{+\infty} d\overline{\boldsymbol{Q}}' \int_{-\infty}^{+\infty} d\overline{\overline{\boldsymbol{Q}}}' \langle\, \overline{\boldsymbol{Q}} \mid \overline{\overline{\boldsymbol{Q}}} \,\rangle \\ \times \langle\, \overline{\overline{\boldsymbol{Q}}} \mid e^{-\overline{\overline{\tau}}\,\overline{\overline{\mathcal{H}}}} \mid \overline{\overline{\boldsymbol{Q}}}' \,\rangle\langle\, \overline{\overline{\boldsymbol{Q}}}' \mid \overline{\boldsymbol{Q}}' \,\rangle\langle\, \overline{\boldsymbol{Q}}' \mid e^{-\overline{\tau}\,\overline{\mathcal{H}}} \mid \overline{\boldsymbol{Q}} \,\rangle \end{aligned} \quad (4.68)$$

Overlap integrals between normal modes are easily resolved thanks to the Duschinsky transformation as follows,

$$\int_{-\infty}^{+\infty} d\overline{\boldsymbol{Q}} \,\langle\, \overline{\boldsymbol{Q}} \mid \overline{\overline{\boldsymbol{Q}}} \,\rangle = \int_{-\infty}^{+\infty} d\overline{\boldsymbol{Q}}\, \delta\left(\overline{\boldsymbol{Q}} - \boldsymbol{J}\overline{\overline{\boldsymbol{Q}}} - \boldsymbol{K}\right) \quad (4.69)$$

The evaluation of the matrix elements involving the time-evolution operator is less trivial, but can be carried out within the Feynmann's path integral formulation of quantum mechanics.[294] The final results is the following:

$$\langle\, \overline{\boldsymbol{Q}} \mid e^{-\overline{\mathcal{H}}\overline{\tau}} \mid \overline{\boldsymbol{Q}}' \,\rangle = \sqrt{\frac{\det(\overline{\boldsymbol{a}})}{(2\pi\hbar)^N}} \exp\left(\frac{i}{\hbar}\left[\frac{1}{2}\overline{\boldsymbol{Q}}^{\mathrm{T}}\,\overline{\boldsymbol{b}}\,\overline{\boldsymbol{Q}} + \frac{1}{2}\overline{\boldsymbol{Q}}'^{\mathrm{T}}\,\overline{\boldsymbol{b}}\,\overline{\boldsymbol{Q}}' - \overline{\boldsymbol{Q}}'^{\mathrm{T}}\,\overline{\boldsymbol{a}}\,\overline{\boldsymbol{Q}}\right]\right) \quad (4.70)$$

where the diagonal matrices $\boldsymbol{a}$ and $\boldsymbol{b}$ are defined as,

$$\begin{aligned} \overline{a}_{ij} &= \frac{\overline{\omega}_i}{\sinh\left(\hbar\overline{\tau}\,\overline{\omega}_i\right)}\delta_{ij} & \overline{\overline{a}}_{ij} &= \frac{\overline{\overline{\omega}}_i}{\sinh\left(\hbar\overline{\overline{\tau}}\,\overline{\overline{\omega}}_i\right)}\delta_{ij} \\ \overline{b}_{ij} &= \frac{\overline{\omega}_i}{\tanh\left(\hbar\overline{\tau}\,\overline{\omega}_i\right)}\delta_{ij} & \overline{\overline{b}}_{ij} &= \frac{\overline{\overline{\omega}}_i}{\tanh\left(\hbar\overline{\overline{\tau}}\,\overline{\overline{\omega}}_i\right)}\delta_{ij} \end{aligned} \quad (4.71)$$

The diagonal matrices $\boldsymbol{c}$ and $\boldsymbol{d}$, together with the non-diagonal matrices $\boldsymbol{C}$ and $\boldsymbol{D}$, are introduced here as well for convenience,

$$\begin{aligned} \bar{c}_{ij} &= \frac{\overline{\omega}_i}{\hbar} \coth\left(\frac{\overline{\omega}_i \hbar \overline{\tau}}{2}\right) \delta_{ij} \qquad & \bar{\bar{c}}_{ij} &= \frac{\overline{\overline{\omega}}_i}{\hbar} \coth\left(\frac{\overline{\overline{\omega}}_i \hbar \overline{\overline{\tau}}}{2}\right) \delta_{ij} \\ \bar{d}_{ij} &= \frac{\overline{\omega}_i}{\hbar} \tanh\left(\frac{\overline{\omega}_i \hbar \overline{\tau}}{2}\right) \delta_{ij} \qquad & \bar{\bar{d}}_{ij} &= \frac{\overline{\overline{\omega}}_i}{\hbar} \tanh\left(\frac{\overline{\overline{\omega}}_i \hbar \overline{\overline{\tau}}}{2}\right) \delta_{ij} \end{aligned} \tag{4.72}$$

and,

$$\boldsymbol{C} = \bar{\bar{\boldsymbol{c}}} + \boldsymbol{J}^{\mathrm{T}} \bar{\boldsymbol{c}} \boldsymbol{J} \qquad \boldsymbol{D} = \bar{\bar{\boldsymbol{d}}} + \boldsymbol{J}^{\mathrm{T}} \bar{\boldsymbol{d}} \boldsymbol{J} \tag{4.73}$$

Combining Eqs. 4.70 and 4.68, the integration can be carried out over the initial-state normal modes, leading to the following expression for the auto-correlation function,

$$\begin{aligned} \chi(t) = \sqrt{\frac{\det(\bar{\boldsymbol{a}}\,\bar{\bar{\boldsymbol{a}}})}{(2\pi i\hbar)^{2N}}} \int \mathrm{d}\overline{\overline{\boldsymbol{Q}}} \int \mathrm{d}\overline{\overline{\boldsymbol{Q}}}' \exp\left(\frac{i}{\hbar}\left[\frac{1}{2}\overline{\overline{\boldsymbol{Q}}}^{\mathrm{T}} \bar{\bar{\boldsymbol{b}}}\, \overline{\overline{\boldsymbol{Q}}} + \frac{1}{2}\overline{\overline{\boldsymbol{Q}}}'^{\mathrm{T}} \bar{\bar{\boldsymbol{b}}}\, \overline{\overline{\boldsymbol{Q}}}' - \overline{\overline{\boldsymbol{Q}}}^{\mathrm{T}} \bar{\bar{\boldsymbol{a}}}\, \overline{\overline{\boldsymbol{Q}}}'\right]\right) \\ \times \exp\left\{\frac{i}{\hbar}\left[\frac{1}{2}\left(\boldsymbol{K}^{\mathrm{T}} + \overline{\overline{\boldsymbol{Q}}}'^{\mathrm{T}} \boldsymbol{J}^{\mathrm{T}}\right) \bar{\boldsymbol{b}} \left(\boldsymbol{J}\,\overline{\overline{\boldsymbol{Q}}}' + \boldsymbol{K}\right)\right.\right. \\ + \frac{1}{2}\left(\boldsymbol{K}^{\mathrm{T}} + \overline{\overline{\boldsymbol{Q}}}^{\mathrm{T}} \boldsymbol{J}^{\mathrm{T}}\right) \bar{\boldsymbol{b}} \left(\boldsymbol{J}\,\overline{\overline{\boldsymbol{Q}}} + \boldsymbol{K}\right) \\ \left.\left. - \left(\boldsymbol{K}^{\mathrm{T}} + \overline{\overline{\boldsymbol{Q}}}^{\mathrm{T}} \boldsymbol{J}^{\mathrm{T}}\right) \bar{\boldsymbol{a}} \left(\boldsymbol{J}\,\overline{\overline{\boldsymbol{Q}}}' + \boldsymbol{K}\right)\right]\right\} \end{aligned} \tag{4.74}$$

The evaluation of the cross-correlation function from Eq. 4.74 is not practical, since the normal modes of the two states are coupled through matrices $\bar{\boldsymbol{a}}$, $\bar{\bar{\boldsymbol{a}}}$, $\bar{\boldsymbol{b}}$ and $\bar{\bar{\boldsymbol{b}}}$. Those couplings can be however removed by changing the coordinate system from $\left(\overline{\overline{\boldsymbol{Q}}}, \overline{\overline{\boldsymbol{Q}}}'\right)$ to $(\boldsymbol{Z}, \boldsymbol{U})$ through the following linear transformation,

$$\begin{aligned} \boldsymbol{Z} &= \frac{1}{\sqrt{2}}\left(\overline{\overline{\boldsymbol{Q}}} + \overline{\overline{\boldsymbol{Q}}}'\right) \\ \boldsymbol{U} &= \frac{1}{\sqrt{2}}\left(\overline{\overline{\boldsymbol{Q}}} - \overline{\overline{\boldsymbol{Q}}}'\right) \end{aligned} \tag{4.75}$$

In the $(\boldsymbol{Z}, \boldsymbol{U})$ basis, the autocorrelation function can be efficiently expressed in terms of the $\boldsymbol{c}$, $\boldsymbol{d}$, $\boldsymbol{C}$ and $\boldsymbol{D}$ matrices as follows,

$$\begin{aligned} \chi(t) = \Upsilon(t) \exp\left(-\boldsymbol{K}^{\mathrm{T}} \bar{\boldsymbol{d}}\, \boldsymbol{K}\right) \int \mathrm{d}\boldsymbol{Z} \exp\left(-\frac{1}{2}\boldsymbol{Z}^{\mathrm{T}} \boldsymbol{D} \boldsymbol{Z} - \sqrt{2}\boldsymbol{v}^{\mathrm{T}} \boldsymbol{Z}\right) \\ \times \int \mathrm{d}\boldsymbol{U} \exp\left(-\frac{1}{2}\boldsymbol{U}^{\mathrm{T}} \boldsymbol{C}\, \boldsymbol{U}\right) \end{aligned} \tag{4.76}$$

where $\boldsymbol{v}^T = \boldsymbol{K}^T \bar{\boldsymbol{d}} \boldsymbol{J}$ and,

$$\Upsilon(t) = \sqrt{\frac{\det(\overline{\boldsymbol{a}}\,\overline{\overline{\boldsymbol{a}}})}{(2\pi i\hbar)^{2N}}} \tag{4.77}$$

The main advantage of Eq. 4.76 over the previous formulations is that the integral over the $\boldsymbol{U}$ and $\boldsymbol{Z}$ coordinates are factorized, so they can be evaluated separately with the well-known analytic formula for the integral of a multidimensional Gaussian function,[295]

$$\int_{-\infty}^{+\infty} d^N\boldsymbol{x}\; e^{-\boldsymbol{x}^T\boldsymbol{B}\boldsymbol{x}+\boldsymbol{v}^T\boldsymbol{x}} = \frac{(\sqrt{\pi})^N}{(\det\boldsymbol{B})^{1/2}} \exp\left(\frac{1}{4}\boldsymbol{v}^T\boldsymbol{B}^{-1}\boldsymbol{v}\right) \tag{4.78}$$

Using Eq. 4.78 to solve the integrals in Eq. 4.76, the following final result is obtained,

$$\chi(t) = \sqrt{\frac{\det(\overline{\boldsymbol{a}}\,\overline{\overline{\boldsymbol{a}}})}{(i\hbar)^{2N}\det(\boldsymbol{C}\,\boldsymbol{D})}} \times \exp\left(-\boldsymbol{K}^{\mathrm{T}}\,\overline{\boldsymbol{d}}\,\boldsymbol{K} + \boldsymbol{v}^{\mathrm{T}}\,\boldsymbol{D}^{-1}\,\boldsymbol{v}\right) \tag{4.79}$$

Eq. 4.79 is the key result for the TD formulation of vibronic spectroscopy. Indeed, it expresses analytically the transition dipole moment autocorrelation function for any time t, so that spectra can be computed at the FC level as discrete Fourier transform by means, for example, of a Fast Fourier Transform (FFT) algorithm.

4.4.2 Inclusion of HT terms

The autocorrelation function $\chi(t)$ is the only quantity needed to compute the spectrum at the FC level. When HT terms are also included in the expansion given in Eq. 4.17, the other tensors in Eq. 4.65 needs to be computed. Let us start begin from the first-order terms, namely $\chi_l(t)$ and $\chi^l(t)$. The same strategy employed for the FC case up to Eq. 4.68 is used here to recast $\chi_l(t)$ as,

$$\begin{aligned}\chi_l(t) = \int_{-\infty}^{+\infty} d\overline{\boldsymbol{Q}} \int_{-\infty}^{+\infty} d\overline{\boldsymbol{Q}}' \int_{-\infty}^{+\infty} d\overline{\overline{\boldsymbol{Q}}} \int_{-\infty}^{+\infty} d\overline{\overline{\boldsymbol{Q}}}' \langle\, \overline{\boldsymbol{Q}} \mid \overline{\overline{\boldsymbol{Q}}} \,\rangle \\ \langle\, \overline{\overline{\boldsymbol{Q}}} \mid \overline{\overline{\mathcal{Q}}}_l e^{-\overline{\overline{\tau}}\,\overline{\overline{\mathcal{H}}}} \mid \overline{\overline{\boldsymbol{Q}}}' \,\rangle \langle\, \overline{\overline{\boldsymbol{Q}}}' \mid \overline{\boldsymbol{Q}}' \,\rangle \langle\, \overline{\boldsymbol{Q}}' \mid e^{-\overline{\tau}\,\overline{\mathcal{H}}} \mid \overline{\boldsymbol{Q}} \,\rangle\end{aligned} \tag{4.80}$$

$\langle\, \overline{\overline{\mathcal{Q}}}_l \mid$ is an eigenbra of $\overline{\overline{\mathcal{Q}}}_l$, thus,

$$\langle\, \overline{\overline{\boldsymbol{Q}}} \mid \overline{\overline{\mathcal{Q}}}_l e^{-\overline{\overline{\tau}}\,\overline{\overline{\mathcal{H}}}} \mid \overline{\overline{\boldsymbol{Q}}}' \,\rangle = \langle\, \overline{\overline{\boldsymbol{Q}}} \mid \overline{\overline{\mathcal{Q}}}_l e^{-\overline{\overline{\tau}}\,\overline{\overline{\mathcal{H}}}} \mid \overline{\overline{\boldsymbol{Q}}}' \,\rangle \tag{4.81}$$

As a consequence, the integrand is simply scaled by a factor equal to $\overline{\overline{\mathcal{Q}}}_l$, which can be rewritten in terms of $\mathbf{U}$ and $\mathbf{Z}$ from Eq. 4.75 as,

$$\begin{aligned}\langle\, \overline{\boldsymbol{Q}} \mid \overline{\overline{\mathcal{Q}}}_l e^{-\overline{\overline{\tau}}\,\overline{\overline{\mathcal{H}}}} e^{-\overline{\tau}\,\overline{\mathcal{H}}} \mid \overline{\boldsymbol{Q}} \,\rangle =& \frac{1}{\sqrt{2}} \langle\, \overline{\boldsymbol{Q}} \mid U_l e^{-\overline{\overline{\tau}}\,\overline{\overline{\mathcal{H}}}} e^{-\overline{\tau}\,\overline{\mathcal{H}}} \mid \overline{\boldsymbol{Q}} \,\rangle \\ &+ \frac{1}{\sqrt{2}} \langle\, \overline{\boldsymbol{Q}} \mid Z_l e^{-\overline{\overline{\tau}}\,\overline{\overline{\mathcal{H}}}} e^{-\overline{\tau}\,\overline{\mathcal{H}}} \mid \overline{\boldsymbol{Q}} \,\rangle\end{aligned} \tag{4.82}$$

With the previous equation, $\chi_l(t)$ can be computed in terms of the FC autocorrelation function $\chi(t)$ given in Eq. 4.76. First, the second term, involving Z_l, of the previous equation can be rewritten as,

$$\begin{aligned}&\langle\, \overline{\boldsymbol{Q}} \mid Z_l e^{-\overline{\overline{\tau}}\,\overline{\overline{\mathcal{H}}}} e^{-\overline{\tau}\,\overline{\mathcal{H}}} \mid \overline{\boldsymbol{Q}} \,\rangle = \Upsilon(t)\, \exp\left(-\boldsymbol{K}^{\mathrm{T}}\, \overline{\boldsymbol{d}}\, \boldsymbol{K}\right) \\ &\times \int \mathrm{d}\boldsymbol{Z}\, Z_l \exp\left(-\frac{1}{2}\boldsymbol{Z}^{\mathrm{T}}\boldsymbol{D}\boldsymbol{Z} - \sqrt{2}\boldsymbol{v}^{\mathrm{T}}\,\boldsymbol{Z}\right) \int \mathrm{d}\boldsymbol{U} \exp\left(-\frac{1}{2}\boldsymbol{U}^{\mathrm{T}}\,\boldsymbol{C}\,\boldsymbol{U}\right)\end{aligned} \tag{4.83}$$

At a given time t, $\chi_l(t)$, is a function of $\boldsymbol{v}$, $\boldsymbol{C}$ and $\boldsymbol{D}$. The integral given in Eq. 4.83 can be expressed in terms of derivatives of $\chi(t)$ with respect to elements of $\boldsymbol{v}$ as,

$$\frac{\partial \chi(t)}{\partial v_l} = -\sqrt{2}\langle\, \overline{\boldsymbol{Q}} \mid Z_l e^{-\overline{\overline{\tau}}\,\overline{\overline{\mathcal{H}}}} e^{-\overline{\tau}\,\overline{\mathcal{H}}} \mid \overline{\boldsymbol{Q}} \,\rangle \tag{4.84}$$

The integral containing U_k vanishes by symmetry since the integrand is odd with respect to U_k. The final result is thus,

$$\begin{aligned}\chi_l(t) = -\frac{1}{2}\frac{\partial \chi(t)}{\partial v_l} &= -\frac{1}{2}\chi(t)\left[\sum_{m=1}^{N_{\mathrm{vib}}} {D_{lm}}^{-1} v_m + \sum_{m=1}^{N_{\mathrm{vib}}} {D_{ml}}^{-1} v_m^{\star}\right] \\ &= -\frac{1}{2}\chi(t)\,\eta_l\end{aligned} \tag{4.85}$$

where the derivative of the FC autocorrelation function has been evaluated by differentiation of the final result given in Eq. 4.79. The $\boldsymbol{\eta}$ vector has been defined as,

$$\boldsymbol{\eta} = \boldsymbol{D}^{-1}\boldsymbol{v} + \{\boldsymbol{D}^{-1}\}^{T}\boldsymbol{v}^{\star} = 2\boldsymbol{D}^{-1}\Re\left(\boldsymbol{v}\right) \tag{4.86}$$

where the last equality follows from the fact that $\boldsymbol{D}$ is symmetric. The calculation of $\chi^{l}(t)$ is analogous to $\chi_l(t)$, with the only difference that, when the closure relation given in Eq. 4.67 is applied, $\overline{\overline{\mathcal{Q}}}_l$ acts on the ket vector $\mid \overline{\overline{\boldsymbol{Q}}}' \,\rangle$ instead of the $\langle\, \overline{\boldsymbol{Q}} \mid$ with eigenvalue $\overline{\overline{\mathcal{Q}}}'_l$. From Eq. 4.75, it follows that,

$$\langle\, \overline{\boldsymbol{Q}} \mid e^{-\overline{\overline{\tau}}\,\overline{\overline{\mathcal{H}}}}\overline{\overline{\mathcal{Q}}}_l e^{-\overline{\tau}\,\overline{\mathcal{H}}} \mid \overline{\boldsymbol{Q}} \,\rangle = \frac{1}{\sqrt{2}}\langle\, \overline{\boldsymbol{Q}} \mid e^{-\overline{\overline{\tau}}\,\overline{\overline{\mathcal{H}}}}(Z_l - U_l)e^{-\overline{\tau}\,\overline{\mathcal{H}}} \mid \overline{\boldsymbol{Q}} \,\rangle \tag{4.87}$$

Hence, $\chi_l(t) = \chi^{l}(t)$, since the integral containing U_k is null. The extension of this approach to higher-order correlation functions is straightforward. For example, the second-order tensor $\chi^{l}_{j}(t)$, which is the only quantity, in addition to $\chi_l(t)$ and $\chi^{l}(t)$, needed to compute spectra at the HT level, can be expressed as follows,

$$\chi^{l}_{j}(t) = \frac{1}{2}\langle\, \overline{\boldsymbol{Q}} \mid \left(Z_j + U_j\right) e^{-\overline{\overline{\tau}}\,\overline{\overline{\mathcal{H}}}} \left(Z_l - U_l\right) e^{-\overline{\tau}\,\overline{\mathcal{H}}} \mid \overline{\boldsymbol{Q}} \,\rangle \tag{4.88}$$

As already discussed above, only terms containing odd powers of $\boldsymbol{U}$ are non-null, thus Eq. 4.88 can be rewritten as,

$$\begin{aligned}\chi_j^l(t) =& \frac{1}{2}\langle \overline{\boldsymbol{Q}} \mid Z_j e^{-\overline{\tau}\,\overline{\overline{\mathcal{H}}}} Z_l e^{-\overline{\tau}\,\overline{\mathcal{H}}} \mid \overline{\boldsymbol{Q}} \rangle \\ & - \frac{1}{2}\langle \overline{\boldsymbol{Q}} \mid U_j e^{-\overline{\tau}\,\overline{\overline{\mathcal{H}}}} U_l e^{-\overline{\tau}\,\overline{\mathcal{H}}} \mid \overline{\boldsymbol{Q}} \rangle\end{aligned} \tag{4.89}$$

Also in this case, the two terms of the previous equation can be efficiently computed as derivatives of $\chi(t)$. The first term can be expressed in two possible ways:

$$\langle \overline{\boldsymbol{Q}} \mid Z_j e^{-\overline{\tau}\,\overline{\overline{\mathcal{H}}}} Z_l e^{-\overline{\tau}\,\overline{\mathcal{H}}} \mid \overline{\boldsymbol{Q}} \rangle = -2\frac{\partial \chi(t)}{\partial D_{jl}} = \frac{1}{2}\frac{\partial^2 \chi(t)}{\partial v_j \partial v_l} \tag{4.90}$$

To evaluate the previous expressions, the following properties of derivatives of a general matrix $\boldsymbol{A}$, are useful,

$$\begin{aligned}\frac{\partial \det(\boldsymbol{A})}{\partial A_{ij}} &= \det(\boldsymbol{A}) \left(\boldsymbol{A}^{-1}\right)_{ij} \\ \frac{\partial {A^{-1}}_{kl}}{\partial A_{ij}} &= -\left(\boldsymbol{A}^{-1}\right)_{ki} \left(\boldsymbol{A}^{-1}\right)_{jl}\end{aligned}$$

Using the previous relations, the quantity defined in Eq. 4.90 can be computed, starting with $\partial\chi(t)/\partial D_{jl}$ as,

$$\begin{aligned}-2\frac{\partial \chi(t)}{\partial D_{jl}} =& -\frac{1}{2\det(\boldsymbol{D})}\frac{\partial \det(\boldsymbol{D})}{\partial D_{jl}}\chi(t) + \frac{\partial}{\partial D_{jl}}\left(\boldsymbol{v}^T \boldsymbol{D}^{-1}\boldsymbol{v}\right)\chi(t) \\ =& {D^{-1}}_{jl}\,\chi(t) + 2\chi(t)\sum_{a,b=1}^{N_{\text{vib}}} {D^{-1}}_{al} {D^{-1}}_{jb} v_a^\star v_b \\ =& \chi(t)\left(2\eta_j\eta_l + {D^{-1}}_{jl}\right)\end{aligned} \tag{4.91}$$

If instead the integral is computed from the second equality of Eq. 4.90, the following result is obtained:

$$\begin{aligned}\frac{1}{2}\frac{\partial^2 \chi(t)}{\partial v_j \partial v_l} =& \frac{1}{2}\chi(t)\left[\sum_{m=1}^{N_{\text{vib}}} {D_{jm}}^{-1} v_m + \sum_{m=1}^{N_{\text{vib}}} {D_{mj}}^{-1} v_m^\star\right] \\ & \times \left[\sum_{m=1}^{N_{\text{vib}}} {D_{lm}}^{-1} v_m + \sum_{m=1}^{N_{\text{vib}}} {D_{ml}}^{-1} v_m^\star\right] + \frac{1}{2}\chi(t)\left({D^{-1}}_{jl} + {D^{-1}}_{lj}\right) \\ =& \chi(t)\left[2\eta_j\eta_l + \left(\boldsymbol{D}^{-1}\right)_{jl}\right]\end{aligned} \tag{4.92}$$

which is, as expected, equivalent to Eq. 4.91. The calculation of the second term of Eq. 4.89 can be recast as,

$$\langle \overline{\boldsymbol{Q}} \mid U_j e^{-\overline{\tau}\,\overline{\overline{\mathcal{H}}}} U_l e^{-\overline{\tau}\,\overline{\mathcal{H}}} \mid \overline{\boldsymbol{Q}} \rangle = -2\frac{\partial \chi(t)}{\partial C_{jl}} \tag{4.93}$$

and the calculation of the derivative of the FC autocorrelation function with respect to C_{jl} is easier, since the dependence of $\chi(t)$ on $\boldsymbol{C}$ appears only in the prefactor $\mathrm{Y}(t)$ (see Eq. 4.79). By considering that,

$$\frac{\partial \chi(t)}{\partial C_{jl}} = -\frac{1}{2}\left(\boldsymbol{C}^{-1}\right)_{jl}\chi(t) \tag{4.94}$$

the final result is the following:

$$\langle\, \overline{\boldsymbol{Q}} \mid \overline{\overline{Q}}_j e^{-\overline{\overline{\tau}}\,\overline{\overline{\mathcal{H}}}} \overline{\overline{Q}}_l e^{-\overline{\tau}\,\overline{\mathcal{H}}} \mid \overline{\boldsymbol{Q}}\,\rangle = \left(\boldsymbol{C}^{-1}\right)_{jl}\chi(t) + \chi(t)\left[2\eta_j\eta_l + \left(\boldsymbol{D}^{-1}\right)_{jl}\right] \tag{4.95}$$

Please note that only the real part of the matrix elements is used in the derivations. For the sake of readability, the real-part symbol was omitted, so that $\partial\chi(t)/\partial v_l$ should be read as $\partial\chi(t)/\partial\Re(v_l)$. The same holds for the derivatives with respect to elements of $\boldsymbol{C}$.

To conclude, is is important to make a note on the computational cost associated to the evaluation of the autocorrelation function, both at the FC and at the FCHT level. As can be easily seen from Eq. 4.79, the bottleneck associated to the computation of $\chi(t)$ is the inversion of the $\boldsymbol{C}$ and $\boldsymbol{D}$ matrices that are, for the AH and VH models, non-diagonal. The calculation of the inverse is performed by means of LU decomposition,[124] which allows to compute also the determinant of $\boldsymbol{C}$ and $\boldsymbol{D}$, entering in the prefactor $\mathrm{Y}(t)$ of Eq. 4.79. Since the cost of the LU decomposition grows with the third power of the dimension of the matrices, the scaling of the overall algorithm is N_{vib}^3. As already mentioned above, the Fourier integral is computed through a numerical evaluation, by sampling $\chi(t)$ on a discrete grid of N_{grid} points, thus the overall scaling of the algorithm is $N_{\mathrm{grid}} \times N_{\mathrm{vib}}^3$. This scaling is much more favorable if $\boldsymbol{J} = \boldsymbol{I}$ as, for example, in the VG and AS cases. In those cases, the $\boldsymbol{C}$ and $\boldsymbol{D}$ matrices are defined as,

$$\boldsymbol{C} = \overline{\overline{c}} + \overline{\boldsymbol{c}} \qquad\qquad \boldsymbol{D} = \overline{\overline{d}} + \overline{\boldsymbol{d}} \tag{4.96}$$

and thus are both diagonal, so their inverses scale linearly with the number of modes N_{vib}.

The scaling increases if HT terms are included. First of all, the number of terms to be included in the expansion given in Eq. 4.64 grows as $\mathcal{O}\left(N_{\mathrm{vib}}^2\right)$. The evaluation of each term requires the calculation of the $\boldsymbol{\eta}$ vector, since the elements of $\boldsymbol{C}^{-1}$ and $\boldsymbol{D}^{-1}$ are already available from the FC calculation. The cost of the evaluation of $\boldsymbol{\eta}$ is proportional to N_{vib}^2, thus is still negligible with respect to the matrix inversion. However, we note that, if the $\chi_j^l(t)$ tensors are evaluated directly using, for example, the first relation of Eq. 4.92 with an actual summation for each term, without storing the $\boldsymbol{\eta}$ vector as an intermediate quantity, the computational cost would increase significantly, since the elements of $\boldsymbol{\eta}$ would be computed several times for each iteration.

4.5 Selected applications

The theoretical framework presented above, including both the support of internal coordinates and the TD formulation is now applied to the simulation of vibronic spectra of two medium-sized organic molecules. The first case is imidazole, whose absorption spectrum will be studied both in vacuum and in solvent, where solvation effects will be included both with the Polarizable Continuum Model (PCM) and by performing QM calculation on a cluster consisting of imidazole and two explicit water molecules. As will be discussed in the following, the structural changes associated to the electronic excitation differ if solvent effects are included, and only a proper choice of the internal coordinates provides a reliable reproduction of the vibronic bandshape.
The second test-case studied here is a camphore derivative, namely the epicamphore. For this molecular system, the theoretical models outlined above will be used to simulate its ECD spectrum, with particular care on the impact of the choice of the vibronic model and of the coordinate system on the final spectrum. In all cases, the calculations were performed at the DFT (for ground states) and TD-DFT level (for excited states), using the B3LYP exchange-correlation functional and the SNSD basis set.[296]

4.5.1 OPA spectrum of imidazole in water

Imidazole derivatives are interesting models to more complex biological systems, like histidine, as their spectroscopic properties can provide some insights on the latter's. Therefore, several studies, both experimental and theoretical, are available for a wide range of imidazole derivatives.[297,298,299] Here, we will study the one-photon absorption spectrum of imidazole, with particular care on the effect of the choice of the coordinates on the final bandshape. We will focus on the first band of the OPA spectrum of imidazole, corresponding to a $\pi \rightarrow \pi^*$ excitation, to the S_2 electronic excited state (see Fig. 4.2 for a representation of the equilibrium geometries in each electronic state).

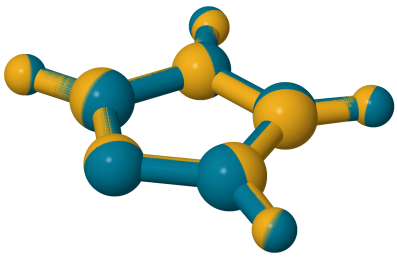

FIGURE 4.2: Graphical representation of the equilibrium geometry of the S_0 (in yellow) and S_2 (in blue) electronic states of imidazole, computed in vacuum at the B3LYP/SNSD level.

The comparison of the computed OPA spectra obtained with Cartesian coordinates, DICs and WICs (see Sec. 4.2 for details) within both TD (solid lines) and TI (dashed lines) approaches is reported in Fig. 4.4. In all cases, solvent effects were neglected. Furthermore, vibronic simulations were performed at the AH|FC level, thus explicitly optimizing the geometry of the S_2 electronic state, and taking into account mode-mixing effects. We note that the bandshape of the three spectra obtained with the different coordinates systems

are very close. As noticed from Fig. 4.2, where the equilibrium geometries of the S_0 and S_2 states are reported after superposition, the geometrical deformation between the two electronic states is negligible. As mentioned above, for small geometrical rearrangements, all coordinate systems give equivalent results. It is also noteworthy that, within the same coordinates system, equivalent results are obtained with the TD and TI algorithms. In the same way, this is a consequence of the limited geometrical deformation between the two electronic states too since this means that mode-mixing effects (corresponding to off-diagonal terms of $\boldsymbol{J}$) are small, and the elements of the shift vector $\boldsymbol{K}$ have low magnitude. As a result, the efficiency of the prescreening scheme in the TI algorithm does not need to be particularly efficient, and a nearly complete convergence (> 99 %) is easily obtained here. This means, in practice, that all non-negligible terms are included in the sum-over-states expansion, and thus the TI results must be equivalent to the TD ones, which are fully converged by definition.

In Fig. 4.5, the same comparison is reported for calculations performed including solvent effects (water) by means of the polarizable continuum model (PCM). Vibronic simulations were performed at the AH|FC level with different coordinate systems, employing however only the TD algorithm. Indeed, TI calculations led to poor convergences ($<$ 20%) in all cases. As for calculations in vacuum, this trend can be understood on the basis of the geometrical deformation associated to the electronic excitation.

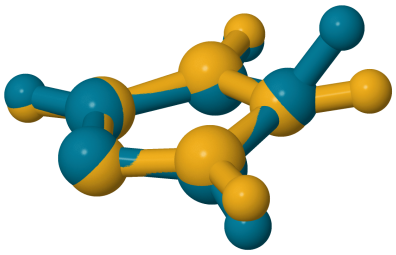

FIGURE 4.3: Graphical representation of the equilibrium geometry of the S_0 (in yellow) and S_2 electronic states of imidazole, computed at the B3LYP/SNSD level. Solvent effects (water) were included by means of PCM.

As shown in Fig. 4.3, in this case, even if the five-membered ring is planar in the S_0 electronic state, a significant out-of-plane deformation occurs after the transition to the S_2 excited state. As remarked before, those deformations are described inaccurately in Cartesian coordinates, resulting in a poor definition of the Duschinsky matrix $\boldsymbol{J}$, with large, unphysical mode-couplings that make a large number of vibronic progressions active, thus leading to an overestimation of the vibronic broadening. This is highlighted in Fig. 4.5, where, even if a relatively small half-width at half-maximum (HWHM) of 100 cm^{-1} is used to reproduce broadening effects for each vibronic peak, the overall broadening is clearly overestimated, with a band spanning over 20000 cm^{-1}. This inaccuracy is corrected in the DIC and WIC spectra, and in both cases the overall broadening is smaller. We also note that the two internal coordinates sets (DICs and WICs) provide nearly equivalent results. This means that the non-redundant coordinates obtained from the SVD of the redundant $\boldsymbol{B}$ matrix already decouples internal coordinates of different types, and thus a further decoupling is not necessary.

As already mentioned above, the inaccurate description of large-amplitude motions in terms of Cartesian coordinates leads to large off-diagonal terms in

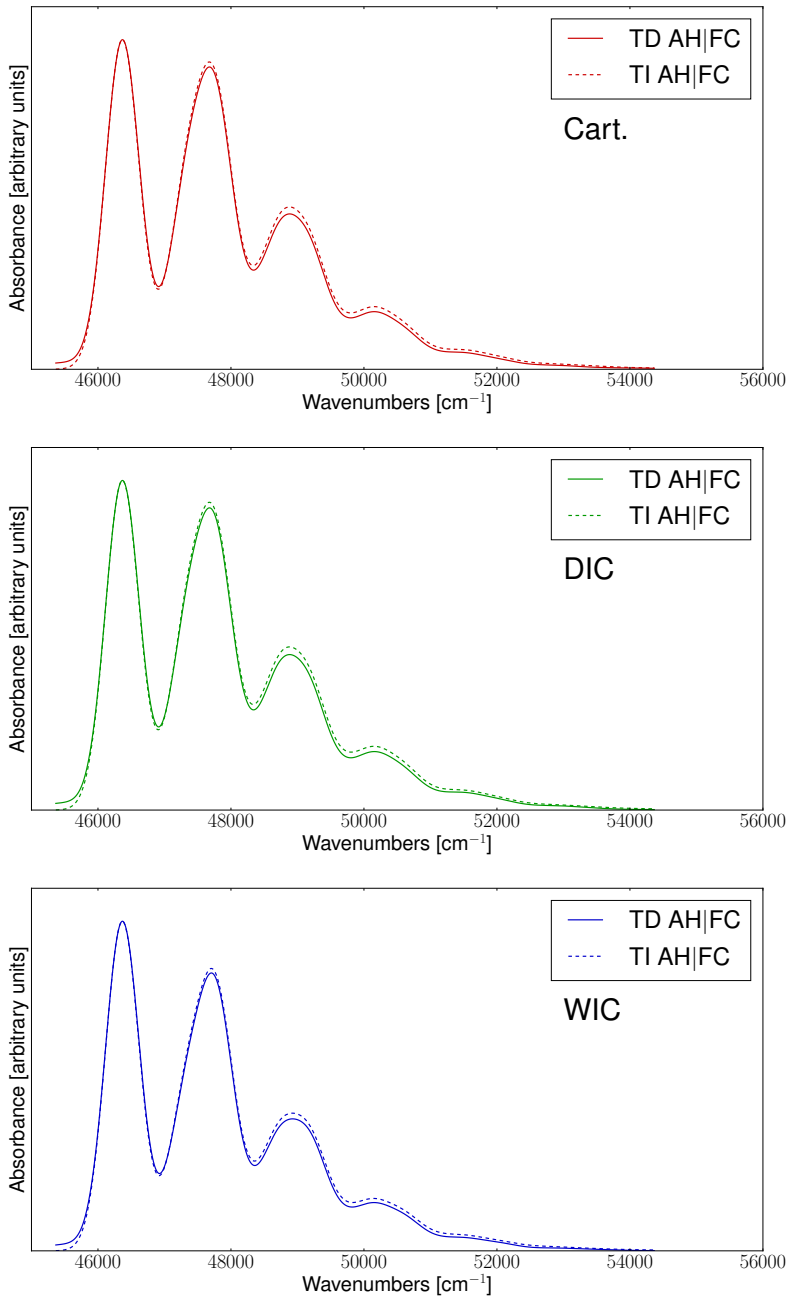

FIGURE 4.4: Theoretical OPA spectrum for the $S_2 \longleftarrow S_0$ transition of imidazole in vacuum at the TD (solid lines) and TI (dashed lines) AH|FC levels using Cartesian coordinates (red lines) DICs (green lines) and WICs (blue lines). Gaussian distribution functions with HWHM of 300 cm^{-1} have been used to simulate the broadening effects. The highest value of absorbance in cartesian coordinates is approximately 5.25 lower than the one obtained using DICs.

$\boldsymbol{J}$, which are not present in internal coordinates. The nearly block-diagonal structure of the Duschinsky matrix in internal coordinates opens the possibility of treating normal modes belonging to different blocks at different levels of approximation. For instance, anharmonic models may be used for a limited number of low-frequency modes, while the harmonic approximation is used for the other vibrations. The development of such anharmonic models will be described in details in Chapter 6, and here we will only verify the block-diagonal structure of $\boldsymbol{J}$ in DICs. For imidazole, the reduced-dimensionality scheme described above identifies five strongly mixed normal modes (the five lowest-energy ones), which are however decoupled from the others. Indeed, this block can be identified by setting η=0.8 in the algorithm used in the RD calculations. In Fig. 4.6, the spectrum obtained by neglecting the coupling elements of $\boldsymbol{J}$ between modes of different blocks is reported, together with the spectrum obtained using the full expression of $\boldsymbol{J}$. The overall shape of the two spectra is quite similar, with a slightly narrower and more resolved shape with the block-shaped $\boldsymbol{J}$. This result confirms the fact that couplings between the modes belonging to different blocks are small. This also confirms that the effect of LAMs can be recovered, as a first approximation, with symmetric broadening functions, provided that internal coordinates are employed.

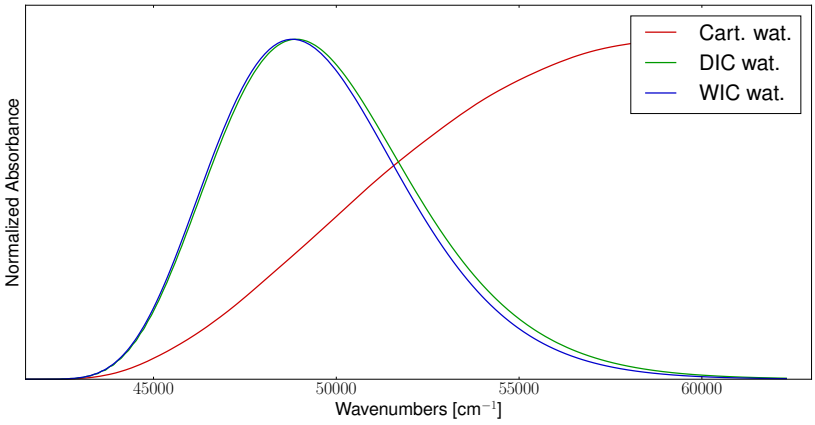

FIGURE 4.5: Theoretical OPA spectra of imidazole in water simulated at the TD AH|FC level with Cartesian coordinates (red line), DICs (green line) and WICs (blue line). Gaussian broadening functions with HWHMs of 100 cm^{-1} have been used to simulate broadening effects.

In order to test the impact of the choice of the vibronic model, the OPA spectrum of imidazole has been simulated also with VH as well. The theoretical spectra calculated at the TD VH|FC level using Cartesian coordinates and DICs are reported in Fig. 4.7. At the equilibrium geometry of S_0, two normal modes in the S_2 electronic state have imaginary frequencies, so they cannot be described at the harmonic level. As already mentioned for the RD scheme, a proper treatment of those normal modes would require the inclusion of anharmonicity. However, as a first approximation, they can be neglected, by

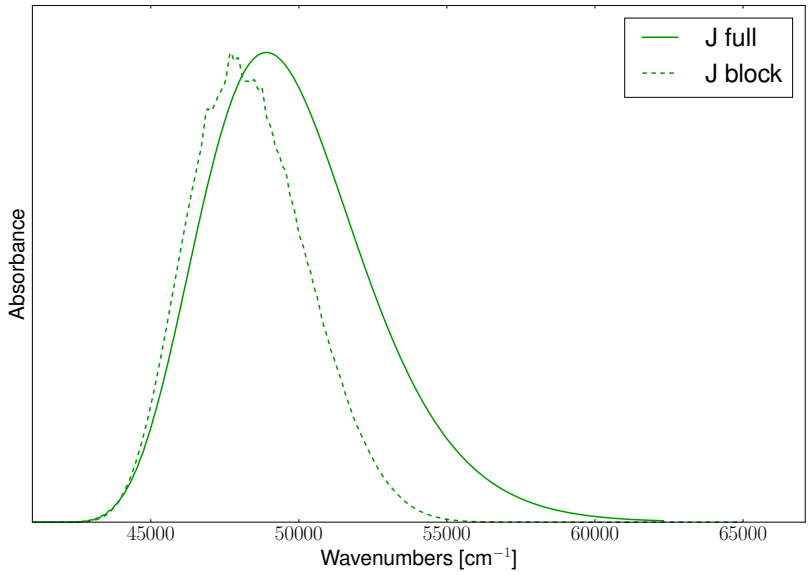

FIGURE 4.6: Theoretical OPA spectra of imidazole in water simulated at the TD AH|FC level using DICs with the full Duschinsky matrix $\boldsymbol{J}$ (solid green line) and a block Duschinsky matrix, where the coupling elements between the five lowest energy normal modes and the other modes have been neglected. Gaussian broadening functions with HWHM of 100 cm^{-1} have been used to simulate the broadening effects.

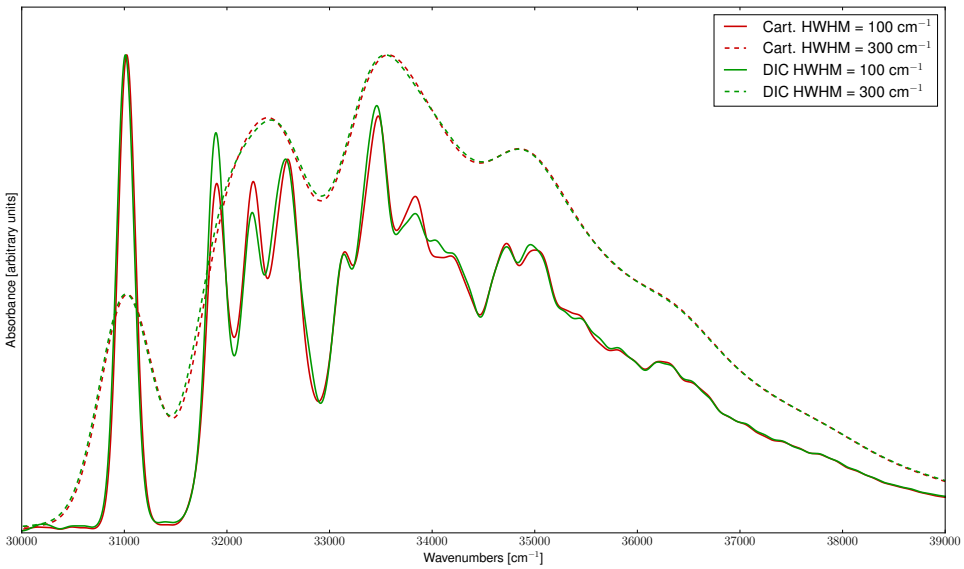

FIGURE 4.7: Theoretical OPA spectra of the $S_2 \longleftarrow S_0$ transition of imidazole in water simulated at the TD VH|FC level using cartesian (red line) and delocalized internal coordinates (green line). Gaussian broadening functions with an HWHM of 100 cm^{-1} (solid line) and 300 cm^{-1} (dashed line) have been used to simulate broadening effects.

uncoupling them from the others using the RD scheme presented earlier. In the Cartesian case, η must be set to 0.4 to remove only the two imaginary frequency modes, whereas in internal coordinates it can be set to 0.7. This suggests that they are more mixed in the Cartesian representation than when DICs are used. Even if the theoretical spectra obtained using the different coordinates systems are nearly equivalent (only slight differences can be detected in the spectrum, where a broadening function with an HWHM of 100 cm^{-1} is used), the definition of the Duschinsky transformation changes significantly.

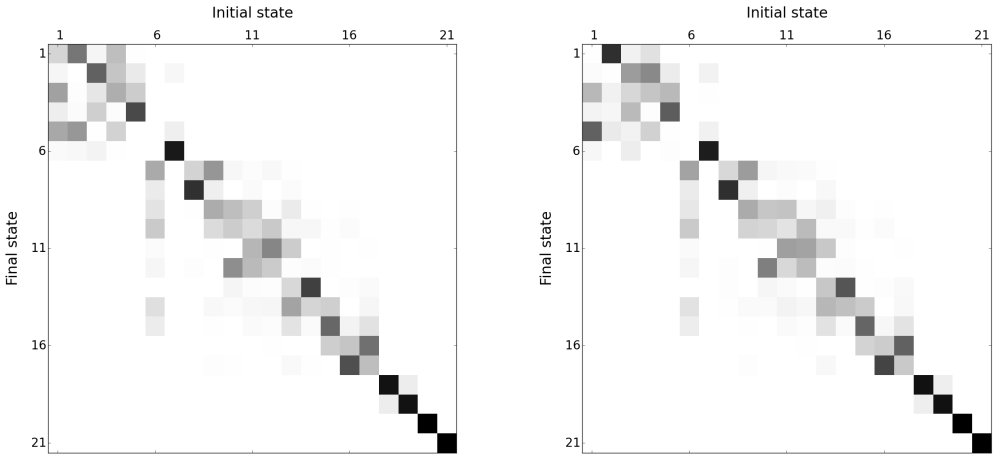

FIGURE 4.8: Graphical representation of the Duschinsky matrix $\boldsymbol{J}$ for the $S_2 \longleftarrow S_0$ transition of imidazole in water at the VH|FC level using Cartesian (left panel) and internal coordinates (right panel). The representation is obtained as follows: the elements $J_{ji}^2 / \left(\sum_{i=1}^{N_{vib}} J_{ji}^2\right)$ are calculated and a shade of gray is associated to each element (j,i) in the figure based on the equivalence 0: white; 1: black.

As shown in the graphical representation of $\boldsymbol{J}$ reported in Fig. 4.8, the couplings between the two normal modes associated to imaginary frequencies and the others is larger in the Cartesian case than in the internal one. For example, mode $\overline{\overline{1}}$ (ring deformation) is mostly coupled to the mode $\overline{2}$ (ring deformation) in internal coordinates, whereas 4 modes ($\overline{\overline{1}}$-$\overline{\overline{4}}$) are needed to describe the projection on the initial state modes in the Cartesian representation. As for the low-frequency modes discussed before, imaginary-frequency modes in internal coordinates are less coupled to the rest of the system, paving the route toward a more accurate treatment for them using, for example, low-dimensional anharmonic models. We should note however, that a notable coupling has been neglected to build the block, an approximation, which should be first tested before aiming at more accurate results.
Specific solvent effects have been simulated by including two explicit water

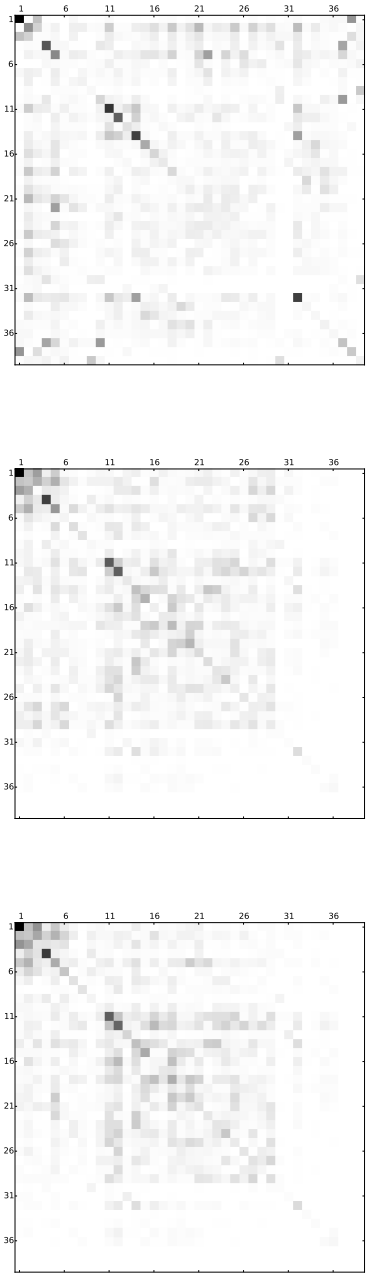

FIGURE 4.9: Graphical representation of the Sharp and Rosenstock matrix $\boldsymbol{C}$ for the $S_2 \longleftarrow S_0$ transition of imidazole in water at the VH|FC level. The representation is obtained by calculating the square of the elements of $\boldsymbol{C}$ and normalizing them with respect to the maximum value of $\{C_{ij}\}^2$ (0.51 for Cart., 0.32 for DICs in both cases). In order to facilitate the visual comparison, the highest maximum (0.51) was used to divide each element of the three matrices. A shade of gray is associated to each element (*i,j*) in the figure with white for 0 and black for 1.

molecules in the QM calculation (a graphical representation of the imidazole-2(H_2O) cluster is reported in Fig. 4.10). The results of the vibronic simulations, carried out at the TD AH|FC level, are reported in Fig. 4.11. Even for this case, the spectrum in Cartesian coordinates is much more broadened with respect to the ones in internal coordinates. For the simulations performed using DICs (green lines), both the standard algorithm used to generate the molecular topology (dashed line), and the one developed to support the presence of hydrogen bonds described in Chapter 2 (solid line), have been used. Even if the results obtained with the two different algorithms are nearly equivalent, the definition of the Duschinsky transformation changes significantly. The most significant changes are visible in the Sharp and Rosenstock $\boldsymbol{C}$ matrix.[266,277] As discussed in the previous sections, within the recursive formulation proposed by Ruhoff,[279] the FC integrals between two vibronic states can be related to lower-quanta ones through those matrices, and the influence of the coupling between the final state modes on the FC integrals is directly related to $\boldsymbol{C}$. The $\boldsymbol{C}$ matrix calculated using Cartesian coordinates, DICs with the standard connectivity and DICs with modified connectivity in the presence of H bonds are reported in Fig. 4.9. We note that the number of off-diagonal couplings between the modes is larger in the Cartesian representation than for any internal coordinate set, which would mean a greater contribution from combination bands in theory and often more low-intensity transitions. Furthermore, using DICs, the structure of $\boldsymbol{C}$ changes with the topology used. Indeed, even if for the high-energy modes the elements of $\boldsymbol{C}$ are nearly equivalent, for the lowest frequency modes, involving variations of the hydrogen bonds, the couplings with the other modes are significantly smaller when the modified topology is used. This example shows that, in the presence of weak bonds, such as hydrogen bonds, a careful choice of the coordinate system is critical to describe correctly the normal modes and especially to limit their coupling, even if those differences have a negligible impact on the final vibronic spectrum.

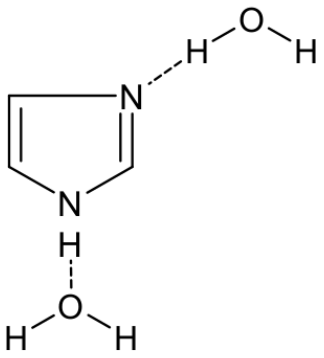

FIGURE 4.10: Structure of the cluster imidazole-2H_2O used in the vibronic simulations.

4.5.2 ECD spectrum of (1S)-dehydro-epicamphore

The third system, which has been chosen to test the reliability of our theoretical formulation is (1S,4R)-4,7,7-trimethylbicyclo[2.2.1]hept-5-en-2-one (the structure is reported in Fig. 4.12), also known as (1S)-dehydro-epicamphor. The molecule will be referred in the following simply as epicamphore.

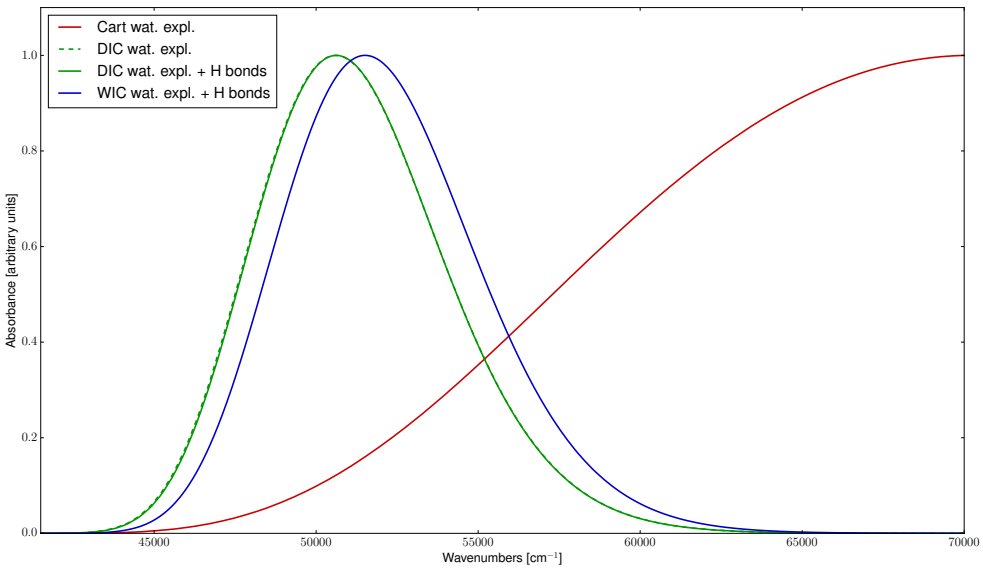

FIGURE 4.11: Theoretical OPA spectra of the $S_2 \longleftarrow S_0$ transition of imidazole in water, where solvent effects have been simulated adding two explicit water molecules in the QM calculation. All simulations have been performed at the TD AH|FC level, using cartesian (red line), delocalized (green line) and weighted internal coordinates (blue line) using the standard connectivity matrix (solid lines) and the one, which has been modified to support the presence of hydrogen bonds (dashed lines). Gaussian distribution functions with HWHM of 100 cm^{-1} have been used to reproduce broadening effects.

From a theoretical point of view, the definition of a non-redundant set of internal coordinates for this system and, more in general, for bicyclic compounds, is quite challenging. In fact, due to its complex topology, with two fused rings, the definition of a non-redundant Z-matrix is far from being straightforward. On the other hand, DICs and WICs can be easily built since only the molecular topology is required. While for several years only the ECD and the CPL spectra of (1R)-camphorquinone had been measured,[300] an extensive study of the experimental ECD and CPL spectra of camphore derivatives has been provided recently by Longhi and co-workers.[301] Thanks to this extensive experimental study, the reliability of the computational model can be checked on more systems. Here, we will focus on epicamphor since, because of its flexibility upon the electronic excitation, which makes the choice of the coordinates system critical to obtain a correct reproduction of the vibronic bandshape of the ECD spectrum.

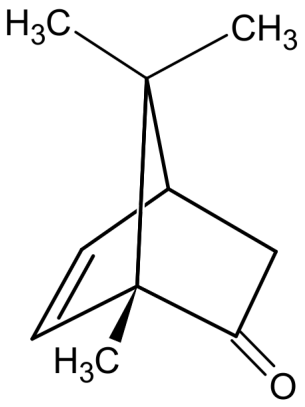

FIGURE 4.12: Graphical representation of the molecular structure of (1S)-dehydro-epicamphor.

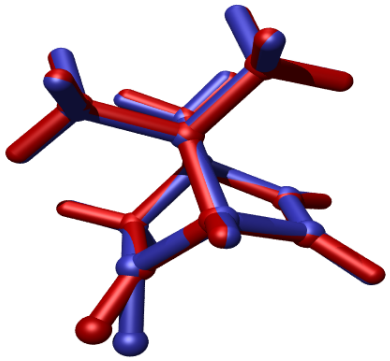

FIGURE 4.13: Graphical representation of the optimized structures of the S_0 (red) and S_1 (blue) electronic states of (1S)-dehydro-epicamphor

The first bright absorption of epicamphor is associated to the $S_1 \leftarrow S_0$ ($\pi \rightarrow \pi^*$) electronic transition. The graphical representation of the equilibrium geometries of the two electronic states, reported in Fig. 4.13, shows that the largest distortion involves an out-of-plane motion of the carbonyl group. This deformation, as already pointed out by Longhi and co-workers,[301] defines the sign of the ECD and CPL spectrum according to the so-called octant rule.[281]

The ECD spectra of epicamphore calculated at the TD AH|FC level using different coordinates systems are reported in Fig. 4.14 Similarly to imidazole, DICs and WICs give nearly equivalent results, therefore further supporting the reliability of the simpler DICs algorithm. However, the spectrum obtained in Cartesian coordinates is significantly broader and less intense (by a factor of about 10). For imidazole, the difference between the coordinate systems was detectable from a visual analysis of the structure of both the Duschinsky matrix $\boldsymbol{J}$ and the Sharp and Rosenstock $\boldsymbol{C}$ matrix.

However, as shown in Fig. 4.15 (top panels), in this case little differences are visible between $\boldsymbol{J_x}$ and $\boldsymbol{J_s}$. The difference between the two sets of coordinates is more evident from the structure of the $\boldsymbol{C}$ matrix, which is remarkably more diagonal when DICs are used, as shown in the lower panel of Fig. 4.15

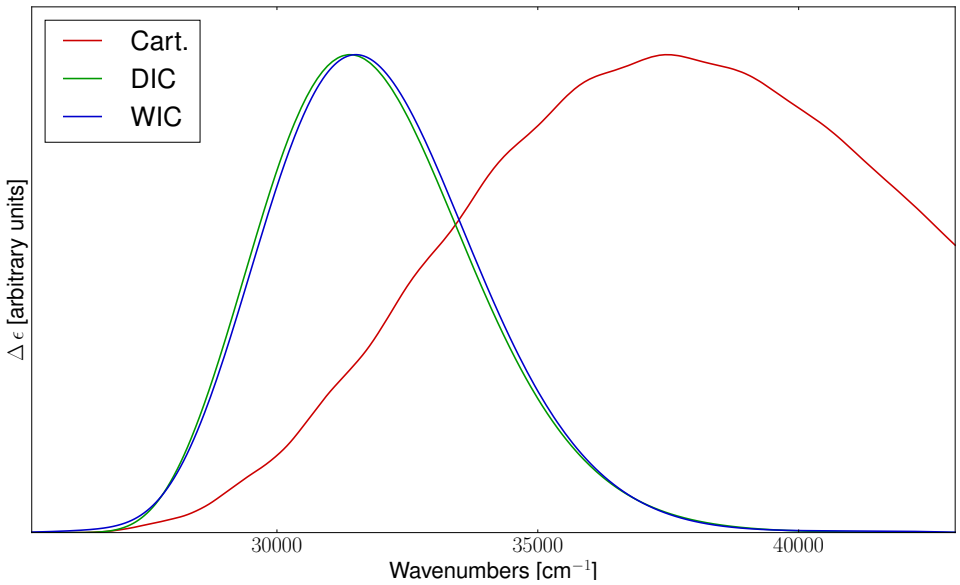

FIGURE 4.14: Theoretical ECD spectrum for the $S_1 \longleftarrow S_0$ transition of epicamphor calculated at the TD AH|FC level using Cartesian coordinates (solid red line), DICs (solid green line) and WICs (solid blue line). Gaussian distribution functions with HWHMs of 100 cm^{-1} have been used to reproduce broadening effects.

(the plot of the matrices obtained with WICs are not reported, and are equivalent to DICs). In more detail, in Cartesian coordinates, a large coupling between the out-of-plane C=O wagging (the lowest energy mode, number 1) and the C=O stretching (mode 47), is present. This large coupling arises from the inaccurate description of out-of-plane motions as linear combinations of Cartesian coordinates, and it disappears when DICs are employed.
The theoretical results have been next compared with the spectrum recorded by Longhi and co-workers,[301] shown in Fig. 4.16. It is noteworthy that, even if the resolution of the experimental spectrum is low, and single vibronic peaks cannot be detected, the reproduction of the overall bandshape is rather poor in Cartesian coordinates, since the convolution of all the vibronic transitions gives an excessively broadened spectrum. With DICs, the agreement between experimental and theoretical spectra becomes satisfactory, even if a constant shift between the two spectra is still present. Since the experimental spectrum has been recorded in ethanol solution, the optimized structures and frequencies of both electronic states have been calculated in this solvent too, using the IEF-PCM.[302,303] At this level, the absolute position of the spectrum is reproduced satisfactorily, and the bandshape does not change significantly. For the sake of completeness, HT effects have been included in the simulation as well. However, unlike other camphore derivatives,[304] in this case HT effects are negligible and the AH|FC and the AH|FCHT spectra are nearly superimposable.

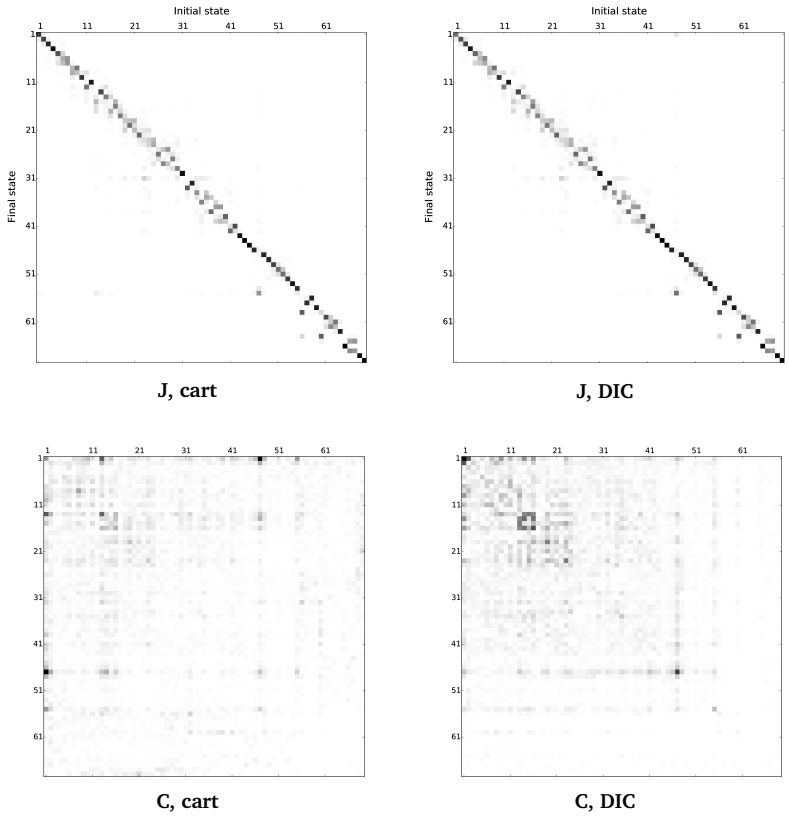

FIGURE 4.15: Graphical representation of the Duschinsky matrix $\boldsymbol{J}$ (upper panels) and of the Sharp and Rosenstock matrix $\boldsymbol{C}$ (lower panels) for the $S_1 \longleftarrow S_0$ transition of epicamphor in vacuum simulated at the TD AH|FC level using Cartesian coordinates (left panels) and DICs (right panels). The representations are the same as in Fig. 4.8 (for $\boldsymbol{J}$) and Fig. 4.9 (for $\boldsymbol{C}$).

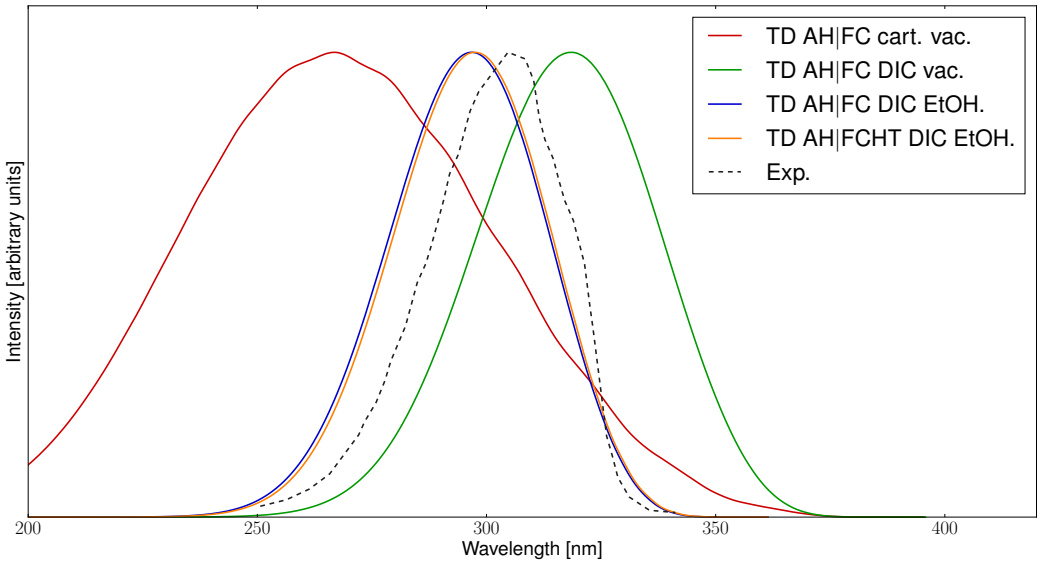

FIGURE 4.16: Comparison between the experimental ECD spectrum for the $S_1 \longleftarrow S_0$ transition of epicamphor (taken from Ref.[301]) and the theoretical results in Cartesian coordinates and DICs computed at the TD AH|FC levels in vacuum and solvent (ethanol). Solvent effects have been included by means of PCM. Gaussian distribution functions with HWHMs of 100 cm^{-1} have been used to reproduce the broadening effects.

4.6 Calculation of rate of non-radiative processes

In the previous sections, a general TD theoretical framework was applied to the calculation of different electronic spectra. However, the same framework can be generalized also to compute rates of radiative and non-radiative processes. In fact, in the previous derivation, the rate of absorption and emission of light was linked to their respective cross section, and then to experimental observable, through the Beer-Lambert law. However, the microscopic rates can be directly used to compute rates of different radiative and non-radiative processes.
This section is organized as follows: in the first part, the generalization of the TD method to the calculation of rates of three different processes, namely the inter-system crossing (ISC), the internal conversion (IC) and the fluorescence, withing an adiabatic picture, will be presented. Then, the framework will be extended to support a diabatic representation of the molecular states, highlighting the main different with the adiabatic case.

4.6.1 The adiabatic picture

As a first step, the formulation of the TD framework for the calculation of fluorescence and ISC rates will be presented. In fact, this extension is much simpler than the one needed to compute IC rates, which will be discussed later in detail.

Let us begin with the analysis of ISC processes. In ISC, the molecular transitions of interest involve vibrational levels of two electronic states of different spin symmetry, like a singlet and a triplet. The molecular Hamiltonian given in Eq. 2.1 does not depend on the spin variables, and thus it could not take into account transitions between states of different symmetry. However, it is well known[36,305] that Eq. 2.1 holds only in the non-relativistic limit. When relativistic effects are included, couplings between states of different spin, known as spin-orbit coupling (SOC), appear. Without going into details, these terms will be collected here in a single operator $\mathcal{H}_{\text{SO}}$, which has non-null cross matrix elements between electronic states of different spins. For non-heavy atoms, this term is usually small compared to the other interactions included in Eq. 2.1, thus its effect can be included through first-order perturbation theory, by taking as a reference $\mathcal{H}_{\text{mol}}$. In this case too, we will employ the adiabatic representation, thus neglecting non-adiabatic effects. Within this framework, the initial and final vibronic states of a transition, where vibronic has the meaning given at the beginning of the chapter, can be represented as $|\,\overline{\phi}\,\rangle|\,\overline{\psi}_i\,\rangle$ and $|\,\overline{\overline{\phi}}\,\rangle|\,\overline{\overline{\psi}}_f\,\rangle$, where $\overline{\phi}$ and $\overline{\overline{\phi}}$ are electronic states with different spin symmetry. As for the radiative case, also here the transition probability p_{if} between the two states introduced above can be derived through the FGR given Eq. 2.9. The main difference with the absorption case is that, in ISC, the perturbation is not represented by a time-dependent electromagnetic field, but by the time-independent Hamiltonian $\mathcal{H}_{\text{SO}}$. A derivation similar to the one aready described above leads to the following relation,[292,306,307]

$$k_{mn} = \frac{2\pi}{\hbar} \left| \langle\, \overline{\phi}\, \overline{\psi}_i \mid \mathcal{H}_{\text{SO}} \mid \overline{\overline{\phi}}\, \overline{\overline{\psi}}_f \,\rangle \right|^2 \delta\left(\overline{\overline{E}}_f - \overline{E}_i\right) \tag{4.97}$$

where k_{if} is the rate constant for the $|\,\overline{\phi}\,\overline{\psi}_i\,\rangle \rightarrow |\,\overline{\overline{\phi}}\,\overline{\overline{\psi}}_f\,\rangle$ transition. The overall rate constant k^{ISC} is obtained summing all the state-to-state constants k_{if} over all the possible initial and final states, by weighing the former by their respective population. In our derivation, thermal equilibrium for the initial electronic state will be assumed, thus the Boltzmann distribution is used. This approximation is valid if the ISC process is sufficiently slow, thus allowing the population of the initial state to reach equilibrium before the ISC begins. Under this approximation, the expression for the rate is the following:

$$k^{\text{ISC}} = \frac{2\pi}{Z\hbar} \sum_{i,f} \left| \langle\, \overline{\phi}\, \overline{\psi}_i \mid \mathcal{H}_{\text{SO}} \mid \overline{\overline{\phi}}\, \overline{\overline{\psi}}_f \,\rangle \right|^2 e^{-\beta \overline{E}_i} \delta\left(\left| \breve{\overline{\overline{E}}}_f - \breve{\overline{E}}_i \right| + E_{\text{ad}} \right) \tag{4.98}$$

The main difference between Eq. 4.97 and its equivalent for the absorption case (see Eq. 4.51) is that the latter depends on the frequency of the incident light ω, while this dependence is not present in the ISC case. The matrix element of the spin-orbit coupling $\mathcal{H}_{\text{SO}}$ can be approximated as a Taylor series, as done for the transition dipole moments,

$$\langle \overline{\phi}\,\overline{\psi}_i \mid \mathcal{H}_{\mathrm{SO}} \mid \overline{\overline{\phi}}\,\overline{\overline{\psi}}_f \rangle = H^e_{\mathrm{SO}}(\boldsymbol{Q}^{\mathrm{eq}}) \langle \overline{\psi}_i \mid \overline{\overline{\psi}}_f \rangle + \sum_{i=1}^{N_{\mathrm{vib}}} \left(\frac{\partial H^e_{\mathrm{SO}}}{\partial Q_i} \right)_{\mathrm{eq}} \langle \overline{\psi}_i \mid Q_i \mid \overline{\overline{\psi}}_f \rangle \tag{4.99}$$

where the electronic component of the spin-orbit coupling $\mathcal{H}_{\mathrm{SO}}$ is given by,

$$\mathcal{H}^e_{\mathrm{SO}} = \langle \overline{\phi} \mid \mathcal{H}_{\mathrm{SO}} \mid \overline{\overline{\phi}} \rangle \tag{4.100}$$

By combining the previous expansion with Eq. 4.98 and keeping, for the moment, only zeroth-order terms, k^{ISC} can be expressed as,[307,308]

$$k^{\mathrm{ISC}} = \frac{2\pi}{\hbar} H^e_{\mathrm{SO}}(\boldsymbol{Q}^{\mathrm{eq}})^2 f(E_{\mathrm{ad}}, T) \tag{4.101}$$

where the temperature-dependent FC weighted density of states (FC-DOS), $f(E_{\mathrm{ad}}, T)$ is defined as,

$$f(E_{\mathrm{ad}}, T) = \frac{1}{Z} \sum_{i,f} \left| \langle \overline{\psi}_i \mid \overline{\overline{\psi}}_f \rangle \right|^2 e^{-\beta \overline{E}_i} \delta \left(\left| \overline{\overline{E}}_f - \breve{\overline{E}}_i \right| + E_{\mathrm{ad}} \right) \tag{4.102}$$

As for the one-photon absorption and emission spectra, the TD formalism can be exploited to compute the FC-DOS. Following the same strategy used in the previous section, it is easy to show that, at the FC level, k^{ISC} can be computed as,

$$k^{\mathrm{ISC}} = H^e_{\mathrm{SO}}(\boldsymbol{Q}^{\mathrm{eq}})^2 \int_{-\infty}^{+\infty} \mathrm{d}t\, e^{iE_{\mathrm{ad}}t}\, \chi(t) \tag{4.103}$$

where the FC correlation function $\chi(t)$ has been given in Eq. 4.79. The extension of the previous expansion to HT effects is trivial, and k^{ISC} can be written in terms of the tensors defined in Eq. 4.65 as,

$$k^{\mathrm{ISC}} = \int_{-\infty}^{+\infty} \mathrm{d}t\, e^{iE_{\mathrm{ad}}t} \left[\chi(t) H^e_{\mathrm{SO}} \left(\overline{\overline{\boldsymbol{Q}}}^{\mathrm{eq}} \right)^2 + \sum_{k=1}^{N_{\mathrm{vib}}} H^e_{\mathrm{SO}}(\boldsymbol{Q}^{\mathrm{eq}}) \left(\frac{\partial H^e_{\mathrm{SO}}}{\partial Q_k} \right) \chi_k(t) + \sum_{k=1}^{N_{\mathrm{vib}}} H^e_{\mathrm{SO}}(\boldsymbol{Q}^{\mathrm{eq}}) \left(\frac{\partial H^e_{\mathrm{SO}}}{\partial Q_k} \right) \chi^k(t) + \sum_{k,l=1}^{N_{\mathrm{vib}}} \left(\frac{\partial H^e_{\mathrm{SO}}}{\partial Q_k} \right) \left(\frac{\partial H^e_{\mathrm{SO}}}{\partial Q_l} \right) \chi^l_k(t) \right] \tag{4.104}$$

A similar approach can be followed for the calculation of radiative processes, such as the fluorescence rate k_F. However, in this case, the transition is not induced by the SOC, but is determined by spontaneous emission processes, whose rate can be computed from the Einstein relation given in Eq. 4.52. The sum-over-state expression given in Eq. 4.53 provides the emitted intensity I_{em}, which is equal to $\hbar\omega\sigma_{\mathrm{em}}$, where σ_{em} is the absorption cross section associated to the spontaneous emission. Thus, it is easy to show that, within the TD formalism, σ_{em} can be expressed, at the FC level, as,

$$\sigma_{\text{em}}(\omega) = \frac{4\omega^3}{3\hbar c^3} |\boldsymbol{\mu}^e|^2 \int_{-\infty}^{+\infty} \mathrm{d}t\, \chi(t)\, e^{i(\omega_{\text{ad}}-\omega)t} \tag{4.105}$$

By definition, the rate constant is equal to the overall cross section $\sigma_{\text{em}}^{\text{tot}}$, which is given by the integral of $\sigma_{\text{em}}(\omega)$ over all the possible frequencies, thus,

$$k^{\text{F}} = \sigma_{\text{em}}^{\text{tot}} = \int \sigma_{\text{em}}(\omega)\, d\omega \tag{4.106}$$

Also in this case, the extension of the previous equation to support HT terms is trivial and can be done following the same strategy presented for one-photon spectroscopies.
The last type of non-adiabatic effect studied here is internal conversion (IC), thus non-radiative transitions induced by non-adiabatic couplings given in Eq. 2.5. The cross matrix element of the term in the molecular Hamiltonian associated to the non-adiabatic effects, reported in Eq. 4.107, between two molecular states $\overline{\phi} \times \overline{\psi}_n$ and $\overline{\overline{\phi}} \times \overline{\overline{\psi}}_m$, can be expressed as,[293]

$$\begin{aligned}
\langle\, \overline{\phi}\,\overline{\psi}_i \mid \mathcal{H}_{\text{NAC}} \mid \overline{\overline{\phi}}\,\overline{\overline{\psi}}_f \,\rangle &= -\hbar^2 \sum_{k=1}^{N_{\text{vib}}} \langle\, \overline{\phi}\,\overline{\psi}_i \mid \frac{\partial \overline{\overline{\phi}}}{\partial \overline{\overline{Q}}_k} \frac{\partial \overline{\overline{\psi}}_f}{\partial \overline{\overline{Q}}_k} \,\rangle \\
&= -\hbar^2 \sum_{k=1}^{N_{\text{vib}}} \langle\, \overline{\psi}_i \mid \langle\, \overline{\phi} \mid \frac{\partial \overline{\overline{\phi}}}{\partial \overline{\overline{Q}}_k} \,\rangle \frac{\partial}{\partial \overline{\overline{Q}}_k} \mid \overline{\overline{\psi}}_f \,\rangle \\
&= \sum_{k=1}^{N_{\text{vib}}} \langle\, \overline{\psi}_i \mid \langle\, \overline{\phi} \mid \overline{\overline{\mathcal{P}}}_k \mid \overline{\overline{\phi}} \,\rangle \overline{\overline{\mathcal{P}}}_k \mid \overline{\overline{\psi}}_f \,\rangle
\end{aligned} \tag{4.107}$$

where $\overline{\overline{\mathcal{P}}}_k$ is the momentum operator associated to the k-th mode of the final state. We define the vector of the electronic non-adiabatic coupling $\boldsymbol{\Gamma}$ as,

$$\Gamma_k(\boldsymbol{Q}) = \langle\, \overline{\phi} \mid \overline{\overline{\mathcal{P}}}_k \mid \overline{\overline{\phi}} \,\rangle \tag{4.108}$$

where the elements of $\boldsymbol{\Gamma}$ depend on the nuclear displacement $\boldsymbol{Q}$ through the wavefunctions $\overline{\phi}$ and $\overline{\overline{\phi}}$. As in the previous case, at the FC level, $\boldsymbol{\Gamma}$ can be approximated as a constant equal to its value at the equilibrium position $\boldsymbol{\Gamma}(\boldsymbol{Q}^{\text{eq}})$ and, under those approximations, Eq. 4.107 can be rewritten as,

$$\langle\, \overline{\phi}\,\overline{\psi}_i \mid \mathcal{H}_{\text{NAC}} \mid \overline{\overline{\phi}}\,\overline{\overline{\psi}}_f \,\rangle = \sum_{k=1}^{N_{\text{vib}}} \Gamma_k(\boldsymbol{Q}^{\text{eq}}) \langle\, \overline{\psi}_i \mid \overline{\overline{\mathcal{P}}}_k \mid \overline{\overline{\psi}}_f \,\rangle \tag{4.109}$$

Eq. 4.109 already highlights the peculiarity of the TD formulation of IC with respect to the previous approaches. Indeed, the matrix elements of the perturbation, even at the FC level, are not proportional to the FC integrals between the vibrational wavefunctions involved in the transition, but is determined by the expectation value of the momentum operator $\overline{\overline{\mathcal{P}}}_k$. Integrals involving the momentum operator have never been encountered up to this point, and thus a generalization of the TD framework is needed. To derive the TD expression for the rate of internal conversion k_{IC}, the starting point is, as previously, the Fermi Golden Rule with $\mathcal{H}_{\text{NAC}}$ as a perturbation,

$$k^{\mathrm{IC}} = \frac{2\pi}{Z\hbar} \sum_{i,f} \left| \langle\, \overline{\phi}\, \overline{\psi}_i \mid \mathcal{H}_{\mathrm{NAC}} \mid \overline{\overline{\phi}}\, \overline{\overline{\psi}}_f \,\rangle \right|^2 e^{-\beta \overline{E}_i} \delta \left(\left| \overline{\overline{E}}_f - \breve{\overline{E}}_i \right| + E_{\mathrm{ad}} \right) \tag{4.110}$$

By combining the previous equation with the FC approximation of the non-adiabatic couplings given in Eq. 4.109, the following result is obtained,

$$k^{\mathrm{IC}} = \sum_{k,l=1}^{N_{\mathrm{vib}}} k^{\mathrm{IC}}_{k,l} \tag{4.111}$$

where $k^{\mathrm{IC}}_{k,l}$ is the contribution of the k-th and h-th modes to the overall IC rate, which can be expressed in a sum-over-states form as,

$$k^{\mathrm{IC}}_{k,l} = \frac{2\pi}{\hbar\, Z}\, \Gamma^e_{kl} \sum_{i,f} e^{-\beta \overline{E}_i} \langle\, \overline{\psi}_i \mid \overline{\overline{\mathcal{P}}}_k \mid \overline{\psi}_i \,\rangle \langle\, \overline{\psi}_i \mid \overline{\overline{\mathcal{P}}}_l \mid \overline{\overline{\psi}}_f \,\rangle \delta \left(\left| \overline{\overline{E}}_f - \overline{E}_i \right| - E_{\mathrm{ad}} \right) \tag{4.112}$$

The $\mathbf{\Gamma}e$ matrix has, as entries, the product of the electronic part of the non-adiabatic coupling,

$$\Gamma^e_{kh} = \langle\, \overline{\phi} \mid \overline{\overline{\mathcal{P}}}_k \mid \overline{\overline{\phi}} \,\rangle \langle\, \overline{\phi} \mid \overline{\overline{\mathcal{P}}}_h \mid \overline{\overline{\phi}} \,\rangle \tag{4.113}$$

Starting from Eq. 4.112, a TD formulation of $k^{k,h}_{\mathrm{IC}}$ can be obtained. Following the same procedure presented above for one-photon spectroscopies, the rate constant can be expressed as,[293,309]

$$k^{\mathrm{IC}}_{kl}(t) = \frac{\Gamma^e_{kl}}{Z} \int_{-\infty}^{+\infty} dt\, e^{iE_{\mathrm{ad}}t}\, \chi^{\mathrm{IC}}_{kl}(t) \tag{4.114}$$

where the time-dependent correlation function $\chi^{\mathrm{IC}}_{kl}(t)$ is defined as,

$$\chi^{\mathrm{IC}}_{kl} = \int_{-\infty}^{+\infty} d\overline{\boldsymbol{Q}} \langle\, \overline{\boldsymbol{Q}} \mid \overline{\overline{\mathcal{P}}}_k e^{-\overline{\overline{\tau}}\, \overline{\overline{\mathcal{H}}}} \overline{\overline{\mathcal{P}}}_l e^{-\overline{\tau}\, \overline{\mathcal{H}}} \mid \overline{\boldsymbol{Q}} \,\rangle \tag{4.115}$$

The closure relations given in Eq. 4.67 can then be employed together with the expression for the propagator for an harmonic oscillator reported in Eq. 4.70 to express the previous integral as,

$$\begin{aligned}
\chi^{\mathrm{IC}}_{kl}(t) = &- \sqrt{\frac{\det(\overline{\boldsymbol{a}}\, \overline{\overline{\boldsymbol{a}}})}{(2\pi i\hbar)^{2N}}} \int d\overline{\overline{\boldsymbol{Q}}} \int d\overline{\overline{\boldsymbol{Q}}}' \\
&\times \frac{\partial}{\partial \overline{\overline{Q}}_k} \exp\left(\frac{i}{\hbar} \left[\frac{1}{2} \overline{\overline{\boldsymbol{Q}}}^{\mathrm{T}}\, \overline{\overline{\boldsymbol{b}}}\, \overline{\overline{\boldsymbol{Q}}} + \frac{1}{2} \overline{\overline{\boldsymbol{Q}}}'^{\mathrm{T}}\, \overline{\overline{\boldsymbol{b}}}\, \overline{\overline{\boldsymbol{Q}}}' - \overline{\overline{\boldsymbol{Q}}}^{\mathrm{T}}\, \overline{\overline{\boldsymbol{a}}}\, \overline{\overline{\boldsymbol{Q}}}' \right] \right) \\
&\times \frac{\partial}{\partial \overline{\overline{Q}}'_l} \exp\left\{ \frac{i}{\hbar} \left[\frac{1}{2} \left(\boldsymbol{K}^{\mathrm{T}} + \overline{\overline{\boldsymbol{Q}}}'^{\mathrm{T}}\, \boldsymbol{J}^{\mathrm{T}} \right) \overline{\boldsymbol{b}} \left(\boldsymbol{J}\, \overline{\overline{\boldsymbol{Q}}}' + \boldsymbol{K} \right) \right.\right. \\
&\left.\left. + \frac{1}{2} \left(\boldsymbol{K}^{\mathrm{T}} + \overline{\overline{\boldsymbol{Q}}}^{\mathrm{T}}\, \boldsymbol{J}^{\mathrm{T}} \right) \overline{\boldsymbol{b}} \left(\boldsymbol{J}\, \overline{\overline{\boldsymbol{Q}}} + \boldsymbol{K} \right) - \left(\boldsymbol{K}^{\mathrm{T}} + \overline{\overline{\boldsymbol{Q}}}^{\mathrm{T}}\, \boldsymbol{J}^{\mathrm{T}} \right) \overline{\boldsymbol{a}} \left(\boldsymbol{J}\, \overline{\overline{\boldsymbol{Q}}}' + \boldsymbol{K} \right) \right] \right\}
\end{aligned} \tag{4.116}$$

$$= -\mathrm{Y}(t) \int d\overline{\overline{\boldsymbol{Q}}} \int d\overline{\overline{\boldsymbol{Q}}}' \frac{\partial}{\partial \overline{\overline{Q}}_k} \exp\left[\overline{f}\left(\overline{\overline{\boldsymbol{Q}}}, \overline{\overline{\boldsymbol{Q}}}'\right)\right] \frac{\partial}{\partial \overline{\overline{Q}}'_l} \exp\left[\overline{\overline{f}}\left(\overline{\overline{\boldsymbol{Q}}}, \overline{\overline{\boldsymbol{Q}}}'\right)\right]$$

where, for the sake of simplicity the exponents of the exponential have been collected in functions $\overline{f}\left(\overline{\overline{\boldsymbol{Q}}}, \overline{\overline{\boldsymbol{Q}}}'\right)$ and $\overline{\overline{f}}\left(\overline{\overline{\boldsymbol{Q}}}, \overline{\overline{\boldsymbol{Q}}}'\right)$. Using the derivative with respect to the l-th mode, the following result is obtained,

$$\chi^{\mathrm{IC}}_{kl}(t) = -\mathrm{Y}(t) \int d\overline{\overline{\boldsymbol{Q}}} \int d\overline{\overline{\boldsymbol{Q}}}' \frac{\partial}{\partial \overline{\overline{Q}}_k} \exp\left[\overline{f}\left(\overline{\overline{\boldsymbol{Q}}}, \overline{\overline{\boldsymbol{Q}}}'\right)\right] \gamma_l \exp\left[\overline{\overline{f}}\left(\overline{\overline{\boldsymbol{Q}}}, \overline{\overline{\boldsymbol{Q}}}'\right)\right] \tag{4.117}$$

with the scaling factor γ_l defined as,

$$\gamma_l = \left[\boldsymbol{J}^T\left(\overline{\boldsymbol{b}} - \overline{\boldsymbol{a}}\right)\boldsymbol{K} + \boldsymbol{J}^T\overline{\boldsymbol{b}}\boldsymbol{J}\overline{\overline{\boldsymbol{Q}}}' - \boldsymbol{J}^T\overline{\boldsymbol{a}}\boldsymbol{J}\overline{\overline{\boldsymbol{Q}}}\right]_l \tag{4.118}$$

where the l subscript means that the l-th component of the vector has to be taken. Further derivation with respect to the k-th mode will return three terms. Two of them correspond to the derivative of the exponential functions, whereas the third one is associated to the derivative of the scaling factor γ_l. The final result is the following,

$$\chi^{\mathrm{IC}}_{kl}(t) = -\mathrm{Y}(t) \int d\overline{\overline{\boldsymbol{Q}}} \int d\overline{\overline{\boldsymbol{Q}}}' \gamma_{l,k} \exp\left[\overline{f}\left(\overline{\overline{\boldsymbol{Q}}}, \overline{\overline{\boldsymbol{Q}}}'\right)\right] \exp\left[\overline{\overline{f}}\left(\overline{\overline{\boldsymbol{Q}}}, \overline{\overline{\boldsymbol{Q}}}'\right)\right] \tag{4.119}$$

where,

$$\gamma_{k,l} = \left[\gamma_k\gamma_l + \gamma_h\left(\overline{\overline{\boldsymbol{b}}}\,\overline{\overline{\boldsymbol{Q}}} - \overline{\overline{\boldsymbol{a}}}\,\overline{\overline{\boldsymbol{Q}}}'\right)_l - \left(\boldsymbol{J}^T\overline{\boldsymbol{a}}\boldsymbol{J}\right)_{lk}\right] \tag{4.120}$$

As expected, Eq. 4.120 contains powers of the position operator up to the second-order. This result had to be expected, since the initial formula contained two momentum operators. To obtain more compact relations, it is useful to introduce the following matrices;

$$\begin{aligned} \boldsymbol{E} &= \boldsymbol{b} - \boldsymbol{a} & \boldsymbol{a}_J &= \boldsymbol{J}^T\boldsymbol{a}\boldsymbol{J} \\ \boldsymbol{G} &= \boldsymbol{J}^T\boldsymbol{E}\boldsymbol{K} & \boldsymbol{b}_J &= \boldsymbol{J}^T\boldsymbol{b}\boldsymbol{J} \end{aligned} \tag{4.121}$$

which are defined for both initial and final electronic states. Using the definition of these matrices, Eq. 4.120 can be rewritten as,

$$\begin{aligned} \gamma_{l,k} = &-\left(\overline{a}_J\right)_{lk} + \left[G_l + \left(\overline{\boldsymbol{b}}_J\overline{\overline{\boldsymbol{Q}}}'\right)_l - \left(\overline{\boldsymbol{a}}_J\overline{\overline{\boldsymbol{Q}}}\right)_l\right] \\ &\times \left[G_k + \left(\overline{\boldsymbol{b}}_J\overline{\overline{\boldsymbol{Q}}}'\right)_k - \left(\overline{\boldsymbol{a}}_J\overline{\overline{\boldsymbol{Q}}}\right)_k + \left(\overline{\overline{\boldsymbol{b}}}\,\overline{\overline{\boldsymbol{Q}}} - \overline{\overline{\boldsymbol{a}}}\,\overline{\overline{\boldsymbol{Q}}}'\right)_k\right] \end{aligned} \tag{4.122}$$

By collecting the previous terms based on the power of the coordinates, the following result is obtained;

$$
\begin{aligned}
\gamma_{l,k} = & -\left(\overline{\boldsymbol{a}}_J\right)_{lk} + G_k\, G_l \\
& + G_l \left[\left(\overline{\overline{\boldsymbol{b}}} - \overline{\boldsymbol{a}}_J\right) \overline{\overline{\boldsymbol{Q}}}\right]_k - G_k \left(\overline{\boldsymbol{a}}_J \overline{\overline{\boldsymbol{Q}}}\right)_l \\
& + G_l \left[\left(\overline{\boldsymbol{b}}_J - \overline{\overline{\boldsymbol{a}}}\right) \overline{\overline{\boldsymbol{Q}}}'\right]_k - G_k \left(\overline{\boldsymbol{b}}_J \overline{\overline{\boldsymbol{Q}}}'\right)_l \\
& + \left[\left(\overline{\overline{\boldsymbol{b}}} - \overline{\boldsymbol{a}}_J\right) \overline{\overline{\boldsymbol{Q}}}\right]_k \left(\overline{\boldsymbol{a}}_J \overline{\overline{\boldsymbol{Q}}}\right)_l + \left[\left(\overline{\boldsymbol{b}}_J - \overline{\overline{\boldsymbol{a}}}\right) \overline{\overline{\boldsymbol{Q}}}'\right]_k \left(\overline{\boldsymbol{b}}_J \overline{\overline{\boldsymbol{Q}}}'\right)_l \\
& - \left[\left(\overline{\overline{\boldsymbol{b}}} - \overline{\boldsymbol{a}}_J\right) \overline{\overline{\boldsymbol{Q}}}\right]_k \left(\overline{\boldsymbol{b}}_J \overline{\overline{\boldsymbol{Q}}}'\right)_l - \left[\left(\overline{\boldsymbol{b}}_J - \overline{\overline{\boldsymbol{a}}}\right) \overline{\overline{\boldsymbol{Q}}}'\right]_k \left(\overline{\boldsymbol{a}}_J \overline{\overline{\boldsymbol{Q}}}\right)_l
\end{aligned}
\tag{4.123}
$$

Eq. 4.123 contains additional terms, which are not present in the transition dipole moment autocorrelation function of one-photon spectroscopies at the HT level. In Eq. 4.89, each second-order term involves the product of one component of $\overline{\overline{\boldsymbol{Q}}}$ and one component of $\overline{\overline{\boldsymbol{Q}}}'$. However, if Eq. 4.123 is used together with Eq. 4.116, terms depending on the second power of $\overline{\overline{\boldsymbol{Q}}}$ and on the second power of $\overline{\overline{\boldsymbol{Q}}}'$ also need to be computed. The evaluation of those terms requires the introduction of new correlation functions,

$$
\begin{aligned}
\chi^{lk}(t) &= \langle\, \overline{\mathbf{0}} \mid \overline{\overline{\mathcal{Q}}}_l \overline{\overline{\mathcal{Q}}}_k e^{-i\overline{\overline{\mathcal{H}}}\overline{\tau}} e^{-i\overline{\mathcal{H}}\tau} \mid \overline{\mathbf{0}} \,\rangle \\
\chi_{lk}(t) &= \langle\, \overline{\mathbf{0}} \mid e^{-i\overline{\overline{\mathcal{H}}}\overline{\tau}} \overline{\overline{\mathcal{Q}}}_l \overline{\overline{\mathcal{Q}}}_k e^{-i\overline{\mathcal{H}}\tau} \mid \overline{\mathbf{0}} \,\rangle
\end{aligned}
\tag{4.124}
$$

Following the same strategy as for OP spectroscopies, the two tensors defined in Eq. 4.124 can be expressed in terms of the $(\boldsymbol{Z}, \boldsymbol{U})$ set. Thanks to this transformation, the previous equations can be expressed as derivative of the FC time-dependent autocorrelation function $\chi(t)$ defined in Eq. 4.79, leading to the following relations,

$$
\chi^{lk}(t) = \chi_{lk}(t) = \chi(t) \left(2\eta_k \eta_l + \left(\boldsymbol{D}^{-1}\right)_{kl} - \left(\boldsymbol{C}^{-1}\right)_{kl}\right)
\tag{4.125}
$$

which is equivalent to Eq. 4.95, with the exception of the sign of the factor of $\left(\boldsymbol{C}^{-1}\right)_{kl}$. The definition of these additional tensors allows to express Eq. 4.116 in the following way,

$$
\begin{aligned}
\chi^{\mathrm{IC}}_{kl}(t) = & \; k^{\mathrm{NAC}}_{kl}\, \chi(t) + \sum_{i=1}^{N_{\mathrm{vib}}} k^{\mathrm{NAC}}_{kl,i} \chi_i(t) \\
& + \sum_{i,j=1}^{N_{\mathrm{vib}}} \left(k^{\mathrm{NAC}}_{kl,ij} \chi_{ij}(t) + k^{\mathrm{NAC}}_{kl,i,j} \chi^j_i(t) + k^{\mathrm{NAC}}_{kl,,ij} \chi^{i,j}(t)\right)
\end{aligned}
\tag{4.126}
$$

where the k^{NAC}_{kl} tensors are defined as,

$$
\begin{aligned}
k^{\mathrm{NAC}}_{kl} =& G_k G_l - \left(\overline{\boldsymbol{a}}_J\right)_{kl} \\
k^{\mathrm{NAC}}_{kl,i} =& G_l \left(\overline{\overline{\boldsymbol{b}}} + \overline{\boldsymbol{b}}_J - \overline{\boldsymbol{a}}_J - \overline{\overline{\boldsymbol{a}}}\right)_{li} - G_k \left(\overline{\boldsymbol{a}}_J + \overline{\boldsymbol{b}}_J\right)_{li} \\
=& G_l \left(\boldsymbol{B} - \boldsymbol{A}\right)_{ki} - G_k \left(\overline{\boldsymbol{a}}_J + \overline{\boldsymbol{b}}_J\right)_{li} \\
k^{\mathrm{NAC}}_{kl,ij} =& \sum_{i=1}^{N_{\mathrm{vib}}} \left(\overline{\overline{\boldsymbol{b}}} - \overline{\boldsymbol{a}}_J\right)_{ki} \times \sum_{i=1}^{N_{\mathrm{vib}}} \left(\overline{\boldsymbol{a}}_J\right)_{li} \\
k^{\mathrm{NAC}}_{kl,,ij} =& \sum_{i=1}^{N_{\mathrm{vib}}} \left(\overline{\boldsymbol{b}}_J - \overline{\overline{\boldsymbol{a}}}\right)_{ki} \times \sum_{i=1}^{N_{\mathrm{vib}}} \left(\overline{\boldsymbol{b}}_J\right)_{li} \\
k^{\mathrm{NAC}}_{kl,i,j} =& - \sum_{i=1}^{N_{\mathrm{vib}}} \left(\overline{\overline{\boldsymbol{b}}} - \overline{\boldsymbol{a}}_J\right)_{ki} \times \sum_{i=1}^{N_{\mathrm{vib}}} \left(\overline{\boldsymbol{b}}_J\right)_{li} \\
& - \sum_{i=1}^{N_{\mathrm{vib}}} \left(\overline{\boldsymbol{b}}_J - \overline{\overline{\boldsymbol{a}}}\right)_{ki} \times \sum_{i=1}^{N_{\mathrm{vib}}} \left(\overline{\boldsymbol{a}}_J\right)_{li}
\end{aligned}
\tag{4.127}
$$

Those relations, together with Eq. 4.114, allow to compute the correlation function χ^{IC}_{kl} at any time t, and then the rate constant k^{IC} through a numerical evaluation of the Fourier transform. As for the ISC case, a complete Fourier transform of the correlation function is not needed, since the integral only needs to be known at the frequency corresponding to $\omega = E_{\mathrm{ad}}/\hbar$. This makes the calculation of the Fourier integral faster than for one-photon spectroscopies.

4.6.2 Interconversion rates: a diabatic representation

For all the three phenomena treated above, the adiabatic representation of the molecular Hamiltonian was taken as reference, and the terms responsible for transitions between molecular states of two different electronic states, were introduced through first-order perturbation theory. However, as noted above, non-adiabatic effects can become large in several cases, such as for closely spaced electronic states. In those cases, a quasi-diabatic representation, where non-adiabatic effects are minimized, is better suited to perform the simulations.
As already reported in the previous section, for two electronic state, the diabatic representation of the molecular Hamiltonian can be defined as,

$$
\mathcal{H}^{\mathrm{ve}} = \begin{pmatrix} \overline{\mathcal{T}} & 0 \\ 0 & \overline{\overline{\mathcal{T}}} \end{pmatrix} + \begin{pmatrix} \overline{\mathcal{V}}^{\mathrm{dia}} & \mathcal{V}^{\mathrm{dia}}_{\mathrm{c}} \\ \mathcal{V}^{\mathrm{dia}}_{\mathrm{c}} & \overline{\overline{\mathcal{V}}}^{\mathrm{dia}} \end{pmatrix}
\tag{4.128}
$$

where the Hamiltonian given in Eq. 4.128 is obtained from the adiabatic one after an unitary transformation, parametrized through a rotation angle θ, of the adiabatic electronic states, as already discussed in Chapter 2. For the sake of coherence with the notation used for one-photon spectroscopies, quantities relative to the initial state have been denoted with a single overbar, and those of the final electronic state with a double overbar. In the following

derivation, the Hamiltonian will be partitioned in a reference part $\mathcal{H}^{(0)}$ and a perturbation part $\Delta\mathcal{H}$,

$$\mathcal{H}^{\text{ve}} = \underbrace{\begin{pmatrix} \overline{\mathcal{T}} & 0 \\ 0 & \overline{\overline{\mathcal{T}}} \end{pmatrix} + \begin{pmatrix} \overline{\mathcal{V}}^{\text{dia}} & 0 \\ 0 & \overline{\overline{\mathcal{V}}}^{\text{dia}} \end{pmatrix}}_{=\mathcal{H}^{(0)}} + \underbrace{\begin{pmatrix} 0 & \mathcal{V}_{\text{c}}^{\text{dia}} \\ \mathcal{V}_{\text{c}}^{\text{dia}} & 0 \end{pmatrix}}_{=\Delta\mathcal{H}} \tag{4.129}$$

The rotation angle θ, giving the transformation from the adiabatic to the diabatic representation, is related to the ratio between the off-diagonal and diagonal parts of the potential operator of the Hamiltonian given in Eq. 4.128 as,[310]

$$2\theta\left(\boldsymbol{Q}\right) = \arctan\left(\frac{2\mathcal{V}_{\text{c}}^{\text{dia}}\left(\boldsymbol{Q}\right)}{\overline{\mathcal{V}}^{\text{dia}}\left(\boldsymbol{Q}\right) + \overline{\overline{\mathcal{V}}}^{\text{dia}}\left(\boldsymbol{Q}\right)}\right) \tag{4.130}$$

The inverse relations of the previous equation, expressing the diagonal and off-diagonal parts of the potential operator in the diabatic representation in terms of the rotation angle $\theta\left(\boldsymbol{Q}\right)$, are the following,

$$\begin{aligned} \overline{\mathcal{V}}^{\text{dia}}\left(\boldsymbol{Q}\right) &= \cos^2\theta\left(\boldsymbol{Q}\right)\overline{\mathcal{V}}^{\text{adia}}\left(\boldsymbol{Q}\right) + \sin^2\theta\left(\boldsymbol{Q}\right)\overline{\overline{\mathcal{V}}}^{\text{adia}}\left(\boldsymbol{Q}\right) \\ \overline{\overline{\mathcal{V}}}^{\text{dia}}\left(\boldsymbol{Q}\right) &= \sin^2\theta\left(\boldsymbol{Q}\right)\overline{\mathcal{V}}^{\text{adia}}\left(\boldsymbol{Q}\right) + \cos^2\theta\left(\boldsymbol{Q}\right)\overline{\overline{\mathcal{V}}}^{\text{adia}}\left(\boldsymbol{Q}\right) \\ \mathcal{V}_{\text{c}}^{\text{dia}}\left(\boldsymbol{Q}\right) &= \cos\theta\left(\boldsymbol{Q}\right)\sin\theta\left(\boldsymbol{Q}\right)\Delta E \end{aligned} \tag{4.131}$$

where $\overline{\mathcal{V}}^{\text{adia}}$ and $\overline{\overline{\mathcal{V}}}^{\text{adia}}$ are the potential operators of the adiabatic states and ΔE is their energetic separation $\left(\overline{\mathcal{V}}^{\text{adia}}\left(\boldsymbol{Q}\right) - \overline{\overline{\mathcal{V}}}^{\text{adia}}\left(\boldsymbol{Q}\right)\right)$. From now on, for the sake of readability, the dependence of $\mathcal{V}$ and θ on the nuclear coordinates $(\boldsymbol{Q})$ will not be explicitly noted and implicitly assumed.

The diagonal part of the Hamiltonian can be approximated through a second-order Taylor expansion in terms of the nuclear coordinates $\boldsymbol{Q}$, as in the adiabatic case. Thanks to this choice, the reference Hamiltonian $\mathcal{H}^{(0)}$ is an harmonic oscillator Hamiltonian, where however the frequencies changes with the rotation angle $\theta\left(\boldsymbol{Q}\right)$. Several ways of approximating the off-diagonal part $\mathcal{V}_{\text{c}}^{\text{dia}}\left(\boldsymbol{Q}\right)$ have been proposed. In the simplest approximation, corresponding to a FC-like model, this coupling is assumed to be constant.[307] As in the HT model, first-order terms can be included in the Taylor expansion, which corresponds to the widely used linear-coupling model (LCM).[94,311]. However, it has been shown that, in several cases, terms up to the second-order must be included in the treatment to correctly reproduce non-adiabatic effects.[95,312] If $\mathcal{V}_{\text{c}}^{\text{dia}}\left(\boldsymbol{Q}\right)$ is expanded as a second-order Taylor series, the so-called quadratic vibronic coupling (QVC) model is obtained.

The first- and second-order terms of the Taylor expansion of the diabatic potential (both the diagonal and off-diagonal parts), which are the parameters defining the QVC model, can be related to the corresponding quantities in the adiabatic representation by direct differentiation of the three relations given in Eq. 4.131 with respect to the nuclear coordinates. The following final results are obtained,

$$\left(\frac{\partial\overline{\mathcal{V}}^{\text{dia}}}{\partial Q_i}\right) = -\sin 2\theta \left(\frac{\partial\theta}{\partial Q_i}\right)\Delta E + \cos^2\theta\left(\frac{\partial\overline{\overline{\mathcal{V}}}^{\text{adia}}}{\partial Q_i}\right) + \sin^2\theta\left(\frac{\partial\overline{\mathcal{V}}^{\text{adia}}}{\partial Q_i}\right)$$

$$\begin{aligned}\left(\frac{\partial^2\overline{\mathcal{V}}^{\text{dia}}}{\partial Q_i\partial Q_j}\right) &= -2\cos 2\theta\left(\frac{\partial\theta}{\partial Q_i}\right)\left(\frac{\partial\theta}{\partial Q_j}\right)\Delta E \\ &\quad - \sin 2\theta\left[\left(\frac{\partial\theta}{\partial Q_i}\right)\left(\frac{\partial\Delta E}{\partial Q_j}\right) + \left(\frac{\partial\theta}{\partial Q_j}\right)\left(\frac{\partial\Delta E}{\partial Q_i}\right)\right] \\ &\quad + \cos^2\theta\left(\frac{\partial^2\overline{\mathcal{V}}^{\text{adia}}}{\partial Q_i\partial Q_j}\right) + \sin^2\theta\left(\frac{\partial^2\overline{\overline{\mathcal{V}}}^{\text{adia}}}{\partial Q_i\partial Q_j}\right)\end{aligned} \tag{4.132}$$

A similar relation is obtained for the derivatives of the final state $\overline{\overline{\mathcal{V}}}^{\text{dia}}$ starting from Eq. 4.132 by interchanging $\overline{\mathcal{V}}^{\text{adia}}$ and $\overline{\overline{\mathcal{V}}}^{\text{adia}}$. The following relation can be derived for the first-order derivative of $\mathcal{V}_{\text{c}}^{\text{dia}}$:

$$\left(\frac{\partial\mathcal{V}_{\text{c}}^{\text{dia}}}{\partial Q_i}\right) = \cos 2\theta\left(\frac{\partial\theta}{\partial Q_i}\right)\Delta E + \frac{1}{2}\sin 2\theta\left(\frac{\partial\Delta E}{\partial Q_i}\right) \tag{4.133}$$

and, for the second derivatives,

$$\begin{aligned}\left(\frac{\partial^2\mathcal{V}_{\text{c}}^{\text{dia}}}{\partial Q_i\partial Q_j}\right) &= -2\sin 2\theta\left(\frac{\partial\theta}{\partial Q_i}\right)\left(\frac{\partial\theta}{\partial Q_j}\right)\Delta E + \cos 2\theta\left(\frac{\partial^2\theta}{\partial Q_i\partial Q_j}\right) \\ &\quad + \cos 2\theta\left(\frac{\partial\theta}{\partial Q_i}\right)\left(\frac{\partial\Delta E}{\partial Q_j}\right) + \cos 2\theta\left(\frac{\partial\Delta E}{\partial Q_i}\right)\left(\frac{\partial\theta}{\partial Q_j}\right) + \frac{1}{2}\sin 2\theta\left(\frac{\partial^2\Delta E}{\partial Q_i\partial Q_j}\right)\end{aligned} \tag{4.134}$$

Up to this point, no assumptions on the vibronic model employed in the simulation have been made in the derivation of Eqs. 4.132, 4.133 and 4.134. However, the expansion of the potential energy surface (PES) is usually performed about the stationary point of at least one of the two adiabatic PESs, thus the gradient of this reference PES is null. For this reason, the gradient of ΔE coincides with the gradient of one of the two PESs. A further simplification of the previous equations is obtained within the so-called weak coupling limit.[313] The weak coupling limit is obtained from our formulation by neglecting mode-mixing effects, as well as the terms proportional to the gradient of ΔE. Under those assumptions, Eq. 4.132 becomes,

$$\left(\frac{\partial^2\overline{\mathcal{V}}^{\text{dia}}}{\partial Q_i\partial Q_j}\right) = 2\cos 2\theta\left(\frac{\partial\theta}{\partial Q_i}\right)\left(\frac{\partial\theta}{\partial Q_j}\right)\Delta E + \cos^2\theta\left(\frac{\partial^2\overline{\mathcal{V}}^{\text{adia}}}{\partial Q_i\partial Q_j}\right) \tag{4.135}$$

Taking the diagonal part of the previous equation and using Eq. 4.133, the final result is obtained,

$$(\omega_i^{\text{dia}})^2 = (\omega_i^{\text{adia}})^2 + \frac{1}{\Delta E}\left(\frac{\partial \mathcal{V}_c^{\text{dia}}}{\partial Q_i}\right)^2 \tag{4.136}$$

which is equivalent to the relation employed in Ref. 313 for the weak coupling regime.

The previous derivation is not sufficient to compute the derivative of the diabatic couplings $\mathcal{V}_c^{\text{dia}}$, since the derivatives of the angle θ have no formal definition. Those quantities are commonly computed numerically,[314] by finite differentiation. The main advantage of numerical approaches is their generality, since they can be applied to any diabatization scheme. Their main drawback is the dependence of the results (*i.e.* their accuracy and their stability) on the grid used for the numerical differentiation. This issue is solved with analytical approaches, where the derivatives are computed at a single reference geometry, using closed-form expressions. Analytical approaches cannot be applied to all diabatization schemes, and those, for which this analytical derivation is possible are particularly appealing for vibronic calculations. As already remarked in Chapter 2, in this thesis the DQΦ method[149,315] will be employed, for which analytical expressions for the derivatives of the off-diagonal diabatic couplings $\mathcal{V}_c^{\text{dia}}$ can be easily determined in terms of the derivatives of three quantities, the dipole- and quadrupole moments and the electrostatic potential. Those derivatives are readily available for most electronic structure methods,[32,316,317] thus the derivatives of the diabatic potential can be obtained with a limited computational cost.

The starting point for our derivation is Eq. 4.133, which relates the derivatives of the diabatic potential $\left(\frac{\partial \mathcal{V}_c^{\text{dia}}}{\partial Q_i}\right)$ to the gradient of the adiabatic PESs, available from electronic structure calculations, and to the derivative of the angle θ with respect to the normal modes. A closed-form expression for the latter can be obtained by direct differentiation of Eq. 2.65:

$$\frac{\partial \theta}{\partial Q_i} = \frac{B\frac{\partial A}{\partial Q_i} - A\frac{\partial B}{\partial Q_i}}{(A^2+B^2)^2} \tag{4.137}$$

where A and B are defined in Eqs. 2.64 and 2.63, respectively. Analytical expressions for the first-order derivatives of A and B with respect to the normal coordinates can, in turn, be obtained from the first-order derivatives of the dipole and quadrupole moments, by direct differentiation of Eqs. 2.63 and 2.64. Assuming that only the electric dipole contributes to A and B, *i.e.*, $\alpha = 0$ and $\beta = 0$, the first derivatives are,

$$\begin{aligned}
\frac{\partial A}{\partial Q_i} &= -\frac{1}{2}\left(\overline{\boldsymbol{\mu}}\frac{\partial \overline{\boldsymbol{\mu}}}{\partial Q_i} + \overline{\overline{\boldsymbol{\mu}}}\frac{\partial \overline{\overline{\boldsymbol{\mu}}}}{\partial Q_i} + 4\boldsymbol{\mu}_c\frac{\partial \boldsymbol{\mu}_c}{\partial Q_i} + \overline{\boldsymbol{\mu}}\frac{\partial \overline{\overline{\boldsymbol{\mu}}}}{\partial Q_i} + \overline{\overline{\boldsymbol{\mu}}}\frac{\partial \overline{\boldsymbol{\mu}}}{\partial Q_i}\right) \\
\frac{\partial B}{\partial Q_i} &= \boldsymbol{\mu}_c \cdot \left(\frac{\partial \overline{\boldsymbol{\mu}}}{\partial Q_i} - \frac{\partial \overline{\overline{\boldsymbol{\mu}}}}{\partial Q_i}\right) + \frac{\partial \boldsymbol{\mu}_c}{\partial Q_i} \cdot \left(\overline{\boldsymbol{\mu}} - \overline{\overline{\boldsymbol{\mu}}}\right)
\end{aligned} \tag{4.138}$$

The generalization of the previous equation to support the quadrupole moments and electrostatic potential is straightforward. The same procedure can

be applied also to second-order derivatives, in order to support QVC models, provided that the second derivatives of the properties are also available.

$$\begin{aligned}\frac{\partial^2\theta}{\partial Q_i\partial Q_j} =& \frac{1}{A^2+B^2}\left[\left(\frac{\partial B}{\partial Q_j}\right)\left(\frac{\partial A}{\partial Q_i}\right)-\left(\frac{\partial B}{\partial Q_i}\right)\left(\frac{\partial A}{\partial Q_j}\right)\right.\\ &\left.+B\left(\frac{\partial^2 A}{\partial Q_i\partial Q_j}\right)-A\left(\frac{\partial^2 B}{\partial Q_i\partial Q_j}\right)\right]\\ &-\frac{1}{\left(A^2+B^2\right)^2}\left(2A\frac{\partial A}{\partial Q_j}+2B\frac{\partial B}{\partial Q_j}\right)\times\left(B\frac{\partial A}{\partial Q_j}-A\frac{\partial B}{\partial Q_j}\right)\end{aligned} \tag{4.139}$$

The theoretical derivation presented up to this point is enough to determine all the parameters of the diabatic Hamiltonian introduced in Eq. 4.128. The internal conversion rate, which is related to the off-diagonal diabatic couplings (see the partition of the Hamiltonian presented in Eq. 4.129), can be computed in the same way as the ISC and IC rates in the adiabatic representation. Thus, the IC rate constant is computed as,

$$k^{\mathrm{IC,dia}} = \frac{1}{Z}\int_{-\infty}^{+\infty} \mathrm{d}t\, e^{iE_{\mathrm{ad}}t}\,\mathrm{Tr}\left(\mathcal{V}_{\mathrm{c}}^{\mathrm{dia}} e^{-\overline{\overline{\tau}}\,\overline{\overline{\mathcal{H}}}}\mathcal{V}_{\mathrm{c}}^{\mathrm{dia}} e^{-\overline{\tau}\,\overline{\mathcal{H}}}\right) \tag{4.140}$$

Since $\mathcal{V}_{\mathrm{c}}^{\mathrm{dia}}$ is a function of the position operator like the transition dipole moment, Eq. 4.140 can be evaluated in the same way as for the radiative decay. However, as mentioned above, in the most complete QVC model, second derivatives of the diabatic coupling $\mathcal{V}_{\mathrm{c}}^{\mathrm{dia}}$ are needed too, and the treatment of such terms within the TD framework has not been described yet. However, thanks to the flexibility of our methodology, those terms can be easily computed as well. The additional contribution to the time-dependent correlation, collected here in the $\chi^{\mathrm{dia}}(t)$ function, is the following,

$$\begin{aligned}\chi^{\mathrm{dia}}(t) = \int_{-\infty}^{+\infty} d\boldsymbol{Q}\Bigg[&\frac{1}{2}\sum_{j,k=1}^{N_{\mathrm{vib}}}\mathcal{V}_c^{\mathrm{dia}}\left(\boldsymbol{Q}^{\mathrm{eq}}\right)\left(\frac{\partial^2\mathcal{V}_c^{\mathrm{dia}}}{\partial\overline{\overline{Q}}_j\partial\overline{\overline{Q}}_k}\right)\left\langle\,\overline{\boldsymbol{Q}}\,\middle|\, e^{-\overline{\overline{\tau}}\,\overline{\overline{\mathcal{H}}}}\overline{\overline{Q}}_j\overline{\overline{Q}}_k e^{-\overline{\tau}\,\overline{\mathcal{H}}}\,\middle|\,\overline{\boldsymbol{Q}}\,\right\rangle\\ &+\frac{1}{2}\sum_{j,k=1}^{N_{\mathrm{vib}}}\left(\frac{\partial^2\mathcal{V}_c^{\mathrm{dia}}}{\partial\overline{\overline{Q}}_j\partial\overline{\overline{Q}}_k}\right)\mathcal{V}_c^{\mathrm{dia}}\left(\boldsymbol{Q}^{\mathrm{eq}}\right)\left\langle\,\overline{\boldsymbol{Q}}\,\middle|\,\overline{\overline{Q}}_j\overline{\overline{Q}}_k e^{-\overline{\overline{\tau}}\,\overline{\overline{\mathcal{H}}}}e^{-\overline{\tau}\,\overline{\mathcal{H}}}\,\middle|\,\overline{\boldsymbol{Q}}\,\right\rangle\\ &+\frac{1}{2}\sum_{jkl=1}^{N_{\mathrm{vib}}}\left(\frac{\partial\mathcal{V}_c^{\mathrm{dia}}}{\partial\overline{\overline{Q}}_j}\right)\left(\frac{\partial^2\mathcal{V}_c^{\mathrm{dia}}}{\partial\overline{\overline{Q}}_k\partial\overline{\overline{Q}}_l}\right)\left\langle\,\overline{\boldsymbol{Q}}\,\middle|\,\overline{\overline{Q}}_j e^{-\overline{\overline{\tau}}\,\overline{\overline{\mathcal{H}}}}\overline{\overline{Q}}_k\overline{\overline{Q}}_l e^{-\overline{\tau}\,\overline{\mathcal{H}}}\,\middle|\,\overline{\boldsymbol{Q}}\,\right\rangle\\ &+\frac{1}{2}\sum_{jkl=1}^{N_{\mathrm{vib}}}\left(\frac{\partial^2\mathcal{V}_c^{\mathrm{dia}}}{\partial\overline{\overline{Q}}_j\partial\overline{\overline{Q}}_k}\right)\left(\frac{\partial\mathcal{V}_c^{\mathrm{dia}}}{\partial\overline{\overline{Q}}_l}\right)\left\langle\,\overline{\boldsymbol{Q}}\,\middle|\,\overline{\overline{Q}}_j\overline{\overline{Q}}_k e^{-\overline{\overline{\tau}}\,\overline{\overline{\mathcal{H}}}}\overline{\overline{Q}}_l e^{-\overline{\tau}\,\overline{\mathcal{H}}}\,\middle|\,\overline{\boldsymbol{Q}}\,\right\rangle\\ &+\frac{1}{4}\sum_{jklm=1}^{N_{\mathrm{vib}}}\left(\frac{\partial^2\mathcal{V}_c^{\mathrm{dia}}}{\partial\overline{\overline{Q}}_j\partial\overline{\overline{Q}}_k}\right)\left(\frac{\partial^2\mathcal{V}_c^{\mathrm{dia}}}{\partial\overline{\overline{Q}}_l\partial\overline{\overline{Q}}_m}\right)\left\langle\,\overline{\boldsymbol{Q}}\,\middle|\,\overline{\overline{Q}}_j\overline{\overline{Q}}_k e^{-\overline{\overline{\tau}}\,\overline{\overline{\mathcal{H}}}}\overline{\overline{Q}}_l\overline{\overline{Q}}_m e^{-\overline{\tau}\,\overline{\mathcal{H}}}\,\middle|\,\overline{\boldsymbol{Q}}\,\right\rangle\Bigg]\end{aligned} \tag{4.141}$$

The first two terms have been derived within the TD framework for the IC rate constants. The other three terms (that, following the notation introduced in Eq. 4.66, are $\chi_j^{kl}(t)$, $\chi_{jk}^{l}(t)$ and $\chi_{jk}^{lm}(t)$, contain three and four different position operators, which need to be derived. The formulas become more cumbersome and difficult to treat, but all those matrix elements can be obtained as successive derivatives of the FC autocorrelation function $\chi(t)$ with respect to the elements of the matrix $\boldsymbol{C}$ and the vector $\boldsymbol{v}$ as,

$$\begin{aligned}
\chi_j^{kl}(t) =& -\frac{\partial^2\chi(t)}{\partial C_{kj}\partial v_l} - \frac{\partial^2\chi(t)}{\partial C_{lj}\partial v_k} + \frac{\partial^2\chi(t)}{\partial C_{kl}\partial v_j} - \frac{1}{4}\frac{\partial^3\chi(t)}{\partial v_k\partial v_l\partial v_j} \\
\chi_{jk}^{l}(t) =& -\frac{\partial^2\chi(t)}{\partial C_{kj}\partial v_l} + \frac{\partial^2\chi(t)}{\partial C_{lj}\partial v_k} + \frac{\partial^2\chi(t)}{\partial C_{kl}\partial v_j} - \frac{1}{4}\frac{\partial^3\chi(t)}{\partial v_k\partial v_l\partial v_j} \\
\chi_{jk}^{lm}(t) =& -\frac{\partial^2\chi(t)}{\partial C_{kl}\partial C_{mj}} - \frac{1}{4}\frac{\partial^3\chi(t)}{\partial C_{kl}\partial v_j\partial v_m} + \frac{1}{4}\frac{\partial^3\chi(t)}{\partial C_{kj}\partial v_l\partial v_m} + \frac{1}{4}\frac{\partial^3\chi(t)}{\partial C_{lj}\partial v_k\partial v_m} \\
&+ \frac{1}{4}\frac{\partial^3\chi(t)}{\partial C_{km}\partial v_l\partial v_j} + \frac{1}{4}\frac{\partial^3\chi(t)}{\partial C_{lm}\partial v_k\partial v_j} - \frac{1}{4}\frac{\partial^3\chi(t)}{\partial C_{jm}\partial v_k\partial v_l} \\
&+ \frac{1}{16}\frac{\partial^4\chi(t)}{\partial v_k\partial v_l\partial v_m\partial v_j}
\end{aligned} \tag{4.142}$$

By exploiting, as done before, the simple properties of the derivative of an exponential function, it is possible to obtain analytic expression also for the higher order derivatives present in Eq. 4.142. The result are all reported in the following equation:

$$\begin{aligned}
\frac{\partial^2\chi(t)}{\partial C_{kl}\partial v_j} =& -\frac{1}{2}\chi(t)\left(\boldsymbol{C}^{-1}\right)_{kl}\eta_j \\
\frac{\partial^3\chi(t)}{\partial C_{kl}\partial v_j\partial v_m} =& -\frac{1}{2}\chi(t)\left(\boldsymbol{C}^{-1}\right)_{kl}\left[\left(\boldsymbol{D}^{-1}\right)_{jm} + \left(\boldsymbol{D}^{-1}\right)_{mj} + \eta_j\eta_m\right] \\
\frac{\partial^2\chi(t)}{\partial C_{kl}\partial C_{jm}} =& -\frac{1}{2}\chi(t)\left[\left(\boldsymbol{C}^{-1}\right)_{lk}\left(\boldsymbol{C}^{-1}\right)_{mj} - \left(\boldsymbol{C}^{-1}\right)_{mk}\left(\boldsymbol{C}^{-1}\right)_{lj}\right] \\
\frac{\partial^3\chi(t)}{\partial v_k\partial v_l\partial v_j} =& \chi(t)\left[\left(\left(\boldsymbol{D}^{-1}\right)_{jk} + \left(\boldsymbol{D}^{-1}\right)_{kj}\right)\eta_l + \left(\left(\boldsymbol{D}^{-1}\right)_{jl} + \left(\boldsymbol{D}^{-1}\right)_{lj}\right)\eta_k\right. \\
&\left. + \left(\left(\boldsymbol{D}^{-1}\right)_{kl} + \left(\boldsymbol{D}^{-1}\right)_{lk}\right)\eta_j + \eta_l\eta_k\eta_j\right]
\end{aligned} \tag{4.143}$$

$$
\begin{aligned}
\frac{\partial^4 \chi(t)}{\partial v_k \partial v_l \partial v_j \partial v_m} =& \chi(t) \Bigg\{ \left(\left(\boldsymbol{D}^{-1} \right)_{jk} + \left(\boldsymbol{D}^{-1} \right)_{kj} \right) \eta_l \eta_m \\
&+ \left(\left(\boldsymbol{D}^{-1} \right)_{jl} + \left(\boldsymbol{D}^{-1} \right)_{lj} \right) \eta_k \eta_m \\
&+ \left(\left(\boldsymbol{D}^{-1} \right)_{kl} + \left(\boldsymbol{D}^{-1} \right)_{lk} \right) \eta_j \eta_m \\
&+ \left(\left(\boldsymbol{D}^{-1} \right)_{kj} + \left(\boldsymbol{D}^{-1} \right)_{jk} \right) \left(\left(\boldsymbol{D}^{-1} \right)_{lm} + \left(\boldsymbol{D}^{-1} \right)_{ml} \right) \\
&+ \left(\left(\boldsymbol{D}^{-1} \right)_{lj} + \left(\boldsymbol{D}^{-1} \right)_{jl} \right) \left(\left(\boldsymbol{D}^{-1} \right)_{km} + \left(\boldsymbol{D}^{-1} \right)_{mk} \right) \\
&+ \left(\left(\boldsymbol{D}^{-1} \right)_{kl} + \left(\boldsymbol{D}^{-1} \right)_{lk} \right) \left(\left(\boldsymbol{D}^{-1} \right)_{jm} + \left(\boldsymbol{D}^{-1} \right)_{mj} \right) \Bigg\}
\end{aligned}
$$

4.7 Calculation of rates: selected applications

4.7.1 Rate of $T_1 \rightarrow S_0$ ISC in biphenyl

The first test-case studied here is biphenyl, for which the ISC rate has been computed. Following the same computational protocol already employed in the previous applications, all electronic structure calculations have been performed at the B3LYP/SNSD level. A graphical representation of the equilibrium geometries of the ground singlet (S_0) and triplet (T_1) states is reported in Fig. 4.17.

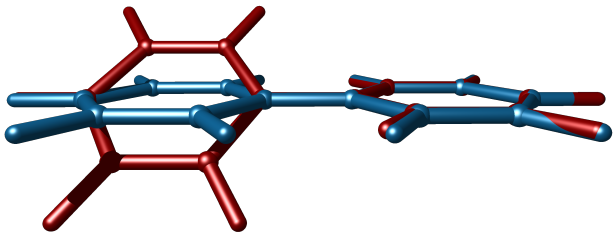

FIGURE 4.17: Graphical representation of the superimposed equilibrium geometries of the S_0 (red) and T_1 (blue) electronic states of biphenyl computed at the B3LYP/SNSD level.

This graphical representation shows that a large geometrical shift is present between the equilibrium geometries of the two electronic states. In fact, the angle between the two phenyl rings is 40° for S_0 and near null for T_1. Thus,

a large-amplitude distortion is involved in the electronic transition and, as a consequence, the choice of the coordinates system used in the simulation is expected to play a key role on the description of vibronic effects. Following the same procedure already presented in the previous section for imidazole and epicamphore, the difference between two coordinates systems can be highlighted through a graphical representation of the Sharp and Rosenstock matrices, as well as of the Duschinsky matrix $\boldsymbol{J}$ and of the shift vector $\boldsymbol{K}$. The graphical representation of the shift vector in Cartesian coordinates ($\boldsymbol{K_x}$) and DICs ($\boldsymbol{K_s}$), reported in Fig. 4.18, shows that the overall structure of $\boldsymbol{K}$ is similar in the two representations, but discrepancies are detected for the higher-energy modes (highest index, corresponding to C–H stretching modes).

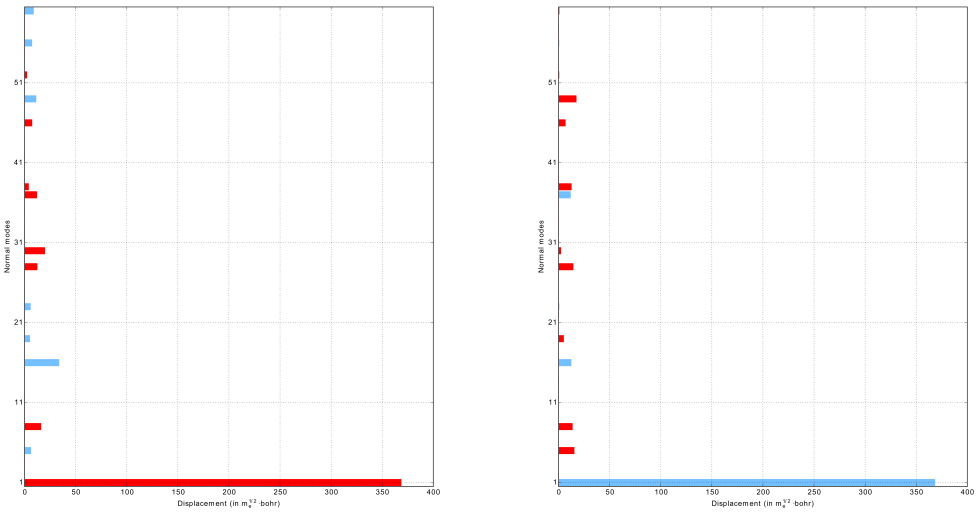

FIGURE 4.18: Representation of the shift vector between the normal coordinates of the T_1 and S_0 states of biphenyl using Cartesian coordinates (left panel) and DICs (right). Blue bars correspond to positive displacements and red bars to negative ones.

These modes have a slightly higher shift in the Cartesian representation than in DICs. This effect is a direct consequence of the poor description of torsional modes as linear combination of Cartesian coordinates, which leads to an incorrect definition of the Duschinsky transformation. Since, as mentioned above, the magnitude of a vibronic progression of a mode is proportional, when mode-mixing effects are neglected, to the component of the shift vector $\boldsymbol{K}$ of this mode, this difference will have a major impact on the reproduction of vibronic effects. The effect is much more evident from the graphical representations of the Sharp and Rosenstock $\boldsymbol{C}$ in the two coordinates systems reported in Fig. 4.19. First of all, the diagonal elements of $\boldsymbol{C}$ for the C−H stretching modes are larger in Cartesian coordinates than in DICs. As discussed above, the i-th diagonal element of $\boldsymbol{C}$ determine the intensity of

progressions of the i-th mode, thus this further confirms that FC integrals involving excitations C–H modes will be larger in Cartesian coordinates. Furthermore, $\boldsymbol{C}$ is much sparser in Cartesian coordinates, FC integrals involving combination bands of these modes will be larger as well. This difference in the relative weights of the FC integrals will have an impact on the computed ISC rate.

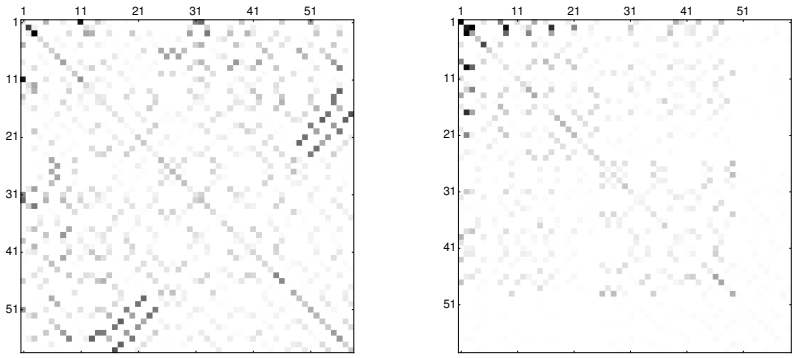

FIGURE 4.19: Graphical representation of the Sharp and Rosenstock $\boldsymbol{C}$ matrix associated to the $T_1 \rightarrow S_0$ transition of biphenyl, computed in Cartesian coordinates (left panel) DICs (right panel), based on AH|FC calculations. The same normalization factor of 0.33, corresponding to the highest magnitude of the two coupling matrices, has been used to facilitate the visual comparison. The representation is obtained as in Fig. 4.9

To further check the difference between Cartesian coordinates and DICs, the phosphorescence spectrum has been computed in the two representations. In fact, as discussed in the theoretical section, at the FC level, the ISC rate is proportional to the corresponding vibronic spectrum (i.e. the phosphorescence spectrum) computed at $\omega = E_{\text{ad}}/\hbar$. Thus, a large difference in the computed spectrum has a direct impact on the ISC rate. As shown in Fig. 4.20, the phosphorescence spectrum computed at the TI AH|FC level for this transition is reproduced correctly only using internal coordinates, whereas significant discrepancies compared to experiment are present in Cartesian coordinates. Let us remark that the simulation of the phosphorescence spectrum has been carried out using the reduced-dimensionality scheme presented in Ref. 275 to neglect the contributions due to the torsional normal mode. In the Cartesian case, also an in-plane ring deformation mode, which is strongly mixed to the torsion through the Duschinsky matrix, has been neglected.
The main difference between the two spectra is related to the presence of intense vibronic transition also in the low-energy range of the spectrum (19000-21000 cm^{-1}) for the Cartesian spectrum, which are not present in its counterpart in DICs. The presence of those transitions can be explained on the basis of the analysis of the structure of the shift vector $\boldsymbol{K}$. In fact, in Cartesian coordinates the shift of the C–H stretching modes is higher, and thus the progressions of these modes are more intense. This explains the presence

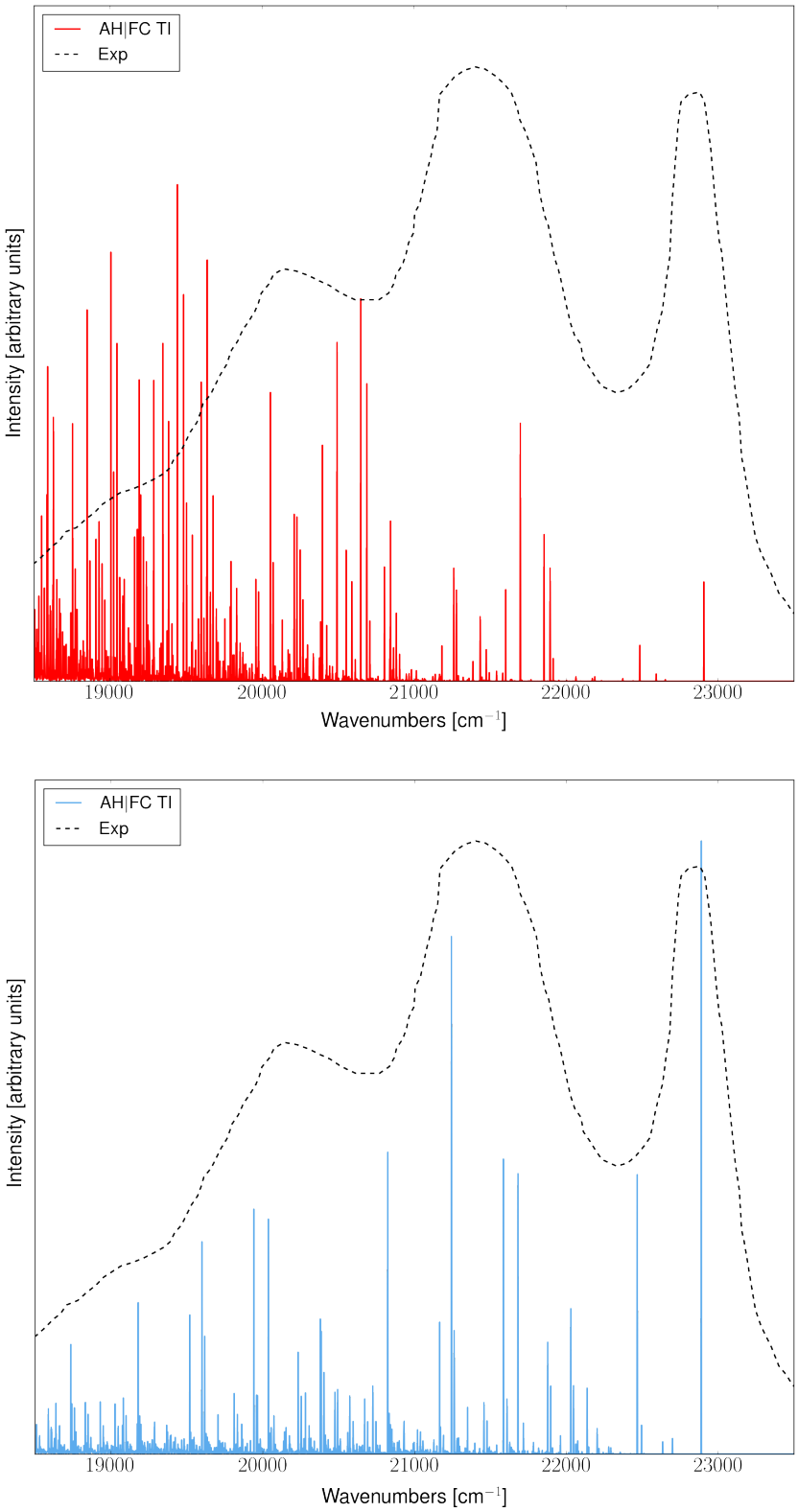

FIGURE 4.20: Comparison of the $T_1 \rightarrow S_0$ phosphorescence spectrum of biphenyl computed at the TI AH|FC level in Cartesian coordinates (upper panel) and DICs (lower panel) with the experimental one (dashed curve), taken from Ref. 318

of higher-energy transition when Cartesian coordinates are used. Furthermore, the coupling of these modes with the other vibrations is higher in the Cartesian representation, as highlighted by the sparse structure of $\boldsymbol{C}$, and this increases the intensity of combination bands involving C–H stretching modes, thus explaining the higher number of intense transition with respect to the spectrum obtained in DICs.
Based on those observations, the ISC rate has been computed at the AH|FC level. The equilibrium value of the spin-orbit coupling calculated at the CASSCF(6,6)/6-311+G* level of theory is 0.2 cm^{-1}. By combining this value with the vibronic density of states (see Eq. 4.102), the ISC rate constant was found to be 4.64×10^4 s^{-1}. The calculated value (in vacuum) is in fair agreement with the experimental values of the ISC rate, which are 2×10^4 s^{-1} in methylcyclohexane-isopentane,[319] or 0.74-0.80 $\times$ 10^4 s^{-1} in *n*-hexane.[320] The experimental data were obtained at 300 K, thus temperature effects were included in our simulations. As shown in Fig. 4.21, temperature effects are relevant, and leads to a constant decrease of the ISC rate.

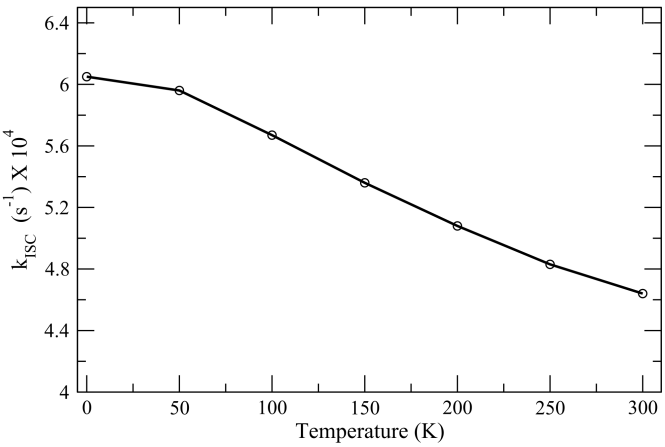

FIGURE 4.21: Temperature dependence of the rate constant for the $T_1 \rightarrow S_0$ ISC of biphenyl in gas phase.

In order to further improve the agreement with the experimental data, calculations were performed also by including solvent effects by means of PCM (*n*-hexane) in the calculation of the electronic spin-orbit coupling. For the vibronic part, the density of states obtained in vacuum was employed. The computed k^{ISC} is in this case 1.16×10^4 s^{-1}, which is in a better agreement with the experimental data.[320]

4.7.2 Temperature dependence of IC rate of [123]-tetramantane

The second system studied in this section is [123]-tetramantane, whose structure is reported in Fig. 4.22, for which the IC rate constant k^{IC} has been computed.

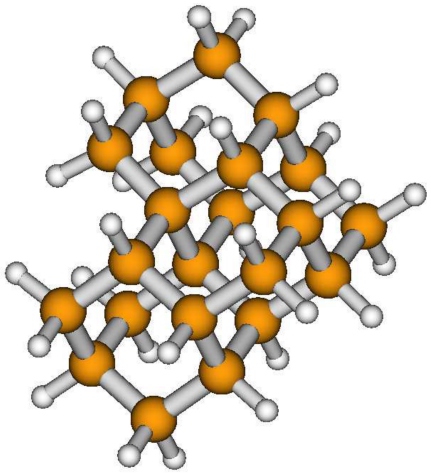

FIGURE 4.22: Optimized ground-state geometry of [123]-tetramantane computed at the B3LYP/TZVP level of theory. The brown and white spheres represent, the C and H atoms respectively.

Also in this case, electronic structure calculations were performed at the (TD-)DFT level, using the B3LYP functional and the TZVP basis set. On the basis of the analysis of the electronic excited states, the fourth excited singlet state (S_4, which is mainly a HOMO $\rightarrow$ (LUMO+1) transition) is the one displaying the highest oscillator strength, which is seven times more intense than for the $S_0 \rightarrow S_1$ transition (corresponding to the HOMO-LUMO excitation). Since the S_1 and S_4 states are relatively close in energy (energy gap of 0.45 eV at the S_0 equilibrium geometry), it is possible that, after electronic excitation to the S_4 state, the molecule decays to S_1 by internal conversion, followed by a fluorescent emission to S_0. For this reason, the rate constant of internal conversion from the S_4 to the S_1 state is of interest and was studied here. For the vibronic part, equilibrium geometries and harmonic frequencies were computed at the TD-DFT level. The non-adiabatic couplings were determined with CASSCF(6,5)/6-311G* calculations performed at the equilibrium geometry of the lower state. In order to limit the computational cost of the simulation, only the sum over the diagonal elements k_{ii}^{IC} were included in the sum given in Eq. 4.111. This choice is based on an earlier theoretical study on azulene[293] has shown that about 96% of the total rate constant comes from the diagonal terms. This approximation allows to save an N-fold increase of computation time, N being the number of vibrational normal modes of the system, which in case of [123]-tetramantane is equal to 144. The resulting IC rate constant, computed at 300 K, is 1.44×10^{10} s^{-1}.
It is interesting to analyze the temperature dependence of the IC rate constant. As shown in Fig. 4.23, where the value of k^{IC} at different temperatures is reported, the rate constant increases gradually with temperature in the given range, the relative increase from 0 K to 300 K being about 55%. Once again, this trend can be ascribed entirely to vibronic effects, since the non-adiabatic coupling vector does not vary with temperature. This variation has a contrasting nature compared to that of ISC in the previous example. This might stem from the fact that for the former, the rate expression goes beyond the Franck-Condon level of approximation. As already remarked above, the IC rate consists of both FC- and HT-like terms. This might be the cause for the change in the behavior of the overall function with temperature.
Comparing to the experimentally determined[321] excited state decay rate ($\sim 2.4\times10^{9}$ s^{-1}) of [123]-tetramantane, it can be predicted that internal conversion might be an important decay channel for the excited state relaxation of diamondoids, especially in the presence of a large number of close excited electronic states.

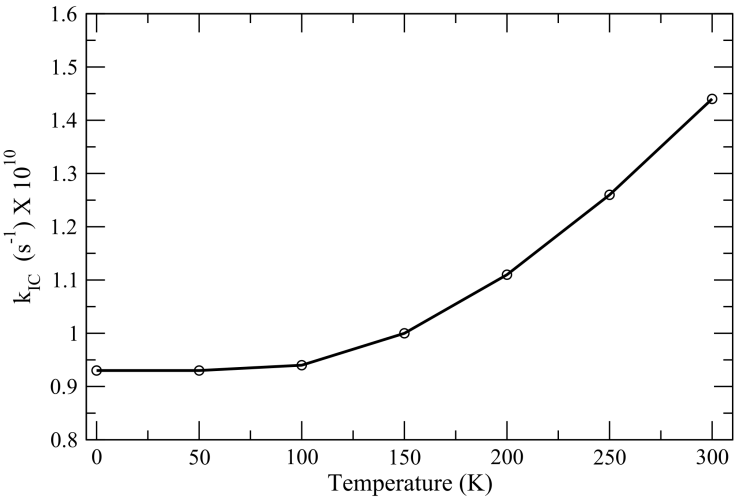

FIGURE 4.23: Temperature dependence of the rate constant for the $S_4 \rightarrow S_1$ IC of [123]-tetramantane in the gas phase.

Chapter 5

Non-linear spectroscopies

In the theoretical framework presented in the previous section, the Fermi Golden Rule was used to compute transition probabilities between different molecular levels, giving spectroscopic observables and rate constants. In the present section, we will discuss how this framework can be extended to support spectroscopic techniques relying on non-linear optical effects, and whose description is not possible within first-order time-dependent perturbation theory. We will focus on two spectroscopic techniques, namely resonance Raman (RR) and its chiral extension, resonance Raman Optical Activity (RROA). First, the expression of the molecular properties that are related to the spectroscopic observables in RR and RROA experiments will be derived. This will serve as basis for the extension of the TD framework introduced in the previous chapter to RR and RROA spectroscopies. Finally, the theory will be tested on two medium-sized organic molecules.

5.1 General theory of RR and RROA scattering

To describe non-linear optical effects, like the ones on which RR and RROA are based, first-order time-dependent perturbation theory is insufficient, and higher-order effects must be included. As for the OP case, we will assume the time-dependent perturbation to correspond to a monochromatic electromagnetic wave with frequency ω. In the previous part, only the electric and magnetic dipole terms were kept in the expansion of the perturbing potential for the simulation of the spectra. By including also the interaction terms associated to the magnetic dipole and electric quadrupole, the perturbing potential can be expressed as,[46,322]

$$\Delta\mathcal{V}(t) = -\sum_{\eta=x,y,z}\left[E_\eta(t)\mu_\eta + B_\eta(t)m_\eta + \frac{1}{3}\sum_{\rho=x,y,z}\left(\frac{\partial E_\eta(t)}{\partial R_\rho}\right)\Theta_{\eta\rho}\right] \tag{5.1}$$

where Θ the electric quadrupole moment. The previous equation can be used to compute the first-order correction $|\,\Psi_n^{(1)}\,\rangle$ to the n-th molecular state $|\,\Psi_n^{(0)}\,\rangle$ (where the (0) superscript highlights that the eigenfunction is obtained without the perturbing potential) as,

$$
\begin{aligned}
|\,\Psi_n^{(1)}\,\rangle = \sum_{m\neq n}\Bigg[& \sum_{\eta=x,y,z} a_\eta^{mn} E_\eta + \sum_{\eta=x,y,z} b_\eta^{mn} E_\eta^\star \\
& + \sum_{\eta=x,y,z} c_\eta^{mn} B_\eta + \sum_{\eta=x,y,z} d_\eta^{mn} B_\eta^\star \\
& + \sum_{\eta,\rho=x,y,z} e_{\eta\rho}^{mn} \left(\frac{\partial E_\eta}{\partial R_\rho}\right) + \sum_{\eta,\rho=x,y,z} e_{\eta\rho}^{mn} \left(\frac{\partial E_\eta^\star}{\partial R_\rho}\right)\Bigg] |\,\Psi_m^{(0)}\,\rangle
\end{aligned}
\tag{5.2}
$$

We note that the previous expansion contains first-order powers of the electric field and its gradient, as well as of its magnetic field. Through first-order perturbation theory, the following expressions for the coefficients of Eq. 5.2 is obtained:

$$
\begin{aligned}
a_\eta^{mn} &= \frac{\langle\,\Psi_m \mid \mu_\eta \mid \Psi_n\,\rangle}{2\,(\omega_{nm}-\omega)} & b_\eta^{mn} &= \frac{\langle\,\Psi_m \mid \mu_\eta \mid \Psi_n\,\rangle}{2\,(\omega_{nm}+\omega)} \\
c_\eta^{mn} &= \frac{\langle\,\Psi_m \mid m_\eta \mid \Psi_n\,\rangle}{2\,(\omega_{nm}-\omega)} & d_\eta^{mn} &= \frac{\langle\,\Psi_m \mid m_\eta \mid \Psi_n\,\rangle}{2\,(\omega_{nm}+\omega)} \\
e_{\eta\rho}^{mn} &= \frac{\langle\,\Psi_m \mid \Theta_{\eta\rho} \mid \Psi_n\,\rangle}{6\,(\omega_{nm}-\omega)} & f_{\eta\rho}^{mn} &= \frac{\langle\,\Psi_m \mid \Theta_{\eta\rho} \mid \Psi_n\,\rangle}{6\,(\omega_{nm}+\omega)}
\end{aligned}
\tag{5.3}
$$

Combining Eqs. 5.2 and 5.3, the first-order correction to the wavefunction can be expressed in terms of the transition electric dipole, electric quadrupole and magnetic dipole moments. The first-order correction to the wavefunction can be used to compute the correction to the average of any molecular properties. For example, the average of the dipole operator over the n-th state ($\langle\mu_\eta\rangle_{nn}$) can be expressed in terms of the components of the electromagnetic field as follows,

$$
\begin{aligned}
\langle\mu_\eta\rangle_{nn} = \sum_{\rho=x,y,z}\Bigg[& \alpha_{\eta\rho} E_\rho + \frac{1}{\omega}\alpha'_{\eta\rho}\left(\frac{\partial E_\rho}{\partial t}\right) + \mathcal{G}_{\eta\rho} B_\rho + \frac{1}{\omega}\mathcal{G}'_{\eta\rho}\left(\frac{\partial B_\rho}{\partial t}\right) \\
& + \sum_{\rho'=x,y,z}\frac{1}{3}\left(\mathcal{A}_{\eta,\rho\rho'}\left(\frac{\partial E_\rho}{\partial R'_\rho}\right) + \frac{1}{\omega}\mathcal{A}'_{\eta,\rho\rho'}\left(\frac{\partial^2 E_\rho}{\partial R_{\rho'}\partial t}\right)\right)\Bigg]
\end{aligned}
\tag{5.4}
$$

where the six tensors $\boldsymbol{\alpha}$, $\boldsymbol{\alpha}'$ (polarizability tensors), $\boldsymbol{\mathcal{G}}$, $\boldsymbol{\mathcal{G}}'$ (electric dipole-magnetic dipole tensors), $\boldsymbol{\mathcal{A}}$ and $\boldsymbol{\mathcal{A}}'$ (electric dipole-electric quadrupole tensors) are defined as,

$$
\begin{aligned}
\alpha_{\eta\rho} &= \frac{2}{\hbar}\sum_{m\neq n}\frac{\omega_{mn}\Re\left(\langle\,\Psi_n\mid\mu_\eta\mid\Psi_m\,\rangle\langle\,\Psi_m\mid\mu_\rho\mid\Psi_n\,\rangle\right)}{{\omega_{mn}}^2-\omega^2}\\
\alpha'_{\eta\rho} &= -\frac{2}{\hbar}\sum_{m\neq n}\frac{\omega_{mn}\Im\left(\langle\,\Psi_n\mid\mu_\eta\mid\Psi_m\,\rangle\langle\,\Psi_m\mid\mu_\rho\mid\Psi_n\,\rangle\right)}{{\omega_{mn}}^2-\omega^2}\\
\mathcal{G}_{\eta\rho} &= \frac{2}{\hbar}\sum_{m\neq n}\frac{\omega_{mn}\Re\left(\langle\,\Psi_n\mid\mu_\eta\mid\Psi_m\,\rangle\langle\,\Psi_m\mid m_\rho\mid\Psi_n\,\rangle\right)}{{\omega_{mn}}^2-\omega^2}\\
\mathcal{G}'_{\eta\rho} &= -\frac{2}{\hbar}\sum_{m\neq n}\frac{\omega_{mn}\Im\left(\langle\,\Psi_n\mid\mu_\eta\mid\Psi_m\,\rangle\langle\,\Psi_m\mid m_\rho\mid\Psi_n\,\rangle\right)}{{\omega_{mn}}^2-\omega^2}\\
\mathcal{A}_{\eta,\rho\rho'} &= \frac{2}{\hbar}\sum_{m\neq n}\frac{\omega_{mn}\Re\left(\langle\,\Psi_n\mid\mu_\eta\mid\Psi_m\,\rangle\langle\,\Psi_m\mid\Theta_{\rho\rho'}\mid\Psi_n\,\rangle\right)}{{\omega_{mn}}^2-\omega^2}\\
\mathcal{A}'_{\eta,\rho\rho'} &= -\frac{2}{\hbar}\sum_{m\neq n}\frac{\omega_{mn}\Im\left(\langle\,\Psi_n\mid\mu_\eta\mid\Psi_m\,\rangle\langle\,\Psi_m\mid\Theta_{\rho\rho'}\mid\Psi_n\,\rangle\right)}{{\omega_{mn}}^2-\omega^2}
\end{aligned}
\tag{5.5}
$$

Eq. 5.4 can be rewritten in a complex form as,

$$
\langle\mu_\eta\rangle_{nn} = \sum_{\rho=x,y,z}\left[\tilde{\alpha}_{\eta\rho}E_\rho + \tilde{\mathcal{G}}_{\eta\rho}B_\rho + \frac{1}{3}\sum_{\rho'=x,y,z}\tilde{\mathcal{A}}_{\eta,\rho\rho'}\left(\frac{\partial E_\rho}{\partial R'_\rho}\right)\right] \tag{5.6}
$$

where,

$$
\begin{aligned}
\tilde{\alpha}_{\eta\rho} &= \alpha_{\eta\rho} - i\alpha'_{\eta\rho}\\
\tilde{\mathcal{G}}_{\eta\rho} &= \mathcal{G}_{\eta\rho} - i\mathcal{G}'_{\eta\rho}\\
\tilde{\mathcal{A}}_{\eta,\rho\rho'} &= \mathcal{A}_{\eta,\rho\rho'} - i\mathcal{A}'_{\eta,\rho\rho'}
\end{aligned}
\tag{5.7}
$$

For a monochromatic wave, the magnetic field and the gradient of the electric field are related to the electric field through the following relations,

$$
\boldsymbol{B} = \frac{1}{c}\boldsymbol{n}_I\times\boldsymbol{E} \qquad\qquad \left(\frac{\partial\boldsymbol{E}}{\partial R_i}\right) = \frac{\omega}{c}\left(\boldsymbol{n}_I\right)_i\boldsymbol{E} \tag{5.8}
$$

where $\boldsymbol{n}_I$ is a unit vector pointing in the direction of the light propagation. Using Eq. 5.8, Eq. 5.6 can be expressed as,

$$
\langle\mu_\eta\rangle_{nn} = \tilde{\alpha}_{\eta\rho}E_\rho + \tilde{\mathcal{G}}_{\eta\rho}\epsilon_{\rho\delta\lambda}n_{I,\delta}E_\lambda + \frac{\omega}{3c}\mathcal{A}_{\eta,\rho\rho'}n_{\rho'}E_\rho \tag{5.9}
$$

where the Einstein convention has been used to implicitly carry out the summation over the repeated indexes. The previous relation is more practical than the one given in Eq. 5.6 when applied to scattering problems. Higher-order corrections like the product between the magnetic dipole and electric quadrupole moments could be, in principle, included in Eq. 5.4. The electric dipole moment is the leading term in the expansion of Eq. 5.1 thus these terms can be, as a first approximation, neglected. When the frequency ω approaches any transition frequency ω_{mn}, the transition tensors given in Eq. 5.5

diverge. This is a direct consequence of the failure of first-order perturbation theory when absorption processes become relevant. This divergence is however not present if we consider that each molecular state $|\,\Psi_m\,\rangle$ has a finite lifetime γ_m, due to energy relaxation processes (such as internal conversion or spontaneous emission). The finite lifetime can be included in the previous relations by substituting the transition frequency ω_{mn} by $\omega_{mn} - i\gamma_m$. In this way, when ω matches a transition frequency, the denominator of the fractions present in Eq. 5.5 have a residual, pure imaginary component which prevents divergences.
Up to now, only averages of molecular properties have been considered. As already stressed in Chapter 2, spectra are in most cases determined by transition values of operators, and not on vibrational averages. Following the same strategy already used for the derivation of Eq. 5.4, the transition dipole moment can be written as,[46,58]

$$\langle \boldsymbol{\mu} \rangle_{mn} = \langle\, \Psi_m \mid \boldsymbol{\mu} \mid \Psi_n \,\rangle + \langle\, \Psi_m \mid \boldsymbol{\mu} \mid \Psi_n \,\rangle^{\star} \tag{5.10}$$

In order to derive the perturbation to the transition dipole moment induced by the presence of an electromagnetic oscillating field, the first-order correction to the molecular wavefunction given in Eq. 5.2 must be combined with the previous expression. By including only terms associated to the electric dipole moment, the following final result is obtained,

$$\langle \mu_\eta \rangle_{mn} = \sum_{\rho=x,y,z} \alpha_{mn,\eta\rho} E_\rho e^{-i(\omega-\omega_{mn})t} \tag{5.11}$$

where,

$$\begin{aligned} \alpha_{mn,\tau\rho} =& \frac{1}{\hbar} \sum_{j\neq n,m} \frac{\langle\, \Psi_m \mid \mu_\tau \mid \Psi_j \,\rangle \langle\, \Psi_j \mid \mu_\rho \mid \Psi_n \,\rangle}{\omega_{jn} - \omega - i\gamma_j} \\ &+ \frac{1}{\hbar} \sum_{j\neq n,m} \frac{\langle\, \Psi_m \mid \mu_\rho \mid \Psi_j \,\rangle \langle\, \Psi_j \mid \mu_\tau \mid \Psi_n \,\rangle}{\omega_{jn} + \omega + i\gamma_j} \end{aligned} \tag{5.12}$$

and similar equations are obtained for the transition electric dipole-magnetic dipole coupling tensors $\mathcal{G}_{mn,\eta\rho}$ and $\mathcal{G}'_{mn,\eta\rho}$, as well as for the electric dipole-electric quadrupole tensors $\mathcal{A}_{mn,\eta,\rho\rho'}$ and $\mathcal{A}^{mn'}_{mn,\eta,\rho\rho'}$. Eq. 5.12 is also known as Placzeck formula for the transition probability tensor,[323] and is the starting point for the simulation of spectra based on light-scattering phenomena, like Raman effect.
These new transition tensors are the key quantities needed to provide a description of scattering processes. Within a classical model of light scattering phenomena, a sample is irradiated by an electromagnetic radiation of frequency ω_{I}, which induces an oscillating electron density (and, for magnetic systems, currents). The density can oscillate at the same frequency of the incident light (ω_{I}), leading to elastic (or Rayleigh) scattering. However, the frequency of oscillation can be different to ω_{I}, leading to inelastic (or Raman)

scattering. The oscillating density leads to the emission of the electromagnetic radiation, with an electric field, which is related to its multipolar moments through the following relation:

$$\boldsymbol{E}\left(\boldsymbol{R},t\right)=\frac{{\omega_{\mathrm{I}}}^{2}}{4\pi}e^{i(\boldsymbol{k}\boldsymbol{R}-\omega_{\mathrm{I}}t)}\Big[\left(1-\boldsymbol{n}_{\mathrm{D}}{\boldsymbol{n}_{\mathrm{D}}}^{T}\right)\boldsymbol{\mu}-\frac{1}{c}\boldsymbol{n}_{\mathrm{D}}\times\boldsymbol{m}-\frac{i\omega_{\mathrm{I}}}{3c}\left(\boldsymbol{\Theta}\boldsymbol{n}_{\mathrm{D}}-\boldsymbol{n}_{\mathrm{D}}\left({\boldsymbol{n}_{\mathrm{D}}}^{T}\boldsymbol{\Theta}\boldsymbol{n}_{\mathrm{D}}\right)\right)\Big] \tag{5.13}$$

where $\boldsymbol{n}_{\mathrm{D}}$ is the unit vector pointing in the direction along which the scattered radiation is recorded. The quantum counterpart of Eq. 5.13 can be derived by substituting the classical vectors $\boldsymbol{\mu}$, $\boldsymbol{m}$ and $\boldsymbol{\Theta}$ with their averages $\langle\boldsymbol{\mu}\rangle_{nn}$, $\langle\boldsymbol{m}\rangle_{nn}$ and $\langle\boldsymbol{\Theta}\rangle_{nn}$ over the state $|\,\Psi_n\,\rangle$ of interest. The previous relation must be modified to support also non-elastic scattering. As can be proven using quantum electrodynamics,[324] Raman scattering can occur only if $\omega_{\mathrm{I}}-\omega_{\mathrm{S}}$ correspond to a transition frequency ω_{mn}, where ω_{S} is the frequency of the scattered radiation. In this case, the electric field of the scattered radiation is still given by Eq. 5.13, provided that transition properties are used in place of the state-bound ones. The induced dipoles are obtained from Eq. 5.4 and, combined with Eq. 5.13, can be used to express the scattered wave in terms of the transition tensors,

$$E_{\mathrm{D},eta}=\frac{\omega_{\mathrm{S}}^{2}}{4\pi R}e^{i\omega_{\mathrm{S}}(R/c-t)}\sum_{\rho=x,y,z}a_{mn,\eta\rho}E_{\rho} \tag{5.14}$$

where $R=|\boldsymbol{R}|$ and,[325]

$$a_{\eta\rho}^{mn}=\alpha_{\eta\rho}^{mn}+\frac{1}{c}\left[\epsilon_{\delta\lambda\rho}n_{\mathrm{I},\lambda}\mathcal{G}_{\eta\delta}^{mn}+\epsilon_{\delta\lambda\eta}n_{\mathrm{D},\lambda}\mathcal{G}_{\delta\rho}^{\prime mn}+\frac{1}{3}i\omega\left(n_{\mathrm{I},\delta}\mathcal{A}_{\eta,\delta\rho}^{mn}-n_{\mathrm{I},\delta}\mathcal{A}_{\rho,\delta\eta}^{\prime mn}\right)\right] \tag{5.15}$$

Particular care must be paid when using the previous equation since, in Eq. 5.14, the electric fields are expressed with respect to a space-fixed frame, whereas the transition tensors are, in most cases, computed in a molecule-fixed frame. For this reason, the latter representation must be converted to the former before using Eq. 5.14. Only after this transformation, can the scattered intensity be obtained from the square value of the electric field $\boldsymbol{E}^{\mathrm{D}}$ starting from Eq. 5.14. The final result will depend on the transition frequency, on the relative polarization of the light, as well as on the orientation of the molecule.[325] In most applications, Raman experiments are performed on isotropic sample, where the molecules are randomly oriented, and thus each value of the cosine director angles is equally probable. Thus, the dependence on the molecular orientation can be removed by doing an isotropic average of the scattering intensity.

The quantity which is recorded in actual Raman experiments depend on the experimental setup. In standard Raman experiments, the intensity of the scattered light I_{S} is directly recorded. I is a function of the polarization of the incident (p_{I}) and scattered (p_{S}) light, as well as in the angle θ between n_{I} and

n_D, and is thus usually referred to as $I\left(p_I, p_S, \theta\right)$, In the most standard configuration, the polarization of the incident light is perpendicular to the direction of propagation, and the scattered light is recorded with $\theta = 90°$ and with polarization parallel to the direction of propagation. The resulting intensity is indicated as $I\left(\perp_I, \|_S, 90°\right)$. Within this configuration, the scattered intensity is given by the following relation,

$$I_S\left(\frac{\pi}{2}; \|^S + \perp^S; \perp^I; \omega_I, \omega_S\right) = k{\omega_s}^2 I_I \frac{45a^2 + 7g^2 + 5d^2}{45} \tag{5.16}$$

where a (isotropic polarizability), g (symmetric anisotropy) and d (asymmetric anisotropy) are given by,

$$\begin{aligned} a =& \frac{1}{3}\left(\alpha_{mn,xx} + \alpha_{mn,yy} + \alpha_{mn,zz}\right) \\ g^2 =& \frac{1}{2}\left(\left|\alpha_{mn,xx} - \alpha_{mn,yy}\right|^2 + \left|\alpha_{mn,xx} - \alpha_{mn,zz}\right|^2 + \left|\alpha_{mn,zz} - \alpha_{mn,yy}\right|^2\right) \\ &+ \frac{3}{4}\left(\left|\alpha_{mn,xy} + \alpha_{mn,yx}\right|^2 + \left|\alpha_{mn,xz} + \alpha_{mn,zx}\right|^2 + \left|\alpha_{mn,yz} + \alpha_{mn,zy}\right|^2\right) \\ d^2 =& \frac{3}{4}\left(\left|\alpha_{mn,xy} - \alpha_{mn,yx}\right|^2 + \left|\alpha_{mn,xz} - \alpha_{mn,zx}\right|^2 + \left|\alpha_{mn,yz} - \alpha_{mn,zy}\right|^2\right) \end{aligned} \tag{5.17}$$

Changing the scattering geometry, a different relation compared to the one given in Eq. 5.16 is obtained. However, in all cases the intensity can be expressed in terms only of a, g^2 and d^2 since, as discussed, for example, in Ref. 46, those are the only components of the transition tensors giving non-null contributions after the isotropic averaging. To derive the previous relation, contributions arising from $\mathcal{G}$ and $\mathcal{A}$ tensors have been neglected, since they are smaller than the ones proportional to $\boldsymbol{\alpha}$.

In the chiral counterpart of Raman, namely Raman Optical Activity (ROA), the difference of the intensity of the scattered light obtained with an incident light with right-handed (I_S^r) and left-handed (I_S^l) polarization is recorded. This difference is usually known as circularly intensity difference (CID), and is non-null only for chiral samples. Being related to I_S, also the CID is a function of p_I, p_S and θ. However, unlike Raman, a wider range of experimental setups is employed in ROA, which can be divided in three main classes:

1. incident circular polarization (ICP), where the spectrum is reported as the difference of the intensity of the scattered light obtained with left and right-handed circularly polarized light, without imposing a polarization of the scattered light.

2. scattered circular polarization (SCP), where the spectrum is reported as the difference of the intensity of the scattered light obtained with left and right-handed circularly polarized light, without imposing a polarization of the incident light.

3. dual circular polarization (DCP), in which the relative polarization of the incident and scattered lights is modulated either in phase (DCP_I) or out-of-phase (DCP_{II}).

In addition to the polarization, the relative angle between the directions of the incident and the scattered light can be modified. In most experiments, the relative angle is set to 0° (forward scattering), 90° (right angle scattering) or 180° (backward scattering). A third parameter which can be modified is the relative angle between the between the transmission axis of the linear polarization analyzer and the plane of the scattered light. The most interesting values are,

1. 0°, corresponding to the depolarized scattering (referred to in the following with a z subscript)
2. 90°, corresponding to the polarized scattering (referred to in the following with a x subscript)
3. the so-called magic angle (which corresponds approximately to 54°) scattering, which allows to remove the contributions due to the $\mathcal{A}$ and $\mathcal{A}'$ tensors (referred to in the following with a $*$ subscript)
4. all possible angles are averaged out, which corresponds to the so-called unpolarized scattering

The isotropic distribution of the molecules can be used to express the intensity in terms of a limited number of invariants, that are given in the following,[46,325,326]

$$\alpha^2 = \frac{1}{9}\Re\left(\alpha^s_{mn,\rho\rho}\{\alpha^s_{mn,\eta\eta}\}^\star\right) \tag{5.18}$$

$$\beta_s(\alpha)^2 = \frac{1}{2}\Re\left(3\alpha^s_{mn,\rho\eta}\{\alpha^s_{mn,\rho\eta}\}^\star - \alpha^s_{mn,\rho\rho}\{\alpha^s_{mn,\eta\eta}\}^\star\right) \tag{5.19}$$

$$\beta_a(\alpha)^2 = \frac{3}{2}\Re\left(3\alpha^a_{mn,\rho\eta}\{\alpha^a_{mn,\rho\eta}\}^\star\right) \tag{5.20}$$

$$\alpha\mathcal{G} = \frac{1}{9}\Im\left(\alpha^s_{mn,\rho\rho}\{\mathcal{G}^s_{mn\eta\eta}\}^\star\right) \tag{5.21}$$

$$\beta_s(\mathcal{G})^2 = \frac{1}{2}\Im\left(3\alpha^s_{mn,\rho\eta}\{\mathcal{G}^s_{mn,\rho\eta}\}^\star - \alpha^s_{mn,\rho\rho}\{\mathcal{G}^s_{mn,\eta\eta}\}^\star\right) \tag{5.22}$$

$$\beta_a(\mathcal{G})^2 = \frac{3}{2}\Im\left(3\alpha^a_{mn,\rho\eta}\{\mathcal{G}^a_{mn,\rho\eta}\}^\star\right) \tag{5.23}$$

$$\alpha\mathcal{G}' = \frac{1}{9}\Im\left(\alpha^s_{mn,\rho\rho}\{\mathcal{G}'^s_{mn,\eta\eta}\}^\star\right) \tag{5.24}$$

$$\beta_s(\mathcal{G}')^2 = \frac{1}{2}\Im\left(3\alpha^s_{mn,\rho\eta}\{\mathcal{G}'^s_{mn,\rho\eta}\}^\star - \alpha^s_{mn,\rho\rho}\{\mathcal{G}'^s_{mn,\eta\eta}\}^\star\right) \tag{5.25}$$

$$\beta_a(\mathcal{G}')^2 = \frac{3}{2}\Im\left(3\alpha^a_{mn,\rho\eta}\{\mathcal{G}'^a_{mn,\rho\eta}\}^\star\right) \tag{5.26}$$

$$\beta_s(\mathcal{A})^2 = \frac{\omega}{2}\Im\left(i\alpha^s_{mn,\rho\eta}\left(\epsilon_{\rho\delta\lambda}\mathcal{A}_{mn,\delta,\lambda\eta}\right)^{s\star}\right) \tag{5.27}$$

$$\beta_a(\mathcal{A})^2 = \frac{\omega}{2}\Im\left(i\alpha^a_{mn,\rho\eta}\left(\epsilon_{\rho\delta\lambda}\mathcal{A}_{mn,\delta,\lambda\eta}\right)^{a\star} + i\alpha^a_{mn,\rho\eta}\left(\epsilon_{\rho\lambda\delta}\mathcal{A}_{mn,\lambda,\delta\lambda}\right)^{a\star}\right) \quad (5.28)$$

$$\beta_s(\mathcal{A}')^2 = \frac{\omega}{2}\Im\left(i\alpha^s_{mn,\rho\eta}\left(\epsilon_{\rho\delta\lambda}\mathcal{A}'_{mn,\delta,\lambda\eta}\right)^{s\star}\right) \quad (5.29)$$

$$\beta_a(\mathcal{A})^2 = \frac{\omega}{2}\Im\left(i\alpha^a_{mn,\rho\eta}\left(\epsilon_{\rho\delta\lambda}\mathcal{A}'_{mn,\delta,\lambda\eta}\right)^{a\star} + i\alpha^a_{mn,\rho\eta}\left(\epsilon_{\rho\eta\delta}\mathcal{A}'_{mn,\lambda,\delta\lambda}\right)^{a\star}\right) \quad (5.30)$$

where the complex conjugate is represented by the $\star$ superscript, whereas the s and a superscripts indicate the symmetric and antisymmetric components of a bidimensional tensor, defined as follows:

$$\begin{aligned} T^s_{mn,\rho\eta} &= \frac{T_{mn,\rho\eta} + T_{mn,\eta\rho}}{2} \\ T^a_{mn,\rho\eta} &= \frac{T_{mn,\rho\eta} - T_{mn,\eta\rho}}{2} \end{aligned} \quad (5.31)$$

where $\boldsymbol{T}$ can be any one of the five scattering tensor. We note that $\epsilon_{\rho\delta\lambda}\mathcal{A}_{mn,\delta,\lambda\eta}$ and $\epsilon_{\rho\eta\delta}\mathcal{A}_{mn,\lambda,\delta\lambda}$ are two-dimensional tensors, with indexes ρ and η, since a contractions over δ and λ are implicitly performed in their definition. For each combination of scattering geometries, the CID is expressed as a different linear combination of the invariants reported above. The definition of the CID for the most common experimental setups employed in ROA experiments is reported in Tab. 5.1.

5.1.1 Vibronic theory of RR and RROA

The theoretical framework derived presented in the previous section showed that the key quantity for the simulation of RR and RROA spectra are the five tensors $\boldsymbol{\alpha}$, $\boldsymbol{\mathcal{G}}$, $\boldsymbol{\mathcal{G}}'$, $\boldsymbol{\mathcal{A}}$ and $\boldsymbol{\mathcal{A}}'$. In order to develop a single theoretical derivation, supporting both RR and RROA, it is useful to introduce the following general tensor,[327]

$$T_{mn,\rho\eta} = \frac{1}{\hbar}\sum_{j\neq m,n}\left[\frac{\langle\,\Psi_m \mid P^{\mathrm{A}}_\rho \mid \Psi_j\,\rangle\langle\,\Psi_j \mid P^{\mathrm{B}}_\eta \mid \Psi_n\,\rangle}{\omega_{jn} - \omega_{\mathrm{I}} + i\gamma_j} + \frac{\langle\,\Psi_m \mid P^{\mathrm{B}}_\rho \mid \Psi_j\,\rangle\langle\,\Psi_j \mid P^{\mathrm{A}}_\eta \mid \Psi_n\,\rangle}{\omega_{jn} + \omega_{\mathrm{I}} - i\gamma_j}\right] \quad (5.32)$$

$\boldsymbol{P}^{\mathrm{A}}$ and $\boldsymbol{P}^{\mathrm{B}}$ are general operators, which can be the electric dipole, the magnetic dipole or the electric quadrupole operator. The equivalence rules given in Tab. 5.2 can be used to recover the definition of all the five transition tensors. For $\boldsymbol{\mathcal{A}}_{mn}$ and $\boldsymbol{\mathcal{A}}'_{mn}$, the index η in Eq. 5.32 collects both the indexes corresponding to the quadrupole operator.

Within the theoretical framework described up to this point, no particular assumption has been made on the value of the frequency of the incident light ω_{I}. However, as mentioned above, we will focus on the resonant version of Raman and ROA spectroscopies. Resonance conditions are satisfied when

ICP(0°)	$8\left(45\alpha G+7\beta_s(G)^2+5\beta_a(G)^2+\beta_s(A)^2-\beta_a(A)^2-45\alpha\mathcal{G}+5\beta_s(\mathcal{G})^2-5\beta_a(\mathcal{G})^2-3\beta_s(\mathcal{A})^2+\beta_a(\mathcal{A})^2\right)$
ICP_x(90°)	$4\left(45\alpha G+7\beta_s(G)^2+5\beta_a(G)^2+\beta_s(A)^2-\beta_a(A)^2\right)$
ICP_z(90°)	$8\left(3\beta_s(G)^2+5\beta_a(G)^2-\beta_s(A)^2+\beta_a(A)^2\right)$
$\mathrm{ICP}_\star$(90°)	$\frac{40}{3}\left(9\alpha G+2\beta_s(G)^2+2\beta_s(G)^2\right)$
ICP_u(90°)	$4\left(45\alpha G+13\beta_s(G)^2+15\beta_a(G)^2-\beta_s(A)^2+\beta_a(A)^2\right.$
ICP(180°)	$8\left(45\alpha G+7\beta_s(G)^2+5\beta_a(G)^2+\beta_s(A)^2-\beta_a(A)^2+45\alpha\mathcal{G}-5\beta_s(\mathcal{G})^2+5\beta_a(\mathcal{G})^2+3\beta_s(\mathcal{A})^2-\beta_a(\mathcal{A})^2\right)$
SCP(0°)	$8\left(-45\alpha G-7\beta_s(G)^2-5\beta_a(G)^2+\beta_s(A)^2+\beta_a(A)^2+45\alpha\mathcal{G}-5\beta_s(\mathcal{G})^2+5\beta_a(\mathcal{G})^2-3\beta_s(\mathcal{A})^2-\beta_a(\mathcal{A})^2\right)$
SCP_x(90°)	$4\left(-45\alpha\mathcal{G}-13\beta_s(\mathcal{G})^2-15\beta_a(\mathcal{G})^2-\beta_s(\mathcal{A})^2-\beta_a(\mathcal{A})^2\right)$
SCP_z(90°)	$4\left(-3\beta_s(\mathcal{G})^2-5\beta_a(\mathcal{G})^2-\beta_s(\mathcal{A})^2-\beta_a(\mathcal{A})^2\right)$
$\mathrm{SCP}_\star$(90°)	$8\left(-3\beta_s(\mathcal{G})^2-5\beta_a(\mathcal{G})^2-\beta_s(\mathcal{A})^2-\beta_a(\mathcal{A})^2\right)$
SCP_u(90°)	$\frac{40}{3}\left(-9\alpha\mathcal{G}-2\beta_s(\mathcal{G})^2-2\beta_a(\mathcal{G})^2\right)$
SCP(180°)	$8\left(-45\alpha G-7\beta_s(G)^2-5\beta_a(G)^2+\beta_s(A)^2+\beta_a(A)^2+-45\alpha\mathcal{G}+5\beta_s(\mathcal{G})^2-5\beta_a(\mathcal{G})^2+3\beta_s(\mathcal{A})^2+\beta_a(\mathcal{A})^2\right)$
DCP_I(0°)	$8\left(45\alpha G+\beta_s(G)^2+5\beta_a(G)^2-\beta_s(A)^2-\beta_a(A)^2+-45\alpha\mathcal{G}-\beta_s(\mathcal{G})^2-5\beta_a(\mathcal{G})^2-\beta_s(\mathcal{A})^2-\beta_a(\mathcal{A})^2\right)$
DCP_I(90°)	$2\left(45\alpha G+13\beta_s(G)^2+15\beta_a(G)^2-\beta_s(A)^2+\beta_a(A)^2+-45\alpha\mathcal{G}-13\beta_s(\mathcal{G})^2-15\beta_a(\mathcal{G})^2-\beta_s(\mathcal{A})^2-\beta_a(\mathcal{A})^2\right)$
DCP_I(180°)	$16\left(3\beta_s(G)^2+\beta_s(A)^2-3\beta_s(\mathcal{G})^2+\beta_s(\mathcal{A})^2\right)$
DCP_{II}(0°)	$16\left(3\beta_s(G)^2+\beta_s(A)^2+3\beta_s(\mathcal{G})^2-\beta_s(\mathcal{A})^2\right)$
DCP_{II}(90°)	$2\left(45\alpha G+13\beta_s(G)^2+15\beta_a(G)^2-\beta_s(A)^2+\beta_a(A)^2++45\alpha\mathcal{G}+13\beta_s(\mathcal{G})^2+15\beta_a(\mathcal{G})^2+\beta_s(\mathcal{A})^2+\beta_a(\mathcal{A})^2\right)$
DCP_{II}(180°)	$8\left(45\alpha G+\beta_s(G)^2+5\beta_a(G)^2-\beta_s(A)^2-\beta_a(A)^2++45\alpha\mathcal{G}+\beta_s(\mathcal{G})^2+5\beta_a(\mathcal{G})^2+\beta_s(\mathcal{A})^2-\beta_a(\mathcal{A})^2\right)$

TABLE 5.1: Equivalence table to obtain the definition of the ROA intensity $\mathrm{I}_{\mathrm{ROA}}$ in terms of linear combinations of ROA invariants for different experimental setups.

$\boldsymbol{T}$	$\boldsymbol{\alpha}$	$\boldsymbol{\mathcal{G}}$	$\boldsymbol{\mathcal{G}'}$	$\boldsymbol{\mathcal{A}}$	$\boldsymbol{\mathcal{A}'}$
$\boldsymbol{P}^{\mathrm{A}}$	$\boldsymbol{\mu}$	$\boldsymbol{\mu}$	$\boldsymbol{m}$	$\boldsymbol{\mu}$	$\boldsymbol{\Theta}$
$\boldsymbol{P}^{\mathrm{B}}$	$\boldsymbol{\mu}$	$\boldsymbol{m}$	$\boldsymbol{\mu}$	$\boldsymbol{\Theta}$	$\boldsymbol{\mu}$

TABLE 5.2: Equivalence table to build the five transition tensors required in ROA spectroscopy using Eq. 5.32.

the energy of the incident light matches the energy of a single electronic excited state (the case of multiple resonant states will be treated in the following), and for the resonance case Eq. 5.32 can be simplified. In fact, the denominator of the first term is small for all vibrational levels of the intermediate-state, and thus the second term is negligible with respect to the first one, and can be discarded. For the same reason, the sum over j can be restricted to the vibrational levels of the intermediate-state. Here, an additional approximation will be performed, since temperature effects will be neglected. This way, the initial state $|\,\Psi_n\,\rangle$ is the vibrational ground state of the electronic ground state ($|\,\overline{\phi}\,\rangle|\,\overline{\psi}_0\,\rangle$, following the notation introduced in the previous chapter). Using those approximations, Eq. 5.32 can be expressed as,

$$T_{0k,\rho\eta} = \frac{1}{\hbar}\sum_{j=1}^{+\infty}\frac{\langle\,\overline{\psi}_k\,|\,P_{\rho}^{\mathrm{A},e}\,|\,\overline{\overline{\psi}}_j\,\rangle\langle\,\overline{\overline{\psi}}_j\,|\,P_{\eta}^{\mathrm{B},e}\,|\,\overline{\psi}_0\,\rangle}{\omega_{j0}-\omega_{\mathrm{I}}-i\gamma} \tag{5.33}$$

where the BO approximation has been used to simplify Ψ_j and Ψ_m. Furthermore, $\boldsymbol{P}^{\mathrm{A},e}$ and $\boldsymbol{P}^{\mathrm{B},e}$ are the electric components of the general transition properties $\boldsymbol{P}^{\mathrm{A}}$ and $\boldsymbol{P}^{\mathrm{B}}$ associated to the intermediate electronic state. We note that Eq. 5.33 holds only for vibrational transitions, where the final state $|\,\overline{\psi}_k\,\rangle$ corresponds to a vibrational level of the electronic ground state.
Using Eq. 5.33, the transition tensor $\boldsymbol{T}$ can be computed based on TI and TD approaches, as for one-photon vibronic spectroscopy. Here, we will briefly describe the TI route, and in the next section the TD method will be described more in detail.
In the TI method, Eq. 5.33 is expressed in terms of Franck-Condon integrals using the expansion of the transition property given in Eq. 4.17. As already mentioned for one-photon spectroscopies, within the harmonic approximation, FC integrals can be evaluated through either analytical[278,328] or recursive[279,329] expressions, thus it is in principle possible to evaluate the transition tensors by carrying out explicitly the sum in Eq. 5.33. Several TI-based approaches have been proposed in the literature and their main limitation is the lack of reliable prescreening systems for the selection of the most relevant transitions.[330,331,332] In order to overcome those limitations of the TI approach, a time-dependent (TD) model, which will be described in the next section, is better suited to perform RR and RROA simulations. The prescreening scheme proposed for OPA/OPE can be modified to support RR and RROA,[333] but its application suffers from several limitations. First, contrary to one-photon spectroscopies, the transition moments involving $\boldsymbol{P}^{\mathrm{A},e}$

and $\boldsymbol{P}^{\mathrm{B},e}$ are not symmetric, so this means in theory keeping track and combining two separate terms, with the difficulty of establishing a reliable prediction pattern to select the most intense transitions. The latter point is a second difficulty for this prescreening since, as already noted for ECD and CPL, it generally performs worse if intensity and transition probability are not directly connected. Those limitations could be overcome by selecting more transitions to compute per class, and checking *a posteriori* the reliability. However, the latter is not possible for RR and RROA, where analytical sum rules are not available due to the frequency appearing in the denominator. While more complete prescreening scheme could be devised, the impossibility of evaluating rigorously their reliability strongly hampers their use in black-box procedures.

5.2 Time-dependent formulation

In this section, the general TD framework introduced in the previous chapter will generalized to RR and RROA spectroscopies. Let us begin from RR, whose simulation requires only the polarizability tensor $\boldsymbol{\alpha}_{mn}$. The starting point of the TD theory is the expression of the sum-over-states formula given in Eq. 5.33 in the time domain using the mathematical properties of the Fourier transform. For RR, the transition from the frequency domain to the time domain is done trough the following relation,[334,335,336,337,338]

$$\frac{1}{x} = \frac{i}{\hbar}\int_0^{+\infty} e^{-ixt/\hbar}\mathrm{d}t\,, \tag{5.34}$$

which can be used to express the polarizability tensor as,

$$\alpha_{0k,\rho\eta} = \frac{i}{\hbar^2}\sum_{j=1}^{+\infty}\int_0^{+\infty} \mathrm{d}t\,\langle\,\overline{\psi}_k \mid \mu^e_\rho \mid \overline{\overline{\psi}}_j\,\rangle\langle\,\overline{\overline{\psi}}_j \mid \mu^e_\eta \mid \overline{\psi}_0\,\rangle\, e^{-it(\omega_{j0}-\omega_\mathrm{I}-i\gamma)} \tag{5.35}$$

Following the same strategy already employed for the TD formulation of one-photon spectroscopies, the previous equation can be expressed in a more compact form in terms of the time-evolution operator $e^{-i\overline{\overline{\mathcal{H}}}\overline{\tau}}$ as,

$$\begin{aligned}\alpha^k_{0k,\rho\eta} &= \frac{i}{\hbar^2}\int_0^{+\infty} \mathrm{d}t\,\langle\,\overline{\psi}_k \mid \mu^e_\rho e^{-i\overline{\overline{\mathcal{H}}}\overline{\tau}}\mu^e_\eta \mid \overline{\psi}_0\,\rangle\, e^{-it(\omega_\mathrm{ad}-\omega_\mathrm{I}-i\gamma)} \\ &= \frac{i}{\hbar^2}\int_0^{+\infty} \mathrm{d}t\,\chi^{\mathrm{RR}}_{\mathrm{full},0k,\rho\eta}(t)\, e^{-it(\omega_\mathrm{ad}-\omega_\mathrm{I}-i\gamma)}\end{aligned} \tag{5.36}$$

where the cross-correlation function $\chi^{\mathrm{RR}}_k(t)$ is defined as,

$$\boldsymbol{\chi}^{\mathrm{RR}}_{\mathrm{full},0k} = \langle\,\overline{\psi}_k \mid \boldsymbol{\mu}^e \otimes e^{-i\overline{\overline{\mathcal{H}}}\overline{\tau}}\boldsymbol{\mu}^e \mid \overline{\psi}_0\,\rangle \tag{5.37}$$

The cross-correlation function above is the counterpart of the auto-correlation function $\chi_\mathrm{full}(t)$ given in Eq. 4.62 for RR spectroscopy. Before describing how $\boldsymbol{\chi}^{\mathrm{RR}}_{\mathrm{full},0k}$ can be computed, it is useful to highlight the differences between

$\boldsymbol{\chi}^{\mathrm{RR}}_{\mathrm{full},0k}$ and $\chi_{\mathrm{full}}(t)$. As discussed in the previous chapter, $\chi_{\mathrm{full}}(t)$ can be expressed as a trace, since the wavefunction appearing in the bra and the ket are equal. As a result, it can be evaluated as the trace in the basis formed by the eigenfunction of the position operator by exploiting the Feynmann path integral theory. This simplification is not possible for the cross-correlation function $\boldsymbol{\chi}^{\mathrm{RR}}_{\mathrm{full},0k}$, since the wavefunctions appearing on the bra and on the ket are different. A further difference between $\chi_{\mathrm{full}}(t)$ and $\boldsymbol{\chi}^{\mathrm{RR}}_{\mathrm{full},0k}$ is that the former includes two time-evolution operators ($e^{-i\overline{\mathcal{H}}\overline{\tau}}$ and $e^{-i\overline{\overline{\mathcal{H}}}\overline{\tau}}$), whereas only $e^{-i\overline{\overline{\mathcal{H}}}\overline{\tau}}$ appears in Eq. 5.37. This is a consequence of neglecting the temperature effects. In fact, in this case, $|\,\overline{\psi}_0\,\rangle$ is the only populated vibrational level of the initial electronic state, thus the trace is equivalent to the expectation value over $|\,\overline{\psi}_0\,\rangle$.

Several strategies can be implemented to compute $\boldsymbol{\alpha}_{0k}$ starting from Eq. 5.36. In the most accurate methods, the time-evolution of the cross-correlation function is simulated using full quantum dynamics approaches, by solving explicitly the time-dependent Schrödinger equation.[339,340] The computational cost of those approaches is usually high, since an accurate sampling of the intermediate-state PES is usually required and make them applicable only to small-size systems. To limit the computational cost, both PESs can be approximated as harmonic, as already done for OP spectroscopies. In this case, closed-form expression can be derived for $\boldsymbol{\chi}^{\mathrm{RR}}_{\mathrm{full},0k}$. Such approaches have already been employed in the literature, but in most cases were combined with simplified vibronic models, based on the FC approximation[336,337,341,342] and neglecting mode-mixing effects.[97,98] Furthermore, the extension to RROA has been proposed, up to our knowledge, only in Refs. 343 and 344, where however the so-called short-time approximation is used to compute the RROA spectra, which is well suited for pre-resonance conditions, but is ill-suited to describe strong resonances. The TD formulation has been used also in Ref.[327] to derive formal properties of the different transition tensors, but in practice the simulations were performed at the TI level, using the independent mode harmonic oscillator model (IMDHO, equivalent to the VG model described in Chapter 4).[97,335,337] Here, since the TD framework introduced in Chapter 4 is extended to RR and RROA spectroscopies, it includes a full support, at the harmonic level, of mode-mixing and HT effects, as well as the possibility of performing calculations in internal coordinates. We note that, for OP spectroscopies, the TI and TD approaches are complementary, since the latter gives access to the overall bandshape with a limited computational cost, whereas the former allows to assign individual vibronic bands. This is not true for RR spectroscopy, where the two approaches provide the same information, so that the TD approach is usually preferred due to its higher numerical stability and reliability.

The TD equivalent of Eq. 5.33 can be derived starting from Eq. 5.36 and using the general transition properties $\boldsymbol{P}^{\mathrm{A}}$ and $\boldsymbol{P}^{\mathrm{B}}$ instead of the electric transition dipole moment,

$$T^{j}_{0k,\rho\eta} = \frac{i}{\hbar^2}\int_0^{+\infty} \mathrm{d}t \,\langle\, \overline{\psi}_k \mid P^{\mathrm{A},e}_{\rho} e^{-i\overline{\overline{\mathcal{H}}}\overline{\tau}} \{P^{\mathrm{B},e}_{\eta}\}^{\star} \mid \overline{\psi}_0 \,\rangle\, e^{-it(\omega_{\mathrm{ad}}-\omega_{\mathrm{I}}-i\gamma)} \tag{5.38}$$

For the sake of simplicity, the vibrational ground state $\mid \overline{\psi}_0 \,\rangle$ will be labeled in the following as $\mid \overline{\mathbf{0}} \,\rangle$. As already mentioned above, only fundamental transitions will be included in the treatment, so that in the final state only one mode, with index k, is singly excited. Using the Dirac notation, the final state will be labeled as $\mid \overline{\mathbf{1}}_k \,\rangle = \mid \overline{\mathbf{0}} + 1_k \,\rangle$. At the FC level (the inclusion of HT effects will be discussed in the next subsection), Eq. 5.38 can be rewritten as,

$$T_{0k,\rho\eta} = \frac{i}{\hbar^2}\, \mathrm{P}^{\mathrm{A},e}_{\rho}\left(\overline{\overline{\boldsymbol{Q}}}^{\mathrm{eq}}\right) \{\mathrm{P}^{\mathrm{B},e}_{\eta}\}^{\star}\left(\overline{\overline{\boldsymbol{Q}}}^{\mathrm{eq}}\right) \int_0^{+\infty} \mathrm{d}t \,\langle\, \overline{\mathbf{1}}_k \mid e^{-i\overline{\overline{\mathcal{H}}}\overline{\tau}} \mid \overline{\mathbf{0}} \,\rangle\, e^{-it(\omega_{\mathrm{ad}}-\omega_{\mathrm{I}}-i\gamma)} \tag{5.39}$$

The cross-correlation function $\langle\, \overline{\mathbf{1}}_k \mid e^{-i\overline{\overline{\mathcal{H}}}\overline{\tau}} \mid \overline{\mathbf{0}} \,\rangle$, labeled in the following as $\chi^{\mathrm{RR}}_{0k}(t)$, can be expressed as follows, following the same strategy adopted for the autocorrelation function,

$$\begin{aligned}\chi^{\mathrm{RR}}_{0k}(t) =& \sqrt{\frac{\det \overline{\overline{\boldsymbol{a}}}}{(2\pi\hbar)^{N_{\mathrm{vib}}}}} \int_{-\infty}^{+\infty} d\overline{\overline{\boldsymbol{Q}}} \int_{-\infty}^{+\infty} d\overline{\overline{\boldsymbol{Q}}}' \\ &\times \langle\, \overline{\mathbf{1}}_k \mid \overline{\boldsymbol{Q}}' \,\rangle \exp\left(\frac{i}{\hbar}\left[\frac{1}{2}\overline{\overline{\boldsymbol{Q}}}'^{\mathrm{T}}\,\overline{\overline{\boldsymbol{b}}}\,\overline{\overline{\boldsymbol{Q}}}' + \frac{1}{2}\overline{\overline{\boldsymbol{Q}}}^{\mathrm{T}}\,\overline{\overline{\boldsymbol{b}}}\,\overline{\overline{\boldsymbol{Q}}} - \overline{\overline{\boldsymbol{Q}}}^{\mathrm{T}}\,\overline{\overline{\boldsymbol{a}}}\,\overline{\overline{\boldsymbol{Q}}}'\right]\right) \langle\, \overline{\boldsymbol{Q}} \mid \overline{\mathbf{0}} \,\rangle\end{aligned} \tag{5.40}$$

where the definition of $\overline{\overline{\boldsymbol{a}}}$ and $\overline{\overline{\boldsymbol{b}}}$ was given in the previous chapter. The coordinates representation of the vibrational wavefunctions $\mid \overline{\mathbf{0}} \,\rangle$ and $\mid \overline{\mathbf{1}}_k \,\rangle$ is the following,

$$\begin{aligned}\langle\, \overline{\boldsymbol{Q}} \mid \overline{\mathbf{0}} \,\rangle &= \prod_{i=1}^{N_{\mathrm{vib}}} \left(\frac{\overline{\omega}_i}{\pi\hbar}\right)^{1/4} \exp\left(-\frac{\overline{\omega}_i \overline{Q}_i^2}{2\hbar}\right) = \frac{(\det \overline{\boldsymbol{\Gamma}})^{1/4}}{\pi^{N_{\mathrm{vib}}/4}} \exp\left(-\frac{\overline{\boldsymbol{Q}}^T\,\overline{\boldsymbol{\Gamma}}\,\overline{\boldsymbol{Q}}}{2}\right) \\ \langle\, \overline{\mathbf{1}}_k \mid \overline{\boldsymbol{Q}}' \,\rangle &= \sqrt{\frac{\overline{\omega}_k}{2\hbar}}\overline{Q}'_k \prod_{i=1}^{N_{\mathrm{vib}}} \left(\frac{\overline{\omega}_i}{\pi\hbar}\right)^{1/4} \exp\left(-\frac{\overline{\omega}_i \overline{Q}_i'^2}{2\hbar}\right) \\ &= \sqrt{\frac{\overline{\Gamma}_k}{2}}\overline{Q}'_k \,\frac{(\det \overline{\boldsymbol{\Gamma}})^{1/4}}{\pi^{N_{\mathrm{vib}}/4}} \exp\left(-\frac{\overline{\boldsymbol{Q}}'^T\,\overline{\boldsymbol{\Gamma}}\,\overline{\boldsymbol{Q}}'}{2}\right)\end{aligned} \tag{5.41}$$

with $\overline{\boldsymbol{\Gamma}}$ being the diagonal matrix with the reduced frequencies of the initial state. By including the previous definitions in Eq. 5.40, the following result is obtained,

$$
\begin{aligned}
\chi_{0k}^{\mathrm{RR}}(t) = & \sqrt{\frac{\det \overline{\mathbf{\Gamma}}\overline{\boldsymbol{a}}}{(2\pi\hbar)^{2N_{\mathrm{vib}}}}} \int_{-\infty}^{+\infty} d\overline{\overline{\boldsymbol{Q}}} \int_{-\infty}^{+\infty} d\overline{\overline{\boldsymbol{Q}}}' \sqrt{\frac{\overline{\omega}_k}{2\hbar}} \overline{Q}'_k \\
& \times \exp\left(\frac{i}{\hbar}\left[\frac{1}{2}\overline{\overline{\boldsymbol{Q}}}'^{\mathrm{T}}\,\overline{\overline{\boldsymbol{b}}}\,\overline{\overline{\boldsymbol{Q}}}' + \frac{1}{2}\overline{\overline{\boldsymbol{Q}}}^{\mathrm{T}}\,\overline{\overline{\boldsymbol{b}}}\,\overline{\overline{\boldsymbol{Q}}} - \overline{\overline{\boldsymbol{Q}}}^{\mathrm{T}}\,\overline{\overline{\boldsymbol{a}}}\,\overline{\overline{\boldsymbol{Q}}}'\right]\right) \\
& \times \exp\left(-\frac{\left(\boldsymbol{K}^T + \overline{\overline{\boldsymbol{Q}}}^T \boldsymbol{J}^T\right) \overline{\mathbf{\Gamma}} \left(\boldsymbol{J}\overline{\overline{\boldsymbol{Q}}} + \boldsymbol{K}\right)}{2}\right) \\
& \times \exp\left(-\frac{\left(\boldsymbol{K}^T + \overline{\overline{\boldsymbol{Q}}}'^T \boldsymbol{J}^T\right) \overline{\mathbf{\Gamma}} \left(\boldsymbol{J}\overline{\overline{\boldsymbol{Q}}}' + \boldsymbol{K}\right)}{2}\right) \\
= & \sqrt{\frac{\det \overline{\mathbf{\Gamma}}\overline{\boldsymbol{a}}}{(2\pi\hbar)^{2N_{\mathrm{vib}}}}} \int_{-\infty}^{+\infty} d\overline{\overline{\boldsymbol{Q}}} \int_{-\infty}^{+\infty} d\overline{\overline{\boldsymbol{Q}}}' \sqrt{\frac{\overline{\omega}_k}{2\hbar}}\, \overline{Q}'_k\, \chi(t,0)
\end{aligned}
\tag{5.42}
$$

where $\chi(t,0)$ corresponds to the FC autocorrelation function $\chi(t)$ in the limit T $\to$ 0 K. In fact, in the limit of null temperature, $\beta \to +\infty$, which means that $\overline{\boldsymbol{a}} \to \mathbf{0}$ and $\overline{\boldsymbol{b}} \to \overline{\mathbf{\Gamma}}$ since,

$$
\begin{aligned}
\sinh\left(\hbar\overline{\tau}\,\overline{\omega}_i\right) &\longrightarrow +\infty \\
\tanh\left(\hbar\overline{\tau}\,\overline{\omega}_i\right) &\longrightarrow 1
\end{aligned}
\tag{5.43}
$$

From Eq. 4.73, this means that also $\overline{\boldsymbol{c}} \to \overline{\mathbf{\Gamma}}$ and $\overline{\boldsymbol{d}} \to \overline{\mathbf{\Gamma}}$. By substituting these relations in Eq. 4.79, Eq. 5.42 is recovered. $\chi(t,0)$ can be expressed as,

$$
\chi(t,0) = \langle\, \overline{\mathbf{0}} \mid e^{-i\overline{\overline{\mathcal{H}}}\overline{\tau}} \mid \overline{\mathbf{0}}\, \rangle \tag{5.44}
$$

and computed from Eq. 4.79. For OP spectroscopies, the tensors $\chi_{ijk\ldots}^{lmn\ldots}(t)$ were introduced to compute the autocorrelation function at the HT level. Their counterpart at 0 K are obtained as,

$$
\chi_{ijk\ldots}^{lmn\ldots}(t,0) = \langle\, \overline{\mathbf{0}} \mid \overline{\overline{\mathcal{Q}}}_i \overline{\overline{\mathcal{Q}}}_j \overline{\overline{\mathcal{Q}}}_k \ldots e^{-i\overline{\overline{\mathcal{H}}}\overline{\tau}} \overline{\overline{\mathcal{Q}}}_l \overline{\overline{\mathcal{Q}}}_m \overline{\overline{\mathcal{Q}}}_n \ldots \mid \overline{\mathbf{0}}\, \rangle \tag{5.45}
$$

Unlike OP spectroscopies, where $\chi(t)$ is the only quantity needed to simulate the spectrum at the FC level, for RR and RROA $\chi(t,0)$ is not sufficient to perform FC simulations. In fact, in the integral given in Eq. 5.42, the autocorrelation function $\chi(t,0)$ is scaled by $\overline{Q}'_k$. The Duschinsky transformation can be used to express $\overline{Q}'_k$ as,

$$
\overline{Q}'_k = \sum_{l=1}^{N_{\mathrm{vib}}} J_{kl} \overline{\overline{Q}}'_l + K_k \tag{5.46}
$$

This allows expressing Eq. 5.44 in terms of the general tensors defined in Eq. 5.45 as,

$$\begin{aligned}\chi_{0k}^{\mathrm{RR}}(t) &= \sqrt{\frac{\overline{\Gamma}_k}{2}}\left(\sum_{l=1}^{N_{\mathrm{vib}}} J_{kl}\langle\,\overline{\mathbf{0}}\mid\overline{\overline{\mathcal{Q}}}_l e^{-i\overline{\overline{\mathcal{H}}}\overline{\tau}}\mid\overline{\mathbf{0}}\,\rangle + K_k\langle\,\overline{\mathbf{0}}\mid e^{-i\overline{\overline{\mathcal{H}}}\overline{\tau}}\mid\overline{\mathbf{0}}\,\rangle\right)\\ &= \sqrt{\frac{\overline{\Gamma}_k}{2}}\left(\sum_{l=1}^{N_{\mathrm{vib}}} J_{kl}\chi_l(t,0) + K_k\chi(t,0)\right)\end{aligned} \tag{5.47}$$

The tensor $\chi_l(t,0)$ can be computed using Eq. 4.85 in terms of the element of the $\boldsymbol{\eta}$ vector introduced in Eq. 4.86 as follows,

$$\chi_{0k}^{\mathrm{RR}}(t) = \sqrt{\frac{\overline{\Gamma}_k}{2}}\left(-\frac{1}{\sqrt{2}}\sum_{l=1}^{N_{\mathrm{vib}}} J_{kl}\eta_l + K_k\right)\chi(t,0) \tag{5.48}$$

where $\boldsymbol{\eta}$ is computed Eq. 4.86 by setting $\overline{\boldsymbol{d}} = \boldsymbol{I}$. Combining Eqs. 5.39 and 5.48, the element $(\rho\eta)$ of the general transition operator $\boldsymbol{T}_{0k}$ is the following:

$$\begin{aligned}T_{0k,\rho\eta} = \frac{i}{\hbar}\sqrt{\frac{\overline{\Gamma}_k}{2}} P_{\rho}^{\mathrm{A},e}\left(\overline{\overline{\boldsymbol{Q}}}^{\mathrm{eq}}\right) P_{\eta}^{\mathrm{B},e}\left(\overline{\overline{\boldsymbol{Q}}}^{\mathrm{eq}}\right)\\ \times\int_0^{+\infty}\mathrm{d}t\left(\mathbf{K}-\frac{1}{\sqrt{2}}\mathbf{J}\boldsymbol{\eta}\right)_k\chi(t,0)\; e^{-it(\omega_{\mathrm{ad}}-\omega_{\mathrm{I}}-i\gamma)}\end{aligned} \tag{5.49}$$

It should be noted that the evaluation of the previous integral does not increase the computational time with respect to the OP case, since $\boldsymbol{\eta}$ is already needed to compute $\chi(t,0)$. Furthermore, the multiplication by the Duschinsky matrix, that would, in principle, increase the computational time, can be performed after the integration, since $\mathbf{J}$ is a time-independent quantity.
In Eq. 5.49, the transition tensor $\boldsymbol{T}_{0k}$ is factorized as the product between a purely electronic term and the Fourier transform of the cross-correlation function, that is determined only by nuclear properties. A direct consequence of this factorization is that only a limited subset of the invariants among the ones given in Eqs. 5.18-5.30 are actually needed to compute the RROA spectrum. In fact, by choosing, without loss of generality, the z axis of the reference system along the electric dipole moment $\boldsymbol{\mu}$, the only non-null element of $\boldsymbol{\alpha}_{0k}$ is $\alpha_{0k,zz}$. As a consequence, $\boldsymbol{\alpha}_{0k}^{a} = \mathbf{0}$ and $\beta_a(\mathcal{G}) = \beta_a(\mathcal{G}') = \beta_a(\mathcal{A}) = \beta_a(\mathcal{A}') = 0$. Furthermore, $\beta_s(A) = \mathbf{0}$, since, in Eq. 5.27, $\alpha_{0k,\rho\eta} \neq 0$ only for $\rho = \eta = z$ and, for the same reason, $\mathcal{A}^{s}_{0k,\delta,\lambda\eta} \neq 0$ only for $\delta = z$, but in those cases $\epsilon_{zz\eta} = 0$, and therefore $\beta_s(\mathcal{A}) = 0$. For the same reason, $\beta_s(\mathcal{A}') = 0$. The same relations have been derived by Nafie and co-workers in Refs. 63 and 345 within the so-called single electronic state limit (SES), where mode-mixing and frequency change effects are neglected by including only one resonant electronic state. However, the previous discussion shows that the same relations hold also if mode-mixing and frequency changes effects are included, provided that the Franck-Condon approximation is used and a single intermediate-state is considered.

When multiple excited states are included in the treatment, the RROA spectrum can be computed from the relations given in Eqs. 5.18-5.30, provided that the general transition tensors is obtained as a sum over all the N_{res} resonant states,

$$\boldsymbol{T}_{0k} = \sum_{l=1}^{N_{\text{res}}} \boldsymbol{T}_{0k}^{l} \tag{5.50}$$

where $\boldsymbol{T}_{0k}^{l}$ is the transition tensor obtained for the l-th resonant state.[327,333] In this case, the transition dipole moments for each transition has, in general, a different orientation, and therefore it is not possible to choose a coordinates system where each transition dipole moment is aligned along the same axis. Therefore, the simplified relations derived for the FC case do not hold for multiple resonant excited states.[346,347]

5.2.1 Inclusion of HT effects

The generalization of the previous theoretical framework to the inclusion of HT effects can be done following the same strategy employed for the FC case. By combining the expansion of the transition dipole moment given in Eq. 4.17 and the SOS expression given in Eq. 5.33, it is possible to derive the following relation,

$$\begin{aligned}
T_{0k,\rho\eta} = & \frac{1}{\hbar} \sum_{k=1}^{+\infty} \Bigg[P_{\rho}^{\mathrm{A},e}\left(\overline{\overline{\boldsymbol{Q}}}^{\mathrm{eq}}\right) \{P_{\eta}^{\mathrm{B},e}\}^{\star}\left(\overline{\overline{\boldsymbol{Q}}}^{\mathrm{eq}}\right) \frac{\langle\, \overline{\psi}_k \mid \overline{\overline{\psi}}_j \,\rangle\langle\, \overline{\overline{\psi}}_j \mid \overline{\psi}_0 \,\rangle}{\omega_{j0} - \omega_{\mathrm{I}} - i\gamma} \\
& + \sum_{m=1}^{N_{\text{vib}}} \left(\frac{\partial P_{\rho}^{\mathrm{A},e}}{\partial \overline{\overline{Q}}_m}\right)_{\mathrm{eq}} \{P_{\eta}^{\mathrm{B},e}\}^{\star}\left(\overline{\overline{\boldsymbol{Q}}}^{\mathrm{eq}}\right) \frac{\langle\, \overline{\psi}_k \mid \overline{\overline{Q}}_m \mid \overline{\overline{\psi}}_j \,\rangle\langle\, \overline{\overline{\psi}}_j \mid \overline{\psi}_0 \,\rangle}{\omega_{j0} - \omega_{\mathrm{I}} - i\gamma} \\
& + \sum_{m=1}^{N_{\text{vib}}} P_{\rho}^{\mathrm{A},e}\left(\overline{\overline{\boldsymbol{Q}}}^{\mathrm{eq}}\right) \left(\frac{\partial P_{\eta}^{\mathrm{B},e}}{\partial \overline{\overline{Q}}_j}\right)_{\mathrm{eq}}^{\star} \frac{\langle\, \overline{\psi}_k \mid \overline{\overline{\psi}}_j \,\rangle\langle\, \overline{\overline{\psi}}_j \mid \overline{\overline{Q}}_m \mid \overline{\psi}_0 \,\rangle}{\omega_{j0} - \omega_{\mathrm{I}} - i\gamma} \\
& + \sum_{l,m=1}^{N_{\text{vib}}} \left(\frac{\partial P_{\rho}^{\mathrm{A},e}}{\partial \overline{\overline{Q}}_l}\right)_{\mathrm{eq}} \left(\frac{\partial P_{\eta}^{\mathrm{B},e}}{\partial \overline{\overline{Q}}_m}\right)_{\mathrm{eq}}^{\star} \frac{\langle\, \overline{\psi}_k \mid \overline{\overline{Q}}_l \mid \overline{\overline{\psi}}_j \,\rangle\langle\, \overline{\overline{\psi}}_j \mid \overline{\overline{Q}}_m \mid \overline{\psi}_0 \,\rangle}{\omega_{j0} - \omega_{\mathrm{I}} - i\gamma} \Bigg]
\end{aligned} \tag{5.51}$$

where the first term correspond to the pure FC contribution, the second and the third ones to the mixed FC/HT terms, and the last one to the pure HT contribution. Using Eq. 5.34 to express the previous relation in the time domain, the last three terms can be computed as Fourier Transform of the following cross-correlation function,

$$\begin{aligned}
\chi_{0k}^{\mathrm{RR},j} &= \langle\, \overline{\mathbf{1}}_k \mid e^{-i\overline{\overline{\mathcal{H}}}\overline{\tau}}\overline{\overline{Q}}_k \mid \overline{\mathbf{0}} \,\rangle \\
\chi_{0k,j}^{\mathrm{RR}} &= \langle\, \overline{\mathbf{1}}_k \mid \overline{\overline{Q}}_k e^{-i\overline{\overline{\mathcal{H}}}\overline{\tau}} \mid \overline{\mathbf{0}} \,\rangle \\
\chi_{0k,j}^{\mathrm{RR},l} &= \langle\, \overline{\mathbf{1}}_k \mid \overline{\overline{Q}}_j e^{-i\overline{\overline{\mathcal{H}}}\overline{\tau}}\overline{\overline{Q}}_l \mid \overline{\mathbf{0}} \,\rangle
\end{aligned} \tag{5.52}$$

Starting from Eq. 5.52, it is easy to show that the cross-correlation functions given in the previous equation can be related to the autocorrelation functions at 0 K as follows,

$$\begin{aligned}
\chi^{\mathrm{RR}}_{0k,j} &= \frac{i}{\hbar}\sqrt{\frac{\overline{\Gamma}_k}{2}}\left(K_k\chi_j(t,0) + \sum_{i=1}^{N_{\mathrm{vib}}} J_{ki}\chi_{ij}(t,0)\right) \\
\chi^{\mathrm{RR},j}_{0k} &= \frac{i}{\hbar}\sqrt{\frac{\overline{\Gamma}_k}{2}}\left(K_k\chi^j(t,0) + \sum_{i=1}^{N_{\mathrm{vib}}} J_{ki}\chi^j_i(t,0)\right) \\
\chi^{\mathrm{RR},l}_{0k,j} &= \frac{i}{\hbar}\sqrt{\frac{\overline{\Gamma}_k}{2}}\left(K_k\chi^l_j(t,0) + \sum_{i=1}^{N_{\mathrm{vib}}} J_{ki}\chi^l_{ij}(t,0)\right)
\end{aligned} \tag{5.53}$$

where the tensors $\chi_j(t,0)$, $\chi^j(t,0)$, $\chi_{ij}(t,0)$, $\chi^l_j(t,0)$ and $\chi^l_{ij}(t,0)$ can be computed using the relations derived in the previous chapter. Also in this case, it is useful to compare the computational cost of the simulation of a RR spectrum at the FCHT level with the OP equivalent. The only additional tensor that needs to be computed is $\chi^l_{ij}(t,0)$, which is a three-indexes tensor and whose calculation increases the computational cost by a factor of N_{vib}, as can be understood from Eq. 4.142.
The general transition tensor $\boldsymbol{T}_{0k}$ defined in Eq. 5.32 can be expressed, using the definitions introduced in Eq. 5.38, as follows:

$$\boldsymbol{T}_{0k} = \frac{i}{\hbar}\sqrt{\frac{\overline{\Gamma}_k}{2}}\int_0^{+\infty} \mathrm{d}t\left[\boldsymbol{\chi}^{\mathrm{FC}}_{0k} + \boldsymbol{\chi}^{\mathrm{FCHT,1}}_{0k} + \boldsymbol{\chi}^{\mathrm{FCHT,2}}_{0k} + \boldsymbol{\chi}^{\mathrm{HT}}_{0k}\right] \tag{5.54}$$

where the cross-correlation function matrices $\chi^{\mathrm{FCHT,1}}_{0k}$, $\chi^{\mathrm{FCHT,2}}_{0k}$ and χ^{HT}_{0k}) are defined as,

$$\begin{aligned}
\boldsymbol{\chi}^{\mathrm{FC}}_{0k} &= \boldsymbol{P}^{\mathrm{A},e}\left(\overline{\overline{\boldsymbol{Q}}}^{\mathrm{eq}}\right) \otimes \{\boldsymbol{P}^{\mathrm{B},e}\}^{\star}\left(\overline{\overline{\boldsymbol{Q}}}^{\mathrm{eq}}\right)\chi^{\mathrm{RR}}_{0k}(t) \\
\boldsymbol{\chi}^{\mathrm{FCHT,1}}_{0k} &= \sum_{l=1}^{N_{\mathrm{vib}}}\left(\frac{\partial \boldsymbol{P}^{\mathrm{A},e}}{\partial \overline{\overline{Q}}_l}\right)_{\mathrm{eq}} \otimes \{\boldsymbol{P}^{\mathrm{B},e}\}^{\star}\left(\overline{\overline{\boldsymbol{Q}}}^{\mathrm{eq}}\right)\chi^{\mathrm{RR}}_{0k,l} \\
\boldsymbol{\chi}^{\mathrm{FCHT,2}}_{0k} &= \sum_{l=1}^{N_{\mathrm{vib}}} \boldsymbol{P}^{\mathrm{A},e}\left(\overline{\overline{\boldsymbol{Q}}}^{\mathrm{eq}}\right) \otimes \left(\frac{\partial \boldsymbol{P}^{\mathrm{B},e}}{\partial \overline{\overline{Q}}_l}\right)^{\star}_{\mathrm{eq}}\chi^{\mathrm{RR}l}_{0k} \\
\boldsymbol{\chi}^{\mathrm{HT}}_{0k} &= \sum_{l,m=1}^{N_{\mathrm{vib}}}\left(\frac{\partial \boldsymbol{P}^{\mathrm{A},e}}{\partial \overline{\overline{Q}}_l}\right)_{\mathrm{eq}} \otimes \left(\frac{\partial \boldsymbol{P}^{\mathrm{B},e}}{\partial \overline{\overline{Q}}_m}\right)^{\star}_{\mathrm{eq}}\chi^{\mathrm{RR},m}_{0k,l}
\end{aligned} \tag{5.55}$$

5.2.2 Gauge invariance

As has been already discussed in the literature,[344,346,348,349,350] for a given molecular structure, the definition of the transition properties $\boldsymbol{\mu}_{mn}$, $\boldsymbol{m}_{mn}$ and $\boldsymbol{\Theta}_{mn}$ changes with the origin of the reference axes used in the simulation. This effect is usually known as gauge-dependence. Let us consider, for example,

two reference systems with origin in $\boldsymbol{x}^0$ and $\boldsymbol{x}^0 + \boldsymbol{a}$, respectively. The transition properties in the first ($\boldsymbol{\mu}_{mn}\left(\boldsymbol{x}^0\right)$, $\boldsymbol{m}_{mn}\left(\boldsymbol{x}^0\right)$, $\boldsymbol{\Theta}_{mn}\left(\boldsymbol{x}^0\right)$) and in the second reference system ($\boldsymbol{\mu}_{mn}\left(\boldsymbol{x}^0 + \boldsymbol{a}\right)$, $\boldsymbol{m}_{mn}\left(\boldsymbol{x}^0 + \boldsymbol{a}\right)$, $\boldsymbol{\Theta}_{mn}\left(\boldsymbol{x}^0 + \boldsymbol{a}\right)$) are related by the following transformation:

$$\begin{aligned}
\boldsymbol{\mu}_{mn}\left(\boldsymbol{x}^0 + \boldsymbol{a}\right) &= \boldsymbol{\mu}_{mn}\left(\boldsymbol{x}^0\right) \\
\boldsymbol{m}_{mn}\left(\boldsymbol{x}^0 + \boldsymbol{a}\right) &= \boldsymbol{m}_{mn}\left(\boldsymbol{x}^0\right) + \frac{1}{2}\boldsymbol{a} \times \boldsymbol{p}_{mn} \\
\Theta_{mn,\rho\eta}\left(\boldsymbol{x}^0 + \boldsymbol{a}\right) &= \boldsymbol{\Theta}_{mn,\rho\eta}\left(\boldsymbol{x}^0\right) - \frac{3}{2}a_\rho \mu_{mn,\eta} - \frac{3}{2}a_\eta \mu_{mn,\rho} + \boldsymbol{a} \cdot \boldsymbol{\mu}_{mn}\delta_{\rho\eta}
\end{aligned} \tag{5.56}$$

The relations given in Eq. 5.56 can be used to express the transition properties as Taylor expansion (as in Eq. 4.17) and to derive relations between the equilibrium value of the transition property and its derivatives in the two different coordinates systems. For the sake of simplicity, we will now use the FC approximation to derive those relations, with a single resonant state. Under those approximations, the following relations can be derived,[346]

$$\begin{aligned}
\boldsymbol{\alpha}_{mn}\left(\boldsymbol{x}^0 + \boldsymbol{a}\right) &= \boldsymbol{\alpha}_{mn}\left(\boldsymbol{x}^0\right) \\
\mathcal{G}_{mn,\rho\eta}\left(\boldsymbol{x}^0 + \boldsymbol{a}\right) &= \mathcal{G}_{mn,\rho\eta}\left(\boldsymbol{x}^0\right) + \frac{i}{2}\omega_{\mathrm{ad}}\epsilon_{\eta\lambda\delta}a_\lambda \alpha_{mn,\rho\delta} \\
\mathcal{G}'_{mn,\rho\eta}\left(\boldsymbol{x}^0 + \boldsymbol{a}\right) &= \mathcal{G}'_{mn,\rho\eta}\left(\boldsymbol{x}^0\right) + \frac{i}{2}\omega_{\mathrm{ad}}\epsilon_{\eta\lambda\delta}a_\lambda \alpha_{mn,\rho\delta} \\
\mathcal{A}_{mn,\rho,\eta\delta}\left(\boldsymbol{x}^0 + \boldsymbol{a}\right) &= \mathcal{A}_{mn,\rho,\eta\delta}\left(\boldsymbol{x}^0\right) - \frac{3}{2}a_\eta \alpha_{mn,\delta\rho} - \frac{3}{2}a_\delta \alpha_{mn,\rho\eta} + \delta_{\eta\delta}a_\lambda \alpha_{mn,\rho\lambda} \\
\mathcal{A}'_{mn,\rho,\eta\delta}\left(\boldsymbol{x}^0 + \boldsymbol{a}\right) &= \mathcal{A}'_{mn,\rho,\eta\delta}\left(\boldsymbol{x}^0\right) - \frac{3}{2}a_\eta \alpha_{mn,\delta\rho} - \frac{3}{2}a_\delta \alpha_{mn,\rho\eta} + \delta_{\eta\delta}a_\lambda \alpha_{mn,\rho\lambda}
\end{aligned} \tag{5.57}$$

Despite the origin-dependence of the individual transition tensors, by using Eq. 5.57 to compute the invariants, it can be shown that all the terms depending on the origin shift $\boldsymbol{a}$ cancel out. However, the transformation rules given in Eq. 5.56 holds only for electronic wavefunctions obtained with a complete basis-set. When a finite-size basis set is employed, the relation between $\boldsymbol{m}_{mn}\left(\boldsymbol{x}^0 + \boldsymbol{a}\right)$ and $\boldsymbol{m}_{mn}\left(\boldsymbol{x}^0\right)$ does not hold anymore,[351] and therefore the gauge-invariance of the RROA intensities is not guaranteed. This limitation can be overcome with the so-called gauge-independent atomic orbitals (GIAO),[352,353] in which a magnetic field-dependent phase factor is included in order to remove the gauge dependence of the transition magnetic dipole moment also for finite basis sets. Another solution is to compute the electric transition dipole and quadrupole moments using the so-called velocity representation (labeled in the following as $\boldsymbol{\mu}^p_{mn}$ and $\boldsymbol{\Theta}^p_{mn}$, respectively).[351,354]. The relation between $\boldsymbol{\mu}^p_{mn}$ and $\boldsymbol{\Theta}^p_{mn}$ and their length-gauge counterpart is,

$$\begin{aligned}\boldsymbol{\mu}_{mn} &= -\frac{i\hbar}{E_m - E_n}\sum_{a=1}^{N_{\text{at}}}\langle\, \phi_m \mid \boldsymbol{p}_a \mid \phi_n \,\rangle = -\frac{i\hbar}{E_m - E_n}\boldsymbol{\mu}^p_{mn} \\ \boldsymbol{\Theta}_{mn} &= -\frac{i\hbar}{E_m - E_n}\sum_{a=1}^{N_{\text{at}}}\langle\, \phi_m \mid \boldsymbol{p}_a \otimes \boldsymbol{r}_a \mid \phi_n \,\rangle = -\frac{i\hbar}{E_m - E_n}\boldsymbol{\Theta}^p_{mn}\end{aligned} \tag{5.58}$$

where E_m and E_n are the energies of the electronic states involved in the transition, computed at the same geometry used for the calculation of the transition properties. The transition tensors in the velocity representation are origin-dependent too, but this dependence cancels out for the invariants.[346] However, at variance with the length representation, in this case the gauge-invariance holds also for finite basis sets in this case, and so is valid in practice for quantum-chemical calculations. Therefore, in the following, all transition properties will be computed in the velocity representation.
The previous discussion is valid only at the FC level and including only a single intermediate-state. As discussed in Ref. 346, the further inclusion of HT effects requires the transformation of the first-order derivatives of the transition properties from the length to the velocity representation. This can be done by differentiation of both sides of Eq. 5.58 with respect to the normal mode Q_k,[346]

$$\begin{aligned}\frac{\partial \boldsymbol{\mu}_{mn}}{\partial Q_k} &= \frac{i\boldsymbol{\mu}^p_{mn}}{\omega^2_{mn}}\frac{\partial \omega_{mn}}{\partial Q_k} - \frac{i}{\omega_{mn}}\frac{\partial \boldsymbol{\mu}^p_{mn}}{\partial Q_k} \\ \frac{\partial \boldsymbol{\Theta}_{mn}}{\partial Q_k} &= \frac{i\boldsymbol{\Theta}^p_{mn}}{\omega^2_{mn}}\frac{\partial \omega_{mn}}{\partial Q_k} - \frac{i}{\omega_{mn}}\frac{\partial \boldsymbol{\Theta}^p_{mn}}{\partial Q_k}\end{aligned} \tag{5.59}$$

where $\omega_{mn} = (E_m - E_n)/\hbar$ and $\partial\omega_{mn}/\partial Q_k$ can be expressed as $\left(\overline{\overline{g}}_k - \overline{g}_k\right)/\hbar$, where $\overline{\boldsymbol{g}}$ and $\overline{\overline{\boldsymbol{g}}}$ are the gradient of the initial- and intermediate-state PESs computed at the same geometry as the one used to compute the transition properties. This reference geometry is different whether adiabatic or vertical models are used. For vertical models, all the quantities are computed at the equilibrium geometry of the ground electronic state, and therefore $\overline{\boldsymbol{g}} = \boldsymbol{0}$ and $\overline{\overline{\boldsymbol{g}}}$ is the gradient of the intermediate-state PES which is used to build the Duschinsky transformation.[268] Furthermore, the energy separation ω_{mn} is the vertical excitation energy. The calculation is less trivial for adiabatic models, since the transition properties are computed at the equilibrium geometry of the intermediate-state PES. For this nuclear configuration, $\overline{\overline{\boldsymbol{g}}} = \boldsymbol{0}$, whereas $\overline{\boldsymbol{g}}$ is in general non null and not available, since it is not involved in the definition of the Duschinsky transformation. In order to avoid an additional gradient computation, $\overline{\boldsymbol{g}}$ can be extrapolated using the harmonic approximation of the initial state PES as follows,

$$\overline{\mathbf{g}} = \frac{1}{\hbar}\overline{\boldsymbol{H}}\left(\overline{\overline{\boldsymbol{x}}}^{\text{eq}} - \overline{\boldsymbol{x}}^{\text{eq}}\right) \tag{5.60}$$

where $\overline{\boldsymbol{H}}$ is the Hessian of the initial state, whereas $\overline{\boldsymbol{x}}^{\mathrm{eq}}$ and $\overline{\overline{\boldsymbol{x}}}^{\mathrm{eq}}$ are the equilibrium geometries of the initial and intermediate electronic states, respectively. The energy separation ω_m can be computed using the same extrapolation, which gives the following result,

$$\omega_{mn} = \frac{1}{\hbar}\left[\overline{\overline{E}} - \overline{E} + \frac{1}{2}\left(\overline{\overline{\boldsymbol{x}}}^{\mathrm{eq}} - \overline{\boldsymbol{x}}^{\mathrm{eq}}\right)^T \overline{\boldsymbol{H}} \left(\overline{\overline{\boldsymbol{x}}}^{\mathrm{eq}} - \overline{\boldsymbol{x}}^{\mathrm{eq}}\right)\right] \tag{5.61}$$

where $\overline{E}$ and $\overline{\overline{E}}$ are the adiabatic energies of the ground and intermedate electronic states. In Ref. 346 it is shown that, even if the derivatives of the transition properties are computed within the velocity representation using the transformation given in Eq. 5.59, the gauge-invariance of the RROA intensities is not ensured. In fact, in order for the invariants $\beta_s(\mathcal{G})^2$, $\beta_a(\mathcal{G})^2$, $\beta_s(\mathcal{A})^2$, $\beta_a(\mathcal{A})^2$ (as well as their counterpart obtained using $\mathcal{G}'$ and $\mathcal{A}'$) to be gauge invariant, the polarizability tensor must be symmetric, and this is not the case when HT effects are included. To conclude, let us remark that the issue of the origin-dependence is even more problematic when multiple intermediate-states are included in the simulation. In fact, in this case an additional gauge-dependent term appears in the definition of the $\beta_s(\mathcal{G})^2$ and $\beta_s(\mathcal{G}')^2$ invariants. A possible solution to this problem has been proposed in Ref. 346, by assuming that all the resonant states have the same excitation energy, which is set to the average of the excitation energies of the resonant states.

5.3 Examples of application

The TD theory of RR and RROA is applied in this section to the simulation of the spectra of two organic molecules, (5,6)-dimethyluracil and the methyl ester of naproxen. In the first case, the RR spectrum will computed with different coordinates systems, to highlight the impact of the choice of the coordinates in the simulation of RR spectra. For naproxen, both RR and RROA spectra will be simulated, in order to check the reliability of the various vibronic models for both spectroscopies. In all cases, if not otherwise specified, electronic structure calculations have been performed at the (TD-)DFT level, with the B3LYP exchange-correlation functional and the SNSD basis set.[355] If not otherwise specified, the damping parameter was set to 100 cm^{-1}, and the Fourier integral was computed by sampling the cross-correlation function in 2^{12} points, for an overall propagation time of 10^{-12} s.

5.3.1 The effect of the choice of the coordinates: RR spectrum of (5,6)-dimethyluracil

The first example used to test the TD-RR theory is 5,6-dimethyluracil (referred to in the following as 5,6-DMU). The study of the electronic properties of nucleobases is of great interest both from a practical and a theoretical points of view.[356,357,358] First of all, the interaction of nucleobases and their derivatives with UV-vis light is at the heart of most DNA photodamage

processes, therefore the study of the photochemical properties of nucleobase can give insights into the mechanism of those processes. RR spectroscopy has been applied in the last years to characterize the short-time dynamics of excited states of a large number of nucleobase derivatives.[359,360,361] Even if several experimental spectra are therefore available, their interpretation usually relies on approximated vibronic models,[362,363,364] neglecting either HT or mode-mixing effects. Furthermore, nucleobases usually undergo significant geometry changes upon electronic excitation, thus a correct description of vibronic properties of such flexible molecules requires an appropriate coordinates system.

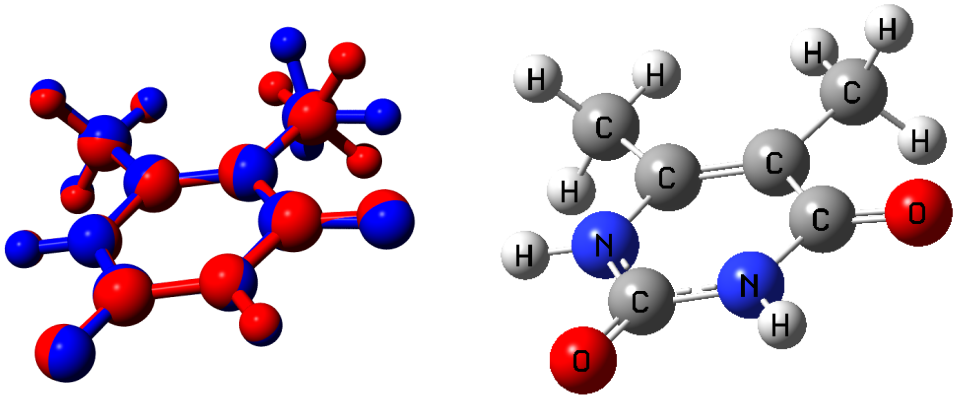

FIGURE 5.1: Superposition of the optimized geometries of the S_0 (in red) and S_2 (in blue) electronic states of 5,6-DMU. The S_0 structure is used as reference for the atom type definition (right structure).

Here, we will focus on the RR spectrum of 5,6-DMU with an incident wavelength set to match the $S_2 \leftarrow S_0$ ($n \rightarrow \pi^*$) electronic transition, since experimental data are available only in resonance with this state.[361] The equilibrium geometries of the S_0 and S_2 states, calculated without including solvent effects, are reported in Fig. 5.1. This graphical representation shows that, even if in both electronic states the ring is planar, one of the methyl residues is rotated by $\approx 60^\circ$ upon excitation. Fig. 5.2 shows the RR spectrum simulated with different models for the intermediate-state PES, with the simulations done at the FC level in all cases. As shown in the upper left panel, the theoretical spectrum calculated at the AH level by using Cartesian coordinates is dominated by an intense band in the low-energy region, corresponding to normal modes involving the torsion of the methyl groups. The overall band-shape calculated at the VG level in Cartesian coordinates, reported in the upper right panel of Fig. 5.2, is significantly different from the AH one in Cartesian coordinates, since the low-energy intense peak is not present anymore, while various peaks appear in the region between 800 and 2000 cm^{-1}.

Let us recall that, when experimental results are poorly reproduced by using adiabatic models in Cartesian coordinates due to the presence of large-amplitude deformations, vertical models in Cartesian coordinates are usually employed instead to obtain more reliable results.[88,272] In fact, as noted in the previous chapter, the VG model is the only one in which internal and Cartesian coordinates provide equivalent results, and for this reason the inaccuracy of vibronic models in Cartesian coordinates is partially recovered. However, in this case, as can be shown by comparison of the upper right and lower panels of Fig. 5.2, the RR spectrum calculated at the AH level in DICs is not equivalent to the VG one. The differences between the two theoretical spectra are mainly due to the strong influence of mode-mixing effects, and therefore the VG model is ill-suited to reproduce the spectrum. On the other hand, use of the more refined VH model, which includes mode-mixing effects, is not straightforward due to the presence of four imaginary frequencies at the ground-state geometry, which would require the inclusion of anharmonic terms in the expansion of the excited-state PES.

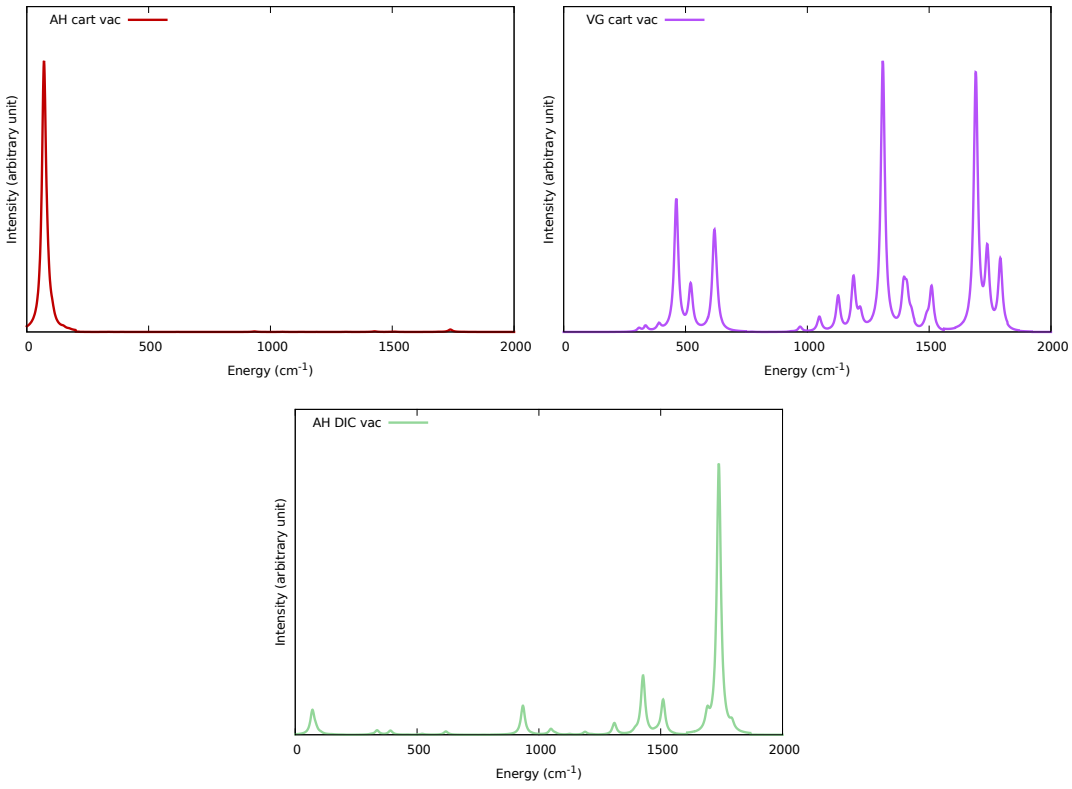

FIGURE 5.2: Comparison of the theoretical RR spectra of 5,6-DMU calculated by using different coordinates system and different models for the excited state PES: AH in Cartesian coordinates (upper panel, left), VG in Cartesian coordinates (upper panel, right), AH in DICs (lower panel). The intensity of each spectrum has been rescaled with respect to the most intense band, and Lorentzian distribution functions with an HWHM of 10 cm^{-1} have been applied to each peak to reproduce broadening effects.

In order to check the accuracy of the results obtained with different coordinates systems and models for the excited-state PES, the theoretical results have been compared to the experimental data, taken from Ref. 361. The experimental spectrum has been recorded in water, and to reproduce the laboratory conditions, solvent effects have been taken into account by mean of PCM. The inclusion of solvent effects strongly modifies the equilibrium geometry of the S_2 state of (5,6)-DMU, since the six-term ring undergoes a distortion from the planar geometry upon the electronic excitation. Furthermore, a large-amplitude rotation of one of the methyl groups is still present. The theoretical results obtained in aqueous solution are reported in Fig. 5.3. As shown in the left panel, the agreement between the theoretical results obtained with AH in Cartesian coordinates and the experimental spectrum is rather poor. Conversely, the agreement becomes significantly better when DICs are used with the AH model, as reported in the right panel. In order to check the influence of the internal coordinate sets, the spectrum obtained with ZICs is reported as well, in the left panel. First of all, the Z-matrix which has been used is a standard one, and no dummy atoms are introduced in order to keep the correct symmetry of the system. In fact, our goal is to compare the performance of automatized algorithms for the generation of internal coordinates, and therefore, no *ad-hoc* Z-matrices have been used (a complete definition of the Z-matrix can be found in Ref. 338). The ZIC spectrum reported in the left panel of Fig. 5.3 shows that the use of Z-matrix coordinates does not improve the agreement between experimental and theoretical results with respect to the Cartesian case. In particular, the most intense bands are still observed in the 900-1100 cm $^{-1}$ spectrum range, compared to about 1700 cm $^{-1}$ in the DIC case and in experiment. In fact, as previously pointed out, Z-matrix coordinates are poorly suited for the description of ring deformations, since one of the bond lengths and valence angles involving ring atoms are not included in the definition of the internal coordinates. As a consequence, DICs are more suitable when electronic excitations are associated to ring deformations.

In conclusion, it should be noted that slight differences between theoretical and experimental results are still present, even if DICs are used. Indeed, the intensity of the bands under 1200 cm^{-1} is underestimated, and an additional band at about 1480 cm^{-1} is present in the theoretical spectrum. The major limitation of our simulations lies in the description of solvent effects by means of PCM, since some first-shell water molecules interact specifically with the solute, which are not reproduced by continuum models.[365,366] Therefore, the inclusion of at least part of the first solvation shell in the QM part of the calculation should further improve the theoretical results. However, as discussed in the previous chapter for imidazole, a proper generation of intermolecular internal coordinates is not straightforward, and has not been investigated here.

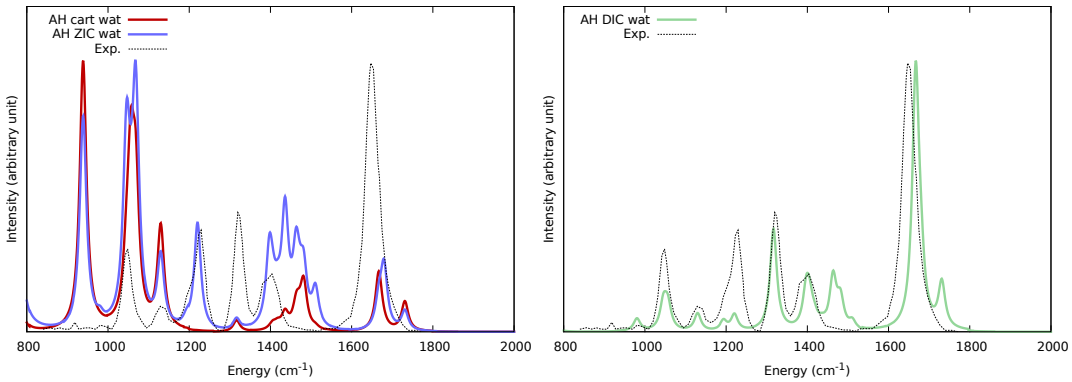

FIGURE 5.3: Comparison of the theoretical and experimental (taken from Ref. 361) RR spectrum of 5,6-DMU. Vibronic calculations were performed at the AH level with Cartesian and Z-matrix coordinates (left panel) and DICs (right panel). Solvent effects have been included by means of PCM. The intensity of each spectrum has been normalized with respect to the most intense band, and Lorentzian distribution functions with HWHMs of 10 cm^{-1} have been applied to each peak to reproduce the broadening effects.

5.3.2 Naproxen: from the OPA to the RROA spectrum

The second molecule studied here is the deuterated methyl ester of the (S)-(+)-6-methoxy-α-methyl-2-naphtaleneacetic acid, denoted as naproxen-OCD_3 for the sake of simplicity, which is one of the first organic molecules for which an RROA spectrum has been experimentally recorded, together with other ibuprofen derivatives, by Nafie and co-workers.[367]

From a computational point of view, the only theoretical analysis of the RROA spectrum of Naproxen-OCD_3 is, up to our knowledge, the one done by Reiher and co-workers,[327] which has been recently extended to the free acid forms of ibuprofen and naproxen.[368] The first work uses a TI theory based on the Kramers-Krönig transform,[363,369] and uses the VG model to describe the intermediate-state PES and the FC approximation for the transition dipole moment. The second study, carried out on the acid form of naproxen-OCD_3, is based on a different theoretical formulation, relying on the complex polarizability approach introduced by Schatz and coworkers[343,344] where resonance effects are included only through a complex lifetime factor, thus neglecting vibronic effects. To complete those analyses, all vibronic models presented in the previous chapter will be employed, in order to fully characterize the RR and RROA spectra of naproxen-OCD_3, with

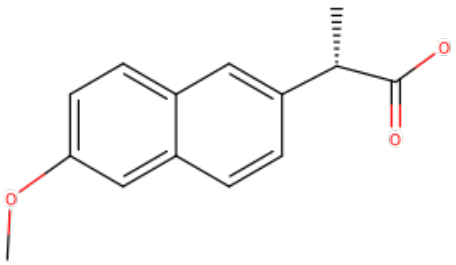

FIGURE 5.4: Graphical representation of the structure of naproxen-OCD_3.

particular care to the effects of the choice of the coordinates system on the spectral bandshape, and to the relevance of HT effects.
The experimental RROA spectrum has been recorded with an incident wavelength of 512 nm, thus significantly distant from the first intense absorption band, which is detected around 320 nm.[367] However, the experimental spectrum is monosignated, and this has been interpreted as a signature of resonance enhancement. For example, in the ROA spectrum of ibuprofen, whose electronic spectrum is blue-shifted with respect to naproxen-OCD_3, this enhancement is not detected.[367,368] In addition to the band at about 320 nm, a second, more intense band, is present at higher energy, which can contribute to the resonance enhancement through interference effects. As discussed in Ref. 327, simulations performed at the TD-DFT level predict two bands, one at about 320 nm and a second one at about 280 nm. However, the computed intensity of the lowest-energy transition is higher than the second one, in disagreement with experimental findings. For this reason, in the calculations presented in Ref. 327, adiabatic excitation energies were shifted in order to match the experimental spectrum. With the aim of extending this analysis, the excitation energies and the respective oscillator strengths of the two lowest-energy excitations have been computed using different exchange-correlation functionals, and the results are reported in Tab. 5.3.

	S_1		S_2		S_3	
	ΔE	f	ΔE	f	ΔE	f
B3LYP	320.54	0.0870	286.40	0.0168	252.70	0.1304
CAM-B3LYP	294.32	0.0911	266.02	0.0298	228.81	0.0027
PBE0	319.46	0.0884	284.59	0.0157	249.39	0.4320
LC-ωHPBE	279.90	0.0829	253.21	0.0593	215.72	1.6516
M062X	293.58	0.0901	263.92	0.0341	228.56	1.2172
MN15	304.73	0.0908	273.83	0.0231	235.86	1.0168

TABLE 5.3: Excitation energy and dipole strength of the three lowest-energy electronic excited states of naproxen-OCD_3 computed using different exchange-correlation functionals. The SNSD basis set has been employed in all cases. Energies are reported in nm, the dipole strength in atomic units.

The results of the simulation confirm the trend noticed in Ref. 327 since, in all cases, the first transition has an oscillator strength higher than the second one. In addition, a transition (excitation to the S_3 electronic state) with high oscillator strength is present at about 250 nm and could also have a relevant effect in the resonance enhancement, and will be considered in the following analysis. We also note that excitation energies are significantly overestimated by all long-range corrected functionals (CAM-B3LYP and LC-ωPBE) as well as the Minnesota functionals (M06-2X and MN15). For this reason, B3LYP and PBE0 will be considered in the following.

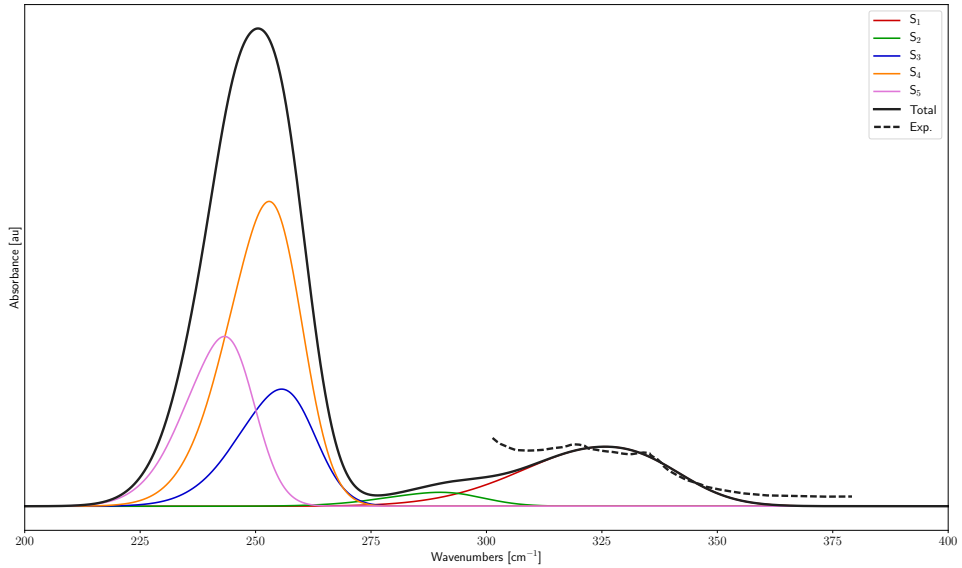

FIGURE 5.5: Experimental[367] (dashed, black line) and theoretical (solid, black line) OPA spectra of naproxen-OCD_3, computed at the VG|FC level by including the three lowest-energy excited states. The contributions of the single excited states are also reported (solid, red line for the S_1 state, solid green line for the S_2 state and solid, blue line for the S_3 state). Electronic structure calculations were performed at the B3LYP/SNSD level. Gaussian distribution functions with HWHMs of 1000 cm^{-1} were used to simulate the broadening effects. Solvent effects (CCl_4) were included by means of PCM.

The comparison between the experimental[367] and theoretical OPA and ECD spectra, computed at the VG|FC level, are reported in Figs. 5.5 and 5.6. As expected, the computed intensity of the high-energy tail of the OPA spectrum is lower than the experimental one. However, the increase in the intensity of the experimental spectrum at 300 nm could also be associated to the presence of the pattern of bands at about 300 nm. For this reason, in contrast with the analysis reported in Ref. 327, the vertical excitation energies have not been shifted in the RR simulations. The discrepancy between theoretical and experimental results is less evident for the ECD spectrum, reported in Fig. 5.6, even if in this case as well the intensity of the second band is slightly underestimated with respect to the experiment. Those results seem to confirm the reliability of the magnetic transition dipole moments computed at the B3LYP/SNSD level, which are involved in the calculation of the $\mathcal{G}$ and $\mathcal{G}'$ tensors. Thus, provided that the transition quadrupole moments are described correctly, a reliable reproduction of the RROA spectrum is expected.

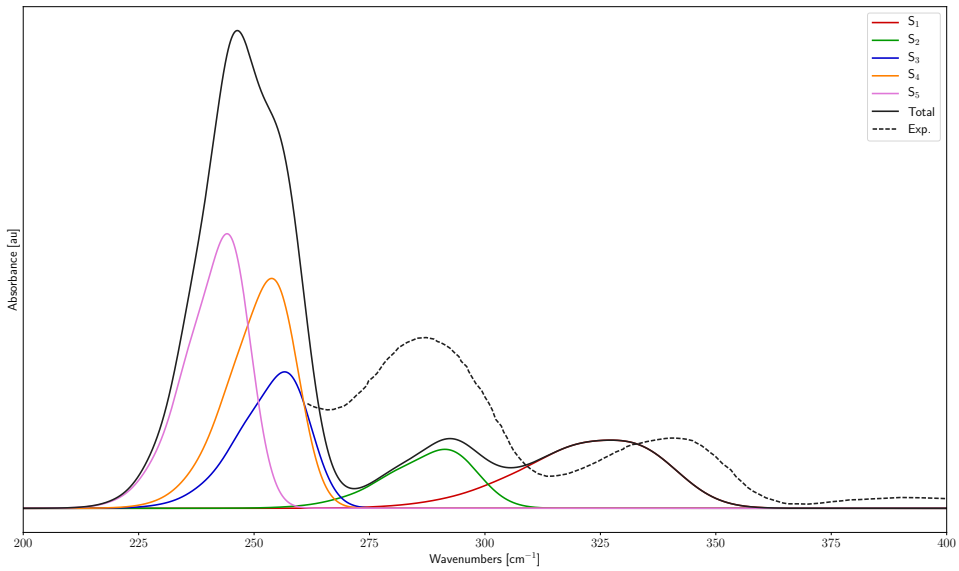

FIGURE 5.6: Experimental[367] (dashed, black line) and theoretical (solid, black line) ECD spectra of naproxen-OCD_3, computed at the VG|FC level by including the three lowest-energy excited states. The contributions of the single excited states are also reported (solid, red line for the S_1 state, solid green line for the S_2 state and solid, blue line for the S_3 state). Electronic structure calculations were performed at the B3LYP/SNSD level. Gaussian distribution functions with HWHMs of 1000 cm^{-1} were used to simulate the broadening effects. Solvent effects (CCl_4) were included by means of PCM.

The computed RR spectra for the S_1 and S_2 electronic states simulated using different vibronic models and coordinate systems are reported in Fig. 5.7. Considering only S_1 as intermediate state, AH|FC results in Cartesian coordinates and DICs are nearly superimposable, and only minor differences are present between 800 and 1200 cm^{-1}. This equivalence suggests that the geometry deformation upon electronic excitation is small, since only in this case

should the results obtained in the two different representations be equivalent. This is further confirmed by the equivalence of the AH and VG results.

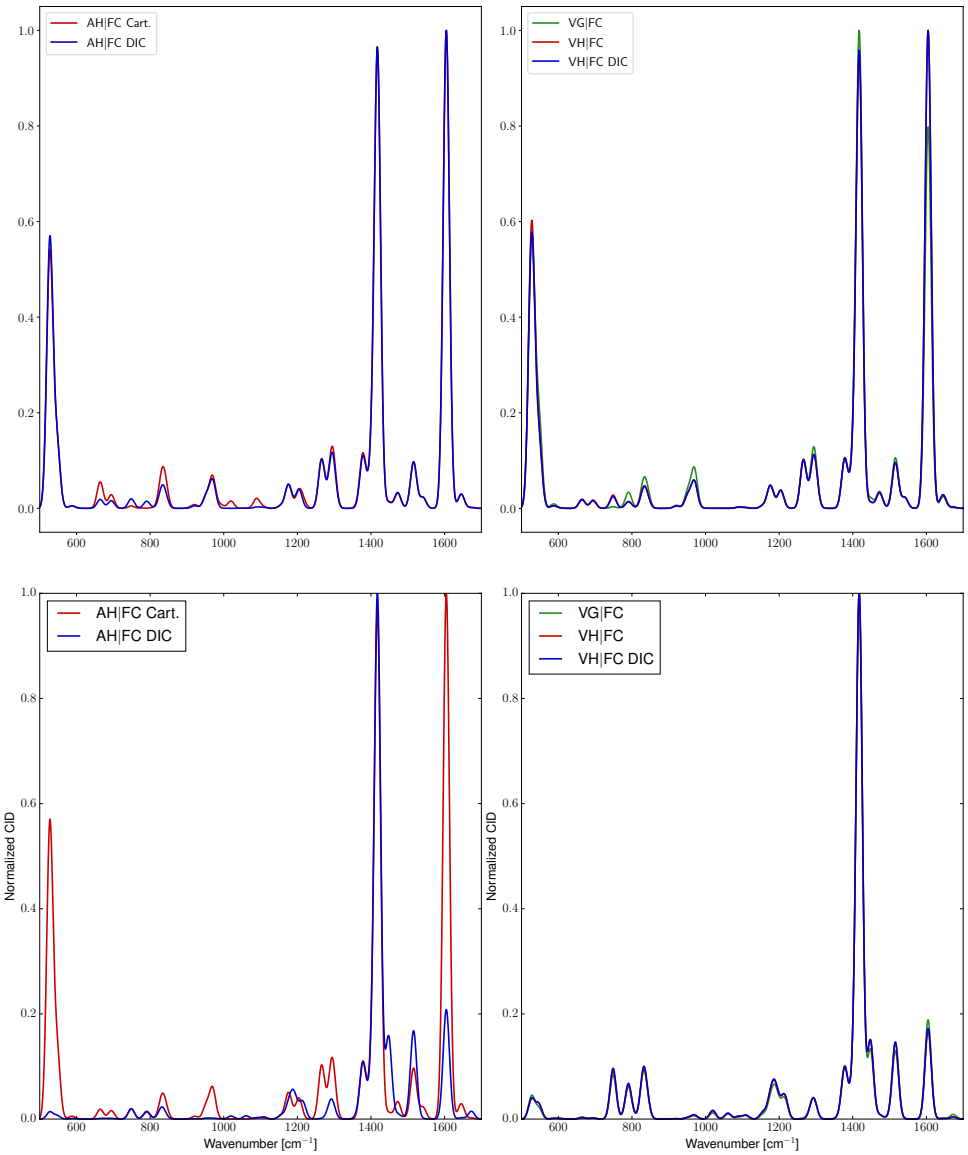

FIGURE 5.7: RR DCP(180°) spectra of naproxen-OCd_3 for resonance with the S_1 (upper panels) and S_2 (lower panels) electronic states, computed at the FC level using adiabatic (left panel, red line for AH|FC in cartesian coordinates, blue line for AH|FC in DICs) and vertical (right panel, green line for VG|FC, blue line for VH|FC in cartesian coordinates, red line for VH|FC in DICs) models. Solvent effects (CCl_4) have been included by means of PCM. Lorentzian functions with HWHMs of 10 cm^{-1} have been used to simulate the broadening effects.

For S_2, the equivalence between the various vibronic models disappears. For example, significant differences are present between the AH|FC spectra in Cartesian coordinates and DICs (left panel), especially in the lower energy region of the spectrum, below 1300 cm^{-1}. As a matter of fact, the excitation

to the S_2 electronic state is accompanied by a torsion along the dihedral angle between the naphtyl moiety and the carboxyl group. Because of the presence of this large amplitude motion (LAM), Cartesian and internal coordinates provide different results. It is interesting to note that the spectra computed using vertical models are equivalent to the adiabatic ones in internal coordinates. As discussed in the theoretical section of Chapter 4, this equivalence, that has been already noticed for other systems,[88] is caused by the fact that, within the simpler VG model, Cartesian and internal coordinates are equivalent.

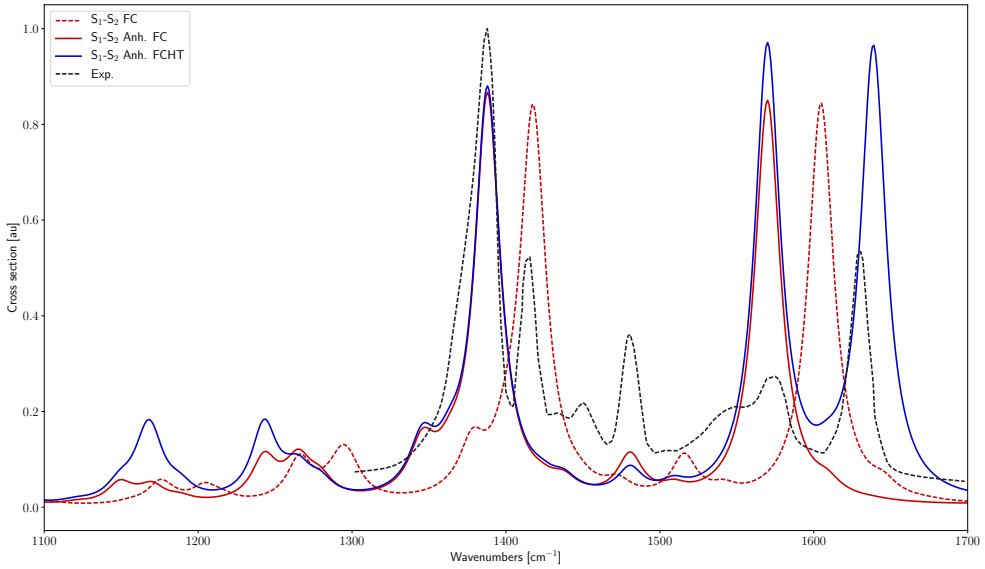

FIGURE 5.8: Experimental[367] and computed RR $DCP_I(180°)$ spectra of naproxen-OCd_3 computed by including the S_1 and S_2 electronic states. Simulations were performed at the AH|FC (red line) and AH|FCHT (blue line) level using the harmonic (dashed line) and anharmonic wavenumbers for the ground state. Lorentzian functions with HWHMs of 10 cm^{-1} were used to reproduce the broadening effects. An incident wavelength of 28572 cm^{-1} (350 nm) was used, and γ was set to 100 cm^{-1}. Solvent effects (CCl_4) were included by means of PCM.

Based on those observations, the full RR spectrum, obtained by including resonance effects from the two excited states is reported in Fig. 5.8. The AH|FC spectrum provides a satisfactory reproduction of the bandshape at the qualitative level, especially in the region about 1400 cm^{-1}. The agreement worsens at about 1600 cm^{-1}, where the experimental spectrum displays two bands, whereas in the theoretical results only a single band is present. In order to improve the accuracy of the theoretical results, the calculation were performed using the anharmonic frequencies of the ground (S_0) state instead of the harmonic ones. As expected, most of the bands are red-shifted, and a significant improvement in the position of the band at about 1400 cm^{-1} is observed. However, the intense band present in the experimental spectrum at about 1600 cm^{-1} is not present in the theoretical counterpart. This

band is however detectable in the spectrum computed at the AH|FCHT level, which indicates that FC simulations are not sufficient to reproduce correctly the experimental results. However, the inclusion of HT effects worsens the agreement between theoretical and experimental results in the region about 1400 cm^{-1}, where the intensity of the bands is underestimated. As shown in Fig. 5.7, the RR spectrum obtained in resonance with the S_2 state displays an intense band at about 1400 cm^{-1} thus, as already noticed in Ref. 327, the discrepancy might be caused by an incorrect reproduction of the relative dipole strengths of the two excited states, causing an incorrect reproduction of the overall bandshape.

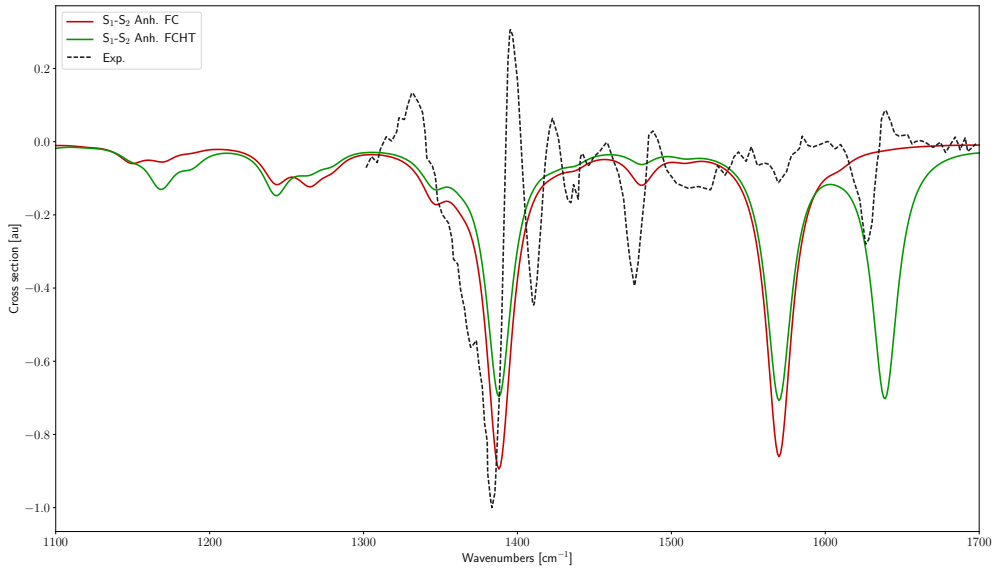

FIGURE 5.9: Experimental[367] and computed RROA $DCP_I(180°)$ spectra of naproxen-OCD_3 computed by including the S_1 and S_2 electronic states. Simulations were performed at the AH|FC (red line) and AH|FCHT (blue line) level, using the harmonic (dashed line) and the anharmonic frequencies for the ground state. Lorentzian functions with HWHMs of 10 cm^{-1} were used to reproduce the broadening effects. An incident wavelength of 28572 cm^{-1} (350 nm) was used, and γ was set to 100 cm^{-1}. Solvent effects (CCl_4) were included by means of PCM.

Based on the previous results, the RROA spectrum has been computed at the AH|FC level by including the S_1 and S_2 electronic states in the treatment, and the results are reported in Fig. 5.9. As expected, the RROA spectrum computed at the AH|FC level is proportional to the RR one, displaying two intense bands, one at about 1400 cm^{-1} and a second one at about 1600 cm^{-1}. The RROA spectrum is negative, and thus has an opposite sign with respect to the ECD one, in agreement with the analysis reported in Ref. 367. Similarly to what has been already noticed for RR, the inclusion of HT effects increases the intensity of the band at about 1650 cm^{-1} and the intensity of this band is significantly overestimated with respect to the experimental one.
To conclude, the effects of the higher excited states has been evaluated by simulating the full RROA spectrum obtained by including also the S_3, S_4 and

S_5 excited states in the simulations. In fact, as already shown in Figs. 5.5 and 5.6, even if the separation between the excitation energies of those states and ω_I is larger than for the S_1 and S_2 states, they have an higher rotatory strength, and therefore their resonance effect could be not negligible. The RROA spectra of the S_3, S_4 and S_5 excited states were computed at the VG level, in order to avoid geometry optimizations of such highly excited electronic states. The results reported in Fig. 5.10 show that the inclusion of those states does not change significantly the bandshape computed at the FC level, but lowers the intensity of the band at about 1600 cm^{-1}, leading to a better agreement with the experimental results.

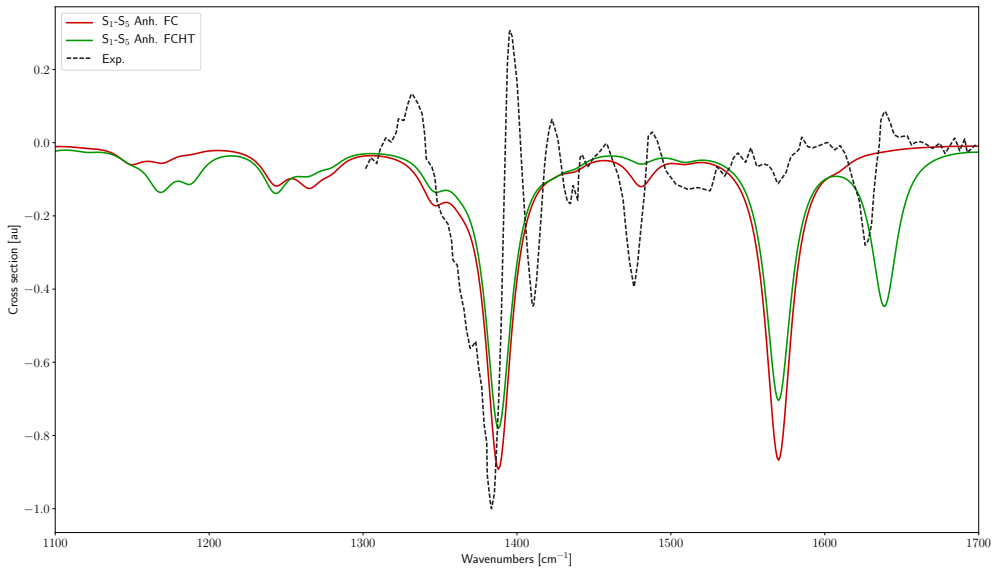

FIGURE 5.10: Experimental[367] and computed RROA $DCP_I(180°)$ spectra of naproxen-OCD_3 computed in $CCl_4$by including the five (S_1-S_5) lowest-energy electronic states. Simulations were performed at the AH level for the S_1 and S_2 states and at the VG level for the S_3, S_4 and S_5 ones, using the FC (solid, red line) and the FCHT (solid, green line) approximation. Frequencies of the ground state were computed at the anharmonic level. Lorentzian functions with HWHMs of 10 cm^{-1} were used to reproduce the broadening effects. An incident wavelength of 28572 cm^{-1} (350 nm) was used, and γ was set to 100 cm^{-1}.

Chapter 6

Anharmonic spectroscopy of excited states

In Chapter 4, harmonic models for the simulation of vibrational signatures in electronic spectra based on the harmonic approximation were presented and anharmonic mode, like LAMs, were simply excluded from the treatment after the application of a reduced-dimensionality scheme. In practice, this means that any simulations done in truncated, with the impact of such an approximation depending on the system and spectroscopy. To overcome this limitation, it is necessary to take into proper account those discarded modes in the vibronic treatment. In Chapter 3, an hybrid scheme was presented, based on the RPH theory, which makes possible the computation of anharmonic frequencies for molecular systems characterized by a single, highly anharmonic mode. This model is extended here to vibronic spectroscopy. As already discussed above, anharmonic calculations on electronic excited states are limited to small-size systems, due to high computational cost of the generation of the anharmonic force field. For this reason, the development of hybrid schemes, where anharmonic effects are included only for a relevant subset of coordinates, is particularly appealing.
Another way to improve the accuracy of vibronic simulation with a limited impact on the overall computational cost is by simply correcting the band positions, including anharonic effects only for the energies. In the second part of this chapter, the extension vibrational second order perturbation theory (VPT2) to the calculation of anharmonic frequencies of electronic excited states is presented. Unlike the hybrid harmonic-DVR scheme presented above, VPT2 is not accurate in treating flexible systems, but is effective for the study of semi-rigid ones. Furthermore, it allows to study multiple, coupled anharmonic degrees of freedom, thus providing a more balanced representation with respect to the previous model, where anharmonic effects were included only for a single degree of freedom. Furthermore, thanks to the development and implementation of analytical formulas for the calculation of harmonic frequencies at the TD-DFT level,[41,100] anharmonic force-fields can be computed also for systems with several dozens of atoms possible with a limited computational cost. This makes the excited-states formulation of VPT2 is particularly appealing. Throughout this chapter, if not mentioned otherwise, VPT2 will refer to GVPT2 with the GAUSSIAN-16[262] default parameters or those used in the reference works cited as source of the data.

6.1 Effective anharmonic vibronic models: an hybrid harmonic-DVR approach

In this section, we will present the extension of the hybrid DVR-harmonic scheme introduced in Sec. 3.2 to vibronic spectroscopy. The extension of vibrational models based on the RPH to spectroscopies involving multiple electronic states is far from being straightforward and has been presented, to our knowledge, only in Ref. 99, where it was applied to a relatively small system, CF_3^+. Here, a general framework will be presented, supporting all vibronic models introduced in Chapter 4 at the harmonic level.

6.1.1 Extension to vibronic models

In the hybrid DVR-harmonic scheme presented in Chapter 3, vibrational levels were computed through the two, coupled Schrödinger equations associated to the LAM (see Eq 3.51) and to the N'_{vib} orthogonal modes (see Eq. 3.52), treated as harmonic. Applied to vibronic spectroscopies, these equations for the initial state of the vibronic transitions are the following,

$$\begin{aligned}\left[\overline{\mathcal{T}}_{N'_{\text{vib}}}(\overline{\boldsymbol{Q}}^p)+\overline{\mathcal{V}}_{N'_{\text{vib}}}(\overline{\boldsymbol{Q}}^p;\bar{l})\right]\overline{\chi}_{N'_{\text{vib}},k}\left(\bar{l},\overline{\boldsymbol{Q}}^p\right)&=\overline{E}_{N'_{\text{vib}},k}(\bar{l})\,\overline{\chi}_{N'_{\text{vib}},k}\left(\bar{l},\overline{\boldsymbol{Q}}^p\right)\\ \left[\overline{\mathcal{T}}_{\text{LAM}}(\bar{l})+\overline{\mathcal{V}}_{\text{LAM}}\left(\bar{l}\right)+\overline{E}_{N'_{\text{vib}},k}(\bar{l})\right]\overline{\chi}_{\text{LAM},i(k)}\left(\bar{l}\right)&=\overline{E}_{\text{tot},i(k)}\,\overline{\chi}_{\text{LAM},i(k)}\left(\bar{l}\right)\end{aligned} \tag{6.1}$$

and, for the final state,

$$\begin{aligned}\left[\overline{\overline{\mathcal{T}}}_{N'_{\text{vib}}}(\overline{\overline{\boldsymbol{Q}}}^p)+\overline{\overline{\mathcal{V}}}_{N'_{\text{vib}}}(\overline{\overline{\boldsymbol{Q}}}^p;\bar{\bar{l}})\right]\overline{\overline{\chi}}_{N'_{\text{vib}},h}\left(\bar{\bar{l}},\overline{\overline{\boldsymbol{Q}}}^p\right)&=\overline{\overline{E}}_{N'_{\text{vib}},k}(\bar{\bar{l}})\,\overline{\overline{\chi}}_{N'_{\text{vib}},k}\left(\bar{\bar{l}},\overline{\overline{\boldsymbol{Q}}}^p\right)\\ \left[\overline{\overline{\mathcal{T}}}_{\text{LAM}}(\bar{\bar{l}})+\overline{\overline{\mathcal{V}}}_{\text{LAM}}\left(\bar{\bar{l}}\right)+\overline{\overline{E}}_{N'_{\text{vib}},k}(\bar{\bar{l}})\right]\overline{\overline{\chi}}_{\text{LAM},i(k)}\left(\bar{\bar{l}}\right)&=\overline{\overline{E}}_{\text{tot},i(k)}\,\overline{\overline{\chi}}_{\text{LAM},i(k)}\left(\bar{\bar{l}}\right)\end{aligned} \tag{6.2}$$

Even if the same indexes have been used in Eqs. 6.1 and 6.2, it is important noting that they refer to different projected modes, and the LAM coordinate can be different between the initial ($\bar{l}$) and the final ($\bar{\bar{l}}$) states. In fact, as already mentioned in the previous section, in the ICPH and RPH models, a geometry optimization is performed for each point of the scan, and thus the coordinate l describing the LAM is different for the initial and final states. The orthogonal modes are obtained as eigenvectors of the projected Hessian, where the projector operator is a function of l, thus they depend on the electronic state of interest as well. However, even if the previous equations can be solved separately with monodimensional anharmonic models, the use of multidimensional approaches is required to compute transition properties, such as the FC factors. To show this point, let us express the LAM coordinate of the final state $\bar{\bar{l}}$ as,

$$\bar{\bar{l}} = \bar{l} + \sum_{i=1}^{N'_{\text{vib}}} c_i \left(\bar{l}\right) \overline{Q}_i^p \tag{6.3}$$

where all the coefficients c_i are, in the most general case, non-null. Eq. 6.3 shows that different types of coordinates (*i.e.* harmonic and variationally anharmonic) will be mixed. For this reason, if the motion along $\bar{\bar{l}}$ is treated at the anharmonic level, both $\bar{l}$ and $\overline{\boldsymbol{Q}}^p$ must be treated on the same footing, which would require the development of multi-dimensional anharmonic models. A major simplification is obtained by imposing that $\bar{l} = \bar{\bar{l}}$ to prevent the mixing of coordinates treated at different levels of theory, and monodimensional anharmonic models can be safely employed. To use this approximation in practice, one of the two electronic states has to be chosen as reference to perform the constrained optimization (for ICPH) or the IRC calculation (for RPH), and the energies of the other state must be computed on the same geometries. Clearly, the definition of the reference electronic state will have a crucial impact on the computed bandshape, since the results will be more accurate for this state. If temperature effects are neglected, all transitions will start from the vibrational ground level of the initial electronic state, whereas a virtually infinite number of final states are possible. For this reason, more accurate results will be obtained by choosing as a reference the final electronic state. If temperature effects are included and relevant, then any choice of the reference state will have its strengths and limitations.
Even if the LAM coordinate is assumed to be equal for the two electronic states, this is not necessarily true for the projected harmonic modes $\overline{\boldsymbol{Q}}^p$ and $\overline{\overline{\boldsymbol{Q}}}^p$. Within the formulation of the hybrid DVR-harmonic scheme for a single electronic state (see Sec. 3.2), the projected modes were defined as the eigenvectors of the projected Hessian (Eq. 3.46) computed at the equilibrium position. In vibronic spectroscopy, the expansion of the PES is not necessarily performed about an equilibrium position, thus the following, more general expansions must be used,

$$\begin{aligned}
\overline{\mathcal{V}}^p\left(l\right) &= \overline{E}_0^p + \{\overline{\boldsymbol{g}}_{\boldsymbol{x}}^p\left(l\right)\}^T \overline{\boldsymbol{Q}}_{\boldsymbol{x}}^p + \frac{1}{2}\{\overline{\boldsymbol{Q}}_{\boldsymbol{x}}^p\}^T \overline{\boldsymbol{H}}_{\boldsymbol{x}}^p\left(l\right) \overline{\boldsymbol{Q}}_{\boldsymbol{x}}^p \\
\overline{\overline{\mathcal{V}}}^p\left(l\right) &= \overline{\overline{E}}_0^p + \{\overline{\overline{\boldsymbol{g}}}_{\boldsymbol{x}}^p\left(l\right)\}^T \overline{\overline{\boldsymbol{Q}}}_{\boldsymbol{x}}^p + \frac{1}{2}\{\overline{\overline{\boldsymbol{Q}}}_{\boldsymbol{x}}^p\}^T \overline{\overline{\boldsymbol{H}}}_{\boldsymbol{x}}^p\left(l\right) \overline{\overline{\boldsymbol{Q}}}_{\boldsymbol{x}}^p
\end{aligned} \tag{6.4}$$

and similar relations can be obtained for internal coordinates. Starting from Eq. 6.4 and following the same ideas already presented in Chapter 4, vertical and adiabatic models can be defined for the projected modes. The main difference between the theory presented here and the harmonic models defined in Chapter 4 is that, in the latter case, $\overline{\boldsymbol{g}} = \boldsymbol{0}$ both for adiabatic and for vertical models, whereas, within this framework, the gradient is null only for the reference state used in the scan, which can be either the initial or the final one, and only if the RPH model is employed. In fact, in the ICPH framework, the constrained optimization is performed in the space orthogonal to the normal mode corresponding to the LAM Q_{LAM}. However, since the LAM coordinate is equivalent to Q_{LAM} only at the equilibrium position, but will be expressed

as a linear combination of an arbitrary number of coordinates along the LAM, the gradient can have a non-null component orthogonal to $\boldsymbol{a}_{\mathrm{LAM}}(l)$. Since, as discussed in Chapter 3, if the LAM deviates significantly from Q_{LAM} along the scan, the monodimensional approximation is invalid, we will neglect the gradient term for the reference state also for ICPH calculations.
Let us now present the derivation of adiabatic models starting from Eq. 6.4. As discussed in Chapter 4, in adiabatic models the harmonic expansion is performed about the respective equilibrium positions of the initial and final electronic states. When working with projected modes, this means that, for each point of the scan, the energy of each electronic state must be minimized while keeping the LAM coordinate fixed by performing, for instance, a constrained optimization. This step is quite straightforward for the reference electronic state of the scan. However, for the other electronic state (referred in the following as "second state"), the geometry optimization is less trivial, and the definition of the projector operator to be used in the constrained optimization is different for the ICPH or the RPH models,

1. in ICPH, it might seem tempting to perform the constrained optimization of the second state in the space orthogonal to the normal mode describing the LAM at the equilibrium position (Q_{LAM}). However, in ICPH, the geometry is optimized during the scan, thus the expression of the LAM in terms of the reference set of coordinates (Cartesian or non-redundant internal coordinates) changes with l. In order to build consistently the projector operator, an analytical form of each coordinate as a function of l is necessary, which can be obtained for instance through a B-spline fitting procedure. For Cartesian coordinates $\boldsymbol{x}_{\mathrm{LAM}}(l)$, the projector operator is obtained as,

$$\mathbf{P}_{\boldsymbol{x}}^{\mathrm{ICPH}} = \boldsymbol{t}_{\mathrm{LAM}}\boldsymbol{t}_{\mathrm{LAM}}{}^{T} \qquad \text{with} \qquad \boldsymbol{t}_{\mathrm{LAM}} = \frac{d\boldsymbol{x}_{\mathrm{LAM}}}{dl} \Big/ \left|\frac{d\boldsymbol{x}_{\mathrm{LAM}}}{dl}\right|^{2} \tag{6.5}$$

   If internal coordinates are employed, the procedure is the same, but the non-redundant internal coordinates must be fitted as a function of l to obtain $\boldsymbol{s}_{\mathrm{LAM}}(l)$. Then, the projector is obtained from Eq. 3.43.

2. for RPH, the calculation is simpler, since the tangent vector to the curve $\boldsymbol{a}_{\mathrm{LAM}}(l)$ defining the LAM is given by the gradient of the PES of the reference state used in the scan. In this case,

$$\mathbf{P}_{\boldsymbol{x}}^{\mathrm{RPH}} = \frac{\boldsymbol{g}_{\boldsymbol{x}}\boldsymbol{g}_{\boldsymbol{x}}{}^{T}}{|\boldsymbol{g}_{\boldsymbol{x}}|^{2}} \tag{6.6}$$

   In this case, the fitting of the coordinates along the scan with a B-spline is not necessary, and $\mathbf{P}_{\boldsymbol{x}}^{\mathrm{RPH}}$ is employed in the constrained optimization for the second state. Again, for internal coordinates the projector given in Eq. 3.44 must be employed.

Once the appropriate projector operator is build, it is possible to determine the equilibrium positions ($\boldsymbol{x}^{p,\mathrm{eq}}(l)$ in Cartesian coordinates and $\boldsymbol{s}^{p,\mathrm{eq}}(l)$ in internal coordinates) of the two electronic states for a given value of the LAM coordinate l. For each value of l, the normal modes of the initial ($\overline{\boldsymbol{L}}^{p}(l)$) and final ($\overline{\overline{\boldsymbol{L}}}^{p}(l)$) states are obtained as eigenvectors of the projected Hessian matrix, and the projected frequencies ($\overline{\boldsymbol{\omega}}^{p}(l)$ and $\overline{\overline{\boldsymbol{\omega}}}^{p}(l)$ respectively) from the corresponding eigenvalues. The Hessian matrices are computed at a stationary point for both electronic states, thus all entries of $\overline{\boldsymbol{\Omega}}^{p}(l)$ and $\overline{\overline{\boldsymbol{\Omega}}}^{p}(l)$ are positive. Following the same procedure described in Chapter 4 for the harmonic case (see Eq. 4.11), a Duschinsky transformation for the projected modes can be built as,

$$\overline{\boldsymbol{Q}}_{\boldsymbol{x}}^{p}(l) = \boldsymbol{J}_{\boldsymbol{x}}^{p}(l)\,\overline{\overline{\boldsymbol{Q}}}_{\boldsymbol{x}}^{p}(l) + \boldsymbol{K}_{\boldsymbol{x}}^{p}(l) \tag{6.7}$$

In Cartesian coordinates, $\boldsymbol{J}_{\boldsymbol{x}}^{p}(l)$ and $\boldsymbol{K}_{\boldsymbol{x}}^{p}(l)$ are given as,

$$\begin{aligned} \boldsymbol{J}_{\boldsymbol{x}}^{p} &= \{\overline{\boldsymbol{L}}_{\boldsymbol{x}}^{p}\}^{T}\,\overline{\overline{\boldsymbol{L}}}_{\boldsymbol{x}} \\ \boldsymbol{K}_{\boldsymbol{x}}^{p} &= \{\overline{\boldsymbol{L}}_{\boldsymbol{x}}^{p}\}^{T}\left(\overline{\overline{\boldsymbol{x}}}^{p,\mathrm{eq}} - \overline{\boldsymbol{x}}^{p,\mathrm{eq}}\right) \end{aligned} \tag{6.8}$$

and, in internal coordinates,

$$\begin{aligned} \boldsymbol{J}_{\boldsymbol{s}}^{p} &= \{\overline{\boldsymbol{L}}_{\boldsymbol{s}}^{p}\}^{-1}\,\overline{\overline{\boldsymbol{L}}}_{\boldsymbol{s}}^{p} \\ \boldsymbol{K}_{\boldsymbol{s}}^{p} &= \{\overline{\boldsymbol{L}}_{\boldsymbol{s}}^{p}\}^{-1}\left(\overline{\overline{\boldsymbol{s}}}^{p,\mathrm{eq}} - \overline{\boldsymbol{s}}^{p,\mathrm{eq}}\right) \end{aligned} \tag{6.9}$$

Since $\overline{\boldsymbol{L}}_{\boldsymbol{s}}^{p}$ is not orthogonal, thus its inverse must be computed explicitly. The application of the harmonic-DVR scheme to vertical models is simpler than to the adiabatic ones, since the same reference geometry is used for the harmonic expansion of both PESs. The projected normal modes and harmonic frequencies of the reference state are obtained in the same way as for adiabatic models, i.e. by diagonalization of the projected Hessian at each point of the scan. The elements of the Duschinsky transformation can be computed using the projected gradient and Hessian instead of their full-dimensional counterpart as,

$$\begin{aligned} \{\boldsymbol{J}_{\boldsymbol{x}}^{p}\}^{T}\overline{\overline{\boldsymbol{H}}}^{p}\boldsymbol{J}_{\boldsymbol{x}}^{p} &= \overline{\overline{\boldsymbol{\Omega}}}^{2} \\ \boldsymbol{K}_{\boldsymbol{x}}^{p} &= -\boldsymbol{J}_{\boldsymbol{x}}^{p}\{\overline{\overline{\boldsymbol{\Omega}}}^{p}\}^{-2}\{\boldsymbol{J}_{\boldsymbol{x}}^{p}\}^{T}\{\overline{\boldsymbol{L}}_{\boldsymbol{x}}^{p}\}^{T}\overline{\overline{\boldsymbol{g}}}_{\boldsymbol{x}}^{p} \end{aligned} \tag{6.10}$$

where the projected gradient and Hessian ($\overline{\overline{\boldsymbol{g}}}_{\boldsymbol{x}}^{p}$ and $\overline{\overline{\boldsymbol{H}}}_{\boldsymbol{s}}^{p}$) are computed from Eq. 6.5 (for ICPH) or from Eq. 6.6 (for RPH). Here, the projector is computed systematically from the quantities defined in the reference state. Again, the equivalent of Eq. 6.10 for internal coordinates can be derived starting from Eqs. 4.31 and 4.32.

We already stressed above that, independently of the type of spectroscopy, the reference state used in the scan calculation can correspond either to the initial or to the final state. For this reason, the projector operators given in Eqs. 6.5 and 6.6 were not labeled with any overbar. However, some care must be paid when the reference state of the scan is the final one and vertical models are employed. Indeed, in order for the relations given in Eq. 6.10 to hold,

the gradient must be null for the initial state, but this is not the case if the reference state of the scan is the final one. In those cases, the VH model cannot be employed. However, the VG model can still be used, by assuming that the extrapolated equilibrium geometry of the initial state is the actual one. In this case, the shift vector computed at the VG level using this extrapolated geometry of the initial state as reference is the same as if computed using the final state as reference, thus the Duschinsky transformation is the same. We stress that this problem is not present when adiabatic models are used, since in this case the geometry of each electronic state is optimized for each value of l.
The definition of the Duschinsky transformation for the orthogonal modes allows to compute transition dipole moments between harmonic wavefunctions of the N'_{vib} orthogonal harmonic modes. Those quantities must then be combined with the transition dipole moment between wavefunctions associated to the LAM to obtain the full-dimensional spectrum. Starting from the factorization introduced in Eqs. 3.51 and 3.52, the general sum-over-states expression reported in Eq. 4.56 for the harmonic case can be rewritten as,

$$I(\omega) = \alpha\omega^{\beta} \sum_{m,j(m)} \left| \boldsymbol{\mu}_{j(m),0(0)} \right|^2 \delta \left(\frac{\left| \overline{\overline{E}}_{\text{tot},j(m)} - \overline{E}_{\text{tot},0(0)} \right|}{\hbar} - \omega \right) \tag{6.11}$$

where,

$$\boldsymbol{\mu}_{j(m),0(0)} = \langle\, \overline{\chi}_{\text{LAM},0(0)}\left(l\right) \overline{\chi}_{N'_{\text{vib}},0}\left(l, \overline{\boldsymbol{Q}}^{p}\right) \mid \boldsymbol{\mu}^{e}\left(l, \overline{\boldsymbol{Q}}^{p}\right) \mid \overline{\overline{\chi}}_{\text{LAM},j(m)}\left(l\right) \overline{\overline{\chi}}_{N'_{\text{vib}},m}\left(l, \overline{\overline{\boldsymbol{Q}}}^{p}\right) \,\rangle \tag{6.12}$$

For simplicity, only transitions starting from the vibrational ground state ($\overline{\chi}_{\text{LAM},0(0)}\left(l\right) \times \overline{\chi}_{N'_{\text{vib}},0}\left(l, \overline{\boldsymbol{Q}}^{p}\right)$) were considered. Furthermore, without loss of generality, the transition dipole moment $\boldsymbol{\mu}^{e}$ has been expressed in terms of the initial state projected modes $\overline{\boldsymbol{Q}}^{p}$. To compute the transition dipole moment, it is convenient to carry out first the integral over the projected modes $\overline{\boldsymbol{Q}}^{p}$ to obtain the LAM-specific transition dipole moment $\boldsymbol{\mu}^{e}_{m0}\left(l\right)$. In practice, this means solving first,

$$\boldsymbol{\mu}^{e}_{m0}\left(l\right) = \langle\, \overline{\chi}_{N'_{\text{vib}},0}\left(l, \overline{\boldsymbol{Q}}^{p}\right) \mid \boldsymbol{\mu}^{e}\left(l, \overline{\boldsymbol{Q}}^{p}\right) \mid \overline{\overline{\chi}}_{N'_{\text{vib}},m}\left(l, \overline{\overline{\boldsymbol{Q}}}^{p}\right) \,\rangle \tag{6.13}$$

so that,

$$\boldsymbol{\mu}_{j(m),0(0)} = \langle\, \overline{\chi}_{\text{LAM},0(0)}\left(l\right) \mid \boldsymbol{\mu}^{e}_{m}\left(l\right) \mid \overline{\overline{\chi}}_{\text{LAM},j(m)}\left(l\right) \,\rangle \tag{6.14}$$

For a given value of l, the integral in Eq. 6.13 involves only harmonic wavefunctions, thus it can be carried out using the theoretical framework presented in Chapter 4, employing either the TI or the TD approach, after expansion of $\boldsymbol{\mu}^{e}\left(l, \overline{\boldsymbol{Q}}^{p}\right)$ as a Taylor series in function of $\boldsymbol{Q}^{p}$ as follows,

$$\boldsymbol{\mu}^{e}\left(l, \overline{\boldsymbol{Q}}^{p}\right) = \boldsymbol{\mu}^{e}\left(l, \overline{\boldsymbol{Q}}^{p,\text{eq}}\right) + \sum_{i=1}^{N_{\text{vib}}} \left(\frac{\partial \boldsymbol{\mu}^{e}}{\partial \overline{Q}^{p}_{i}} \right)_{\text{eq}} \overline{Q}^{p}_{i} \tag{6.15}$$

where both the equilibrium value and the first derivatives of the transition dipole moment are functions of l. For the sake of clarity, we will refer to the zero-th and first-order approximations of the dipole given in Eq. 6.15 as $\mathrm{FC}_{N'_{\mathrm{vib}}}$ and $\mathrm{FCHT}_{N'_{\mathrm{vib}}}$, in order to avoid confusion with the standard Franck-Condon and Herzberg-Teller models. The second integral required to obtain the full transition dipole moment involves the LAM coordinate l, and can be expressed as in Eq. 6.14 The expression given in Eq. 6.14 involves the LAM wavefunctions, that are computed through the variational, DVR-based approach, and thus the evaluation of the integral needs to be carried out numerically. The diagonal approximation for the DVR basis functions can be effectively used to express the integral as,[251,370]

$$\langle \overline{\chi}_{\mathrm{LAM},0(0)}(l) \mid \boldsymbol{\mu}^e_m(l) \mid \overline{\overline{\chi}}_{\mathrm{LAM},j(m)}(l) \rangle = \sum_{k=1}^{N_{\mathrm{DVR}}} \overline{\overline{C}}_{j(m),k}\, \overline{C}_{0(0),k}\, \boldsymbol{\mu}^e_m(l_k) \tag{6.16}$$

where $\overline{C}$ and $\overline{\overline{C}}$ are the matrices of the eigenfunctions of $\mathcal{H}_{\mathrm{LAM}}$ for each state expressed in the DVR basis. As anticipated above, Eq. 6.16 holds only if the same DVR basis set is employed for the expansion of the LAM wavefunctions of the two electronic states, and therefore if the same curve $\boldsymbol{a}_{\mathrm{LAM}}(l)$ is used to define the LAM in the two electronic states. This condition is met in the theoretical framework presented here since, as discussed above, monodimensional vibronic models can be employed if the same geometries are used for both electronic states.

To use Eq. 6.16 in practice, the transition dipole moment $\boldsymbol{\mu}^e_{m0}$ must be computed at each point of the DVR grid $(l_1, ..., l_{\tilde{n}})$. Those values can be obtained, for each final state $\overline{\overline{\chi}}_{N'_{\mathrm{vib}},m(0)}\left(l, \overline{\overline{\boldsymbol{Q}}}^p\right)$, from the transition dipole moment $\boldsymbol{\mu}^e_{m0}$ at each point of the QM grid along the scan $(\tilde{l}_1, ..., \tilde{l}_{\tilde{n}})$, and by fitting those values using the B-spline representation as already done for the electronic energies. The matrices of the eigenfunctions $\overline{C}$ and $\overline{\overline{C}}$ are obtained by diagonalization of the Hamiltonian given in Eq. 3.52 in the DVR basis set. To compute the second term of the potential energy ($E_{N'_{\mathrm{vib}},k}(l)$ in Eq. 3.52), arising from the vibrational energy of the N'_{vib} harmonic modes, the projected frequencies $\omega^p_i(l)$ are also fitted using B-splines, and the term is computed, for each value of l, from the Schrödinger equation for the N'_{vib} orthogonal modes (see Eqs. 6.1 and 6.2). It is important noting that, due to the presence of this second term, a different Schrödinger equation is obtained for each final state $\overline{\overline{\chi}}_{N'_{\mathrm{vib}},m}\left(l, \overline{\overline{\boldsymbol{Q}}}^p\right)$.

The general theory outlined above can be simplified to reduce the overall computational cost. Significant saving is achieved by neglecting the dependence of the vibrational energy of the N'_{vib} harmonic modes $\boldsymbol{Q}^p$ on l. Under this approximation, $E_{N'_{\mathrm{vib}},k}(l)$ can be approximated as $E_{N'_{\mathrm{vib}},k}(l_0)$ in equation 3.52, where l_0 is the LAM coordinate at some reference geometry. The vibrational Schrödinger equation associated to the LAM, given in Eq. 3.52, can then be rewritten as,

$$\left[\mathcal{T}\left(l\right)+\mathcal{V}\left(l\right)\right]\chi_{\mathrm{LAM},i(k)}\left(l\right)=\left(E_{\mathrm{tot},i(k)}-E_{N'_{\mathrm{vib}},k}\left(l_0\right)\right)\chi_{\mathrm{LAM},i(k)}\left(l\right) \tag{6.17}$$

where the energy of the i-th state of the LAM does not depend anymore on k. With this approximation, Eq. 6.11 becomes,

$$\begin{aligned} I(\omega)=\alpha\omega^{\beta}\sum_{m,j(m)}&\left|\left\langle\,\overline{\chi}_{\mathrm{LAM},0(0)}\left(l\right)\mid\boldsymbol{\mu}^{e}_{m0}(l)\mid\overline{\overline{\chi}}_{\mathrm{LAM},j(m)}\left(l\right)\,\right\rangle\right|^{2}\\ &\times\delta\left(\frac{\left|\overline{\overline{E}}_{m}+\overline{\overline{E}}_{j(m)}-\overline{E}_{0}\right|}{\hbar}-\omega\right)\end{aligned} \tag{6.18}$$

This equation can be further simplified within the Franck-Condon approximation for the N'_{vib} orthogonal modes $\boldsymbol{Q}^{p}$, so that $\boldsymbol{\mu}^{e}_{m0}\left(l\right)$ can be rewritten as,

$$\boldsymbol{\mu}^{e}_{m0}=\boldsymbol{\mu}^{e}_{m0}\left(l,\boldsymbol{Q}^{p,\mathrm{eq}}\right)\times\left\langle\,\overline{\overline{\chi}}_{N'_{\mathrm{vib}},m}\left(l,\overline{\overline{\boldsymbol{Q}}}^{p}\right)\mid\overline{\chi}_{N'_{\mathrm{vib}},0}\left(l,\overline{\boldsymbol{Q}}^{p}\right)\,\right\rangle \tag{6.19}$$

where $\boldsymbol{\mu}^{e}_{m0}\left(l,\boldsymbol{Q}^{p,\mathrm{eq}}\right)$ is the electric transition dipole moment computed, for each value of l, computed at the equilibrium configuration of the orthogonal modes. While this simplification does not bring any significant computational saving, it can be used to separate the contributions to the transition dipole moment of the LAM from the ones of the orthogonal modes. To further simplify the sum-over-states expression in Eq. 6.18, the dependence of the nuclear wavefunctions $\overline{\chi}_{N'_{\mathrm{vib}},0}\left(l,\overline{\boldsymbol{Q}}^{p}\right)$ and $\overline{\overline{\chi}}_{N'_{\mathrm{vib}},m}\left(l,\overline{\overline{\boldsymbol{Q}}}^{p}\right)$ on the IRC parameter l can also be also neglected, leading to the final result,

$$\begin{aligned} I(\omega)=\alpha\omega^{\beta}\sum_{m,j(m)}&\left|\left\langle\,\overline{\chi}_{\mathrm{LAM},0(0)}\left(l\right)\mid\boldsymbol{\mu}^{e}_{m}(l)\mid\overline{\overline{\chi}}_{\mathrm{LAM},j(m)}\left(l\right)\,\right\rangle\right|^{2}\\ &\times\left|\left\langle\,\overline{\overline{\chi}}_{N'_{\mathrm{vib}},m}\left(l,\overline{\overline{\boldsymbol{Q}}}^{p}\right)\mid\overline{\chi}_{N'_{\mathrm{vib}},0}\left(l,\overline{\boldsymbol{Q}}^{p}\right)\,\right\rangle\right|^{2}\delta\left(\frac{\overline{\overline{E}}_{m}+\overline{\overline{E}}_{j(m)}-\overline{E}_{0}}{\hbar}-\omega\right)\end{aligned} \tag{6.20}$$

which is equivalent to the expression used in previous works.[371,372].

6.2 Examples of application

The theoretical framework derived in the previous section will be now applied to the simulation of the high-resolution vibronic spectra of two organic system, namely bithiophene and cyclobutanone. In the former, the LAM coordinate corresponds to the low-energy torsional mode between the two thiophene group. This motion is well separated, in terms of energy, from the other vibrations of the molecule, and thus its coupling with the latter will be neglected, adopting this way the simplified model. For cyclobutanone, the LAM associated to the structural occurring upon the electronic excitation is

a ring-deformation, and in this case the more complete formulation will be employed to simulate the vibronic spectra.

6.2.1 OPA and OPE spectra of bithiophene

The first system on which the theoretical framework presented above is tested is bithiophene, and more specifically the OPA and OPE spectra for transitions involving the S_0 and S_1 states. Electronic structure calculations will be performed at the (TD)-DFT level, using the B3LYP and CAM-B3LYP exchange-correlation functionals, with the addition of the D3BJ correction to account for dispersion effects.[373] This choice is based on the benchmark reported in Ref. 372, where this electronic structure method was proven to be the most accurate for the reproduction of the vibrational properties of thiophene and bithiophene.

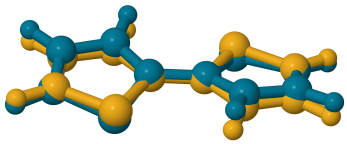

FIGURE 6.1: Graphical representation of the equilibrium structures of bithiophene in the S_0 and S_1 electronic states.

Bithiophene has two isomers, corresponding to the *trans* and *cis* configurations, which differ in the relative orientation of the two rings. As discussed in Ref. 372, the *trans* isomer (referred in the following as *trans*-2T) is the most stable one, and will be studied in the present work. *trans*-2T is planar in the S_1 state, and non-planar in S_0, with a dihedral angle between the two thiophene groups of $\approx 160°$. The electronic excitation is accompanied by a large-amplitude distortion and, as discussed in the previous chapter, the choice of the coordinate system used in the simulation is expected to be relevant to reproduce correctly the vibronic spectrum.

In Fig. 6.2, the theoretical OPA spectra, computed at the TD AH|FC level using Cartesian coordinates and DICs, are reported together with the experimental spectrum, taken from Ref. 374. The TD algorithm has been used since, due to the high flexibility of bithiophene, the convergence of the TI algorithm to recover the total intensity is very slow. As expected, the computed spectra are very different depending on the coordinates system, the shape being significantly broader with Cartesian coordinates than with DICs. Another important aspect is that, while the spectra have been normalized to facilitate the comparison of the band-shape, the intensity is also halved for Cartesian coordinates. The spectrum is computed at the FC level, therefore the difference between Cartesian and internal coordinates is directly connected to the definition of the Duschinsky transformation. In the previous chapter, it was shown that a larger vibronic broadening in Cartesian coordinates can be caused both by the presence of large, unphysical couplings between the LAM and the other modes in the definition of $\boldsymbol{J}$, and this coupling can have stronger impacts, depending on the structure of $\boldsymbol{K}$. For 2T, the main source of inaccuracy is the incorrect definition of $\mathbf{J}$, as highlighted in Fig. 6.2, where the spectra computed at the AS|FC level, therefore neglecting the mode-mixing effects, are also plotted along their AH|FC counterpart. The AS spectra are

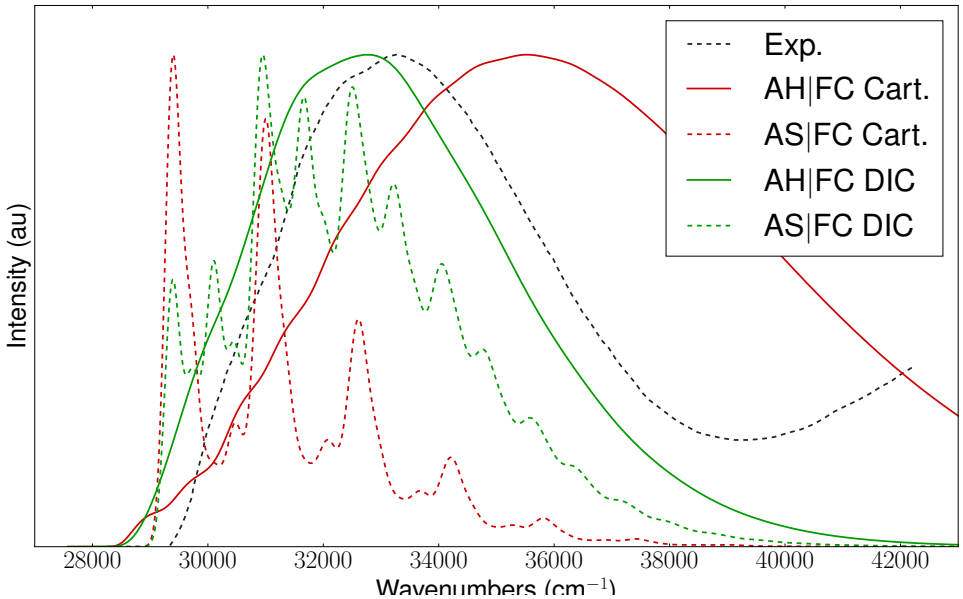

FIGURE 6.2: Theoretical OPA spectrum for the $S_1 \longleftarrow S_0$ transition of *trans*-2T computed with Cartesian coordinates (red line) and DICs (green line) at the TD AH|FC (solid lines) and TD AS|FC (dashed lines) level, together with the experimental spectrum, taken from Ref. 374. Gaussian functions with HWHMs of 100 cm^{-1} have been used to reproduce the broadening effects. IEF-PCM (*n*-hexane) has been used to reproduce solvent effects.

significantly less broadened than the AH ones, even though the same Gaussian broadening functions with HWHMs of 100 cm^{-1} have been used each time. Therefore, mode-mixing effects are relevant in both cases, since they enhance the intensity of a large-number of vibronic transitions, at expense of the maximum of intensity, which is lowered. Anyway, even at the AS level, the agreement between the theoretical spectrum based on Cartesian coordinates and the experimental one[374] is still unsatisfactory since, for example, the intensities of the lowest energy transitions are overestimated. On the other hand, the agreement is better both at the AH and AS levels if DICs are used.

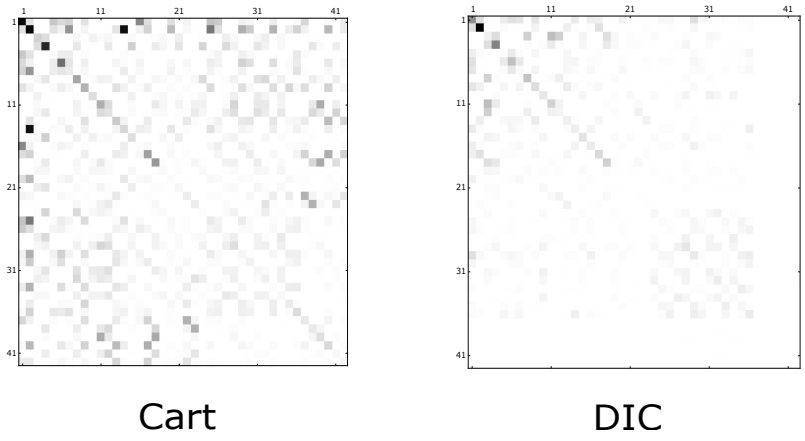

FIGURE 6.3: Graphical representation of the Sharp and Rosenstock $\boldsymbol{C}$ matrix for the $S_1 \longleftarrow S_0$ transition of bithiophene computedin *n*-hexane with Cartesian coordinates (left panel) and DICs (right panel).

Following the analysis reported in the previous chapter, the couplings effects between the final-states modes, which contribute to the intensity of the combination bands, has been evaluated from the magnitude of the elements of the Sharp and Rosenstock $\boldsymbol{C}$ matrix. The graphical representation of $\boldsymbol{C}$ for 2T in Cartesian coordinates and DICs, reported in Fig. 6.3, confirms that, if the latter are used, the torsional mode (corresponding to first mode) is mildly coupled from the others, whereas significant couplings are present with the high-frequency modes when Cartesian coordinates are employed.
In order to further improve the accuracy of the theoretical results, the DVR-based approach described in the previous section has been used to compute vibronic transitions involving the torsional motion along the dihedral angle θ between the two rings. Among the various high-resolution spectra available in the literature,[374,375] the laser-induced fluorescence (LIF) spectrum of bithiophene, taken from Ref. 375 will be used as reference. In order to highlight the influence of the barrier height on the overall spectroscopic properties, calculations were performed both at the B3LYP and at the CAM-B3LYP-D3BJ level, where the latter is expected to provide the most accurate results. As shown in Fig. 6.4, the PES has a similar shape in both cases, with two equivalent minima, corresponding to the distorted geometry, and a local

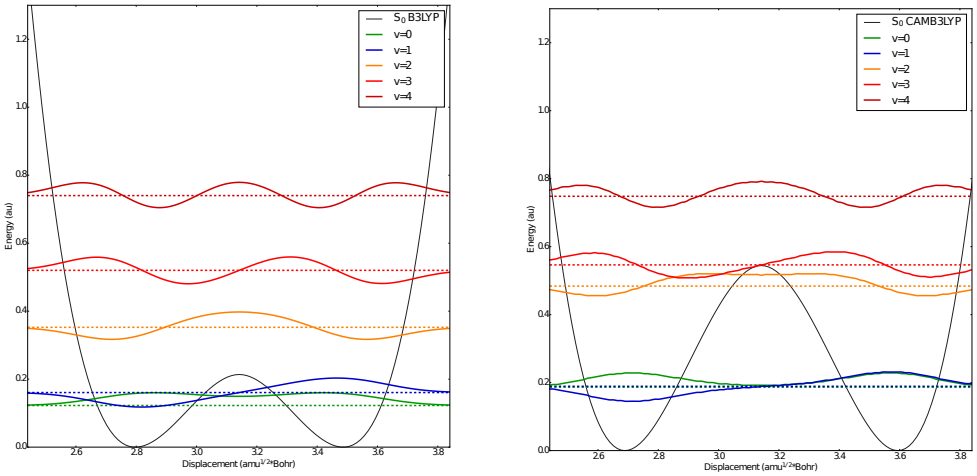

FIGURE 6.4: PES of the S_0 state of 2T obtained after a relaxed scan along the dihedral angle between the thiophene rings of 2T (black line), computed at the B3LYP/SNSD and CAM-B3LYP-D3BJ/SNSD level of theory. The vibrational energies of the first 5 levels computed using the DVR approach are reported using horizontal, dotted lines, together with their respective wavefunctions (solid lines).

maximum, corresponding to the planar configuration. The energy difference between this planar configuration and the minima is however significantly different between the two electronic structure approaches, since the barrier computed at the CAM-B3LYP-D3BJ level is twice higher than the one obtained with B3LYP.

The energy barrier has a strong impact on the vibrational energies computed variationally, with two possible limiting cases. If the vibrational energy is small with respect to the barrier, two nearly degenerate vibrational levels are present, corresponding to functions localized in each well. Due to the symmetry of the PES, the final vibrational wavefunctions are the symmetric and antisymmetric linear combination of wavefunctions localized around the two minima, and the splitting between those two levels is small with respect to their energy. This condition is met for the two lowest-energy levels computed at the CAM-B3LYP-D3BJ level, where the barrier (42.57 cm^{-1}) is larger than the vibrational energies of the first two vibrational states (15.20 and 15.50 cm^{-1}), so that the splitting between them is negligible (0.30 cm^{-1}). For the second and third vibrational levels, the degeneracy of the states is removed and the splitting increases, since the vibrational energies (39.00 and 44.82 cm^{-1}) are in this case comparable to the height of the barrier. For the B3LYP PES, due to the too low barrier height, the energy splitting between the first two vibrational states (3.11 cm^{-1}) is overestimated with respect to experimental data ($\approx$ 1 cm^{-1}).[375] It should be stressed out that, while only the region of th PES about the two minima of the *trans* conformers is shown in Fig. 6.4 (corresponding to l between 2.4 and 3.8 $amu^{1/2}\cdot$ Bohr), the DVR computations were performed for values of θ ranging from 0 to 360 degrees

(l between 0 and 6.28), using periodic boundary conditions for the DVR basis functions.

In order to compute the Franck-Condon factors for vibrational levels involving the LAM, the PES along the torsional angle θ was also computed at the TD-CAM-B3LYP-D3BJ/SNSD level also for the S_1 state, with the results reported in Figure 6.5. The values of the potential energy of the excited state have been computed at the same geometries as those obtained along the relaxed scan of S_0. Indeed, as already recalled in the previous section, the DVR-based variational approach can be used to compute Franck-Condon factors only if the PESs of both states are sampled with the same nuclear configuration. The shape of the S_1 PES is significantly different from S_0, since the equilibrium geometry here is planar. Therefore, the vibrational levels are nearly equally spaced, with a spacing larger than for S_0, which is consistent with the fact that the PES of the S_1 state is significantly steeper.

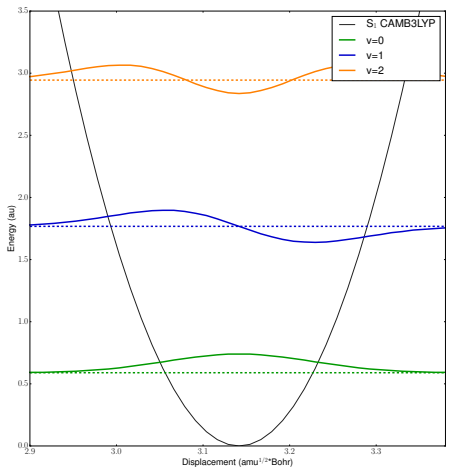

FIGURE 6.5: PES of the S_1 state of 2T obtained after a relaxed scan along the dihedral angle between the thiophene rings (black line), computed at the CAM-B3LYP-D3BJ/SNSD level of theory. The computed vibrational energies of the first 3 levels are reported using horizontal, dotted lines, together with their respective vibrational wavefunctions (solid lines).

The OPE spectra along the torsional motion is reported in Fig. 6.6 together with the experimental LIF results, taken from Ref. 375. The spectrum has been computed twice, with the ground and the first vibrational excited level of S_1 as starting levels of the transitions, since the experimental vibronic progressions were recorded separately for each of those cases. Considering first the vibronic spectrum from the vibrational ground state (reported in the left panel of Fig. 6.6), the agreement in the band positions is very good for the first transitions, but the computed ones tend to be underestimated at higher quanta. Except for the first transition, the relative intensities are also qualitatively comparable to experiment, reproducing the trend in the band pattern. The discrepancies between the theoretical and the experimental results can be ascribed to the limitations of our DVR approach. First of all, the representation of the S_1 PES is not the most accurate one, since it is sampled at the nuclear configurations obtained for the scan of the relaxed S_0 state. Nevertheless, the quality of the description of the S_1 PES is critical for the intensities of the vibronic bands, whereas the main inaccuracy concerns the position of the bands. A further major approximation employed in those simulations is the use of the adiabatic approximation to decouple the LAM and the other normal modes. For 2T, this coupling may be large especially for higher-energy levels of the S_0 state, for which the reproduction of the vibrational energies

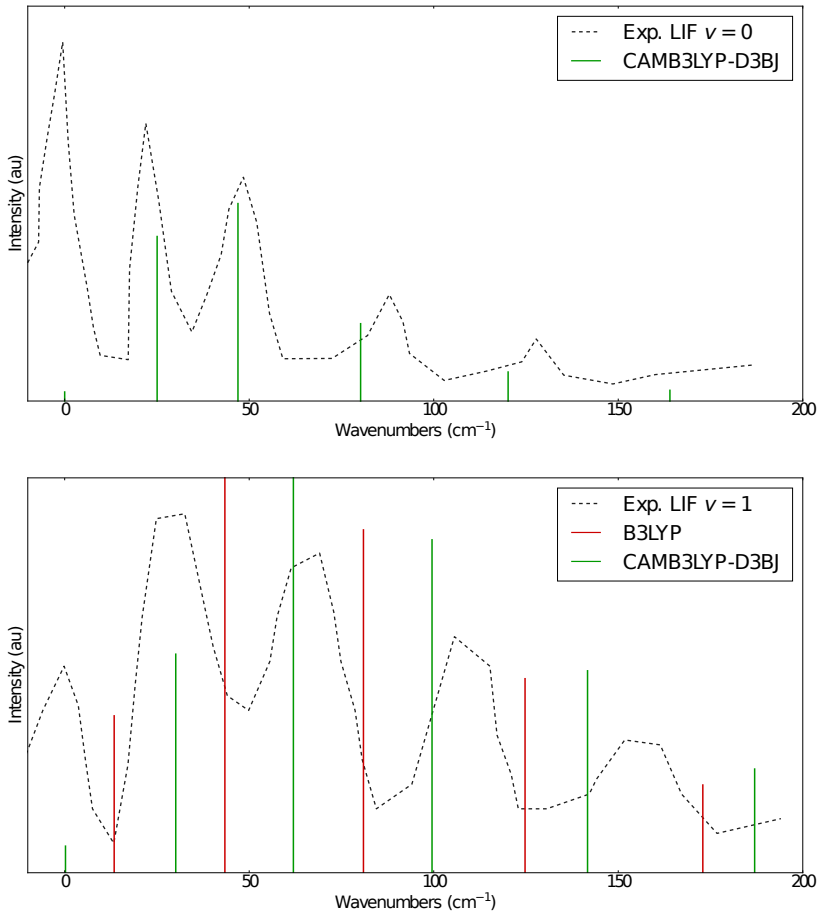

FIGURE 6.6: Theoretical OPE spectra for the $S_1 \longrightarrow S_0$ transition of 2T computed at the B3LYP (red line) and CAM-B3LYP-D3BJ (green line) level from the ground (upper panel) and the first excited (lower panel) vibrational level of te S_1 electronic state. The experimental LIF spectrum, taken from Ref. 375, is also reported.

is less accurate. The situation is more complex for the transitions from the first excited vibrational state, where the band energies seem systematically underestimated and their relative intensities overestimated. However, the improvement is significant especially when compared with the results obtained using the harmonic approximation, which predicts a constant spacing of the levels of 40 cm^{-1}. The quality of the results is significantly worse also if a PES with a lower energy barrier between the two minima is employed, such as the one computed at the B3LYP level (reported in Fig. 6.4). In fact, as shown in the lower panel of Fig. 6.6, the reproduction of the band position is in this case poor, and does not allow an univocal assignment of every band. Those results show that the DVR-based approach, when coupled with high-accuracy electronic structure methods, provides a significant improvement in the description of large-amplitude motions.

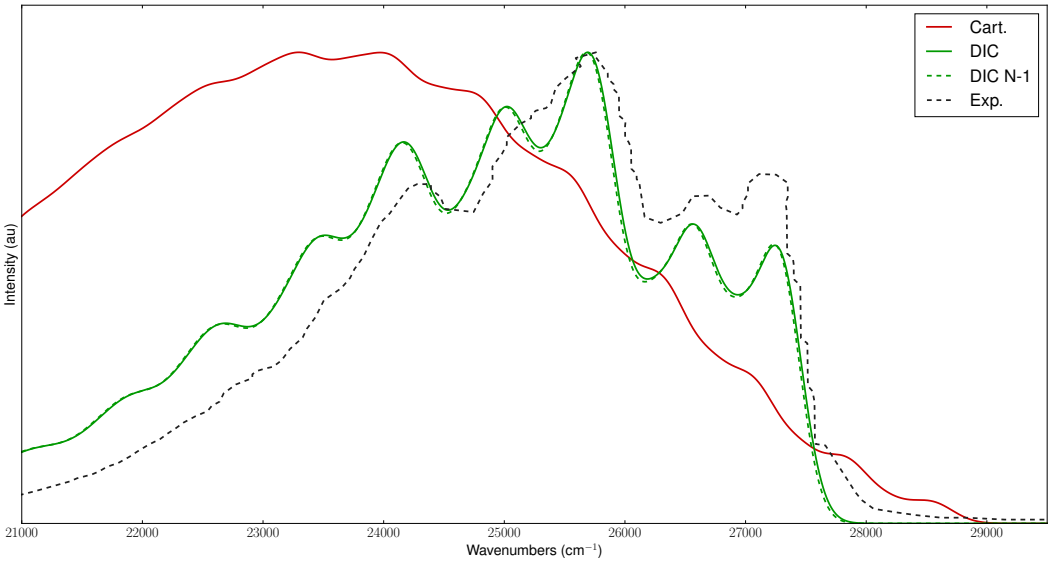

FIGURE 6.7: Theoretical OPE spectrum for the $S_1 \longrightarrow S_0$ transition of 2T computed at the CAM-B3LYP-D3BJ/SNSD level of theory using Cartesian coordinates (red line) and DICs (green lines), using the reduced-dimensionality scheme to isolate the LAM, treated separately and combined within the hybrid DVR-harmonic scheme (solid line) or simply discarded (dashed line). The experimental spectrum was taken from Ref. 376

The results shown above have been used to simulate the full OPE spectrum of 2T using the hybrid DVR-harmonic approach presented in the theoretical section, and the results are reported in Fig. 6.7. In all cases, the electronic structure calculations have been performed at the CAM-B3LYP-D3BJ level, and the vibronic spectra have been computed at the TI AH|FC level for the N'_{vib} harmonic modes, explicitly excluding the mode associated to the LAM using the reduced-dimensionality schemes introduced in the previous chapter. The vibronic spectrum for the N'_{vib} modes has been convoluted with the progressions due to the LAM to obtain the full spectrum. Any variation of the orthogonal modes along the LAM is ignored. As shown in Fig. 6.7, the

agreement is satisfactory for the spectrum computed using DICs, whereas it is poor if Cartesian coordinates are used. Those results show that, if the LAM is strongly coupled to the other N'_{vib} modes, such as when Cartesian coordinates are used, the accuracy of the results is poor independently of the method used to describe the LAM. A more accurate reproduction of the experimental spectrum is obtained using DICs, since in this case the coupling between the LAM and the other modes is lower, increasing the accuracy of the hybrid DVR-harmonic approach. The DICs spectrum has been compared also to the one obtained including only the N'_{vib} harmonic block, and neglecting the vibronic transitions involving the LAM. As shown in Fig. 6.7, the two spectra are nearly superimposable. We recall that, to reproduce the experimental broadening, a distribution function (in the present case Gaussian functions with HWHMs of 200 cm^{-1}) is superimposed to each vibronic peak. This value, which has been chosen to match the experimental data, is much larger than the separation between the vibrational levels of the LAMs, and therefore the convolution of all the vibronic transitions involving the LAM is equivalent to an overall broadening of the vibronic spectrum obtained for the $N_{\text{vib}} - 1$ harmonic block. This is true only for low-resolution spectra, since, when high-resolution spectra are simulated (such as for the LIF spectrum described above), an explicit inclusion of the vibronic transitions of the LAM is mandatory.

6.2.2 A challenging case: cyclobutanone

Bithiophene is characterized by a LAM which can be described using directly the primitive internal coordinates (PICs) or linear combinations of them. This allowed to use the ICPH model to compute the vibronic progression involving the torsional mode. However, for more complex LAMs, such a simple description is usually impossible. For example, a large class of cyclic molecules, which are planar in the ground state and undergo a deformation upon electronic excitation, cannot be described trivially in terms of PICs.[132,133] In those cases, the LAM can be efficiently described using the RPH model, since the planar configuration is a transition state for the electronic excited state, so that the LAM can be parametrized using the intrinsic reaction path connecting the transition state to a minimum.

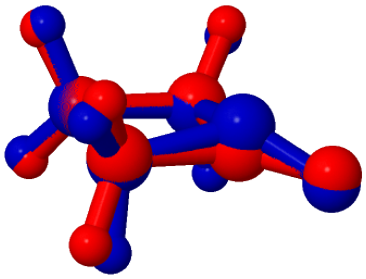

FIGURE 6.8: Graphical representation of the equilibrium geometries of cylobutanone of the S_0 (in red) and S_1 (in blue) electronic states, computed at the B3LYP/SNSD level.

The high-resolution experimental spectra of several cyclic compounds have been recorded by Laane and co-workers, both within the IR and UV-vis energy ranges, so that vibronic transitions can be singled out.[377,378,379] In most cases, the interpretation of these experimental data is based on semi-empirical

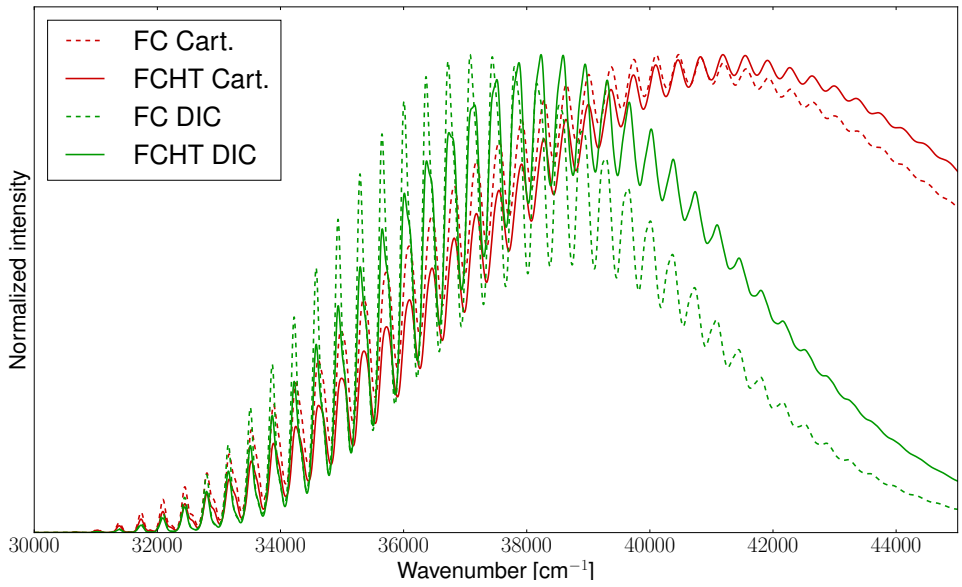

FIGURE 6.9: OPA spectrum of the $S_1 \leftarrow S_0$ transition of cyclobutane computed at the AH|FC (dashed lines) and AH|FCHT (solid lines) levels using Cartesian (red lines) and delocalized internal (green lines) coordinates at the harmonic level. Gaussian functions with HWHMs of 50 cm^{-1} have been used to reproduce the broadening effects.

vibrational Hamiltonians (mono- and bi-dimensional) for the PES along the LAM, whose parameters have been determined by fitting the theoretical vibrational energies to experimental data.[377,379] Those analyses proved that monodimensional Hamiltonians can be satisfactory only if applied to represent the energy levels of a narrow sample of cases, such as four-membered[380] and five-membered rings with a double bound.[381,382] For more complex systems,[383] monodimensional models are not sufficient, and only a bidimensional Hamiltonian can reproduce correctly experimental data. Characterizations of those experimental data using PES obtained from *ab initio* calculations, not involving any empirical parameter obtained through a fitting to experimental data are scarce. Here, we will focus on the simulation of the one-photon absorption spectrum of cyclobutanone for the $S_1 \leftarrow S_0$ transition, using the experimental data reported in Refs. 384 and 380 as reference.
The OPA spectra of cyclobutanone for the $S_1 \leftarrow S_0$ transition computed at the harmonic level, using the AH|FC and AH|FCHT models in Cartesian and internal coordinates, are plotted in Fig. 6.9. The main vibronic progression, characterized by bands with a constant spacing of ≈ 300 cm^{-1}, is due to the ring-inversion mode, which corresponds to the LAM. In fact, as shown in Fig. 6.8, the ring of cyclobutanone is planar in the S_0 state, but the planarity is lost in the excited, S_2 state, due to a pyramidalization of the C=O group, accompanied by a deformation of the four-membered ring. As already discussed in Chapter 4, in presence of similar deformations, significant differences are expected between the spectrum in Cartesian and in internal coordinates. In fact, as shown in Fig. 6.9 the band-shape is narrower in DICs than

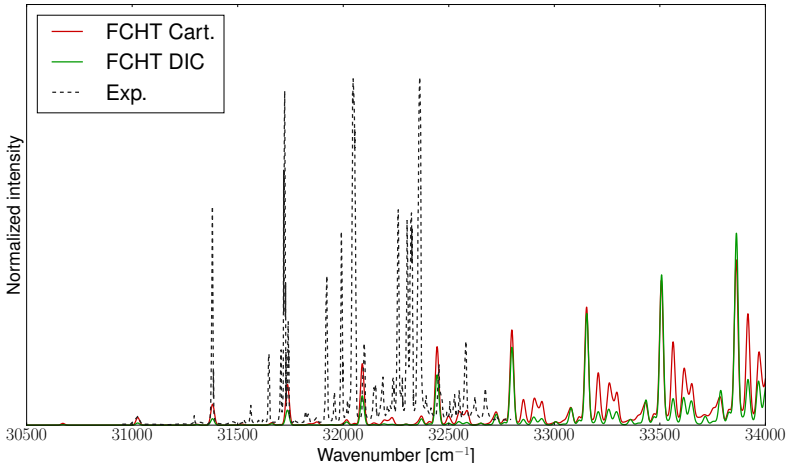

FIGURE 6.10: Experimental[380] and theoretical OPA spectra of the $S_1 \longleftarrow S_0$ transition of cyclobutanone computed at the AH|FCHT level using Cartesian coordinates (red line) and DICs (green line) at the harmonic level. Gaussian functions with HWHMs of 10 cm^{-1} have been used to reproduce the broadening effects.

in Cartesian coordinates, due to the reduced coupling between the LAM and the other modes. Furthermore, HT effects are not negligible, especially in internal coordinates, and they cause a shift of the spectral maximum towards higher energies. The difference between the two coordinates systems is even more evident if a lower HWHM is employed, so that vibronic transitions can be singled out. As shown in Fig. 6.10, where the theoretical OPA spectrum, broadened by means of Gaussian functions with HWHMs of 10 cm^{-1}, is compared to the experimental, high-resolution fluorescence excitation spectrum, taken from Ref. 380. For both Cartesian and internal coordinates, the vibronic progression of the LAM is reproduced incorrectly. More precisely, the intensity of the bands in the computed spectra increases constantly with the energy also above 34000 cm^{-1}, whereas, in the experimental data, the spectrum reaches a maximum for the fourth band and then decreases.
In order to improve the accuracy of the simulation, the vibronic spectrum has been simulated using the anharmonic model described before. A major difficulty, however, is that the description of the LAM as a fixed linear combination of primitive internal coordinates is less trivial than for the previous system, so the RPH framework will be employed. Furthermore, the S_1 state, with a saddle point for the planar configuration, has been taken as reference in the IRC calculation, and the same geometries have been used for the fitting of the S_0 PES. The PES along the LAM, shown in Fig. 6.11, has a significantly different shape in the ground and excited electronic states. This difference has a significant impact on the pattern of the vibrational energy levels, since in the first case they are nearly equispaced, with the spacing decreasing slowly with the increasing energy. On the other hand, for the double-well potential, two different regions can be identified. For vibrational energies below the barrier of the double-well (which is approximately 1300 cm^{-1}), couples

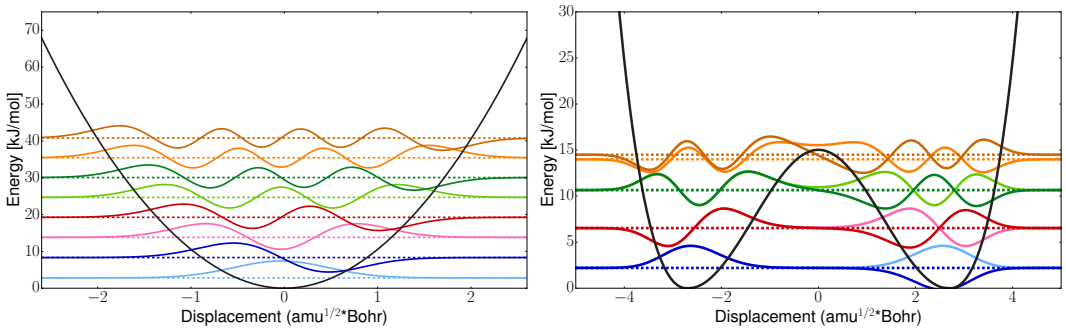

FIGURE 6.11: Graphical representation of the PES along the ring inversion mode for the S_0 (left panel) and S_1 (right panel) electronic states of cyclobutanone, computed at the B3LYP/SNSD level of theory and using the RPH framework. The vibrational levels and wavefunctions, computed using the variational, DVR-based approach, are also reported.

of nearly-degenerate states are present, which are symmetric and antisymmetric with respect to the planar configuration, respectively. For energies comparable and above the barrier, the splitting between nearly-degenerate states increases. It is noteworthy that this trend cannot be reproduced, even at a qualitative level, using an harmonic description, where the spacing is constant.

When the coupling between N'_{vib} harmonic modes is taken into account, the vibronic progression involving vibrational states where only the LAM is excited can be computed at the lowest level of approximation by neglecting three effects, namely the variation of the ZPVE based on the projected harmonic modes along the LAM, the variation of the transition dipole moment along the LAM and the change of the intensity of the $\langle\, \overline{\overline{\mathbf{0}}} \mid \overline{\mathbf{0}} \,\rangle$ integral for the harmonic modes. By neglecting all those effects, the variational calculation is performed directly on the PES explored during the IRC calculation, and the intensity of the transitions is given by FC_{LAM} integrals between LAM-specific vibrational wavefunctions.

Fig. 6.12 reports the OPA spectrum by only considering the vibrational progressions along the LAM. Already, an improvement over the original, full-dimensional albeit purely harmonic calculations shown in Fig. 6.10 can be observed. However, the agreement with the experiment is still not satisfactory, especially for the higher-energy transitions. Inclusion of the variation of the transition dipole moment along the LAM (green line in Fig. 6.12) results in a significant gain in accuracy. To explain this difference, it should be remarked that, in the FC_{LAM} simulation, considering the symmetry of the system, only transitions to states which are symmetric with respect to the top of the well have non-null intensity, since the initial, ground state is symmetric as well. On the other hand, in the FCHT_{LAM} simulations, only transitions to antisymmetric states become allowed, due to the antisymmetry of the latter. For the lowest-energy transitions, the difference is minimal, since the couples of symmetric/antisymmetric states are nearly-degenerate. On the other hand, for higher-energy states, as the splitting increases, such a constraint

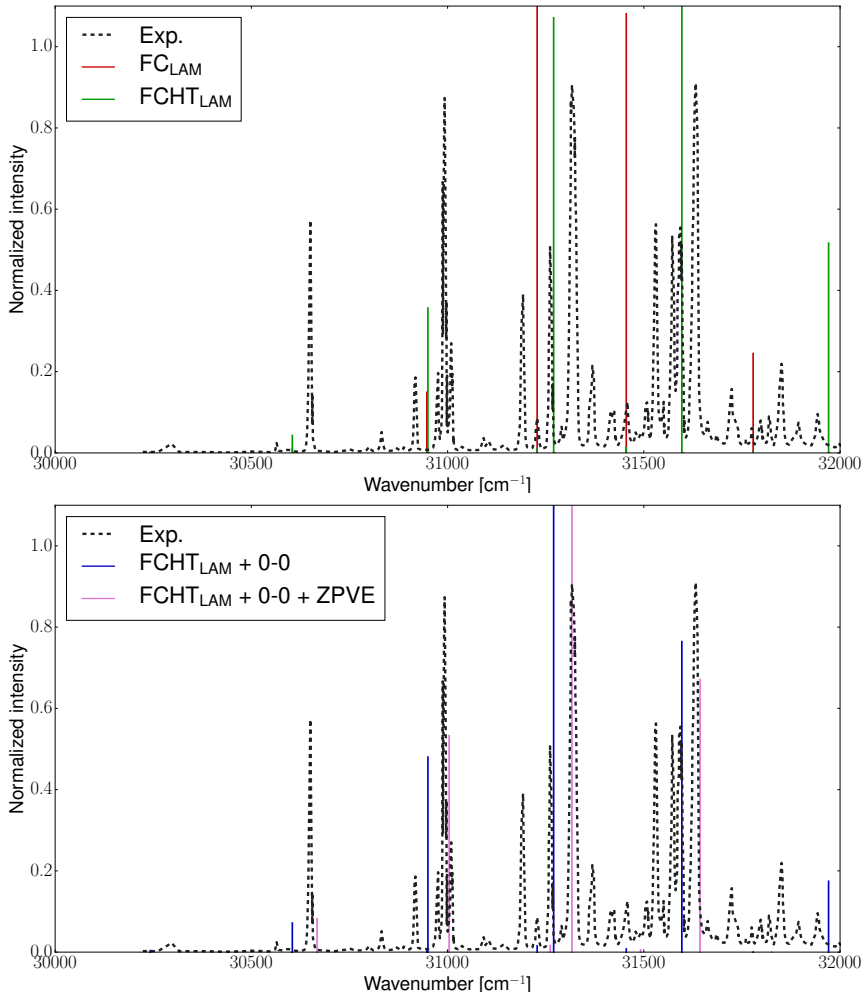

FIGURE 6.12: Experimental[380] (dashed, black line) and theoretical OPA spectra of the $S_1 \leftarrow S_0$ transition of cyclobutanone computed at the B3LYP/SNSD level, using the RPH model and including vibronic transitions involving only the ring-inversion mode. The spectra obtained by neglecting the variation of the transition dipole moment along the LAM (solid, red line) and including it (solid, green line) are reported. To facilitate the comparison between theoretical and experimental results, the theoretical spectra have been shifted to match the experimental value of the energy of the 0-0 transition.

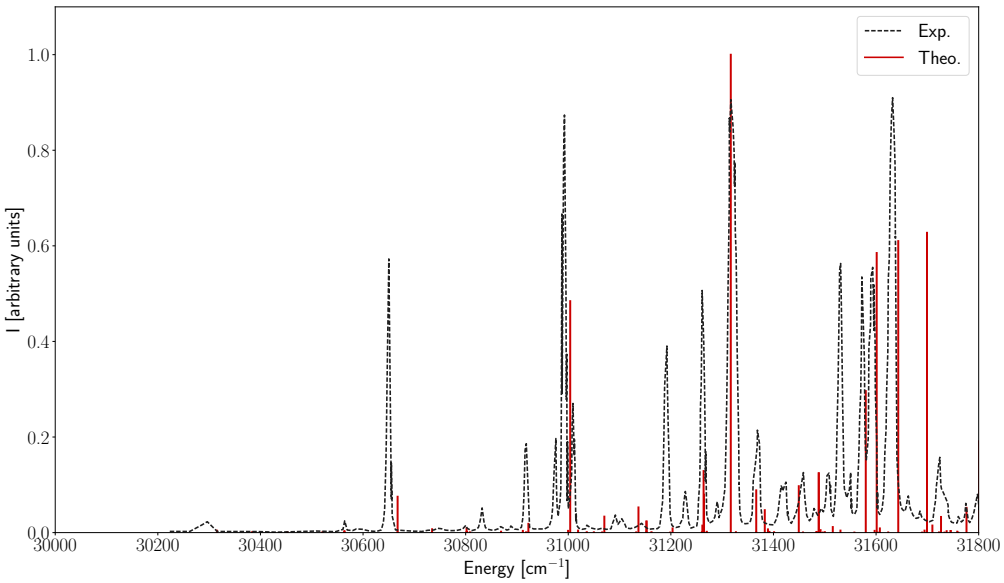

FIGURE 6.13: Experimental[380] (dashed, black line) and theoretical OPA spectrum for the $S_1 \leftarrow S_0$ transition of cyclobutanone computed at the B3LYP/SNSD level, using the RPH model, together with the hybrid DVR-harmonic model.To facilitate the comparison between theoretical and experimental results, the computed spectrum has been shifted to match the experimental value of the energy of the 0-0 transition.

has a significant impact on the computed band-shape. To refine further the quality of the theoretical results, the other two effects, namely the variation of the intensity of the 0-0 transition and Fig. 6.12). As expected, inclusion of the variation of the intensity of the 0-0 transition associated to the projected modes $\boldsymbol{Q}^p$ (spectrum in solid, blue line) changes only the relative intensity of the bands but not their positions. More precisely, the relative intensities of the most intense bands are improved, even if those of the two lowest-energy bands are still underestimated. Inclusion of the variation of the ZPVE leads to a better agreement in the band-positions with respect to experiment, with the position of the first 5 bands reproduced with an accuracy within 10 cm^{-1}. Finally, the full-dimensional OPA spectrum of cyclobutanone computed using the hybrid harmonic-DVR scheme is reported in Fig. 6.13. The transitions involving the N'_{vib} harmonic modes have been simulated with the VH model. For each geometry along the IRC, all N'_{vib} projected harmonic frequencies are positive, and therefore all modes have been included in the simulation. The overall band-shape is well reproduced correctly, even if discrepancies are still present in the intensities of several bands between 31400 and 31800 cm^{-1}. However, those bands correspond to transitions to vibrational states, with energy comparable to the height of the well, and thus their intensity strongly depends on the accuracy in the reproduction of this height. For this reason, to further improve the accuracy of the results, more refined electronic structure methods would be necessary in the calculation of the PES.

6.3 Perturbative anharmonic simulations on electronic excited states: the TD-DFT/VPT2 approach

6.3.1 General theory

The combination of harmonic vibronic models in internal coordinates with the variational, DVR-based scheme introduced in the previous section significantly improves the reliability of purely harmonic models when treating systems displaying some degree of flexibility. However, the main limitation of the previous approach is that anharmonic effects are included only for a single degree of freedom, while treating all the other modes as harmonic.
Thus, the theory presented in the previous chapter is ill-suited for the study of semi-rigid systems where a single coordinate characterized by strong anharmonic effects cannot be identified. Here, we propose an alternative approach, where anharmonic frequencies of excited states are computed using VPT2 (see Chapter 3 for more details about VPT2). Clearly, the main advantage of this approach over the hybrid DVR-harmonic one introduced above is the possibility of including anharmonic effects for all vibrational degrees of freedom, without the need of specifying a coordinate for which anharmonic effects are to be included.
To apply VPT2 to electronically excited states, high-order derivatives of energy and properties are needed. Those properties can be computed by numerical methods, such as finite differentiation[385] or fitting approaches,[386] or using analytical formulas for the derivatives. The main advantage of the former class of approaches is their generality, since they can be applied to any electronic-structure approach, but their computational cost grows significantly when high-order derivatives are needed and they can suffer from numerical instability. For the ground state, analytic formulas and implementations of cubic and quartic force constants, which are the input data for VPT2 calculations, have been proposed in the literature at the Hartree-Fock and DFT levels.[387,388,389,390,391] For excited states, analytical second-order geometrical derivatives of excitation energies have been recently derived within the time-dependent density functional theory (TDDFT) and and its Tamm-Dancoff approximation (TDA).[41,100,392] This made possible the calculation of analytical first and second derivatives of electronic excitation energies for very large systems, with up to several dozens of atoms. Thanks to this, it is possible to build the cubic and semi-diagonal quartic force constants, necessary to compute the vibrational energies at the VPT2 level, by numerical differentiation, in the same way as is now commonly done for the ground state,

$$
\begin{aligned}
k_{ijk} = \frac{\partial^3 \mathcal{V}}{\partial q_i \partial q_j \partial q_k} = \frac{1}{3}\Bigg[& \sqrt{\frac{\hbar}{\omega_i}} \frac{k_{jk}(+\delta Q_i) - k_{jk}(-\delta Q_i)}{2\delta Q_i} \\
& + \sqrt{\frac{\hbar}{\omega_j}} \frac{k_{ik}(+\delta Q_j) - k_{ik}(-\delta Q_j)}{2\delta Q_j} \\
& + \sqrt{\frac{\hbar}{\omega_k}} \frac{k_{ij}(+\delta Q_k) - k_{ij}(-\delta Q_k)}{2\delta Q_k} \Bigg] \\
k_{iijk} = \frac{\partial^4 \mathcal{V}}{\partial {q_i}^2 \partial q_j \partial q_k} = & \frac{\hbar}{\omega_i} \frac{k_{jk}(+\delta Q_i) - k_{jk}(-\delta Q_i)}{\delta {Q_i}^2} \\
k_{iijj} = \frac{\partial^4 \mathcal{V}}{\partial {q_i}^2 \partial {q_j}^2} = & \frac{1}{2}\Bigg[\frac{\hbar}{\omega_i} \frac{k_{jj}(+\delta Q_i) - k_{jj}(-\delta Q_i)}{\delta {Q_i}^2} \\
& + \frac{\hbar}{\omega_j} \frac{k_{ii}(+\delta Q_j) - k_{ii}(-\delta Q_j)}{\delta {Q_j}^2} \Bigg]
\end{aligned}
\tag{6.21}
$$

The standard formulation of VPT2,[67,75] if used with the quartic force-field of an excited state, allows to compute anharmonic energies, as well as transition properties[393] between vibrational levels of the excited state. However, in vibronic spectroscopy, transition between vibrational levels of different electronic states are of interest. The extension of VPT2 to vibronic transitions has been proposed in the literature,[42,43] but due to its high computational cost it has been applied only to small-size systems, with up to 10 atoms. For this reason, an alternative, more affordable way is needed to deal with medium-to-large molecular systems. The approach adopted here is to focus on the band positions. Following eq. 3.11, the transition energy between vibronic states $|\,\bar{i}\,\rangle$ and $|\,\bar{\bar{f}}\,\rangle$ is,

$$
\begin{aligned}
\Delta E_{if} = & E_{\text{ad}} + \breve{\bar{\bar{E}}}_0 - \breve{\bar{E}}_0 + \sum_{k=1}^{N_{\text{vib}}} \left(\bar{\bar{v}}_k^f \bar{\bar{\omega}}_k - \bar{v}_k^i \bar{\omega}_k \right) \\
& + \sum_{k,l=1}^{N_{\text{vib}}} \left(\bar{\bar{\chi}}_{kl} \left[\bar{\bar{v}}_k^f \bar{\bar{v}}_k^f + \frac{1}{2}\left(\bar{\bar{v}}_k^f + \bar{\bar{v}}_l^f \right) \right] - \bar{\chi}_{kl} \left[\bar{v}_k^i \bar{v}_l^i + \frac{1}{2}\left(\bar{v}_k^i + \bar{v}_k^i \right) \right] \right)
\end{aligned}
\tag{6.22}
$$

Assuming that all transitions originate from the vibrational ground state of the initial electronic state (*i.e.* neglecting temperature effects), the previous equation can be recast as,

$$
\Delta E_{if} = E_{\text{ad}} + \sum_{k=1}^{N_{\text{vib}}} \bar{\bar{v}}_k^f \bar{\bar{\omega}}_k + \sum_{k,l=1}^{N_{\text{vib}}} \bar{\bar{\chi}}_{kl} \left[\bar{\bar{v}}_k^f \bar{\bar{v}}_l^f + \frac{1}{2}\left(\bar{\bar{v}}_k^f + \bar{\bar{v}}_l^f \right) \right] \tag{6.23}
$$

An alternative form of Eq. 6.23 can be derived using the VPT2 fundamental energies (ν_{1_k}),

$$\Delta E_{if} = E_{\text{ad}} + \sum_{k=1}^{N_{\text{vib}}} \overline{\overline{v}}_k \overline{\overline{\nu}}_{1_k} + \sum_{k=1}^{N_{\text{vib}}} \overline{\overline{\chi}}_{kk} \overline{\overline{v}}_k^f (\overline{\overline{v}}_k^f - 1) + \sum_{k \neq l=1}^{N_{\text{vib}}} \overline{\overline{\chi}}_{kl} \overline{\overline{v}}_k^f \overline{\overline{v}}_l^f \tag{6.24}$$

Inclusion of anharmonic effects in vibronic calculations can be derived with an alternate version of Eq. 6.24, where the terms proportional to the χ matrix are ignored,

$$\Delta E_{if} = E_{\text{ad}} + \sum_{k=1}^{N_{\text{vib}}} \overline{\overline{v}}_k^f \overline{\overline{\nu}}_{1_k} \tag{6.25}$$

Alternatively, the Duschinsky transformation can be employed to estimate the anharmonic corrections to be applied on the harmonic frequencies of a given state (generally the excited one). To do so, the harmonic frequencies and reference data (generally, the VPT2 results) for the fundamentals of the other state are needed. Assuming that all data are available for the initial state, then a set of scaling factors to correct the anharmonic energies in the final one and new, corrected data can be obtained through the relation,[394]

$$\overline{\overline{\nu}}_l = \left(\sum_{k=1}^{N_{\text{vib}}} {J_{kl}}^2 \frac{\overline{\nu}_k^{\text{anh}}}{\overline{\omega}_k} \right) \overline{\overline{\omega}}_l \tag{6.26}$$

In some of the following examples the reliability of this method will be compared with the full VPT2 treatment. We note here that all the molecular systems studied in the following are semi-rigid since for more flexible systems, characterized by LAMs, the accuracy of VPT2 is low.

6.3.2 Absorption spectrum of phenyl radical

A first illustrative case is the absorption spectrum of phenyl radical. Spectroscopic techniques (usually time-resolved) are routinely used for the characterization of radicals and, for phenyl radical, the high-resolution IR[395,396] and electronic[397,398] spectra are available in the literature. In particular, the importance of vibronic effects on the electronic spectrum has been investigated[399,400] using models of different level of sophistication. In the second work, anharmonic frequencies were derived for the D_1 state through the extrapolation based on the Duschinsky transformation. Here, the reliability of this approximation will be checked by computing the anharmonic frequencies of the excited, D_1 state at the VPT2 level.
The harmonic and anharmonic frequencies for the D_0 and D_1 electronic states of phenyl, computed at the B3LYP/SNSD level, are reported in Fig. 6.1. This comparison shows that, in this case, the extrapolation scheme based on the Duschinsky transformation is significantly more reliable than for anisole (*vide infra*) since, for the majority of the modes, the deviation between the extrapolated and VPT2 anharmonic frequencies is below 10 cm^{-1}. A graphical representation of the deviation between the two sets of wavenumbers

Mode	Symm.	Harm. S_0	Anharm. S_0	Harm. S_1	Scal. S_1	Anharm. S_1
1	A_1	400.134	390.917	299.660	292.846	289.887
2	B_1	423.944	416.150	354.322	347.358	347.732
3	B_2	594.236	588.095	527.707	522.086	528.533
4	A_1	614.264	609.520	590.751	586.151	581.805
5	B_1	667.807	650.805	682.305	674.965	665.291
6	B_1	719.920	706.433	764.050	751.747	746.189
7	A_2	814.178	792.719	787.816	767.042	767.253
8	A_1	893.238	869.735	923.361	907.573	907.658
9	B_1	968.277	941.104	966.685	941.689	938.953
10	A_2	981.849	968.928	997.068	969.097	970.741
11	A_1	995.120	968.135	999.879	985.481	982.110
12	A_1	1014.756	999.397	1017.064	999.206	1001.350
13	B_1	1046.795	1025.039	1024.006	997.041	995.905
14	B_2	1068.810	1060.485	1048.727	1035.589	1040.082
15	B_2	1171.064	1157.918	1118.088	1103.633	1093.978
16	A_1	1171.845	1156.986	1213.744	1198.077	1193.132
17	B_2	1302.373	1277.038	1241.510	1222.394	1219.820
18	B_2	1334.222	1309.661	1349.836	1324.526	1320.665
19	B_2	1459.878	1431.567	1395.244	1368.014	1372.508
20	A_1	1467.893	1436.368	1442.357	1411.234	1411.309
21	B_2	1571.771	1529.905	1521.746	1490.773	1484.554
22	A_1	1629.513	1592.817	1632.013	1588.648	1578.686
23	A_1	3159.398	3016.322	3137.459	2998.836	3026.061
24	B_2	3165.760	3028.737	3137.860	3004.743	3003.548
25	A_1	3179.364	3040.669	3160.153	3020.954	3008.177
26	B_2	3181.599	3050.657	3165.820	3032.806	3029.222
27	A_1	3191.353	3077.070	3184.981	3068.758	3073.908

TABLE 6.1: Harmonic, anharmonic and extrapolated wavenumbers for the D_0 and D_1 states of phenyl radical computed at the B3LYP/SNSD level.

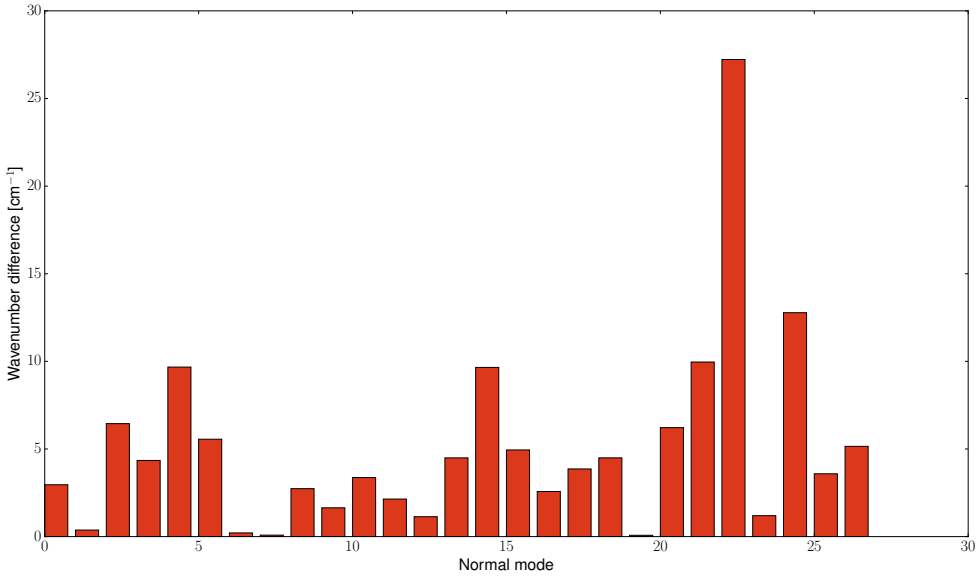

FIGURE 6.14: Plot of the absolute value of the difference between the anharmonic frequencies for the D_1 state of phenyl radical computed using the extrapolation based on the Duschinsky transformation and at the VPT2 level.

(see Fig. 6.14) shows that the largest difference is present for the higher-wavenumber modes, above 3000 cm^{-1}, corresponding to the C–H stretchings. Those modes are usually affected by strong anharmonic couplings, and therefore the extrapolation scheme, which assumes that the anharmonic correction to the PES is transitive between the electronic states, is inaccurate. Conversely, for the other modes, the accuracy is better due to the limited mode-mixing associated to the electronic transition.
The vibronic absorption spectrum for the $D_1 \leftarrow D_0$ transition of the phenyl radical computed using three different sets of frequencies – harmonic for both states, anharmonic (VPT2) for both states and anharmonic (VPT2) for the D_0 state and anharmonic (extrapolated) for the D_1 one – is reported in Fig. 6.15. As already noticed before, the spectrum computed at the harmonic level is shifted towards higher energies with respect to the two anharmonic ones, which are nearly superimposable. This is an expected outcome since the main vibronic progressions of the spectrum of phenyl correspond to excitation of two modes (4 and 8) with low wavenumbers (below 1000 cm $^{-1}$), a region in which the extrapolation scheme is reliable.

6.3.3 High-resolution OPA spectrum of anisole

The second test-case system studied here is anisole, the methyl ester of phenol (the structure is reported in Fig. 6.16). The spectroscopic properties of anisole in gas phase have been characterized using a wide range of experimental techniques, ranging from rotational[401] to vibrational[402,403] and electronic spectroscopies.[404,405,406] More recently, dimers[407] and van der Waals complexes of anisole have also been characterized spectroscopically.[408,409,410]

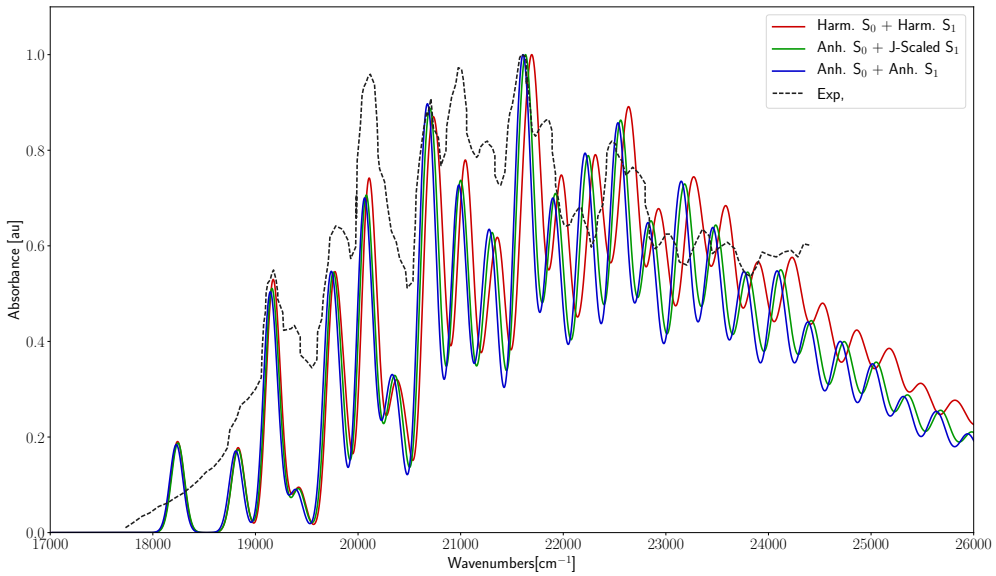

FIGURE 6.15: Theoretical OPA spectrum for the $D_1 \leftarrow D_0$ transition of phenyl radical, computed at the AH|FC level using the harmonic frequencies for both the electronic states (solid, red line), the anharmonic frequency for the S_0 state and the extrapolated ones for the S_1 state (solid, green line) and the anharmonic frequencies for both states (solid, blue line). Broadening effects have been included with Gaussian functions with HWHMs of 75 cm^{-1}.

From a theoretical point of view, the high-resolution vibronic spectrum of free anisole has been simulated at the AH|FC level[394] with the anharmonic frequencies of the excited electronic state (S_1) obtained through the extrapolation scheme introduced above.

As discussed in the reference theoretical work,[394] this extrapolation scheme provides a systematic improvement of the theoretical one-photon absorption (OPA) spectrum compared to the experimental one.[406] Here, the reliability of the extrapolation will be further tested by comparing those frequencies to the anharmonic ones, computed at the VPT2 level.

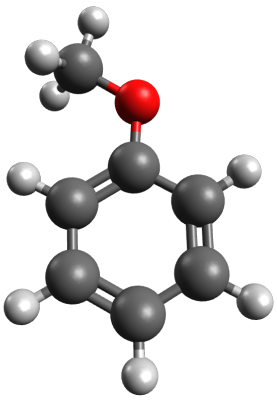

FIGURE 6.16: Molecular structure of anisole.

The harmonic and anharmonic wavenumbers of the ground and excited electronic states are reported in Tabs. 6.2 and 6.3, together with the experimental ones for the S_1 state, taken from Ref. 394. For the sake of consistency with the original theoretical work used as reference here,[394] electronic structure calculations have been performed at the B3LYP/6-311+G(d,p) level. For the ground electronic state, a full, direct VPT2 treatment leads to an overall lowering of most wavenumbers, with the exception of the fourth mode,

Mode	Harm.	Anharm.	HRAO	Mode	H	A	HRAO
1	90.43	83.05	92.56	22	1178.28	1164.19	1164.26
2	204.10	128.53	192.67	23	1194.35	1180.15	1179.14
3	255.86	252.02	254.90	24	1201.47	1178.01	1177.50
4	267.52	326.13	241.57	25	1271.41	1238.54	1238.48
5	421.90	416.25	416.26	26	1334.51	1303.56	1303.42
6	445.94	437.48	441.08	27	1356.98	1338.77	1339.16
7	517.18	508.79	510.84	28	1473.86	1440.00	1435.84
8	560.35	553.80	553.00	29	1484.96	1451.00	1450.62
9	629.06	623.21	622.98	30	1493.10	1454.16	1450.34
10	696.94	694.19	693.58	31	1505.53	1470.40	1470.69
11	763.71	761.68	762.01	32	1526.54	1497.62	1498.45
12	797.18	783.97	783.50	33	1624.19	1582.63	1582.76
13	827.41	811.83	812.00	34	1641.96	1601.25	1601.55
14	893.78	883.08	882.03	35	3002.56	2819.80	2812.86
15	971.16	958.03	957.91	36	3060.48	2894.14	2888.20
16	989.48	980.56	980.66	37	3131.99	2993.66	2991.28
17	1009.26	994.05	994.35	38	3163.07	3005.47	3005.64
18	1040.58	1024.13	1018.33	39	3170.49	3035.63	3035.83
19	1065.01	1041.73	1041.20	40	3186.65	3044.40	3043.40
20	1102.25	1082.63	1082.63	41	3193.97	3073.76	3074.75
21	1169.31	1146.96	1144.84	42	3204.08	3087.85	3087.99

TABLE 6.2: Comparison of the theoretical frequencies, computed at the harmonic and anharmonic (VPT2) levels, of the S_0 electronic state of anisole. Electronic structure calculations have been performed at the B3LYP/6-311+G(d,p) level.

Mode	Harm.	Anharm.	Scal.	RD-HRAO	Exp.[406]
1	63.05	272.66	61.15	62.95	66
2	78.41	84.36	74.11	86.76	85
3	135.76	90.19	103.59	151.79	140
4	196.89	214.57	210.66	193.91	197
5	253.58	232.57	249.76	248.92	256
6	374.48	368.27	370.57	383.23	372
7	436.26	429.32	428.05	431.20	421
8	439.95	501.03	433.04	472.27	436
9	517.18	500.15	511.86	505.59	509
10	527.70	514.24	522.45	513.39	524
11	546.03	539.85	540.06	537.23	538
12	600.76	639.13	592.84	607.36	595
13	625.72	625.95	622.66	620.75	620
14	678.51	732.90	671.15	706.93	670
15	780.78	765.32	767.82	765.47	772
16	856.76	848.28	848.53	839.50	845
17	973.59	952.92	958.66	956.29	960
18	989.52	969.66	972.93	970.60	972
19	1005.95	979.69	986.82	985.90	982
20	1034.30	1017.35	1013.94	1006.83	1008
21	1143.46	1120.22	1121.53	1115.68	1118
22	1151.93	1126.95	1136.58	1127.34	1127
23	1159.64	1140.87	1144.56	1141.35	1135
24	1183.19	1151.11	1161.45	1159.95	1161
25	1278.16	1236.68	1246.91	1236.95	1258
26	1309.62	1281.06	1282.96	1282.82	1277
27	1395.35	1359.16	1370.24	1359.78	1364
28	1419.44	1381.56	1386.67	1385.03	1389
29	1447.79	1400.48	1415.95	1402.13	1417
30	1457.23	1423.70	1423.11	1413.14	1424
31	1475.82	1437.98	1445.91	1441.32	1446
32	1482.91	1443.78	1444.21	1437.54	1443
33	1494.87	1448.56	1460.11	1452.44	1454
34	1521.22	1460.07	1483.56	1470.30	1482
35	3030.33	2935.65	2846.15	2933.33	2928
36	3099.48	2959.25	2931.04	2947.07	2980
37	3152.67	3008.49	3013.30	3006.01	3025
38	3170.29	3023.41	3022.15	3031.52	3042
39	3199.72	3088.89	3063.79	3050.99	3066
40	3207.43	3018.43	3058.30	3046.15	3078
41	3222.05	3122.60	3098.07	3102.47	3117
42	3228.20	3005.11	3109.82	3079.25	3128

TABLE 6.3: Comparison of the theoretical wavenumbers, computed at the harmonic and anharmonic (VPT2) levels, of the S_1 electronic state of anisole with the experimental data, taken from Ref. 406. Electronic structure calculations have been performed at the B3LYP/6-311+G(d,p) level.

that displays an anharmonic correction of +59 cm^{-1}. As emerges from an hindered rotor analysis,[157] this mode, together with the lowest-energy one (with harmonic wavenumber of $\overline{\omega}_1$=90.43 cm^{-1}), corresponds to torsions about the two single C−O bonds of the molecule. Such large-amplitude modes (LAMs) are highly anharmonic, and thus poorly described at a perturbative level based on a quartic force field. In order to get more reliable results, all couplings between the LAMs and the other modes have been canceled,[259] and LAMs have been treated using the hindered rotor model (the combined model is referred to as Hindered Rotor Anharmonic Oscillator, HRAO).[68,260] As shown in Tab. 6.2, for most modes, the difference between the full-dimensionality and the HRAO results is below 2 cm^{-1}, with the exception of modes 18, 28, 35, 36. Therefore, the couplings between the two LAMs and the other modes is not critical, and thus the HRAO model, where those couplings are neglected, is a satisfactory approach.

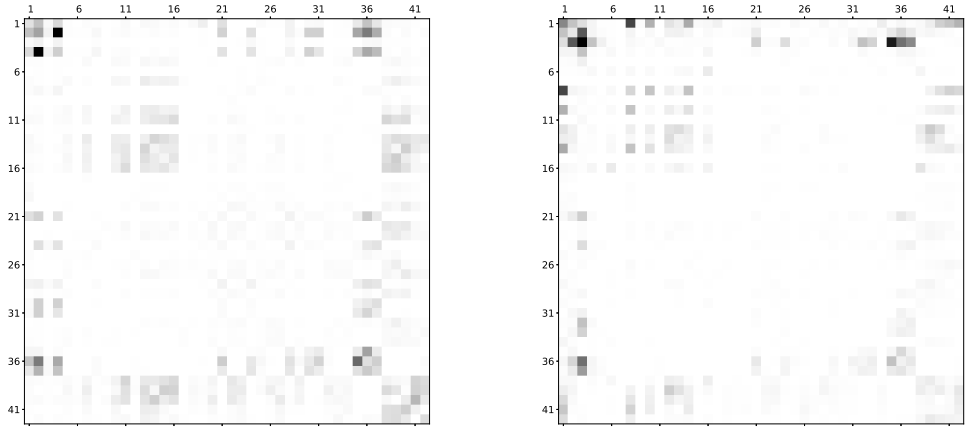

FIGURE 6.17: Graphical representation of the anharmonic **Y** matrix of anisole in the S_0 (left panel) and S_1 (right panel) states. The representation has been obtained as follows: the elements $Y_{ij}{}^2$ are calculated and normalized to 1. Then, a shade of gray is associated to each element (i,j) in the figure based on the equivalence (0, white; 1, black). The normalization factor is 284.31 cm^{-1} for the S_0 state and 648.64 cm^{-1} for the S_1 state.

To further evaluate the extent of the coupling between the modes, a graphical representation of the anharmonic **Y** matrix, whose definition can be found in Ref. 411, is given in Fig. 6.17. Without going into the details of the derivation, the **Y** matrix is simply a rewriting of the VPT2 anharmonic matrix χ where the terms are gathered based on the mode indexes involved, so the diagonal terms Y_{ii} contains only terms depending on mode i, and off-diagonal terms Y_{ij} are the sum of elements depending on to different indexes, i and j. Since χ contains the anharmonic correction to transition energies, **Y** can provide insights on the direct impact of mode coupling on the anharmonic correction. The graphical representation of **Y** for the ground, S_0 state, is reported in the left panel of Fig. 6.17. As expected, most of the couplings between the LAMs

(modes 1 and 4) and the other modes are nearly null, with the exception of modes 35 and 36, which are in fact among the ones displaying the largest deviation between the full-dimensional and the HRAO schemes. For the excited state S_1, modes 2 and 3 are the ones corresponding to the torsions along the two C−O single bonds, as confirmed by the graphical representation of the Duschinsky matrix **J**, reported in Fig. 6.18.

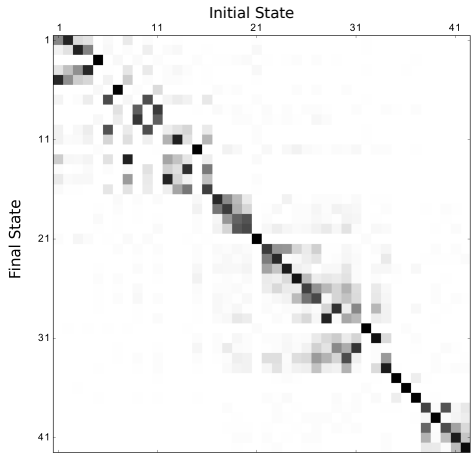

FIGURE 6.18: Graphical representation of the Duschinsky matrix **J** for the $S_1 \leftarrow S_0$ transition of anisole. The representation is obtained as already discussed for Fig. 6.17.

For this state as well, the **Y** matrix (right panel of Fig. 6.17) shows a coupling of those modes mainly with mode 36. However, in addition to the two internal rotations, a low-frequency mode (with a harmonic wavenumber of ω_1 = 63.05 cm^{-1}) is present. The plot of the Duschinsky transformation shows that this mode corresponds to mode 5 of the ground state, with harmonic wavenumber of 421 cm^{-1}). This mode is an out-of-plane deformation of the ring, and the lowering of its frequency is probably due to the transfer of electron density to $\pi^\star$ orbitals of the aromatic ring upon electronic excitation, which makes the ring less stable. The anharmonic wavenumber of the electronic state S_1 at the VPT2 level, which are collected in Tab. 6.3, show that full-dimensional VPT2 calculations lead to an unphysical anharmonic correction for the first mode (the anharmonic wavenumber is approximately three times larger than its harmonic counterpart). To obtain more reliable results, the force constants involving the first mode have been neglected, and this mode has been treated at the harmonic level.[259] Furthermore, the two torsional modes have been treated at the HRAO level, and the results (labeled as reduced-dimensionality HRAO, RD-HRAO) are collected in Tab. 6.3, together with the results obtained using the extrapolation based on the Duschinsky transformation ***J*** ("Scal."). At variance with the ground electronic state, in this case the difference between the full-dimensional and the RD-HRAO models is more significant in this case, above 2 cm^{-1} for the majority of the modes. This means, in practice, that the coupling between

the LAMs and the other modes is larger than for the ground state, and therefore the difference between the reduced- and the full-dimensional systems is higher. This result reveals that there is a strong change in the anharmonic component of the PES between the two electronic states, and in this case the extrapolation technique based on the Duschinsky transformation is expected to work poorly.

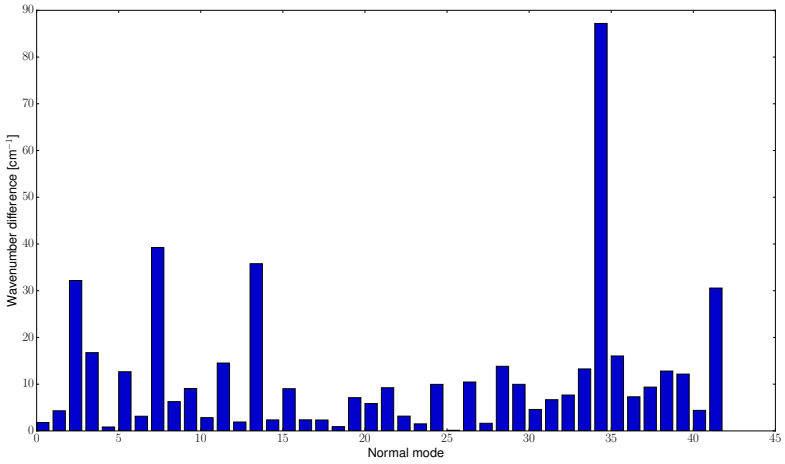

FIGURE 6.19: Graphical representation of the difference between the anharmonic wavenumbers computed at the VPT2 level and the ones determined using the extrapolation based on the Duschinsky transformation.

In fact, as shown in Fig. 6.19, the difference between the anharmonic frequencies computed using the two approaches is significant, above 20 cm^{-1} for several modes. It is noteworthy that the difference is large not only for the low-energy modes, but also for the higher ones, with the largest deviation occurring for mode 34. This further confirms that anharmonic effects are significantly different for the two electronic states, and the extrapolation technique is, in this case, inaccurate. Finally, the anharmonic frequencies computed using both approaches have been used to simulate the OPA spectrum of anisole at the AH|FC level, within the TI framework. The results of the simulation are reported in Fig. 6.20 and compared with experiment, from Ref. 406.

Inclusion of anharmonic effects for the S_1 state, either using the extrapolation approach or the VPT2 one, leads to an overall red-shift of the bands, with this shift being larger for the RD-VPT2 frequencies than for the extrapolated ones. This trend can be observed, for example, in the region between 800 and 1500 cm^{-1} (with respect to the 0-0 transition) of the spectrum, which is reported in the middle panel of Fig. 6.20 and is characterized by three intense bands (at about 550, 750 and 950 cm^{-1}, respectively). The position of those bands is overestimated at the harmonic level, and this inaccuracy is only partially corrected using the extrapolated anharmonic frequencies. Frequencies computed at the VPT2 level for both S_0 and S_1 electronic states provide even better band positions, resulting in an overall improvement in the quality of

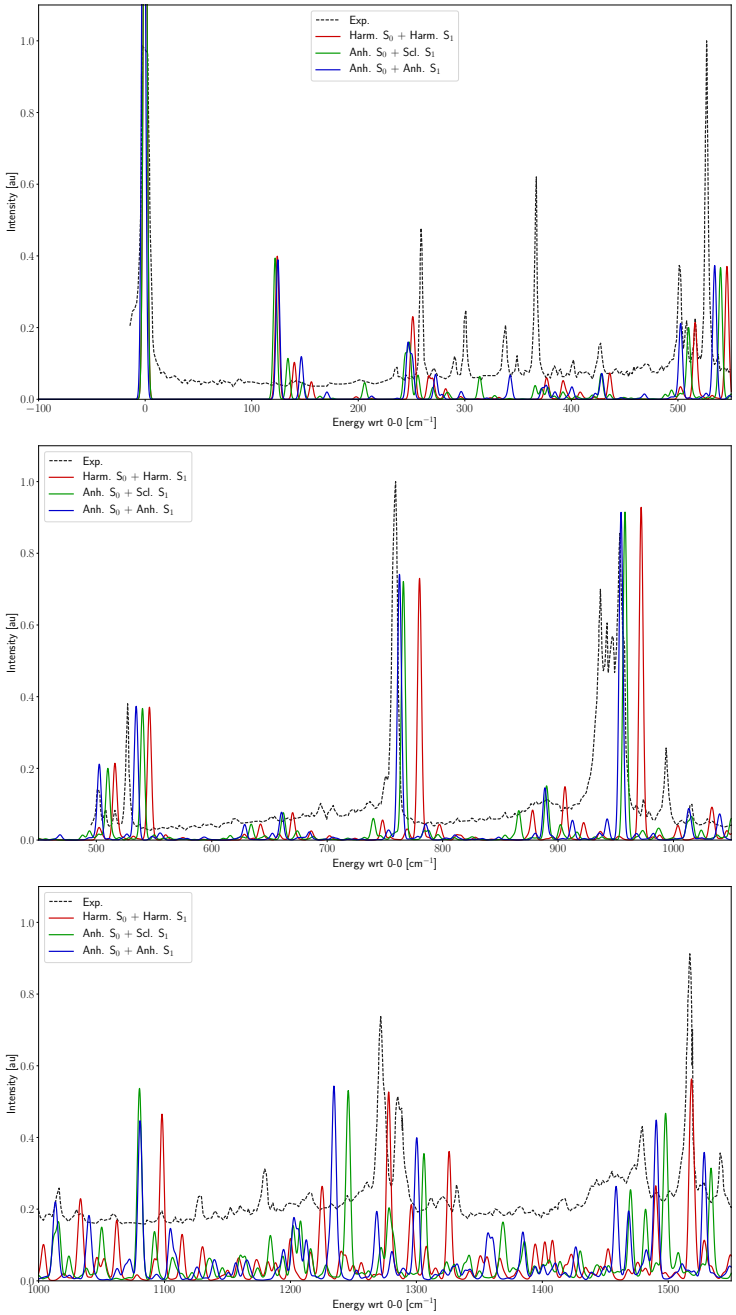

FIGURE 6.20: Comparison of the theoretical (TI AH|FC level) and experimental[406] OPA spectrum of anisole for the $S_1 \leftarrow S_0$ transition. Theoretical spectra have been computed using the harmonic frequencies for both electronic states (solid red line), the anharmonic frequencies for the S_0 state and the extrapolated ones for the S_1 state (solid, green line) and the anharmonic frequencies for both states (solid, blue line). Gaussian functions with HWHMs of 2 cm^{-1} have been used to reproduce the broadening effects.

the spectrum. A similar trend is detected also for other regions of the spectrum, even if in this case the agreement can be less satisfactory, especially in the 0-500 cm^{-1} range. However, this energy range contains large-amplitude motions, which could not be treated at a satisfactory level of theory in this study.

Chapter 7

High-resolution core electrons spectroscopy

In the previous chapters, which focused on the calculation of vibronic processes, only valence excitation were considered. However, the theoretical framework holds for any kind of electronic excitation, and thus can support also transitions involving core electrons. In more detail, the impact of vibrational effects on X-ray absorption (XAS) and photoabsorption (XPS) spectroscopies will be analyzed.
Regarding the former technique, we focus here on Near-Edge X-ray Absorption Spectroscopy (NEXAFS),[412] which corresponds to the energy range 30-40 eV higher than the energy of inner-shell core orbitals, in which transitions from excitations from these core orbitals to valence, virtual orbitals are present. The standard resolution of experimental NEXAFS spectra is usually much lower than for valence, OPA spectra. However, thanks to the increasing power of synchrotron light sources, the accuracy of experimental NEXAFS spectra is growing quickly and, in most cases, a full interpretation of those data requires theoretical calculation. From a qualitative point of view, it is well known that the intensity of a band in a NEXAFS spectrum is proportional to the p contribution of the final virtual orbital on the atom from which the core electron is excited. Such a simple selection rule can be used only for a qualitative interpretation of experimental spectra but, in order to characterize fully high-resolution NEXAFS spectra, *ab initio* simulations are in most cases required. In particular, as shown in the literature,[413,414] the inclusion of vibronic effects is mandatory to reproduce correctly the relative intensity of bands in a NEXAFS spectrum. Here, pyridine and two of its fluorinated derivatives (2-fluoropyridine and 2,6-difluoropyridine) will be used to test the reliability of DFT-based approaches to reproduce vibrationally-resolved NEXAFS spectra.
In the second part of the chapter, this analysis will be extended to XPS spectroscopy, in which the energy is higher than the binding energy of the core electrons, which are thus removed from the molecule. This is a significant difference with NEXAFS spectroscopy, where core electrons are excited towards a virtual, unoccupied orbital. The simulation of XPS spectra will be performed not using DFT-based approaches, but using Green Function-based (GF) methods. In these methods (also known as electron propagator theories, EPT) properties of cationic state, such as their ionization energies (IEs)

are computed from the one-particle Green function,[415] thus without explicitly computing any wavefunction for the cationic states. Since the exact one-particle Green function is not known, a perturbation expansion in powers of the correlation potential is usually employed. The zeroth-order approximation corresponds to IEs computed at the Koopmans' theorem level, but correlation effects can be included through higher-order approximations of the one-particle Green function. In more detail, the IEs are obtained as eigenvalues of a one-particle operator, where correlation effects are included in the so-called self-energy matrix, and the eigenfunctions are known as Dyson orbitals. The EPTs can be divided in two classes, the diagonal ones,[416,417,418] in which the Dyson orbitals are proportional to the HF canonical orbitals, and the more complete, non-diagonal approaches, where the full self-energy matrix is employed.[416,419] Diagonal approaches are usually well-suited to study valence ionizations, which are not associated to strong orbital relaxation effects. On the other hand, non-diagonal approaches are required to study ionization accompanied by strong relaxations, such as the ones involving core electrons. In the present thesis, the performance of different propagator approaches in the simulation of vibrationally-resolved NEXAFS spectra will be tested, with the aim of finding the best compromise between efficiency and accuracy. In addition to the standard EPT approaches, a new GF-based methods will be presented, referred to as the second-order approximation of the one-particle Green function with a transition operator reference (TOEP2). This method is particularly appealing to simulate XPS spectra of large-sized systems. In the transition operator method, grand-canonical Hartree-Fock theory, where spin-orbitals may have fractional occupation numbers, is used to obtain the reference orbitals, to express the one-particle Green function. With a grand-canonical reference, the relaxation effects is integrated in the definition of the orbitals, and therefore more accurate results are obtained even for low-order approximations of the one-particle Green function.[420,421] Core IEs obtained at the TOEP2 level are usually more accurate than those obtained using standard EPT, both diagonal and non-diagonal.[104,105] Here, we introduce a new implementation of the TOEP2 theory coupled with the maximum overlap method (MOM)[232,422] to increase its reliability.

7.1 DFT simulation of vibrationally-resolved NEXAFS spectra

7.1.1 Computational protocol

Let us begin with the simulation of the NEXAFS spectra. Before presenting the details of the vibronic calculations, let us briefly describe the electronic structure methods used in the calculations. Core excited states have been computed with two different electronic structure methods. The first one is the so-called transition potential DFT (TP-DFT).[423,424] In TP-DFT, the Kohn-Sham equations are solved by lowering the occupation number of the core orbitals involved in the excitation from 1 to 1/2. The excitation energies

are then obtained as differences between the energy of the virtual orbital to which the core electron is excited and the energy of the core orbital itself. We note here that TP-DFT can be considered as an improvement with respect to the standard Koopmans' approach, where excitation energies are computed simply as differences between the energies of the orbitals involved in the transition. Indeed, upon the excitation of a core-electron, a molecular system undergoes strong orbital relaxation effects (i.e. strong changes in the orbitals), which are not taken into account in a Koopman-based approach. The lowering of the occupation number allows to partially recover those effects. We note here that the formulation of TP-DFT approach for Hartree-Fock (HF) theory, also known as transition-operator self consistent field (TO-SCF), will be analyzed more in detail in the next section.
As an alternative to TP-DFT, calculations were performed also at the TD-DFT level, within the so-called restricted excitation window formulation of TD-DFT (description of the method can be found, for example, in Ref. 425). Within the REW-TD-DFT formalism, a set of active occupied molecular orbitals is defined, and only excitations starting from those orbitals are actually computed. This approximation strongly reduces the size of the electronic excitations space, and thus limits the computational cost of such simulations. We note that the calculation of core excitations within the standard formulation of TD-DFT is significantly higher, since core excitations corresponds to inter eigenvalues of the Casida equations, which cannot be reached with standard subspace iteration diagonalization techniques. We note here that more refined methods, based on the S&I algorithm presented in Chapter 3 for VDMRG, have been proposed,[226,227] in which the coupling between the core and the valence occupied orbitals is not neglected.
For the calculations on pyridine, 2-fluoropyridine and 2,6-difluoropyridine presented in the following, a different set of active orbitals has been chosen for each type of transition. For all computations involving excitations from the N atom, only the N1s orbital has been included in the active set. This approximation is based on the consideration that the nitrogen's 1s orbital is the lowest-energy one, and the energy gap with the closest occupied orbital (the C1s core orbitals) is 100 eV. For this reason, couplings with other core orbitals are expected to be small, and thus can be neglected. For the C1s spectra, all 1s orbitals of equivalent carbon atoms have been treated together. Therefore, for the calculations involving excitations from the ortho and meta C atoms of pyridine and 2,6-difluoropyridine (which belong to the C_{2v} point group), the active range included two molecular orbitals, corresponding to linear combinations of the 1s orbitals of the equivalent C atoms. For 2-fluoropyridine, which belongs to the C_s point group, each C1s orbital was included in a separate set of active orbitals. Several basis sets were tested for the calculations. The double-ζ SNSD basis set,[355] already employed in the previous chapters, has been used as reference. To improve the description of the core orbitals, which is a mandatory requirement for the study of core excitations, the EPR-III basis set,[426] which was built the accurate calculation of hyperfine constants, has been also employed. EPR-III is a triple-ζ basis set with diffuse functions and two d and one f polarization functions for the atoms from B

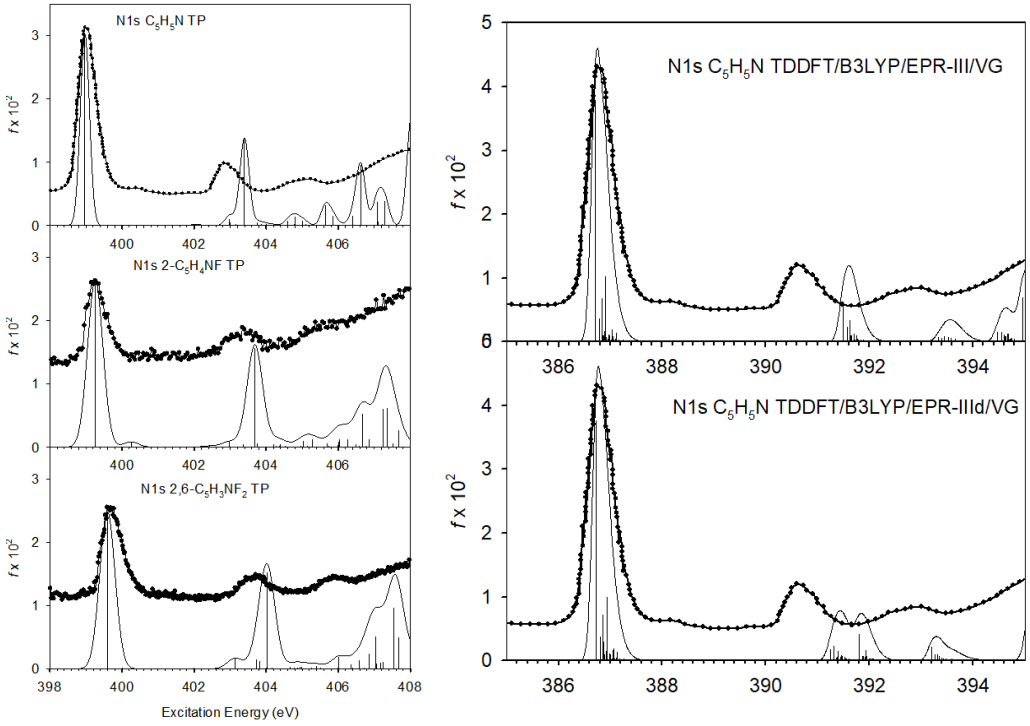

FIGURE 7.1: Comparison of the experimental N1s NEXAFS spectra of pyridine with theoretical results obtained by neglecting vibronic effects (left panel) and by including them at the VG|FC level (right panel). Pure electronic spectra are reported also for 2-fluoropyridine and 2,6-difluoropyridine in the left panel. Experimental energy scale has been shifted in order to match the first calculated N1s peak (taken from Ref. 427)

to F. Furthermore, an additional *s* function is present for these atoms. To improve also the description of the valence molecular orbitals, a third basis set has been employed, referred to as EPR-IIId, which is obtained by adding diffuse polarization functions (*p* on hydrogen and *d* on atoms from B to F taken from the aug-cc-pVTZ basis set) to the EPR-III set.

7.1.2 Results

To facilitate the presentation of the results, the N1s NEXAFS spectra will be discussed first, followed by the C1s one. In each case, standard electronic structure calculations will be shown first, followed by a description of the impact of vibronic effects, starting from pyridine as a model. The differences observed for the NEXAFS spectra of the fluorinated derivatives will be discussed next.

Let us begin our analysis from the spectrum obtained with excitations from the N1s orbital. In Fig. 7.1, the experimental N1s NEXAFS spectra of pyridine and of its two F-derivatives are compared with the spectra computed with the TP-DFT method. The experimental profiles have been shifted on the energy scale in order to match the most intense peak of the spectrum. We note

that the theoretical electronic spectra correctly describe the main features of the experiment, regarding both the energy separation among the peaks and the intensity pattern. The first and strongest peak of the pyridine spectrum (left panel of Fig. 7.1) is assigned to the N1s$\rightarrow 1\pi^\star$ transition, at about 399.0 eV. A very weak bump appears in the experiment at the higher energy side of the main peak, with an energy separation of about 1.4 eV, which is missing in the calculated spectrum. This small structure has been attributed to the N1s transition to the $2\pi^\star$ orbital, which is dipole-forbidden in C_{2v} symmetry but could gain intensity through vibronic coupling effects. A second band, corresponding to a N1s $\rightarrow 3\pi^\star$ transition, is present at about 404 eV, with a significantly lower intensity with respect to the first transition. The higher-energy region, around the ionization threshold, contains several weak transitions of mixed Rydberg and valence excitations, which are however not detected in the experimental data due to the limited resolution.
The N1s NEXAFS spectrum of pyridine has been computed also at the TD-DFT level, using different combinations of exchange-correlation functionals and basis sets. The results of this small benchmark, which are reported in Ref. 427 show that the best reproduction of the bandshape is obtained with the B3LYP hybrid functional in conjunction with the EPR-III basis set. For this reason, this setup has been chosen to perform also vibronic calculations. In the right panel of Fig. 7.1, the experimental N1s spectrum of pyridine is reported together with the vibronic spectrum calculated at the VG|FC level. The vibronic spectrum has been obtained by including in the simulation only the five excited states, with the highest oscillator strength in the energy range between 386 and 394 eV. A direct comparison of the left and right panels of Fig. 7.1 shows that the inclusion of vibronic effects does not change significantly the relative intensities of the most intense transitions. However, we note that, when vibronic effects are taken into account, the shape of the most intense band changes slightly, being more broadened towards higher energies. We note that this improves the agreement with the experimental results compared to the spectra obtained at the purely electronic level.
The corresponding spectra for 2-fluoropyridine and 2,6-difluoropyridine reproduce the pattern of the pyridine spectrum, with a slight increase of the excitation energies going from pyridine to 2,6-difluoropyridine, due to the withdrawal of valence electron charge induced by the fluorine atoms. However, this does not affect the relative energy separation between the excited states. Furthermore, we note that, in 2-fluoropyridine, the N1s $\rightarrow 2\pi^\star$ transition becomes dipole-allowed and appears in the calculated spectrum at about 400.2 eV.
Based on the results reported for the N1s spectra, the C1s NEXAFS spectra of the 3 pyridines derivatives were also simulated. The results obtained at the TP-DFT and TD-DFT levels without the inclusion of vibronic effects are reported in Fig. 7.2. The TP-DFT spectrum of pyridine is characterized by a sharp double-peak band around 286 eV followed by weaker features starting at about 288 eV and reaching a maximum near 290 eV. The theory reproduces only qualitatively the experiment, since the relative intensity of the double-peak feature at 286 eV (in the experiment the first peak is less

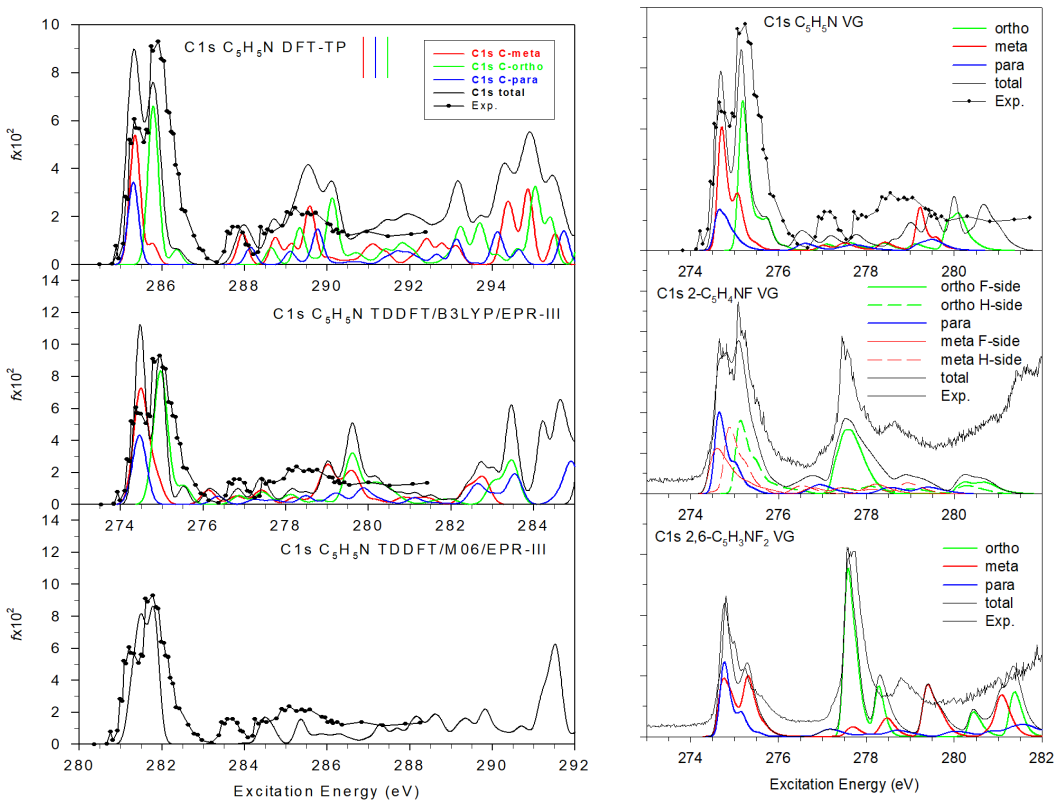

FIGURE 7.2: Comparison of the experimental N1s NEXAFS spectra of pyridine with theoretical results obtained at the pure electronic level (left panel) and at the VG|FC level (right panel) performing electronic structure calculations with TP-DFT (upper panel) and TD-DFT (middle and lower panel). Experimental energy scale has been shifted in order to match the first calculated C1s peak (figure taken from Ref. 427)

intense than the second one) is reversed in the calculation. The double peak-structure of this first band can be rationalized by taking into account that it is ascribed to the three different C1s $\rightarrow$ LUMO transitions. Thus, the relative excitation energies reflect the relative energy of the core orbitals. The ortho C1s is the closest to the electronegative N atom, which depletes electron density and thus induces a larger excitation energy by approximately 0.5 eV, in good agreement with experiment. The higher-energy region, above 290 eV, is quite complicated, since it encompasses transitions to many final virtual orbitals, including $\sigma^\star$(C-H) antibonding orbitals as well as diffuse Rydberg states. Although this spectral region is extremely congested, preventing a detailed assignment of all the calculated spectral features, the calculation is in good agreement with the experiment. Thus, TP-DFT reproduces satisfactorily the relative excitation energies, but not their intensities, in particular for the first band at 286 eV.

To check if the error in the intensity is associated to an inaccuracy of the electronic structure calculation or to the neglect of vibronic effects, spectra were simulated also at the TD-DFT level, with the B3LYP and M06-2X exchange-correlation functionals, in conjunction with the EPR-III basis set. The results of the simulation, which are reported in the left panel of Fig. 7.2, show that the reversed intensity distribution for the first double peak is coherent with the one obtained at the TP-DFT level. This finding suggests that the disagreement with the experiment should not be ascribed to problems with the electronic structure but rather to the absence of vibrational contributions.

The vibronic NEXAFS spectrum calculated at the VG|FC level for C1s excitations in pyridine in the energy range 274-281 eV is compared with the experimental results in the right panel of Fig. 7.2. The 29 excited states corresponding to the largest oscillator strength (11 associated to excitations from the ortho carbons, 11 from the meta ones and 7 from the para) have been included in the computations. The results shown that the inclusion of vibronic effects corrects the inaccuracy in the reproduction of the double-peak structure in the low-energy range of the spectrum. As already remarked above, this pattern is poorly reproduced in the purely electronic spectrum, since the intensity of the first peak is expected to be larger than that of the second one. The inclusion of vibronic effects modifies the relative intensities of the two peaks, and a better match with the experimental results is reached. To understand the origin behind this effect, the vibronic NEXAFS spectra for excitations from the C1s orbital of each non-equivalent C atom to the LUMO ($1\pi^\star$) virtual orbital are shown separately in the left panel of Fig. 7.3. Even if the vibronic band-shapes are nearly equivalent for the excitations starting from the C1s orbitals of the ortho and meta atoms, a larger number of intense vibronic transition are present for the spectrum associated to the para C1s $\rightarrow$ LUMO excitation. As a consequence, the FC factor associated to the 0-0 transition is less intense than for the other C1s orbitals, and the vibronic broadening is larger. Since, as already remarked above, the band associated to the para C1s $\rightarrow$ LUMO transition lies in the low-energy region of the double peak signal, the relative intensity of the first sub-peak decreases, giving a better match with the experimental results. To conclude, it is worth noting

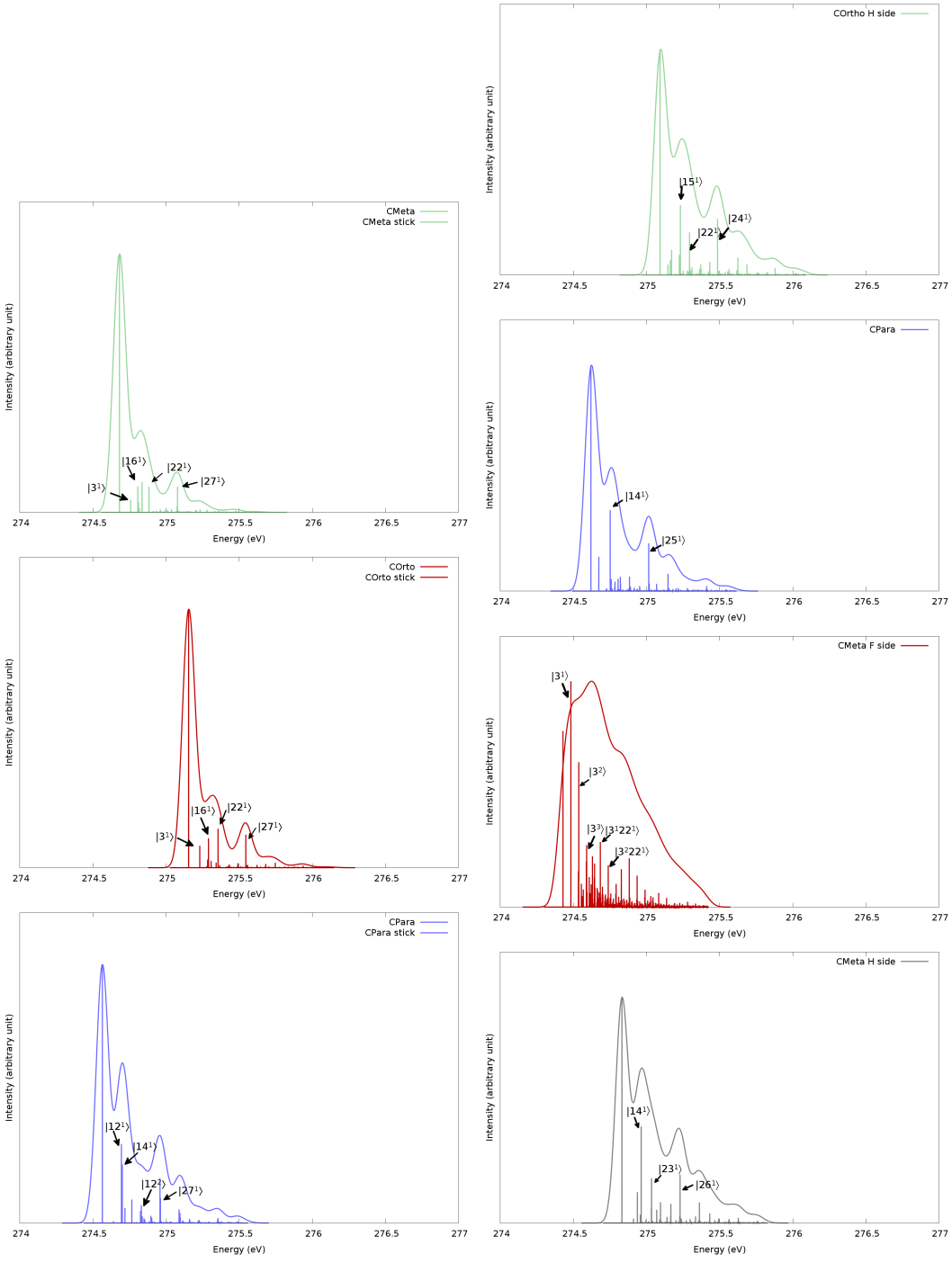

FIGURE 7.3: Vibronic NEXAFS spectra for the excitations of C1s core orbitals of pyridine (left panel) and 2-fluoropyridine (right panel). The single contribution of each C1s orbital are reported separately. (Figure taken from Ref. 427)

that the active normal modes are associated to in-plane deformations of the ring, since the extrapolated equilibrium geometry of the excited states associated to bright transitions is, in every case, planar, and therefore vibronic transitions involving out-of-plane deformations are inactive by symmetry.
Focusing now on the fluorinated derivatives of pyridine, the C1s NEXAFS vibronic spectrum of 2-fluoropyridine are reported in the right panels of Fig. 7.2, together with the shifted experimental spectrum. In this case, the 27 excited states with the largest value of the oscillator strengths have been included in the simulation. Like for pyridine, the low-energy region of the experimental spectrum is characterized by a double-peak structure, where the first peak is less intense than the second one. As shown in Fig. 7.2, this spectral pattern is well reproduced by including vibronic effects. The contribution of each C1s core orbital to the overall vibronic NEXAFS spectrum are reported separately in the right panel of Fig. 7.3. The carbon directly bonded to the fluorine atom gives a signal at significantly higher energy, due to polarization effects, and has not been included in Fig. 7.3. Comparison of those spectra shows that the vibronic band-shape is similar for three of them, except for the excitation from the C meta atom lying on the same side as the F atom, giving a significantly broader spectrum. Similarly to pyridine, only few vibronic transitions (whose assignment is reported in the spectrum) have a noticeable intensity for the first three C1s orbitals, thus leading to a limited spectral broadening. On the other hand, for the fourth excitation, several overtones and combination bands have non-negligible intensities, and therefore the spectrum is significantly broader. Since the C1s $\rightarrow$ LUMO transition starting from the C meta atom lying on the F side contributes to the low-energy sub-peak of the double-peak structure present in the experimental spectrum, the inclusion of vibronic effects decreases the relative intensity of this peak. As a result, a better match with the experimental data is reached.
To conclude, the NEXAFS vibronic spectrum for 2,6-difluoropyridine simulated at the VG|FC level is reported in the lower panels of Fig. 7.2, where the 34 excited state with the largest oscillator strengths have been included. For this system, the inclusion of vibronic effects does not affect significantly the simulated band-shape. In fact, the shapes of the two most intense peaks of the experimental spectrum (at about 275 and 278 eV) are nearly unchanged with respect to their VE counterparts, even if the intensity of the first band decreases slightly. A more relevant difference is present in the energy region above 279 eV, where the inclusion of vibronic effects leads to an overall decrease of the intensity for most bands, giving a better matching with the experimental results.

7.2 Efficient calculation of XAS spectra: the TOEP2 approach

The analysis reported in the previous chapter is now extended to X-ray photoelectron spectroscopy (XPS). As shown by the examples of the previous section, DFT-based approaches provide an accurate reproduction of relative

transition energies for core-electron excitations. However, large inaccuracies are present in their absolute value, with deviations of up to 10 eV with respect to the experimental data. More importantly, this error is highly dependent on the DFT exchange-correlation functional. In order to get more accurate results, more suitable electronic structure approaches are needed. As already remarked above, Green function (GF)-based techniques will be used here to simulate photoelectron spectra. The most appealing feature of GF-based algorithms is that ionization potentials (IP) are computed as pole of the single-particle GF (also known as propagator),[103,415] thus without computing explicitly the wavefunction of the cationic state. Since the exact one-particle GF is not known, it is usually approximated by mean of perturbation theory. Depending on the level of approximation of the propagator, different GF approaches are obtained, which are usually divided in two main classes, diagonal and non-diagonal.[103] Without going into the details of the theory, which will be discussed below, here it is sufficient for now to mention that diagonal approaches neglect orbital-relaxation effects (*i.e.* change of the occupied orbitals upon ionization),[416,418,428] whereas this effects are properly included in non-diagonal approaches,[416,419] however at the price of an higher computational cost. For valence ionizations, accurate results are obtained already with diagonal approaches in most cases. However, for core ionizations, which are the target of this chapter, orbital relaxation effects are usually large, and non-diagonal approaches are in most cases needed to reproduce reliably experimental data. However, the high computational cost of non-diagonal approaches makes them applicable, in most cases, only to small-size systems. With the aim of targeting larger molecules, of several dozens of atoms, a new GF-based approach is presented here, referred to as second-order transition-operator electron propagator (TOEP2),[104,105] which uses orbitals arising from a gran-canonical HF calculation as a reference. As is proven with several test cases, the use of a grand-canonical HF reference provides accurate results even for low-order perturbation theory, thus strongly reducing the computational costs.[104,105] Here, the reliability of TOEP2 will be checked not only in the reproduction of core ionization energies, but also for full XPS vibronic spectra.

7.2.1 Electron propagator methods

Before introducing the TOEP2 theory, it is useful to recall the main theoretical aspects of GF-based approaches. As already remarked above, in those methods, ionization energies are determined as poles of the electron propagator, referred to in the following as $G(E)$, which is usually expressed in a basis of one-particle functions ϕ. The matrix elements $G(E)_{pq}$ between two basis functions ϕ_p and ϕ_q can be expressed as,[103]

$$G_{pq}(E) = \lim_{\eta \to 0} \left[\sum_r \frac{\langle \Phi_0^N \mid \hat{a}_p^\dagger \mid \Phi_r^{N-1} \rangle \langle \Phi_r^{N-1} \mid \hat{a}_q \mid \Phi_0^N \rangle}{E - E_0^N + E_r^{N-1} - i\eta} + \sum_s \frac{\langle \Phi_0^N \mid \hat{a}_q \mid \Phi_s^{N+1} \rangle \langle \Phi_s^{N+1} \mid \hat{a}_p^\dagger \mid \Phi_0^N \rangle}{E + E_0^N - E_s^{N+1} + i\eta} \right] \tag{7.1}$$

where Φ_r^{N-1} and Φ_s^{N+1} are "N-1" and "N+1"-electron states with energy E_r^{N-1} and E_s^{N+1}, respectively. $|\, \Phi_0^N \,\rangle$ is the exact electronic ground-state wavefunction, and η is a positive, infinitesimal quantity, which is used to avoid singularities in the definition of $G(E)$. Finally, $\hat{a}_p^\dagger$ and $\hat{a}_q$ are fermionic second-quantization creation and annihilation operators, respectively. Eq. 7.1 shows that $G(E)$ has poles for $E = E_0^N - E_r^{N-1} + i\eta$ and $E = E_r^{N+1} - E_0^N + i\eta$, *i.e.* when E approaches the energy of an ionization or of an electron attachment. To compute the poles of $G(E)$, it is useful to express the one-particle Green function in the vector space composed by all the combinations of second-quantization operators changing the number of electrons by $\pm$ 1. A consistent definition of the scalar product between two elements $\boldsymbol{a}$ and $\boldsymbol{a}'$ of this vector space, and of the action of the Hamiltonian superoperator $\mathcal{H}$ on $\boldsymbol{a}$ is obtained using the following rules:[429]

$$\begin{aligned} (\boldsymbol{a}|\boldsymbol{a}') &= \langle \Phi_0^N \mid \left[\boldsymbol{a}^\dagger, \boldsymbol{a}'\right]_+ \mid \Phi_0^N \rangle \\ \mathcal{H}\boldsymbol{a} &= [\boldsymbol{a}, H] \end{aligned} \tag{7.2}$$

where the square brakets represent the commutator, whereas the square brackets with the $+$ subscript represent the anticommutator. From Eq. 7.2, it is possible to express the inverse of the electron-propagator matrix as,[103]

$$\boldsymbol{G}^{-1}(E) = E\boldsymbol{I} - \boldsymbol{F} - \boldsymbol{\Sigma}(E) \tag{7.3}$$

where $\boldsymbol{F}$ is the matrix representation of the Fock operator. $\boldsymbol{\Sigma}(E)$ is the so-called self-energy matrix, and contains the corrections to $\boldsymbol{G}(E)$ due to correlation effects. When E approaches the energy of a pole, $\det\left(\boldsymbol{G}^{-1}(E)\right) = 0$, thus the poles are the eigenvalues of the following generalized one-electron equation,

$$\left[\boldsymbol{F} + \boldsymbol{\Sigma}(E)\right] \boldsymbol{C}^{\mathrm{EP}} = \boldsymbol{C}^{\mathrm{EP}} E \tag{7.4}$$

where $\boldsymbol{C}^{\mathrm{EP}}$ is the transformation matrix from the atomic basis to the so-called Dyson orbitals ψ_p^{Dyson}. The Dyson orbitals are, in general, not normalized, and their norm π_p is defined as the pole strength. As will be discussed in more detail in the following section, the pole strength determines the intensities of peaks in a photoelectron spectrum. The relation between π_p and $\boldsymbol{C}^{\mathrm{EP}}$ is the following,[430]

$${\pi_p}^{-1} = 1 - \left(\{\boldsymbol{C}^{\mathrm{EP}}\}^\dagger \frac{d\boldsymbol{\Sigma}}{dE} \boldsymbol{C}^{\mathrm{EP}} \right)_{pp} \tag{7.5}$$

Eq. 7.4 must be solved iteratively, since E appears on both sides of the equation. Different expressions for $\mathbf{\Sigma}(E)$ are obtained, depending on the perturbation order used to approximate the ground-state wavefunction. Within the diagonal approaches, only the diagonal elements of $\mathbf{\Sigma}(E)$ are kept. This approximation simplifies the solution of Eq. 7.4, since the $\boldsymbol{F} + \mathbf{\Sigma}(E)$ matrix is diagonal in the canonical molecular orbitals basis, thus the Dyson orbitals are proportional to the canonical ones. The lowest-order non-zero contribution to $\mathbf{\Sigma}$ is obtained at the second-order (usually referred to as second-order electron propagator, EP2), and can be expressed as,

$$\omega_k = \epsilon_k + \sum_a \sum_{i<j} \frac{|\langle ka||ij\rangle|^2}{\omega_k + \epsilon_a - \epsilon_i - \epsilon_j} + \sum_i \sum_{a<b} \frac{|\langle ki||ab\rangle|^2}{\omega_k + \epsilon_i - \epsilon_a - \epsilon_b} \tag{7.6}$$

where ω_k is the energy of the pole, ϵ_k are the orbital energies and $\langle ij||kl\rangle$ are two-electron integrals. Furthermore, i, j, k label occupied orbitals and a, b virtual ones. The second term is usually referred to as the two holes-one particle (2h-1p) term and the third one as two particle-one hole (2p-1h) term. The arithmetic scaling of Eq. 7.6 is governed by the evaluation of the second term, which scales as OV^2, where O is the number of occupied orbitals and V is the number of the virtual ones. Beyond its efficiency, the EP2 approach usually underestimates experimental ionization energies. Third-order terms can be included in the so-called third-order electron propagator (EP3) approach, and in this case the experimental results are usually overestimated.[430] More accurate results are obtained within the so-called outer valence Green function (OVGF) approach,[416,428] where higher-order terms are included in an approximate way. Even if the diagonal approximation is retained, the main limitation of the OVGF approach is the arithmetic scaling as OV^4. More efficient approaches, such as the partial third order approximation (P3)[417] and the renormalized partial third-order approximation (P3+)[418] have been devised, and will be used in the following.

As already remarked above, diagonal approaches are well-suited if orbital relaxation effects are not relevant, and their accuracy decreases as the differences between canonical and Dyson orbitals increase. To obtain more accurate results, the full self-energy matrix $\mathbf{\Sigma}$ is needed to compute the poles from Eq. 7.4, using non-diagonal approaches. Among them, here the non-diagonal, renormalized second-order approach (NR2)[419] and the third-order algebraic diagrammatic construction (ADC(3))[416] will be employed. It is noteworthy that, besides the generation of the full self-energy matrix (which scales as O^2V^3 for NR2 and as OV^4 for ADC(3)), the computational cost of non-diagonal approaches increases also because of the diagonalization step. The range of applicability of non-diagonal approaches is strongly limited by their computational costs, and therefore, to tackle also larger-size systems, more efficient approaches must be developed. The main limitation of the standard propagator approaches presented above in describing ionizations accompanied by significant relaxation effects is the large difference between

the canonical HF and the Dyson orbitals. For this reason high-order approximations of the propagator must be used to obtain reliable results.[431] To get results of the same quality using lower-order approximations of the one-body Green function, a different set of reference orbitals must be used.
In this respect, molecular orbitals obtained by solving grand-canonical HF equations,[432,433] where fractional occupation numbers are used, are particularly appealing for the simulation of ionization processes. In grand-canonical Hartree-Fock theory, the one-particle density operator $\boldsymbol{\rho}$ is defined as,[434]

$$\boldsymbol{\rho} = \prod_i \left[1 - \langle \boldsymbol{n}_i \rangle + \boldsymbol{n}_i \left(2\langle \boldsymbol{n}_i \rangle - 1\right)\right] \tag{7.7}$$

where $\boldsymbol{n}_i$ is the occupation number operator for the i-th orbital. Even if the occupation numbers are usually determined under equilibrium conditions by statistical thermodynamics, Eq. 7.7 is valid also for general ensembles, which do not necessarily correspond to any equilibrium distribution. Therefore, the population can be tuned to obtain grand-canonical orbitals, which are closer to those of the ionic state, to obtain a better reference for a perturbative expansion of the propagator. Once the distribution n_i is set, the elements of the Fock matrix $\boldsymbol{F}$ and the density matrix $\boldsymbol{P}$ in the atomic basis are given by,[105,435]

$$P_{\mu\nu} = \sum_{i=1}^{N_{\text{occ}}} n_i C_{\mu i} C_{\nu i} \tag{7.8}$$

$$F_{\mu\nu} = h_{\mu\nu} + \sum_{i=1}^{N_{\text{occ}}} \langle \mu i || \nu i \rangle n_i \tag{7.9}$$

where μ and ν label two atomic basis functions, while the sum over i includes the N_{occ} occupied spin-orbitals. $\boldsymbol{C}$ is the matrix with the coefficients of the molecular orbitals in terms of the basis set and $\boldsymbol{n}$ is the vector of the occupation numbers. In the following, the transition operator (TO) approach, which is the counterpart of the TS-DFT approach for the HF theory, will be employed. As for TS-DFT, also in TO calculations the occupation numbers are 1 for all the occupied orbitals, with the exception of one orbitals, usually the one involved in the ionization, for which it is set to 0.5. By lowering the occupation number of the orbital involved in the transition, the resulting orbitals are better-suited to perform propagator calculations.[104,105]
The orbital energies obtained from a TO computation provide already a qualitative estimate of the ionization energies, which are significantly more reliable than the ones obtained by direct application of the Koopmans' theorem level.[436] However, it has been proven that, in most cases, the accuracy of those results is comparable to that of standard, non-diagonal approaches, which is still not satisfactory (with errors above 1 eV) for core ionizations.[104,105] To further improve the accuracy of the results, perturbative corrections to the one-particle Green function must be computed based on the spin-orbitals of the TO-SCF calculation. This is done, in practice, by replacing the pure reference state, $|\,\Psi_0^N\,\rangle$, of Eq. 7.1 with a reference ensemble

defined by $|\,\Phi^{\mathrm{GC}}\,\rangle$ defined as,

$$|\,\Phi^{\mathrm{GC}}\,\rangle = \frac{\left(|\,\Phi_0^N\,\rangle + |\,\Phi_f^{N-1}\,\rangle\right)}{\sqrt{2}} \tag{7.10}$$

where $|\,\Phi_f^{N-1}\,\rangle$ is a core-ionized state. Starting from $|\,\Phi^{\mathrm{GC}}\,\rangle$, low-order, self-energy improvements to TO orbital energies can be obtained, in a way similar to standard, GF-based theories[104,420,421] by employing grand-canonical density operators and generalizing the usual self-energy formulas through the introduction of spin-orbital occupation numbers.[437,438] In this manner, the electron propagator may adapted to the calculation of the IE of a specific orbital in which strong orbital relaxation are relevant, but avoiding the evaluation of otherwise necessary self-energy corrections of high-order. As for standard, canonical orbitals, the first non-zero contribution for grand-canonical orbitals still arises from the second-order term. The expression for the pole energy ω_k using the diagonal, second-order correction for general occupation numbers n_r, is the following:[104,420,421]

$$\omega_k = \epsilon_k + \sum_{r,s<t} \frac{|\langle kr||st\rangle|^2}{\omega_k + \epsilon_r - \epsilon_s - \epsilon_t} \cdot \left[n_r\left(1 - n_s - n_t\right) + n_s n_t\right] \tag{7.11}$$

where ϵ_n are the grand-canonical orbital energies. The sum over r, s, t includes both the (possibly fractionally) occupied and the virtual orbitals. If standard HF orbitals are employed, and therefore the occupation number is 1 for the occupied orbitals and 0 for the virtual ones, the only non-null terms are obtained for $n_r = 0, n_s = n_t = 1$ and $n_r = 1, n_s = n_t = 0$, which corresponds to the standard second-order, diagonal approximation of the propagator given in Eq. 7.6. On the other hand, if the TO method is used, and therefore, besides the occupied and virtual orbitals, an orbital k has a fractional occupation number n_k, Eq. 7.11 can be expressed as,

$$\begin{aligned}\omega_k =& \epsilon_k + \sum_a \sum_{i<j} \frac{|\langle ka||ij\rangle|^2}{\omega_k + \epsilon_a - \epsilon_i - \epsilon_j} n_i n_j + \sum_i \sum_{a<b} \frac{|\langle ki||ab\rangle|^2}{\omega_k + \epsilon_i - \epsilon_a - \epsilon_b} \\ &+ \sum_i \sum_a \frac{|\langle ki||ka\rangle|^2}{\omega_k + \epsilon_i - \epsilon_a - \epsilon_k}(1 - n_k)\end{aligned} \tag{7.12}$$

In this case, the sum over i and j includes also the fractionally-occupied orbital k. Eq. 7.12 differs from the standard expression of the EP2 propagator given in Eq. 7.6 in two respects. First of all, the terms in the sum of the 2h-1p term are scaled by the occupation numbers. Furthermore, a third, additional term is present, involving the bielectronic integrals $\langle ki||ka\rangle$. As for all the diagonal approaches, the pole ω_k appears on both sides of Eq. 7.12, which therefore must be solved iteratively by taking as a first guess for ω_k the orbital energy obtained from the TO calculation.

In practice, SCF calculations with fractional occupation numbers raise additional issues with respect to the standard case. Indeed, during the SCF procedure, the energy order of the orbitals may change, and when such change occurs, the components of the vector $\boldsymbol{n}$ must be permuted in a consistent way. This can be done using the maximum-overlap criterion (MOM).[104,232,422] Let $\boldsymbol{C}^{(m)}$ and $\boldsymbol{C}^{(m+1)}$ be the matrix coefficient of the molecular orbitals in terms of the basis set for two successive SCF cycles (m-th and "m+1"-th). An overlap matrix $\boldsymbol{O}$ can be built as follows:

$$\boldsymbol{O} = \{\boldsymbol{C}^{(m+1)}\}^T \boldsymbol{S} \boldsymbol{C}^{(m)} \tag{7.13}$$

where $\boldsymbol{S}$ is the overlap matrix of the atomic basis functions. For each occupied orbital k of the m-th SCF cycle, the k-th row of the $\boldsymbol{O}$ matrix ($\boldsymbol{O}_k$) is considered and the squared elements of its components are computed. The maximum of those values determines the index h of molecular orbital of the "m+1"-th cycle most similar to the k-th one of the m-th cycle. Thus, the occupation number vector at the $m+1$-th cycle ($\boldsymbol{n}^{(m+1)}$) is built from the previous one ($\boldsymbol{n}^{(m)}$) setting $n_h^{(m+1)} = n_k^{(m)}$. Even if for valence ionization of small- and medium-size systems the order of the molecular orbitals remains usually unchanged during the SCF cycles, this is not the case for core ionizations. The energy difference between the core orbitals centered on atoms of the same type is usually small, and therefore changes in the orbital order are frequent.

7.2.2 Simulation of vibrationally-resolved XPS spectra

To use, in practice, the approaches described above to simulate vibrationally-resolved XPS spectra, the theoretical framework presented in Chapter 4 must be generalized to support also photoelectron spectroscopy. In this case, the electronic states involved in the transition are the ground electronic state of the neutral molecule and a cationic state. For the sake of coherence with the notation employed in Chapter 4, the former will be labeled with a single overbar, and the latter with a double overbar. The only quantity which must be changed with respect to the sum-over-states expression given in Eq. 4.56 to simulate photoelectron spectra is the electronic coupling, which is given by the transition dipole moment for standard, OPA spectroscopy, but has a different expression for photoelectron spectroscopy. The electronic wavefunction of the cationic state can be approximated as $\overline{\overline{\Psi}} = \overline{\overline{\Psi}}^{N_{\text{ele}}-1} \otimes \overline{\overline{\Psi}}_c$, where $\overline{\overline{\Psi}}^{N_{\text{ele}}-1}$ is the electronic wavefunction of the $N_{\text{ele}}-1$ electrons of the cation, whereas $\overline{\overline{\Psi}}_c$ is the unbound wavefunction of the electron, which has been ionized. As discussed in Refs. 102 and 439, this factorization can be used to express the electronic coupling as follows:

$$k_i^e = K \cdot \langle\, \overline{\psi}_i^{\text{Dyson}} \mid \boldsymbol{\mu} \mid \overline{\overline{\Psi}}_c \,\rangle \tag{7.14}$$

where i labels the orbital, from which the electron is ionized, and $\mid \overline{\psi}_i^{\text{Dyson}} \rangle$ is the Dyson orbital associated to this ionization. As already recalled above, $\mid \overline{\psi}_i^{\text{Dyson}} \rangle$ is not normalized, and its squared norm P_i^2 is given by the squared

value of the pole strength π_i. Thus, $|\,\overline{\psi}_i^{\text{Dyson}}\,\rangle$ can be expressed as $P_i \cdot |\,\overline{\phi}'_i\,\rangle$, where $P_i = \sqrt{\pi_i}$ and $|\,\overline{\phi}'_i\,\rangle$ is the normalized Dyson orbital. In principle, both $\langle\,\overline{\phi}'_i \mid \boldsymbol{\mu} \mid \overline{\overline{\Psi}}_c\,\rangle$ and P_i change with the nuclear coordinates. The nuclear dependence of the first term is usually neglected and the electric transition dipole moment is assumed to be the same for all transitions.[103] Under these approximations, the sum-over-states expression given in Eq. 4.56 can be generalized to photoelectron spectroscopy as,

$$\sigma(\omega) = \alpha\omega \sum_{i,f} \rho_i \{P_i^{\text{eq}}\}^2 \left|\langle\,\overline{\psi}_i \mid \overline{\overline{\psi}}_f\,\rangle\right|^2 \delta(E_{\text{ad}} + \breve{\overline{\overline{E}}}_f - \breve{\overline{E}}_i - \omega_0) \tag{7.15}$$

where σ is the photoionization cross section and α is a fixed proportionality constant. In the following, all the theoretical spectra will be reported using relative unities, and therefore α will be set to match the experimental results. It should be noted that considering the pole strength as a constant is equivalent to a zeroth-order Taylor expansion with respect to the nuclear coordinates, which is equivalent to the FC approximation of the transition dipole moment. In order to check the reliability of this approximation, also first order terms can be included in the treatment, following the same strategy used to support HT effects.[280]

7.2.3 TOEP2: selected applications

FIGURE 7.4: Graphical representation of the equilibrium geometry of ethanol for the two stable conformers in the S_0 state, computed at the B3LYP/SNSD level. The structure reported on the left will be labelled as (a), the one reported on the right one will be labelled as (b).

The first case used to test the reliability of TOEP2 is ethanol (EtOH), for which the XPS spectrum in the energy range between 290 and 295 eV will be simulated. The experimental, high-resolution XPS spectrum of EtOH has been recently recorded using synchrotron light,[440,441] and is characterized by the presence of two main bands, associated to the ionization of the electrons of the two C1s core orbitals. The broadening of the two bands is not equivalent, and several vibronic transitions can be singled out in the experimental spectrum. For this reason, ethanol is a suitable test-case to check the reliability of the approaches described above in the simulation of XPS spectra. Furthermore, thanks to its rather small size, both diagonal and non-diagonal approaches can be employed to compute IEs, gradients and pole strengths

(*i.e.* the quantities needed to simulate the vibronic XPS spectrum) with a limited computational cost.

		C_α	C_β	$\Delta(C_\alpha\text{-}C_\beta)$
OVGF	cc-pVTZ	294.67	293.04	1.63
	aug-cc-pVTZ	294.76	293.11	1.65
P3	cc-pVTZ	293.98	292.19	1.69
	aug-cc-pVTZ	294.08	292.38	1.70
NR2	cc-pVTZ	293.40	291.76	1.64
	aug-cc-pVTZ	293.42	291.79	1.66
ADC(3)	cc-pVTZ	294.71	293.16	1.55
	aug-cc-pVTZ	294.80	293.22	1.58
TOEP2	cc-pVTZ	292.68	291.03	1.65
	aug-cc-pVTZ	292.70	291.04	1.66
	EPR-IIId	292.61	290.06	1.65
Exp.[440]		292.01	290.04	1.70

TABLE 7.1: Vertical ionization energies (in eV) for the C1s orbitals of ethanol computed using different combinations of propagator methods and basis sets.

In Tab. 7.1, the ionization potentials for the C1s core orbitals of ethanol, computed using different combinations of propagator approaches and basis sets, are reported. Two non-equivalent equilibrium structures (referred to as (a) and (b) in the following) are present in the ground state, whose structures are reported in Fig. 7.4. The main difference between the two structures is the position of the H atom bonded to the O atom, which is closer to the methyl group in the (b) conformer than in the (a) one. Since the energy separation between the two minima is comparable to the vibrational energies,[440] the IEs have been computed for each conformer. As already mentioned in the theoretical section, relaxation effects may be relevant for core ionizations and, for this reason, the diagonal approximation of the one-electron Green function is usually insufficient, and non-diagonal approaches are needed to simulate reliably the IEs. This is confirmed by the results reported in Tab. 7.1, since both diagonal methods OVGF and P3 overestimate the IEs of both C1s orbitals by 1.5-2 eV on average, independently on the basis set. The accuracy increases significantly when employing the TOEP2 approach, as shown in the last three rows of Tab. 7.1, with the difference between the theoretical results and the experimental data decreasing below 0.7 eV for both C1s orbitals. It is worth noting that the relative value of the ionization potentials for the two C 1s orbitals, which was already satisfactory for OVGF and P3, remains accurate at the TOEP2 level. In order to further check the reliability of the TOEP2 results, the ionization potentials have been computed also with the EPR-IIId basis set already used to compute vibrationally-resolved NEXAFS spectra in the previous section. With this basis set, the difference between theoretical

and computed ionization potentials decreases further by 0.1 eV, whereas the difference between the two ionization potentials is nearly unchanged. Ionization energies have been computed also with the non-diagonal approaches NR2 and ADC(3), and their results are reported in Tab. 7.1 too. By employing the NR2 approach, the difference with the experimental data decreases with respect to the OVGF and P3 results, but the discrepancy is still above 1 eV, therefore larger than for TOEP2. With the more refined ADC(3) approach, the agreement between the theoretical and the experimental data worsens, becoming even poorer than the one obtained using the diagonal approaches described above. This is probably due to an incomplete description of the orbital relaxation effects even if non-diagonal, third-order terms are included at the ADC(3) level, and higher order terms should be included to obtain more reliable results. Therefore, for this test case, the TOEP2 approach is the most reliable propagator method in the reproduction of both the absolute and the relative value of the ionization energies for the C1s core orbitals.

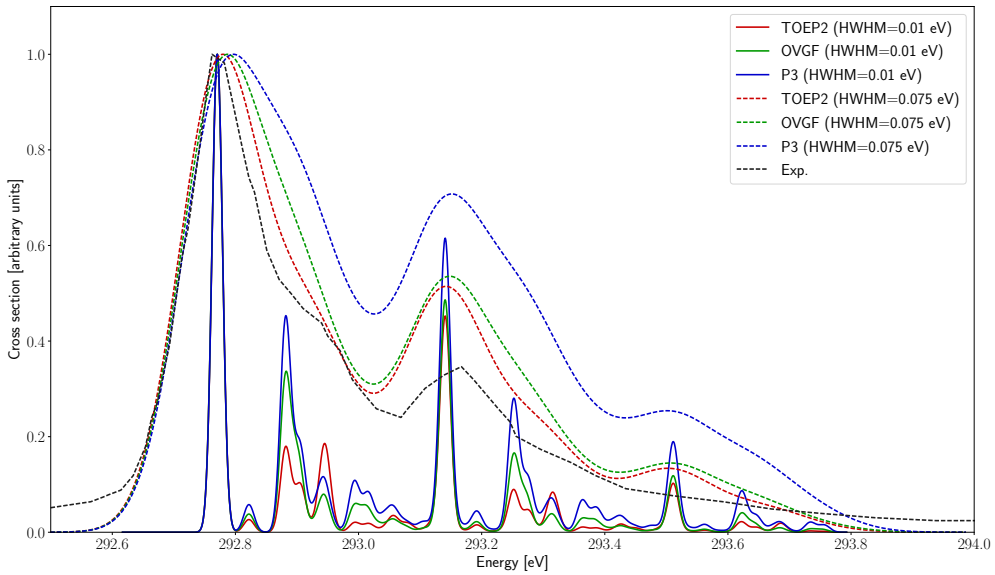

FIGURE 7.5: XPS spectrum for the ionization of the C_α1s electron of ethanol computed at the VG|FC level using different diagonal propagator methods (TOEP2 in red, OVGF in green, P3 in blue) using Gaussian functions with HWHMs of 0.01 eV (solid lines) and 0.075 eV (dashed lines) to simulate the broadening effects.

In order to simulate the XPS spectrum of ethanol at the VG level, the different propagator methods have been employed to compute the gradient of the PES of the cationic state at the equilibrium geometry of the neutral one, using in all cases the cc-pVTZ basis set. As a first step, the XPS spectrum for the ionization of the C_α (*i.e.* the C atom directly bonded to the O atom) 1s orbital has been computed. For the sake of simplicity, all computations have been performed for the (a) conformer, since, as will be discussed in the following, the results for the (b) conformer are equivalent. The results obtained using the diagonal approaches are reported in Fig. 7.5, whereas the ones obtained with

the non-diagonal ones are given in Fig. 7.6. To facilitate the comparison of the bandshapes, all the spectra have been shifted to match the 0-0 transition with the one computed at the TOEP2 level. The comparison of the theoretical spectra obtained with Gaussian broadening functions with smaller HWHMs (0.01 eV) shows that, even if the overall bandshape is reproduced consistently by the three diagonal approaches, slight differences are present regarding the intensity of the bands in the higher-energy region of the spectrum. In more detail, the computed intensity of those bands is lower at the TOEP2 level than at the OVGF (or P3) one. This difference is still detectable with larger HWHHs (0.075 eV). The comparison of the spectra with the experimental results shows that the bandshape is reproduced more accurately if the TOEP2 and OVGF approaches are used, whereas the accuracy decreases for P3. The same spectrum has been simulated also using the non-diagonal approaches NR2 and ADC(3), and the results are reported in Fig. 7.6, together with the TOEP2 spectrum. In this case as well, the spectra have been shifted to match the energy of the 0-0 transition to the one computed at the TOEP2 level. It is noteworthy that the NR2 and ADC(3) spectra are nearly superimposable, even if, as for P3, the intensity of the bands in the higher-energy region of the spectrum is overestimated with respect to experiment. Therefore, in this case the TOEP2 approach is the most reliable also in the reproduction of the bandshape of the XPS spectrum.

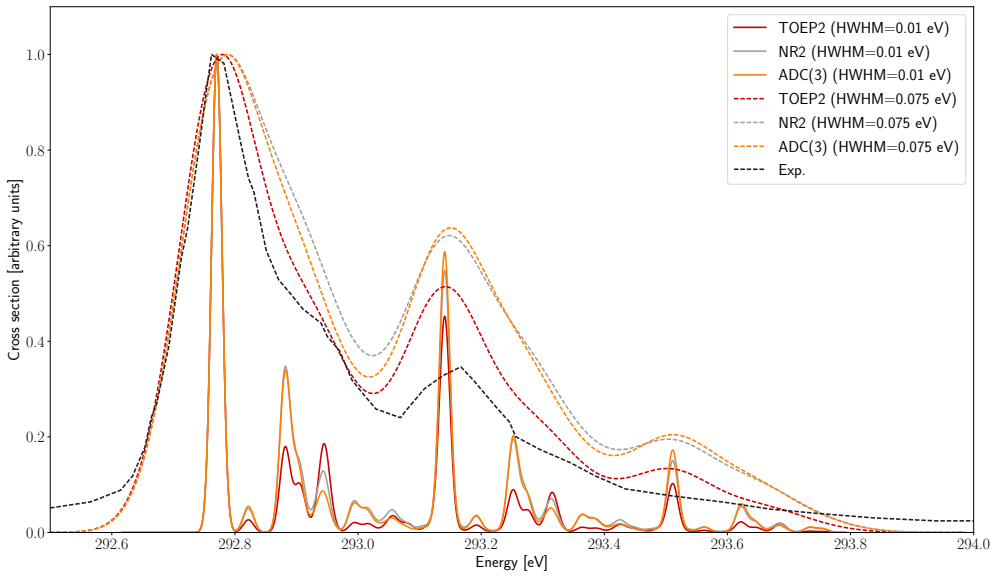

FIGURE 7.6: XPS spectrum for the ionization of the C_α 1s electron of ethanol computed at the VG|FC level using different non-diagonal propagator methods (NR2 in gray, ADC(3) in orange) and the TOEP2 approach (in red). Gaussian functions with HWHMs of 0.01 eV (solid lines) and 0.075 eV (dashed lines) have been used to simulate the broadening effects.

Based on the previous results, TOEP2 has thus been employed to simulate the full XPS spectrum. In order to get a reliable reproduction of the experimental data, the ionization of the 1s orbital has been computed for the C_α and C_β

atoms in both conformers. The electronic energy difference between the two conformers, computed at the B3LYP/SNSD level is 7.704 meV, which corresponds to an abundance of 57 % of (a) and 43 % of (b) at room temperature. Those values have been used to weight the spectra of the two conformers and to obtain the overall spectrum.

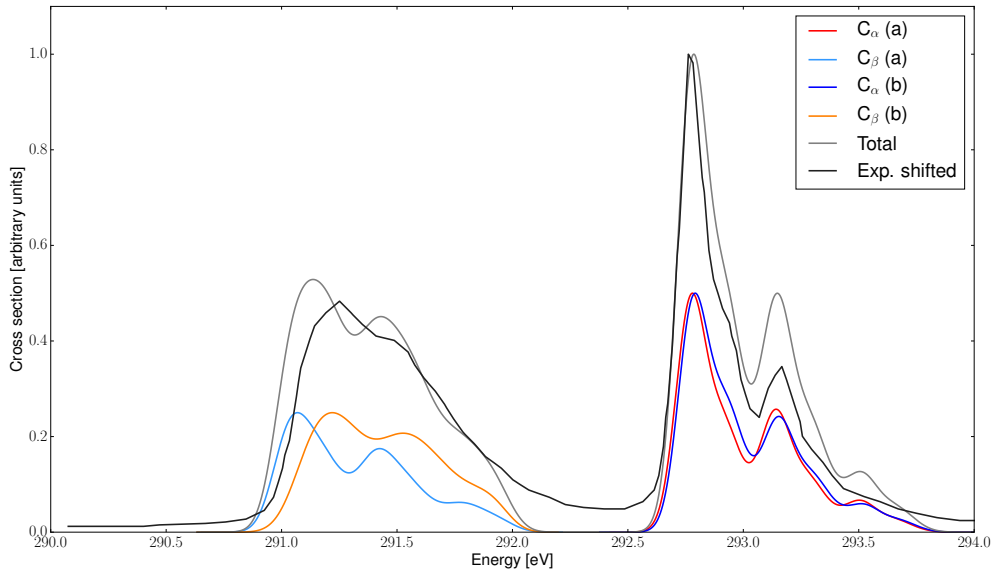

FIGURE 7.7: Comparison of the theoretical XPS spectrum for the ionization of the C1s core electrons of ethanol, computed at the VG|FC level (solid, gray line) with the experimental one (solid, black line, taken from Ref. 440). The latter has been shifted by 0.5 eV to facilitate the comparison of the bandshapes. Gaussian functions with HWHMs of 0.075 eV have been used to simulate broadening effects. The spectra for the individual contributions for the ionization of the (a) (solid red line for the C_α1s orbital, solid light blue line for the C_β1s orbital) and the (b) conformer (solid orange line for the C_α1s orbital, solid blue line for the C_β1s orbital) are reported.

The comparison between the spectrum computed at the TOEP2/cc-pVTZ level within the VG|FC model, and the experimental results, reported in Fig. 7.7, shows that, even if the computed spectrum is shifted by approximately 0.5 eV with respect to the experimental one, the relative position of the bands, as well as their shape, is reproduced accurately. In order to highlight the relevance of vibrational effects, the VG spectrum is compared to the vertical energy (VE) one, where vibrational effects are neglected, in Fig. 7.8. This comparison shows that the relative intensity of the bands associated to the ionization of the core orbitals of the C_α and C_β atoms is poorly reproduced at the VE level. This is due to the fact that the impact of molecular vibrations is different for the two bands, the broadening being more significant for the C_β atom than for the C_α one.
This effect can be detected also in Fig. 7.7, where the contribution of each C atom and of each conformer is reported. In fact, it is evident that, for both conformers, more extended progressions are detected for the ionization of

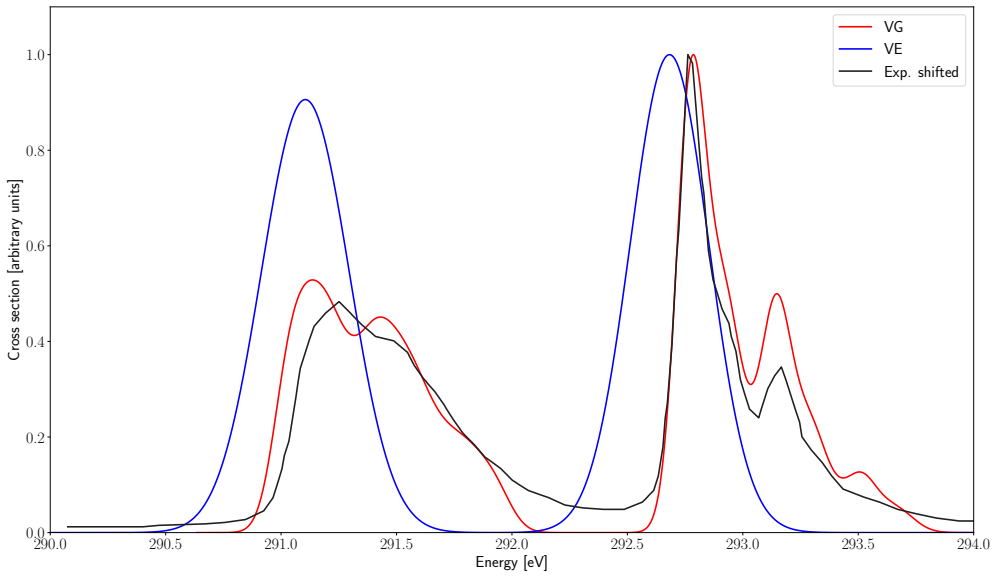

FIGURE 7.8: Comparison of the theoretical XPS spectrum for the ionization of the C1s core electrons of ethanol, computed at the VG|FC (solid, red line) and VE (solid, blue line) with the experimental one (solid, black line, taken from Ref. 440). The latter has been shifted by 0.5 eV to facilitate the comparison of the bandshapes. Gaussian functions with HWHMs of 0.075 eV for the VG spectrum, and with an HWHM of 0.25 eV for the VE spectrum, have been used to simulate broadening effects.

the 1s orbital of C_β than the one of C_α, and therefore the intensity maximum decreases. It should also be noted that, for the ionization of the C_α 1s orbital, the spectra obtained for the (a) and (b) conformers are nearly superimposable. On the other hand, both positions and shapes of the bands associated to the ionization of the C_β 1s orbital are different. Those results are in agreement with the analysis given in Ref. 441, where the difference in the ionization energies of the C_β 1s orbitals was ascribed to a different interaction, in the cationic state, between the positive hole in the C_β atom and the hydroxyl group. To further highlight the different impact of vibrational effects in the two bands of the XPS spectrum, a graphical representation of the shift vector $\boldsymbol{K}$ for the ionization of the two C 1s core orbitals for the (a) conformer is reported in Fig. 7.9 (the results for the (b) conformer have not been included for the sake of simplicity, as they are nearly equivalent to the ones obtained for the first conformer). For the ionization of the C_β core orbital, the largest component of $\boldsymbol{K}$ is the one associated to the torsion along the H-O-C_α-C_β dihedral angle (mode 3 in Fig. 7.9, $K_3 \approx 34$ $m_e^{1/2}$ · Bohr), while the others are at least three times smaller. On the other hand, for the ionization of the C_α 1s orbital, the magnitude of the shift vector decreases significantly for all components, especially for the torsional mode, where in this case $K_3 \approx 5.5$ $m_e^{1/2}$ · Bohr. Since, within the VG|FC model, the intensity of the progressions increases with the magnitude of the shift vector,[97,372] the broadening is larger for the C_β atom due to the larger shift of

the torsional motion. This result is coherent with the analysis reported elsewhere,[440] where the difference between the two spectra is ascribed to the different contributions of the torsional mode. However, it should be noted that, in the previous study,[441] the AH|FC model was employed, and therefore harmonic frequencies of the core-ionized state at its equilibrium geometry were explicitly computed. However, the core-ionization of the C_β orbital causes a large-amplitude distortion along the H-O-C_α-C_β dihedral angle. As already discussed in the previous section, large-amplitude distortions are poorly described by adiabatic models in Cartesian coordinates, and therefore, in Ref. 441 a monodimensional, anharmonic model was used to improve the description of the torsional mode. Here the simpler VG|FC model, which is better-suited to treat large-amplitude motions has been employed since, as discussed in Chapter 4, for vertical models Cartesian and internal coordinates give equivalent results. Furthermore, the computational cost of a VG simulation is significantly smaller than that of an AH simulation, since the core-ionized state is not optimized, and the calculation of the frequencies of the cationic state is avoided.[442]

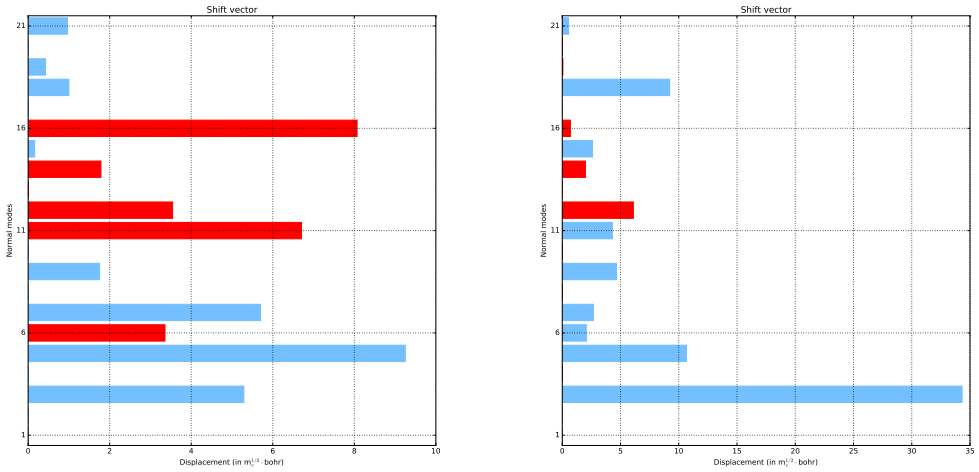

FIGURE 7.9: Graphical representation of the shift vector **K** associated to the ionization of the C_α (left panel) and the C_β (right panel) 1s core orbitals of ethanol, computed at the VG|FC level. Positive values are represented with blue bars, negative values are represented with red bars. The components of $\boldsymbol{K}$ are reported in $m_e^{1/2} \cdot$ Bohr.

As a final check of the reliability of our computational setup, the XPS spectrum has been simulated also for chloroethane. Like ethanol, an experimental spectrum of chloroethane recorded with high-resolution, in which single vibronic bands are detected is available in the literature.[440] However, unlike ethanol, in this case the vibronic broadening of the bands associated to the ionization of the two C 1s orbitals is nearly equivalent. Thus, the TOEP2 approach can be used to check if this trend is caused by a different vibronic broadening. The comparison of the theoretical and experimental results is reported in Fig. 7.10, where electronic structure calculations were performed

at the TOEP2/cc-pVTZ level, and vibronic calculations at the VG|FC level. Also in this case, the overall bandshape is reproduced accurately, both for the band associated to the ionization of the C_α 1s orbital, with an intense peak at about 292 eV and a second shoulder at 292.4 eV, and for the C_β peak, which is less broadened. With respect to ethanol, in this case the shape of the bands is similar for the ionization of the two C 1s orbitals, and in both cases the broadening is less pronounced compared to the one of the C_α ionization of ethanol. In fact, the torsional degree of freedom associated to the H-O-C_α-C_β dihedral angle, which was the main origin of the broadening in the previous case, is not present for chloroethane, and this reduces the overall broadening of the spectrum.

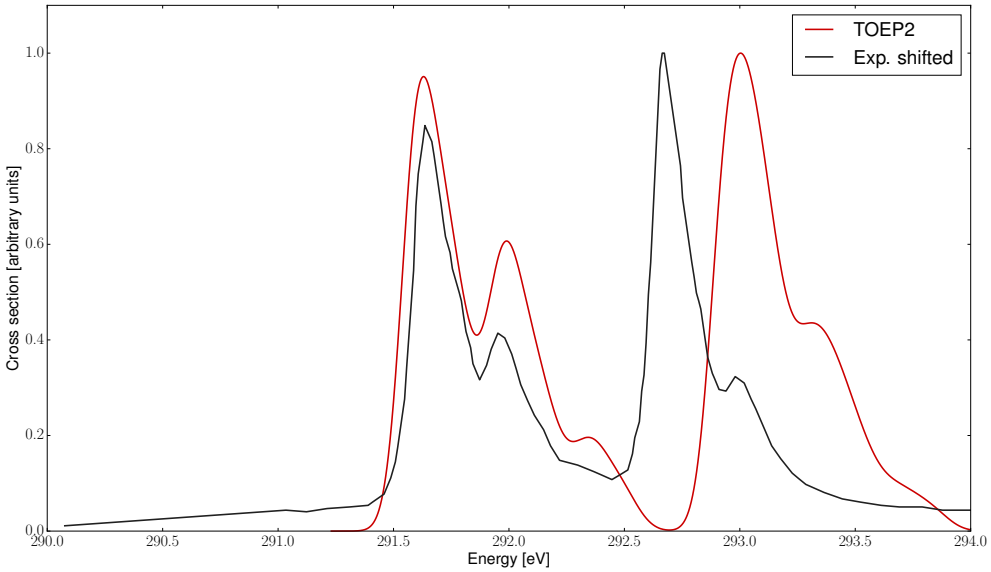

FIGURE 7.10: Comparison of the theoretical XPS spectrum for the ionization of the C 1s core electrons of chloroethane, computed at the TOEP2 VG|FC level with the experimental results (solid, black line, taken from Ref. 440). Gaussian functions with an HWHM of 0.075 eV have been used to simulate broadening effects. The experimental spectrum has been shfited by 0.5 eV to facilitate the comparison with the computed spectra.

To support this analysis, a graphical representation of the shift vector for the two ionizations is reported in Fig. 7.11. As expected and at variance with ethanol, the order of magnitude of the components of $\boldsymbol{K}$ for the two ionizations is similar (let us recall that, for the VG model, the spectrum depends only on the squared values of the components of $\boldsymbol{K}$, and therefore their sign is not relevant). As a consequence, the bandshape is similar as well.
Also in this case, the most important source of inaccuracy in the reproduction of the experimental data lies in the computation of the IEs, the one for the C_α 1s orbital being overestimated by 0.5 eV and that of the C_β orbital by 0.9 eV. Contrary to ethanol, the difference between the theoretical and experimental ionization energy changes for the two core orbitals, and therefore,

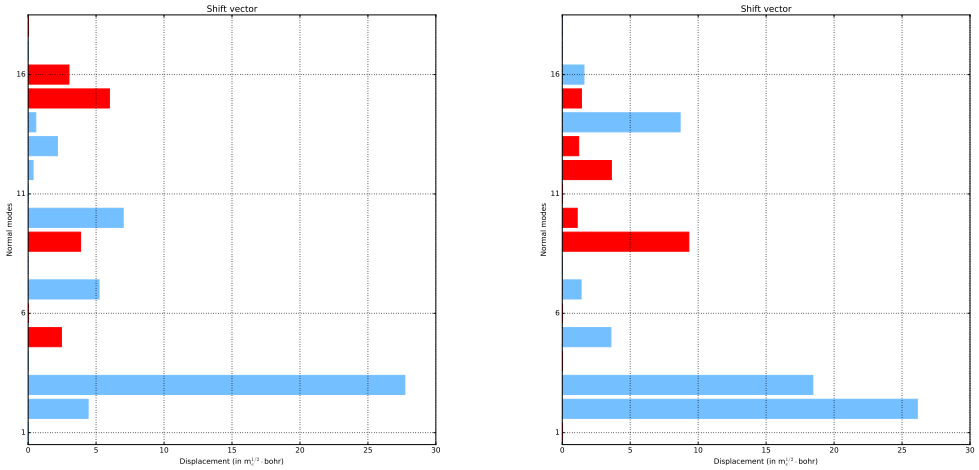

FIGURE 7.11: Graphical representation of the shift vector $\boldsymbol{K}$ associated to the ionization of the C_α (left panel) and the C_β (right panel) 1s core orbitals of chloroethane, computed at the VG|FC level. Positive shifts are represented with blue bars, negative values are represented with red bars. The components of $\mathbf{K}$ are reported in $\text{aum}^{1/2} \cdot \text{Bohr}$.

even if a constant shift is applied to the experimental spectrum, the theoretical and experimental spectra do not overlap. However, as shown in Tab. 7.2, where the IEs obtained using higher-order propagator methods are reported, the accuracy of the theoretical results is not recovered using more accurate propagator approaches. Using the larger EPR-IIId basis set, the computed and experimental splittings between the two C 1s ionization energy are in better agreement, with a difference below 0.1 eV. In this case too, TOEP2 is the approach providing the best theoretical estimate of the IEs.

		C_α	C_β	$\Delta(C_\alpha\text{-}C_\beta)$
OVGF	cc-pVTZ	295.44	293.60	1.88
	aug-cc-pVTZ	295.10	293.64	1.46
P3	cc-pVTZ	294.48	292.80	1.54
	aug-cc-pVTZ	294.22	292.80	1.42
NR2	cc-pVTZ	293.81	292.37	1.44
	aug-cc-pVTZ	293.69	292.24	1.45
ADC(3)	cc-pVTZ	295.16	293.75	1.41
	aug-cc-pVTZ	296.07	292.95	3.12
TOEP2	cc-pVTZ	292.85	291.57	1.28
	aug-cc-pVTZ	292.83	291.56	1.29
	EPR-IIId	292.61	291.43	1.18
Exp.[440]		292.10	290.00	1.10

TABLE 7.2: Vertical ionization energies (in eV) for the C 1s orbitals of chloroethane computed using different combinations of propagator methods and basis sets.

Chapter 8

Conclusions and perspectives

The main objective of this PhD project has been the development of theoretical methods for the simulation of vibrational and vibrationally-resolved electronic spectra, with the aim of targeting large-sized, possibly flexible systems of several dozens of atoms in a cost-effective way. In general terms, the simulation of molecular vibrations relies on two steps. The first one concerns the calculation of the potential energy surface (PES) through electronic structure calculations (ESCs), which defines the potential entering in the vibrational Schrödinger equation. Solving the latter determines the molecular motion. The second issue is related to the solution of the vibrational Schrödinger equation itself, whose complexity strongly depends on the level of approximation of the PES.
The simplest models for molecular vibrations are based on the harmonic approximation, which is particularly appealing since it leads to an analytic solution of the vibrational Schrödinger equation. Going back to the two points mentioned above, this means that the calculation of vibrational energies is possible directly from the output of ESCs, and does not require the development of any specific algorithm for the solution of the Schrödinger equation. Vibrational energies determine the band positions in molecular spectra, but are not sufficient to simulate full spectra, since also transition properties, which are directly related to the band intensities, are required. The complexity associated to the evaluation of these transition moments at the harmonic level is significantly different for vibrational and vibronic spectroscopies. In fact, even if for both spectroscopies, transition properties can be computed analytically, in the first case only a finite number of transitions have non-null intensity, whereas in vibronic spectroscopy a virtually infinite number of transitions can in principle be active. This makes the simulation of the latter much less trivial. One of the main objectives of the present thesis has been the development of theoretical approaches for the simulation of vibronic spectra at the harmonic level for large-size and potentially flexible systems at an affordable computational cost. This framework combines two components for targeting large systems, *i.e.* a time-dependent (TD) algorithm and a description of molecular properties in terms of curvilinear internal coordinates. Within TD algorithms, vibronic spectra are computed as the Fourier transform of an appropriate autocorrelation function, thus avoiding the need of evaluating explicitly the contribution of each vibronic transition, as in the parallel, time-independent (TI) approaches.[268,285] Within this thesis, the transition dipole moment autocorrelation function is computed analytically,

within the Feynmann path integral theory.[91] An additional, major advantage of TD algorithms over the TI ones is the possibility of including temperature effects effectively, without a significant increase of the computational cost. This second aspect makes TD particularly appealing when studying flexible systems, usually displaying a large number of low-frequency modes, which are significantly populated already at room temperature. At variance with most TD-based approaches recently proposed in the literature,[97,98,443] which are based on simplified vibronic models, the theory has been kept here as general as possible, supporting different representations of the PES of the excited states involved in the transition, as well as different levels of approximation for the property surface (PS). Clearly, the harmonic approximation limits the application of this TD framework to semi-rigid systems, displaying limited structural deformations upon electronic excitation. The extension to more flexible systems would require, in principle, the inclusion of anharmonic effects, but a cost-effective alternative is offered by the generalization of the framework to curvilinear, internal coordinates, still at the harmonic level. As already discussed in the literature,[86,200] a careful choice of internal coordinates allows to strongly reduce mode-couplings, and this results in an improvement of the accuracy in simulations, especially for flexible systems. Like TD, the internal coordinates framework has been kept as general as possible, therefore supporting the same vibronic models as in Cartesian coordinates. It is worth noting that the definition of a general, black-box internal coordinates-framework is not a trivial task. In fact, unlike for Cartesian coordinates, the definition of a non-redundant set of internal coordinates for a given molecular structure is not unique, and this definition has a strong impact on the reliability of the simulations. Within this thesis, various algorithms already applied to geometry optimizations[120,127,129,131,135] have been tested. Based on the results of our simulations, the so-called delocalized internal coordinates (DICs)[120] prove to be the most reliable for spectroscopic simulations, in particular if compared to the widely used Z-matrix internal coordinates,[135] especially when dealing with complex molecular topologies. The use of internal coordinates allows to concentrate anharmonic effects over a limited number of degrees of freedom, which improves the reliability of harmonic simulations for flexible systems or systems having LAMs. However, in order to get a correct description of this class of molecules, the inclusion of anharmonic effects is mandatory. This usually leads to a steep increase in the computational cost, both in the generation of the PES and in the solution of the vibrational Schrödinger equation. Thus, the development of efficient anharmonic algorithms is critical to target also large-size systems. In this thesis, two different methods for the simulation of vibrational spectra at the anharmonic level have been presented. The first one is designed to target systems, where anharmonic effects are relevant mostly for a single degree of freedom, whereas they are negligible for the other modes. Within this model, the highly anharmonic degree of freedom, usually corresponding to a large-amplitude mode (LAM), is treated with a fully-numerical variational approach, in which the PES is computed explicitly along the LAM,

and vibrational levels are obtained by applying the discrete variable representation (DVR) theory.[192] They correspond to the "exact" vibrational levels, since no approximations are made both for the PES and in the solution of the Schrödinger equation. The coupling of the LAM with the other modes, treated as harmonic, is then recovered within the so-called internal coordinates (ICPH)[76] and reaction path (RPH) Hamiltonian[77] models. With respect to most existing formulations of ICPH and RPH, the theory presented in this thesis has been generalized to support internal coordinates,[114,179] based on the framework already defined for harmonic vibronic models. This allows to reduce the couplings between the LAM and the remaining, harmonic modes, with a consequent increase in the reliability of the simulations.
The main limitation of this hybrid DVR-harmonic algorithm is that it is based on an unbalanced description of different modes, the LAM being treated with high accuracy, whereas the other modes are described as harmonic. Thus, this method cannot be applied to molecular systems with multiple anharmonic degrees of freedom, which require multidimensional anharmonic models. To target also this class of system, the density matrix renormalization group (DMRG) algorithm, commonly applied to electronic structure problems,[30,444,445] has been generalized to vibrational problems (VDMRG). The main advantage of VDMRG over standard variational approaches is that vibrational wavefunctions are parametrized as a matrix-product states (MPSs),[224] which are much more flexible than standard CI expansions. The derivation of VDMRG has been done within the so-called second-generation formulation of DMRG,[82,216] in which, similarly to wavefunctions, operators are expressed in a compact form, as matrix product operators (MPOs). The main advantage of this formulation over the original, first-generation one,[80] is the possibility of supporting any type of Hamiltonian starting from its second-quantization (SQ) form. In our implementation, we used the Watson Hamiltonian in Cartesian-based normal modes, by exploiting the bosonic second-quantization operators.[111] Clearly, the use of such a Hamiltonian provides a much less accurate representation of the potential with respect to the one used in the hybrid DVR-harmonic scheme. However, the main advantage of the Watson Hamiltonian is the possibility of expressing it in a compact, SQ form, thus allowing an efficient formulation of VDMRG. In its standard formulation, the DMRG algorithm provides the ground state energies, *i.e.* zero-point vibrational energies in vibrational structure calculations, which is of little interest for most practical applications. Indeed, the energy of highly-excited states (as for example, X−H stretching modes), and the associate transition frequencies, are of higher interest. To target also those states, an energy-specific extension of VDMRG has been presented, which uses shift-and-invert (S&I) algorithms[207] coupled with subspace iteration diagonalization techniques[167,168] to optimize excited states without the need of any constraint. The S&I formulation of VDMRG has been coupled with root-homing procedures[231] based on a maximum-overlap criterion[104,422] to further increase the reliability of the optimization algorithm. As shown for several test cases, the coupling of S&I VDMRG with root-homing allows to

compute variational energies of highly-excited vibrational states of molecular systems with several dozens of modes, which are currently the limit of most of the more advanced variational algorithms.[72,207]
At the beginning of this section, we showed that harmonic vibronic models are much more complex than their counterpart applied to vibrational spectroscopies. It is thus clear that the extension of anharmonic models to vibronic models is extremely challenging, and has been scarcely discussed in the literature.[42,43,44,99,446] First, the ESCs are much more expansive than for electronic ground states, thus the cost associated to the generation of the anharmonic PES is higher. The complexity of the vibrational part of the simulation depends on the spectroscopy of interest. In fact, the calculation of vibrational energies and transition properties between vibrational levels of the same electronic state is as complex as its equivalent for ground-states. In this respect, we presented in this thesis the extension of second-order perturbation theory (VPT2) to excited states, where anharmonic force fields at the time-dependent density-functional theory (TD-DFT) level. Thanks to the recent development of analytic formulae for TD-DFT harmonic frequencies,[41,100] anharmonic PES for systems with several dozens of atoms have become doable with an affordable computational cost. For vibronic spectroscopies, however, the calculation of transition properties between vibrational levels of different electronic states is required, and this makes the vibrational part of the simulation much more complex than for purely vibrational spectroscopies. In this thesis, the hybrid DVR-harmonic scheme has been generalized to vibronic transitions. This extension poses two major challenges. First of all, a single coordinate describing the LAM for both electronic states involved in the transition must be defined. This means, in practice, that if the PES is computed through a relaxed scan calculation (as for ICPH), one of the two electronic states has to be chosen as reference for the scan, and this choice will have a critical impact on the overall band-shape. The second challenge is related to the description of the harmonic degrees of freedom. As a matter of fact, vibronic transitions will involve, in general, simultaneous excitations of both the LAM and the harmonic modes, where the latter change, in the most general case, along the LAM. To build a framework coherent with full-harmonic models, transition moments involving the harmonic modes must be computed based on the same vibronic models defined for the full-harmonic case. This requires, in practice, the extension of each vibronic model to projected harmonic modes,[77] which change along the LAM. However, thanks the integration of the hybrid DVR-harmonic scheme within the vibronic models introduced above, an automatic support of different models, both in Cartesian and in internal coordinates, is possible.
From another point of view, the simulation of vibronic spectra is further complicated by the fact that a wide range of phenomena can occur after an electronic excitation. Among them, non-radiative processes, such as inter-system crossing (ISC) and internal conversion (IC). To model correctly photochemical processes, those effects must be included in calculations too. Within this thesis, the harmonic, internal-coordinates based TD framework has been

generalized to support the calculation of IC and ISC rates. For IC, two, parallel formulations have been defined. The first one is based on an adiabatic representation of the PESs, in which the rate is determined by non-adiabatic couplings between the electronic states. The second formulation is based, however, on a diabatic representation of the PESs, in which IC rates are determined by off-diagonal couplings in the potential energy operator. The former representation is well-suited for electronic states separated by large energy gaps, but leads to severe instabilities when this gap is small. In this case, more reliable results are obtained within a diabatic picture. From a computational point of view, the extension of the TD framework to IC rates is not straightforward independently on the representation and requires the calculation of high-order correlation function. In this thesis, the generality of the TD framework has been exploited to compute those correlation functions with only minor modifications to the existing theory.
The support of linear absorption spectroscopies is not sufficient for building a complete framework for the simulation of molecular spectra, and more advanced techniques, such as the ones based on non-linear optical effects, must be supported as well. In this thesis, a computational approach for the simulation vibrational resonance Raman (RR) and its chiral counterpart, resonance Raman Optical Activity (RROA), has been presented. These spectroscopies involve transitions between vibrational levels of the same electronic state, but the experiment is carried out with a laser, whose frequency matches the electronic excitation to a so-called intermediate electronic state. For this reason, the intensity of the bands in a RR or RROA spectrum is determined by vibronic contributions involving this intermediate state. Similarly to non-radiative decay rates, the TD theory has been extended to the simulation of RR and RROA spectra. From a practical point of view, this required the extension of the framework to the calculation of cross-correlation functions in place of the standard, transition dipole moment autocorrelation function. In this case as well, the generality of the TD theory developed for one-photon spectroscopy, has been exploited to support both Cartesian and in internal coordinates. In particular, the extension to internal coordinates is very interesting when studying flexible systems, for which an incorrect definition of the coordinates set can lead to a significant redistribution of band intensities in the whole energy range of the spectrum, and not only for the modes associated to the LAM.
Another class of spectroscopies studied in this thesis are the ones involving excitations of core electrons. From a theoretical point of view, this extension does not require any significant modification to the vibronic models, since only the nature of the electronic states involved in the transition changes. However, the impact of vibronic effects on core electron spectroscopies, such as near-edge X-ray absorption spectroscopy (NEXAFS) and X-ray photoionizations (XPS), is much less explored than for their valence counterpart. In fact, for several decades, the poor resolution of NEXAFS and XPS measurements hindered the identification of vibronic bands in experimental spectra, and simulations performed at the purely electronic level were sufficient to interpret experimental data. However, thanks to the increasing power of

synchrotron light sources, the accuracy of experimental spectra is quickly improving and, even if vibronic bands can only rarely be singled out, the inclusion of vibronic effects is becoming crucial to get a correct reproduction of the intensity pattern of experimental spectra. This has been shown, in this thesis, for the NEXAFS spectra of several pyridine derivatives, whose C1s and N1s spectra have been computed with DFT-based methods, coupled to the simpler Vertical Gradient (VG) vibronic model. The analysis has then been extended to XPS for which, however, electronic structure calculations were performed using Green function (GF)-based approaches. Still with the aim of targeting large-size systems, a new, cost-effective GF-based method has been developed, namely second-order transition operator electron propagator theory (TOEP2). The main feature of TOEP2 is that grand-canonical HF orbitals[421] are used in place of the standard, HF ones. Ionization energies are then computed as poles of the second-order approximation of the one-electron GF. In this way, accurate results, even better than the most accurate standard GF approaches, are obtained already at the second order, while the theory remains applicable also to large-sized systems with a limited computational cost. The reliability of TOEP2 has been checked not only for vertical ionization energies, but also for full vibronic, XPS spectra, where all the quantities defining the vibronic model are computed at the TOEP2 level. In this respect, it is important to note that in photoelectron spectrum some care must be paid when computing transition dipole moments, since the two electronic states involved in the transition have a different number of electrons. This makes the calculation of transition dipole moments more difficult, but this can still be done within GF-based theories.

The theoretical framework presented in this thesis pave the way towards new developments. Regarding vibrational spectroscopies, we already mentioned that the hybrid DVR-harmonic scheme and VDMRG represent two extremes among variational approaches regarding the scalability with respect to the system size. In the former, a single degree of freedom is treated nearly exactly, with highly accurate anharmonic models, whereas the harmonic approximation is used for the remaining modes. Conversely, in VDMRG, all modes are treated variationally, using however a less local representation of the PES, less accurate than for the hybrid DVR-harmonic scheme. To fully exploit the advantages of both methods, hybrid algorithms, where variational calculations are carried out only on a subset of anharmonic modes, comprising more than a single mode, like RPH, must be devised. In this respect, the hybrid DVR-harmonic scheme can be extended to multiple degrees of freedom based on the generalization of the ICPH and RPH models to 2 and 3 dimensions. This leads to the so-called reaction surface Hamiltonian (RSH)[188] and the reaction volume Hamiltonian (RVH)[447] models, whose formulation has been however limited until now only to Cartesian coordinates. A major issue associated to RSH and RVH compared to RPH is that the expression for the kinetic energy operator is much more complex,[122] thus making the evaluation of the vibrational Hamiltonian less trivial. The extension of RSH and RVH to more than 3 degrees of freedom is less appealing, due to the

high computational cost associated to an explicit scan along more than 3 vibratonal degrees of freedom. Another interesting development of the hybrid harmonic-DVR theory would be the inclusion of anharmonic effects also for the small-amplitude modes (SAMs), currently treated at the harmonic level, using cheaper anharmonic models, such as perturbative ones.[67,69] Also the coupling of VDMRG with perturbation theory is particularly appealing and would reduce the size of the variational Hamiltonian, with a consequent strong reduction of the overall computational costs. From a practical point of view, the combination of the DMRG algorithm with perturbation theories could be done following recent works done in the field of electronic structure calculations.[448,449] The further combination of a coupled VDMRG-perturbative treatment with RPH-based approaches would lead to multiscale models where, for a given molecule, modes are treated at increasing levels of theory (harmonic models, perturbative treatment, VDMRG, RPH-based approaches), therefore allowing to tackle large-size systems at a feasible computational cost. Regarding the partition of the vibrational Hamiltonian in a variational and a perturbative part, measures taken from quantum information theory have already been proven, for now on electronic structure calculations,[244,245] to be reliable in identifying states involved in strong variational corrections.

An additional limitation of the anharmonic models presented in this thesis is related to the reference coordinates system. For the hybrid DVR-harmonic scheme, internal coordinates were used but the actual calculations were carried out in internal coordinates-based normal modes. However, internal coordinates could be in principle also directly used to define the vibrational Hamiltonian, without computing normal modes. The support of similar models, also known as local modes-based approaches,[72] would require the support of more complex Hamiltonians including, for example, off-diagonal quadratic terms in the potential expansion.[73,74,172] Nevertheless, couplings between different coordinates are usually strongly reduced if local modes are employed, therefore allowing a block-partition of the Hamiltonian, with a consequent gain in the computational efficiency of the procedure. Local modes-based approaches are particularly appealing in connection with VDMRG. In fact, it is well-known[81,82] that the efficiency of DMRG-based algorithms is maximal for Hamiltonians not containing long-range interactions. For this reason, using local modes, even more compact MPSs would probably be sufficient to represent converged wavefunctions, with a consequent additional gain in efficiency. From a practical point of view, this extension would require the generalization of VDMRG, currently based on Hermite polynomials, to more general basis sets. This in turn requires the use of a different SQ form of the vibrational Hamiltonian, based on the so-called n-mode representation of the potential.[110,162] Unlike for the standard bosonic SQ, the n-mode representation of the potential fulfill several symmetry constraints, such as the conservation of the number of particles. Consequently, MPSs must also be adapted to respect those symmetry constraints. This task can hardly be done within first-generation DMRG algorithms but is possible within a second-generation, MPS-based formulation[221] such as the one

employed here.
Regarding vibronic spectroscopy, the models presented in this thesis can be improved in two respects. First, anharmonic effects were included in vibronic spectroscopy only for a single degree of freedom, within the hybrid DVR-harmonic scheme, while all the other models were based on the harmonic approximation. Thus, the extension of multidimensional anharmonic approaches described above to vibronic spectroscopy would allow to target even larger systems. In this respect, perturbative approaches, based on VPT2 have been proposed in the literature,[42,43] but most of them relied on Cartesian coordinates-based Hamiltonians. Their extension to internal coordinates[158] has not been discussed, but would probably allow to target quite flexible systems. A second limitation of the vibronic models presented throughout this thesis is that at most two interacting electronic states are supported. This limits the range of applicability of the models in the description of both radiative and non-radiative phenomena. Indeed, for several non-linear optical spectroscopies, which will be discussed more in detail in the following, at least three electronic states are involved, and thus their description within the framework described here would not be possible. Furthermore, it is known that non-radiative phenomena are usually governed by non-equilibrium effects, whereas the models presented here assume that thermal equilibrium is reached in the electronic initial state. As for non-linear spectroscopies, also the inclusion of non-equilibrium effects requires the development a three electronic states-based model. In more detail, the molecule is assumed to be in equilibrium with the first state, and is excited to the second electronic state. Then, non-radiative decay occurs between this second state and the third one before the realization thermal equilibrium. Even if analytical approaches for the calculation of rates under those conditions have been proposed in the literature,[94,96] they have been limited to simplified vibronic models, such as the linear coupling model.[94] The further extension of those frameworks to more refined vibronic models, and in particular to internal coordinates, would increase the reliability of non-radiative decay rates calculations.
All the perspectives discussed up to this point are based on the further increase on the accuracy of vibrational and vibronic models. However, from a parallel point of view, the theoretical framework can be extended also in terms of the number of supported spectroscopies. In particular, regarding non-linear ones, even if here only RR and RROA were discussed, the framework is general enough to be extended to additional non-linear techniques, such as two-photon absorption (TPA),[450] hyper resonance Raman,[390,451] and magnetic circular dichroism (MCD).[452] The main issue associated to the extension of the vibronic framework to those spectroscopies lies in the electronic structure calculations, which require the calculation of higher-order molecular response functions,[51,57,390] and more specifically excited to excited transition moments. However, the vibronic part is in most cases similar to the one developed for one-photon and RR spectroscopies, and would need

only minor technical changes in theory. A more challenging task is the further extension to multidimensional spectroscopies,[453] such as IR-UV pump-probe techniques, for which the relevance of vibronic effects has already been proven in the literature.[454] Even if in this case the molecular properties are the same as those involved in linear one-photon spectroscopies, the vibronic part requires the calculation of high-order correlation functions,[455] for which only very simplified vibronic models have been proposed.[456,457]

Bibliography

[1] Laane, J. *Frontiers of Molecular Spectroscopy*; Elsevier Science, 2011.

[2] Quack, M.; Merkt, F. *Quack, Martin and Merkt, Frederic*; Wiley, 2011.

[3] Jensen, P.; Bunker, P. *Computational Molecular Spectroscopy*; Wiley, 2000.

[4] Pretsch, E.; Bühlmann, P.; Badertscher, M. *Structure Determination of Organic Compounds*; Springer-Verlag Berlin Heidelberg, 2009.

[5] Kaupp, M.; Bühl, M.; Malkin, V. *Calculation of NMR and EPR Parameters: Theory and Applications*; Wiley-VCH, 2004.

[6] Weil, J. A.; Bolton, . J. R. *Electron Paramagnetic Resonance: Elementary Theory and Practical Applications*; Wiley-Interscience, 2007.

[7] Barone, V.; Gyamfi, J. A.; Piserchia, A. *Electron Paramagnetic Resonance: Volume 25*; The Royal Society of Chemistry, 2017; Vol. 25; pp 98–156.

[8] Kroto, H. W. *Molecular Rotation Spectra*; Dover Publications, 1992.

[9] Brown, J. M.; Carrington, A. *Rotational Spectroscopy of Diatomic Molecules*; Cambridge University Press, 2003.

[10] Herbst, E. *Chem. Soc. Rev.* **2001**, *30*, 168–176.

[11] Barone, V.; Biczysko, M.; Puzzarini, C. *Acc. Chem. Res.* **2015**, *48*, 1413–1422.

[12] Fortenberry, R. C. *Int. J. Quantum Chem.* **2017**, *117*, 81–91.

[13] Puzzarini, C.; Stanton, J. F.; Gauss, J. *Int. Rev. Phys. Chem.* **2010**, *29*, 273–367.

[14] Puzzarini, C. *Phys. Chem. Chem. Phys.* **2013**, *15*, 6595–6607.

[15] Demaison, J. *Mol. Phys.* **2007**, *105*, 3109–3138.

[16] Piccardo, M.; Penocchio, E.; Puzzarini, C.; Biczysko, M.; Barone, V. *J. Phys. Chem. A* **2015**, *119*, 2058–2082.

[17] Califano, S. In *Vibrational States*; Sons, J. W. ., Ed.; 1976.

[18] Wilson, E. B. In *Molecular Vibrations: The Theory of Infrared and Raman Vibrational Spectra*; Dover,, Ed.; Dover Publications; New edition edition (March 1, 1980), 1980.

[19] Chalmers, J. M.; Griffiths, P. R. *Handbook of Vibrational Spectroscopy*; Wiley, 2002.

[20] Duncan, M. A. *Int. Rev. Phys. Chem.* **2003**, *22*, 407–435.

[21] Dong, A.; Huang, P.; Caughey, W. S. *Biochemistry (Mosc.)* **1990**, *29*, 3303–3308.

[22] Rauhut, G. *J. Chem. Phys.* **2004**, *121*, 9313–9322.

[23] Schlegel, H. B. *J. Comput. Chem.* **2003**, *24*, 1514–1527.

[24] Schlegel, H. B. *Wiley Interdiscip. Rev.: Comput. Mol. Sci.* **2011**, *1*, 790–809.

[25] Papousek, D.; Aliev, M. In *Molecular Vibrational-rotational Spectra: Theory and Applications of High Resolution Infrared, Microwave and Raman Spectroscopy of Polyatomic Molecules*; Ltd, E. S., Ed.; 1982.

[26] Hoy, A.; Mills, I.; Strey, G. *Mol. Phys.* **1972**, *24*, 1265–1290.

[27] Bowman, J. M.; Carrington, T.; Meyer, H.-D. *Mol. Phys.* **2008**, *106*, 2145–2182.

[28] Matyus, E.; Czak, G.; Csszr, A. G. *J. Chem. Phys.* **2009**, *130*, 134112.

[29] Krylov, A. I. *Annu. Rev. Phys. Chem.* **2008**, *59*, 433–462.

[30] Knecht, S.; Hedegaard, E. D.; Keller, S.; Kovyrshin, A.; Ma, Y.; Muolo, A.; Stein, C. J.; Reiher, M. *CHIMIA International Journal for Chemistry* **2016**, *70*, 244–251.

[31] Burke, K.; Werschnik, J.; Gross, E. K. U. *J. Chem. Phys.* **2005**, *123*, 062206.

[32] Schreiber, M.; Silva-Junior, M. R.; Sauer, S. P. A.; Thiel, W. *J. Chem. Phys.* **2008**, *128*, 134110.

[33] Laurent, A. D.; Jacquemin, D. *Int. J. Quantum Chem.* **2013**, *113*, 2019–2039.

[34] Lakowicz, J. R. In *Principles of Fluorescence Spectroscopy*; Verlag, S., Ed.; 2006.

[35] Baryshnikov, G.; Minaev, B.; Ågren, H. *Chem. Rev.* **2017**, *117*, 6500–6537.

[36] Reiher, M.; Wolf, A. *Relativistic Quantum Chemistry*; Wiley-VCH Verlag GmbH & Co. KGaA, 2009; pp 315–383.

[37] Carter, S.; Handy, N. C.; Rosmus, P.; Chambaud, G. *Mol. Phys.* **1990**, *71*, 605–622.

[38] Boudon, V.; Champion, J.-P.; Gabard, T.; Loëte, M.; Michelot, F.; Pierre, G.; Rotger, M.; Wenger, C.; Rey, M. *J. Mol. Spec.* **2004**, *228*, 620–634.

[39] Furche, F.; Ahlrichs, R. *J. Chem. Phys.* **2002**, *117*, 7433–7447.

[40] Scalmani, G.; Frisch, M. J.; Mennucci, B.; Tomasi, J.; Cammi, R.; Barone, V. *J. Chem. Phys.* **2006**, *124*, 94107–94115.

[41] Liu, J.; Liang, W. *J. Chem. Phys.* **2011**, *135*, 184111.

[42] Luis, J. M.; Bishop, D. M.; Kirtman, B. *J. Chem. Phys.* **2004**, *120*, 813–822.

[43] Luis, J. M.; Kirtman, B.; Christiansen, O. *J. Chem. Phys.* **2006**, *125*, 154114.

[44] Rodriguez-Garcia, V.; Yagi, K.; Hirao, K.; Iwata, S.; Hirata, S. *J. Chem. Phys.* **2006**, *125*, 014109.

[45] Berova, N.; Polavarapu, P.; Nakanishi, H.; Woody, R. W. *Comprehensive Chrioptical Spectroscopy*; Wiley, 2012.

[46] Barron, L. D. *Molecular Light Scattering and Optical Activity*; Cambridge University Press, 2009.

[47] Berova, N.; Woody, R. W. *Circular Dichroism: Principles and Applications*; Wiley, 2000.

[48] Riehl, J. P.; Richardson, F. S. *Chem. Rev.* **1986**, *86*, 1–16.

[49] Riehl, J. P.; Muller, G. *Handbook on the Physics and Chemistry of Rare Earths*; Handbook on the Physics and Chemistry of Rare Earths Supplement C; Elsevier, 2004; Vol. 34; pp 289 – 357.

[50] Ciofini, I.; Daul, C. A. *Coord. Chem. Rev.* **2003**, *238-239*, 187 – 209, Theoretical and Computational Chemistry.

[51] Helgaker, T.; Coriani, S.; Jrgensen, P.; Kristensen, K.; Olsen, J.; Ruud, K. *Chem. Rev.* **2012**, *112*, 543–631.

[52] Bloino, J.; Biczysko, M.; Barone, V. *J. Phys. Chem. A* **2015**, *119*, 11862–11874.

[53] Lin, N.; Santoro, F.; Rizzo, A.; Luo, Y.; Zhao, X.; Barone, V. *J. Phys. Chem. A* **2009**, *113*, 4198–4207.

[54] Santoro, F.; Barone, V. *Int. J. Quantum Chem.* **2010**, *110*, 476–486.

[55] Barone, V.; Baiardi, A.; Biczysko, M.; Bloino, J.; Cappelli, C.; Lipparini, F. *Phys. Chem. Chem. Phys.* **2012**, *14*, 12404–12422.

[56] Macak, P.; Luo, Y.; Norman, P.; Ågren, H. *J. Chem. Phys.* **2000**, *113*, 7055–7061.

[57] Friese, D. H.; Beerepoot, M. T. P.; Ringholm, M.; Ruud, K. *J. Chem. Theory Comput.* **2015**, *11*, 1129–1144.

[58] Long, D. A.; Long, D. *Raman spectroscopy*; McGraw-Hill New York, 1977; Vol. 206.

[59] Quinet, O.; Champagne, B. *J. Chem. Phys.* **2001**, *115*, 6293–6299.

[60] Ligeois, V.; Ruud, K.; Champagne, B. *J. Chem. Phys.* **2007**, *127*, 204105.

[61] Guthmuller, J.; Champagne, B. *J. Chem. Phys.* **2007**, *127*, 164507.

[62] Guthmuller, J.; Champagne, B. *J. Phys. Chem. A* **2008**, *112*, 3215–3223.

[63] Nafie, L. A. *Chem. Phys.* **1996**, *205*, 309–322.

[64] Barone, V. *Wiley Interdiscip. Rev.: Comput. Mol. Sci.* **2016**, *6*, 86–110.

[65] Licari, D.; Baiardi, A.; Biczysko, M.; Egidi, F.; Latouche, C.; Barone, V. *J. Comput. Chem.* **2015**, *36*, 321–334.

[66] Bowman, J. M.; Huang, X.; Handy, N. C.; Carter, S. *J. Phys. Chem. A* **2007**, *111*, 7317–7321.

[67] Barone, V. *J. Chem. Phys.* **2005**, *122*, 14108.

[68] Bloino, J.; Biczysko, M.; Barone, V. *J. Chem. Theory Comput.* **2012**, *8*, 1015–1036.

[69] Changala, P. B.; Baraban, J. H. *J. Chem. Phys.* **2016**, *145*, 174106.

[70] Dawes, R.; Carrington Jr., T. *J. Chem. Phys.* **2005**, *122*, 134101.

[71] Avila, G.; Carrington Jr., T. *J. Chem. Phys.* **2011**, *135*, 064101.

[72] Jacob, C. R.; Reiher, M. *J. Chem. Phys.* **2009**, *130*, 084106.

[73] Panek, P. T.; Jacob, C. R. *ChemPhysChem* **2014**, *15*, 3365–3377.

[74] Panek, P. T.; Jacob, C. R. *J. Phys. Chem. Lett.* **2016**, *7*, 3084–3090.

[75] Nielsen, H. H. *Rev. Mod. Phys.* **1951**, *23*, 90–136.

[76] Tew, D. P.; Handy, N. C.; Carter, S.; Irle, S.; Bowman, J. *Mol. Phys.* **2003**, *101*, 3513–3525.

[77] Miller, W. H.; Handy, N. C.; Adams, J. E. *J. Chem. Phys.* **1980**, *72*, 99–112.

[78] Page, M.; McIver, J. W. *J. Chem. Phys.* **1988**, *88*, 922–935.

[79] Jackels, C. F.; Gu, Z.; Truhlar, D. G. *J. Chem. Phys.* **1995**, *102*, 3188–3201.

[80] White, S. R. *Phys. Rev. Lett.* **1992**, *69*, 2863–2866.

[81] Schollwöck, U. *Rev. Mod. Phys.* **2005**, *77*, 259–315.

[82] Schollwöck, U. *Ann. Phys.* **2011**, *326*, 96 – 192.

[83] Tackett, A. R.; Di Ventra, M. *Phys. Rev. B* **2002**, *66*, 245104.

[84] Reiher, M.; Neugebauer, J. *Phys. Chem. Chem. Phys.* **2004**, *6*, 4621–4629.

[85] Kovyrshin, A.; Neugebauer, J. *J. Chem. Phys.* **2010**, *133*, 174114.

[86] Reimers, J. R. *J. Chem. Phys.* **2001**, *115*, 9103–9109.

[87] Capobianco, A.; Borrelli, R.; Noce, C.; Peluso, A. *Theor. Chem. Acc.* **2012**, *131*, 1181.

[88] Cerezo, J.; Zuniga, J.; Requena, A.; Avila Ferrer, F. J.; Santoro, F. *J. Chem. Theory Comput.* **2013**, *9*, 4947–4958.

[89] Heller, E. J. *Acc. Chem. Res.* **1981**, *14*, 368–375.

[90] Mukamel, S.; Abe, S.; Islampour, R. *J. Phys. Chem.* **1985**, *89*, 201–204.

[91] Ianconescu, R.; Pollak, E. *J. Phys. Chem. A* **2004**, *108*, 7778–7784.

[92] Burghardt, I.; Giri, K.; Worth, G. A. *J. Chem. Phys.* **2008**, *129*, 174104.

[93] Meng, Q.; Meyer, H.-D. *J. Chem. Phys.* **2013**, *138*, 014313.

[94] Izmaylov, A. F.; Mendive-Tapia, D.; Bearpark, M. J.; Robb, M. A.; Tully, J. C.; Frisch, M. J. *J. Chem. Phys.* **2011**, *135*, 234106.

[95] Endicott, J. S.; Joubert-Doriol, L.; Izmaylov, A. F. *J. Chem. Phys.* **2014**, *141*, 034104.

[96] Borrelli, R.; Peluso, A. *J. Chem. Theory Comput.* **2015**, *11*, 415–422.

[97] Neese, F.; Petrenko, T.; Ganyushin, D.; Olbrich, G. *Coord. Chem. Rev.* **2007**, *251*, 288 – 327.

[98] Silverstein, D. W.; Jensen, L. *J. Chem. Phys.* **2012**, *136*, 64111.

[99] Bowman, J. M.; Huang, X.; Harding, L. B.; Carter, S. *Mol. Phys.* **2006**, *104*, 33–45.

[100] Petrone, A.; Lingerfelt, D. B.; Williams-Young, D. B.; Li, X. *J. Phys. Chem. Lett.* **2016**, *7*, 4501–4508.

[101] Lingerfelt, D. B.; Williams-Young, D. B.; Petrone, A.; Li, X. *J. Chem. Theory Comput.* **2016**, *12*, 935–945.

[102] Langhoff, P.; Langhoff, S.; Rescigno, T.; Schirmer, J.; Cederbaum, L.; Domcke, W.; Niessen, W. V. *Chem. Phys.* **1981**, *58*, 71 – 91.

[103] Ortiz, J. V. *Wiley Interdiscip. Rev.: Comput. Mol. Sci.* **2013**, *3*, 123–142.

[104] Flores-Moreno, R.; Zakrzewski, V. G.; Ortiz, J. V. *J. Chem. Phys.* **2007**, *127*, 134106.

[105] Flores-Moreno, R.; Melin, J.; Dolgounitcheva, O.; Zakrzewski, V. G.; Ortiz, J. V. *Int. J. Quantum Chem.* **2010**, *110*, 706–715.

[106] Kupka, H. J. *Transitions in molecular Systems*; Wiley, 2010.

[107] Eckart, C. *Phys. Rev.* **1935**, *47*, 552–558.

[108] Sayvetz, A. *J. Chem. Phys.* **1939**, *7*, 383–389.

[109] Louck, J. D.; Galbraith, H. W. *Rev. Mod. Phys.* **1976**, *48*, 69–106.

[110] Christiansen, O. *J. Chem. Phys.* **2004**, *120*, 2140–2148.

[111] Hirata, S.; Hermes, M. R. *J. Chem. Phys.* **2014**, *141*.

[112] Peng, C.; Ayala, P. Y.; Schlegel, H. B.; Frisch, M. J. *J. Comput. Chem.* **1996**, *17*, 49–56.

[113] Brandhorst, K.; Grunenberg, J. *J. Chem. Phys.* **2010**, *132*, 184101.

[114] Natanson, G. A. *Chem. Phys. Lett.* **1992**, *190*, 209–214.

[115] Pulay, P.; Fogarasi, G. *J. Chem. Phys.* **1992**, *96*, 2856–2860.

[116] Koliha, J.; Djordjevic, D.; Cvetkovic, D. *Linear Algebra and its Applications* **2007**, *426*, 371 – 381.

[117] Grochowski, P. *Theor. Chem. Acc.* **2008**, *121*, 257–266.

[118] Crawford, B.; Overend, J. *J. Mol. Spec.* **1964**, *12*, 307–318.

[119] Torres, E. M.; Gonzalez, J. J. L.; Gomez, M. F. *J. Chem. Phys.* **1999**, *110*, 3302–3308.

[120] Baker, J.; Kessi, A.; Delley, B. *J. Chem. Phys.* **1996**, *105*, 192–212.

[121] Schaad, L.; Hu, J. *J. Mol. Struct.* **1989**, *185*, 203–215.

[122] Lauvergnat, D.; Nauts, A. *J. Chem. Phys.* **2002**, *116*, 8560–8570.

[123] Miyazawa, T. *J. Chem. Phys.* **1958**, *29*, 246–246.

[124] Press, W. H.; Flannery, B. P.; Teukolsky, S. A.; Vetterling, W. T. In *Numerical Recipes in FORTRAN 77*; Press, C. U., Ed.; 1992; Vol. 1.

[125] Lindh, R.; Bernhardsson, A.; Schätz, M. *Chem. Phys. Lett.* **1999**, *303*, 567–575.

[126] Lindh, R.; Bernhardsson, A.; Karlstrom, G.; Malmqvist, P. A. *Chem. Phys. Lett.* **1995**, *241*, 423–428.

[127] Swart, M.; Matthias Bickelhaupt, F. *Int. J. Quantum Chem.* **2006**, *106*, 2536–2544.

[128] Jensen, F.; Palmer, D. S. *J. Chem. Theory Comput.* **2011**, *7*, 223–230.

[129] Pulay, P.; Fogarasi, G.; Pang, F.; Boggs, J. E. *J. Am. Chem. Soc.* **1979**, *101*, 2550–2560.

[130] Fogarasi, G.; Zhou, X.; Taylor, P. W.; Pulay, P. *J. Am. Chem. Soc.* **1992**, *114*, 8191–8201.

[131] von Arnim, M.; Ahlrichs, R. *J. Chem. Phys.* **1999**, *111*, 9183–9190.

[132] Cremer, D.; Pople, J. A. *J. Am. Chem. Soc.* **1975**, *97*, 1354–1358.

[133] Cremer, D. *J. Phys. Chem.* **1990**, *94*, 5502–5509.

[134] Shojaei, S. H. R.; Morini, F.; Deleuze, M. S. *J. Phys. Chem. A* **2013**, *117*, 1918–1929.

[135] Baker, J.; Hehre, W. J. *J. Comput. Chem.* **1991**, *12*, 606–610.

[136] Bakken, V.; Helgaker, T. *J. Chem. Phys.* **2002**, *117*, 9160–9174.

[137] Mead, C. A.; Truhlar, D. G. *J. Chem. Phys.* **1982**, *77*, 6090–6098.

[138] Baer, M. *Chem. Phys. Lett.* **1975**, *35*, 112 – 118.

[139] Halász, G. J.; Vibók, A.; Suhai, S.; Baer, M. *J. Chem. Phys.* **2007**, *127*, 244101.

[140] Tapavicza, E.; Bellchambers, G. D.; Vincent, J. C.; Furche, F. *Phys. Chem. Chem. Phys.* **2013**, *15*, 18336–18348.

[141] Ruedenberg, K.; Atchity, G. J. *J. Chem. Phys.* **1993**, *99*, 3799–3803.

[142] Atchity, G. J.; Ruedenberg, K. *Theor. Chem. Acc.* **1997**, *97*, 47–58.

[143] Nakamura, H.; Truhlar, D. G. *J. Chem. Phys.* **2001**, *115*, 10353–10372.

[144] Werner, H.-J.; Meyer, W. *J. Chem. Phys.* **1981**, *74*, 5802–5807.

[145] Cave, R. J.; Newton, M. D. *Chem. Phys. Lett.* **1996**, *249*, 15–19.

[146] Subotnik, J. E.; Yeganeh, S.; Cave, R. J.; Ratner, M. A. *J. Chem. Phys.* **2008**, *129*, 244101.

[147] Ou, Q.; Subotnik, J. E. *J. Phys. Chem. C* **2013**, *117*, 19839–19849.

[148] Subotnik, J. E.; Alguire, E. C.; Ou, Q.; Landry, B. R.; Fatehi, S. *Acc. Chem. Res.* **2015**, *48*, 1340–1350.

[149] Hoyer, C. E.; Xu, X.; Ma, D.; Gagliardi, L.; Truhlar, D. G. *J. Chem. Phys.* **2014**, *141*, 114104.

[150] Rauhut, G.; Pulay, P. *J. Phys. Chem.* **1995**, *99*, 3093–3100.

[151] Baker, J.; Jarzecki, A. A.; Pulay, P. *J. Phys. Chem. A* **1998**, *102*, 1412–1424.

[152] Merrick, J. P.; Moran, D.; Radom, L. *J. Phys. Chem. A* **2007**, *111*, 11683–11700.

[153] Andersson, M. P.; Uvdal, P. *J. Phys. Chem. A* **2005**, *109*, 2937–2941.

[154] Bouteiller, Y.; Gillet, J.-C.; Grégoire, G.; Schermann, J. P. *J. Phys. Chem. A* **2008**, *112*, 11656–11660.

[155] Watson, J. K. *Mol. Phys.* **1968**, *15*, 479–490.

[156] Meal, J. H.; Polo, S. R. *J. Chem. Phys.* **1956**, *24*, 1126–1133.

[157] Ayala, P. Y.; Schlegel, H. B. *J. Chem. Phys.* **1998**, *108*, 2314–2325.

[158] Isaacson, A. D. *J. Phys. Chem. A* **2006**, *110*, 379–388.

[159] Sibaev, M.; Crittenden, D. L. *J. Comput. Chem.* **2015**, *36*, 2200–2207.

[160] Sibaev, M.; Crittenden, D. L. *Comput. Phys. Commun.* **2016**, *203*, 290–297.

[161] Carter, S.; Culik, S. J.; Bowman, J. M. A. *J. Chem. Phys.* **1997**, *107*, 10458–10469.

[162] Wang, H.; Thoss, M. *J. Chem. Phys.* **2009**, *131*, 024114.

[163] Piccardo, M.; Bloino, J.; Barone, V. *Int. J. Quantum Chem.* **2015**, *115*, 948–982.

[164] Martin, J. M. L.; Lee, T. J.; Taylor, P. M.; François, J.-P. *J. Chem. Phys.* **1995**, *103*, 2589–2602.

[165] Matthews, D. A.; Stanton, J. F. *Mol. Phys.* **2009**, *107*, 213–222.

[166] Kuhler, K. M.; Truhlar, D. G.; Isaacson, A. D. *J. Chem. Phys.* **1996**, *104*, 4664–4670.

[167] Davidson, E. R. *J. Comput. Phys.* **1975**, *17*, 87 – 94.

[168] Sleijpen, G. L. G.; der Vorst, H. A. V. *SIAM Rev.* **2000**, *42*, 267–293.

[169] Scribano, Y.; Lauvergnat, D. M.; Benoit, D. M. *J. Chem. Phys.* **2010**, *133*.

[170] Richter, F.; Thaunay, F.; Lauvergnat, D.; Carbonniére, P. *J. Phys. Chem. A* **2015**, *119*, 11719–11728.

[171] Cheng, X.; Steele, R. P. *J. Chem. Phys.* **2014**, *141*, 104105.

[172] Zimmerman, P. M.; Smereka, P. *J. Chem. Theory Comput.* **2016**, *12*, 1883–1891.

[173] Cerezo, J.; Mazzeo, G.; Longhi, G.; Abbate, S.; Santoro, F. *J. Phys. Chem. Lett.* **2016**, *7*, 4891–4897.

[174] Fukui, K. *Acc. Chem. Res.* **1981**, *14*, 363–368.

[175] Gonzalez, C.; Schlegel, H. B. *J. Chem. Phys.* **1989**, *90*, 2154–2161.

[176] Gonzalez, C.; Schlegel, H. B. *J. Phys. Chem.* **1990**, *94*, 5523–5527.

[177] Marcus, R. A. *J. Chem. Phys.* **1966**, *45*, 4493–4499.

[178] Kato, S.; Kato, H.; Fukui, K. *J. Am. Chem. Soc.* **1977**, *99*, 684–691.

[179] Natanson, G. A.; Garrett, B. C.; Truong, T. N.; Joseph, T.; Truhlar, D. G. *J. Chem. Phys.* **1991**, *94*, 7875–7892.

[180] Fukui, K. *Int. J. Quantum Chem.* **1981**, *20*, 633–642.

[181] Hratchian, H. P.; Schlegel, H. B. *J. Chem. Phys.* **2004**, *120*, 9918–9924.

[182] Hratchian, H. P.; Schlegel, H. B. *J. Chem. Theory Comput.* **2005**, *1*, 61–69.

[183] Hratchian, H. P.; Frisch, M. J.; Schlegel, H. B. *J. Chem. Phys.* **2010**, *133*, 224101.

[184] Beenken, W. J. D.; Lischka, H. *J. Chem. Phys.* **2005**, *123*, 144311.

[185] Lin, C.-K.; Chang, H.-C.; Lin, S. H. *J. Phys. Chem. A* **2007**, *111*, 9347–9354.

[186] Peluso, A.; Borrelli, R.; Capobianco, A. *J. Phys. Chem. A* **2009**, *113*, 14831–14837.

[187] Kreyszig, E. *Differential Geometry*; Dover Publications, 1991.

[188] Carrington, T.; Miller, W. H. *J. Chem. Phys.* **1984**, *81*, 3942–3950.

[189] Taketsugu, T.; Gordon, M. S. *J. Chem. Phys.* **1996**, *104*, 2834–2840.

[190] Luckhaus, D. *Phys. Chem. Chem. Phys.* **2008**, *10*, 6215–6222.

[191] Light, J. C.; Hamilton, I. P.; Lill, J. V. *J. Chem. Phys.* **1985**, *82*, 1400–1409.

[192] Colbert, D. T.; Miller, W. H. *J. Chem. Phys.* **1992**, *96*, 1982–1991.

[193] Muckerman, J. T. *Chem. Phys. Lett.* **1990**, *173*, 200 – 205.

[194] Corey, G. C.; Lemoine, D. *J. Chem. Phys.* **1992**, *97*, 4115–4126.

[195] Szalay, V. *J. Chem. Phys.* **1993**, *99*, 1978–1984.

[196] Marston, C. C.; Balint-Kurti, G. G. *J. Chem. Phys.* **1989**, *91*, 3571–3576.

[197] Karabulut, H.; Sibert, E. L. III. *J. Phys. B: At., Mol. Opt. Phys.* **1997**, *30*, L513.

[198] Bachau, H.; Cormier, E.; Decleva, P.; Hansen, J. E.; Martín, F. *Rep. Prog. Phys.* **2001**, *64*, 1815.

[199] Beenken, W. J. *Chem. Phys.* **2008**, *349*, 250 – 255.

[200] Stendardo, E.; Ferrer, F. A.; Santoro, F.; Improta, R. *J. Chem. Theory Comput.* **2012**, *8*, 4483–4493.

[201] Lawrence, M. C.; Robertson, G. N. *J. Chem. Phys.* **1987**, *87*, 3375–3380.

[202] Kryachko, E. S. *Chem. Phys.* **1990**, *143*, 359–370.

[203] Baiardi, A.; Bloino, J.; Barone, V. *J. Chem. Theory Comput.* **2017**, *13*, 2804–2822.

[204] Tew, D. P.; Handy, N. C.; Carter, S. *Mol. Phys.* **2001**, *99*, 393–402.

[205] Baiardi, A.; Bloino, J.; Barone, V. *J. Chem. Phys.* **2016**, *144*, 084114.

[206] Bulik, I. W.; Frisch, M. J.; Vaccaro, P. H. *J. Chem. Phys.* **2017**, *147*, 044110.

[207] Petrenko, T.; Rauhut, G. *J. Chem. Phys.* **2017**, *146*, 124101.

[208] Kovyrshin, A.; Neugebauer, J. *Chem. Phys.* **2011**, *391*, 147 – 156.

[209] White, S. R. *Phys. Rev. B* **1993**, *48*, 10345–10356.

[210] Daul, S.; Ciofini, I.; Daul, C.; White, S. R. *Int. J. Quantum Chem.* **2000**, *79*, 331–342.

[211] Chan, G. K.-L.; Head-Gordon, M. *J. Chem. Phys.* **2002**, *116*, 4462–4476.

[212] Chan, G. K.-L.; Head-Gordon, M. *J. Chem. Phys.* **2003**, *118*, 8551–8554.

[213] Östlund, S.; Rommer, S. *Phys. Rev. Lett.* **1995**, *75*, 3537–3540.

[214] Pirvu, B.; Murg, V.; Cirac, J. I.; Verstraete, F. *New J. Phys.* **2010**, *12*, 025012.

[215] Dolfi, M.; Bauer, B.; Keller, S.; Kosenkov, A.; Ewart, T.; Kantian, A.; Giamarchi, T.; Troyer, M. *Comput. Phys. Commun.* **2014**, *185*, 3430 – 3440.

[216] Keller, S.; Dolfi, M.; Troyer, M.; Reiher, M. *J. Chem. Phys.* **2015**, *143*.

[217] Hubig, C.; McCulloch, I. P.; Schollwöck, U. *Phys. Rev. B* **2017**, *95*, 035129.

[218] Hubig, C.; McCulloch, I. P.; Schollwöck, U.; Wolf, F. A. *Phys. Rev. B* **2015**, *91*, 155115.

[219] Fortenberry, R. C.; Huang, X.; Yachmenev, A.; Thiel, W.; Lee, T. J. *Chem. Phys. Lett.* **2013**, *574*, 1–12.

[220] Tóth, A. I.; Moca, C. P.; Legeza, O.; Zaránd, G. *Phys. Rev. B* **2008**, *78*, 245109.

[221] Keller, S.; Reiher, M. *J. Chem. Phys.* **2016**, *144*, 134101.

[222] Dorando, J. J.; Hachmann, J.; Chan, G. K.-L. *J. Chem. Phys.* **2007**, *127*, 084109.

[223] Liu, F.; Kurashige, Y.; Yanai, T.; Morokuma, K. *J. Chem. Theory Comput.* **2013**, *9*, 4462–4469.

[224] McCulloch, I. P. *J. Stat. Mech: Theory Exp.* **2007**, *2007*, P10014.

[225] Stratmann, R. E.; Scuseria, G. E.; Frisch, M. J. *J. Chem. Phys.* **1998**, *109*, 8218–8224.

[226] Liang, W.; Fischer, S. A.; Frisch, M. J.; Li, X. *J. Chem. Theory Comput.* **2011**, *7*, 3540–3547.

[227] Peng, B.; Lestrange, P. J.; Goings, J. J.; Caricato, M.; Li, X. *J. Chem. Theory Comput.* **2015**, *11*, 4146–4153.

[228] Yu, X.; Pekker, D.; Clark, B. K. *Phys. Rev. Lett.* **2017**, *118*, 017201.

[229] Paige, C. C.; Parlett, B. N.; van der Vorst, H. A. *Numerical Linear Algebra with Applications* **1995**, *2*, 115–133.

[230] Chen, T.; Demmel, J.; Gu, M.; Saad, Y.; Lehoucq, R.; Sorensen, D.; Maschhoff, K.; Bai, Z.; Day, D.; Freund, R.; Sleijpen, G.; van der Vorst, H.; Li, R. *Templates for the Solution of Algebraic Eigenvalue Problems*; 2000; pp 149–231.

[231] Butscher, W.; Kammer, W. *Journal of Computational Physics* **1976**, *20*, 313–325.

[232] Gilbert, A. T. B.; Besley, N. A.; Gill, P. M. W. *J. Phys. Chem. A* **2008**, *112*, 13164–13171.

[233] Khemani, V.; Pollmann, F.; Sondhi, S. L. *Phys. Rev. Lett.* **2016**, *116*, 247204.

[234] Devakul, T.; Khemani, V.; Pollmann, F.; Huse, D. A.; Sondhi, S. L. *Philos. Trans. Royal Soc. A* **2017**, *375*.

[235] Reiher, M.; Neugebauer, J. *J. Chem. Phys.* **2003**, *118*, 1634–1641.

[236] Baiardi, A.; Paoloni, L.; Barone, V.; Zakrzewski, V. G.; Ortiz, J. V. *J. Chem. Theory Comput.* **2017**, *13*, 3120–3135.

[237] Pirvu, B.; Haegeman, J.; Verstraete, F. *Phys. Rev. B* **2012**, *85*, 035130.

[238] Moritz, G.; Reiher, M. *J. Chem. Phys.* **2007**, *126*.

[239] Boguslawski, K.; Marti, K. H.; Reiher, M. *J. Chem. Phys.* **2011**, *134*.

[240] Sandvik, A. W.; Vidal, G. *Phys. Rev. Lett.* **2007**, *99*, 220602.

[241] Marti, K. H.; Bauer, B.; Reiher, M.; Troyer, M.; Verstraete, F. *New J. Phys.* **2010**, *12*, 103008.

[242] Chib, S.; Greenberg, E. *The American Statistician* **1995**, *49*, 327–335.

[243] Luo, Z.; Ma, Y.; Liu, C.; Ma, H. *J. Chem. Theory Comput.* **2017**, *13*, 4699–4710.

[244] Boguslawski, K.; Tecmer, P.; Legeza, O.; Reiher, M. *J. Phys. Chem. Lett.* **2012**, *3*, 3129–3135.

[245] Stein, C. J.; Reiher, M. *J. Chem. Theory Comput.* **2016**, *12*, 1760–1771.

[246] Battocchio, G.; Madsen, N. K.; Christiansen, O. *Mol. Phys.* **2017**, *115*, 228–240.

[247] Peterson, K. A. *J. Chem. Phys.* **1998**, *109*, 8864–8875.

[248] Ortigoso, J.; Escribano, R.; Burkholder, J. B.; Howard, C. J.; Lafferty, W. J. *J. Mol. Spectrosc.* **1991**, *148*, 346–370.

[249] Ortigoso, J.; Escribano, R.; Burkholder, J. B.; Lafferty, W. J. *J. Mol. Spectrosc.* **1992**, *155*, 25–43.

[250] Ortigoso, J.; Escribano, R.; Burkholder, J.; Lafferty, W. *J. Mol. Spectrosc.* **1993**, *158*, 347–356.

[251] Bacic, Z.; Light, J. C. *Annu. Rev. Phys. Chem.* **1989**, *40*, 469–498.

[252] Delahaye, T.; Nikitin, A.; Rey, M.; Szalay, P. G.; Tyuterev, V. G. *J. Chem. Phys.* **2014**, *141*, 104301.

[253] Georges, R.; Bach, M.; Herman, M. *Mol. Phys.* **1999**, *97*, 279–292.

[254] Carter, S.; Sharma, A. R.; Bowman, J. M. *J. Chem. Phys.* **2012**, *137*, 154301.

[255] Gregurick, S. K.; Fredj, E.; Elber, R.; Gerber, R. B. *J. Phys. Chem. B* **1997**, *101*, 8595–8606.

[256] Gerber, R. B.; Brauer, B.; K. Gregurick, S.; M. Chaban, G. *PhysChemComm* **2002**, *5*, 142–150.

[257] Fornaro, T.; Burini, D.; Biczysko, M.; Barone, V. *J. Phys. Chem. A* **2015**, *119*, 4224–4236.

[258] Fornaro, T.; Carnimeo, I.; Biczysko, M. *J. Phys. Chem. A* **2015**, *119*, 5313–5326.

[259] Schuurman, M. S.; Allen, W. D.; von Ragué Schleyer, P.; Schaefer, H. F. III. *J. Chem. Phys.* **2005**, *122*, 104302.

[260] Barone, V.; Biczysko, M.; Bloino, J.; Puzzarini, C. *J. Chem. Theory Comput.* **2013**, *9*, 1533–1547.

[261] Johnson, C. J.; Wolk, A. B.; Fournier, J. A.; Sullivan, E. N.; Weddle, G. H.; Johnson, M. A. *J. Chem. Phys.* **2014**, *140*, 221101.

[262] Frisch, M. J. et al. Gaussian16 Revision A.03. 2016; Gaussian Inc. Wallingford CT.

[263] Huh, J.; Neff, M.; Rauhut, G.; Berger, R. *Mol. Phys.* **2010**, *108*, 409–423.

[264] Duschinsky, F. *Acta Physicochimica URSS* **1937**, *7*, 551.

[265] Özkan, I. *J Mol. Spectrosc.* **1990**, *139*, 147 – 162.

[266] Santoro, F.; Improta, R.; Lami, A.; Bloino, J.; Barone, V. *J. Chem. Phys.* **2007**, *126*, 084509.

[267] Biczysko, M.; Bloino, J.; Santoro, F.; Barone, V. In *Computational Strategies for Spectroscopy, from Small Molecules to Nano Systems*; Barone, V., Ed.; Wiley: Chichester, 2011; pp 361–443.

[268] Bloino, J.; Biczysko, M.; Santoro, F.; Barone, V. *J. Chem. Theory Comput.* **2010**, *6*, 1256–1274.

[269] Franck, J. *Trans. Faraday Soc.* **1926**, *21*, 536–542.

[270] Condon, E. *Phys. Rev.* **1928**, *32*, 858–872.

[271] Herzberg, G.; Teller, E. *Z. Phys. Chem.* **1933**, *21*, 410.

[272] Götze, J. P.; Karasulu, B.; Thiel, W. *J. Chem. Phys.* **2013**, *139*, 234108.

[273] Karasulu, B.; Götze, J. P.; Thiel, W. *J. Chem. Theory Comput.* **2014**, *10*, 5549–5566.

[274] Dierksen, M.; Grimme, S. *J. Chem. Phys.* **2004**, *120*, 3544–3554.

[275] Pedone, A.; Bloino, J.; Barone, V. *J. Phys. Chem. B* **2012**, *116*, 17807–17818.

[276] Borrelli, R.; Peluso, A. *J. Chem. Phys.* **2006**, *125*, 194308.

[277] Sharp, T. E.; Rosenstock, H. M. *J. Chem. Phys.* **1964**, *41*, 3453–3463.

[278] Islampour, R.; Dehestani, M.; Lin, S. *J. Mol. Spec.* **1999**, *194*, 179–184.

[279] Ruhoff, P. T. *Chem. Phys.* **1994**, *186*, 355 – 374.

[280] Santoro, F.; Lami, A.; Improta, R.; Bloino, J.; Barone, V. *J. Chem. Phys.* **2008**, *128*, 224311.

[281] Alison Rodger, B. N. *Circular dichroism and linear dichroism*; Oxford university press, 1997.

[282] Emeis, C. A.; Oosterhoff, L. J. *J. Chem. Phys.* **1971**, *54*, 4809–4819.

[283] Emeis, C. A.; Oosterhoff, L. J. *Chem. Phys. Lett.* **1967**, *1*, 129 – 132.

[284] Richardson, F. S.; Riehl, J. P. *Chem. Rev.* **1977**, *77*, 773–792.

[285] Barone, V.; Bloino, J.; Biczysko, M.; Santoro, F. *J. Chem. Theory Comput.* **2009**, *5*, 540–554.

[286] Lee, S.-Y.; Heller, E. J. *J. Chem. Phys.* **1979**, *71*, 4777–4788.

[287] Heller, E. J.; Sundberg, R.; Tannor, D. *J. Phys. Chem.* **1982**, *86*, 1822–1833.

[288] Yan, Y. J.; Mukamel, S. *J. Chem. Phys.* **1986**, *85*, 5908–5923.

[289] Tatchen, J.; Gilka, N.; Marian, C. M. *Phys. Chem. Chem. Phys.* **2007**, *9*, 5209–5221.

[290] Borrelli, R.; Capobianco, A.; Peluso, A. *J. Phys. Chem. A* **2012**, *116*, 9934–9940.

[291] Peng, Q.; Niu, Y.; Shi, Q.; Gao, X.; Shuai, Z. *J. Chem. Theory Comput.* **2013**, *9*, 1132–1143.

[292] Etinski, M.; Rai-Constapel, V.; Marian, C. M. *J. Chem. Phys.* **2014**, *140*, 114104.

[293] Niu, Y.; Peng, Q.; Deng, C.; Gao, X.; Shuai, Z. *J. Phys. Chem. A* **2010**, *114*, 7817–7831.

[294] Tannor, D. J. In *Introduction to quantum mechanics: a time-dependent perspective*; Book, U. S., Ed.; 2006.

[295] Milton Abramowitz, I. A. S. *Handbook of Mathematical Functions: with Formulas, Graphs, and Mathematical Tables*; Dover, 1965.

[296] Barone, V.; Cimino, P. *Chem. Phys. Lett.* **2008**, *454*, 139–143.

[297] Jarzecki, A. A.; Spiro, T. G. *J. Raman Spectrosc.* **2001**, *32*, 599–605.

[298] Jarzecki, A. A. *J. Phys. Chem. A* **2009**, *113*, 2926–2934.

[299] Balakrishnan, G.; Jarzecki, A. A.; Wu, Q.; Kozlowski, P. M.; Wang, D.; Spiro, T. G. *J. Phys. Chem. B* **2012**, *116*, 9387–9395.

[300] Luk, C. K.; Richardson, F. S. *J. Am. Chem. Soc.* **1974**, *96*, 2006–2009.

[301] Longhi, G.; Castiglioni, E.; Abbate, S.; Lebon, F.; Lightner, D. A. *Chirality* **2013**, *25*, 589–599.

[302] Cances, E.; Mennucci, B.; Tomasi, J. *J. Chem. Phys.* **1997**, *107*, 3032–3041.

[303] Mennucci, B. *Wiley Interdiscip. Rev.: Comput. Mol. Sci.* **2012**, *2*, 386–404.

[304] Barone, V.; Baiardi, A.; Bloino, J. *Chirality* **2014**, *26*, 588–600.

[305] Henry, B. R.; Siebrand, W. *J. Chem. Phys.* **1971**, *54*, 1072–1085.

[306] Tatchen, J.; Gilka, N.; Marian, C. M. *Phys. Chem. Chem. Phys.* **2007**, *9*, 5209–5221.

[307] Borrelli, R.; Peluso, A. *Phys. Chem. Chem. Phys.* **2011**, *13*, 4420–4426.

[308] Etinski, M.; Tatchen, J.; Marian, C. M. *J. Chem. Phys.* **2011**, *134*, 154105.

[309] Peng, Q.; Niu, Y.; Deng, C.; Shuai, Z. *Chem. Phys.* **2010**, *370*, 215–222.

[310] Wolfgang Domcke, H. K., David R. Yarkony *Conical Intersections: Theory, Computation and Experiment*; World Scientific Publishing Company, 2011.

[311] Islampour, R.; Miralinaghi, M.; Khavaninzadeh, A. *J. Phys. Chem. A* **2011**, *115*, 8860–8869.

[312] Picconi, D.; Lami, A.; Santoro, F. *J. Chem. Phys.* **2012**, *136*, 244104.

[313] Islampour, R.; Miralinaghi, M. *J. Phys. Chem. A* **2009**, *113*, 2340–2349.

[314] Picconi, D.; Barone, V.; Lami, A.; Santoro, F.; Improta, R. *ChemPhysChem* **2011**, *12*, 1957–1968.

[315] Hoyer, C. E.; Parker, K.; Gagliardi, L.; Truhlar, D. G. *J. Chem. Phys.* **2016**, *144*, 194101.

[316] Adamo, C.; Jacquemin, D. *Chem. Soc. Rev.* **2013**, *42*, 845–856.

[317] Laurent, A. D.; Adamo, C.; Jacquemin, D. *Phys. Chem. Chem. Phys.* **2014**, *16*, 14334–14356.

[318] Gustav, K.; Seydenschwanz, C. *Chem. Phys. Lett.* **1984**, *109*, 156 – 159.

[319] Zimmerman, H. E.; Kamm, K. S.; Werthemann, D. P. *J. Am. Chem. Soc.* **1975**, *97*, 3718–3725.

[320] Heinzelmann, W.; Labhart, H. *Chem. Phys. Lett.* **1969**, *4*, 20 – 24.

[321] Richter, R. et al. *Phys. Chem. Chem. Phys.* **2014**, *16*, 3070–3076.

[322] Barron, L. D.; Gray, C. G. *J. Phys. A: Math. Nucl. Gen.* **1973**, *6*, 59.

[323] Placzek, G. *Handbuch der Radiologie VI*; Marx E., 1934; Vol. 2; pp 290–374.

[324] D.P. Craig, T. T. *Molecular Quantum Electrodynamics*; Dover, 1998.

[325] Hecht, L.; Nafie, L. A. *Mol. Phys.* **1991**, *72*, 441–469.

[326] Barron, L.; Escribano, J. *Chem. Phys.* **1985**, *98*, 437–446.

[327] Luber, S.; Neugebauer, J.; Reiher, M. *J. Chem. Phys.* **2010**, *132*, 044113.

[328] Mebel, A. M.; Hayashi, M.; Liang, K. K.; ; Lin, S. H. *J. Phys. Chem. A* **1999**, *103*, 10674–10690.

[329] Malmqvist, P. A.; Forsberg, N. *Chem. Phys.* **1998**, *228*, 227 – 240.

[330] Rush, T. I.; Peticolas, W. L. *J. Phys. Chem.* **1995**, *99*, 14647–14658.

[331] Avila Ferrer, F. J.; Barone, V.; Cappelli, C.; Santoro, F. *J. Chem. Theory Comput.* **2013**, *9*, 3597–3611.

[332] Guthmuller, J. *J Chem Phys* **2016**, *144*, 064106.

[333] Egidi, F.; Bloino, J.; Cappelli, C.; Barone, V. *J. Chem. Theory Comput.* **2014**, *10*, 346–363.

[334] Tannor, D. J.; Heller, E. J. *J. Chem. Phys.* **1982**, *77*, 202–218.

[335] Banerjee, S.; Kröner, D.; Saalfrank, P. *J. Chem. Phys.* **2012**, *137*, 22A534.

[336] Baiardi, A.; Bloino, J.; Barone, V. *J. Chem. Phys.* **2014**, *141*, 114108.

[337] Banerjee, S.; Saalfrank, P. *Phys. Chem. Chem. Phys.* **2014**, *16*, 144–158.

[338] Baiardi, A.; Bloino, J.; Barone, V. *J. Chem. Theory Comput.* **2015**, *11*, 3267–3280.

[339] Gerdts, T.; Manthe, U. *J. Chem. Phys.* **1997**, *107*, 6584–6593.

[340] Ben-Nun, M.; ; Martnez, T. J. *J. Phys. Chem. A* **1999**, *103*, 10517–10527.

[341] Ma, H.; Liu, J.; Liang, W. *J. Chem. Theory Comput.* **2012**, *8*, 4474–4482.

[342] Liang, W.; Ma, H.; Zang, H.; Ye, C. *Int. J. Quantum Chem.* **2015**, *115*, 550–563.

[343] Jensen, L.; Zhao, L. L.; Autschbach, J.; Schatz, G. C. *J. Chem. Phys.* **2005**, *123*, 174110.

[344] Jensen, L.; Autschbach, J.; Krykunov, M.; Schatz, G. C. *J. Chem. Phys.* **2007**, *127*, 134101.

[345] Nafie, L. A. *Theor. Chem. Acc.* **2008**, *119*, 39–55.

[346] Vidal, L. N.; Egidi, F.; Barone, V.; Cappelli, C. *J Chem Phys* **2015**, *142*, 174101.

[347] Vidal, L. N.; Giovannini, T.; Cappelli, C. *J Phys Chem Lett* **2016**, *7*, 3585–3590.

[348] Helgaker, T.; Ruud, K.; Bak, K. L.; Jorgensen, P.; Olsen, J. *Faraday Discuss.* **1994**, *99*, 165–180.

[349] Lestrange, P. J.; Egidi, F.; Li, X. *J. Chem. Phys.* **2015**, *143*, 234103.

[350] Sørensen, L. K.; Guo, M.; Lindh, R.; Lundberg, M. *Mol. Phys.* **2017**, *115*, 174–189.

[351] Luber, S.; Reiher, M. *Chemical Physics* **2008**, *346*, 212 – 223.

[352] Ditchfield, R. *Mol. Phys.* **1974**, *27*, 789–807.

[353] Ruud, K.; Helgaker, T.; Bour, P. *J. Phys. Chem. A* **2002**, *106*, 7448–7455.

[354] Pedersen, T. B.; Koch, H.; Boman, L.; Snchez de Mers, A. M. J. *Chem. Phys. Lett.* **2004**, *393*, 319–326.

[355] Barone, V.; Cimino, P.; Stendardo, E. *J. Chem. Theory Comput.* **2008**, *4*, 751–764.

[356] Ismail, N.; Blancafort, L.; Olivucci, M.; Kohler, B.; Robb, M. A. *J. Am. Chem. Soc.* **2002**, *124*, 6818–6819.

[357] Crespo-Hernandez, C. E.; Cohen, B.; Hare, P. M.; Kohler, B. *Chem. Rev.* **2004**, *104*, 1977–2020.

[358] Improta, R.; Barone, V. *J. Am. Chem. Soc.* **2004**, *126*, 14320–14321.

[359] Billinghurst, B. E.; Loppnow, G. R. *J. Phys. Chem. A* **2006**, *110*, 2353–2359.

[360] Yarasi, S.; Ng, S.; Loppnow, G. R. *J. Phys. Chem. B* **2009**, *113*, 14336–14342.

[361] Sasidharanpillai, S.; Loppnow, G. R. *J. Phys. Chem. A* **2014**, *118*, 4680–4687.

[362] Peticolas, W. L.; Rush, T. *J. Comput. Chem.* **1995**, *16*, 1261–1270.

[363] Neugebauer, J.; Hess, B. A. *J. Chem. Phys.* **2004**, *120*, 11564–11577.

[364] Sun, S.; Brown, A. *J. Phys. Chem. A* **2014**, *118*, 9928.

[365] Amovilli, C.; Barone, V.; Cammi, R.; Cancès, E.; Cossi, M.; Mennucci, B.; Pomelli, C. S.; Tomasi, J. *Adv. Quantum Chem.* **1998**, *32*, 227–261.

[366] Tomasi, J.; Mennucci, B.; Cammi, R. *Chem. Rev.* **2005**, *105*, 2999–3094.

[367] Vargek, M.; Freedman, T. B.; Lee, E.; Nafie, L. A. *Chem. Phys. Lett.* **1998**, *287*, 359–364.

[368] Krausbeck, F.; Autschbach, J.; Reiher, M. *J Phys Chem A* **2016**, *120*, 9740–9748.

[369] Patapoff, T. W.; Turpin, P. Y.; Peticolas, W. L. *J. Phys. Chem.* **1986**, *90*, 2347–2351.

[370] Light, J. C.; Carrington, T. *Adv. Chem. Phys.*; John Wiley & Sons, Inc., 2007; pp 263–310.

[371] Santoro, F.; Lami, A.; Improta, R.; Barone, V. *J. Chem. Phys.* **2007**, *126*, 184102.

[372] Bloino, J.; Baiardi, A.; Biczysko, M. *Int. J. Quantum Chem.* **2016**, *115*, 1543–1574.

[373] Grimme, S.; Antony, J.; Ehrlich, S.; Krieg, H. *J. Chem. Phys.* **2010**, *132*, 154104.

[374] Birnbaum, D.; Kohler, B. E. *J. Chem. Phys.* **1991**, *95*, 4783–4789.

[375] Takayanagi, M.; Gejo, T.; Hanazaki, I. *J. Phys. Chem.* **1994**, *98*, 12893–12898.

[376] Becker, R. S.; de Melo, J. S.; Maçanita, A. L.; Elisei, F. *J. Phys. Chem.* **1996**, *100*, 18683–18695.

[377] Laane, J. *Annu. Rev. Phys. Chem.* **1994**, *45*, 179–211.

[378] Laane, J. *Int. Rev. Phys. Chem.* **1999**, *18*, 301–341.

[379] Laane, J. *J. Phys. Chem. A* **2000**, *104*, 7715–7733.

[380] Zhang, J.; Chiang, W. Y.; Laane, J. *J. Chem. Phys.* **1994**, *100*, 3455–3462.

[381] Sagear, P.; Laane, J. *J. Chem. Phys.* **1995**, *102*, 7789–7797.

[382] Pillsbury, N. R.; Choo, J.; Laane, J.; Drucker, S. *J. Phys. Chem. A* **2003**, *107*, 10648–10654.

[383] Arp, Z.; Meinander, N.; Choo, J.; Laane, J. *J. Chem. Phys.* **2002**, *116*, 6648–6655.

[384] Baba, M.; Hanazaki, I. *J. Chem. Phys.* **1984**, *81*, 5426–5433.

[385] Louant, O.; Champagne, B.; Liégeois, V. *Chem. Phys. Lett.* **2015**, *634*, 249–254.

[386] Carbonniere, P.; Begue, D.; Dargelos, A.; Pouchan, C. *Chem. Phys.* **2004**, *300*, 41–51.

[387] Gaw, J. F.; Yamaguchi, Y.; Schaefer, H. F.; Handy, N. C. *J. Chem. Phys.* **1986**, *85*, 5132–5142.

[388] Colwell, S. M.; Jayatilaka, D.; Maslen, P. E.; Amos, R. D.; Handy, N. C. *Int. J. Quantum Chem.* **1991**, *40*, 179–199.

[389] Maslen, P. E.; Jayatilaka, D.; Colwell, S. M.; Amos, R. D.; Handy, N. C. *J. Chem. Phys.* **1991**, *95*, 7409–7417.

[390] Ringholm, M.; Jonsson, D.; Ruud, K. *J. Comput. Chem.* **2014**, *35*, 622–633.

[391] Ringholm, M.; Jonsson, D.; Bast, R.; Gao, B.; Thorvaldsen, A. J.; Ekström, U.; Helgaker, T.; Ruud, K. *J. Chem. Phys.* **2014**, *140*, 034103.

[392] Liu, J.; Liang, W. *J. Chem. Phys.* **2013**, *138*, 024101.

[393] Bloino, J.; Barone, V. *J. Chem. Phys.* **2012**, *136*, 124108.

[394] Bloino, J.; Biczysko, M.; Crescenzi, O.; Barone, V. *J. Chem. Phys.* **2008**, *128*, 244105.

[395] Radziszewski, J. G.; Nimlos, M. R.; Winter, P. R.; Ellison, G. B. *J. Am. Chem. Soc.* **1996**, *118*, 7400–7401.

[396] Friderichsen, A. V.; Radziszewski, J. G.; Nimlos, M. R.; Winter, P. R.; Dayton, D. C.; David, D. E.; Ellison, G. B. *J. Am. Chem. Soc.* **2001**, *123*, 1977–1988.

[397] Butcher, V.; Costa, M.; Dyke, J.; Ellis, A.; Morris, A. *Chem. Phys.* **1987**, *115*, 261–267.

[398] Radziszewski, J. *Chem. Phys. Lett.* **1999**, *301*, 565–570.

[399] Kim, G.-S.; Mebel, A. M.; Lin, S. H. *Chem. Phys. Lett.* **2002**, *361*, 421–431.

[400] Biczysko, M.; Bloino, J.; Barone, V. *Chem. Phys. Lett.* **2009**, *471*, 143–147.

[401] Desyatnyk, O.; Pszczolkowski, L.; Thorwirth, S.; Krygowski, T. M.; Kisiel, Z. *Phys. Chem. Chem. Phys.* **2005**, *7*, 1708–1715.

[402] Balfour, W. J. *Spectrochim. Acta A* **1983**, *39*, 795–800.

[403] Reddy, B. V.; Rao, G. R. *Vib. Spectrosc.* **1994**, *6*, 231–250.

[404] Balfour, W. J. *J. Mol. Spec.* **1985**, *109*, 60–72.

[405] Matsumoto, R.; Sakeda, K.; Matsushita, Y.; Suzuki, T.; Ichimura, T. *J. Mol. Struct.* **2005**, *735*, 153–167.

[406] Hoffmann, L. J. H.; Marquardt, S.; Gemechu, A. S.; Baumgartel, H. *Phys. Chem. Chem. Phys.* **2006**, *8*, 2360–2377.

[407] Schiccheri, N.; Pasquini, M.; Piani, G.; Pietraperzia, G.; Becucci, M.; Biczysko, M.; Bloino, J.; Barone, V. *Phys. Chem. Chem. Phys.* **2010**, *12*, 13547–13554.

[408] Giuliano, B. M.; Caminati, W. *Angew. Chem.* **2005**, *117*, 609–612.

[409] Giuliano, B. M.; Maris, A.; Melandri, S.; Caminati, W. *J. Phys. Chem. A* **2009**, *113*, 14277–14280.

[410] Pietraperzia, G.; Pasquini, M.; Mazzoni, F.; Piani, G.; Becucci, M.; Biczysko, M.; Michalski, D.; Bloino, J.; Barone, V. *J. Phys. Chem. A* **2011**, *115*, 9603–9611.

[411] Egidi, F.; Williams-Young, D. B.; Baiardi, A.; Bloino, J.; Scalmani, G.; Frisch, M. J.; Li, X.; Barone, V. *J. Chem. Theory Comput.* **2017**, *13*, 2789–2803.

[412] Stöhr, J. *NEXAFS spectroscopy*; Springer-Verlag Berlin Heidelberg, 1992.

[413] Kolczewski, C.; Pättner, R.; Plashkevych, O.; Ägren, H.; Staemmler, V.; Martins, M.; Snell, G.; Schlachter, A. S.; Sant'Anna, M.; Kaindl, G.; Pettersson, L. G. M. *J. Chem. Phys.* **2001**, *115*, 6426–6437.

[414] Fronzoni, G.; Baseggio, O.; Stener, M.; Hua, W.; Tian, G.; Luo, Y.; Apicella, B.; Alfé, M.; de Simone, M.; Kivimäi, A.; Coreno, M. *J. Chem. Phys.* **2014**, *141*, 044313.

[415] Linderberg, J.; Öhrn, Y. *Propagators in quantum chemistry*; Wiley, 2004.

[416] von Niessen, W.; Schirmer, J.; Cederbaum, L. *Computer Physics Reports* **1984**, *1*, 57 – 125.

[417] Ortiz, J. V.; Zakrzewski, V. G. *J. Chem. Phys.* **1996**, *105*, 2762–2769.

[418] Ortiz, J. V. *Int. J. Quantum Chem.* **2005**, *105*, 803–808.

[419] Ortiz, J. V. *J. Chem. Phys.* **1998**, *108*, 1008–1014.

[420] Purvis, G. D.; Öhrn, Y. *J. Chem. Phys.* **1976**, *65*, 917–922.

[421] Ortiz, J.; Basu, R.; Öhrn, Y. *Chem. Phys. Lett.* **1983**, *103*, 29–34.

[422] Besley, N. A.; Gilbert, A. T. B.; Gill, P. M. W. *J. Chem. Phys.* **2009**, *130*, 124308.

[423] Triguero, L.; Pettersson, L. G. M.; Agren, H. *Phys. Rev. B* **1998**, *58*, 8097–8110.

[424] De Francesco, R.; Stener, M.; Fronzoni, G. *J. Phys. Chem. A* **2012**, *116*, 2885–2894.

[425] Stener, M.; Fronzoni, G.; de Simone, M. *Chem. Phys. Lett.* **2003**, *373*, 115–123.

[426] Barone, V. *Structure, magnetic properties and reactivity of open-shell species from Density Functional and Self-Consistent hybrid methods*; World Scientific Publishing, 1995; Chapter 8, p 287.

[427] Baiardi, A.; Mendolicchio, M.; Barone, V.; Fronzoni, G.; Cardenas Jimenez, G. A.; Stener, M.; Grazioli, C.; de Simone, M.; Coreno, M. *J. Chem. Phys.* **2015**, *143*, 204102.

[428] Ortiz, J. V. *Int. J. Quantum Chem.* **2003**, *95*, 593–599.

[429] Goscinski, O.; Lukman, B. *Chem. Phys. Lett.* **1970**, *7*, 573 – 576.

[430] Corzo, H. H.; Galano, A.; Dolgounitcheva, O.; Zakrzewski, V. G.; Ortiz, J. V. *J. Phys. Chem. A* **2015**, *119*, 8813–8821.

[431] Thiel, A.; Schirmer, J.; Köppel, H. *J. Chem. Phys.* **2003**, *119*, 2088–2101.

[432] Slater, J. C.; Mann, J. B.; Wilson, T. M.; Wood, J. H. *Phys. Rev.* **1969**, *184*, 672–694.

[433] Warren, R.; Dunlap, B. *Chem. Phys. Lett.* **1996**, *262*, 384–392.

[434] Abdulnur, S. F.; Linderberg, J.; Öhrn, U.; Thulstrup, P. W. *Phys. Rev. A* **1972**, *6*, 889–898.

[435] Slater, J. C. In *Adv. Quantum Chem.*; Löwdin, P.-O., Ed.; Advances in Quantum Chemistry; Academic Press, 1972; Vol. 6; pp 1–92.

[436] Goscinski, O.; Pickup, B.; Purvis, G. *Chem. Phys. Lett.* **1973**, *22*, 167–171.

[437] Redmon, L. T.; Purvis, G.; Öhrn, Y. *J. Chem. Phys.* **1975**, *63*, 5011–5017.

[438] Corzo, H. H.; Ortiz, J. V. *Mol. Phys.* **2017**, *115*, 545–551.

[439] Ghanty, T. K.; Davidson, E. R. *J. Phys. Chem. A* **1999**, *103*, 8985–8993.

[440] Abu-Samha, M.; Børve, K. J.; Sæthre, L. J.; Thomas, T. D. *Phys. Rev. Lett.* **2005**, *95*, 103002.

[441] Abu-Samha, M.; Børve, K. J. *Phys. Rev. A* **2006**, *74*, 042508.

[442] Ortiz, J. V. *J. Chem. Phys.* **2000**, *112*, 56–68.

[443] Silverstein, D. W.; Jensen, L. *J. Chem. Phys.* **2012**, *136*, 64110.

[444] Keller, S. F.; Reiher, M. *CHIMIA International Journal for Chemistry* **2014**, *68*, 200–203.

[445] Olivares-Amaya, R.; Hu, W.; Nakatani, N.; Sharma, S.; Yang, J.; Chan, G. K.-L. *J. Chem. Phys.* **2015**, *142*, 034102.

[446] Petrenko, T.; Rauhut, G. *J. Chem. Phys.* **2015**, *143*, 234106.

[447] Koch, A.; Billing, G. D. *J. Chem. Phys.* **1997**, *107*, 7242–7251.

[448] Roemelt, M.; Guo, S.; Chan, G. K.-L. *J. Chem. Phys.* **2016**, *144*, 204113.

[449] Freitag, L.; Knecht, S.; Angeli, C.; Reiher, M. *J. Chem. Theory Comput.* **2017**, *13*, 451–459.

[450] Macak, P.; Luo, Y.; ågren, H. *Chem. Phys. Lett.* **2000**, *330*, 447 – 456.

[451] Ringholm, M.; Bast, R.; Oggioni, L.; Ekström, U.; Ruud, K. *J. Chem. Phys.* **2014**, *141*, 134107.

[452] Lin, N.; Solheim, H.; Zhao, X.; Santoro, F.; Ruud, K. *J. Chem. Theory Comput.* **2013**, *9*, 1557–1567.

[453] Oliver, T. A. A.; Lewis, N. H. C.; Fleming, G. R. *Proceedings of the National Academy of Sciences* **2014**, *111*, 10061–10066.

[454] De Sio, A.; Troiani, F.; Maiuri, M.; Réhault, J.; Sommer, E.; Lim, J.; Huelga, S. F.; Plenio, M. B.; Rozzi, C. A.; Cerullo, G.; Molinari, E.; Lienau, C. *Nat. Comm.* **2017**, *7*, 13742.

[455] Rivalta, I.; Nenov, A.; Cerullo, G.; Mukamel, S.; Garavelli, M. *Int. J. Quantum Chem.* **2014**, *114*, 85–93.

[456] Nenov, A.; Rivalta, I.; Cerullo, G.; Mukamel, S.; Garavelli, M. *J. Phys. Chem. Lett.* **2014**, *5*, 767–771.

[457] Nenov, A.; Giussani, A.; Fingerhut, B. P.; Rivalta, I.; Dumont, E.; Mukamel, S.; Garavelli, M. *Phys. Chem. Chem. Phys.* **2015**, *17*, 30925–30936.